THE DOSIMETRY OF A HIGHLY-COLLIMATED BREMSSTRAHLUNG SOURCE IN AIR

A Dissertation
Presented to
The Academic Faculty

by

Michael Paul Shannon

In Partial Fulfillment
of the Requirements for the Degree
Doctor of Philosophy in the
School of George Woodruff School of Mechanical Engineering

Georgia Institute of Technology
August 2009

THE DOSIMETRY OF A HIGHLY-COLLIMATED BREMSSTRAHLUNG SOURCE IN AIR

Approved by:

Dr. Nolan E. Hertel, Advisor
School of Mechanical Engineering
Georgia Institute of Technology

Dr. Wm. David Kulp III
School of Physics
Georgia Institute of Technology

Dr. C.K. Wang
School of Mechanical Engineering
Georgia Institute of Technology

Dr. Adam Stulberg
School of International Affairs
Georgia Institute of Technology

Dr. Chaitanya Deo
School of Mechanical Engineering
Georgia Institute of Technology

Dr. Tanya Palmateer Oxenberg
Uranium Recovery Licensing Branch
U.S. Nuclear Regulatory Commission

Dr. James L. Jones
Nuclear Nonproliferation & Homeland Security Division
Idaho National Laboratory

Date Approved: June 30, 2009

[To Jessica, the love of my life]

ACKNOWLEDGEMENTS

First I wish to acknowledge My Creator who is the reason that this work was conceived, executed and completed. I hope I have honored Him through the work of my hands. To Him be the Glory!

I am deeply beholden to my advisor, Dr. Nolan Hertel for his support and mentorship over the 8 years I have known him. I have served with and for many great leaders and mentors over the course of my adult life. Dr. Hertel is definitely one of the finest, most intellectual, most principled leaders I have ever had the pleasure of serving under. There is absolutely no way I could have done this without him. He has become a true friend and I cherish his support, guidance, patience, and help. Dr. Hertel, thank you!

To Mr. Rob Beimler who believed in me and made this dream of mine a reality!

To the folks of the US Army Dosimetry Center at Redstone Arsenal (Bill Harris, Gail Smith and Debbie Butler) who assisted me in providing dosimetry as well as the use of their sources. You unquestionable dedication to duty and support was a critical component to this effort. Thank you!

There are several within the Georgia Tech community I wish to thank for their help and support to make this research possible. First, a special thanks to Dr. Wayne Whiteman, Valarie Spradling, Christina Tabor, Arlene Smith, Nazia Zakir and Dwayne Blaylock for their fine support. Additionally, thank you to John Graham in the Georgia Tech

Mechanical Engineering Machine Shop, who was instrumental in creating set-ups and widgets for several of my measurements. His hard work and unending dedication was awesome! Thank you John!

To the crew at Georgia Tech Research Institute ITTL both in Quantico (Ron Smith, Kris Young and Vikki Sutton) and here in Atlanta (Miriam Pierce). Your hard work and professionalism ensured that I consistently had the resources I needed to conduct my research. From equipment acquisition to travel to Miriam's pep talks, you folks made it happen. I sincerely appreciate all the help and support!

To Brian Hales who spent a semester assisting me in calibrating, batching and reading the TLDs. Brian spent many hours in the lab working on data and finished his duties by writing a superb report which was above and beyond what was expected. Excellent work Brian. You have a bright future!

To two of my Team Hertel colleagues, Ryan Manger and Eric Burgett. Ryan assisted me in the later stages of my measurement work by enduring a very long and harsh week in the Idaho winter to help finish several measurements. He was instrumental in the acquisition of TLD exposure data. Ryan's help was huge! A very special thanks to Eric Burgett who is an icon in the group. Eric helped me countless times over the past 3 years preparing for measurement trips, setting up equipment, debugging MCNP and just providing an overall helping hand. I appreciate your help Eric!

To the folks at the Defense Threat Reduction Agency over the past three years who made this research possible (Dr. Mark Byers, LTC(R) Mike Johns, James Howell, David Squires, Dr. Jim Lemley, Major Brad Beatty, Peter Zielinski, LTC James Riddick and MAJ Greg Schwarz). I appreciate your help, support and confidence. I could NOT have done this work without you! Also, a special thank you to the test support folks at DTRA (LTC Dan Hauck, Don Gross, Roger Bevins, Derick Duke, and Lucy Combs-Walker). Your assistance in the acquisition of data was fundamental to my success. Thank you for your patience, your understanding and your make it happen attitudes.

To the world-class folks at the Idaho Accelerator Center (Kevin Folkman, Chad O'Neill, Mike Smith and Alan Hunt). You guys were critical to my success. Thanks for all you taught me about accelerators and their related systems. Your help, guidance and tutelage was an invaluable asset to my research. Thanks so much!

A very special thank you to Dr. James Jones and his team at the Idaho National Laboratory. Dr. Jones took a chance on an unknown and hopefully is pleased with the result. James it was a pure pleasure to have worked with you. I admire your vision and the impact of your work on our great nation. You are a shining visionary that I hope to have many more collaborations with throughout my career. James, I couldn't have done it without you, thank you! To John Dwight for your support in providing your fine team to support my research. There are so many folks who assisted me during my time collaborating at the INL, too many to mention here. However, I would like to especially recognize, Lyle Roybal, James Johnson, Dr. Woo Yoon, Dr. Matt Kinlaw, Linda Mayeda,

Kelly Cook, Mike Evans, and Jill Hawkes. Without the support of these fine people, there is no way I could have completed this work. Additionally I would like to thank the INL High Performance Computing Group, including my close friends ICESTORM and HELIOS, who provided support and assistance in my simulation work. There is no way I could have run as many models and as many particles that I did, without this resource. Thanks so much! Finally, a very special thank you to 3 members of the INL team who had the biggest impact on my research, and with whom I spent many countless hours doing experiments; Daren Norman, Kevin Haskell and Rich Watson. You 3 gentlemen were the lynchpin of my entire measurement program. Without each one of you and your support and the resources you brought to bear, there is without question, NO WAY I could have done what I did. Gentlemen, I am forever thankful to each one of you!

To my parents, Bert and Winnie Waller, for your encouragement and belief in me. You have always supported my ambitions and continue to do so through my adult life. I thank you for your support and love!

Last and surely not least, I would like to thank my dear family (Jessica, Rachel, Danica and Hunter) for their love, support and most importantly, their sacrifice over the past 3 years and especially the past year. From being away on measurement trips, to countless hours in my home or work offices, my family gave up so much for me I cannot begin to express my gratitude. I hope that the results of my work have an impact that was worth all of the hours I missed being with these dear and most cherished people. To each of you, I thank you and I love you! Daddy is finally done!

TABLE OF CONTENTS

LIST OF TABLES

LIST OF FIGURES

SUMMARY

The characterization and measurement of the spatial, temporal and energy emission of air-scattered photons, electrons and neutrons generated near 10 MV or greater accelerator-based bremsstrahlung photon sources is becoming important in many applications. The national and homeland security research community is interested in developing technologies which can detect illicit materials at substantial standoff distances in outdoor environments. These systems are referred to as "active" interrogation systems and are defined as inspection systems that take advantage of an externally applied "source" to perform traditional imaging of, or to stimulate characteristic emissions from, an inspected object.

A key concern in the development of these systems is the ability to effectively predict the dose equivalents at long standoff distances from these sources in order to ascertain the operational radiation safety of said systems. Current computational radiation transport simulation tools have the ability to effectively model these systems; however, a paucity of experimental data exists in comparing the results of these simulations.

A methodology to assess the radiation dose surrounding a high-energy bremsstrahlung-based accelerator system for national defense applications was developed. Fluence-to-dose conversion coefficients for the International Commission on Radiation Units and Measurements operational quantity ambient dose equivalent were calculated for photons and electrons up to 25 MeV utilizing the Los Alamos National Laboratory Monte Carlo

N-Particle code, MCNP5 Version 1.51 [1]. Special consideration was given to the treatment of secondary charged particle equilibrium in all simulations. The latest photon and electron cross section data from ENDF/B-VI.8 [2] and the e103 [3] libraries, respectively, were used to perform all calculations.

An extensive set of system simulations was performed to model a prototype high-energy bremsstrahlung-based accelerator system to obtain photon, electron and neutron fluence spectra. These fluence data were folded with the calculated ambient dose equivalent conversion coefficients as well as previously published effective dose conversion coefficients. A set of integral air-scatter measurements for accelerator-generated primary and secondary radiations (photon and neutron) were performed around the prototype system in order to provide a comparative data set from which to determine the total dose equivalent both in the beam (on-axis) and outside of the beam (off-axis). Comparison with system simulation calculations indicate agreement to within 20-30% for the total dose equivalent.

CHAPTER 1

INTRODUCTION

The increased use of the atom in society continues to dictate the need for rigorous study of the effects of radiation interactions with matter. The concepts and quantities used to describe radiation dose are continuously updated to provide the best recommendations to protect both humans and the environment. This need is evident in the development of particle accelerators for use in a wide array of applications including medical diagnostic and treatment applications, basic science research, industrial applications, and national defense applications. Each of these very important applications requires specific study and understanding of not only the development of the systems but more importantly the safe implementation of the systems.

With the growth of the use and development of particle accelerators came the increase in capability, especially particle energies. The ability to predict the effects of these energetic particles as they interact with matter has become a field of great importance. In addition to increasing energies, accelerator systems have been adapted to answer the needs of society. Fresh ideas and concepts are propelling accelerators into a whole new realm of importance. No example is more apparent than in the medical accelerator field. Portable accelerator systems are changing the way in which medical care is provided to populations throughout the globe. Thus the closed facilities used for so many years to house accelerators are making way for more flexible, transportable systems. This has facilitated a movement from massive concrete facilities with unbounded physical barriers to protect people and the environment from the high-energy particles to the need for innovative solutions which rely on novel control methods and highly predictive

capabilities. Beyond the medical world, one such area of current growth is seen in the use of accelerators in national defense and military applications.

Using accelerator systems to protect national sovereignty and interests provides a unique set of challenges as a tradeoff exists between the necessity to deploy systems to protect the greater good while ensuring the safety of the general public. The current world situation has changed the dynamic of employing military machinery. In the past, battlefields and battlelines were drawn on maps which created symmetric areas of operations. Today, the scenario has changed such that an asymmetric battlefield exists. Therefore, the potential of deploying high-energy accelerator-based systems in populated areas has become a reasonable possibility. This paradigm shift leads to the requirement for rigorous study of associated radiation doses from these systems and the development of analytical tools which provide increased prognostic insight and capabilities.

Military planners and advisers require a set of facts during the planning of a military contingency. These facts range from sheer metrics of personnel, terrain, and weather to equipment capabilities and hazards. The motivation for this work is to provide a set of analytical tools which can be applied to the prediction of radiation doses around portable accelerator-based systems being considered for national defense applications. Although a great deal of research and study in accelerator dosimetry has already been performed, the current work was undertaken to provide a greater understanding of the specific phenomenon observed in bremsstrahlung-based systems. This research starts with the calculation of fluence-to-dose conversion coefficients which are energy-dependent conversion coefficients that allow for the direct calculation of dose equivalents if the group fluence of the incident particle is known. Conventionally, conversion coefficients are folded with group particle fluence data and subsequently integrated over the energy regime of interest to obtain a total dose equivalent. After conversion coefficients are

calculated, the research moves to an extensive set of experimental measurements where an actual prototype system is used to compare the analytic predictions. Next, a series of system simulations is performed to apply the fluence-to-dose conversion coefficients to the system from which measurements were performed. Finally, a series of comparisons is performed which provides validation of the predictive methodology. It is the intent of this research to provide a framework from which to develop predictive tools and capabilities. The objectives and organization of the thesis are described in the following sections.

1.1 Objectives

This thesis has two primary objectives. The first objective is to develop a sound analytical prediction methodology to calculate the radiation dose surrounding a high-energy bremsstrahlung-based accelerator system used for national defense applications. This methodology should instill confidence that data obtained via Monte Carlo radiation transport calculations are trustworthy. The second objective is to perform photon and neutron dose measurements within a collimated beam and outside the beam of a high-energy bremsstrahlung-based accelerator system. These measurements provide a validation of the predictions. An ancillary objective is to calculate ambient dose equivalent fluence-to-dose conversion factors in various depths of the ICRU sphere.

1.2 Organization

A discussion of the active interrogation, a review of radiation dosimetry and an overview of MCNP5 are presented in Chapter 2. This includes a review of the fundamental quantities, radiation protection quantities and operational quantities. The ambient dose equivalent calculations are presented in Chapter 3. This includes an explanation of the methodology used to calculate the fluence-to-dose conversion coefficients for photons

and electrons. A brief review of published data is presented with a comparison of the data calculated in the present work. Chapter 4 contains a detailed description of the measurements performed including a discussion of the bremsstrahlung source, the test environment, associated instrumentation, and a description of all measurements and parameters utilized. The analysis and results of all measurements are presented in Section 4.8. Chapter 5 includes an overview of system simulations including results and analysis. In Chapter 6, the measurements are compared to system simulations with analysis concerning trends and points of interest. Chapter 7 includes conclusions and recommendations which lead to Chapter 8 which summarizes future work.

CHAPTER 2

BACKGROUND

For the past century, the importance of ionizing radiation in various applications has increased. From energy applications to industrial processes to defense applications, the atom is used in our society. The current geopolitical world situation has created a necessity to develop novel means by which to keep nations safe from the threat of the illicit use of weapons of mass destruction. One such means utilizes radiation beams to detect illicit materials. Active "interrogation" nuclear material detection systems operate on the premise of using either electromagnetic or particulate radiation generated by a radiation source to stimulate the emission of characteristic (unique) signatures within a suspect target. In general, the radiation source is a radiation generating device (RGD) such as an accelerator or a neutron generator [4]. For the present work, the RGD is a high-energy bremsstrahlung-based accelerator system. It can be argued that the benefits of such systems are large as potentially scores of lives can be saved by their use. However, the radiation protection risks posed by the deployment of such technologies are notable and therefore require study.

The premise for the concept of active interrogation is not new. Wilhelm Röntgen, the pioneer of diagnostic radiology, used penetrating radiation for inspection purposes when he used x-rays to create an image of his wife's hand in 1895 [5]. This discovery arguably led to the most significant advancement in the diagnosis of disease in human history. As the utility of x-rays became more apparent, so did the consequences. The physical consequences birthed the concept of radiation dose which, simply stated, is the amount of

energy imparted per unit mass. This concept necessitated the forging of a new area of study known today as radiological physics. Radiological physics is the science of ionizing radiation and its interaction with matter, with special interest in the energy absorbed. Radiation dosimetry is the quantitative determination of that energy [6].

The growth of the use of ionizing radiation over the past century has necessitated the creation of organizations charged with developing the scientific and technical basis for the definition and application of said radiations. The International Commission on Radiation Units and Measurements (ICRU) was established in 1925 to develop and promulgate internationally accepted recommendations on radiation related quantities and units, terminology, measurement procedures, and reference data for the safe and efficient application of ionizing radiation to medical diagnosis and therapy, radiation science and technology, and radiation protection of individuals and populations [7]. The International Commission on Radiological Protection (ICRP) was established in 1928 to advance for the public benefit the science of radiological protection, in particular by providing recommendations and guidance on all aspects of protection against ionizing radiation [8]. The National Council on Radiation Protection and Measurements (NCRP) was chartered by the U.S. Congress in 1964 to formulate and widely disseminate information, guidance and recommendations on radiation protection and measurements which represent the consensus of leading scientific thinking [9]. From these three organizations, come the philosophy, scientific peer review and promulgation of guidance for radiation protection within the United States and beyond.

The Department of Defense (DOD) is pursuing several active interrogation technologies including electron accelerator-based systems which utilize bremsstrahlung-induced photonuclear detection [10]. One prototype technology, known as the Photonuclear Inspection and Threat Assessment System (PITAS), is being developed by a team of

researchers at the Idaho National Laboratory (INL) [11, 12]. The PITAS technology draws on over two decades of photonuclear inspection research performed at the INL and its' predecessor, the Idaho National Engineering and Environmental Laboratory (INEEL) by Dr. James L. Jones and his team [13-18]. Since the PITAS is being developed for use by the DOD, it is being designed to operate in outdoor environments, under all weather conditions, outside of the traditional facilities/laboratories where most accelerators have operated over the past century. The PITAS prototype will serve as the base case for the present work.

A key concern of employing active interrogation is properly accounting for the radiation dose received by the interrogated object (e.g. a vehicle, container, etc.) as well as both service members and civilians who may be within the immediate vicinity of such a device. Accelerator-based systems operate in a pulsed mode in which the charged particles are delivered in pulses within 1 ns to 1 μs spaced a few milliseconds apart. When used in a standoff mode-of-operation in an outdoor environment, such systems can be deployed with both collimated and uncollimated beams to control the spatial behavior of the radiation emissions. The accelerator nominal operating parameters (e.g. beam current, repetition rate, beam energy, etc.) used in interrogating a suspect object can be selectively varied. Each of these parameters further complicates photon and neutron dose measurements. Furthermore, the pulsed nature of an accelerator radiation field presents a litany of challenges for accurately determining the dose.

From a systems standpoint, the PITAS consists of several sub-systems. For the purposes of this work, the main component of interest is the accelerator-based photon source. The PITAS uses a commercial-off-the-shelf 25 MV electron linear accelerator (LINAC) to produce a beam containing high-energy photons. The generation of bremsstrahlung is accomplished via the interaction of the electrons with a converter. The resulting field is

dominated by high-energy bremsstrahlung photons which are then collimated by a specially-designed collimator. The collimator was designed to maximize photon output while decreasing the radiation dose surrounding the system. The resulting collimated beam serves as the inspection source and is operated in conjunction with a combination of neutron and photon detectors. These detectors are designed to detect both shielded and unshielded special nuclear material (SNM) at much greater standoff distances than is currently possible with alternative technologies.

2.1 Fundamental Quantities

The interaction of radiation with matter results in several phenomenon which have been studied quite extensively over the past century. The ICRU defines physical quantities such as fluence, kerma and absorbed dose which are used in radiation dosimetry [19]. One must first define a metric to characterize the radiation field. The fluence, Φ, is the quotient of dN by da where dN is the number of particles incident on a sphere of cross sectional area da [19]. Since fluence is a radiometric quantity, it does not describe the interaction of radiation with matter.

Radiation interacts with matter in a series of processes whereby the incident particle energy is converted and transferred to the medium. It is the conversion of the incident particle energy from ionizing particles to secondary ionizing particles and subsequent energy deposition that is of interest in radiation dosimetry. The kerma, K, relates the kinetic energy of the charged particles liberated by uncharged particles. In more rigorous terms, it is the quotient dE_{tr} by dm where dE_{tr} is the sum of the initial kinetic energies of all charged particles liberated by uncharged particles in a mass dm of material [19].

The absorbed dose, D, is defined in order to provide a physical measure which can be correlated to the effects of ionizing radiation. It is the quotient of the mean energy imparted by ionizing radiation to matter in a specified volume element divided by the mass of matter in the volume. The unit of absorbed dose is joule per kilogram (J/kg) and its special name is Gray (Gy) [20].

2.2 Protection and Operational Quantities

It is standard convention in radiation protection to utilize conversion coefficients to directly relate the protection quantities to physical quantities. The ICRP defines protection (limiting) quantities as dosimetric quantities specified in the human body. These quantities are not measurable but can be determined by calculation or a combination of calculations and measurements [20]. Operational quantities were developed by the ICRU and are meant to demonstrate compliance with dose limits. These quantities serve as calibration quantities for dose measuring devices used in monitoring and provide a reasonable estimate of the protection quantities [21]. For external irradiation of the body, this is expressed in practical terms, by the goal that the ratio of the value of the appropriate protection quantity, H_{prot} to the measurement of the operational quantity H_{op} is usually less than unity.

$$\frac{H_{prot}}{H_{op}} \leq 1 \tag{2.1}$$

Under this condition, the operational quantity provides an overestimate of the protection quantity. Thus a comparison of these quantities must be conducted in order to ensure that proper operational quantity is used [20].

The ICRP recommended the protection quantities, which included organ absorbed dose, the equivalent dose in an organ or tissue and the effective dose, in *Publication 103* [22]. The effective dose, E, is the sum of the weighted equivalent doses in all the tissues and organs of the body. ICRP *Publication 60* defines 12 designated tissues and organs and a remainder consisting of 10 additional tissues or organs [20]. A great disparity exists in the manner in which the effective dose is calculated. This stems from confusion in mass weighting of certain organs as well as the analytical treatment of the remainder. A thorough review of the calculation of effective dose is presented by Sutton [23].

The operational quantities were defined by the ICRU in Reports 39, 43, 47, and 51 [24-27] and are related to the ICRP protection quantities. The operational quantities are applied to area monitoring in the form of the ambient dose equivalent and directional dose equivalent, and individual monitoring, in the form of the personal dose equivalent. The ambient dose equivalent, $H^*(d)$, at a point in a radiation field is the dose equivalent that would be produced by the corresponding expanded and aligned field in the ICRU sphere at a depth, d, on the radius opposing the direction of the aligned field. The recommended value of d is 10 mm for penetrating radiation and 0.07 mm for low-penetrating radiation [20]. An expanded and aligned radiation field is a hypothetical field where the fluence and its energy distribution are the same as an expanded field, but the fluence is unidirectional [20].

Fundamental quantities such as fluence can be related to the operational quantities, i.e. ambient dose equivalent $H^*(d)$, through measurements and conversion coefficients. Furthermore, the physical quantities can also be related to the protection quantities, i.e. effective dose E, through calculations (simulations) and conversion coefficients. The operational quantities can be related to the protection quantities if one knows the response of the instrument used to make the measurement. To ensure the fidelity of the answer, the instrument must be properly calibrated. The relationship among these concepts, which were originally presented in ICRP Publication 74 and later modified by McDonald, is shown in Figure 1 [20, 28].

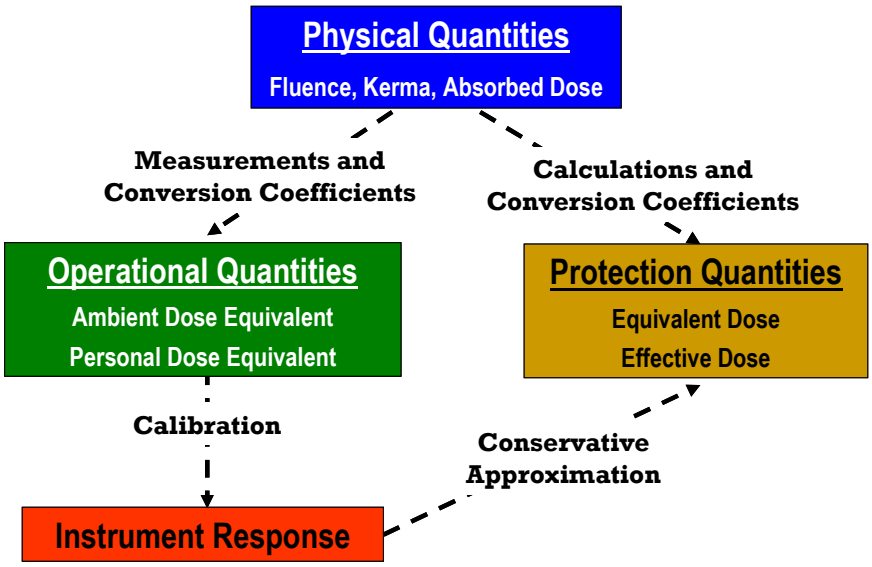

Figure 1. Relationship Between Operational and Protection Quantities. Reprinted from [20, 28].

A key concept in radiation dosimetry is that of charged particle equilibrium (CPE). CPE provides the condition such that if CPE exists at a point in the medium, the kerma is proportional to the absorbed dose. CPE exists for a volume if each charged particle of a

given type and energy leaving the volume is replaced by an identical particle of the same energy entering the volume [6]. The concept of CPE is fundamental to the present work.

2.3 MCNP5

MCNP5 (Monte Carlo N-Particle code) is a Monte-Carlo radiation transport code developed by Los Alamos National Laboratory. MCNP is a general-purpose, continuous-energy, generalized-geometry, time-dependent, coupled neutron/photon/electron Monte Carlo transport code. It can be used in several transport modes: neutron only, photon only, electron only, combined neutron/photon transport where the photons are produced by neutron interactions, neutron/photon/electron, photon/electron, or electron/photon. The neutron energy regime is from 10^{-11} to 20 MeV for all isotopes and up to 150 MeV for some isotopes, the photon energy regime is from 1 keV to 100 GeV, and the electron energy regime is from 1 keV to 1 GeV [1].

The MCNP5 code treats an arbitrary three-dimensional configuration of materials in geometric cells bounded by first- and second-degree surfaces and fourth-degree elliptical tori. Pointwise cross-section data are used. For neutrons, all reactions given in a particular cross-section evaluation (such as ENDF/B-VI) are accounted for. Thermal neutrons are described by both the free gas and thermal particle scattering ($S(\alpha,\beta)$) models. For photons, the code accounts for incoherent and coherent scattering, the possibility of fluorescent emission after photoelectric absorption, and absorption in electron-positron pair production. Electron/positron transport processes account for angular deflection through multiple Coulomb scattering, collisional energy loss with optional straggling, and the production of secondary particles including K x-rays, knock-

on and Auger electrons, bremsstrahlung, and annihilation gamma rays from positron annihilation at rest. Electron transport does not include the effects of external or self-induced electromagnetic fields. Photonuclear physics is available for a limited number of isotopes [29].

The code has its' roots in the earliest days of Los Alamos during the Manhattan Project. Through the years, the capability of the code has grown along with the capabilities of the computer. Today, the code provides a litany of user options for performing calculations and simulations ranging from reactor physics to radiation dosimetry. The code is export controlled and is distributed by the Radiation Safety Information Computational Center (RSICC) at Oak Ridge National Laboratory. The current version and that used in this work is MCNP5 Version 1.51, which was released in February 2009 [29].

Photon cross section data are derived from the "04p" ACE tables and were processed from the ENDF/B-VI.8 library [2]. The ENDF/B-VI.8 photoatomic and atomic relaxation data are based upon the EPDL97 library [2]. This library includes incoherent, coherent, photoelectric and pair production cross sections for incident energies from 1 keV to 100 GeV. The determination of directions and energies of atomically scattered photons requires information different from the sets of angular and energy distributions found on neutron interaction tables. The angular distribution for fluorescence x-rays from the relaxation cascade after a photoelectric event is isotropic. The angular distributions for coherent and incoherent scattering come from sampling the well-known

Thomson and Klein-Nishina formulas, respectively. The energy of an incoherently scattered photon is calculated from the sampled scattering angle [1].

Electron cross section data utilize the e103 library which is derived from the Integrated Tiger Series (ITS) 3.0 codes [3]. The library data contain energies for tabulation, radiative stopping power parameters, bremsstrahlung production cross sections, bremsstrahlung energy distributions, K-edge energies, Auger electron production energies, parameters for the evaluation of the Goudsmit-Saunderson theory for angular deflections based on the Riley cross-section calculation, and Mott correction factors to the Rutherford cross sections also used in the Goudsmit-Saunderson theory. The el03 library also includes the atomic data of Carlson used in the density effect calculation. During the run-time sequence of MCNP5, data are calculated for electron stopping powers and ranges, K x-ray production probabilities, knock-on probabilities, bremsstrahlung angular distributions, and the Landau-Blunck-Leisegang theory of energy-loss fluctuations [1].

CHAPTER 3

AMBIENT DOSE EQUIVALENT CONVERSION COEFFICIENTS

Ambient dose equivalent, by definition, describes the dose equivalent at a point in a radiation field. If energy-dependent particle fluences are known, a set of ambient dose equivalent conversion coefficients can be applied to estimate the total H^*(d) which is defined as

$$H^*(d) = \int \left[\frac{H^*(d)}{\Phi} \right] \Phi(E) dE \qquad (3.1)$$

ICRP Publication 74 provides a set of photon fluence-to-ambient dose equivalent conversion coefficients, however, these coefficients only extend to photon energies of 10 MeV [20]. A few sets of photon H*(10) coefficients for photon energies in excess of 10 MeV are published [30-33]. In addition, the ICRP does not report fluence-to-ambient dose equivalent conversion coefficients for electrons. Pelliccioni published a set of electron conversion coefficients in 1994 [34].

In lieu of this paucity in published and/or recommended data, a set of ambient dose equivalent conversion coefficients for photons and electrons at various depths in the ICRU sphere were calculated. Data are presented for ambient dose equivalent per unit

fluence for photons from 0.01 to 25 MeV and electrons from 1.5 to 25 MeV along with a comparison to published data.

3.1 Methodology

The methodology used to calculate the ambient dose equivalent conversion coefficients has been studied quite extensively over the past 25 years [33]. Special consideration must be given to certain physical processes in order to conduct a valid calculation. This section details some of these considerations as well as describes the method used in the present work.

3.1.1 Overall Special Considerations

The critical component in the calculation of ambient dose equivalent conversion coefficients is the manner in which charged particle buildup is handled within the phantom, in this case, the ICRU sphere. The depth at which charged particle equilibrium is achieved depends upon the energy and type of incident radiation. In order to simplify calculations, many researchers have assumed charged particle equilibrium exists thus applying the kerma approximation [20]. This greatly simplifies the computational model and also is much less computationally expensive. For the photon case, the kerma approximation assumes that, at the point of interest in the phantom (ICRU sphere), all secondary radiations and charged particles are in equilibrium with the primary radiation, therefore, the absorbed dose is equal to the kerma less any energy removed by uncharged radiation (bremsstrahlung and neutrons) [20]. In subsequent sections, the manner in

which charged particle equilibrium is handled will be discussed for the respective incident radiation.

3.1.2 Overall Modeling Approach

Ambient dose equivalent conversion coefficients are calculated by modeling the energy deposition in a specified volume at varying depths in the ICRU sphere. The ICRU sphere is a 30 cm diameter sphere of tissue-equivalent material used in the description of dose equivalent quantities by the ICRU [35]. The material composition and density of the ICRU sphere are shown in Table 1.

Table 1. Material Composition for ICRU Tissue.

Material Constituent	wt %
Hydrogen	10.1
Carbon	11.1
Nitrogen	2.6
Oxygen	76.2
Density = 1.00 g/cm^3	

For each incident particle type, a 15 cm-radius disk source, uniformly emitting parallel monoenergetic particles (monodirectionally) was placed 0.001 cm from the ICRU sphere at the central axis. The volume, used to determine H^*(d), was a compromise between its volume and statistical uncertainty in the computed dose. A trade-off in utilizing Monte Carlo codes is the large number of particle histories required to converge on a statistically accurate answer which must be weighed against the required computational time. Modern multi-processor computer systems have greatly lowered this tradeoff. However

electron transport is computationally expensive, some decisions were made in order to increase simulation run times. The volume selected for these calculations consisted of 0.065 cm^3 (radius of 0.25 cm) spheres of ICRU tissue arrayed along the central axis of the ICRU sphere at depths of 10 mm, 15 mm, 20 mm, 30 mm and 40 mm. A schematic of the model geometry is shown in Figure 2.

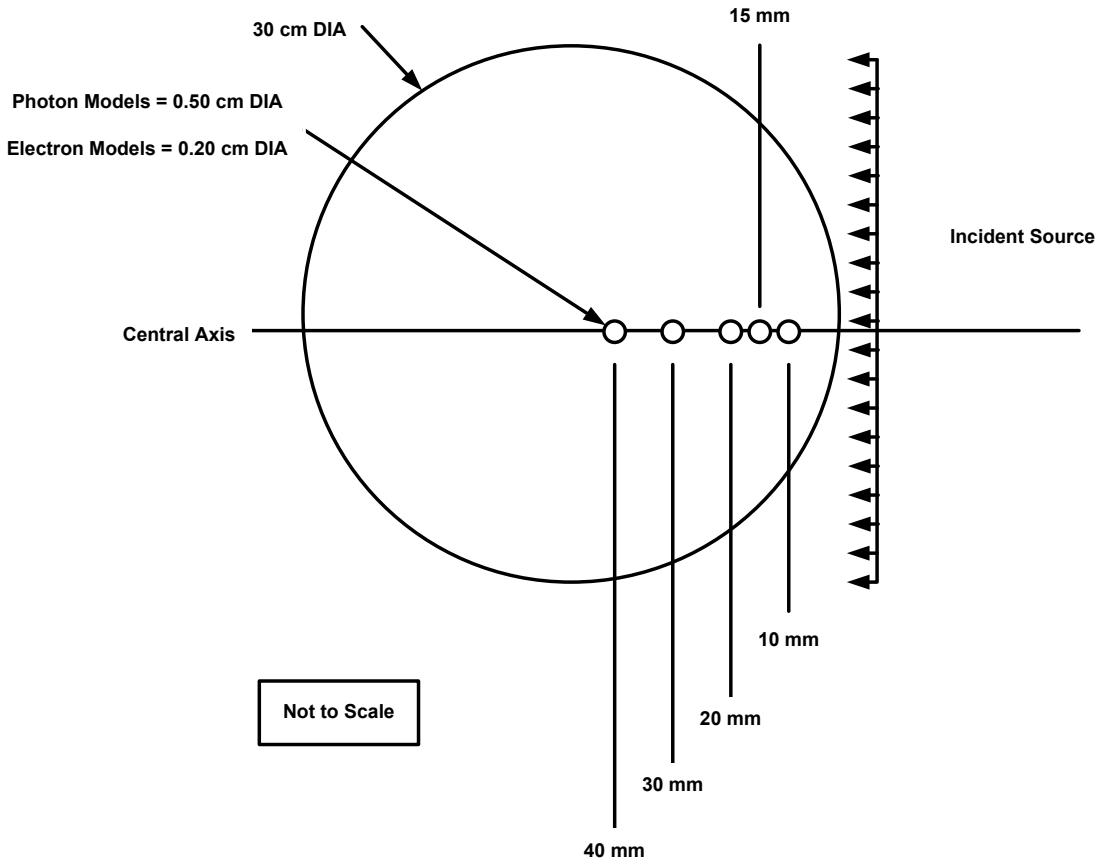

Figure 2. Schematic of Ambient Dose Equivalent Conversion Coefficient Model.

3.2 Photon Conversion Coefficients

3.2.1 Special Considerations

The ICRP adopted the photon fluence-to-ambient dose equivalent conversion coefficients by employing the kerma approximation which assumes that all secondary electrons generated by photons are in equilibrium [20]. The kerma approximation implies that the kinetic energy of the secondary electron is transferred to the medium and deposited locally. The implementation of the kerma approximation for the calculation of photon ambient dose conversion coefficients was evaluated for these computations. There are depths and energies where secondary charged particle equilibrium is not present and dose equivalent data may be skewed by the kerma approximation. The kerma approximation is satisfactory for photons up to 3 MeV. At higher photon energies, the equilibrium becomes increasingly incomplete and although secondary electrons do originate in air and accompany the incident photon beam, there may not be enough intervening air to assume charged particle equilibrium [20].

Historically, the ambient dose equivalent conversion factors have been calculated in vacuo which ignores the effect of air scatter [20, 30]. In 1983, Dimbylow and Francis published a study on the effect of air scatter and consequent electron build-up on the calculation of dose equivalent quantities in the ICRU sphere [35]. They argue that the air scatter contribution, which would be present in practice, has been ignored by assuming the calculations to be in vacuo [35]. Their calculations involved a long cylinder of air containing the ICRU sphere at one end. A key component of the study was to determine the length and radius of the air cylinder in order to attain full secondary

electronic equilibrium at the sphere's surface due to the air. Their study found that for a 10 MeV photon beam, the length of the air cylinder had to be 40 meters which resulted in a significant attenuation of the beam [35]. In addition, they concluded that the inclusion of the dose equivalent produced by photons scattering in the surrounding air, contributes about 2% of the dose equivalent at a depth of 10 mm below 10 MeV [20, 35]. The dose conversion coefficients calculated are essentially those obtained by the kerma approximation.

3.2.2 Calculations and Results

Photon ambient dose equivalent conversion coefficients were calculated in each dose volume (depth in the ICRU sphere) by tracking the recoil electrons using both an energy deposition tally (MCNP5 *f8) and an energy deposition heating tally (MCNP5 f6). The *f8 tally scores the energy deposition of each photon and electron as it enters and exits the cell volume whereas the f6 tally scores the energy fluence of photons crossing a tally region and converts the fluence to energy deposition using a heating number which assumes local energy deposition of secondary electrons (kerma approximation) [1]. The energy regime of interest for the present work requires additional photon conversion coefficients up to 25 MeV. However, for completeness as well as to ensure that the models were correctly predicting the energy deposition, monoenergetic photons from 10 keV to 25 MeV were simulated. Energies were selected based on those published in ICRP Publication 74 with greater resolution in the energy regime of interest for this work [20]. The energy cutoff for electrons and photons were both 1 keV, respectively.

The results for photon H*(10), H*(15), H*(20), H*(30) and H*(40) are shown in Table 2 and Figure 3. The results for H*(10) based on the kerma approximation are shown in Table 3 and Figure 3. The dose contribution below 1 MeV decreases with depth. However, above 3 MeV, the dose contribution increases quite steadily with depth and energy. Note that the H*(10) calculated using the kerma approximation greatly overestimates the dose above 3 MeV. This can be attributed to placing the ICRU sphere in air under a condition of charged particle equilibrium as well as the employment of the kerma approximation. As pointed out by Kim and Kim, as the electron energy increases and the location of the electron is closer to the surface, the kerma approximation becomes invalid because electron equilibrium is incomplete [32].

Several researchers have published photon fluence-to-ambient dose equivalent conversion coefficients for various energies, however, data are generally reported for only the 10mm depth in the ICRU sphere, probably since ICRP Publication 74 makes it clear that the 10 mm depth is preferred for penetrating radiation [20]. This depth is recommended because H*(10) overestimates the effective dose at all energies up to 10 MeV.

As reported, the radius of the tally volume used for the present work was 0.25 cm. Ferrari and Pelliccioni used a 1 cm radius sphere which was based on the assumption that an electron deposits its energy at the point of interaction at electron energies less than 50 keV. This corresponds to electron ranges of less than or equal to 4.3 $x10^{-3}$ g/cm^2 in tissue [30]. Kim and Kim selected a smaller volume, a radius of $4x10^{-3}$ cm for their work,

which corresponds to less than the range of a 0.01 MeV electron in tissue (less than one-tenth of $4x10^{-3}$ g/cm^2 [30].

Data shown in Figure 4 are from Kim and Kim (using MCNP4C), Ferrari and Pelliccioni (using FLUKA), Takesuye and Hertel (using the ACCEPT code from the Integrated Tiger Series system), ICRP Publication 51, ICRP Publication 74 and the present work [32, 30, 36, 37, 20]. These data are also plotted with effective dose conversion coefficients for photons using the AP irradiation geometry [22] in Figure 4 .

The percent difference between published data and the present work for the photon H*(10) calculation is shown in Figure 5 [20, 30, 32]. In order to provide higher resolution in the plot, comparisons are only made up to 10 MeV. A comparison of the present work to Ferrari and Pelliccioni at 20 MeV yields a percent difference of -1.6% [30]. Note the dramatic percent difference from the ICRP-74 calculation which is due to the kerma approximation. A comparison of the present work to ICRP Publication 74 (based on the kerma approximation) for photon H*(10) is shown in Figure 6. Note the good agreement to within 3% above 0.015 MeV

Table 2. Photon Fluence-to-Ambient Dose Equivalent Conversion Coefficients for Various Depths in the ICRU Sphere.

Photon Energy [MeV]	$H^*(10)/\Phi$ [pSv cm^2]	$\delta H^*(10)/\Phi$ [pSv cm^2]	$H^*(15)/\Phi$ [pSv cm^2]	$\delta H^*(15)/\Phi$ [pSv cm^2]	$H^*(20)/\Phi$ [pSv cm^2]	$\delta H^*(20)/\Phi$ [pSv cm^2]	$H^*(30)/\Phi$ [pSv cm^2]	$\delta H^*(30)/\Phi$ [pSv cm^2]	$H^*(40)/\Phi$ [pSv cm^2]	$\delta H^*(40)/\Phi$ [pSv cm^2]
0.01	0.073	0.0004	0.0067	0.0001	0.0006	0.00004	-----	-----	-----	-----
0.015	0.83	0.003	0.40	0.002	0.19	0.001	0.05	0.001	0.010	0.0003
0.02	1.06	0.007	0.78	0.006	0.56	0.006	0.30	0.004	0.15	0.003
0.03	0.82	0.007	0.74	0.007	0.66	0.007	0.54	0.006	0.42	0.005
0.04	0.62	0.007	0.61	0.007	0.59	0.007	0.53	0.006	0.47	0.006
0.05	0.54	0.006	0.54	0.006	0.53	0.006	0.52	0.006	0.48	0.006
0.06	0.52	0.006	0.51	0.006	0.51	0.006	0.51	0.006	0.48	0.006
0.08	0.54	0.006	0.54	0.006	0.53	0.006	0.52	0.006	0.51	0.006
0.1	0.62	0.006	0.62	0.006	0.61	0.006	0.61	0.006	0.58	0.006
0.15	0.91	0.009	0.88	0.009	0.89	0.009	0.88	0.009	0.84	0.008
0.2	1.20	0.01	1.18	0.01	1.16	0.01	1.16	0.01	1.10	0.01
0.3	1.81	0.03	1.77	0.03	1.76	0.03	1.75	0.03	1.62	0.03
0.4	2.34	0.04	2.32	0.04	2.38	0.04	2.23	0.04	2.16	0.04
0.5	2.84	0.05	2.83	0.05	2.85	0.05	2.76	0.05	2.68	0.05
0.6	3.37	0.06	3.31	0.06	3.31	0.06	3.24	0.06	3.06	0.06
0.8	4.27	0.06	4.20	0.06	4.28	0.06	4.19	0.06	3.97	0.06
1	5.08	0.07	5.04	0.07	5.04	0.07	4.89	0.07	4.71	0.07
1.5	7.07	0.13	6.55	0.13	6.77	0.13	6.59	0.13	6.35	0.12
2	8.66	0.16	8.14	0.15	8.50	0.16	8.15	0.15	7.79	0.15
3	10.4	0.19	11.3	0.20	11.1	0.19	10.9	0.19	10.3	0.19
4	10.9	0.19	13.1	0.22	13.4	0.22	12.7	0.21	12.6	0.21
5	10.0	0.19	13.3	0.22	14.9	0.24	14.8	0.23	14.6	0.23
6	9.55	0.18	13.3	0.23	16.0	0.25	17.1	0.26	17.0	0.25
8	8.69	0.18	12.7	0.23	15.9	0.26	20.0	0.28	20.5	0.28
10	8.51	0.19	12.2	0.23	15.6	0.27	20.6	0.29	23.8	0.31
15	8.14	0.20	11.8	0.24	15.2	0.29	20.9	0.32	26.2	0.35
20	8.16	0.21	11.8	0.26	15.3	0.30	22.2	0.34	27.8	0.38
21	7.89	0.21	11.8	0.26	15.4	0.31	22.2	0.34	27.9	0.38
22	8.02	0.21	11.9	0.26	15.0	0.30	22.2	0.35	28.0	0.39
23	8.14	0.21	12.1	0.27	15.4	0.30	22.7	0.36	28.1	0.39
24	8.16	0.22	11.9	0.27	15.9	0.32	22.8	0.36	28.9	0.40
25	8.37	0.22	11.8	0.26	15.6	0.31	22.8	0.36	28.9	0.41

Table 3. Photon Fluence-to-Ambient Dose Equivalent Conversion Coefficients for H*(10) based on Kerma Approximation.

Photon Energy [MeV]	$H^*(10)_{Kerma}/\Phi$ [pSv cm^2]	$\delta H^*(10)_{Kerma}/\Phi$ [pSv cm^2]
0.01	0.073	0.0009
0.015	0.82	0.006
0.02	1.05	0.005
0.03	0.81	0.003
0.04	0.63	0.002
0.05	0.54	0.002
0.06	0.51	0.002
0.08	0.54	0.002
0.1	0.62	0.002
0.15	0.90	0.003
0.2	1.20	0.004
0.3	1.79	0.006
0.4	2.35	0.008
0.5	2.88	0.009
0.6	3.37	0.01
0.8	4.29	0.02
1	5.11	0.02
1.5	6.87	0.02
2	8.38	0.03
3	10.9	0.04
4	13.2	0.05
5	15.3	0.06
6	17.4	0.06
8	21.4	0.08
10	25.5	0.09
15	35.7	0.13
20	46.5	0.17
21	48.7	0.18
22	50.9	0.19
23	53.1	0.20
24	55.4	0.21
25	57.7	0.21

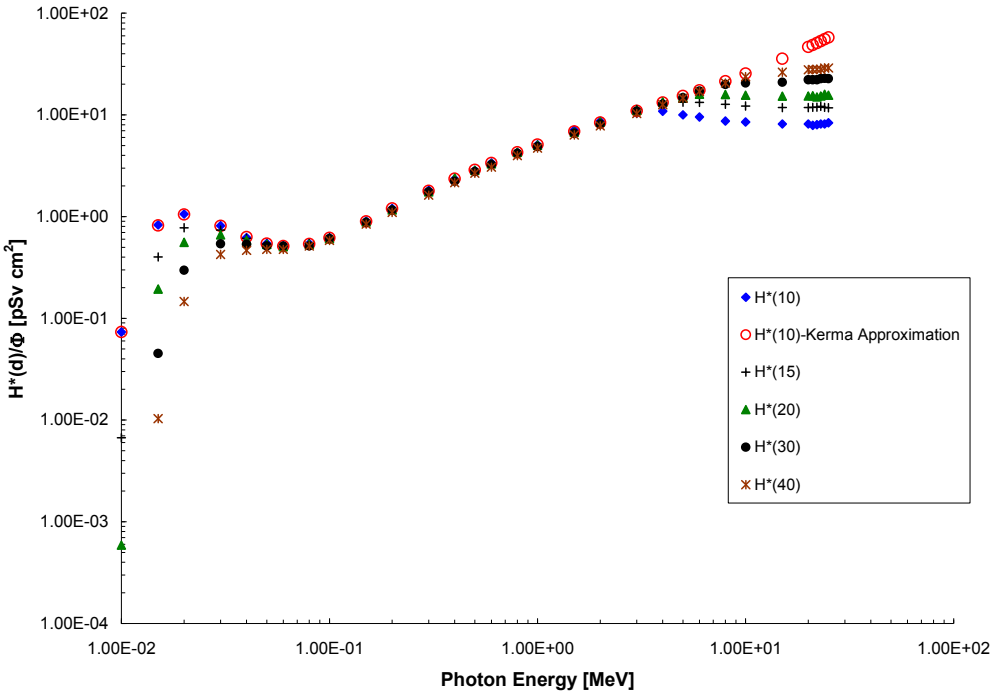

Figure 3. Photon Fluence-to-Ambient Dose Equivalent Conversion Coefficients. (The error bars are smaller than the size of the symbols).

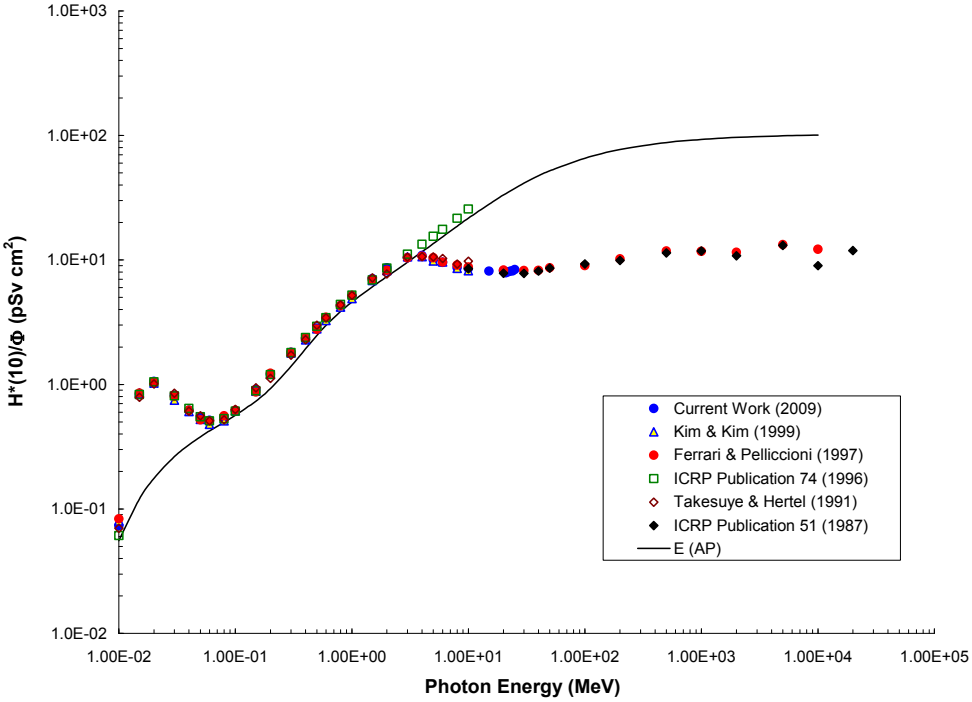

Figure 4. Comparison of Photon Fluence-to-Ambient Dose Equivalent Conversion Coefficient Data to Published Data. Data reprinted from [32, 30,].

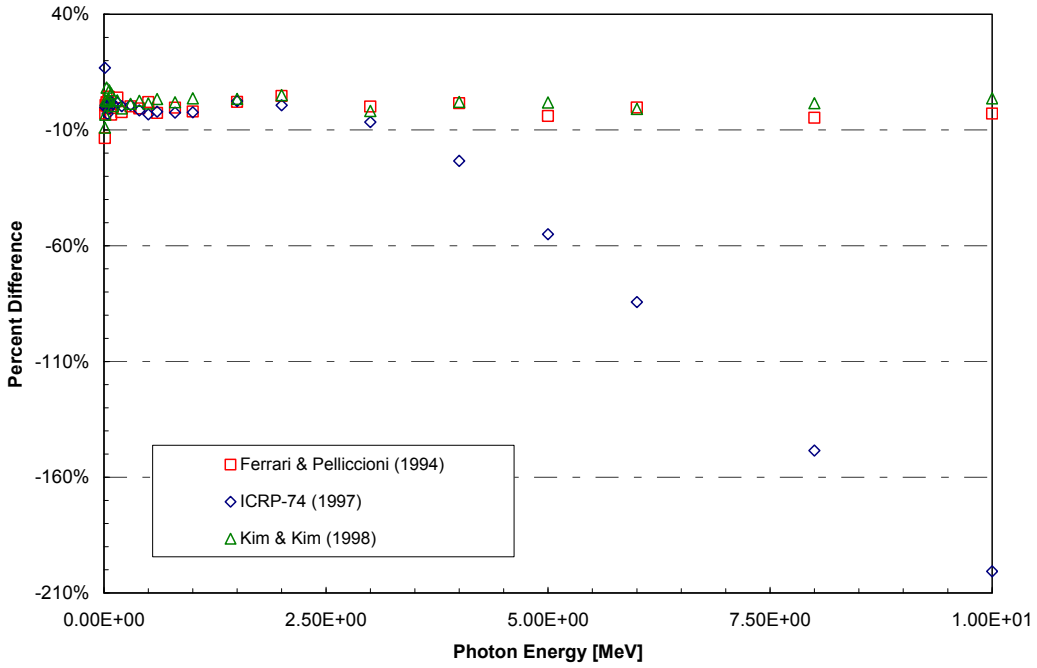

Figure 5. Percent Difference Between Present Work and Published Data for Photon H*(10) Conversion Coefficient Calculation. Data reprinted from [20, 30, 32].

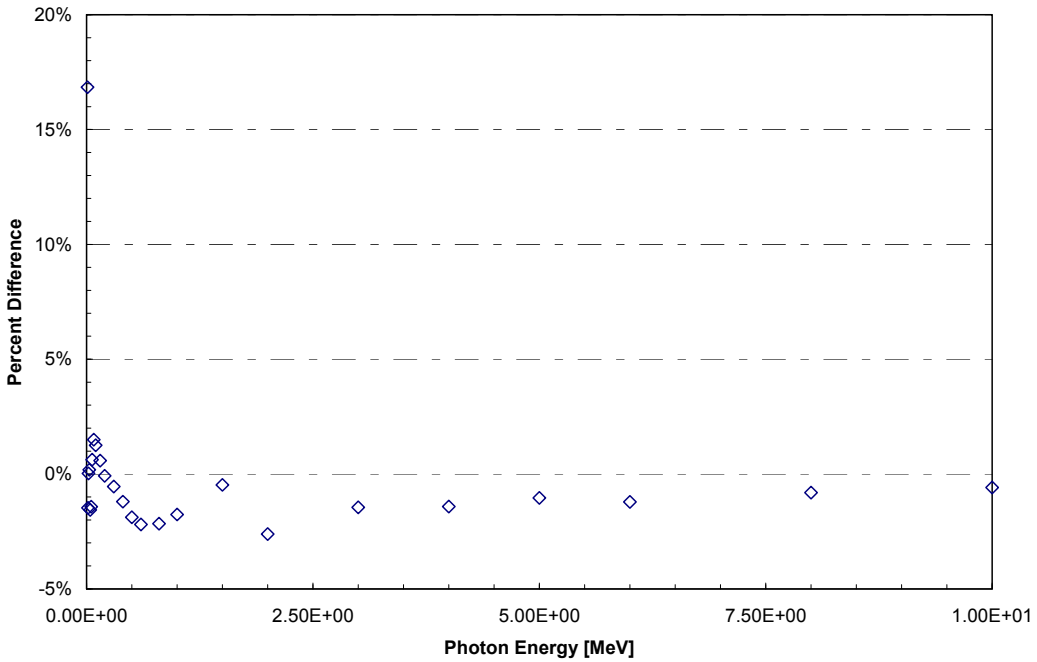

Figure 6. Percent Difference Between ICRP Publication 74 (Kerma Approximation) and Present Work for Photon H*(10) Conversion Coefficient Calculation. Data reprinted from [20].

3.3 Electron Conversion Coefficients

3.3.1 Special Considerations

The amount of published data available for electron ambient dose equivalent conversion coefficients is sparse. As was the case for photons, the calculation of dose equivalent at 10 mm is quite useful as it provides a good estimate of the organ dose and thus the effective dose. Since it was unknown whether the condition of charged particle equilibrium in the air was met, a new set of electron fluence-to-ambient dose equivalent conversion coefficients were calculated. For consistency and completeness, the same methodology employed in the previous section for calculating the photon fluence-to-ambient dose equivalent conversion coefficients was employed. The key difference between the electron case and the photon case was that a slightly smaller volume was used for the calculation of energy deposition. In the electron case, energy deposition was scored in a volume of 4.19×10^{-3} cm^3 (a sphere radius of 0.1 cm) with the remainder of the model the same as the photon case. Since the range of an electron in ICRU tissue will dictate the amount of energy deposited at a given depth, monoenergetic electrons starting at 1.5 MeV were considered. This was done for practicality as well as to speed the calculation runtimes since the range of a 1.5 MeV electron is on the order of 7 mm in ICRU tissue.

3.3.2 Calculations and Results

Electron ambient dose equivalent conversion coefficients were calculated in each dose volume (depth in the ICRU sphere) by tracking the recoil electrons and subsequent bremsstrahlung photons using an energy deposition tally (MCNP5 *f8). The *f8 tally

scores the energy deposition of each electron and any bremsstrahlung photons generated as they enter and exit the cell volume. Transport was conducted in vacuo, following the same arguments used in the photon case. As previously discussed, the energy regime of interest for the present work requires electron conversion coefficients up to 25 MeV. Pelliccioni published electron conversion coefficients from 1.5 to 10 GeV, however, there was not much resolution between the energies of 10 and 30 MeV [33]. Therefore, conversion coefficients were calculated from 20 to 25 MeV in 1 MeV increments. For completeness, as well as to ensure that the models were correctly predicting the energy deposition, monoenergetic electrons from 1.5 MeV to 10 MeV were also considered. These energies were selected based on those published in ICRP Publication 51. The low energy cutoff for electrons and photons was 1 keV.

The results for electron H*(10), H*(15), H*(20), H*(30) and H*(40) are shown in Table 4 and plotted in Figure 7. The dose equivalent grows to a maximum at 4 MeV and then levels out since the stopping power is then fairly constant with energy. The conversion coefficients for the 10 mm depth remain constant above about 8 MeV, a mean value of (312 ± 2.75) pSv-cm^2, and for the 15 mm depth above about 10 MeV a mean value of (315 ± 3.25) pSv-cm^2. The 20 mm and 30 mm cases are constant above about 20 MeV, a mean value on the order of (320 ± 3) pSv-cm^2.

Electron ambient dose equivalent data were calculated by Ferrari and Pelliccioni using the FLUKA code [38]. Similar calculation parameters were used in their work except they only consider a maximum penetration depth of 10 mm. Much like the data

calculated for the present work, above about 8 MeV, the energy deposition is constant. Ferrari and Pelliccioni point out that this is due to the fact that energy deposition becomes fairly constant as the interacting electrons reach relativistic velocities which leads to near constant dose equivalent values [38]. Rogers calculated the dose equivalent in the ICRU slab at various depths utilizing the EGS3 code [39]. Much of this modeling effort was similar to the present work except a slab geometry was employed. Pelliccioni and Ferrari make the argument that it is valid to compare data even though the phantoms are different, since the dose equivalent data are consistent at the depth interval 0.8-1 cm [38]. A closer comparison of the data illustrates a less than 8% difference in dose equivalent between 3 MeV and 30 MeV.

Data calculated for H*(10) for electrons compared to Ferrari and Pelliccioni, Rogers, and ICRP Publication 51 are shown in Figure 8 [38, 39, 27]. Data calculated for H*(15), H*(20), H*(30) and H*(40) for electrons compared to Rogers' published data [39], are shown in Figure 9 through Figure 12. Error bars represent the total statistical error in the energy deposition calculation.

The percent difference between published data and the present work for the electron H*(10) calculation is shown in Figure 13 [37, 38, 39]. The data from the present work compare well with Ferrari and Pelliccioni above 3 MeV, however, below 3 MeV the difference ranges from 25 to 80% [38]. For the present work, the same methodology was employed in all calculations and the Monte Carlo statistical error for the energy deposition calculations was 2.37%, 0.44% and 0.24% for 1.5 MeV, 2 MeV and 2.5 MeV,

respectively. A comparison to Rogers's data showed a 0.8% difference at 1.5 MeV, a 99.5% difference at 2 MeV, and a 1.8% difference at 3 MeV [39]. The cause of these inconsistencies is not clear.

Table 4. Electron Fluence-to-Ambient Dose Equivalent Conversion Coefficients for Various Depths in the ICRU Sphere.

Electron Energy [MeV]	H*(10)/Φ [pSv cm^2]	δH*(10)/Φ [pSv cm^2]	H*(15)/Φ [pSv cm^2]	δH*(15)/Φ [pSv cm^2]	H*(20)/Φ [pSv cm^2]	δH*(20)/Φ [pSv cm^2]	H*(30)/Φ [pSv cm^2]	δH*(30)/Φ [pSv cm^2]	H*(40)/Φ [pSv cm^2]	δH*(40)/Φ [pSv cm^2]
1.5	0.091	0.002	0.071	0.002	0.059	0.002	0.047	0.002	0.045	0.002
2	33.6	0.15	0.13	0.004	0.12	0.004	0.093	0.004	0.082	0.004
2.5	215	1	0.44	0.01	0.17	0.01	0.14	0.01	0.13	0.01
3	368	1	36.3	0.2	0.25	0.01	0.20	0.01	0.19	0.01
4	425	1	315	1	40.7	0.2	0.38	0.01	0.34	0.01
5	384	1	414	1	281	1	0.66	0.03	0.51	0.03
7	329	2	370	2	399	2	236	1	1.87	0.1
8	319	2	344	2	374	2	349	2	55.6	1
10	311	1	322	2	340	2	376	2	319	1
15	304	2	313	2	319	3	326	2	342	2
20	312	3	314	4	320	4	321	3	327	3
21	313	3	310	4	315	4	320	3	323	3
22	315	3	312	4	318	4	322	4	329	3
23	313	3	315	4	318	4	320	4	330	3
24	309	3	319	4	317	4	319	4	317	3
25	312	3	314	4	315	4	323	4	322	3

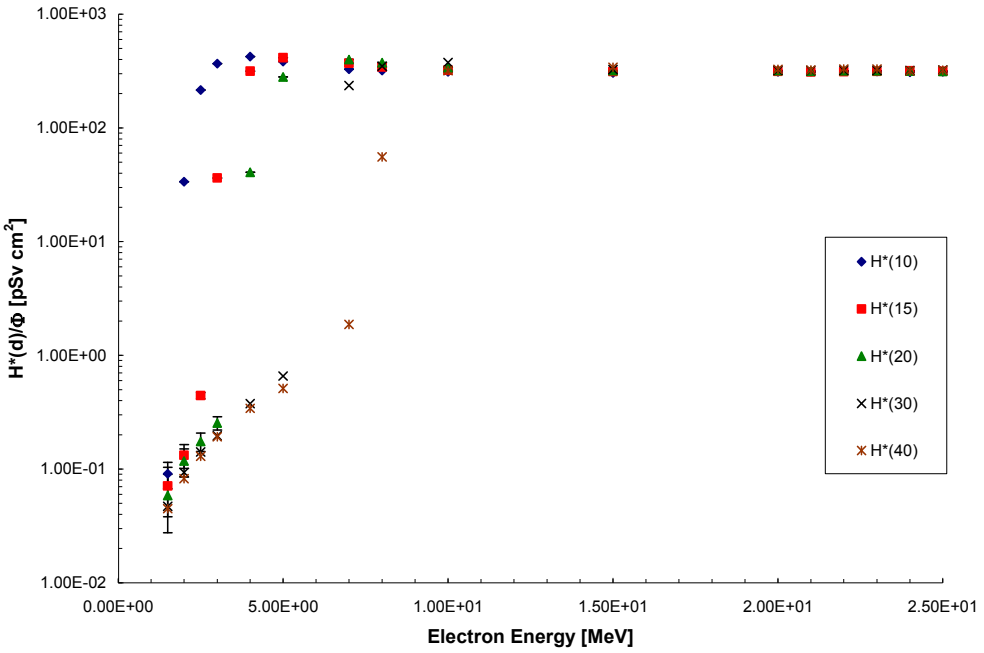

Figure 7. Electron Fluence-to-Ambient Dose Equivalent Conversion Coefficients. (The error bars are smaller than the size of the symbols).

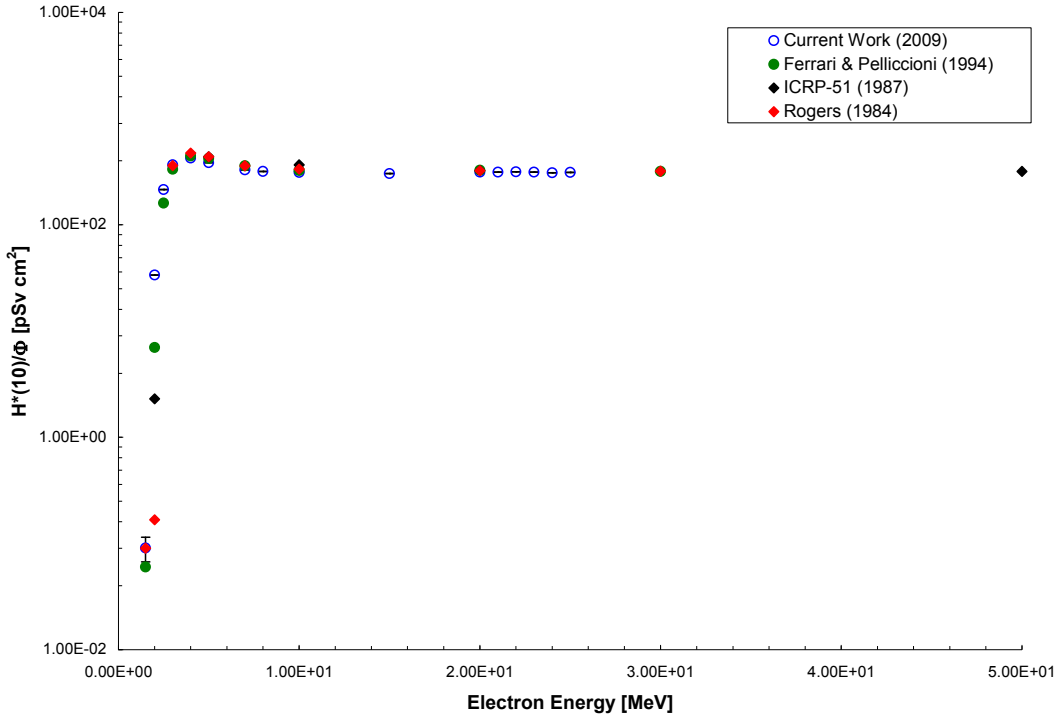

Figure 8. Comparison of Electron Fluence H*(10) Conversion Coefficient Data to Published Data. Data reprinted from [38, 39].

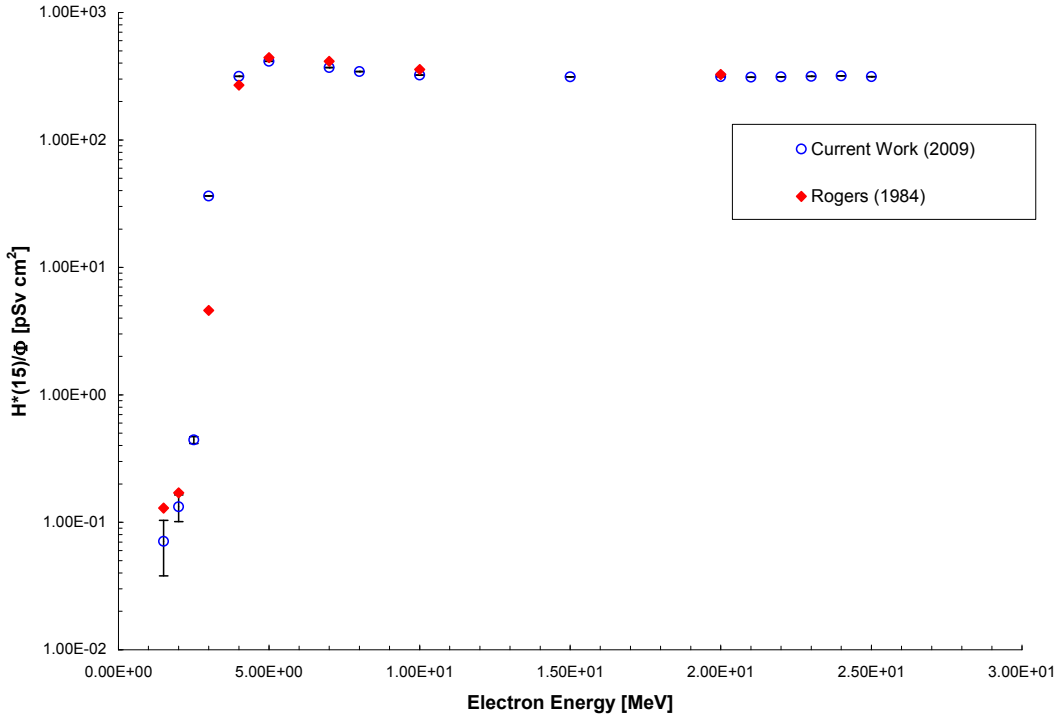

Figure 9. Comparison of Electron Fluence H*(15) Conversion Coefficient Data to Published Data. Data reprinted from [39].

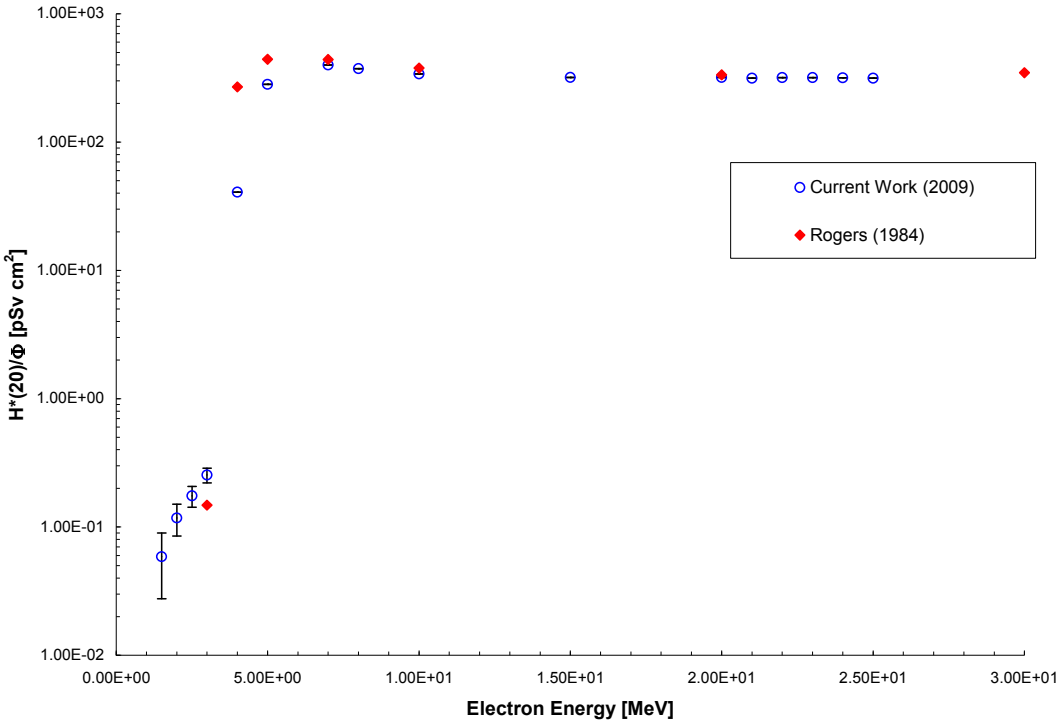

Figure 10. Comparison of Electron Fluence H*(20) Conversion Coefficient Data to Published Data. Data reprinted from [39].

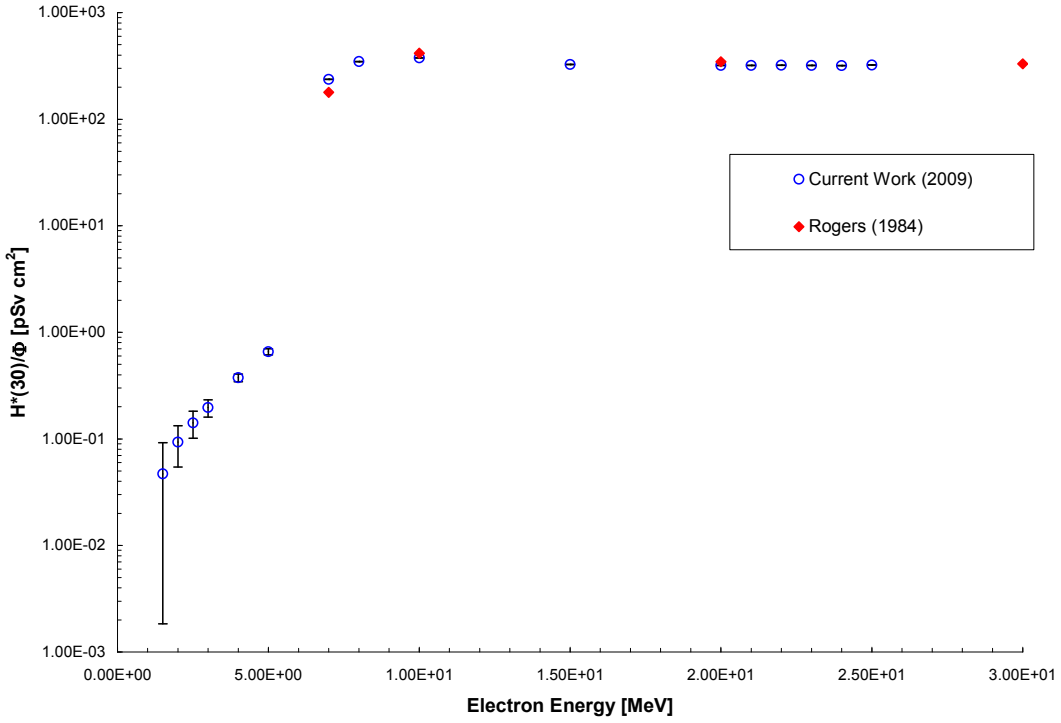

Figure 11. Comparison of Electron Fluence H*(30) Conversion Coefficient Data to Published Data. Data reprinted from [39].

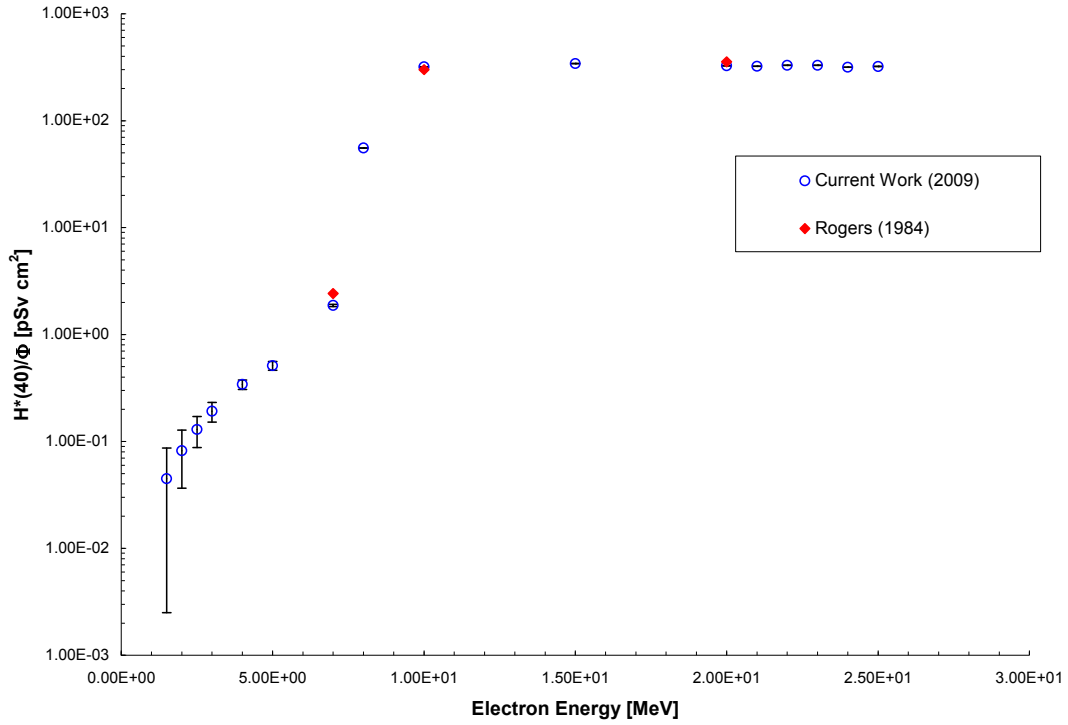

Figure 12. Comparison of Electron Fluence H*(40) Conversion Coefficient Data to Published Data. Data reprinted from [39].

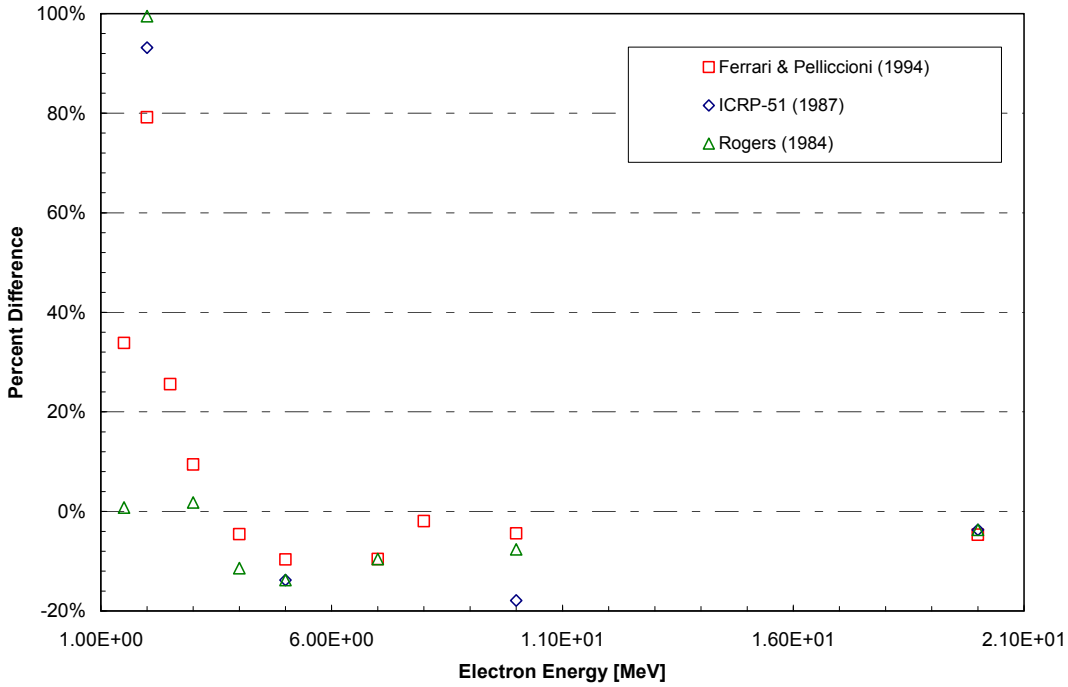

Figure 13. Percent Difference Between Published Data and Present Work for Electron H*(10) Conversion Coefficient Calculation. Data reprinted from [38, 37, 39].

3.4 Neutron Conversion Coefficients

Since the neutron fluence-to-ambient dose equivalent conversion coefficients reported in ICRP Publication 74 were based on the kerma approximation, which is acceptable in the neutron energy regime under consideration in the present work, updated neutron ambient dose equivalent conversion coefficients were not calculated. The neutron fluence-to-ambient dose equivalent conversion coefficients employed in the present work were taken from ICRP Publication 74 [20]. These data are shown in Table 5.

Table 5. Neutron Fluence-to-Ambient Dose Equivalent Conversion Coefficients. Reprinted from [20].

Neutron Energy [MeV]	$H^*(10)/\Phi$ [pSv cm^2]
0.000000001	6.60
0.00000001	9.00
0.00000003	10.6
0.0000001	12.9
0.0000002	13.5
0.000001	13.6
0.000001	13.3
0.000002	12.9
0.00001	12.0
0.00001	11.3
0.00002	10.6
0.0001	9.9
0.0001	9.4
0.0002	8.9
0.001	8.3
0.001	7.9
0.002	7.7
0.01	8.0
0.01	10.5
0.02	16.6
0.03	23.7
0.05	41.1
0.07	60.0
0.1	88.0
0.15	132
0.2	170
0.3	233
0.5	322
0.7	375
0.9	400
1	416
1.2	425
2	420
3	412
4	408
5	405
6	400
7	405
8	409
9	420
10	440
12	480
14	520
15	540
16	555
18	570
20	600
30	515

CHAPTER 4

MEASUREMENTS

Although simulations of dose with radiation transport codes is well established, such simulations need to be compared to be compared to measurements to verify their veracity. The best approach is to conduct measurements of the actual physical processes in order to do a comparison. There are several unique elements of the system studied in the present work including a highly collimated source operated outdoors in the open air in all weather conditions. Most air-scatter measurements conducted to date were more idealized in nature and have looked mainly at isotropic sources. Although the challenges of performing measurements are great in number, the payoff received from possessing quality data is usually even greater.

This chapter describes measurements which were performed using the prototype accelerator system over the course of a calendar year. Measurements were performed under various conditions using both active and passive radiation measurement instrumentation. All measurements were performed on an outdoor test range in two different parts of the United States. Absorbed dose measurements were performed utilizing the recommendations of the ICRU and the American Association of Physicists in Medicine (AAPM). The following sections contain descriptions of the bremsstrahlung source, the measurement instrumentation employed, and the various measurements performed. An analysis of the experimental data and results are then reported.

4.1 Bremsstrahlung Source

The following section will describe the bremsstrahlung source as well as describe the importance of the electron beam energy in an electron LINAC. The relationship between electron energy, beam current and input power will be highlighted. A description of the measurement of beam current for the present work will be presented. Finally, a brief overview of the radiation field around the PITAS prototype will be described.

4.1.1 General Overview

The PITAS prototype bremsstrahlung source consists of a commercial-off-the-shelf electron linear accelerating (standing wave) waveguide coupled to other commercially available sub-systems (i.e. klystron, power supply, etc.) mounted inside a standard cargo container. A sketch of the PITAS prototype is shown in Figure 14. The accelerating waveguide is the component of the accelerator where electrons are accelerated by the electric field of the injected radiofrequency. The electrons are produced with a thermionic triode "gun" and can be injected into the waveguide for a range of pulse widths and amplitudes. The output energy from the LINAC depends on the fixed (physical) parameters of the waveguide (i.e. waveguide length and impedance) as well as dynamic system parameters such as the input power level during each pulse, the microwave frequency and the electron beam current [40].

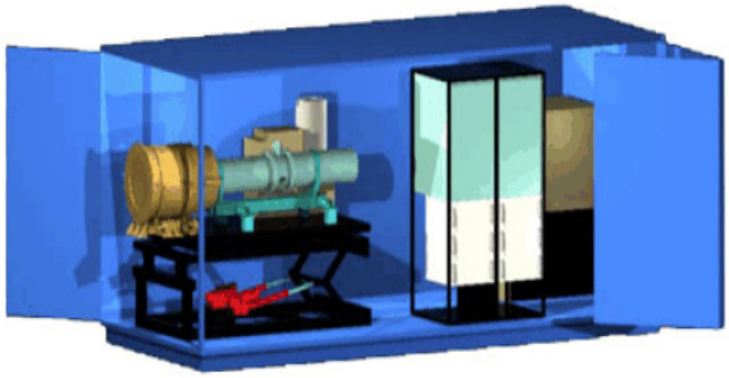

Figure 14. Artist Concept Sketch of PITAS. Reprinted from [11].

For a standing wave accelerator, the energy is proportional to the root of the input power. Since a standing wave accelerator is a highly resonant system, it will only work at a fixed frequency. The energy of the accelerated electrons depends mainly on the amplitude of the oscillations in the waveguide and on the phase of the electron bunches in relation to the standing waves. The amplitude depends on the microwave power, while the phase can be varied by changing the energy of the electrons coming into the system from the electron gun [40].

Since the electric field amplitude is constant throughout the system, the amplitude depends on the balance between incoming microwave power and losses in the microwave system. The average electric field acting on an electron is reduced as the electron beam current is increased, thus the electron energy is reduced. The dependence of energy on beam current is important at high operating currents used for bremsstrahlung production as there is a direct correlation between electron energy, beam current and subsequent bremsstrahlung production. With this relationship, two conflicting effects are observed. First, at constant electron energies, the bremsstrahlung output is proportional to beam

current. Second, x-ray production efficiency is a function of electron energy, decreasing rapidly with falling energy. These effects are illustrated in Figure 15. Note that initially, the first effect is dominant and bremsstrahlung output increases with electron beam current. As the energy drops, the output will reach a well defined maximum [40]. A thorough understanding of this correlated relationship is important in determining system doses as the electron beam energy will dictate the associated doses.

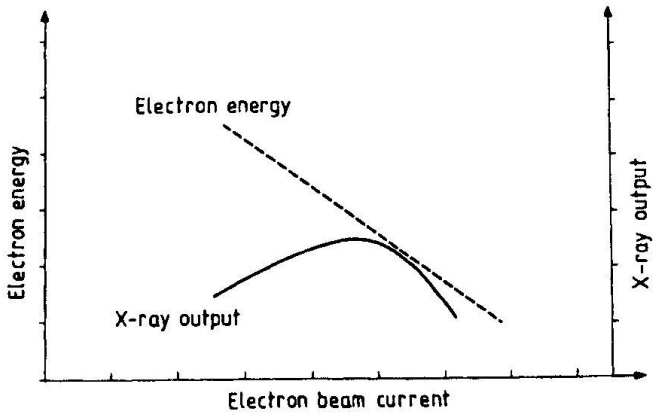

Figure 15. Relationship Between Electron Energy, Beam Current and X-ray Output. Reprinted from [40].

The most common way to control the electron beam energy is to control the beam loading characteristics of the waveguide. At high beam currents, the electron beam energy can be controlled by precisely varying the beam current. If the energy is too low it can be increased by reducing the beam current while if it is too high it can be reduced by increasing the beam current. Feedback is generally controlled by a bending magnet which is used to deflect the beam and provide focusing for the spreading of energies [40]. Through this process, the beam energy can be monitored. For practical deployment

considerations, the PITAS did not employ a bending magnet. Therefore, the characterization of electron beam energy was carried out by purely empirical methods where a series of measurements of load curves were created. Load curves are generated by measuring the photonuclear response of known materials as a function of accelerator input power. Results of those analyses showed that the system operates at a nominal energy of 23-25 MeV. Another approach to determining the electron beam energy was employed in this present work and will be discussed in a subsequent section of this chapter.

The bremsstrahlung photon beam is produced by accelerated electron interactions with a converter. Generally, the converter is made of a high atomic number material since the probability for bremsstrahlung interactions increases with atomic number. In the PITAS prototype, the converter is placed inside a collimator which serves to create a very narrow-solid angle primary beam. The collimator also aids in off-axis dose control by minimizing the amount of radiation incident on the off-target environment. The collimator is specifically tailored for both operational deployment (i.e. lightweight, rugged) and sufficient interrogation of the intended target. The process by which the photon beam is generated is shown in Figure 16.

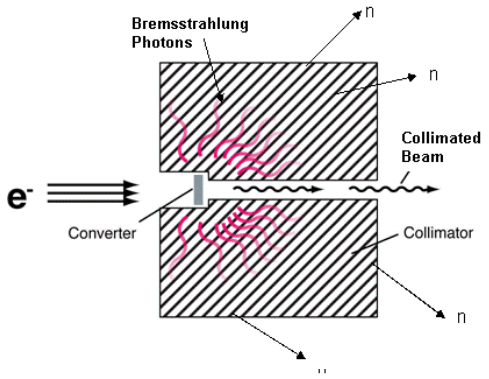

Figure 16. Schematic of Bremsstrahlung Photon Conversion.

4.1.2 Beam Current Measurement

For detailed, accurate simulation of the system, the electron beam energy must be known. Measurement of the beam current is the best monitor available in the PITAS prototype to monitor the bremsstrahlung beam intensity over time. Furthermore, knowing the beam energy is key to modeling the system since the radiation transport (bremsstrahlung production and transport), relies on the electron beam endpoint energy as a starting condition. So a measurement of the PITAS beam current was undertaken. Because of the intensity of the beam this is not a trivial measurement. The electrons exit a thin window at the end of the accelerating waveguide and traveling through air at relativistic energies strike the converter to create bremsstrahlung. The rate and number of electrons hitting the converter is directly proportional to the beam current, which is the basic definition of current. This could be done by using a Faraday cup, a conductive cup that essentially catches the charged particles. An electrical lead is attached to the metallic cup which conducts the current to a measurement device such as an oscilloscope or electrometer. This is normally done in an evacuated beam tube, but in the present work

the beam enters air since the bremsstrahlung conversion takes places after the electrons exit the accelerating waveguide. Traditional Faraday cups are almost always operated in vacuum in order to reduce leakage currents which can skew results. A review of the basics of Faraday cups is presented by Brown and Tautfest [41].

The method used to measure the beam current in the present work employed a very simple approach. A coaxial cable was connected (the center conductor) between the converter and a Tektronix Model TDS3054C Oscilloscope. A second electrical lead was connected from the coaxial cable shield to the system ground. Additionally, the oscilloscope was connected to the system ground. The oscilloscope was set to measure the voltage into a 50Ω terminator. This signal was integrated over time to determine the beam current. A schematic of the beam current measurement is shown in Figure 17.

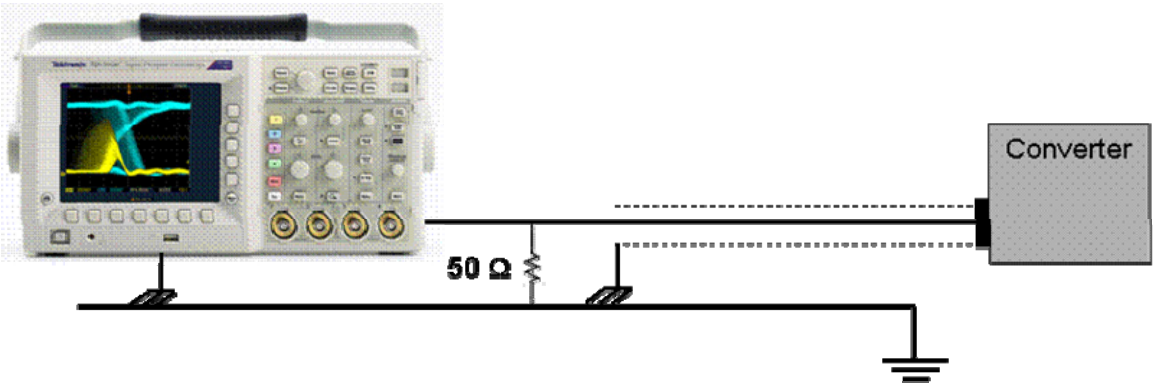

Figure 17. Schematic of Beam Current Measurement.

4.1.3 Overview of Radiation Field

The radiation field created by this system is complex. The following is a description of some of the characteristics of the radiation field observed around the PITAS prototype. First, since an accelerator is used to generate the electron beam, the radiation is pulsed and thus time-dependent. This means that pulses of electrons are delivered for a period of a few microseconds at high repetition rates. The time during which the beam is on is referred to as the duty factor. The duty factor is the product of the pulse width and the repetition rate. For electron accelerators, typical duty factors are about 0.001, which can pose challenges when it comes to accurate radiation measurements.

The accelerated electrons interact in the converter material and produce a considerable amount of bremsstrahlung photons. The collimator serves as a mechanism to create a sharply defined photon beam by directing some of the photons down a narrow tube. Once the photons leave this tube, they will disperse in essentially the same manner as visible light. The photons leave the collimator at 1° of collimation. The photons that scatter into the collimator material interact with this material and the air to produce neutrons through both photonuclear and (n,xn) reactions. Although not dominating, a neutron component is present must be evaluated, particularly near the collimator assembly.

The high-energy photons that exit the collimator, i.e., the primary photon beam, create electrons in the air through the photoelectric effect, compton recoil and pair production

processes. This intensity of this electron field is proportional to the intensity of the photon beam.

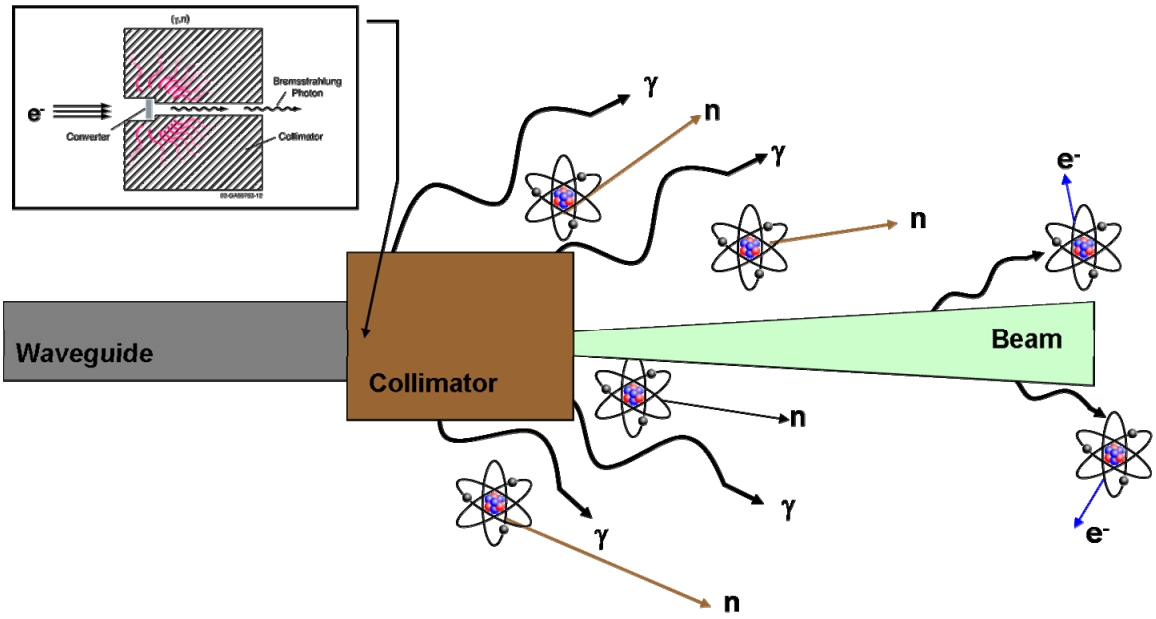

Figure 18. Schematic of PITAS Radiation Field.

4.2 Test Environment

The deployment of the PITAS for military applications requires it to be operated in outdoor environments under various weather and terrain conditions. This requirement led to all PITAS experimental testing to be performed at outdoor testing locations. For the present work, two facilities were utilized for testing, one located in eastern Idaho and one in southern Virginia. Both facilities provided the adequate space as well as operating conditions for successful testing and experimental activities. For each set of measurements, the facility used as well as average environmental conditions will be noted.

4.3 Instrumentation

The conduct of measurements in the vicinity of an accelerator-based source presents challenges which must be addressed in order to ensure the fidelity and quality of experimental data. The following subsections will describe the instrumentation selected to perform the measurements. All equipment was selected to take into account the challenges associated with pulsed source measurements as well as the ability to perform under harsh testing conditions (i.e. outdoors, extreme temperatures, etc.).

4.3.1 Ionization Chambers

The most widely used instrument for measuring absorbed dose is the ionization chamber, which, for simplicity will be referred to as an ion chamber. In general, an ion chamber measures the ionization in a fill gas resulting from interactions in its walls and gas, and in the case of high-energy radiations, outside its walls as well. In the case of photons, the electrons are generated by the three previous reactions mentioned. For neutrons,

recoiling heavy charged particles create the ionization. The collected charge is measured in real-time by an electrometer which is a high impedance voltmeter. The collected charge must be corrected for various effects which are found in a pulsed radiation field. These will be discussed in subsequent sections.

A cavity ionization chamber is of specific interest in this work. It consists of a solid envelope surrounding a gas-filled cavity (usually air) in which an electric field is established to collect the ions formed by the incident radiation. Through the application of cavity theory which is derived from the Bragg-Gray principle, the absorbed dose can be determined in a material of which the cavity wall is made [6]. The Bragg-Gray principle states that the absorbed dose in a given material can be deduced from the ionization produced in a small gas-filled cavity within that material. This relationship is based on the assumption that charged particles produced by the radiation in the wall material of an ion chamber lose a negligible fraction of their energy in traversing the gas cavity [23].

The measurement of absorbed dose in a pulsed radiation field presents challenges for the experimenter. In many absorbed dose measurement scenarios for steady-state sources, the emission of particles and secondary radiations are constant over time. These types of fields are less difficult to characterize as most instruments perform well under a continuous emission source. An accelerator system changes the paradigm as one has to account for the time-dependent changes in the radiation field due to the cyclic nature of the accelerator. Most methods of dosimetry (i.e. ion chambers) which are in use for

measuring continuous radiation from a constant potential x-ray source or from a gamma-ray source can also be used for pulsed radiation provided certain precautions are taken [42]. The time parameters which define the output pulses from a pulsed accelerator are shown in Figure 19. The pulse duration, *t*, is the period during which radiation energy is being emitted by the machine and after a short delay in time is absorbed in the dosimeter. The pulse spacing, *T*, is the interval between corresponding points on successive pulses and is therefore the reciprocal of the pulse repetition frequency [42].

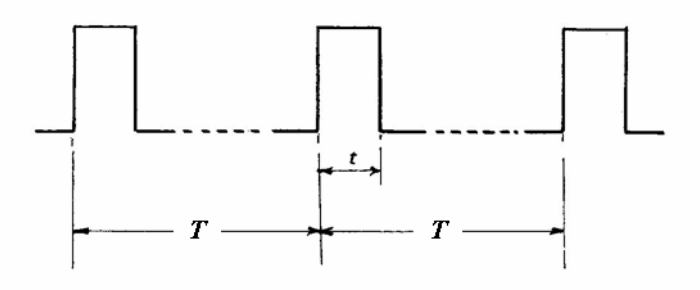

Figure 19. Time Parameters from a Pulsed Radiation Source. Reprinted from [42].

In using ion chambers, the principal disturbing factor is ionic recombination and there are two time parameters of interest, T_1 and T_2 shown in Figure 20. T_1 is the time required for the positive and negative charge clouds generated by the pulse to separate as they drift towards opposite electrodes. No recombination can occur at times greater than T_1. T_2 is the transit time of the slowest ions across the whole gap between the electrodes. At times greater than T_2 there is no ionization in the chamber and subsequent pulses cannot affect the charge collected from earlier pulses. These charge packets are integrated by the electrometer when a train of pulses is delivered [42].

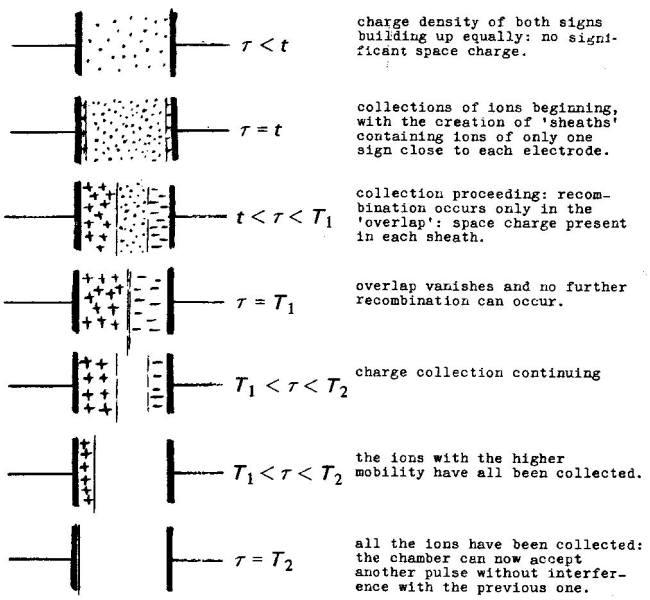

Figure 20. Idealized Charge Density Patterns During the Collection of Ions. Reprinted from [42].

If operating under the condition of $T > T_2 >> t$, the ion chamber will provide a good estimate of the radiation dose with little correction necessary. The condition where $T < T_2$ means the successive pulses will overlap in the chamber and thus increase the amount of recombination. The time required to collect the ions will usually be hundreds of microseconds and a pulse lasting only a few microseconds can be considered to be instantaneous [42].

For most accelerators, the fluctuations between successive pulses is much larger than the overall error of the dosimetric system. Therefore, a monitor is required to ensure that there is consistency in the amount of dose delivered from run to run [42]. In the present work, beam monitoring was accomplished through the measurement of beam current utilizing the same scheme previously discussed.

As reported by Boag, as the voltage difference between the electrodes of an ionization chamber exposed to radiation is increased from zero to higher values, the collected current increases almost linearly with voltage. Above a certain voltage the current increases more slowly. It finally approaches asymptotically the saturation current for the given radiation intensity – which corresponds to the current that would be measured if all the ions formed in the chamber by the radiation were able to reach the electrodes [43]. A plot of a typical saturation curve for an ion chamber is shown in Figure 21.

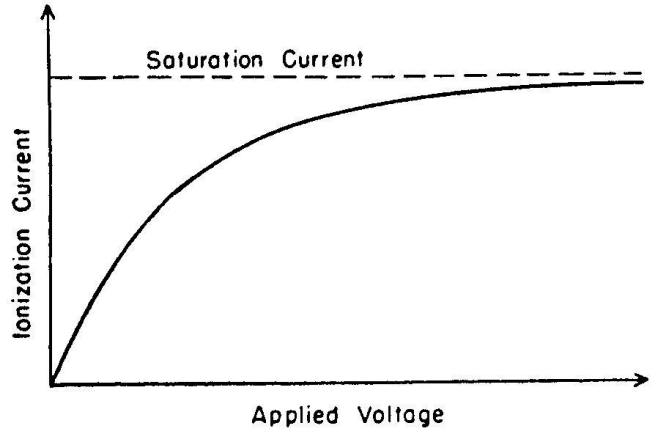

Figure 21. Typical Ion Chamber Saturation Curve. Reprinted from [43].

At low collecting voltages some of the ions produced in the gas meet and neutralize others of opposite sign before they can reach the collector. This is called recombination. Recombination can be reduced by sweeping the ions out of the chamber more rapidly, by increasing the field strength or reducing the distance between the electrodes [43]. The AAPM TG-51 Protocol recommends a correction for incomplete ion collection or ionic recombination. This correction involves collecting ion chamber ionization current readings under standardized test conditions at two-standard applied bias voltages. In general, this is the normal operating bias voltage of the ion chamber and a second bias

voltage which is a reduction of the operating bias voltage by a factor of two. In order to infer the effect of ionic recombination, the data are then applied to the following equation,

$$P_{ion} = \frac{1 - \left(V_H / V_L \right)}{\left(M_{raw}^H / M_{raw}^L \right) - \left(V_H / V_L \right)} \tag{4.1}$$

where V_H is the normal operating bias voltage for the ion chamber (volts) and $M_{raw}{}^H$ is the corresponding ionization current reading (coulombs) , V_L is the lower bias voltage (reducing V_H by a factor of two) (Volts) and $M_{raw}{}^L$ is the corresponding ionization current reading (coulombs). The correction factors for ionic recombination should not exceed 1.05. If a value greater than 1.05 is obtained, another ion chamber should be used to perform the measurement [44]. The ionic recombination correction factor P_{ion} is unitless.

Another phenomenon observed in the pulsed field is the polarity effect. This phenomenon is sometimes observed when current collected from an ion chamber changes in magnitude when the polarity of the collecting potential is reversed [43]. Several authors present potential causes for the polarity effect [45-47]. These effects can vary within measurement sets and can be attributed to cable position as well. The AAPM TG-51 Protocol recommends a correction for the polarity effect which is simply taking two readings with both polarities applied for the standard operating bias voltage. The following correction is then applied

$$P_{pol} = \left| \frac{\left(M_{raw}^{+} - M_{raw}^{-} \right)}{2 M_{raw}} \right| \tag{4.2}$$

where M_{raw}^{+} is the reading when positive charge is collected (coulombs), M_{raw}^{-} is the reading when negative charge is collected (coulombs) and M_{raw} is the standard charge collected (coulombs) [44]. The polarity correction factor P_{pol} is unitless.

Since free air ionization chambers are calibrated under standard environmental conditions of temperature (22°C) and barometric pressure (760 mm Hg), charge readings must be corrected for the fact that measurements are not always made under these conditions. The correction applied involves the recording of the temperature and pressure during the measurement and applying the following equation

$$P_{TP} = \left(\frac{273.2 + T}{273.2 + 22.0} \right) \left(\frac{760}{P} \right) \tag{4.3}$$

where T is the temperature in degrees Celsius and P is the barometric pressure in mm Hg. The temperature-pressure correction factor, $P_{TP,}$ is unitless.

This is the easiest correction to make for every measurement as these data can be continuously monitored and no changes to the ion chamber settings need to be made in order to make this correction. Humid air can affect ion chamber data as condensation inside chamber walls can form. In the range of 20% to 80% relative humidity, no corrections are generally made as the error is only on the order of ± 0.15%. Beyond this band, corrections are made with sophisticated formalisms as presented by Rogers [48].

The final correction that was considered was the electrometer calibration factor, P_{elec}. P_{elec} is simply the calibration factor which corrects the electrometer reading of ion charge to true coulombs. The P_{elec} applied is only applicable to the range being used on the

electrometer. The data to calculate this correction is supplied via a manufacturer's calibration of the electrometer [44]. The correction is calculated such that

$$P_{elec} = \frac{Q_k - Q_m}{Q_k} \tag{4.4}$$

where Q_k is the known charge input into the electrometer (coulombs) and Q_m is the measured charge (coulombs). The electrometer correction factor, $P_{elec,}$ is unitless.

The value used for the charge reading is now based on the product of the actual ionization charge reading given by the electrometer and the four correction factors previously discussed. After these corrections are applied, the electrometer ionization charge reading, M (coulombs) becomes

$$M = (M_{raw})(P_{ion})(P_{pol})(P_{TP})(P_{elec}) \tag{4.5}$$

The Bragg-Gray principle, which governs ion chamber cavity theory, can be stated as

$$D = \frac{(M)\left(\overline{w}/e\right)(S_{w,g})}{M_g} \tag{4.6}$$

where D is the absorbed dose in the wall surrounding the cavity (gray), M is the collected ionization charge within the cavity corrected for the various pulsed source effects as shown in Equation (4.5) (coulombs), $\left(\overline{w}/e\right)$ is the average energy required to produce an ion pair in the gas cavity (joules/coulomb), $(S_{w,g})$ is the mass stopping power ratio for the wall material w and the gas g (unitless) and M_g is the mass of the gas in the cavity (kilograms).

The manufacturers of the ion chambers used in the present work provided a calibration factor, $N_{chamber,}$ which is traceable to the National Institute of Standards and Technology (NIST). $N_{chamber}$ provides the response of the ion chamber under known calibration conditions and can be applied directly in the conversion to absorbed dose. Therefore, the product of the corrected electrometer ionization charge reading, M, as given in equation (4.4) and N is proportional to the absorbed dose in air such that,

$$D = (M)(N_{chamber}) \tag{4.7}$$

where absorbed dose, D, is in units of Gray.

Three different ion chambers were selected to perform measurements for the present work. The first chamber, a 0.1cm^3 tissue equivalent cylindrical ion chamber was used to perform beam energy measurements within a virtual water phantom. The second chamber, an 1800 cm^3 air-filled cylindrical ion chamber was used to perform measurements within the primary beam. The third chamber, a 3300 cm^3 propane-filled cylindrical ion chamber was used to perform off-axis measurements of the scattered beam. Each ion chamber and their operating characteristics are described in the next section.

4.3.1.1 0.1cc Ion Chamber

The 0.1cc ion chamber is manufactured by Far West Technologies, Inc. as Model IC-18G and is designed to make an accurate measurement of absorbed dose at a specific point. The chamber wall is 0.064cm thick and is made from high-purity graphite at a density of 1.80 g/cm^3. The chamber has a cylindrical collecting volume and guarded three-terminal design and is mounted on a 26.7 cm long aluminum stem [49]. The chamber is ideal for

absorbed dose measurements as it can be inserted into a water or tissue equivalent phantom with cabling not interfering with the measurement. A schematic of this chamber and its connections are shown in Figure 22 with specifications listed in Table 6.

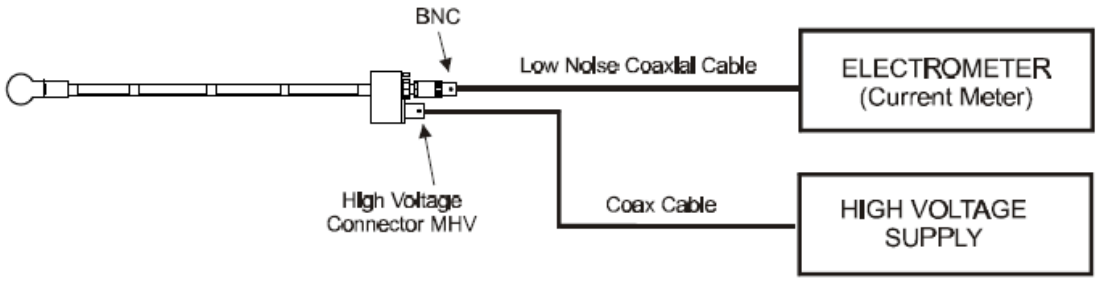

Figure 22. Far West 0.1cc Graphite Tissue Equivalent Ion Chamber. Reprinted from [49].

Table 6. Far West Model IC-18G - 0.1cc Ion Chamber Specifications.

Manufacturer	Far West Technologies, Inc.
Model	IC-18G
Chamber Volume	0.10 cm^3
Operating Bias Voltage	+250 V
Wall Material	Graphite (density = 300 mg/cm^2)
Leakage	5 x 10^{-15} A (typical)
Collection Efficiency	99%
Overall Size	35.7 cm (including connectors)
Weight	94 g

4.3.1.2 1800cc Cylindrical Ion Chamber

The 1800cc cylindrical ion chamber is a reference class device manufactured by RADCAL Corporation as Model RC1800 and is designed to be used by calibration laboratories that employ reference grade electrometers and bias supplies. The chamber wall is 0.33 cm thick and is made from polycarbonate, density of 1.20 g/cm^3. The

chamber has a cylindrical, unsealed collecting volume. The chamber is ideal for low dose rate radiation applications such as shielding leakage, low-level irradiator output and environmental measurements. It is designed to be operated in a pulsed field with a dose rate range of 50 μGy/s to 160 μGy/s [50]. A schematic of this chamber is shown in Figure 23 with specifications listed in Table 7.

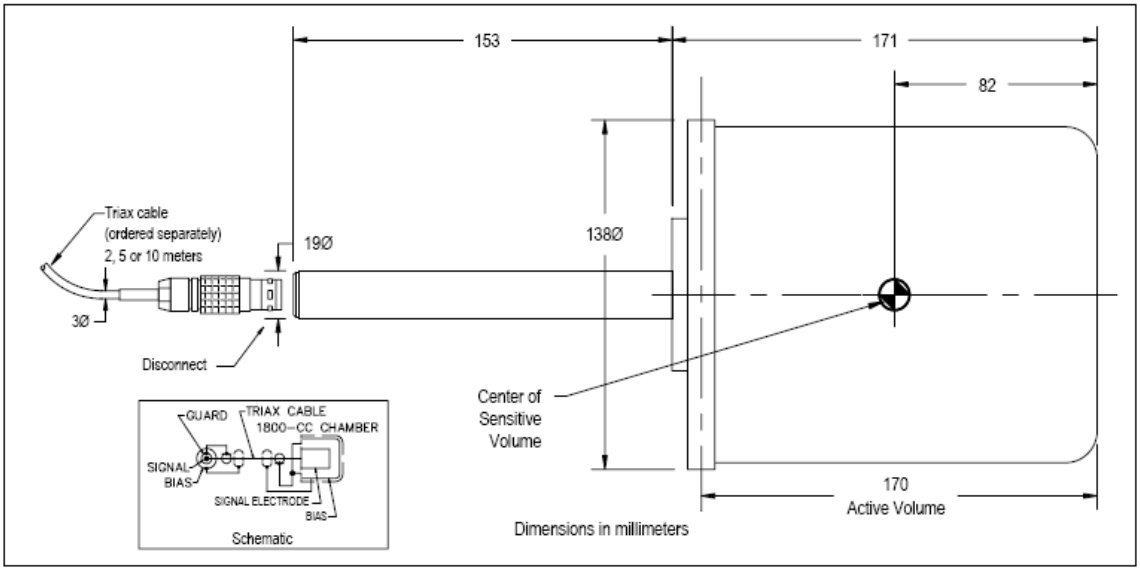

Figure 23. RADCAL Model RC1800 Reference Class Ion Chamber. Reprinted from [50].

Table 7. RADCAL Model RC1800 - 1800cc Ion Chamber Specifications.

Manufacturer	RADCAL Corporation
Model	RC1800
Chamber Volume	1800 cm^3
Operating Bias Voltage	+300 V
Wall Material	Polycarbonate (density = 1.20 g/cm^3)
Leakage	< 1 x 10^{-14} A
Overall Length	32.4 cm
Overall Diameter	13.8 cm
Weight	+/- 0.60 kg

4.3.1.3 3300cc Cylindrical Ion Chamber

The 3300cc cylindrical ion chamber is manufactured by Far West Technologies, Inc. as the Model 1055 Chipmunk and is designed for measuring low levels of radiation ranging from 1 μGy/hr to $1x10^4$ μGy/hr [51]. The chamber wall is 0.3175 cm thick and is made from bakelite and polystyrene at a density of 1.25 g/cm^3. The chamber has a cylindrical, sealed collecting volume and is filled with propane at 1 atm (nominal). Since the Chipmunk is propane-filled and remains under constant pressure, there is no need to apply the pressure-temperature correction, P_{TP}. This chamber was developed by Fermi National Accelerator Laboratory and is deployed at over 300 locations as a "beam-on" monitor at Fermilab [51]. A photograph of this chamber is shown in Figure 24 with specifications listed in Table 8.

Figure 24. Far West Model 1055 Chipmunk Ion Chamber. Reprinted from [52].

Table 8. Far West Model 1055 - 3300cc Ion Chamber Specifications.

Manufacturer	Far West Technologies, Inc.
Model	1055 "Chipmunk"
Chamber Volume	3.40 liters
Operating Bias Voltage	+800 V
Wall Material	Bakelite (density = 1.25 g/cm^3)
Leakage	< 1 x 10^{-14} A
Overall Length	33.02 cm
Overall Diameter	15.24 cm
Weight	10.0 kg

4.3.2 Other Support Equipment

Three different electrometers were used to measure the ionization current from the ion chambers. The Keithley Model 6517A and the Keithley Model 6517B (an upgraded version) were both employed. In addition to ionization current, each electrometer had an associated Type-K thermocouple and relative humidity probe which continuously monitored the ambient conditions around the ion chamber measurement locations. Each electrometer also had a built-in voltage source which provided bias voltage to each ion chamber. A photograph of the Keithley Model 6517B is shown in Figure 25.

Figure 25. Keithley Model 6517B Electrometer. Reprinted from [53].

The Omega iServer iBTX Barometric Pressure and Temperature sensor provided real-time recording of barometric pressure and temperature data throughout the entire measurement periods. The device is accessible via an Ethernet connection which provides a data logging capability. A photograph of this sensor is shown in Figure 26.

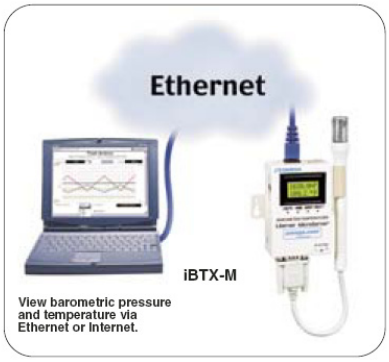

Figure 26. Omega Engineering iBTX Barometric Pressure and Temperature Sensor. Reprinted from [54].

4.3.3 User Interface

A user interface to accommodate multiple measurements using various ion chambers was developed with the National Instruments LabVIEW Version 8.50 software. LabVIEW is a graphical programming environment used to develop sophisticated measurement, test, and control systems using intuitive graphical icons and wires that resemble a flowchart. LabVIEW offers integration with thousands of hardware devices and provides hundreds of built-in libraries for advanced analysis and data visualization [55]. This user interface gave the experimenter the ability to control and monitor multiple ion chambers from a laptop personal computer which was accessed via Windows Remote Desktop.

The LabVIEW interface allows the experimenter to select the ion chamber, bias voltage, the corresponding electrometer and run time, prior to each run. During a run, real-time data were observed including the data being collected from each electrometer (ion chamber charge, relative humidity and temperature) as well as an independent temperature and barometric pressure reading. These data were displayed as both a digital readout as well as plotted on a log sub-screen. When the measurement run was

completed, the software prompted the experimenter to enter any comments concerning the run. These comments plus a second-by-second data set are recorded to a date and time-stamped, formatted text file for post processing. All data files were saved in a user directory automatically with the measurement date and appropriate run number. In addition, LabVIEW automatically saved a screenshot of the user interface which contained all final data from a run for error-checking and archival purposes. An example of the user interface and data presentation is shown in Figure 27.

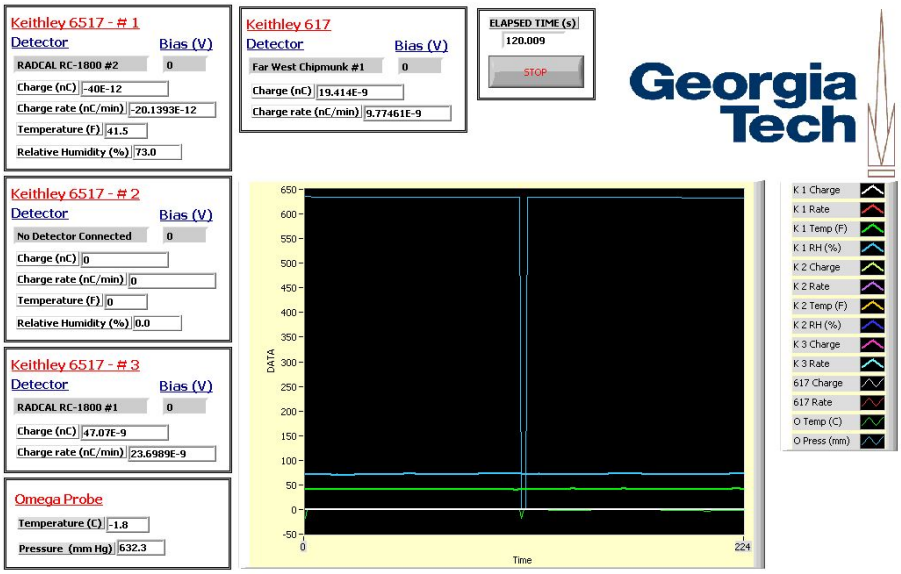

Figure 27. Georgia Tech Measurement System User Interface.

4.3.4 Passive Dosimeters

Due to the pulsed nature of the source and the large radiofrequency electromagnetic background in proximity to the system, the use of active instruments was not always favorable. In addition, there was a requirement for some measurements to be performed using an integrating device such that the data would be colleted based on exposure and measured run times and then read in a post-processing scenario. These factors lead to the

use of passive integrating dosimeters for some measurements. Passive dosimeters, which are widely used in research and personal dosimetry monitoring, have many advantages. In general, they are small in physical size, they have a wide dose range and high dose rate dependence, and they are reusable, which makes them cost effective. The biggest disadvantages of passive dosimeters are the special handling they require throughout their use as well as the amount of time required to prepare and post-process them. Two types of passive dosimeters were selected for use in the present work, thermoluminescent dosimeters (TLDs) and optically stimulated luminescence (OSL) dosimeters. A brief overview of each dosimeter is described in the following subsections with a recap shown in Table 9.

4.3.4.1 Thermoluminescence Dosimeters

Ionizing radiation can produce electron-hole pairs in an inorganic crystal which lead to the formation of excited states with energies that lie in the forbidden gap between the valence band and the conduction band. Some materials will cause the electrons and the holes to remain trapped at activator sites at room temperature. One such material is a thermoluminescent dosimeter (TLD) which has been the mainstay of integrating personnel dosimeters for decades. A TLD is integrating in that the number of trapped electrons and holes will increase with exposure [56]. Upon heating the material, the electrons are excited above the electron trap and into the conduction band, at which point they are free to recombine with a positive ion, producing light. The light can then be read by a photomultiplier tube (PMT). The integral of the current produced by the PMT is linearly proportional to the light produced by the TLD, which is in turn linearly

proportional to the amount of dose absorbed by the TLD. A review of the physics associated with TLDs is found in Horowitz [57].

The TLDs used in the present work were TLD-600s and TLD-700s manufactured by Thermo Scientific. The TLD-600s are extruded rods (1 mm x 1mm x 6 mm) of lithium fluoride enriched to 95.62% ^{6}Li and respond to beta, gamma, and neutron radiation. The TLD-700s are also extruded rods (1 mm x 1mm x 6 mm) of lithium fluoride enriched to 99.63% ^{7}Li and respond to only beta and gamma radiation. [58]. The TLDs were read using a Harshaw Model 3500 TLD Reader.

4.3.4.2 Optically Stimulated Luminescence Dosimeters

Optically stimulated luminescence dosimetry was pioneered by Miller at Batelle-Pacific Northwest Division in the mid-1990s [59-61]. OSL utilizes carbon-doped aluminum oxide (Al_2O_3) as the radiation sensitive material with they key difference from a TLD being that it is read with light and not heat. After being exposed, the amount of radiation exposure is measured by stimulating the Al_2O_3 material with green light (532 nm line) from either a pulsed laser or light emitting diode (LED) source. The resulting blue light emitted from the Al_2O_3 is proportional to the amount of radiation exposure and the intensity of stimulation light. OSL allows for multiple readouts and is used routinely to re-confirm reported radiation doses. Only a fraction of the radiation exposure signal contained in the Al_2O_3 material is depleted upon stimulation with the green light [62]. A review of the solid state physics associated with OSL dosimeters is presented by Yukihara and McKeever [63].

OSL dosimeters are manufactured and marketed by Landauer, Inc. The microStar™ system with the InLight™ Dot dosimeters was used for the present work [62]. The Dot dosimeter contains a single round dosimeter 7.0 mm in diameter and is read using a microStar™ reader, shown in Figure 28. The OSL is read with a short stimulation (1 s) using an array of 38 green LEDs. A PMT is used to collect the subsequent photon emission which is then converted to dose [63].

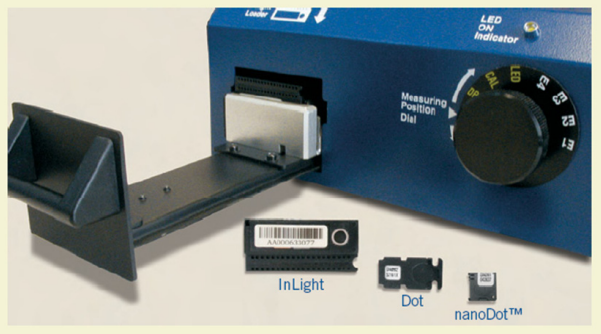

Figure 28. Landauer microStar™ OSL Reader. Reprinted from [62].

Table 9. Summary of Passive Dosimeter Materials & Associated Dosimeter Readers.

TLD Material	Thermo-Fisher TLD-600 Rods (1 mm x 1mm x 6 mm) – ^{6}Li Thermo-Fisher TLD-700 Rods (1 mm x 1mm x 6 mm) – ^{7}Li
TLD Reader	Harshaw Model 3500
OSL Material	Landauer Dot (7 mm diameter) – Al_2O_3
OSL Reader	Landauer microStar™

4.3.5 Bonner Spheres

Neutron dose measurements were performed using a Bonner sphere spectrometer (BSS) system with TLDs as the detector material. The BSS works on the principal of moderation and capture of neutrons and was pioneered by Bramlett, Bonner and Ewing [64]. The Bonner sphere is one of the few systems that can be used across a large range of neutron energies from thermal to hundreds of MeV and has been used in numerous neutron dose equivalent measurements [65]. The Bonner spheres used in the present work were manufactured from high-density (0.95 g/cm^3) polyethylene by Ludlum Measurements, Inc. The BSS system consisted of seven detectors: bare, 2" ball, 3" ball, 5" ball, 8" ball, 10" ball, 10" ball and 12" ball.

4.4 Measurement Normalization

The nature of performing multiple measurements under varied operating conditions and system settings dictates the need to have a consistent method to normalize data points across data sets. This need led to the development of a measurement normalization approach where comparison of quantities across data sets would be technically meaningful. As previously discussed, the beam current was monitored during most measurement sets. This provides the best metric for inter-measurement normalization, as one can relate all data on a per electron basis. The following method was used to normalize the measurements. The average beam current, I_{AVG} (μA) is defined as

$$I_{AVG} = (I_{INST})(f)(t) \tag{4.8}$$

where I_{INST} is the instantaneous (actual) beam current (μA), f is the repetition rate (Hz), and t is the pulse width (μs). The product of I_{AVG} and the measurement run time (s) provides the total charge (Coulombs) delivered during a run, such that

$$Total\ Charge = (I_{AVG})(Run\ Time) \tag{4.9}$$

Therefore, the quotient of a dose value (Gy) and the total charge (μC) provides a normalized dose value in units of Gy/μC. The product of the normalized dose value (Gy/μC), a given beam current (μA) and run time (s), provides the total dose (equivalent) and therefore a consistent comparison between measurement sets. This approach was used in modeling activities as well. Data in the present work are reported in units of Gy/μC and/or Sv/μC using this approach. The assumption used in the present work was that an interrogation will be performed in a 120 second timed run.

4.5 Beam Energy Measurements

The electron beam energy was initially characterized by Idaho National Laboratory utilizing an empirical approach where the waveguide loading conditions were measured and plotted as a series of load curves. In order to corroborate these data with the electron beam energy used in the Monte Carlo simulations, a series of absorbed dose measurements at 3 meters from the collimator were performed and compared to accurately modeled absorbed dose calculations (these data are presented in Chapter 6). The premise is that if the absorbed dose measurements match the absorbed dose simulations, then the electron energy used in the simulations was correct and is, to within some uncertainty, the actual electron energy of the system.

The absorbed dose measurements for beam energy correlation were made directly in front of the PITAS at a distance of 3 meters. In order to effectively measure absorbed dose, a phantom material was needed. Traditional methods call for using a water phantom where a polymethyl methacrylate (PMMA) tank is filled with distilled water. For simplicity, virtual water was used in lieu of a water phantom. Virtual water is a solid slab manufactured from epoxy resins and powders to resemble the radiation transport properties of water. Virtual water slabs are used in radiation oncology applications for routine calibrations and respond (scattering and attenuation) in the same manner as a standard water phantom (equivalent to within 0.5% at photon energies) [66]. The slab used in this measurement was 30 cm x 30 cm x 5 cm. The material composition data for virtual water is shown in Table 10.

Table 10. Material Composition for Virtual Water.

Material Constituent	wt %
Hydrogen	8.02
Carbon	67.03
Nitrogen	2.14
Oxygen	19.1
Chlorine	0.14
Calcium	2.31
Density = 1.04 g/cm^3	

For the purposes of this measurement, a virtual water phantom slab was machined with a 1.27 cm diameter hole through the centerline such that active volume of the Far West 0.1cc tissue equivalent ion chamber was inserted and positioned directly at the centerline of the phantom and primary beam. A photograph of this setup is shown in Figure 29. In order to attenuate the beam and provide a set of absorbed dose responses without moving

the entire measurement apparatus, lead sheets (30.48 cm x 20.32 cm x 0.635 cm) were placed between the virtual water phantom and the incident beam. Measurements were completed with the phantom only and then with individual lead sheets for a total of six (a total thickness of 3.81 cm). A photograph of this setup is shown in Figure 30. A green sighting laser was used to ensure that the beam was at the centerline of the phantom. For all measurements, the ion chamber was operated at a bias voltage of +250V and the integrated ionization current was measured with a Keithley Model 6517 electrometer and user interface as previously discussed. A summary of the measurements performed is shown in Table 11 with average measurement environmental conditions shown in Table 12.

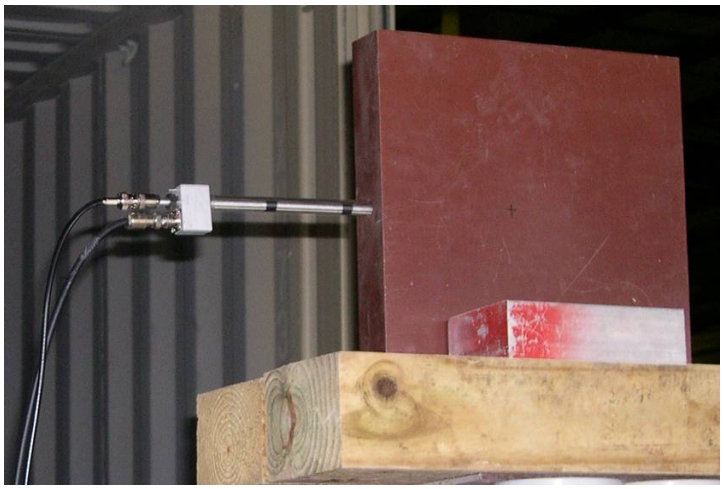

Figure 29. 0.1cc Ion Chamber Positioned Inside the Virtual Water Phantom.

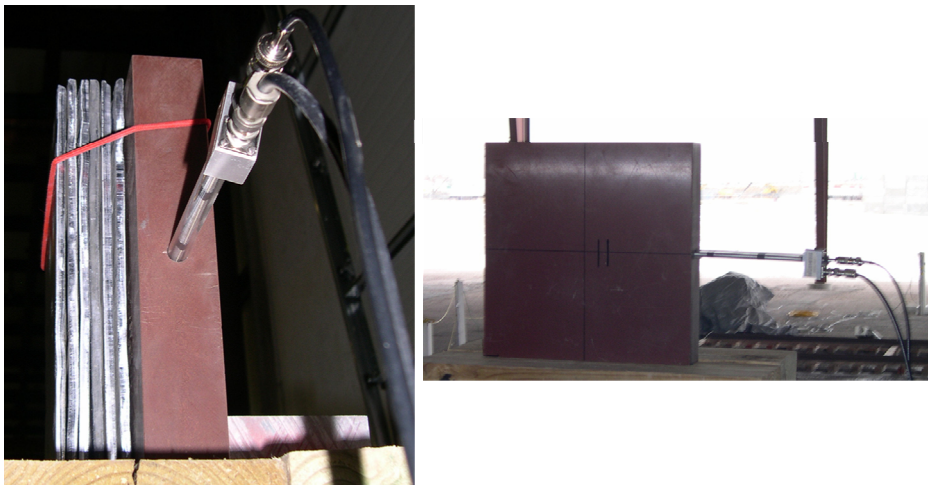

Figure 30. Absorbed Dose Measurement with 0.1cc Ion Chamber.

Table 11. Summary of Beam Energy Absorbed Dose Measurements.

Measurement	No. Runs
Virtual Water Phantom	3
Virtual Water Phantom + 0.635 cm Pb sheet	3
Virtual Water Phantom + 1.27 cm Pb sheet	3
Virtual Water Phantom + 1.91 cm Pb sheet	3
Virtual Water Phantom + 2.54 cm Pb sheet	3
Virtual Water Phantom + 3.18 cm Pb sheet	3
Virtual Water Phantom + 3.81 cm Pb sheet	3

Table 12. Summary of Average Environmental Conditions During Beam Energy Absorbed Dose Measurements.

Testing Facility	Idaho
Temperature	4.40 °C
Barometric Pressure	645 mm Hg
Relative Humidity	63%

4.6 Beam Profile Measurements

The ability to perform high-fidelity downfield dose measurements is predicated on the fact that the shape and size of the photon beam is well understood. The location of measurement positions as well as the difference from the primary beam and the air-scattered beam, hinges on a knowledge of the center of the beam as well as the edges. In order to gain an understanding of the beam size and shape, a series beam profile measurements were performed.

The basis for these measurements was sets of OSL dosimeters which were carefully positioned in order to provide a detailed set of dose data in a matrix array. The size of the matrix grid at close proximity downfield distances (i.e. 10 meters) was quite small while the size grew much bigger at far downfield distances (i.e. 100 plus meters). In all measurements, an attempt was made to ensure consistency in the total number of OSL dosimeters employed.

For logistical purposes, OSL dosimeters were attached to plastic sheeting (with clear adhesive tape) which allowed for the simplistic construction of large arrays at far downfield distances. Beam profile measurements were executed in timed runs of durations lasting several minutes. For all measurements, the center of the OSL dosimeter matrix was placed as close to the predicted beam center as possible. This center position was noted with great care as follow-on downfield measurements would be based on these locations.

Photographs of the set-up of the beam profile measurements are shown in Figure 31 and Figure 32. A summary of beam profiles measurements is shown in Table 13. A summary of the average environmental conditions during the beam profile measurements performed at downfield distances less than 100 meters is shown in Table 14. A summary of the average environmental conditions during the beam profile measurements performed at downfield distances greater than 100 meters is shown in Table 15.

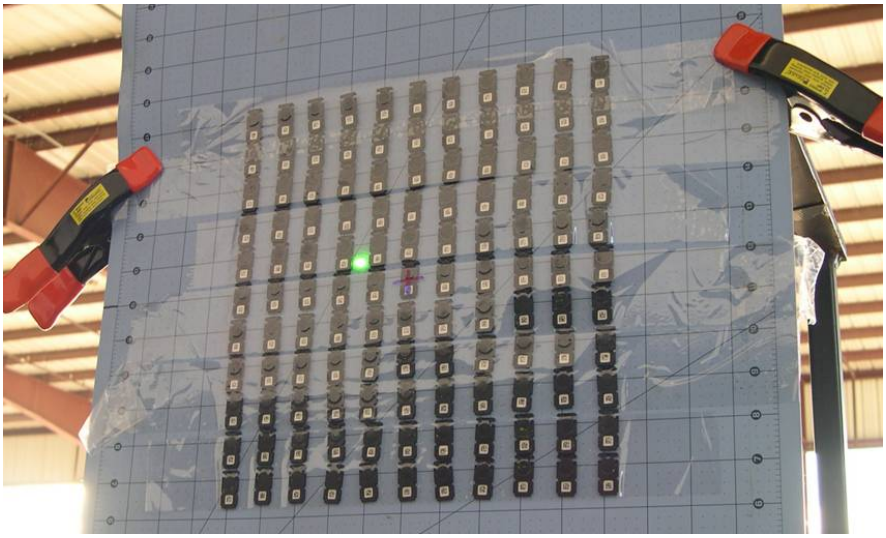

Figure 31. 8 meter Beam Profile Measurement Set-up.

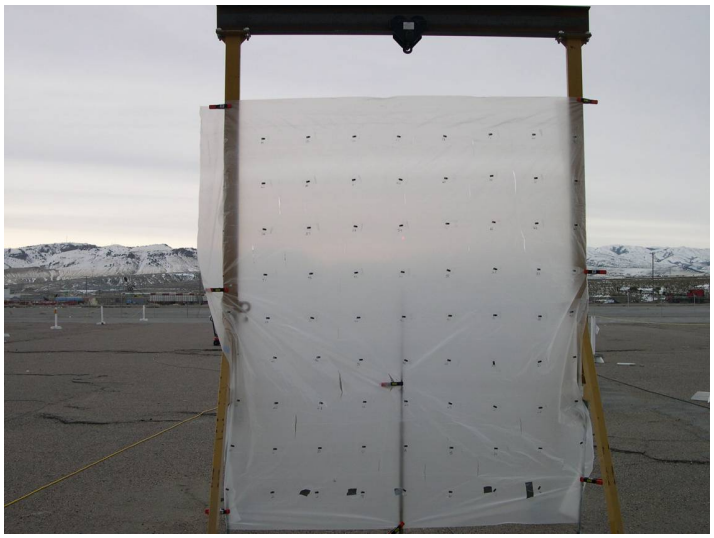

Figure 32. 50 meter Beam Profile Measurement Set-up.

Table 13. Summary of Beam Profile Measurements.

Downfield Distance [m]	Exposure Time [s]	OSL Array	# OSLs Used	Matrix Size [cm]	OSL Spacing [cm]	+ / - [cm]
8	600	11 x 11	121	25.4 x 25.4	2.54 x 2.54	0.635
30	600	6 x 5	30	38.1 x 30.5	7.62 x 7.62	0.635
50	900	9 x 9	81	274 x 274	30.48 x 30.48	1.27
120	600	9 x 9	81	274 x 274	30.48 x 30.48	1.27
170	600	9 x 9	81	274 x 274	30.48 x 30.48	1.27

Table 14. Summary of Average Environmental Conditions During Beam Profile Measurements (at Downfield Distances < 100 meters).

Testing Facility	Idaho
Temperature	5 °C
Barometric Pressure	651 mm Hg
Relative Humidity	45%

Table 15. Summary of Average Environmental Conditions During Beam Profile Measurements (at Downfield Distances > 100 meters).

Testing Facility	Virginia
Temperature	26 °C
Barometric Pressure	755 mm Hg
Relative Humidity	79%

4.7 Downfield Absorbed Dose Measurements

The objective of the present work is to predict doses resulting from the operation of the PITAS. The measurement of doses provides a useful set of data from which to compare computer simulations of dose for a unique radiation source geometry in an outdoor setting. In order to develop a set of comparative data, absorbed dose measurements were conducted at downfield locations from the PITAS prototype. Downfield is described as the area forward of the PITAS where doses result from the primary highly-collimated photon beam, the scattered beam and the area adjacent to the system itself. It should be noted that the contribution from the system decreased, the further downfield the measurements were performed.

Measurement locations were based on downfield distance and off-axis angle (distance). A set of distances and angles were selected and used for all measurements. Due to facility constraints and other testing activities, some measurements were performed at slightly different locations than those conducted at closer downfield distances. This included the prototype being in a non-fixed configuration for some of the measurements, therefore, the measurement geometry was dynamic. In general, off-axis distances were based on beam centerline estimates as dictated by beam profile measurements previously discussed. Every effort was made to ensure that the beam centerline was correlated to the off-axis location and each successive downfield distance location. Error in establishing each measurement location was inherent to the measurement conditions including weather, time of day, etc. Detectors were placed at the height of the central axis of the beam using tripods which were assembled to ensure that an area of direct interaction with

the beam was established thus minimizing any scattering effects. The terrain dictated the height of the detector such that the central axis of the beam was always intersected.

All measurement locations are reported with an uncertainty in off-axis distance in cm. A schematic of the notation for the measurement locations is shown in Figure 33. Absorbed dose measurements were performed using both the RADCAL Model RC1800 ion chamber and the Far West Model 1055 Chipmunk ion chamber. The RADCAL RC1800 was used to perform measurements near the primary beam (i.e. closer to beam centerline). The Far West Model 1055 Chipmunk was used to measure the air-scattered beam (i.e. increased off-axis distances). For all measurements, the RADCAL RC1800 was operated at a bias voltage of +300V and the Far West Model 1055 Chipmunk at a bias voltage of +800V. For both detectors, the integrated ionization current was measured with a Keithley Model 6517 electrometer and user interface as previously discussed. An example of a typical measurement set-up is shown in Figure 34.

A summary of downfield distances and off-axis angles/distances is shown in Table 16 through Table 20 for the primary beam measurements. A summary of downfield distances and off-axis angles/distances is shown in Table 21 through Table 23 for the air-scattered beam measurements. A summary of the average test environmental conditions for the 10 meter through 100 meter measurements is shown in Table 24 and the 170 meter measurements in Table 25.

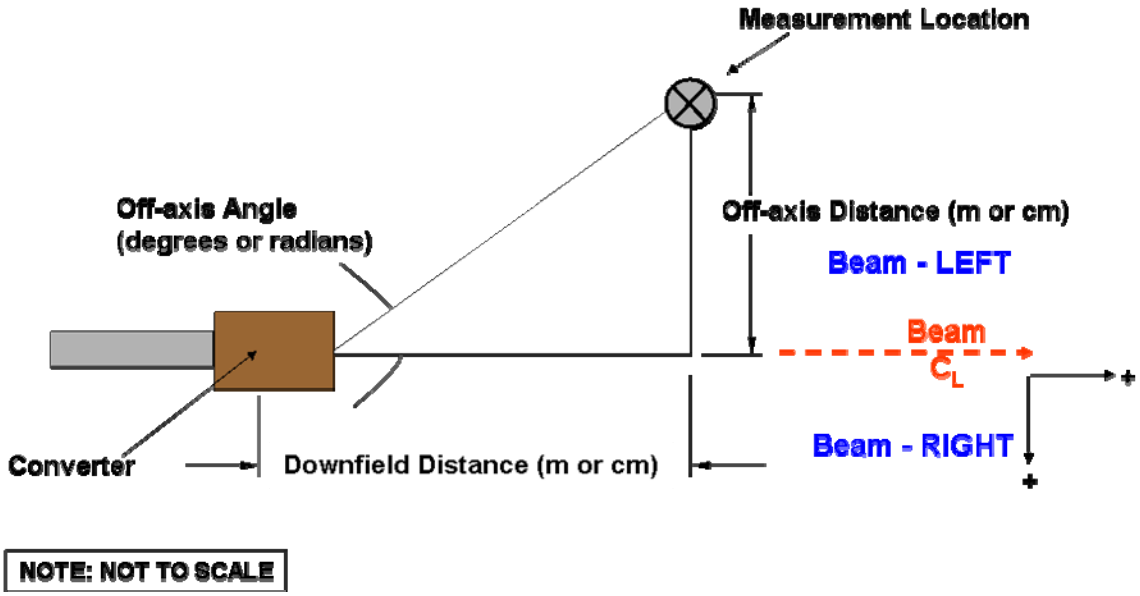

Figure 33. Schematic of Notation Used for Measurement Locations.

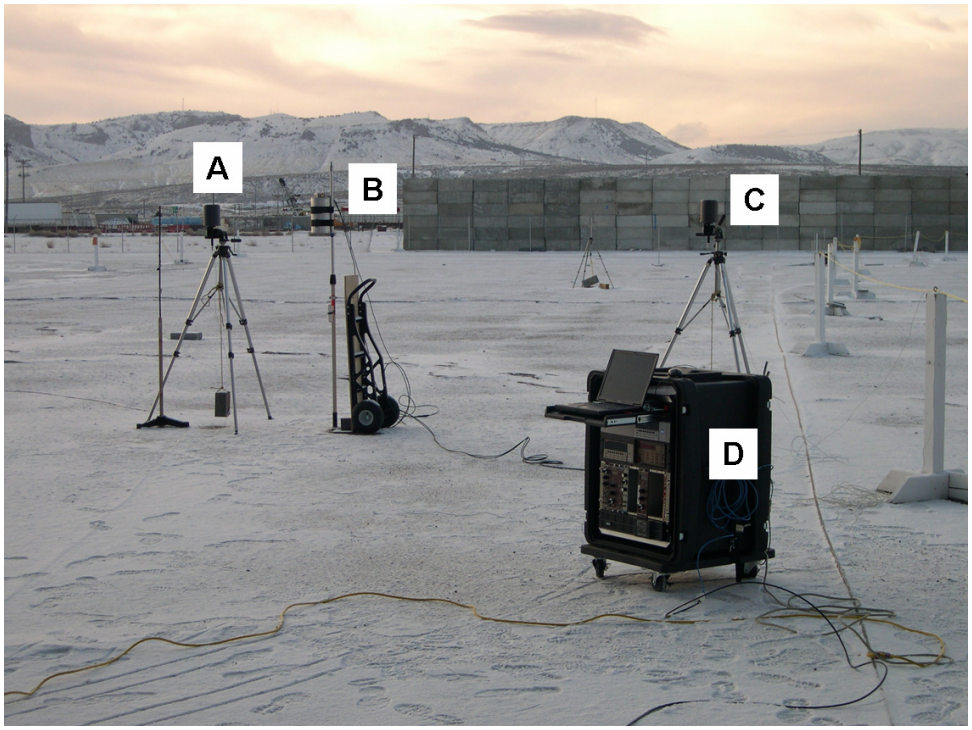

Figure 34. Typical Downfield Measurement Set-up at 50 meters.
Detectors at locations A and C are RADCAL RC1800 Ion Chambers. The detector at location B is a Far West Model 1055 Chipmunk. Location D is the instrument rack which housed the electronics. Note this measurement set taken during the winter in snowy conditions.

Table 16. Off-axis Angles/Distances for 10 meter Downfield Primary Beam Measurement Locations.

Downfield Distance		10 meters	Detector:	RADCAL RC1800	
Orientation from Beam Centerline	Off-axis Angle [degrees]	Off-axis Angle [radians]	Off-Axis Distance [m]	Off-Axis Distance [cm]	+ / - [cm]
Beam RIGHT	0.5	0.009	0.09	8.73	1.27
Beam RIGHT	1	0.017	0.17	17.5	1.27
Beam RIGHT	2	0.035	0.35	34.9	2.54
Beam RIGHT	5	0.087	0.87	87.5	5.08
Beam RIGHT	10	0.175	1.76	176	10.16
Beam RIGHT	20	0.349	3.64	364	10.16
Beam LEFT	-0.5	-0.009	-0.09	-8.73	-1.27
Beam LEFT	-1	-0.017	-0.17	-17.5	-1.27
Beam LEFT	-2	-0.035	-0.35	-34.9	-2.54
Beam LEFT	-5	-0.087	-0.87	-87.5	-5.08
Beam LEFT	-10	-0.175	-1.76	-176	-10.16
Beam LEFT	-20	-0.349	-3.64	-364	-10.16

Table 17. Off-axis Angles/Distances for 25 meter Downfield Primary Beam Measurement Locations.

Downfield Distance		25 meters	Detector:	RADCAL RC1800	
Orientation from Beam Centerline	Off-axis Angle [degrees]	Off-axis Angle [radians]	Off-Axis Distance [m]	Off-Axis Distance [cm]	+ / - [cm]
Beam RIGHT	0.5	0.009	0.22	21.8	1.27
Beam RIGHT	1	0.017	0.44	43.6	1.27
Beam RIGHT	2	0.035	0.87	87.3	5.08
Beam RIGHT	5	0.087	2.19	219	10.16
Beam RIGHT	10	0.175	4.41	441	10.16
Beam RIGHT	14.375	0.251	6.41	641	10.16
Beam LEFT	-0.5	-0.009	-0.22	-21.8	-1.27
Beam LEFT	-1	-0.017	-0.44	-43.6	-1.27
Beam LEFT	-2	-0.035	-0.87	-87.3	-5.08
Beam LEFT	-5	-0.087	-2.19	-219	-10.16
Beam LEFT	-10	-0.175	-4.41	-441	-10.16
Beam LEFT	-14.375	-0.251	-6.41	-641	-10.16

Table 18. Off-axis Angles/Distances for 50 meter Downfield Primary Beam Measurement Locations.

Downfield Distance		50 meters	Detector:	RADCAL RC1800	
Orientation from Beam Centerline	Off-axis Angle [degrees]	Off-axis Angle [radians]	Off-Axis Distance [m]	Off-Axis Distance [cm]	+ / - [cm]
Beam RIGHT	0.5	0.009	0.44	43.6	1.27
Beam RIGHT	1	0.017	0.87	87.3	1.27
Beam RIGHT	2	0.035	1.75	175	10.16
Beam RIGHT	5	0.087	4.37	437	10.16
Beam LEFT	-0.5	-0.009	-0.44	-43.6	-1.27
Beam LEFT	-1	-0.017	-0.87	-87.3	-1.27
Beam LEFT	-2	-0.035	-1.75	-175	-10.16
Beam LEFT	-5	-0.087	-4.37	-437	-10.16

Table 19. Off-axis Angles/Distances for 100 meter Downfield Primary Beam Measurement Locations.

Downfield Distance		100 meters	Detector:	RADCAL RC1800	
Orientation from Beam Centerline	Off-axis Angle [degrees]	Off-axis Angle [radians]	Off-Axis Distance [m]	Off-Axis Distance [cm]	+ / - [cm]
Beam RIGHT	0.078	0.001	0.14	13.6	1.27
Beam RIGHT	0.116	0.002	0.20	20	1.27
Beam RIGHT	0.155	0.003	0.27	27	1.27
Beam RIGHT	0.310	0.005	0.54	54	2.54
Beam LEFT	-0.078	-0.001	-0.14	-13.6	-1.27
Beam LEFT	-0.116	-0.002	-0.20	-20.3	-1.27
Beam LEFT	-0.155	-0.003	-0.27	-27	-1.27
Beam LEFT	-0.310	-0.005	-0.54	-54	-2.54

Table 20. Off-axis Angles/Distances for 170 meter Downfield Primary Beam Measurement Locations.

Downfield Distance		170 meters	Detector:	RADCAL RC1800	
Orientation from Beam Centerline	Off-axis Angle [degrees]	Off-axis Angle [radians]	Off-Axis Distance [m]	Off-Axis Distance [cm]	+ / - [cm]
Beam RIGHT	0.337	0.0059	1.00	100	10.16
Beam RIGHT	0.361	0.0063	1.07	107	10.16
Beam CENTER	0.000	0.000	0.00	0.00	10.16
Beam LEFT	-0.051	-0.001	-0.15	-15	-5.08
Beam LEFT	-0.103	-0.002	-0.31	-31	-5.08
Beam LEFT	-0.154	-0.003	-0.46	-46	-5.08
Beam LEFT	-0.206	-0.004	-0.61	-61	-5.08
Beam LEFT	-0.257	-0.004	-0.76	-76	-10.16
Beam LEFT	-0.308	-0.005	-0.91	-91	-10.16
Beam LEFT	-0.361	-0.006	-1.07	-107	-10.16
Beam LEFT	-0.411	-0.007	-1.22	-122	-10.16

Table 21. Off-axis Angles/Distances for 50 meter Downfield Air-Scattered Beam Measurement Locations.

Downfield Distance		50 meters	Detector:	Far West Chipmunk	
Orientation from Beam Centerline	Off-axis Angle [degrees]	Off-axis Angle [radians]	Off-Axis Distance [m]	Off-Axis Distance [cm]	+ / - [cm]
Beam RIGHT	0.40	0.007	0.4	35	2.54
Beam RIGHT	1.55	0.027	1.4	135	10.16
Beam RIGHT	2.69	0.047	2.4	235	10.16
Beam RIGHT	3.83	0.067	3.4	335	10.16
Beam RIGHT	11.7	0.204	10.4	1035	10.16
Beam RIGHT	14.1	0.247	12.6	1260	10.16
Beam LEFT	-0.40	-0.007	-0.4	-35	-2.54
Beam LEFT	-1.55	-0.027	-1.4	-135	-10.16
Beam LEFT	-2.69	-0.047	-2.4	-235	-10.16
Beam LEFT	-3.83	-0.067	-3.4	-335	-10.16
Beam LEFT	-11.7	-0.204	-10.4	-1035	-10.16
Beam LEFT	-14.1	-0.247	-12.6	-1260	-10.16

Table 22. Off-axis Angles/Distances for 100 meter Downfield Air-Scattered Beam Measurement Locations.

Downfield Distance		100 meters	Detector:	Far West Chipmunk	
Orientation from Beam Centerline	Off-axis Angle [degrees]	Off-axis Angle [radians]	Off-Axis Distance [m]	Off-Axis Distance [cm]	+ / - [cm]
Beam RIGHT	0.40	0.007	0.70	70	2.54
Beam RIGHT	0.97	0.017	1.70	170	10.16
Beam RIGHT	1.55	0.027	2.70	270	10.16
Beam RIGHT	2.12	0.037	3.70	370	10.16
Beam RIGHT	6.11	0.107	10.7	1070	10.16
Beam LEFT	-0.40	-0.007	-0.70	-70	-2.54
Beam LEFT	-0.97	-0.017	-1.70	-170	-10.16
Beam LEFT	-1.55	-0.027	-2.70	-270	-10.16
Beam LEFT	-2.12	-0.037	-3.70	-370	-10.16

Table 23. Off-axis Angles/Distances for 170 meter Downfield Air-Scattered Beam Measurement Locations.

Downfield Distance		170 meters	Detector:	Far West Chipmunk	
Orientation from Beam Centerline	Off-axis Angle [degrees]	Off-axis Angle [radians]	Off-Axis Distance [m]	Off-Axis Distance [cm]	+ / - [cm]
Beam RIGHT	0.050	0.001	0.15	15.0	1.27
Beam RIGHT	0.672	0.012	2.0	200	10.16
Beam RIGHT	1.009	0.018	3.0	300	10.16
Beam RIGHT	1.345	0.023	4.0	400	10.16
Beam RIGHT	1.682	0.029	5.0	500	10.16
Beam LEFT	-0.336	-0.006	-1.0	-100	-5.08
Beam LEFT	-1.345	-0.023	-4.0	-400	-10.16
Beam LEFT	-1.682	-0.029	-5.0	-500	-10.16

Table 24. Summary of Average Environmental Conditions During Downfield Absorbed Dose Measurements from 10 meters Through 100 meters

Testing Facility	Idaho
Temperature	5.75 °C
Barometric Pressure	658 mm Hg
Relative Humidity	28%

Table 25. Summary of Average Environmental Conditions During Downfield Absorbed Dose Measurements at 170 meters.

Testing Facility	Virginia
Temperature	26 °C
Barometric Pressure	755 mm Hg
Relative Humidity	79%

4.8 System Dose Measurements

In addition to understanding the downfield radiation doses created by the PITAS, a need exists to characterize the absorbed dose in close proximity to the system itself. The need for data in this area stems from a concern about radiation doses received by both operators and unintended people who may inadvertently be in the vicinity of the system while operating. Therefore, dose measurements were performed around the system to provide a data set for the characterization of the dose field in the immediate operating area of the PITAS. Dose measurements in the vicinity of the system were carried out using the RADCAL Model RC1800 ion chamber as well as the Bonner sphere spectrometer system for neutron dose equivalent. These measurements will be described in the subsequent subsections.

4.8.1 System Dose Measurements – RADCAL Model RC1800

Measurement locations were selected in order to obtain a good understanding of the dose field around the system. The RADCAL Model RC1800 was mounted on a tripod in the same manner used for downfield measurements. For all measurements, the RADCAL RC1800 was operated at a bias voltage of +300V and the integrated ionization current was measured with a Keithley Model 6517 electrometer and user interface as previously

discussed. An example of a typical measurement set-up is shown in Figure 35. Measurements were performed around the outer perimeter of the cargo container housing the PITAS prototype. A schematic of the measurement locations is shown in Figure 36 with a location summary shown in Table 26. A summary of the average environmental conditions during the measurements are shown in Table 27.

Figure 35. RADCAL Model RC1800 Ion Chamber Set-up for System Dose Measurements.

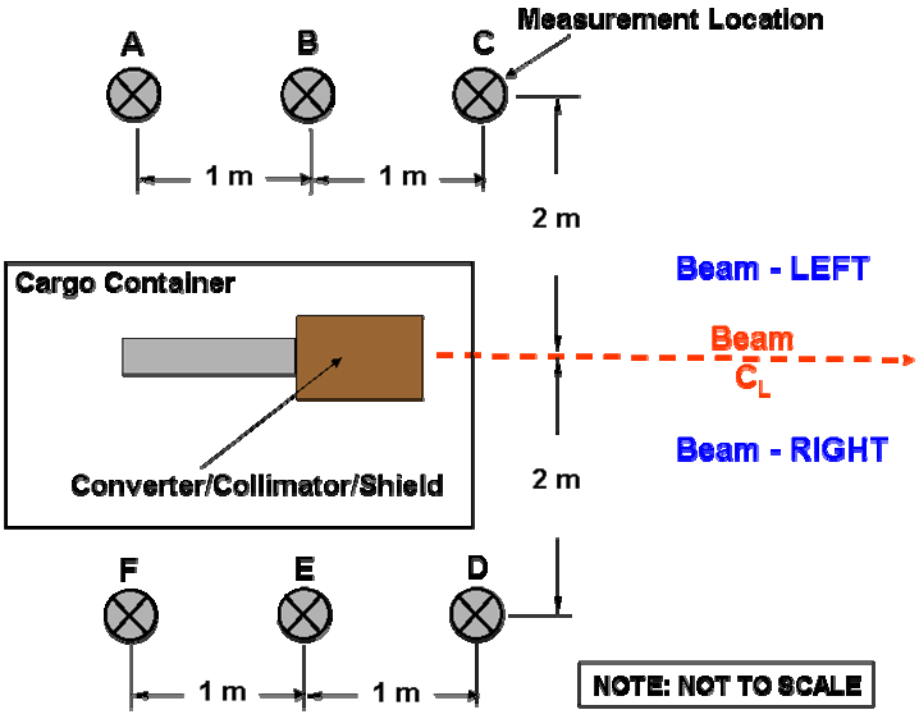

Figure 36. Schematic of System Dose Measurement Locations Performed with RADCAL Model RC1800 Ion Chamber. Note locations are labeled A through F, respectively.

Table 26. System Dose Measurement Locations Performed with RADCAL Model RC1800 Ion Chamber.

System Locations			Detector:	RADCAL RC1800	
Measurement Location	Orientation from Beam Centerline	Point of Reference	Downfield Distance [m]	Off-Axis Distance [m]	+ / - [m]
A	Beam LEFT	End of waveguide	0.00	2.00	0.10
B	Beam LEFT	End of waveguide	1.00	2.00	0.10
C	Beam LEFT	End of waveguide	2.00	2.00	0.10
D	Beam RIGHT	End of waveguide	2.00	2.00	0.10
E	Beam RIGHT	End of waveguide	1.00	2.00	0.10
F	Beam RIGHT	End of waveguide	0.00	2.00	0.10

Table 27. Summary of Average Environmental Conditions During System Absorbed Dose Measurements with RADCAL Model RC1800 Ion Chamber.

Testing Facility	Idaho
Temperature	4 °C
Barometric Pressure	649 mm Hg
Relative Humidity	45%

4.8.2 System Neutron Dose Equivalent Measurements – BSS System with TLDs

The pulsed nature of an accelerator and large radiofrequency field makes it difficult to use an active neutron detector, such as a LiI(Tl) scintillator, to acquire neutron spectra in the immediate vicinity of the accelerator due to problems encountered with detector dead time and pulse pile-up effects. Therefore, for the present work, neutron measurements were performed using a Bonner sphere spectrometer system with a coupled TLD-600/TLD-700 array. TLDs, being passive and integrating in nature, do not suffer from the effects of a scintillator and provide a favorable response over the neutron energy regime of interest. This has been a proven methodology utilized by various researchers and further details are presented by Sweezy [65]. A holder for the TLDs was developed to resemble a BSS scintillator detector. The holder will accommodate an array of 9 TLDs (5 TLD-600s and 4 TLD-700s). Positions A, C, E, G, and I contained TLD-600s while positions B, D, F, and H contained TLD-700s. This convention is shown schematically in Figure 37. A photograph of a typical measurement set-up is shown in Figure 38.

Neutron measurements were performed at three locations around the PITAS prototype as shown in Figure 39. Locations A and B match locations D and E from the RADCAL Model RC1800 measurements reported in the previous section. Location B is directly adjacent to the collimator. A summary of neutron measurement locations is presented in Table 28. A summary of the average environmental conditions during the neutron measurements are shown in Table 29.

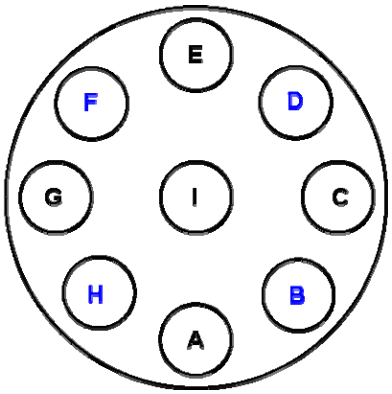

Figure 37. Schematic of TLD Location Convention.
Positions A, C, E, G and I contained TLD-600s. Postions B, D, F and H contained TLD-700s.

Figure 38. Setup of BSS System with TLDs for Neutron Measurements.

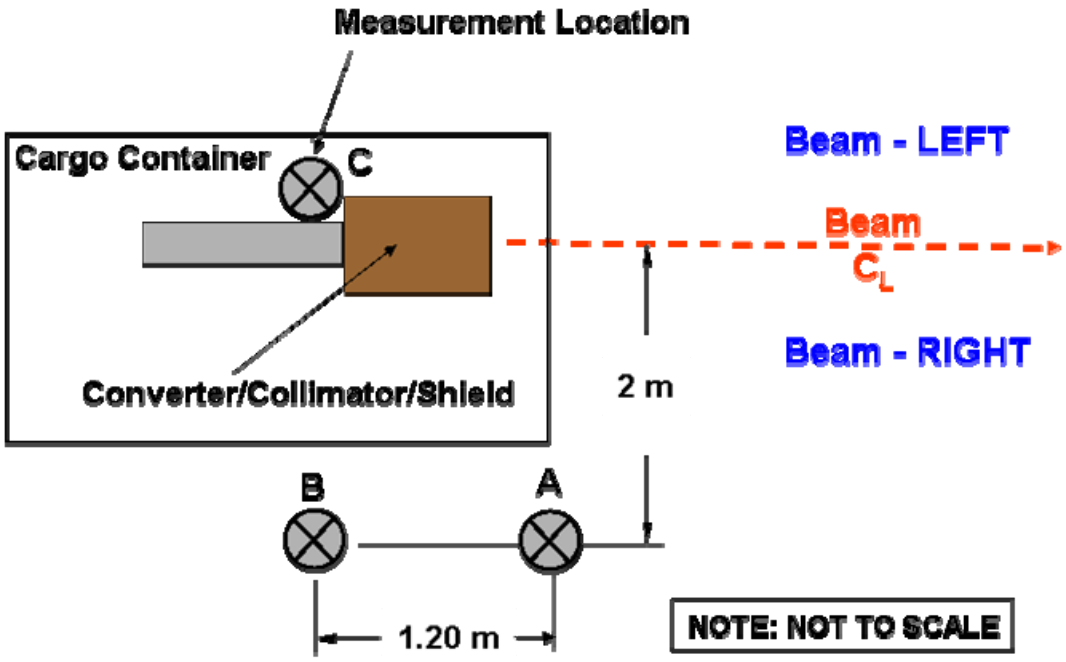

Figure 39. Schematic of System Neutron Measurement Locations Performed with a BSS System and TLDs. Note locations are labeled A through C, respectively.

Table 28. System Neutron Measurement Locations Performed with BSS System and TLDs.

System Locations		Detector: BSS System with TLDs			
Measurement Location	Orientation from Beam Centerline	Point of Reference	Downfield Distance [m]	Off-Axis Distance [m]	+ / - [m]
A	Beam LEFT	Front of container	-1.20	2.00	0.10
B	Beam CENTER	Collimator	-1.20	0.00	0.10
C	Beam RIGHT	Front of container	-1.20	2.00	0.10

Table 29. Summary of Average Environmental Conditions During System Neutron Measurements with BSS System and TLDs.

Testing Facility	Idaho
Temperature	10 °C
Barometric Pressure	655 mm Hg
Relative Humidity	38%

4.9 Results and Analysis

The following section provides data, results and analysis from all measurements performed. Several statistical methods were applied to the evaluation of measurement data. A discussion of these methods, including the assessment of outliers between multiple runs, error estimation and the propagation of errors throughout all measurements, is presented in Appendices B and C, respectively. In the following subsections, experimental data are presented in tabular form as well as plotted graphically to illustrate appropriate trends.

4.9.1 Beam Energy Measurements

Beam energy measurements were performed under the nominal operating parameters given in Table 30. The ionization charge reading, M was only corrected for temperature-pressure P_{TP}, and electrometer calibration P_{elec}, as given in Table 31. Data (with associated relative uncertainty) used to calculate the absorbed dose are given in Table 32. The absorbed dose as a function of lead sheet thickness with associated uncertainties are given in Table 33 and shown in Figure 40. The attenuation of the beam by the Pb sheets follows an expected trend. One can observe the hardening of the photon beam which occurs after three Pb sheets are present. This is visually represented by the slight dip in absorbed dose response at 1.905 cm.

Table 30. Nominal Operating Conditions for Beam Energy Absorbed Dose Measurements.

Parameter	System Setting
Instantaneous Beam Current, I_{INST}	35 mA
Average Beam Current, I_{AVG}	8.4 μA
Repetition Rate, f	60 Hz
Pulse Width, t	4 ms

Table 31. Ionization Charge Correction Factors Applied to Absorbed Dose Beam Energy Measurements.

Correction Factor	Value
Temperature-Pressure Correction, P_{TP}	Varied by Run
Electrometer Calibration Factor, P_{elec}	0.99

Table 32. Data Used to Calculate Absorbed Dose for Beam Energy Measurements.

Parameter	Units	Value	Absolute Uncertainty	Relative Uncertainty
Q	nC	Varied by Run	0.001	Varied by Run
(W/e)	J/C	33.9	1.7	0.05
Sw,g	unitless	0.84	0.01	0.01
M_g	kg	0.143	0.008	0.06
T	°C	Varied by Run	0.1	Varied by Run
P	mm Hg	Varied by Run	1.5	Varied by Run
Q_k	nC	19	0.001	0.00005
Q_m	nC	18.9	0.001	0.00005

Table 33. Absorbed Dose Beam Energy Measurement Data.

Measurement Description	Pb Thickness [cm]	D_{air} [Gy]	δD_{air} [Gy]	D_{air} [Gy/μC]	δD_{air} [Gy/μC]
Virtual Water Phantom Only	0.00	2.07E+00	2E-01	2.47E-01	3E-02
Virtual Water Phantom + 1 sheet lead	0.64	1.68E+00	1E-01	2.00E-01	2E-02
Virtual Water Phantom + 2 sheets lead	1.27	1.21E+00	9E-02	1.44E-01	1E-02
Virtual Water Phantom + 3 sheets lead	1.91	8.05E-01	6E-02	9.59E-02	7E-03
Virtual Water Phantom + 4 sheets lead	2.54	6.21E-01	5E-02	7.39E-02	6E-03
Virtual Water Phantom + 5 sheets lead	3.18	4.49E-01	4E-02	5.35E-02	4E-03
Virtual Water Phantom + 6 sheets lead	3.81	2.63E-01	2E-02	3.14E-02	2E-03

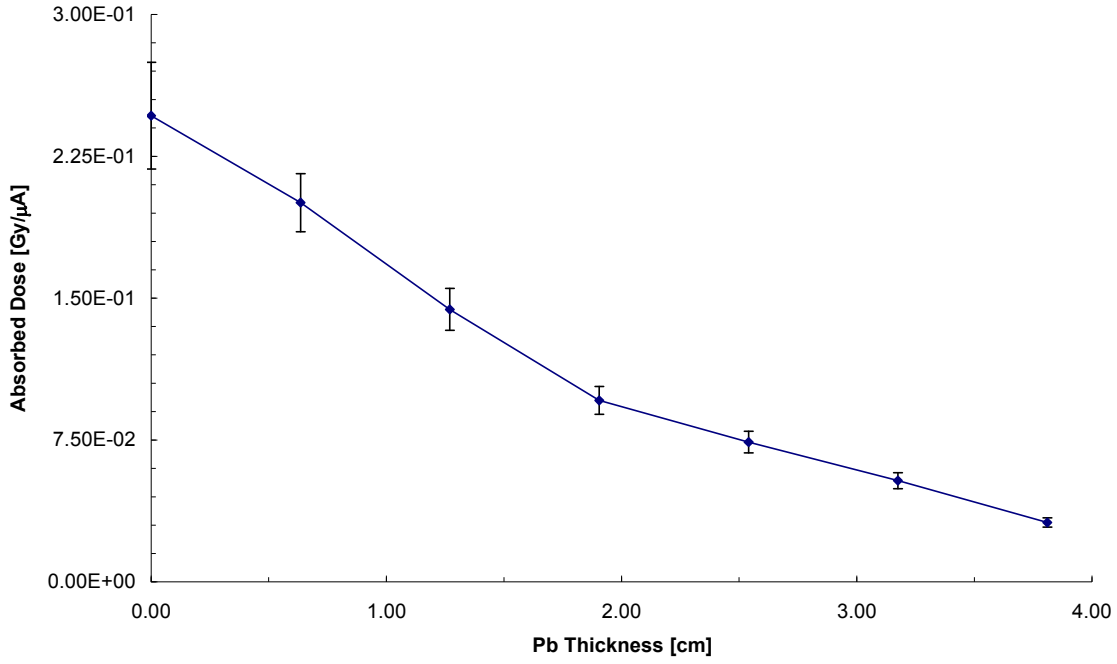

Figure 40. Absorbed Dose Beam Energy Measurements.

4.9.2 Beam Profile Measurements

The beam profile measurements began with a geometrical estimate of the beam size and shape. This simplistic assessment provided a baseline for the comparison of beam profile measurements obtained at various downfield distances. This approach employed the use of similar triangles which simply put states that *if two corresponding sides of two triangles are in proportion, and their included angles are equal, then the triangles are similar.* Therefore, if the length, L_1 and diameter D_1, of the collimator are known, then a similar triangles estimate of the corresponding beam diameter, D_2, can be made at various downfield distances, L_2. This relationship is shown in the schematic in Figure 41 and calculated estimates of beam diameter are given in Table 34.

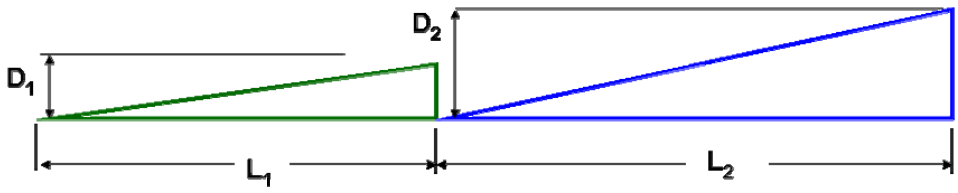

Figure 41. Schematic of Similar Triangles Approach.

Table 34. Projected Beam Diameters at Various Downfield Distances.

Collimator Diameter [m]	Collimator Length [m]	Downfield Distance [m]	Projected Beam Diameter [m]
0.01	0.5	3	0.04
0.01	0.5	8	0.11
0.01	0.5	10	0.14
0.01	0.5	25	0.3
0.01	0.5	30	0.4
0.01	0.5	50	0.7
0.01	0.5	100	1.4
0.01	0.5	120	1.7
0.01	0.5	170	2.4

Beam profile measurement data using OSL dosimeters were translated into contour plots. Plots were also generated with a to-scale overlay of the projected beam diameter. At downfield distances of 8 meters and 50 meters, the entire beam, including the air-scattered secondary beam, were captured within the plot. An estimate of the outer diameter of the scattered beam was made and was roughly two times the projected primary beam diameter. Finally, 3-dimensional plots of all beam profiles are also reported to provide perspective on beam shape. All beam profile data (intensity) are reported in units of Gy/μC. Contour plots for beam profiles measurements in accordance with the above scenarios at 8 meters, 30 meters, 50 meters, 120 meters and 170 meters are shown in Figure 42 through Figure 58.

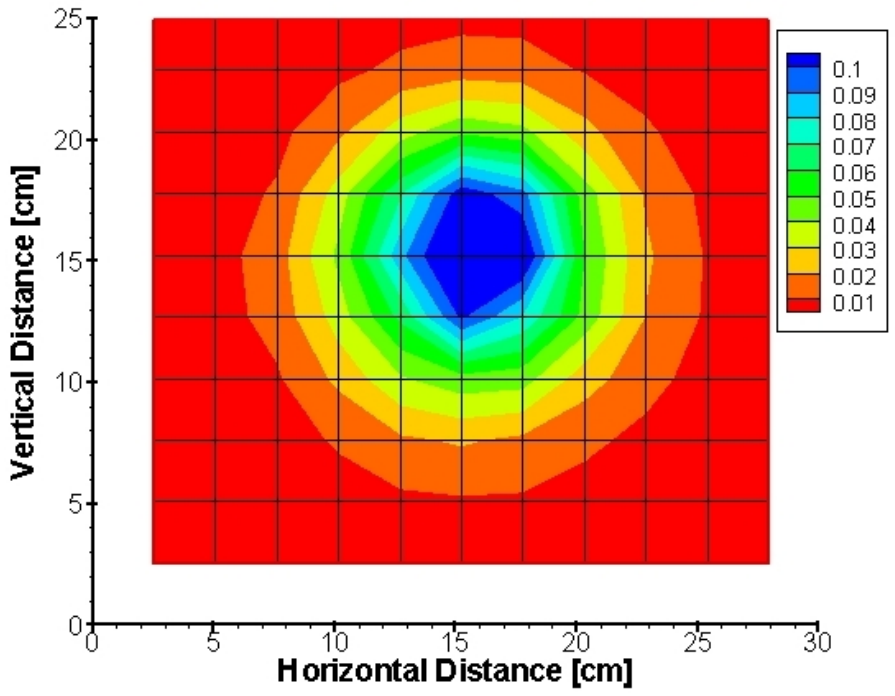

Figure 42. 8 meter 2-Dimensional Beam Profile.

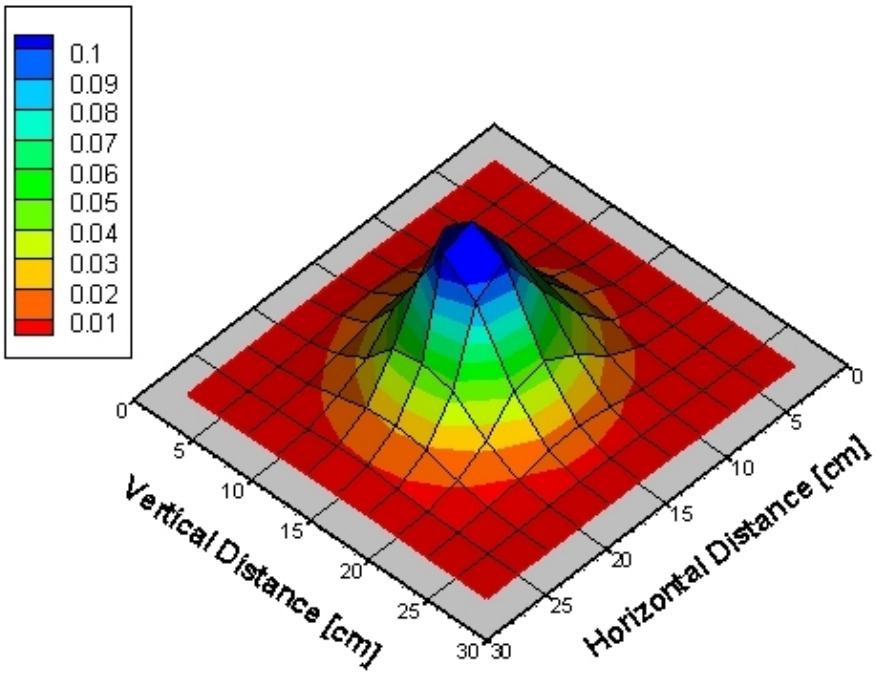

Figure 43. 8 meter 3-Dimensional Beam Profile.

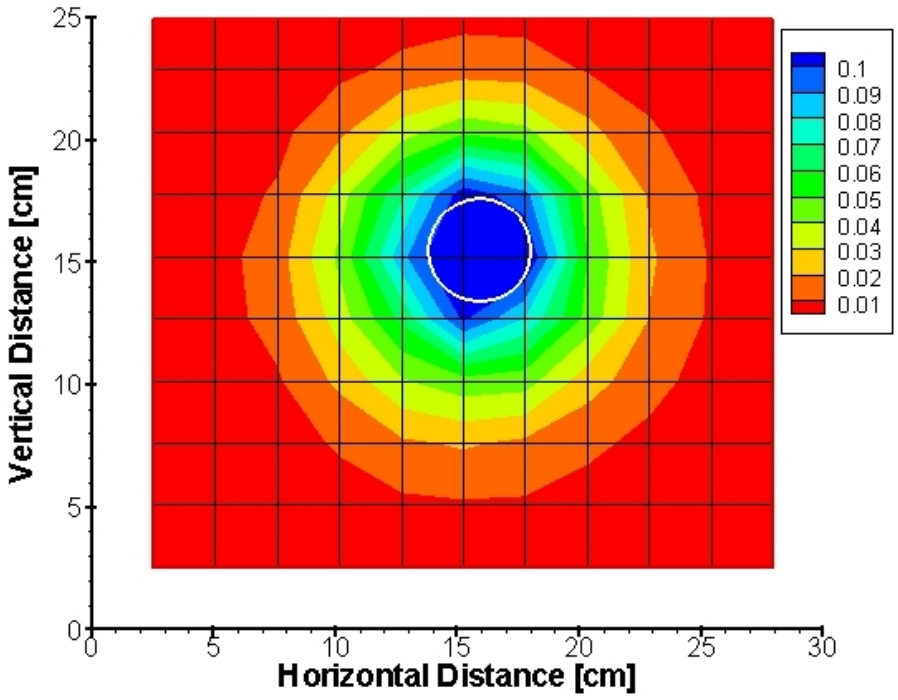

Figure 44. 8 meter 2-Dimensional Beam Profile with Geometrically Calculated Primary Beam Diameter Overlayed.

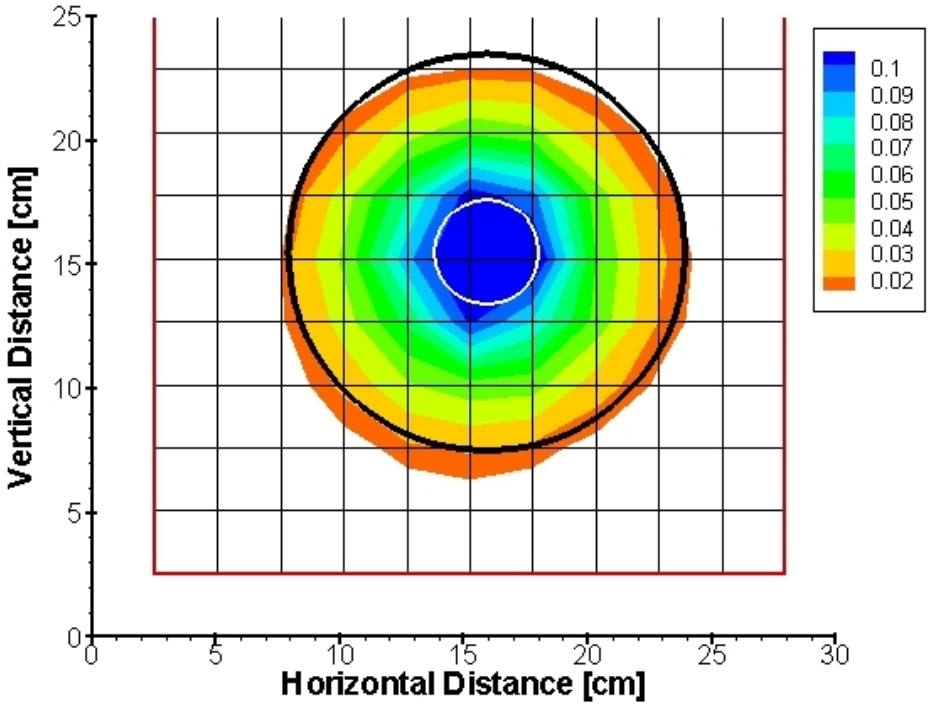

Figure 45. 8 meter 2-Dimensional Beam Profile with Projected Secondary Air-Scattered Beam Diameter Overlayed.

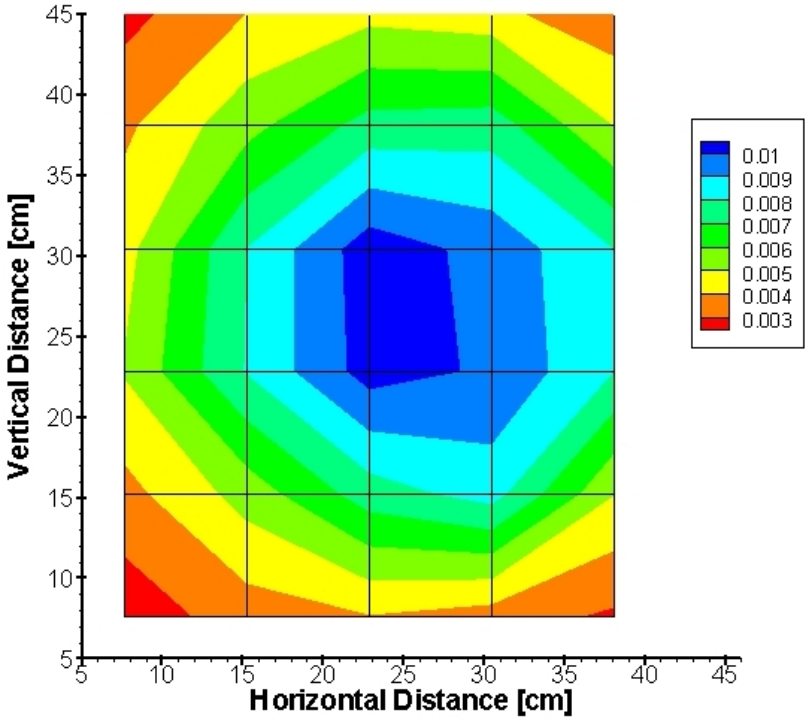

Figure 46. 30 meter 2-Dimensional Beam Profile.

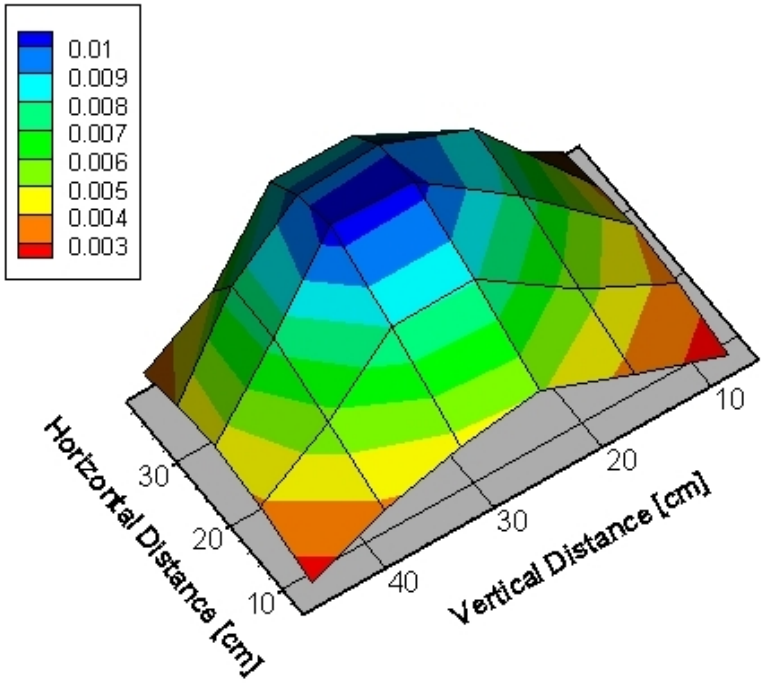

Figure 47. 30 meter 3-Dimensional Beam Profile.

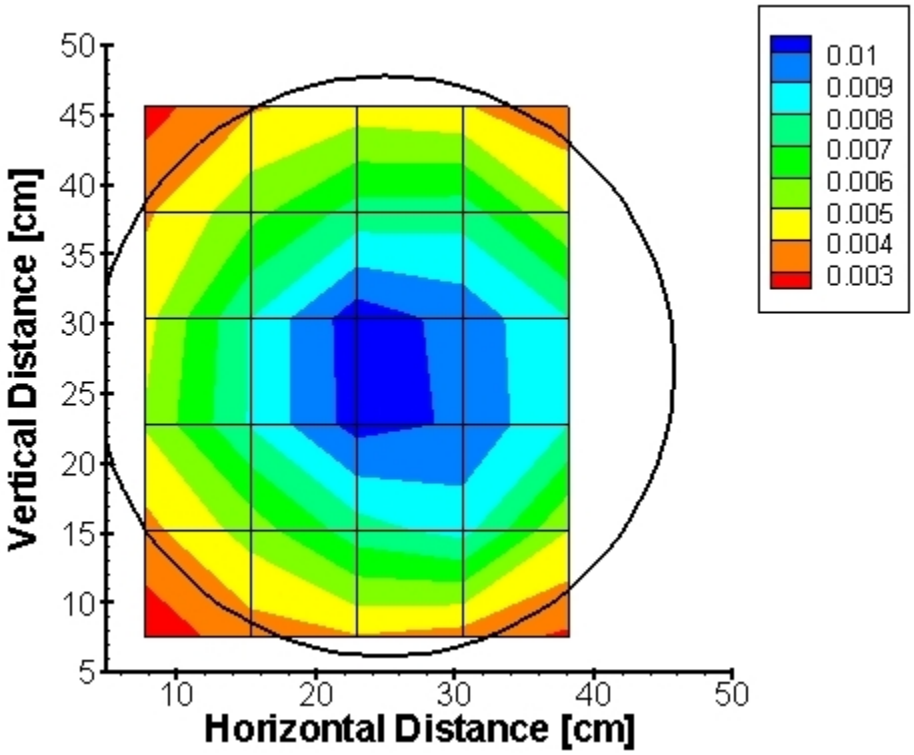

Figure 48. 30 meter 2-Dimensional Beam Profile with Geometrically Calculated Primary Beam Diameter Overlayed. Note the OSL array was not large enough to capture the entire beam.

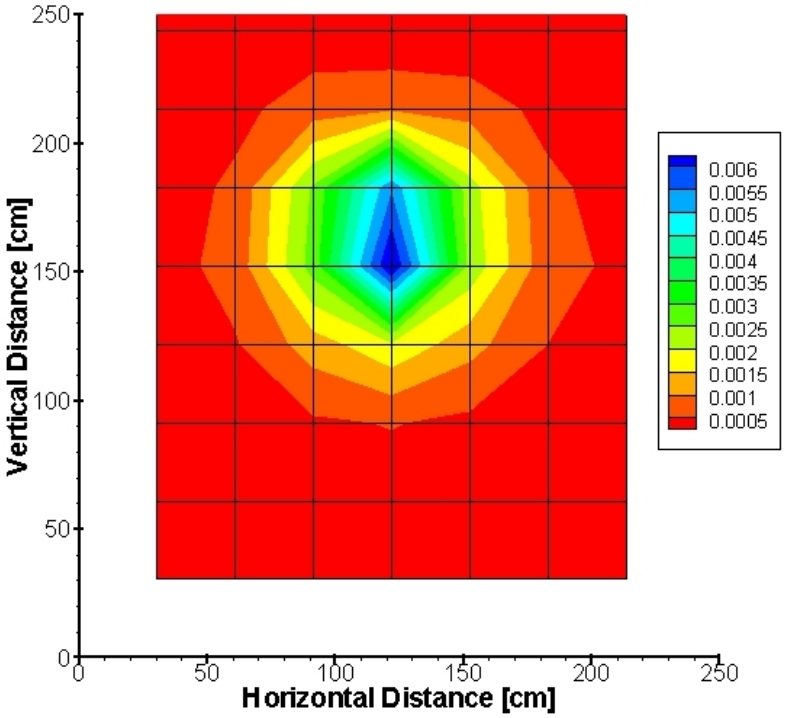

Figure 49. 50 meter 2-Dimensional Beam Profile.

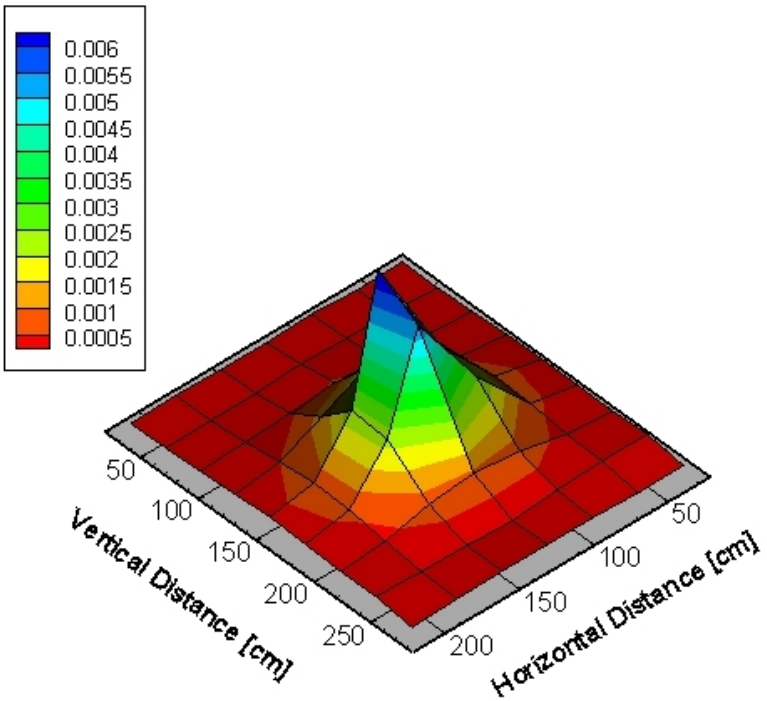

Figure 50. 50 meter 3-Dimensional Beam Profile.

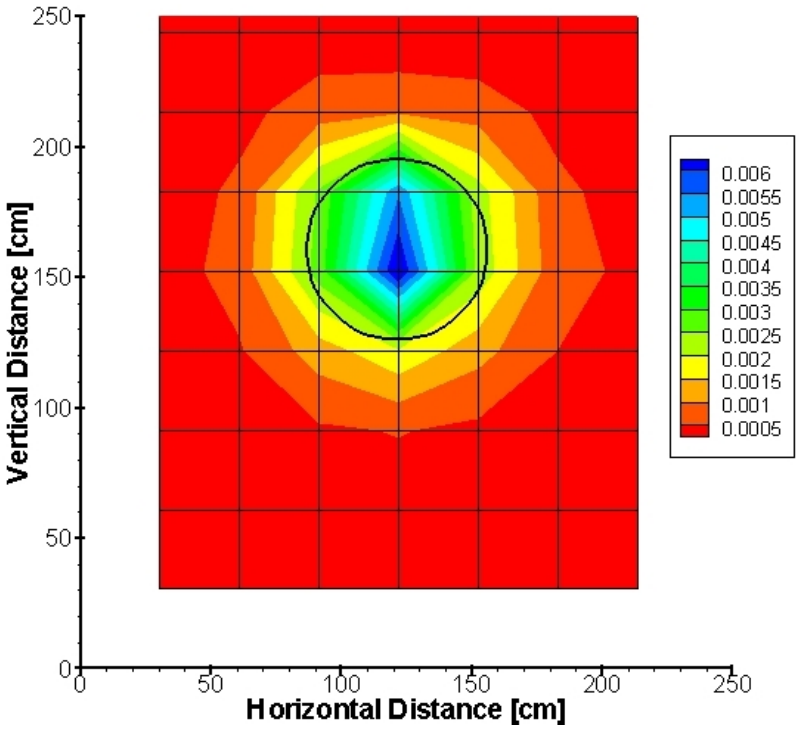

Figure 51. 50 meter 2-Dimensional Beam Profile with Geometrically Calculated Primary Beam Diameter Overlayed.

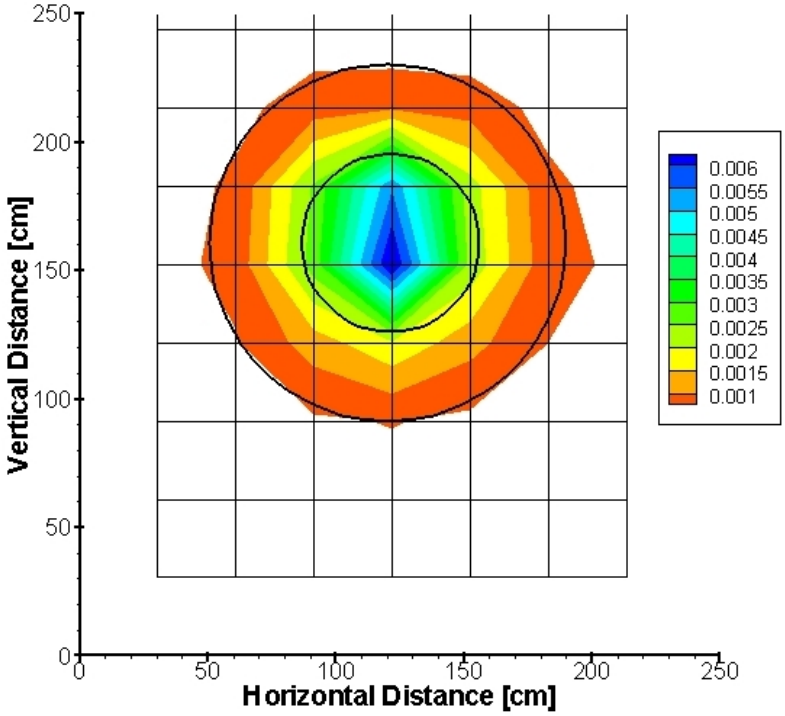

Figure 52. 50 meter 2-Dimensional Beam Profile with Projected Secondary Air-Scattered Beam Diameter Overlayed.

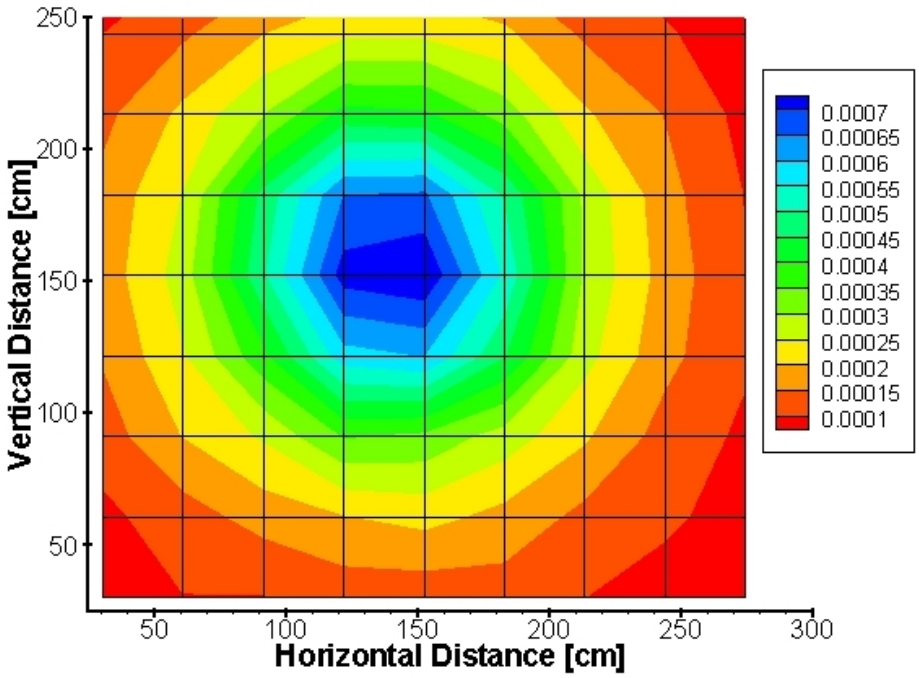

Figure 53. 120 meter 2-Dimensional Beam Profile.

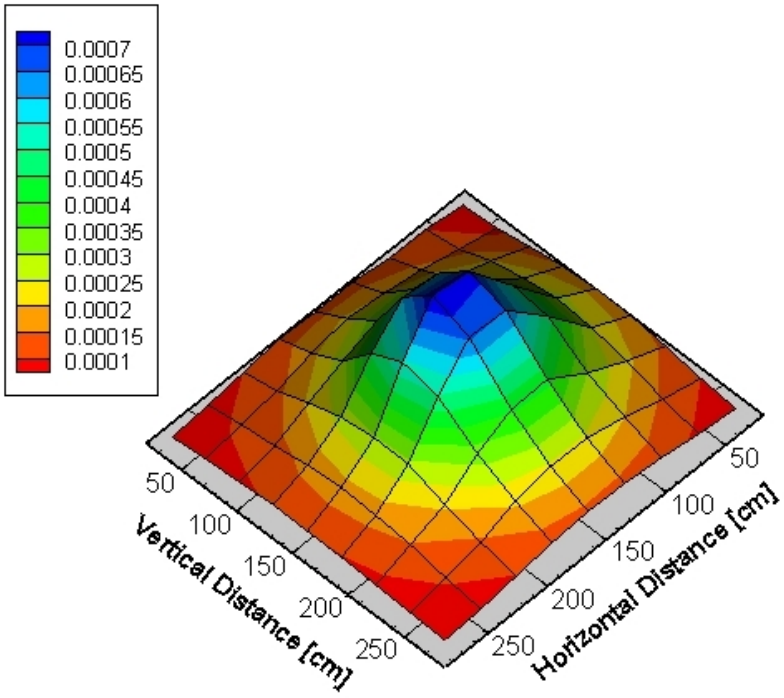

Figure 54. 120 meter 3-Dimensional Beam Profile.

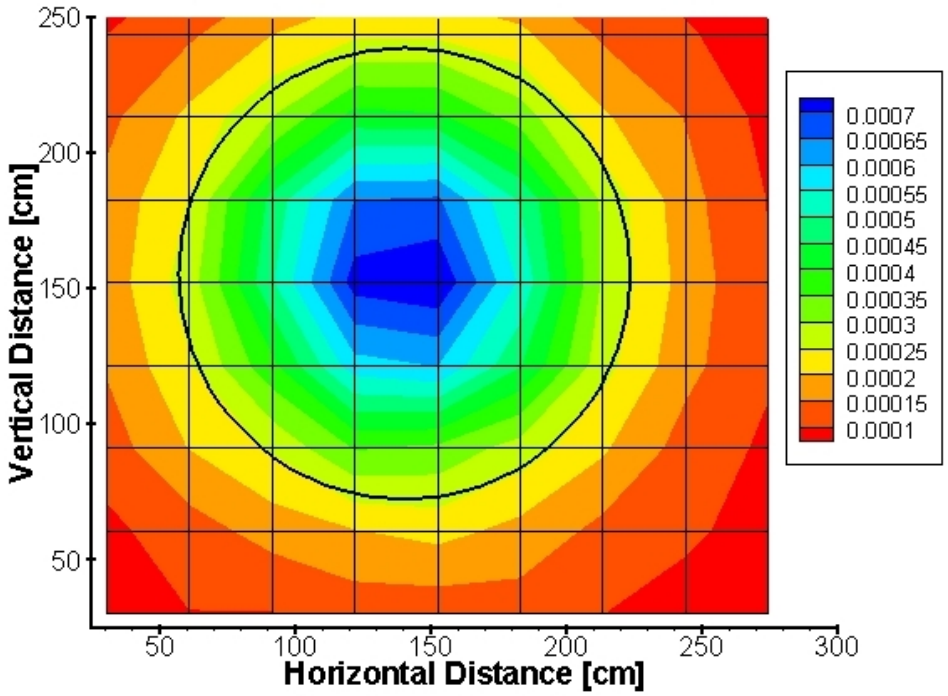

Figure 55. 120 meter 2-Dimensional Beam Profile with Geometrically Calculated Primary Beam Diameter Overlayed.

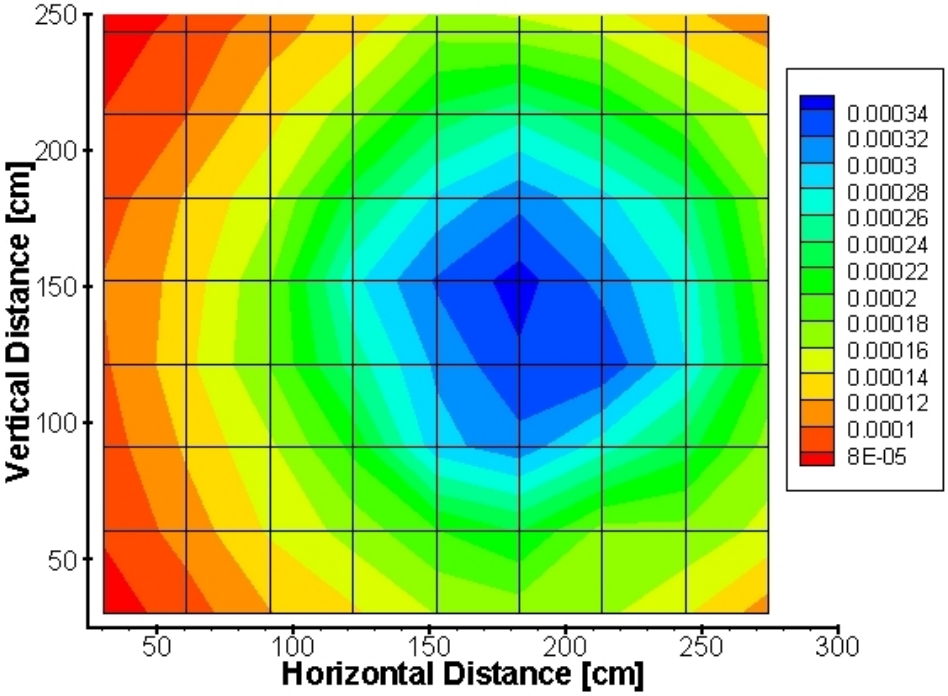

Figure 56. 170 meter 2-Dimensional Beam Profile.

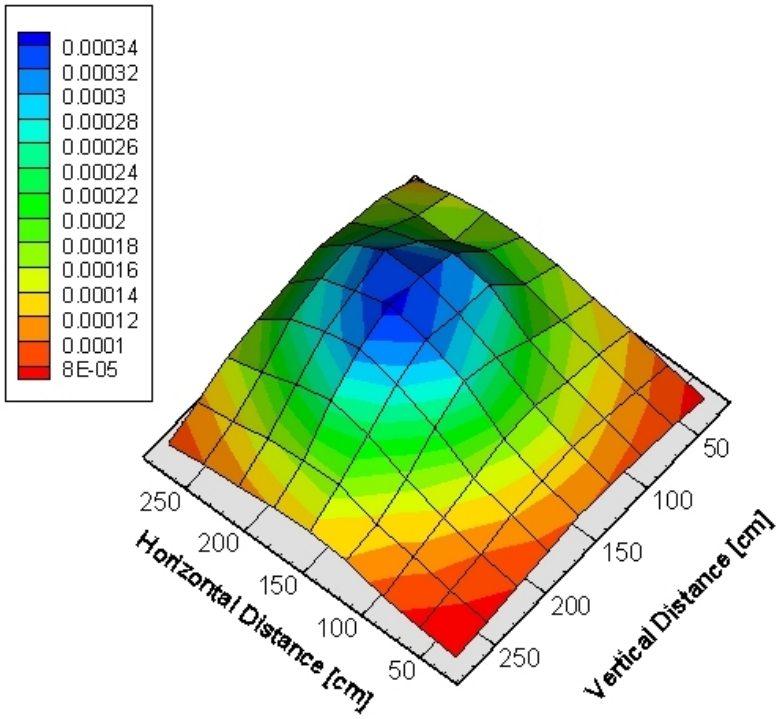

Figure 57. 170 meter 3-Dimensional Beam Profile.

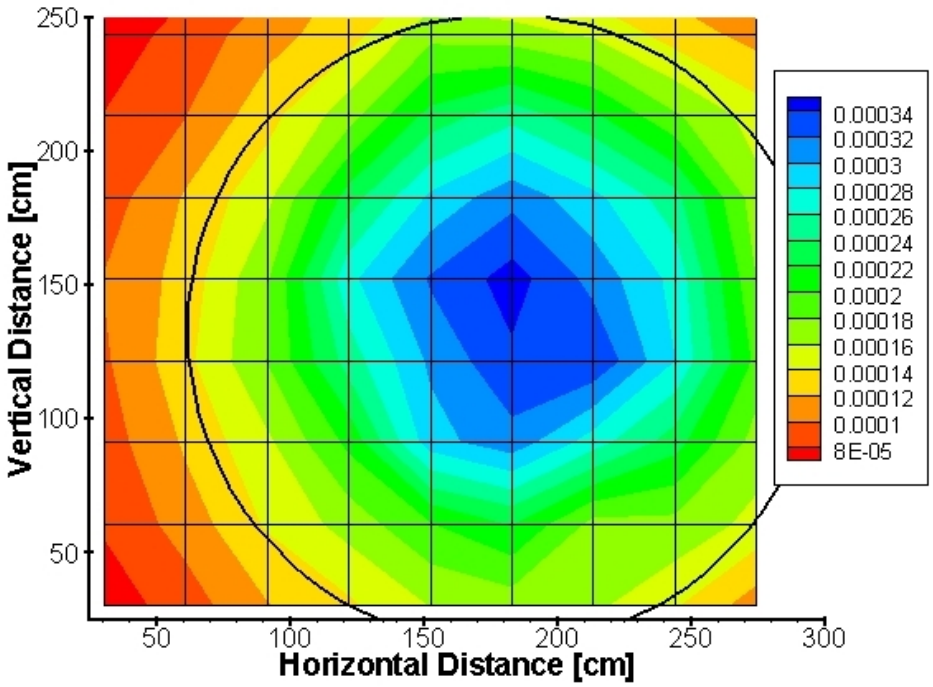

Figure 58. 170 meter 2-Dimensional Beam Profile with Geometrically Calculated Primary Beam Diameter Overlayed. Note the OSL array was not large enough to capture the entire beam.

4.9.3 Downfield Absorbed Dose Measurements

Downfield absorbed dose measurements were performed under the nominal operating parameters given in Table 35 and Table 36. The ionization charge reading, M was corrected for all pulsed effects using equations (4.1) through (4.5). The results of these corrections, which were utilized in all downfield absorbed dose measurements are given in Table 37 and Table 38. Data (with associated relative uncertainty) used to calculate the absorbed doses are given in Table 39 and Table 40. Downfield absorbed doses were calculated using these data and equation (4.7).

The absorbed doses from the primary beam measured with the RADCAL Model RC1800 ion chamber and Far West Model 1055 Chipmunk at downfield distances of 10 meters, 25 meters, 50 meters, 100 meters, and 170 meters are given in Table 41 through Table 48 and shown in Figure 59 through Figure 67.

Table 35. Nominal Operating Conditions for Downfield (< 100 meters) Absorbed Dose Measurements

Parameter	System Setting
Instaneous Beam Current, I_{INST}	35 mA
Average Beam Current, I_{AVG}	8.4 μA
Repetition Rate, f	60 Hz
Pulse Width, t	4 μs

Table 36. Nominal Operating Conditions for Downfield (> 100 meters) Absorbed Dose Measurements

Parameter	System Setting
Instaneous Beam Current, I_{INST}	60 mA
Average Beam Current, I_{AVG}	28.8 μA
Repetition Rate, f	120 Hz
Pulse Width, t	4 μs

Table 37. Ionization Charge Correction Factors Applied to Primary Beam (RADCAL Model RC1800) Downfield Absorbed Dose Measurements.

Correction Factor	Value
Ionic Recombination Correction, P_{ion}	0.999
Polarity Correction, P_{pol}	1.06
Temperature-Pressure Correction, P_{TP}	Varied by Run
Electrometer Calibration Factor, P_{elec}	0.99

Table 38. Ionization Charge Correction Factors Applied to Secondary Beam (Far West Model 1055 Chipmunk) Downfield Absorbed Dose Measurements.

Correction Factor	Value
Ionic Recombination Correction, P_{ion}	1.01
Polarity Correction, P_{pol}	1.01
Electrometer Calibration Factor, P_{elec}	0.99

Table 39. Data Used to Calculate Absorbed Dose for Primary Beam (RADCAL Model RC1800) Downfield Absorbed Dose Measurements.

Parameter	Units	Value	Absolute Uncertainty	Relative Uncertainty
Q	nC	Varied by Run	0.001	Varied by Run
(W/e)	J/C	33.9	1.7	0.05
Sw,g	unitless	0.892	0.001	0.001
M_g	kg	0.00217	0.0001	0.05
$N_{chamber}$	Gy/C	1.56E+04	8.00E+02	0.05
T	°C	Varied by Run	0.1	Varied by Run
P	mm Hg	Varied by Run	1.5	Varied by Run
V_H	V	300	5	0.02
V_L	V	150	5	0.03
$M_{raw}{}^H$	nC	6.24	0.001	0.0002
$M_{raw}{}^L$	nC	6.25	0.001	0.0002
V --- $M_{raw}{}^+$	V	300	5	0.02
V --- $M_{raw}{}^-$	V	-300	5	-0.02
V --- M_{raw}	V	300	5	0.02
$M_{raw}{}^+$	nC	6.24	0.001	0.0002
$M_{raw}{}^-$	nC	-6.95	0.001	-0.0001
M_{raw}	nC	6.24	0.001	0.0002
Q_k	nC	19	0.001	0.0001
Q_m	nC	18.9	0.001	0.0001

Table 40. Data Used to Calculate Absorbed Dose for Primary Beam (Far West Model 1055 Chipmunk) Downfield Absorbed Dose Measurements.

Parameter	Units	Value	Absolute Uncertainty	Relative Uncertainty
Q	nC	Varied by Run	0.001	Varied by Run
(W/e)	J/C	33.9	1.7	0.05
Sw,g	unitless	0.891	0.001	0.001
M_g	kg	0.00412	0.0001	0.02
$N_{chamber}$	Gy/C	4.73E+05	2.40E+04	0.05
V_H	V	800	5	0.006
V_L	V	400	5	0.01
$M_{raw}{}^H$	nC	8.8	0.001	0.0001
$M_{raw}{}^L$	nC	8.76	0.001	0.0001
V --- $M_{raw}{}^+$	V	800	5	0.006
V --- $M_{raw}{}^-$	V	-800	5	0.006
V --- M_{raw}	V	800	5	0.006
$M_{raw}{}^+$	nC	8.56	0.001	0.0001
$M_{raw}{}^-$	nC	-8.73	0.001	0.0001
M_{raw}	nC	8.56	0.001	0.0001
Q_k	nC	19	0.001	0.00005
Q_m	nC	18.9	0.001	0.00005

Table 41. 10 meter (RADCAL Model RC1800) Absorbed Dose Measurement Data.

Orientation from Beam Centerline	Off-axis Angle [degrees]	D_{air} [Gy]	δD_{air} [Gy]	D_{air} [Gy/μC]	δD_{air} [Gy/μC]
Beam RIGHT	0.50	3.42E-02	2E-03	3.40E-05	2E-06
Beam RIGHT	1.00	5.79E-03	4E-04	5.78E-06	4E-07
Beam RIGHT	2.00	9.64E-04	6E-05	9.60E-07	6E-08
Beam RIGHT	5.00	3.07E-04	2E-05	3.06E-07	2E-08
Beam RIGHT	10.00	1.75E-04	1E-05	1.74E-07	1E-08
Beam LEFT	-0.50	9.67E-03	7E-04	9.46E-06	7E-07
Beam LEFT	-1.00	1.44E-03	1E-04	1.43E-06	9.6E-08
Beam LEFT	-2.00	9.71E-04	6E-05	9.63E-07	6.3E-08
Beam LEFT	-5.00	5.15E-04	3E-05	5.14E-07	3.4E-08
Beam LEFT	-10.00	1.51E-04	1E-05	1.51E-07	9.8E-09
Beam LEFT	-20.00	3.59E-05	2E-06	3.57E-08	2.3E-09

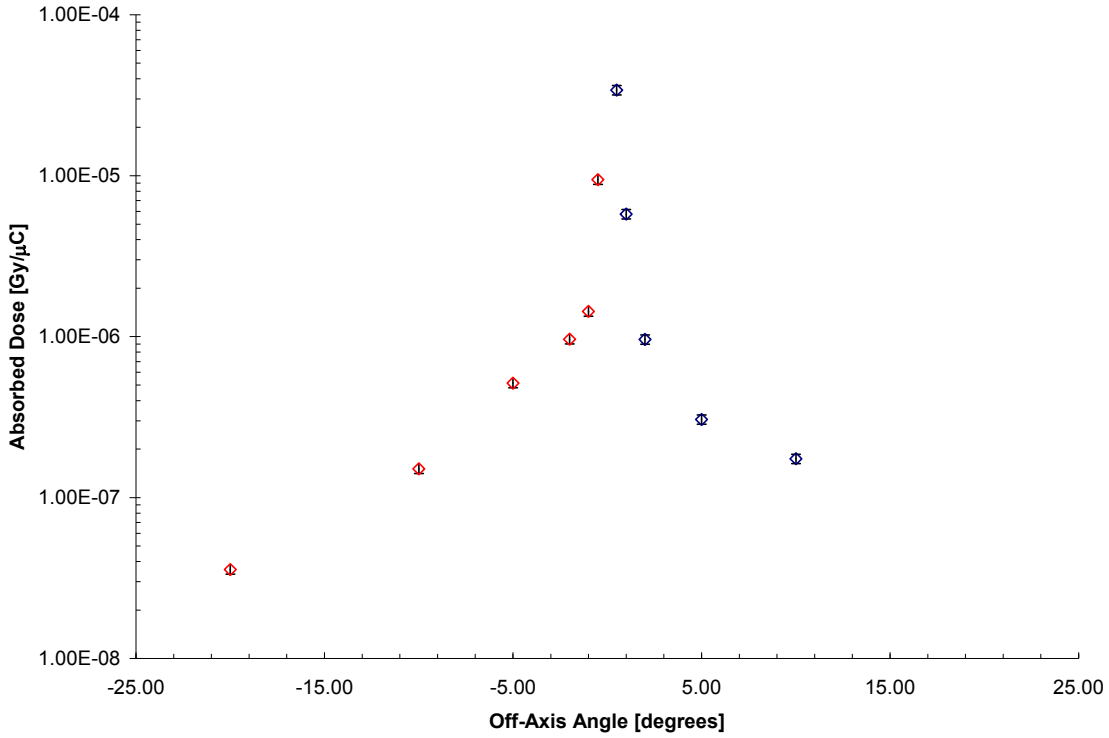

Figure 59. 10 meter Beam (RADCAL Model RC1800) Absorbed Dose Measurement. (The error bars are smaller than the size of the symbols).

Table 42. 25 meter (RADCAL Model RC1800) Absorbed Dose Measurement Data.

Orientation from Beam Centerline	Off-axis Angle [degrees]	D_{air} [Gy]	δD_{air} [Gy]	D_{air} [Gy/μC]	δD_{air} [Gy/μC]
Beam RIGHT	0.50	2.30E-03	2E-04	2.22E-06	2E-07
Beam RIGHT	1.00	2.48E-04	2E-05	2.43E-07	2E-08
Beam RIGHT	2.00	1.17E-04	8E-06	1.14E-07	8E-09
Beam RIGHT	5.00	4.45E-05	3E-06	4.33E-08	3E-09
Beam RIGHT	10.00	2.03E-05	1E-06	1.98E-08	1E-09
Beam RIGHT	14.38	9.99E-06	7E-07	9.75E-09	6.9E-10
Beam LEFT	-0.50	2.72E-03	2E-04	2.69E-06	2E-07
Beam LEFT	-1.00	2.34E-04	2E-05	2.27E-07	1.6E-08
Beam LEFT	-2.00	1.00E-04	7E-06	9.77E-08	6.7E-09
Beam LEFT	-5.00	3.76E-05	3E-06	3.66E-08	2.5E-09
Beam LEFT	-10.00	1.63E-05	1E-06	1.58E-08	1.1E-09
Beam LEFT	-14.38	6.96E-06	5E-07	6.77E-09	4.7E-10

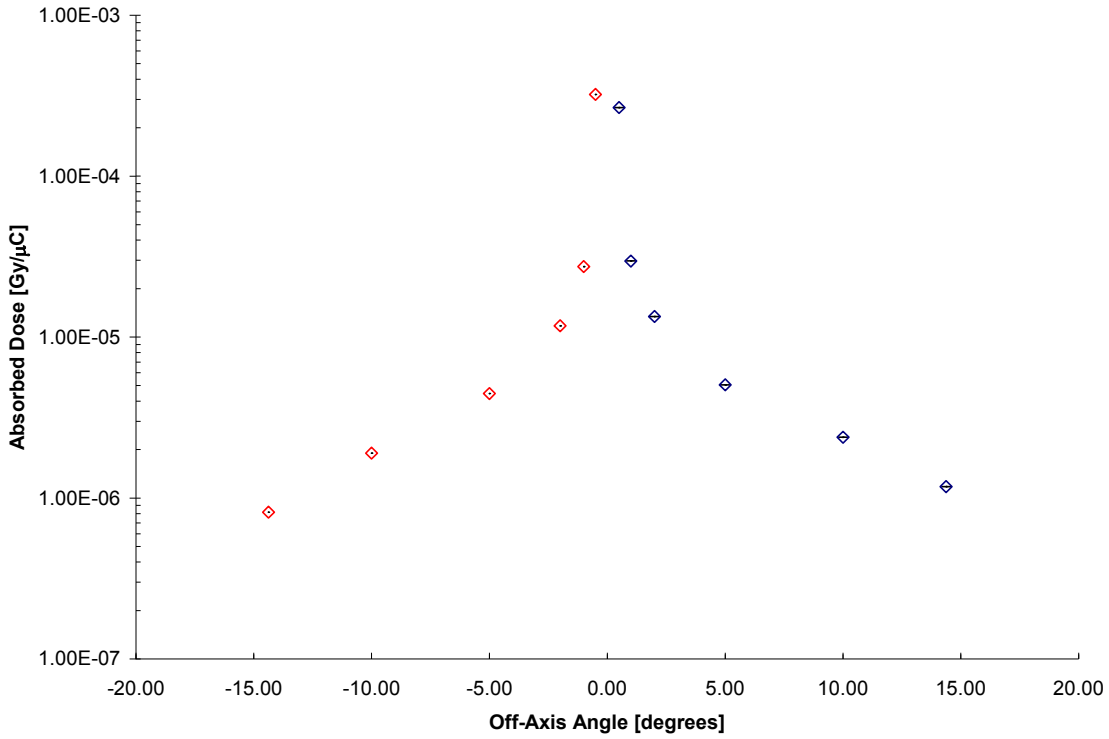

Figure 60. 25 meter (RADCAL Model RC1800) Absorbed Dose Measurement. (The error bars are smaller than the size of the symbols).

Table 43. 50 meter (RADCAL Model RC1800) Absorbed Dose Measurement Data.

Orientation from Beam Centerline	Off-axis Angle [degrees]	D_{air} [Gy]	δD_{air} [Gy]	D_{air} [Gy/μC]	δD_{air} [Gy/μC]
Beam RIGHT	0.50	8.49E-04	6E-05	8.36E-07	6E-08
Beam RIGHT	1.00	7.30E-05	5E-06	7.58E-08	5E-09
Beam RIGHT	2.00	1.97E-05	1E-06	2.00E-08	1E-09
Beam RIGHT	5.00	1.12E-06	7E-08	1.17E-09	7E-11
Beam LEFT	-0.50	9.06E-04	6E-05	9.19E-07	6E-08
Beam LEFT	-1.00	6.64E-05	4E-06	6.95E-08	4.3E-09
Beam LEFT	-2.00	1.69E-05	1E-06	1.71E-08	1.1E-09
Beam LEFT	-5.00	1.77E-06	1E-07	1.79E-09	1.2E-10

Table 44. 50 meter (Far West Model 1055) Absorbed Dose Measurement Data.

Orientation from Beam Centerline	Off-axis Angle [degrees]	D_{air} [Gy]	δD_{air} [Gy]	D_{air} [Gy/μC]	δD_{air} [Gy/μC]
Beam RIGHT	0.4	2.14E-03	1E-04	2.33E-06	1E-07
Beam RIGHT	1.5	2.26E-05	1E-06	2.35E-08	1E-09
Beam RIGHT	2.7	4.60E-04	3E-05	4.82E-07	3E-08
Beam RIGHT	3.8	2.12E-04	1E-05	2.16E-07	1E-08
Beam RIGHT	11.7	1.78E-04	1E-05	1.80E-07	1E-08
Beam RIGHT	14.1	2.16E-04	1E-05	2.27E-07	1E-08
Beam LEFT	-0.4	2.20E-03	1E-04	2.22E-06	1E-07
Beam LEFT	-1.5	1.88E-04	1E-05	1.86E-07	1E-08
Beam LEFT	-2.7	1.40E-04	9E-06	1.42E-07	9E-09
Beam LEFT	-3.8	1.47E-04	1E-05	1.44E-07	1E-08
Beam LEFT	-11.7	1.70E-04	1E-05	1.68E-07	1E-08
Beam LEFT	-14.1	1.52E-04	1E-05	1.51E-07	1E-08

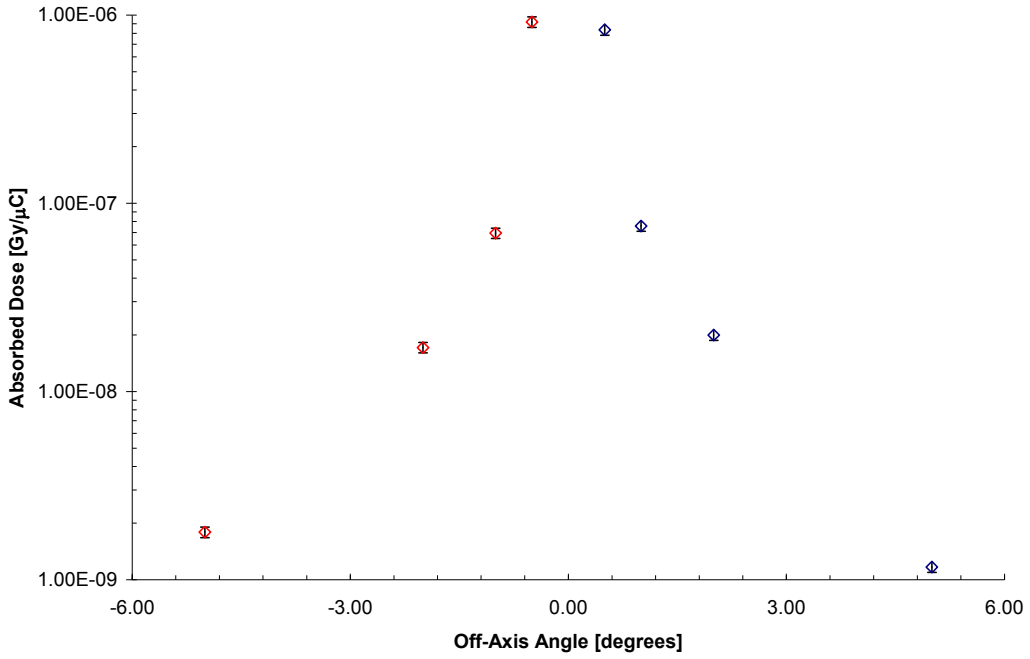

Figure 61. 50 meter (RADCAL Model RC1800) Absorbed Dose Measurement. (The error bars are smaller than the size of the symbols).

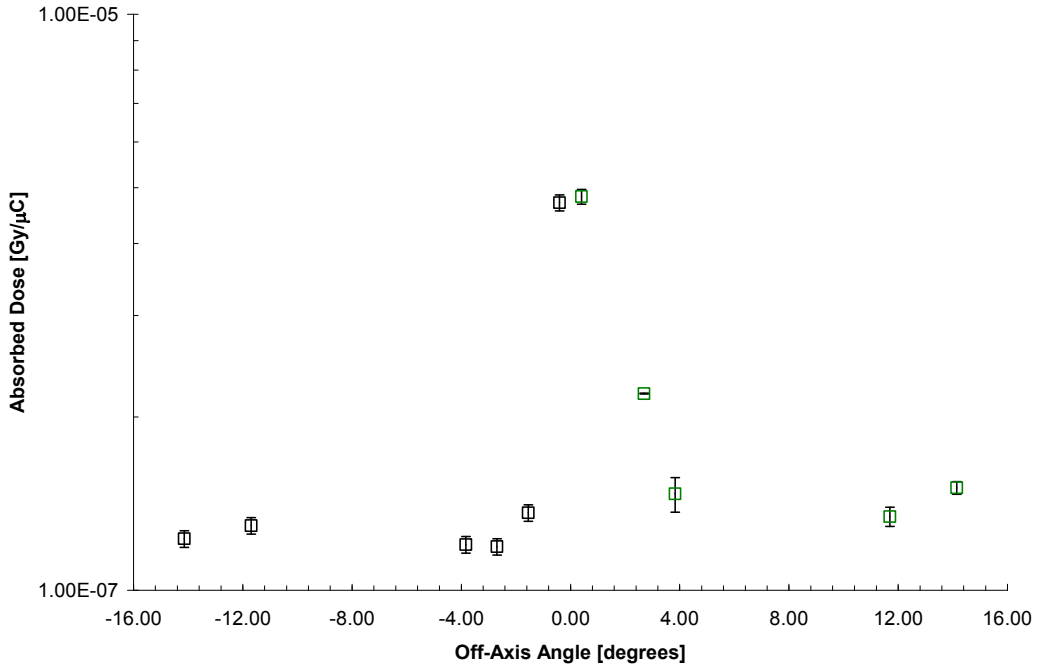

Figure 62. 50 meter (Far West Model 1055) Absorbed Dose Measurement. (The error bars are smaller than the size of the symbols).

Table 45. 100 meter (RADCAL Model RC1800) Absorbed Dose Measurement Data.

Orientation from Beam Centerline	Off-axis Angle [degrees]	D_{air} [Gy]	δD_{air} [Gy]	D_{air} [Gy/μC]	δD_{air} [Gy/μC]
Beam RIGHT	0.08	1.85E-04	1E-05	1.87E-07	1E-08
Beam RIGHT	0.12	4.45E-05	3E-06	4.47E-08	3E-09
Beam RIGHT	0.16	1.93E-05	1E-06	1.94E-08	1E-09
Beam RIGHT	0.31	7.18E-07	5E-08	7.22E-10	5E-11
Beam LEFT	-0.08	2.33E-04	2E-05	2.37E-07	2E-08
Beam LEFT	-0.12	5.54E-05	4E-06	5.62E-08	3.7E-09
Beam LEFT	-0.16	1.94E-05	1E-06	1.95E-08	1.3E-09
Beam LEFT	-0.31	4.20E-07	3E-08	4.26E-10	2.8E-11

Table 46. 100 meter (Far West Model 1055) Absorbed Dose Measurement Data.

Orientation from Beam Centerline	Off-axis Angle [degrees]	D_{air} [Gy]	δD_{air} [Gy]	D_{air} [Gy/μC]	δD_{air} [Gy/μC]
Beam RIGHT	0.4	4.07E-04	3E-05	4.14E-07	3E-08
Beam RIGHT	1.0	2.16E-05	1E-06	2.19E-08	1E-09
Beam RIGHT	1.5	9.56E-06	6E-07	9.65E-09	6E-10
Beam RIGHT	2.1	5.36E-06	4E-07	5.43E-09	4E-10
Beam RIGHT	6.1	1.89E-07	1E-08	1.97E-10	1E-11
Beam LEFT	-0.4	4.87E-04	3E-05	4.92E-07	3E-08
Beam LEFT	-1.0	2.21E-05	1E-06	2.23E-08	1E-09
Beam LEFT	-1.5	9.14E-06	6E-07	9.18E-09	6E-10
Beam LEFT	-2.1	4.77E-06	3E-07	4.79E-09	3E-10
Beam LEFT	-6.1	1.89E-07	1E-08	1.97E-10	1E-11

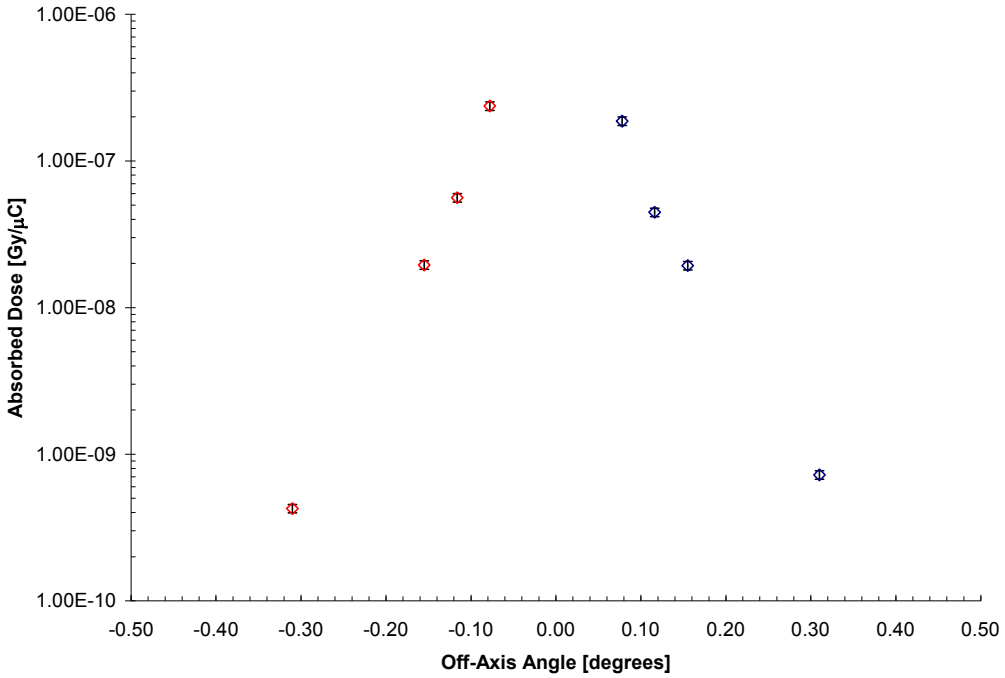

Figure 63. 100 meter (RADCAL Model RC1800) Absorbed Dose Measurement. (The error bars are smaller than the size of the symbols).

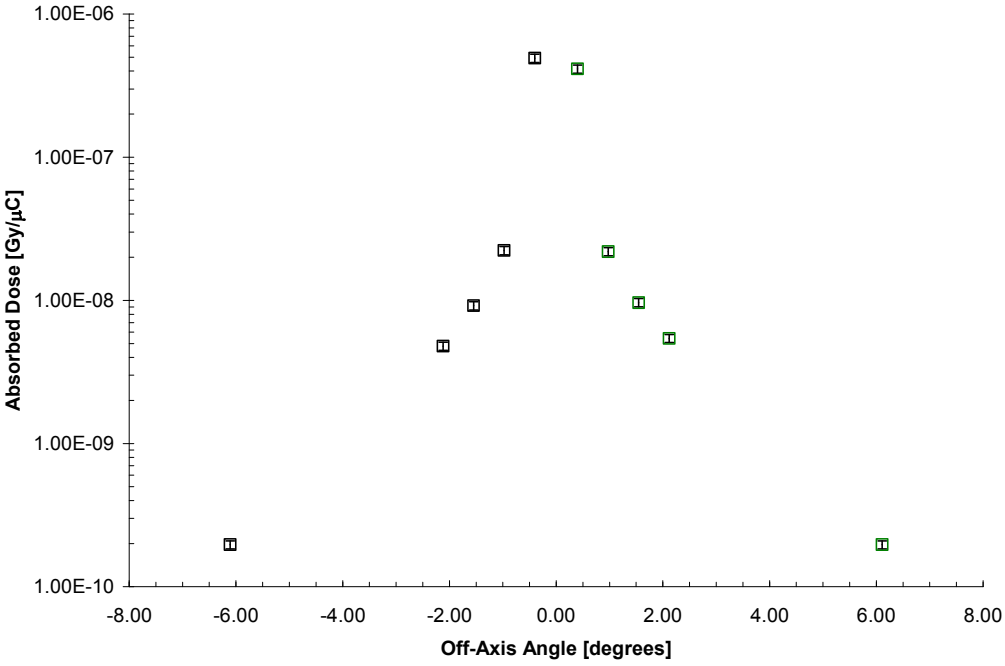

Figure 64. 100 meter (Far West Model 1055) Absorbed Dose Measurement. (The error bars are smaller than the size of the symbols).

Table 47. 170 meter Beam LEFT (RADCAL Model RC1800) Absorbed Dose Measurement Data.

Orientation from Beam Centerline	Off-axis Angle [degrees]	D_{air} [Gy]	δD_{air} [Gy]	D_{air} [Gy/μC]	δD_{air} [Gy/μC]
Beam LEFT	0.00	1.08E-03	1E-04	3.14E-07	3E-08
Beam LEFT	-0.05	1.09E-03	1E-04	3.25E-07	2.9E-08
Beam LEFT	-0.10	1.06E-03	1E-04	3.07E-07	2.8E-08
Beam LEFT	-0.15	1.01E-03	9E-05	3.01E-07	2.7E-08
Beam LEFT	-0.21	9.37E-04	9E-05	2.82E-07	2E-08
Beam LEFT	-0.26	7.93E-04	7E-05	2.32E-07	2E-08
Beam LEFT	-0.31	5.18E-04	5E-05	1.50E-07	1E-08
Beam LEFT	-0.36	5.63E-04	5E-05	1.64E-07	1E-08
Beam LEFT	-0.41	4.55E-04	4E-05	1.32E-07	1E-08

Table 48. 170 meter (Far West Model 1055) Absorbed Dose Measurement Data.

Orientation from Beam Centerline	Off-axis Angle [degrees]	D_{air} [Gy]	δD_{air} [Gy]	D_{air} [Gy/μC]	δD_{air} [Gy/μC]
Beam RIGHT	0.05	6.50E-04	7E-05	1.84E-07	2E-08
Beam RIGHT	0.67	1.95E-04	2E-05	5.67E-08	6E-09
Beam RIGHT	1.01	8.48E-05	9E-06	2.43E-08	2.5E-09
Beam RIGHT	1.35	3.53E-05	4E-06	1.02E-08	1E-09
Beam RIGHT	1.68	3.13E-05	3E-06	8.84E-09	9E-10
Beam RIGHT	2.02	4.44E-05	5E-06	1.24E-08	1E-09
Beam RIGHT	2.36	4.69E-05	5E-06	1.36E-08	1.4E-09
Beam RIGHT	2.69	4.71E-05	5E-06	1.36E-08	1.4E-09
Beam RIGHT	3.03	4.70E-05	5E-06	1.37E-08	1.4E-09
Beam RIGHT	3.37	4.52E-05	5E-06	1.32E-08	1.4E-09
Beam RIGHT	3.70	4.48E-05	5E-06	1.30E-08	1.4E-09
Beam RIGHT	4.04	4.55E-05	5E-06	1.32E-08	1.4E-09
Beam RIGHT	4.37	4.42E-05	5E-06	1.28E-08	1.3E-09
Beam LEFT	-0.34	3.97E-04	4E-05	1.2E-07	1E-08
Beam LEFT	-0.67	6.42E-05	7E-06	1.8E-08	2E-09
Beam LEFT	-1.01	3.88E-05	4E-06	1.1E-08	1.2E-09
Beam LEFT	-1.35	3.91E-05	4E-06	1.1E-08	1.2E-09
Beam LEFT	-1.68	3.74E-05	4E-06	1.1E-08	1E-09

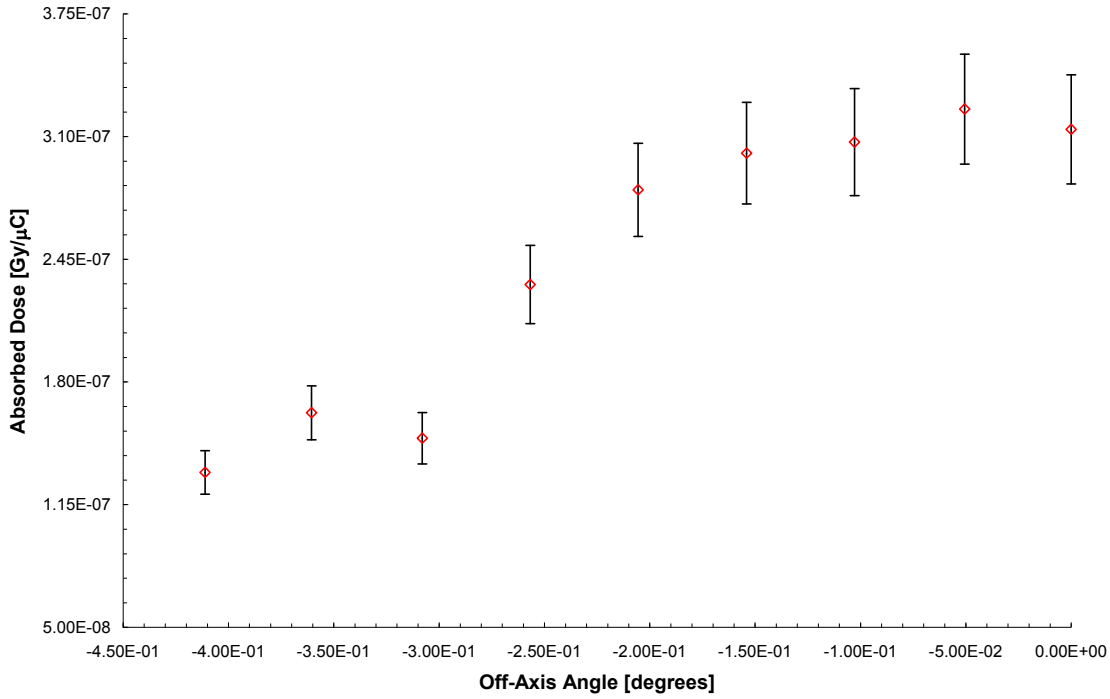

Figure 65. 170 meter Beam LEFT (RADCAL Model RC1800) Absorbed Dose Measurement.

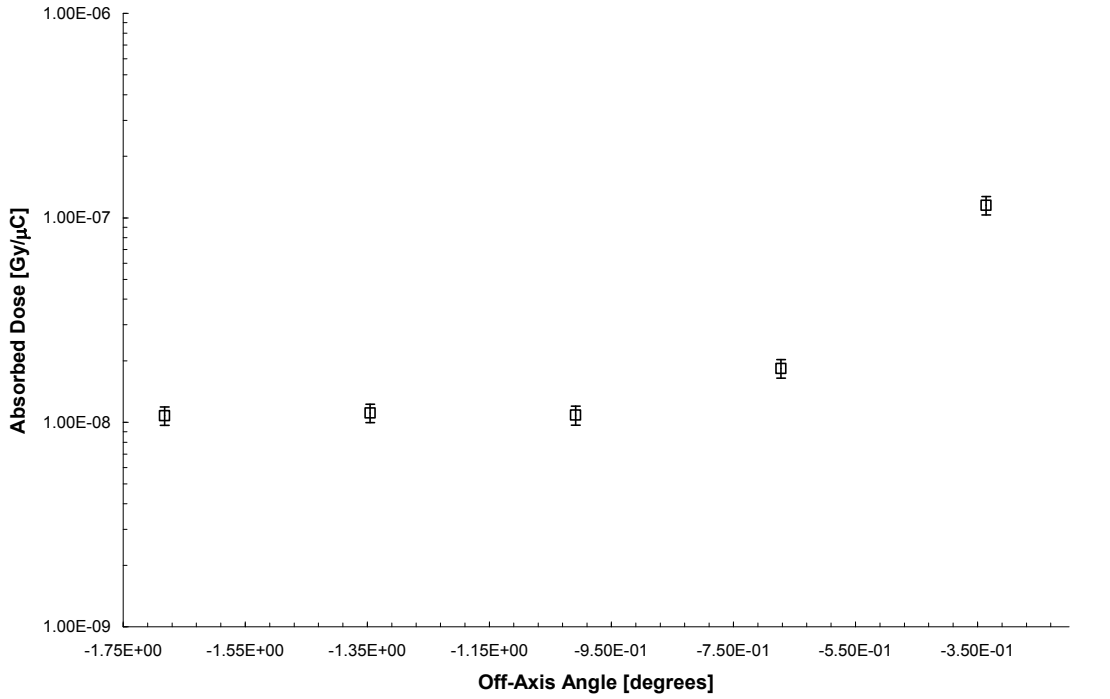

Figure 66. 170 meter Beam LEFT (Far West Model 1055) Absorbed Dose Measurement.

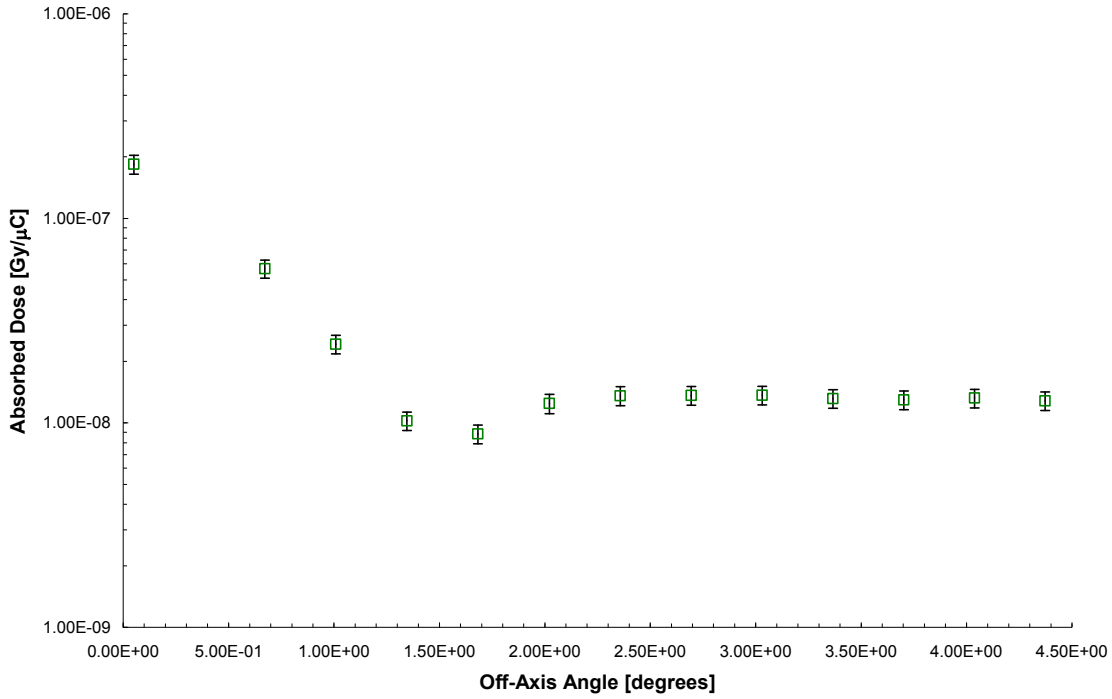

Figure 67. 170 meter Beam RIGHT (Far West Model 1055) Absorbed Dose Measurement.

4.9.4 System Dose Measurements – RADCAL Model RC1800 Ion Chamber

System dose measurements were conducted at six locations under the nominal operating parameters given in Table 49. The ionization charge reading, M was corrected for all pulsed effects using equations (4.1) through (4.5). The results of these corrections, which were utilized in all downfield absorbed dose measurements are given in Table 50. Data (with associated relative uncertainty) used to calculate the absorbed doses are given in Table 51. System absorbed doses were calculated using these data and equation (4.7). System absorbed dose data are given in Table 52.

Table 49. Nominal Operating Conditions for System Absorbed Dose Measurements

Parameter	System Setting
Instaneous Beam Current, I_{INST}	35 mA
Average Beam Current, I_{AVG}	8.4 μA
Repetition Rate, f	60 Hz
Pulse Width, t	4 μs

Table 50. Ionization Charge Correction Factors Applied to System Absorbed Dose Measurements.

Correction Factor	Value
Ionic Recombination Correction, P_{ion}	0.999
Polarity Correction, P_{pol}	1.06
Temperature-Pressure Correction, P_{TP}	Varied by Run
Electrometer Calibration Factor, P_{elec}	0.99

Table 51. Data Used to Calculate Absorbed Dose for System Absorbed Dose Measurements

Parameter	Units	Value	Absolute Uncertainty	Relative Uncertainty
Q	nC	Varied by Run	0.001	Varied by Run
(W/e)	J/C	33.9	1.7	0.05
Sw,g	unitless	0.892	0.001	0.001
M_g	kg	0.00217	0.0001	0.05
$N_{chamber}$	Gy/C	1.56E+04	8.00E+02	0.05
T	°C	Varied by Run	0.1	Varied by Run
P	mm Hg	Varied by Run	1.5	Varied by Run
V_H	V	300	5	0.02
V_L	V	150	5	0.03
$M_{raw}{}^H$	nC	6.24	0.001	0.0002
$M_{raw}{}^L$	nC	6.25	0.001	0.0002
V --- $M_{raw}{}^+$	V	300	5	0.02
V --- $M_{raw}{}^-$	V	-300	5	-0.02
V --- M_{raw}	V	300	5	0.02
$M_{raw}{}^+$	nC	6.24	0.001	0.0002
$M_{raw}{}^-$	nC	-6.95	0.001	-0.0001
M_{raw}	nC	6.24	0.001	0.0002
Q_k	nC	19	0.001	0.0001
Q_m	nC	18.9	0.001	0.0001

Table 52. System Absorbed Dose Measurement Data.

System Dose Position	D_{air} [Gy]	δD_{air} [Gy]	D_{air} [Gy/μC]	δD_{air} [Gy/μC]
A	1.65E-04	1E-05	9.86E-06	1E-06
B	3.47E-04	2E-05	2.08E-05	3E-06
C	3.78E-04	3E-05	2.26E-05	3E-06
D	3.53E-04	3E-05	2.11E-05	3E-06
E	1.27E-03	9E-05	1.82E-05	1.1E-05
F	1.30E-04	9E-06	7.77E-06	1.1E-06

4.9.5 System Neutron Dose Equivalent Measurements – BSS System with TLDs

System neutron dose equivalent measurements were performed using the TLD-based BSS system under the nominal operating conditions given in Table 53. A combination of approximately 225 TLD-600s and TLD-700s were used in the measurements with 10 of each typed being used as controls. Measurements were performed at three locations simultaneously (for 10 minute run times) allowing for the rotation of Bonner spheres between runs. All TLDs were then transported (hand-carried via airplane flight) back to the Georgia Tech TLD Laboratory for post-processing. At no time during the process did the TLDs receive any additional radiation beyond what they were exposed to during irradiation activities. This was closely monitored with the control TLDs employed.

Table 53. Nominal Operating Conditions for Neutron Absorbed Dose Measurements.

Parameter	System Setting
Instaneous Beam Current, I_{INST}	35 mA
Average Beam Current, I_{AVG}	8.4 μA
Repetition Rate, f	60 Hz
Pulse Width, t	4 μs

Within a five-day period, all TLDs were read using a Harshaw Model 3500 TLD Reader at the Georgia Tech TLD Laboratory. All TLD response information was then corrected for background utilizing the mean of the control TLDs. In order to obtain the total response of the TLD-600s to neutrons only, the response to photons are subtracted via the use of the TLD-700s. Since TLD-700s have a negligible response to neutrons, and TLD-600s respond to both neutrons and photons, the TLD-700 reading is used to subtract out

the photon response of the TLD-600s. The response of TLD-600s and TLD-700s to a mixed radiation field is described by

$$R_{600}^{n+\gamma} = R_{600}^{n} + R_{600}^{\gamma} \tag{4.9}$$

$$R_{700}^{n+\gamma} = R_{700}^{n} + R_{700}^{\gamma} \tag{4.10}$$

where $R_{600}^{n+\gamma}$ is the total TLD-600 response to neutrons and photons, R_{600}^{n} is the neutron response, and R_{600}^{γ} is the photon response with the terms $R_{700}^{n+\gamma}$, R_{700}^{n} and R_{700}^{γ} being similarly defined. Since R_{700}^{n} is considered to be negligible compared to R_{600}^{n}, equation (4.10) can be reduced to

$$R_{700}^{n+\gamma} = R_{700}^{\gamma} \tag{4.11}$$

The relationship between the photon response of the two TLD types can be described as

$$k = \frac{R_{700}^{\gamma}}{R_{600}^{\gamma}} \tag{4.12}$$

where k is the photon response ratio. k is experimentally determined by exposing the TLDs to a pure gamma-ray source. Previous measurements of the gamma response ratio indicate that k is independent of gamma-ray energies, thus it can be used for all radiation fields. Equations 4.9, 4.11 and 4.12 can then be combined to provide the total TLD-600 neutron response [65].

$$R_{600}^{n} = R_{600}^{n+\gamma} - \frac{R_{700}^{n+\gamma}}{k} \tag{4.13}$$

The BSS detector data does not provide a direct indication of the measured neutron spectrum, the BSS data must be unfolded to deconvolve the spectrum. The BSS response to a given neutron spectrum is given according to the equation

$$R_j = \int_{E_{\min}}^{E_{\max}} \sigma_j(E)\phi(E)dE \qquad j = 1, 2, \ldots M \tag{4.14}$$

where R_j is the detector count rate of the j^{th} detector to neutrons of energy E in units of counts cm^2 per neutron, $\phi(E)$ is the incident neutron fluence on the surface of the spherical detector, and M is the number of detectors. This equation can be written in matrix form such that

$$R_j = \sum_{k=1}^{N} \sigma_{jk}\phi(k) \qquad j = 1, 2, \ldots M \tag{4.15}$$

where σ_{jk} is the detector response of the j^{th} detector to neutrons in the k^{th} energy interval and N is the total number of energy groups. Since N is generally larger than M, no unique solution exists. In lieu of a unique solution, it is the goal of unfolding to find an appropriate spectrum which satisfies the requirements of physical reality. These requirements mandate that the spectrum be positive (negative solutions are not physical). Other requirements include smoothness, spectral shape and energy cutoff limits [65].

The unfolding program BUNKIUT was used to unfold the BSS data through the employment of the SPUNIT algorithm and the UTA4 response matrix [65, 67-68]. BUNKIUT, utilizing the mathematical formalism just described, provides an iterative solution to the deconvolution of the neutron spectrum. In order to begin unfolding, an initial guess of the anticipated neutron spectrum is needed. Any initial guess may be used, but it is appropriate to select a spectrum that resembles the one which is being measured. For the present work, four starting spectra were used as the starting initial guess. Those spectra include a high energy Maxwellian $(1/E)^x$ (with T=1.4 MeV), an equal lethargy starting spectrum, the National Bureau of Standards (NBS) ^{252}Cf spectrum,

and the NBS ^{252}Cf Room Return spectrum. In addition to neutron spectral information, BUNKIUT provides a neutron dose equivalent calculation in units of rem as well as the quality factor in units of rem/rad. For additional information, Sweezy provides a thorough review of the intricacies of BSS data unfolding, BUNKIUT, the SPUNIT algorithm, etc. [65]. A summary of the unfolding parameters used in the present work are presented in Table 54.

Table 54. BSS Data Unfolding Parameters.

Unfolding Program	BUNKIUT
Unfolding Algorithm	SPUNIT
Response Matrix	UTA4
Starting Spectra	Maxwellian (T=1.4 MeV) Equal Lethargy NBS ^{252}Cf NBS ^{252}Cf Room Return
Energy Intervals	26
Number of Iterations	1000

In order to relate the response of TLDs to the response of a neutron scintillator, characterization measurements were made at Georgia Tech by Sweezy and Howell, et al [65, 69]. These measurements included calibration, corrections for room return and air-scatter and calibration in terms of counts/μC. Due to the consistency of historical measurements, these data were utilized in the present work [65, 69]. A study was performed to determine the validity of these data within the present work and is reviewed by Hales [70]. A summary of the calibration factors used are given in Table 55. In addition, an explanation of the calibration procedure and related activities is presented by Hales [70].

Table 55. BSS-TLD Calibration Factors. Reprinted from [65].

Photon Response Ratio, *k*	1.069
Calibration Factor (*counts/*μ*C)*	3.218×10^7

The data were fit using the aforementioned starting spectra and parameters. The best results were produced utilizing the Maxwellian (T=1.4 MeV) for the starting spectrum. The spectrum observed at Location A is expected as it resembles a photoneutron evaporation spectrum. The spectra at Locations B and C are similar except for a slight shift in the peak where a slightly softer spectrum is observed at the collimator (Location C). The small peaks observed above 1 MeV are attributed to uncollided neutrons, especially at Location B.

The results of the neutron measurements are given in Table 56 through Table 58 and shown in Figure 68 through Figure 70. A complete summary of the unfolded data is presented in Appendix D.

Table 56. Properties of Neutron Spectrum at Location A.

Starting Spectra	ϕ_{total} [neutrons/cm^2/μC]	Dose Equivalent [rem/μC]	Quality Factor [rem/rad]	Percent Error
Maxwellian (T=1.4 MeV)	2.85E+04	4.54E-04	8.38	2.07%
NBS ^{252}Cf	2.85E+04	4.54E-04	8.34	2.37%
NBS ^{252}Cf Room Return	2.84E+04	4.54E-04	8.55	1.88%
Equal Lethargy	2.88E+04	4.54E-04	8.21	2.41%

Table 57. Properties of Neutron Spectrum at Location B.

Starting Spectra	ϕ_{total} [neutrons/cm^2/μC]	Dose Equivalent [rem/μC]	Quality Factor [rem/rad]	Percent Error
Maxwellian (T=1.4 MeV)	2.99E+03	1.06E-03	3.76	11.49%
NBS ^{252}Cf	2.99E+03	1.06E-03	3.84	11.47%
NBS ^{252}Cf Room Return	2.99E+03	1.06E-03	3.69	11.73%
Equal Lethargy	2.99E+03	1.06E-03	3.77	11.38%

Table 58. Properties of Neutron Spectrum at Location C.

Starting Spectra	ϕ_{total} [neutrons/cm^2/μC]	Dose Equivalent [rem/μC]	Quality Factor [rem/rad]	Percent Error
Maxwellian (T=1.4 MeV)	3.90E+04	5.37E-05	2.35	19.98%
NBS ^{252}Cf	3.90E+04	5.37E-05	2.39	19.94%
NBS ^{252}Cf Room Return	3.90E+04	5.37E-05	2.33	20.01%
Equal Lethargy	3.90E+04	5.37E-05	2.39	19.93%

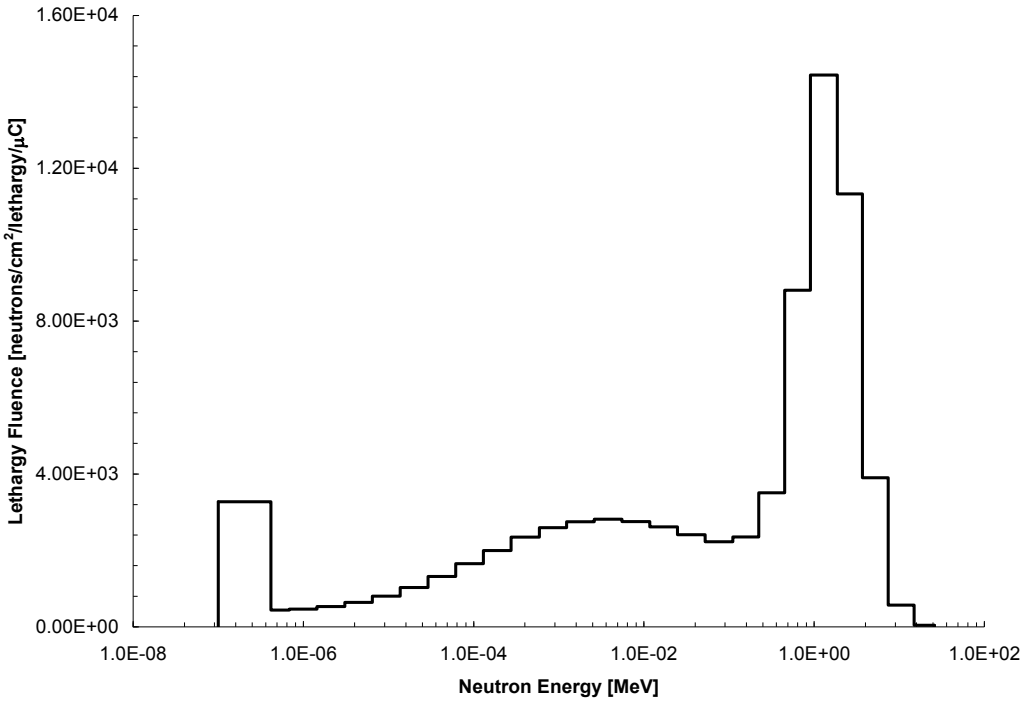

Figure 68. Neutron Spectrum Measured at Location A.

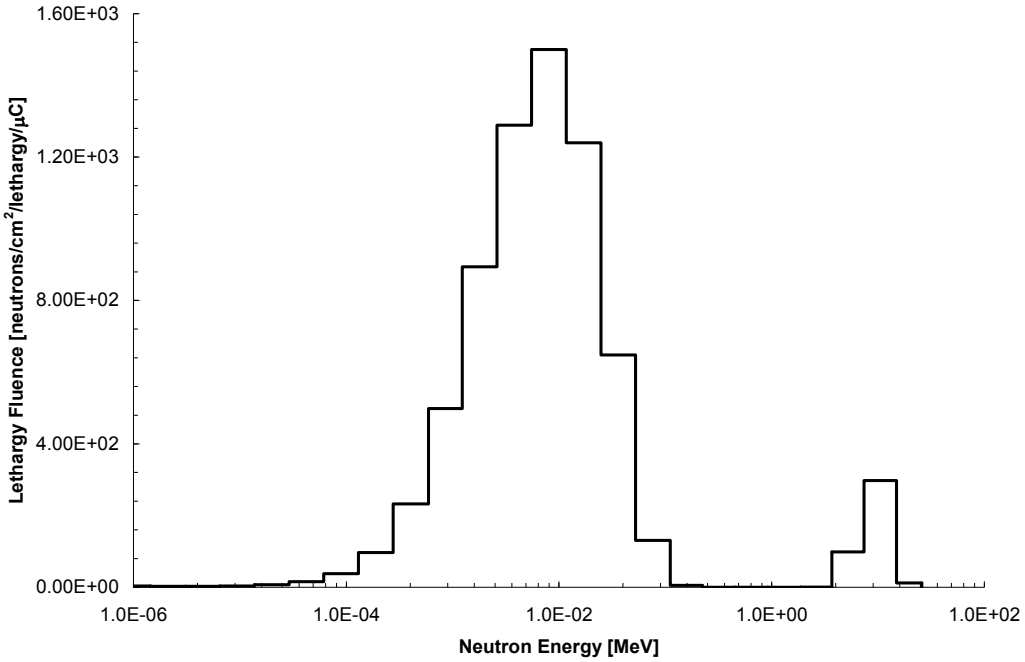

Figure 69. Neutron Spectrum Measured at Location B.

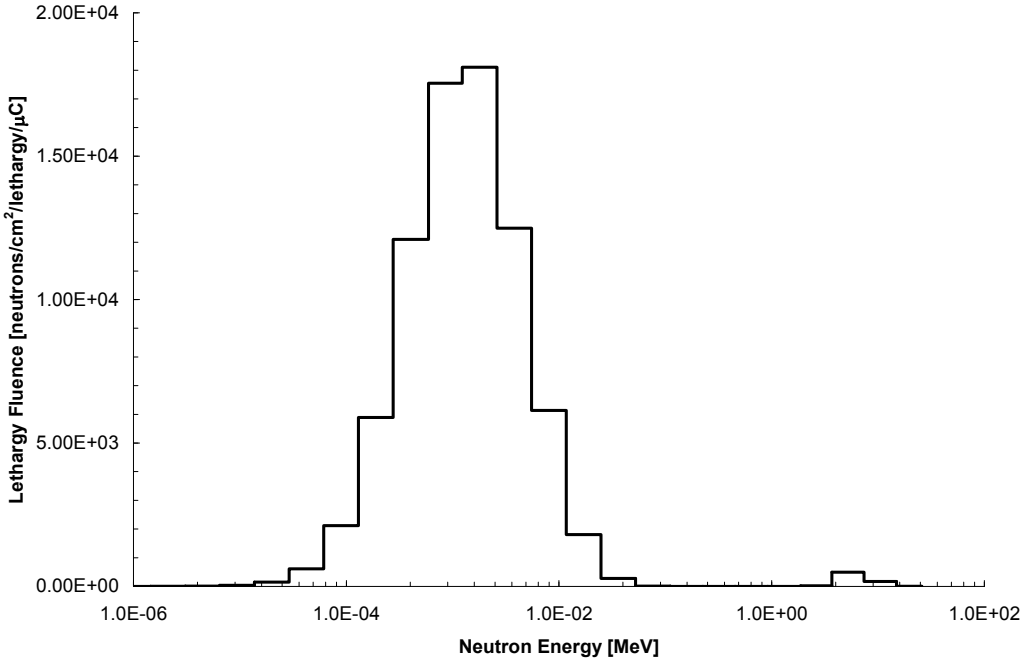

Figure 70. Neutron Spectrum Measured at Location C.

CHAPTER 5

SYSTEM SIMULATION

A key aspect of the present work is to develop a data set in which the conduct of an extensive experimental effort is not essential in solving many of the pressing radiation dosimetry problems. The essence of this capability is reliance on radiation transport modeling and simulation to provide answers and insight such that an exhaustive measurement program is not necessary. In order to accomplish this objective, an extensive simulation and validation effort must be performed. This effort provides verification of the methodology as well as insight into different aspects of system dosimetry.

This chapter describes an extensive set of Monte Carlo simulations which were performed to calculate particle fluence and dose data. The following sections contain a summary of the simulations performed as well as an extensive set of calculated data presented both in tabular and graphical format. An analysis of the simulation data and results is also presented.

5.1 Computational Models & Methodology

An extensive set of computational models were created in order to provide a thorough data set and gain insight into the system dosimetry. All models were developed using the best available data (i.e. dimensions, material properties, etc.) pertaining to the actual prototype system. The selection of material compositions and densities were based on either manufacturer's specifications or published information. MCNP5 Version 1.51, as previously described, was utilized for all simulations [1]. Several options within the MCNP5 code were employed in order to accurately model the physical problem as well as provide answers with the least amount of statistical uncertainty.

A baseline MCNP5 model of the PITAS prototype was developed and used as the basis for all system simulations. The baseline model contained all fundamental system components including the outer shell of the accelerating waveguide, converter, collimator, and cargo container. The PITAS was modeled in dry air as defined by NIST [71]. Later in this chapter, additional simulations are presented where perturbations were made concerning the modeling of the air and some of the PITAS components.

A trade-off exists in modeling physical reality versus the ability for MCNP5 to converge on statistically significant answers in manageable run times. This trade-off was exercised in modeling the experimental facility where most of the measurements were performed. The models did not include all of the fidelity one desires when performing a large-scale study to compare measured data to computed data. The actual facility contains several physical characteristics (i.e. some walls, some structures, etc.) that will have an impact on

measurements, by creating a scattering source for secondary radiations. It is anticipated that this will have an effect on computed data.

The starting source particle was a 25 MeV (monoenergetic) electron which was modeled as a pencil beam of electrons. This means that all simulations started with electrons, bremsstrahlung were then created followed by the subsequent creation of appropriate secondary electrons, neutrons and photons. This approach created simulation run times on the order of tens of hours. All simulation data are presented on a per μC basis as discussed in Section 4.4. In order to be consistent with measurements, the instantaneous beam currents used in all simulation normalization was the same as those used for the measurements. In general, these values were either 8.4 μA or 28.8 μA.

Electron physics was implemented according to the following conditions. The upper energy limit for electrons was set at 25.2 MeV with the low energy cutoff set at 1 keV. Electron production by photons as well as photon production by electrons were both enabled. In addition, biased bremsstrahlung production was employed such that 100 times the analog number of photons were sampled [72]. These photons were each sampled independently for angle and energy with the particle weight being appropriately modified [1].

Photon physics was implemented according to the following conditions. The upper energy limit for detailed photon physics treatment was set at 25.2 MeV. This means that below 25.2 MeV, photons were treated with detailed photons physics such that

photoelectric absorption can result in fluorescent emission, the Thompson and Klein-Nishina differential cross sections are modified by appropriate form factors and Compton profiles take electron binding effects into account including coherent scattering [1]. Doppler energy broadening for photons was not used in system simulations.

Neutron physics was implemented according to the following conditions. The upper energy limit for neutron energy was set at 25.2 MeV. All neutrons received the implicit capture treatment. Photonuclear collision sampling was enabled such that the photon was split at each collision with each of the two parts undergoing a photoatomic or photonuclear event with their particle weights updated accordingly [1].

The two fundamental quantities simulated were energy deposition and particle fluence (photon, electron and neutron). Energy deposition data were used to calculate absorbed dose directly. These simulations are much more computationally expensive. In general, many of the calculations presented herein require large numbers of particle histories and the employment of Monte Carlo variance reduction techniques. Particle fluence data were folded with conversion coefficients to determine ambient dose equivalent and effective dose. This was the primary method employed in computing dose.

Energy deposition was calculated by tracking recoil electrons using an energy deposition tally (MCNP5 *f8). The *f8 tally scores the energy deposition of each photon and electron as it enters and exits the cell volume and assumes the energy deposited is the difference. This tally is not a track length estimator but is more analogous to a pulse-

height detector tally. The energy deposition tally allows for the direct calculation of absorbed dose. The challenge with this tally is running enough particle histories to get a statistically significant solution in a small volume at long distances from the source.

A set of positions for the calculation of particle fluence was employed to provide a consistent data set as well as to provide a basis for comparison to measurement data. These positions were a function of downfield distance and off-axis distance. In order to keep a uniform set of locations for comparative purposes, off-axis distances were based on angles. These angles used the same methodology employed during the measurements. Photon and neutron fluence simulations were performed at angles ranging from -45 degrees to 45 degrees from the beam centerline, at downfield distances of 10, 25, 50, 100, 120 and 170 meters. Electron fluence simulations were much more challenging due to the computationally expensive nature of electron transport. Therefore, electron fluence simulations were only performed at angles ranging from -5 degrees to 5 degrees from the beam centerline, at downfield distances of 10, 25, 50, 100, 120 and 170 meters. A complete summary of the downfield distance, off-axis distance and correlated off-axis angle for particle fluence simulations are given in Table 59 through Table 64.

Table 59. Locations for Particle Fluence Calculations at 10 meters.

Downfield Distance		10 meters			
Orientation from Beam Centerline	Off-axis Angle [degrees]	Off-axis Angle [radians]	Off-Axis Distance [m]	Off-Axis Distance [cm]	Fluence Calculated
Beam CENTER	0.0	0.000	0.0	0.0	Photon, Neutron, Electron
Beam RIGHT	0.5	0.009	0.1	9	Photon, Neutron
Beam RIGHT	1	0.017	0.2	17	Photon, Neutron, Electron
Beam RIGHT	2	0.035	0.3	35	Photon, Neutron, Electron
Beam RIGHT	5	0.087	0.9	87	Photon, Neutron, Electron
Beam RIGHT	10	0.175	1.8	176	Photon, Neutron
Beam RIGHT	20	0.349	3.6	364	Photon, Neutron
Beam RIGHT	30	0.524	5.8	577	Photon, Neutron
Beam RIGHT	45	0.785	10.00	1000	Photon, Neutron
Beam LEFT	-0.5	-0.009	-0.1	-9	Photon, Neutron
Beam LEFT	-1	-0.017	-0.2	-17	Photon, Neutron, Electron
Beam LEFT	-2	-0.035	-0.3	-35	Photon, Neutron, Electron
Beam LEFT	-5	-0.087	-0.9	-87	Photon, Neutron, Electron
Beam LEFT	-10	-0.175	-1.8	-176	Photon, Neutron
Beam LEFT	-20	-0.349	-3.6	-364	Photon, Neutron
Beam RIGHT	-30	-0.524	-5.8	-577	Photon, Neutron
Beam RIGHT	-45	-0.785	-10.00	-1000	Photon, Neutron

Table 60. Locations for Particle Fluence Calculations at 25 meters.

Downfield Distance		25 meters			
Orientation from Beam Centerline	Off-axis Angle [degrees]	Off-axis Angle [radians]	Off-Axis Distance [m]	Off-Axis Distance [cm]	Fluence Calculated
Beam CENTER	0.0	0.000	0.0	0.0	Photon, Neutron, Electron
Beam RIGHT	0.5	0.009	0.2	22	Photon, Neutron, Electron
Beam RIGHT	1	0.017	0.4	44	Photon, Neutron, Electron
Beam RIGHT	2	0.035	0.9	87	Photon, Neutron, Electron
Beam RIGHT	5	0.087	2.2	219	Photon, Neutron
Beam RIGHT	10	0.175	4.4	441	Photon, Neutron
Beam RIGHT	20	0.349	9.1	910	Photon, Neutron
Beam RIGHT	30	0.524	14.4	1443	Photon, Neutron
Beam RIGHT	45	0.785	25.00	2500	Photon, Neutron
Beam LEFT	-0.5	-0.009	-0.2	-22	Photon, Neutron, Electron
Beam LEFT	-1	-0.017	-0.4	-44	Photon, Neutron, Electron
Beam LEFT	-2	-0.035	-0.9	-87	Photon, Neutron, Electron
Beam LEFT	-5	-0.087	-2.2	-219	Photon, Neutron
Beam LEFT	-10	-0.175	-4.4	-441	Photon, Neutron
Beam LEFT	-20	-0.349	-9.1	-910	Photon, Neutron
Beam RIGHT	-30	-0.524	-14.4	-1443	Photon, Neutron
Beam RIGHT	-45	-0.785	-25.00	-2500	Photon, Neutron

Table 61. Locations for Particle Fluence Calculations at 50 meters.

Downfield Distance		50 meters			
Orientation from Beam Centerline	Off-axis Angle [degrees]	Off-axis Angle [radians]	Off-Axis Distance [m]	Off-Axis Distance [cm]	Fluence Calculated
Beam CENTER	0.0	0.000	0.0	0.0	Photon, Neutron, Electron
Beam RIGHT	0.5	0.009	0.4	44	Photon, Neutron, Electron
Beam RIGHT	1	0.017	0.9	87	Photon, Neutron, Electron
Beam RIGHT	2	0.035	1.7	175	Photon, Neutron, Electron
Beam RIGHT	5	0.087	4.4	437	Photon, Neutron
Beam RIGHT	10	0.175	8.8	882	Photon, Neutron
Beam RIGHT	20	0.349	18.2	1820	Photon, Neutron
Beam RIGHT	30	0.524	28.9	2887	Photon, Neutron
Beam RIGHT	45	0.785	50.00	5000	Photon, Neutron
Beam LEFT	-0.5	-0.009	-0.4	-44	Photon, Neutron, Electron
Beam LEFT	-1	-0.017	-0.9	-87	Photon, Neutron, Electron
Beam LEFT	-2	-0.035	-1.7	-175	Photon, Neutron, Electron
Beam LEFT	-5	-0.087	-4.4	-437	Photon, Neutron
Beam LEFT	-10	-0.175	-8.8	-882	Photon, Neutron
Beam LEFT	-20	-0.349	-18.2	-1820	Photon, Neutron
Beam RIGHT	-30	-0.524	-28.9	-2887	Photon, Neutron
Beam RIGHT	-45	-0.785	-50.00	-5000	Photon, Neutron

Table 62. Locations for Particle Fluence Calculations at 100 meters.

Downfield Distance		100 meters			
Orientation from Beam Centerline	Off-axis Angle [degrees]	Off-axis Angle [radians]	Off-Axis Distance [m]	Off-Axis Distance [cm]	Fluence Calculated
Beam CENTER	0.0	0.000	0.0	0.0	Photon, Neutron, Electron
Beam RIGHT	0.5	0.009	0.9	87	Photon, Neutron, Electron
Beam RIGHT	1	0.017	1.7	175	Photon, Neutron, Electron
Beam RIGHT	2	0.035	3.5	349	Photon, Neutron, Electron
Beam RIGHT	5	0.087	8.7	875	Photon, Neutron
Beam RIGHT	10	0.175	17.6	1763	Photon, Neutron
Beam RIGHT	20	0.349	36.4	3640	Photon, Neutron
Beam RIGHT	30	0.524	57.7	5774	Photon, Neutron
Beam RIGHT	45	0.785	100.00	10000	Photon, Neutron
Beam LEFT	-0.5	-0.009	-0.9	-87	Photon, Neutron, Electron
Beam LEFT	-1	-0.017	-1.7	-175	Photon, Neutron, Electron
Beam LEFT	-2	-0.035	-3.5	-349	Photon, Neutron, Electron
Beam LEFT	-5	-0.087	-8.75	-875	Photon, Neutron
Beam LEFT	-10	-0.175	-17.6	-1763	Photon, Neutron
Beam LEFT	-20	-0.349	-36.4	-3640	Photon, Neutron
Beam RIGHT	-30	-0.524	-57.7	-5774	Photon, Neutron
Beam RIGHT	-45	-0.785	-100.00	-10000	Photon, Neutron

Table 63. Locations for Particle Fluence Calculations at 120 meters.

Downfield Distance		120 meters			
Orientation from Beam Centerline	Off-axis Angle [degrees]	Off-axis Angle [radians]	Off-Axis Distance [m]	Off-Axis Distance [cm]	Fluence Calculated
Beam CENTER	0.0	0.000	0.0	0.0	Photon, Neutron, Electron
Beam RIGHT	0.5	0.009	1.05	105	Photon, Neutron, Electron
Beam RIGHT	1	0.017	2.09	209	Photon, Neutron, Electron
Beam RIGHT	2	0.035	4.19	419	Photon, Neutron, Electron
Beam RIGHT	5	0.087	10.50	1050	Photon, Neutron
Beam RIGHT	10	0.175	21.16	2116	Photon, Neutron
Beam RIGHT	20	0.349	43.68	4368	Photon, Neutron
Beam RIGHT	30	0.524	69.28	6928	Photon, Neutron
Beam RIGHT	45	0.785	120.00	12000	Photon, Neutron
Beam LEFT	-0.5	-0.009	-1.05	-105	Photon, Neutron, Electron
Beam LEFT	-1	-0.017	-2.09	-209	Photon, Neutron, Electron
Beam LEFT	-2	-0.035	-4.19	-419	Photon, Neutron, Electron
Beam LEFT	-5	-0.087	-10.50	-1050	Photon, Neutron
Beam LEFT	-10	-0.175	-21.16	-2116	Photon, Neutron
Beam LEFT	-20	-0.349	-43.68	-4368	Photon, Neutron
Beam RIGHT	-30	-0.524	-69.28	-6928	Photon, Neutron
Beam RIGHT	-45	-0.785	-120.00	-12000	Photon, Neutron

Table 64. Locations for Particle Fluence Calculations at 170 meters.

Downfield Distance		170 meters			
Orientation from Beam Centerline	Off-axis Angle [degrees]	Off-axis Angle [radians]	Off-Axis Distance [m]	Off-Axis Distance [cm]	Fluence Calculated
Beam CENTER	0.0	0.000	0.0	0.0	Photon, Neutron, Electron
Beam RIGHT	0.5	0.009	1.48	148	Photon, Neutron, Electron
Beam RIGHT	1	0.017	2.97	297	Photon, Neutron, Electron
Beam RIGHT	2	0.035	5.94	594	Photon, Neutron
Beam RIGHT	5	0.087	14.87	1487	Photon, Neutron
Beam RIGHT	10	0.175	29.98	2998	Photon, Neutron
Beam RIGHT	20	0.349	61.87	6187	Photon, Neutron
Beam RIGHT	30	0.524	98.15	9815	Photon, Neutron
Beam RIGHT	45	0.785	170.00	17000	Photon, Neutron
Beam LEFT	-0.5	-0.009	-1.48	-148	Photon, Neutron, Electron
Beam LEFT	-1	-0.017	-2.97	-297	Photon, Neutron, Electron
Beam LEFT	-2	-0.035	-5.94	-594	Photon, Neutron
Beam LEFT	-5	-0.087	-14.87	-1487	Photon, Neutron
Beam LEFT	-10	-0.175	-29.98	-2998	Photon, Neutron
Beam LEFT	-20	-0.349	-61.87	-6187	Photon, Neutron
Beam RIGHT	-30	-0.524	-98.15	-9815	Photon, Neutron
Beam RIGHT	-45	-0.785	-170.00	-17000	Photon, Neutron

Photon fluences were calculated using two Monte Carlo tally approaches. First, a track length estimate of flux (volume averaged particle flux, MCNP5 f4) was used to calculate the scalar photon flux in a cylinder which approximated the dimensions of the ion chambers used in measurements. The cylinders were modeled using the actual wall material (i.e. polycarbonate or bakelite) that is used in the manufacturing process. Material composition data were obtained from the NIST Electron Sopping Power (ESTAR) database [73]. A set of 17 cylinders were placed at the center of the off-axis angle positions, as previously discussed, and used as flux tally volumes

The second method used to calculate photon fluence was a point detector tally (MCNP5 f5). A point detector is a next event estimator of the flux at a point in space. Contributions to the point detector tally are made at source and collision events throughout the Monte Carlo random walk [1]. In addition, a ray tracing approach is undertaken at surface crossing events. Points detectors can be used to tally neutral particles (i.e., neutrons or photons) and are placed at specified points in the model using Cartesian coordinates, thus point detectors were placed at the points specified in Table 59 through Table 64. Particle fluence data for photons, electrons and neutrons are graphically presented in Appendix E, F, and G, respectively.

Particle fluence data were used to calculate both effective dose and ambient dose equivalent. Fluences were energy binned according to the group structure of the conversion coefficients. Fluence-to-ambient dose equivalent conversion coefficients, as discussed in Chapter 3, were folded with photon, electron and neutron fluences in order

to calculate particle-specific and total ambient dose equivalent. Likewise, published fluence-to-effective dose conversion coefficients were folded with photon, electron and neutron fluences in order to calculate particle-specific and total effective dose.

5.2 Beam Energy Calculations

The estimation of beam energy was performed using a comparison of measurements with model data as described in Chapter 4. A detailed model was developed to confirm the beam energy absorbed dose measurements. Seven different MCNP5 models were developed using two approaches to calculate the absorbed dose inside a virtual water phantom. Each successive model included an additional 0.635 cm layer of lead sheeting which was a direct match to the experiment performed.

In the first approach, an energy deposition tally (MCNP5 *f8) was used to directly calculate the absorbed dose at the center of the virtual water phantom. The energy deposition, in units of MeV, was converted to absorbed dose in Gy/μC in a post processing calculation. In the second approach, the photon fluence at the center of the virtual water phantom was calculated. These fluence data were then folded with a set of energy-dependent kerma factors calculated for virtual water using mass energy–absorption coefficient data obtained from Seltzer [74]. The kerma factor was calculated using the relationship

$$\frac{K}{\phi} = [160.22](E_\gamma) \sum_{i=1}^{n} \left(\frac{\mu_{en}}{\rho} \right)_i \tag{5.1}$$

where $\left(\frac{\mu_{en}}{\rho}\right)$ is the mass energy-absorption coefficient (cm^2/g) of each individual material weighted in a relative sense by its' weight percent in virtual water and E_γ is the photon energy of the corresponding energy bin (MeV). The calculated kerma factors for virtual water are given in Table 65 and shown in Figure 71.

Table 65. Calculated Virtual Water Kerma Factors.

Photon Energy [MeV]	Kerma Factor (pGy-cm^2)
0.01	4.8
0.015	2.0
0.02	1.1
0.03	0.46
0.04	0.29
0.05	0.25
0.06	0.24
0.08	0.30
0.1	0.38
0.15	0.64
0.2	0.92
0.3	1.5
0.4	2.0
0.5	2.6
0.6	3.1
0.8	4.0
1	4.8
1.5	6.6
2	8.1
3	11
4	13
5	15
6	17
8	20
10	24
15	32
20	41
30	59

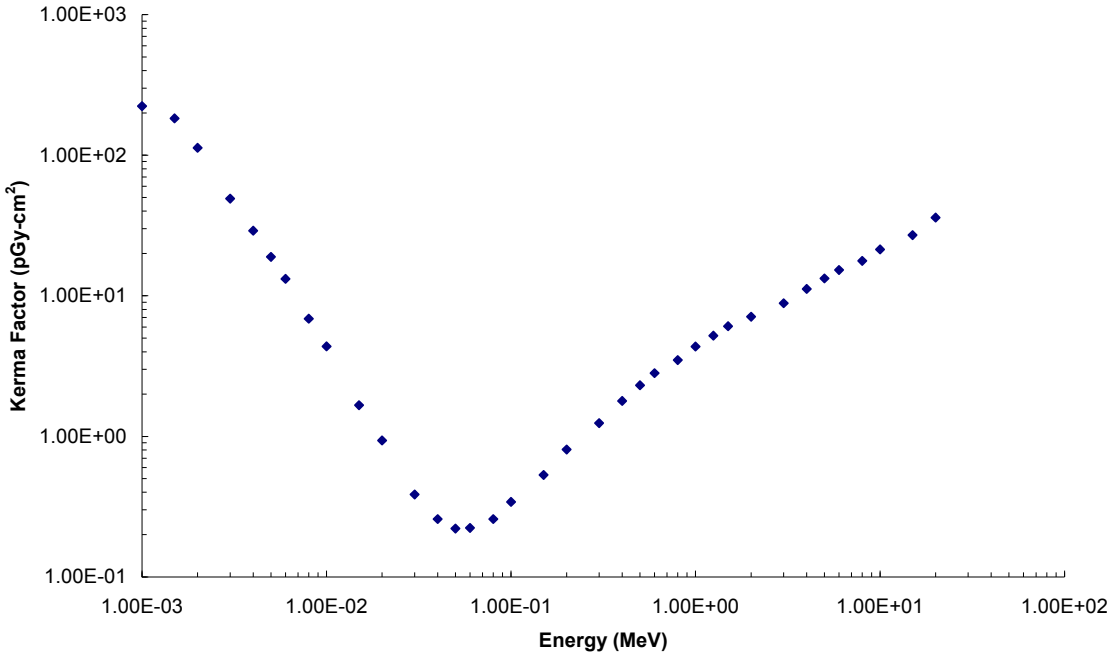

Figure 71. Calculated Kerma Factors for Virtual Water.

In order to bracket the electron beam energy, kerma calculations were performed for incident electron energies of 20, 23, 24, and 25 MeV. Absorbed dose calculations were only performed for the 25 MeV electron energy case. The results of the absorbed doses and kerma calculations in the virtual water phantom utilizing both methods are given in Table 66 through Table 70 and shown in Figure 72.

Table 66. Calculation of Absorbed Dose at 25 MeV for Beam Energy Assessment.

Calculation Description	Pb Thickness [cm]	D [Gy]	δD [Gy]	D [Gy/μC]	δD [Gy/μC]
Virtual Water Phantom Only	0.00	1.05E-15	6E-18	2.29E-01	1E-03
Virtual Water Phantom + 1 sheet lead	0.64	7.54E-16	9E-18	1.65E-01	2E-03
Virtual Water Phantom + 2 sheets lead	1.27	5.34E-16	5E-18	1.17E-01	1E-03
Virtual Water Phantom + 3 sheets lead	1.91	3.87E-16	3E-18	8.44E-02	5E-04
Virtual Water Phantom + 4 sheets lead	2.54	2.74E-16	2E-18	5.99E-02	4E-04
Virtual Water Phantom + 5 sheets lead	3.18	1.94E-16	1E-18	4.24E-02	3E-04
Virtual Water Phantom + 6 sheets lead	3.81	1.41E-16	1E-18	3.07E-02	2E-04

Table 67. Calculation of Kerma at 20 MeV for Beam Energy Assessment.

Calculation Description	Pb Thickness [cm]	Kerma [Gy]	δKerma [Gy]	Kerma [Gy/μC]	δKerma [Gy/μC]
Virtual Water Phantom Only	0.00	3.35E-16	5E-19	1.11E-01	2E-04
Virtual Water Phantom + 1 sheet lead	0.64	2.42E-16	1E-18	7.96E-02	3E-04
Virtual Water Phantom + 2 sheets lead	1.27	1.77E-16	4E-19	5.73E-02	1E-04
Virtual Water Phantom + 3 sheets lead	1.91	1.30E-16	3E-19	4.15E-02	9E-05
Virtual Water Phantom + 4 sheets lead	2.54	9.60E-17	4E-19	3.02E-02	1E-04
Virtual Water Phantom + 5 sheets lead	3.18	7.04E-17	2E-19	2.19E-02	6E-05
Virtual Water Phantom + 6 sheets lead	3.81	5.15E-17	2E-19	1.58E-02	5E-05

Table 68. Calculation of Kerma at 23 MeV for Beam Energy Assessment.

Calculation Description	Pb Thickness [cm]	Kerma [Gy]	δKerma [Gy]	Kerma [Gy/μC]	δKerma [Gy/μC]
Virtual Water Phantom Only	0.00	4.85E-16	7E-19	1.72E-01	3E-04
Virtual Water Phantom + 1 sheet lead	0.64	3.49E-16	6E-19	1.22E-01	2E-04
Virtual Water Phantom + 2 sheets lead	1.27	2.56E-16	9E-19	8.80E-02	3E-04
Virtual Water Phantom + 3 sheets lead	1.91	1.87E-16	4E-19	6.32E-02	1E-04
Virtual Water Phantom + 4 sheets lead	2.54	1.37E-16	5E-19	4.56E-02	2E-04
Virtual Water Phantom + 5 sheets lead	3.18	1.00E-16	2E-19	3.28E-02	8E-05
Virtual Water Phantom + 6 sheets lead	3.81	7.37E-17	2E-19	2.37E-02	6E-05

Table 69. Calculation of Kerma at 24 MeV for Beam Energy Assessment.

Calculation Description	Pb Thickness [cm]	Kerma [Gy]	δKerma [Gy]	Kerma [Gy/μC]	δKerma [Gy/μC]
Virtual Water Phantom Only	0.00	5.44E-16	8E-19	1.97E-01	3E-04
Virtual Water Phantom + 1 sheet lead	0.64	3.90E-16	7E-19	1.39E-01	2E-04
Virtual Water Phantom + 2 sheets lead	1.27	2.85E-16	5E-19	9.99E-02	2E-04
Virtual Water Phantom + 3 sheets lead	1.91	2.08E-16	4E-19	7.17E-02	2E-04
Virtual Water Phantom + 4 sheets lead	2.54	1.53E-16	5E-19	5.15E-02	2E-04
Virtual Water Phantom + 5 sheets lead	3.18	1.12E-16	3E-19	3.71E-02	9E-05
Virtual Water Phantom + 6 sheets lead	3.81	8.20E-17	2E-19	2.67E-02	6E-05

Table 70. Calculation of Kerma at 25 MeV for Beam Energy Assessment.

Calculation Description	Pb Thickness [cm]	Kerma [Gy]	δKerma [Gy]	Kerma [Gy/μC]	δKerma [Gy/μC]
Virtual Water Phantom Only	0.00	1.03E-15	2E-18	2.25E-01	5E-04
Virtual Water Phantom + 1 sheet lead	0.64	7.51E-16	1E-17	1.64E-01	2E-03
Virtual Water Phantom + 2 sheets lead	1.27	5.47E-16	6E-18	1.20E-01	1E-03
Virtual Water Phantom + 3 sheets lead	1.91	4.02E-16	4E-18	8.78E-02	9E-04
Virtual Water Phantom + 4 sheets lead	2.54	2.95E-16	5E-18	6.43E-02	1E-03
Virtual Water Phantom + 5 sheets lead	3.18	2.09E-16	4E-18	4.58E-02	1E-03
Virtual Water Phantom + 6 sheets lead	3.81	1.55E-16	4E-18	3.39E-02	8E-04

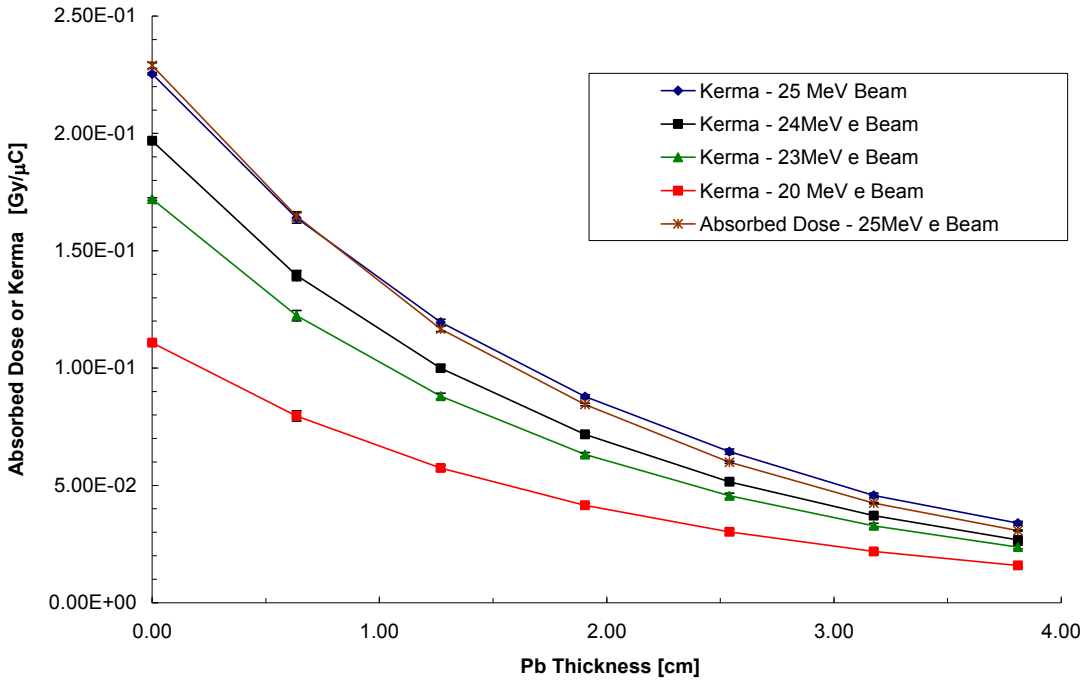

Figure 72. Absorbed Dose and Kerma Calulcation for Beam Energy Assessment. (The error bars are smaller than the size of the symbols).

5.3 Beam Profile Calculations

The shape and size of the photon beam was a critical metric for much of the present work. Therefore, in addition to a simplistic geometric calculation and measurement, as previously reported, the beam profile was calculated. The beam profile calculation employed a simplistic model in order to conserve computational time.

The approach utilized involved a series of photon flux point detector tallies (MCNP5 f5) arrayed along the x-axis (13 total) and y-axis (12 total) at beam centerline. The spacing between the point detectors increased at greater downfield distances proportional to the increased size of the photon beam, however, the total number of detectors employed was

conserved. These tallies provided point photon fluxes which were plotted as a function of horizontal distance and vertical distance, respectively. Beam profile calculations were performed for downfield distances of 8 meters (1 cm spacing between point detectors), 30 meters (4 cm spacing between point detectors) and 50 meters (15 cm spacing between point detectors). Since both the horizontal and vertical plots are the same, only the horizontal data are reported. Calculated horizontal profile plots are shown in Figure 73 through Figure 75.

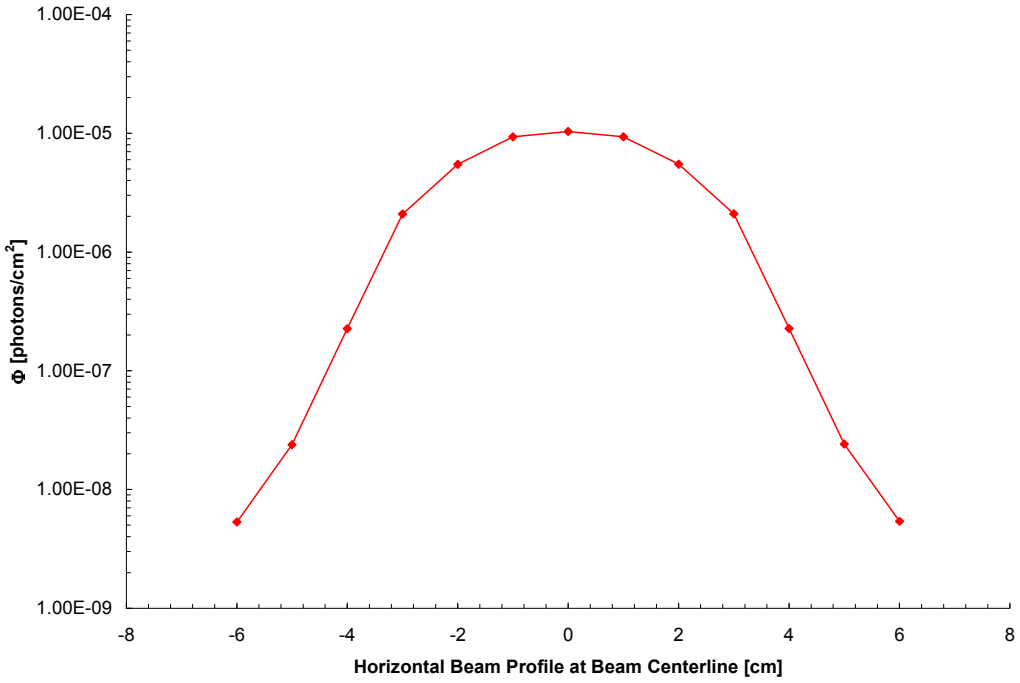

Figure 73. Horizontal Beam Profile Calculation at 8 meter Downfield Distance.

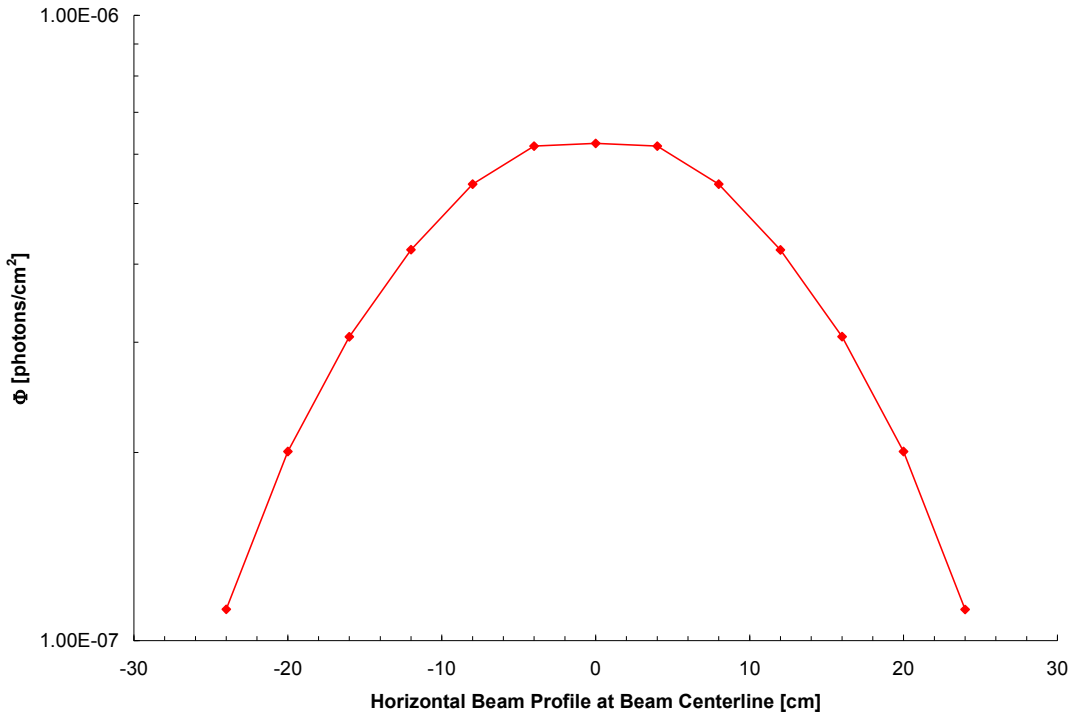

Figure 74. Horizontal Beam Profile Calculation at 30 meter Downfield Distance.

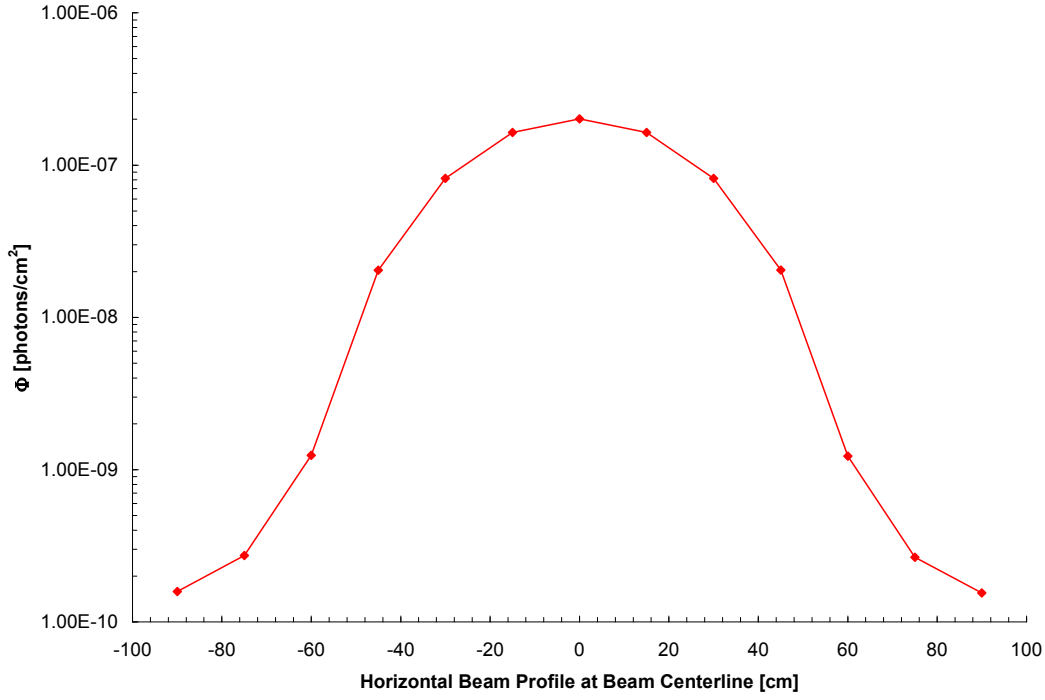

Figure 75. Horizontal Beam Profile Calculation at 50 meter Downfield Distance.

5.4 Secondary Dose Build-up Calculations

The ability of an instrument to accurately measure absorbed dose is predicated on the fact the charged particle equilibrium exists. Charged particle equilibrium, as defined in Chapter 2, is a condition that is fundamental to radiation dosimetry [75]. Since the dose in a photon field stems from the ionization and excitation of the secondary charged particles which are generated via the photoelectric effect, Compton scattering and pair production, achieving CPE in a dose measuring device is required to obtain a reasonable estimate of the dose. The challenge in high-energy bremsstrahlung fields is that current (standard) dosimeters do not provide for CPE above a few MeV. CPE can be obtained by placing tissue-equivalent material (such as a build-up cap) around the dosimeter. This material is generally tissue equivalent plastic or polymethyl methacrylate (PMMA). The challenge with using a build-up cap is ensuring that the low-energy portion of the photon spectrum is not overly attenuated. This attenuation will cause an underestimate in the total dose measured by the dosimeter.

In order to understand the effect of dose build-up in the primary beam, a set of simulations was performed to calculate the build-up. The idea is to ascertain the location (thickness) where the absorbed dose peaks, which is the appropriate thickness of tissue-equivalent material needed to obtain CPE. The build-up simulations utilized the guidance outlined in the ANSI/HPS.N13.11 standard for irradiation phantoms [76]. As outlined in the standard, the model contained a 30 cm x 30 cm x 20 cm PMMA phantom placed at the beam centerline, at a downfield distance of 10 meters. In the downfield (20-cm) dimension, the phantom was sliced into fifteen 1-cm thick sheets of PMMA with a

solid 5-cm section at the end of the phantom. An energy deposition tally (MCNP5 *f8) was used to directly calculate the absorbed dose averaged over the volume of each PMMA thickness. The energy deposition, in units of MeV, was converted to absorbed dose in units of Gy/μC in a post processing calculation. The results of these calculations for a downfield distance of 10 meters are presented in Figure 76. The absorbed dose at a downfield distance of 10 meters at the centerline of the primary beam peaks at approximately 5 cm.

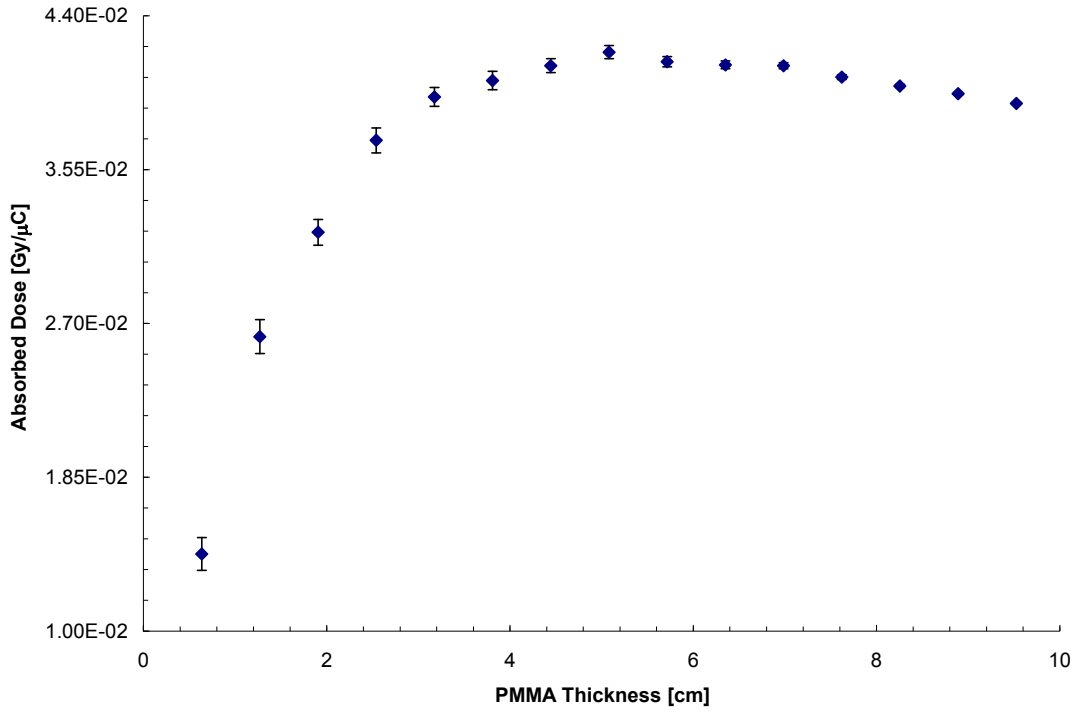

Figure 76. Calculated Dose Build-up in PMMA Phantom at 10 meters (Beam Centerline).

5.5 Effective Dose Calculations

Several approaches exist in the calculation of effective dose. The first principles approach is to use a Monte Carlo model of an anthropomorphic phantom to calculate energy deposition and thus absorbed dose in individual organs. The absorbed dose data are then used to calculate effective dose by employing tissue weighting factors as outlined in the methodology of ICRP Publication 60 [77]. Several groups have simplified this approach by calculating fluence-to-effective dose conversion coefficients much like the ambient dose equivalent conversion coefficients discussed in Chapter 3. Several authors present reviews such works [79-82].

The coefficients are developed based on the irradiation of anatomical phantoms. Since the number of geometries in which the human body may be irradiated is limitless, it has become convention to employ specific geometries which are clearly defined. In general, calculations are carried out assuming whole-body irradiation by broad unidirectional or plane-parallel beams [20]. A schematic of the irradiation geometries is shown in Figure 77. The irradiation geometries employed in this work are defined in ICRP Publication 74 as follows:

Antero-posterior geometry (AP) – The irradiation geometry in which the ionizing radiation is incident on the front of the body in a direction orthogonal to the long axis of the body;

Postero-anterior geometry (PA) – The irradiation geometry in which the ionizing radiation is incident on the back of the body in a direction orthogonal to the long axis of the body;

Lateral geometry(LAT) – The irradiation geometry in which the ionizing radiation is incident from either side of the body in a direction orthogonal to the long axis of the body;

Rotational geometry – The irradiation geometry in which the body is irradiated by a parallel beam of ionizing radiation, from a direction orthogonal to the long axis of the body, which rotates at a uniform rate around the long axis;

Isotropic geometry – Defined by a radiation field in which the particle fluence per unit of solid angle is independent of direction [20].

All effective doses for the present work were calculated using published effective dose conversion coefficients and will be discussed individually in the following subsections. All effective dose data are reported in units of Sv and are normalized on a per μC basis. In addition, the effective dose-weighted average energy in units of MeV, are reported.

5.5.1 Photon Effective Dose Calculations

The photon fluence-to-effective dose conversion coefficients of Sutton et al. were used to calculate effective dose at downfield distances of 10, 25, 50, 100, 120 and 170 meters [79]. These coefficients were folded with photon fluences calculated with MCNP5 as previously discussed. Effective dose for the AP, PA, R-LAT and ROT irradiation geometries were calculated. A summary of the photon effective dose conversion coefficients utilized is presented in Table 71 and shown in Figure 78. Photon effective doses (AP) calculated for the PITAS prototype are given in Table 72 through Table 77. All additional photon effective dose data are reported in Appendix H.

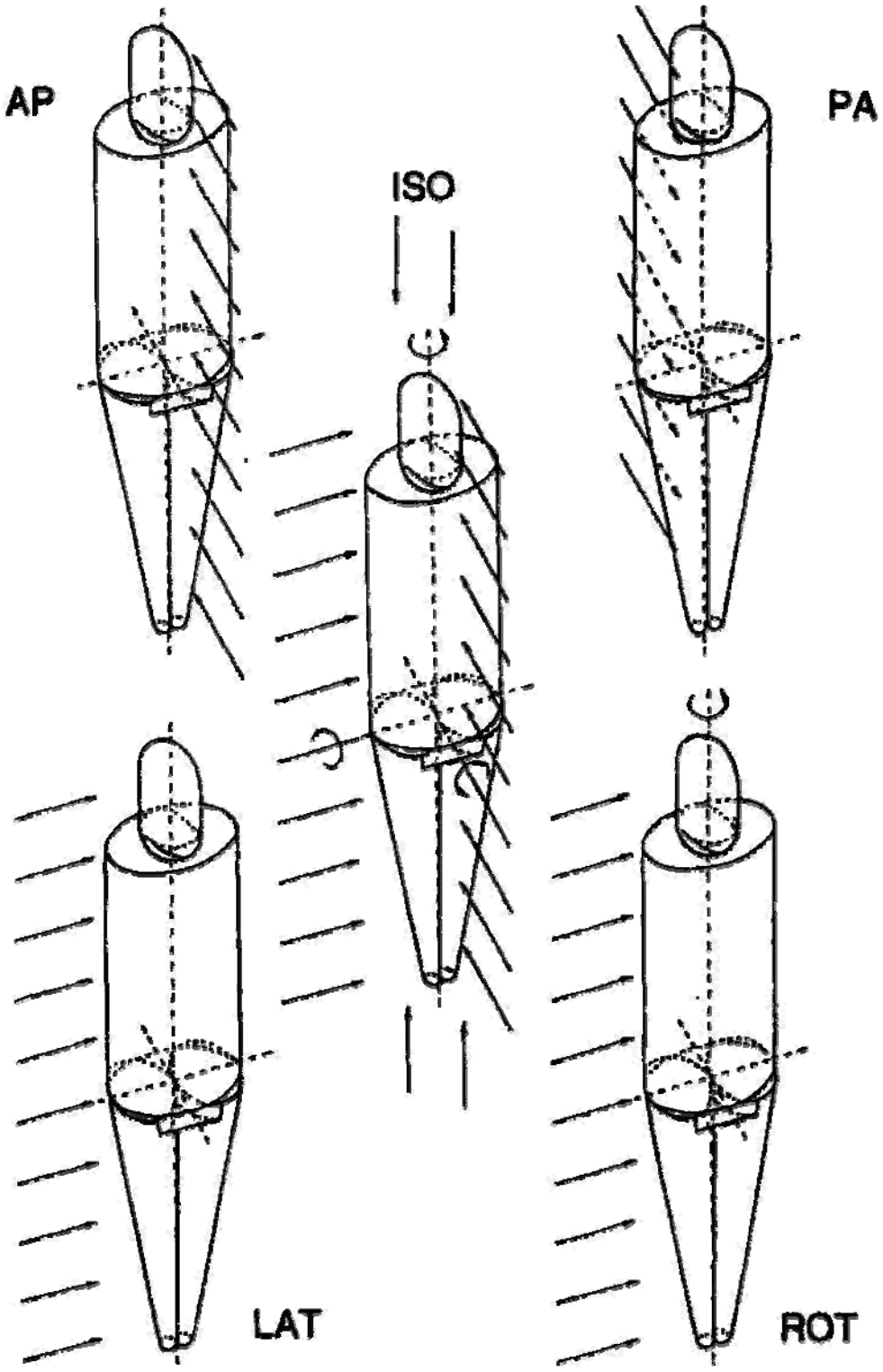

Figure 77. Anthropomorphic Phantom Irradiation Geometries Used in Effective Dose Calculations. Reprinted from [20].

Table 71. Photon Fluence-to-Effective Dose Conversion Coefficients. Reprinted from [79].

ENERGY [MeV]	AP [pSv-cm^2]	PA [pSv-cm^2]	R-LAT [pSv-cm^2]	ROT [pSv-cm^2]
1.00E-02	0.056	0.016	0.012	0.024
1.50E-02	0.120	0.023	0.020	0.053
2.00E-02	0.177	0.037	0.030	0.082
3.00E-02	0.263	0.081	0.053	0.133
4.00E-02	0.33	0.14	0.08	0.18
5.00E-02	0.38	0.20	0.11	0.22
6.00E-02	0.42	0.26	0.13	0.25
8.00E-02	0.50	0.37	0.19	0.32
1.00E-01	0.57	0.48	0.25	0.38
1.50E-01	0.74	0.72	0.39	0.53
2.00E-01	0.93	0.94	0.53	0.70
3.00E-01	1.4	1.3	0.81	1.1
4.00E-01	1.9	1.7	1.1	1.5
5.00E-01	2.5	2.0	1.3	1.9
6.00E-01	3.0	2.3	1.6	2.3
8.00E-01	3.9	2.9	2.1	3.0
1.00E+00	4.6	3.5	2.6	3.6
1.50E+00	6.1	5.0	3.8	5.0
2.00E+00	7.3	6.3	5.0	6.2
3.00E+00	9.6	9.0	7.3	8.4
4.00E+00	12	11	10	10
5.00E+00	14	14	12	12
6.00E+00	15	16	14	14
8.00E+00	19	20	18	18
1.00E+01	22	24	21	21
1.50E+01	28	31	29	28
2.00E+01	33	38	36	35
3.00E+01	41	48	48	46

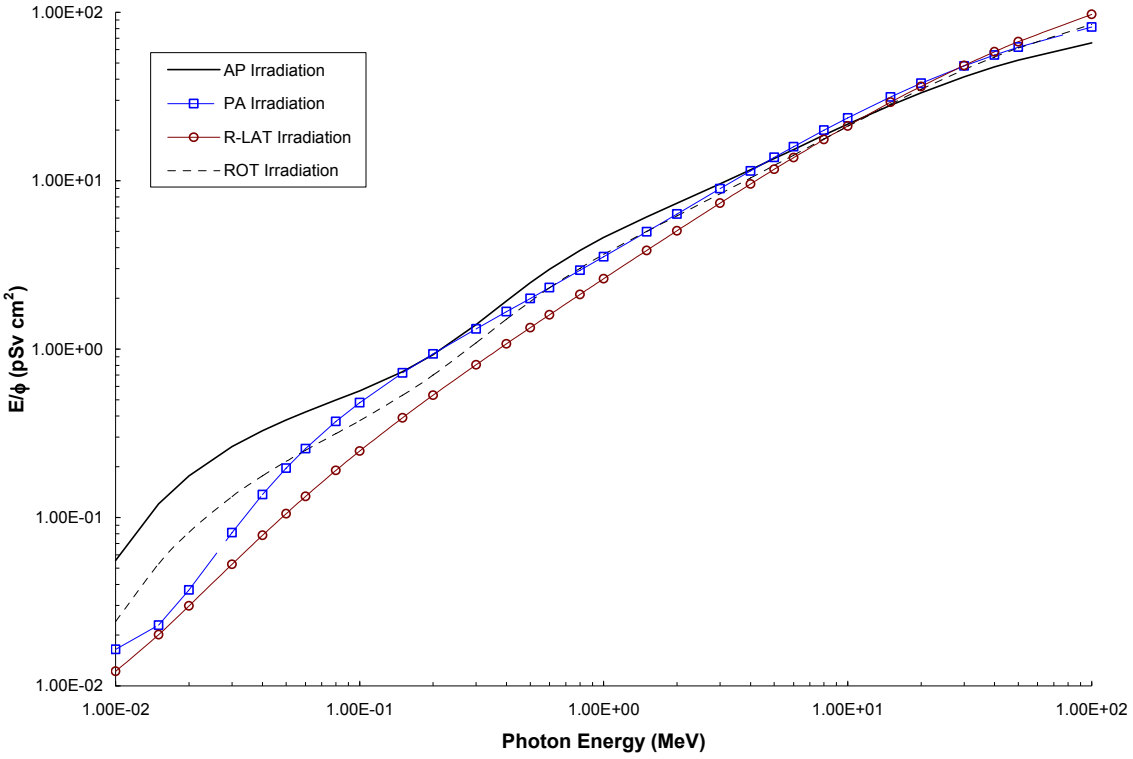

Figure 78. Photon Fluence-to-Effective Dose Conversion Coefficients. Reprinted from [79].

Table 72. Photon Effective Dose (AP) Data at 10 meters.

Orientation from Beam Centerline	Off-Axis Angle	Φ_{TOTAL} [photons/cm^2/source e$^-$]	E (AP) [Sv]	δE (AP) [Sv]	E (AP) [Sv/μC]	δE (AP) [Sv/μC]	E Dose-Weighted Average Energy [MeV]
Beam LEFT	-45	1.80E-10	8.60E-22	5E-24	5.37E-09	3E-11	2.33
Beam LEFT	-30	3.00E-10	1.56E-21	1E-23	9.76E-09	9E-11	2.78
Beam LEFT	-20	5.22E-10	3.83E-21	4E-23	2.39E-08	3E-10	4.04
Beam LEFT	-10	4.58E-10	2.36E-21	5E-23	1.47E-08	3E-10	2.95
Beam LEFT	-5	5.83E-10	3.27E-21	8E-23	2.04E-08	5E-10	3.59
Beam LEFT	-2	9.91E-10	6.42E-21	2E-22	4.01E-08	1E-09	4.40
Beam LEFT	-1	2.20E-09	1.71E-20	5E-22	1.07E-07	3E-09	4.97
Beam LEFT	-0.5	6.28E-07	8.03E-18	2E-20	5.01E-05	1E-07	6.33
Beam CENTER	0	6.48E-06	7.91E-17	7E-20	4.93E-04	4E-07	6.28
Beam RIGHT	0.5	6.27E-07	8.03E-18	2E-20	5.01E-05	1E-07	6.33
Beam RIGHT	1	2.26E-09	1.78E-20	3E-22	1.11E-07	2E-09	4.95
Beam RIGHT	2	1.01E-09	6.67E-21	1E-22	4.16E-08	9E-10	4.42
Beam RIGHT	5	6.06E-10	3.46E-21	1E-22	2.16E-08	9E-10	3.64
Beam RIGHT	10	4.64E-10	2.35E-21	4E-23	1.46E-08	3E-10	2.86
Beam RIGHT	20	5.15E-10	3.79E-21	3E-23	2.37E-08	2E-10	4.06
Beam RIGHT	30	3.03E-10	1.57E-21	1E-23	9.83E-09	9E-11	2.79
Beam RIGHT	45	1.82E-10	8.60E-22	6E-24	5.37E-09	4E-11	2.32

Table 73. Photon Effective Dose (AP) Data at 25 meters.

Orientation from Beam Centerline	Off-Axis Angle	Φ_{TOTAL} [photons/cm^2/source e$^-$]	E (AP) [Sv]	δE (AP) [Sv]	E (AP) [Sv/μC]	δE (AP) [Sv/μC]	E Dose-Weighted Average Energy [MeV]
Beam LEFT	-45	2.54E-11	1.27E-22	1E-24	7.92E-10	7E-12	2.37
Beam LEFT	-30	4.56E-11	2.48E-22	2E-24	1.55E-09	1E-11	2.80
Beam LEFT	-20	7.12E-11	4.08E-22	3E-24	2.54E-09	2E-11	3.08
Beam LEFT	-10	7.77E-11	4.03E-22	5E-24	2.52E-09	3E-11	2.85
Beam LEFT	-5	1.13E-10	6.41E-22	1E-23	4.00E-09	6E-11	3.55
Beam LEFT	-2	2.27E-10	1.42E-21	4E-23	8.84E-09	2E-10	4.22
Beam LEFT	-1	5.15E-10	3.77E-21	1E-22	2.35E-08	7E-10	4.76
Beam LEFT	-0.5	1.06E-07	1.39E-18	3E-21	8.68E-06	2E-08	6.39
Beam CENTER	0	9.26E-07	1.16E-17	9E-21	7.27E-05	6E-08	6.35
Beam RIGHT	0.5	1.06E-07	1.39E-18	2E-21	8.67E-06	1E-08	6.39
Beam RIGHT	1	4.97E-10	3.71E-21	8E-23	2.32E-08	5E-10	4.79
Beam RIGHT	2	2.28E-10	1.44E-21	6E-23	8.97E-09	4E-10	4.25
Beam RIGHT	5	1.12E-10	6.35E-22	2E-23	3.96E-09	1E-10	3.55
Beam RIGHT	10	7.77E-11	4.01E-22	5E-24	2.50E-09	3E-11	2.83
Beam RIGHT	20	7.33E-11	4.13E-22	6E-24	2.58E-09	4E-11	3.07
Beam RIGHT	30	4.52E-11	2.47E-22	2E-24	1.54E-09	1E-11	2.80
Beam RIGHT	45	2.54E-11	1.27E-22	9E-25	7.91E-10	6E-12	2.36

Table 74. Photon Effective Dose (AP) Data at 50 meters.

Orientation from Beam Centerline	Off-Axis Angle	Φ_{TOTAL} [photons/cm^2/source e$^-$]	E (AP) [Sv]	δE (AP) [Sv]	E (AP) [Sv/μC]	δE (AP) [Sv/μC]	E Dose-Weighted Average Energy [MeV]
Beam LEFT	-45	5.22E-12	2.70E-23	5E-25	1.69E-10	3E-12	2.41
Beam LEFT	-30	1.02E-11	5.74E-23	7E-25	3.58E-10	4E-12	2.84
Beam LEFT	-20	1.90E-11	1.41E-22	2E-24	8.80E-10	1E-11	4.00
Beam LEFT	-10	2.14E-11	1.11E-22	2E-24	6.93E-10	1E-11	2.86
Beam LEFT	-5	3.58E-11	2.02E-22	4E-24	1.26E-09	3E-11	3.54
Beam LEFT	-2	7.73E-11	4.94E-22	1E-23	3.08E-09	6E-11	4.20
Beam LEFT	-1	1.64E-10	1.22E-21	2E-23	7.61E-09	1E-10	4.71
Beam LEFT	-0.5	2.45E-08	3.32E-19	6E-22	2.07E-06	4E-09	6.48
Beam CENTER	0	2.01E-07	2.65E-18	2E-21	1.65E-05	1E-08	6.45
Beam RIGHT	0.5	2.46E-08	3.32E-19	8E-22	2.07E-06	5E-09	6.48
Beam RIGHT	1	1.74E-10	1.25E-21	5E-23	7.78E-09	3E-10	4.64
Beam RIGHT	2	7.59E-11	4.87E-22	1E-23	3.04E-09	6E-11	4.21
Beam RIGHT	5	3.51E-11	2.00E-22	4E-24	1.25E-09	2E-11	3.56
Beam RIGHT	10	2.17E-11	1.12E-22	2E-24	6.98E-10	1E-11	2.86
Beam RIGHT	20	1.98E-11	1.41E-22	7E-24	8.78E-10	4E-11	3.95
Beam RIGHT	30	1.01E-11	5.66E-23	8E-25	3.53E-10	5E-12	2.86
Beam RIGHT	45	5.13E-12	2.68E-23	4E-25	1.67E-10	3E-12	2.43

Table 75. Photon Effective Dose (AP) Data at 100 meters.

Orientation from Beam Centerline	Off-Axis Angle	Φ_{TOTAL} [photons/cm^2/source e$^-$]	E (AP) [Sv]	δE (AP) [Sv]	E (AP) [Sv/μC]	δE (AP) [Sv/μC]	E Dose-Weighted Average Energy [MeV]
Beam LEFT	-45	8.16E-13	4.72E-24	5E-26	2.95E-11	3E-13	2.59
Beam LEFT	-30	1.94E-12	1.15E-23	1E-25	7.19E-11	8E-13	2.92
Beam LEFT	-20	3.98E-12	3.02E-23	3E-25	1.89E-10	2E-12	4.02
Beam LEFT	-10	5.66E-12	3.03E-23	5E-25	1.89E-10	3E-12	2.95
Beam LEFT	-5	1.14E-11	6.60E-23	2E-24	4.12E-10	1E-11	3.62
Beam LEFT	-2	2.73E-11	1.77E-22	4E-24	1.10E-09	3E-11	4.21
Beam LEFT	-1	5.90E-11	4.21E-22	2E-23	2.63E-09	1E-10	4.59
Beam LEFT	-0.5	5.02E-09	7.25E-20	1E-22	4.52E-07	7E-10	6.65
Beam CENTER	0	3.95E-08	5.62E-19	4E-22	3.51E-06	2E-09	6.65
Beam RIGHT	0.5	5.02E-09	7.25E-20	1E-22	4.53E-07	7E-10	6.65
Beam RIGHT	1	5.95E-11	4.22E-22	2E-23	2.63E-09	1E-10	4.63
Beam RIGHT	2	2.84E-11	1.80E-22	7E-24	1.12E-09	5E-11	4.19
Beam RIGHT	5	1.16E-11	6.61E-23	2E-24	4.13E-10	1E-11	3.61
Beam RIGHT	10	5.75E-12	3.06E-23	6E-25	1.91E-10	4E-12	2.93
Beam RIGHT	20	3.95E-12	3.01E-23	2E-25	1.88E-10	1E-12	4.02
Beam RIGHT	30	1.91E-12	1.14E-23	1E-25	7.10E-11	7E-13	2.95
Beam RIGHT	45	8.30E-13	4.77E-24	1E-25	2.98E-11	7E-13	2.60

Table 76. Photon Effective (AP) Dose Data at 120 meters.

Orientation from Beam Centerline	Off-Axis Angle	Φ_{TOTAL} [photons/cm^2/source e$^-$]	E (AP) [Sv]	δE (AP) [Sv]	E (AP) [Sv/μC]	δE (AP) [Sv/μC]	E Dose-Weighted Average Energy [MeV]
Beam LEFT	-45	4.78E-13	2.90E-24	4E-26	1.81E-11	2E-13	2.68
Beam LEFT	-30	1.21E-12	7.31E-24	1E-25	4.56E-11	7E-13	2.95
Beam LEFT	-20	2.56E-12	1.97E-23	2E-25	1.23E-10	1E-12	4.02
Beam LEFT	-10	3.90E-12	2.12E-23	3E-25	1.32E-10	2E-12	2.96
Beam LEFT	-5	8.56E-12	4.91E-23	2E-24	3.06E-10	1E-11	3.63
Beam LEFT	-2	2.05E-11	1.34E-22	4E-24	8.37E-10	3E-11	4.27
Beam LEFT	-1	4.03E-11	3.04E-22	6E-24	1.90E-09	4E-11	4.69
Beam LEFT	-0.5	3.23E-09	4.76E-20	2E-22	2.97E-07	1E-09	6.70
Beam CENTER	0	2.51E-08	3.67E-19	5E-22	2.29E-06	3E-09	6.72
Beam RIGHT	0.5	3.23E-09	4.76E-20	1E-22	2.97E-07	6E-10	6.71
Beam RIGHT	1	5.61E-11	3.41E-22	8E-23	2.13E-09	5E-10	4.30
Beam RIGHT	2	2.06E-11	1.33E-22	5E-24	8.31E-10	3E-11	4.24
Beam RIGHT	5	8.28E-12	4.87E-23	1E-24	3.04E-10	9E-12	3.71
Beam RIGHT	10	3.91E-12	2.17E-23	5E-25	1.35E-10	3E-12	3.00
Beam RIGHT	20	2.56E-12	1.97E-23	3E-25	1.23E-10	2E-12	4.05
Beam RIGHT	30	1.22E-12	7.35E-24	2E-25	4.59E-11	1E-12	2.97
Beam RIGHT	45	4.65E-13	2.84E-24	2E-26	1.77E-11	1E-13	2.67

Table 77. Photon Effective Dose (AP) Data at 170 meters.

Orientation from Beam Centerline	Off-Axis Angle	Φ_{TOTAL} [photons/cm^2/source e$^-$]	E (AP) [Sv]	δE (AP) [Sv]	E (AP) [Sv/μC]	δE (AP) [Sv/μC]	E Dose-Weighted Average Energy [MeV]
Beam LEFT	-45	1.51E-13	1.01E-24	1E-26	6.32E-12	7E-14	2.84
Beam LEFT	-30	4.32E-13	2.86E-24	5E-26	1.78E-11	3E-13	3.07
Beam LEFT	-20	1.06E-12	8.33E-24	1E-25	5.20E-11	9E-13	4.08
Beam LEFT	-10	1.77E-12	1.04E-23	2E-25	6.47E-11	9E-13	3.09
Beam LEFT	-5	4.25E-12	2.65E-23	1E-24	1.66E-10	6E-12	3.82
Beam LEFT	-2	1.16E-11	7.73E-23	3E-24	4.83E-10	2E-11	4.33
Beam LEFT	-1	2.45E-11	1.76E-22	9E-24	1.10E-09	5E-11	4.71
Beam LEFT	-0.5	1.33E-09	2.05E-20	5E-23	1.28E-07	3E-10	6.86
Beam CENTER	0	1.01E-08	1.57E-19	2E-22	9.78E-07	1E-09	6.88
Beam RIGHT	0.5	1.32E-09	2.05E-20	4E-23	1.28E-07	2E-10	6.85
Beam RIGHT	1	2.28E-11	1.71E-22	6E-24	1.07E-09	4E-11	4.74
Beam RIGHT	2	1.06E-11	7.44E-23	2E-24	4.64E-10	1E-11	4.40
Beam RIGHT	5	4.08E-12	2.59E-23	5E-25	1.61E-10	3E-12	3.83
Beam RIGHT	10	1.92E-12	1.07E-23	6E-25	6.71E-11	4E-12	3.04
Beam RIGHT	20	1.03E-12	8.32E-24	9E-26	5.19E-11	6E-13	4.10
Beam RIGHT	30	4.35E-13	2.85E-24	3E-26	1.78E-11	2E-13	3.08
Beam RIGHT	45	1.58E-13	1.03E-24	2E-26	6.43E-12	1E-13	2.80

5.5.2 Electron Effective Dose Calculations

The electron fluence-to-effective dose conversion coefficients of Ferrari and Pelliccioni were used to calculate effective dose at downfield distances of 10, 25, 50, 100, 120 and 170 meters [38]. These coefficients were folded with electron fluences calculated with MCNP5 as previously discussed. The contribution from electrons at far off-axis distances are not reported since calculating electron fluences at those locations was too computationally expensive. An interesting observation from these data was the high electron fluences observed directly off the beam's central axis (within 1 to 2 degrees).

Effective dose for the AP, PA, R-LAT and ISO irradiation geometries were calculated. A summary of the electron effective dose conversion coefficients utilized is presented in Table 78 and shown in Figure 79. Electron effective doses (AP) calculated for the PITAS prototype are given in Table 79 through Table 84. All additional electron effective dose data are reported in Appendix I.

Table 78. Electron Fluence-to-Effective Dose Conversion Coefficients. Reprinted from [38].

ENERGY [MeV]	AP [pSv-cm^2]	PA [pSv-cm^2]	R-LAT [pSv-cm^2]	ISO [pSv-cm^2]
5.00E+00	71.9	7.37	8.95	20.7
1.00E+01	152	42.7	20.5	51.2
2.00E+01	248	124	81.1	112
2.50E+01	274	194	109	138
3.00E+01	299	264	136	163

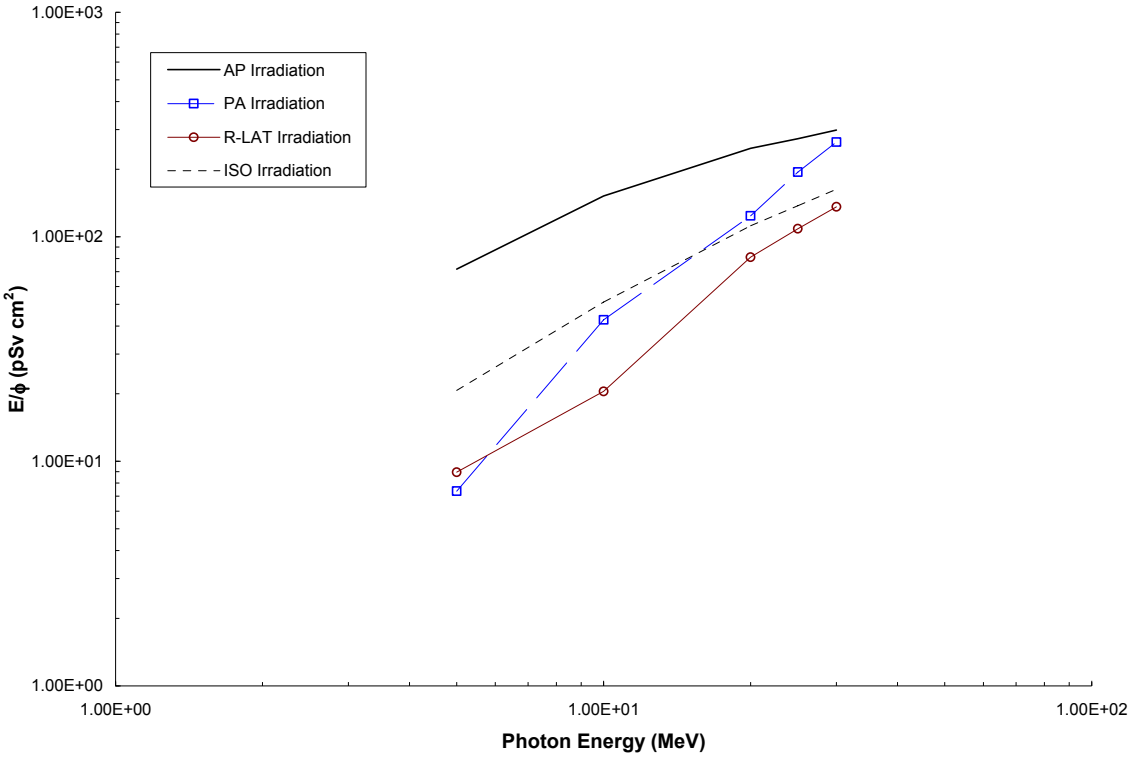

Figure 79. Electron Fluence-to-Effective Dose Conversion Coefficients. Reprinted from [38].

Table 79. Electron Effective Dose (AP) Data at 10 meters.

Orientation from Beam Centerline	Off-Axis Angle	Φ_{TOTAL} [electrons/cm^2/source e$^-$]	E (AP) [Sv]	δE (AP) [Sv]	E (AP) [Sv/μC]	δE (AP) [Sv/μC]
Beam LEFT	-5	8.73E-11	6.67E-21	5E-22	4.16E-08	3E-09
Beam LEFT	-2	3.17E-10	2.69E-20	8E-22	1.68E-07	5E-09
Beam LEFT	-1	8.27E-10	7.46E-20	1E-21	4.65E-07	6E-09
Beam CENTER	0	4.54E-09	4.42E-19	9E-22	2.76E-06	6E-09
Beam RIGHT	1	8.14E-10	7.31E-20	6E-22	4.56E-07	4E-09
Beam RIGHT	2	3.15E-10	2.68E-20	7E-22	1.67E-07	5E-09
Beam RIGHT	5	7.97E-11	5.94E-21	4E-22	3.70E-08	2E-09

Table 80. Electron Effective Dose (AP) Data at 25 meters.

Orientation from Beam Centerline	Off-Axis Angle	Φ_{TOTAL} [electrons/cm^2/source e$^-$]	E (AP) [Sv]	δE (AP) [Sv]	E (AP) [Sv/μC]	δE (AP) [Sv/μC]
Beam LEFT	-2	7.59E-11	6.07E-21	1E-22	3.79E-08	7E-10
Beam LEFT	-1	2.23E-10	1.90E-20	2E-22	1.18E-07	2E-09
Beam LEFT	-0.5	7.37E-10	6.73E-20	4E-22	4.20E-07	3E-09
Beam CENTER	0	2.00E-09	1.92E-19	7E-22	1.20E-06	4E-09
Beam RIGHT	0.5	7.37E-10	6.76E-20	5E-22	4.22E-07	3E-09
Beam RIGHT	1	2.20E-10	1.86E-20	2E-22	1.16E-07	1E-09
Beam RIGHT	2	7.85E-11	6.44E-21	2E-22	4.02E-08	1E-09

Table 81. Electron Effective Dose (AP) Data at 50 meters.

Orientation from Beam Centerline	Off-Axis Angle	Φ_{TOTAL} [electrons/cm^2/source e$^-$]	E (AP) [Sv]	δE (AP) [Sv]	E (AP) [Sv/μC]	δE (AP) [Sv/μC]
Beam LEFT	-2	2.51E-11	1.94E-21	9E-23	1.21E-08	5E-10
Beam LEFT	-1	7.74E-11	6.23E-21	1E-22	3.89E-08	9E-10
Beam LEFT	-0.5	2.69E-10	2.37E-20	2E-22	1.48E-07	1E-09
Beam CENTER	0	8.00E-10	7.59E-20	4E-22	4.74E-07	2E-09
Beam RIGHT	0.5	2.66E-10	2.37E-20	2E-22	1.48E-07	1E-09
Beam RIGHT	1	7.65E-11	6.24E-21	1E-22	3.90E-08	9E-10
Beam RIGHT	2	2.57E-11	1.97E-21	9E-23	1.23E-08	5E-10

Table 82. Electron Effective Dose (AP) Data at 100 meters.

Orientation from Beam Centerline	Off-Axis Angle	Φ_{TOTAL} [electrons/cm^2/source e$^-$]	E (AP) [Sv]	δE (AP) [Sv]	E (AP) [Sv/μC]	δE (AP) [Sv/μC]
Beam LEFT	-2	6.46E-12	4.63E-22	3E-23	2.89E-09	2E-10
Beam LEFT	-1	2.36E-11	1.80E-21	5E-23	1.13E-08	3E-10
Beam LEFT	-0.5	9.13E-11	7.84E-21	1E-22	4.89E-08	9E-10
Beam CENTER	0	2.85E-10	2.64E-20	2E-22	1.65E-07	1E-09
Beam RIGHT	0.5	8.96E-11	7.68E-21	1E-22	4.79E-08	7E-10
Beam RIGHT	1	2.35E-11	1.80E-21	5E-23	1.12E-08	3E-10
Beam RIGHT	2	6.46E-12	4.63E-22	3E-23	2.89E-09	2E-10

Table 83. Electron Effective Dose (AP) Data at 120 meters.

Orientation from Beam Centerline	Off-Axis Angle	Φ_{TOTAL} [electrons/cm^2/source e$^-$]	E (AP) [Sv]	δE (AP) [Sv]	E (AP) [Sv/μC]	δE (AP) [Sv/μC]
Beam LEFT	-2	4.51E-12	3.03E-22	2E-23	1.89E-09	2E-10
Beam LEFT	-1	1.59E-11	1.25E-21	5E-23	7.77E-09	3E-10
Beam LEFT	-0.5	6.52E-11	5.63E-21	1E-22	3.52E-08	7E-10
Beam CENTER	0	2.10E-10	1.93E-20	2E-22	1.21E-07	1E-09
Beam RIGHT	0.5	6.52E-11	5.59E-21	1E-22	3.49E-08	8E-10
Beam RIGHT	1	1.67E-11	1.24E-21	5E-23	7.73E-09	3E-10
Beam RIGHT	2	4.36E-12	2.97E-22	2E-23	1.85E-09	1E-10

Table 84. Electron Effective Dose (AP) Data at 170 meters.

Orientation from Beam Centerline	Off-Axis Angle	Φ_{TOTAL} [electrons/cm^2/source e$^-$]	E (AP) [Sv]	δE (AP) [Sv]	E (AP) [Sv/μC]	δE (AP) [Sv/μC]
Beam LEFT	-1	7.95E-12	5.76E-22	6E-23	3.59E-09	4E-10
Beam LEFT	-0.5	3.26E-11	2.92E-21	1E-22	1.82E-08	9E-10
Beam CENTER	0	1.17E-10	1.11E-20	3E-22	6.92E-08	2E-09
Beam RIGHT	0.5	3.26E-11	2.92E-21	1E-22	1.82E-08	9E-10
Beam RIGHT	1	7.95E-12	5.76E-22	6E-23	3.59E-09	4E-10

5.5.3 Neutron Effective Dose Calculations

The neutron fluence-to-effective dose conversion coefficients of Sutton et al. were used to calculate effective dose at downfield distances of 10, 25, 50, 100, 120 and 170 meters [79]. These coefficients were folded with neutron fluences calculated with MCNP5 as previously discussed. Effective dose for the AP, PA, R-LAT and ROT irradiation geometries were calculated. A summary of the neutron effective dose conversion coefficients utilized is shown in Figure 80 and given in Table 85. Neutron effective doses (AP) calculated for the PITAS prototype are given in Table 86 through Table 91. All additional neutron effective dose data are reported in Appendix J.

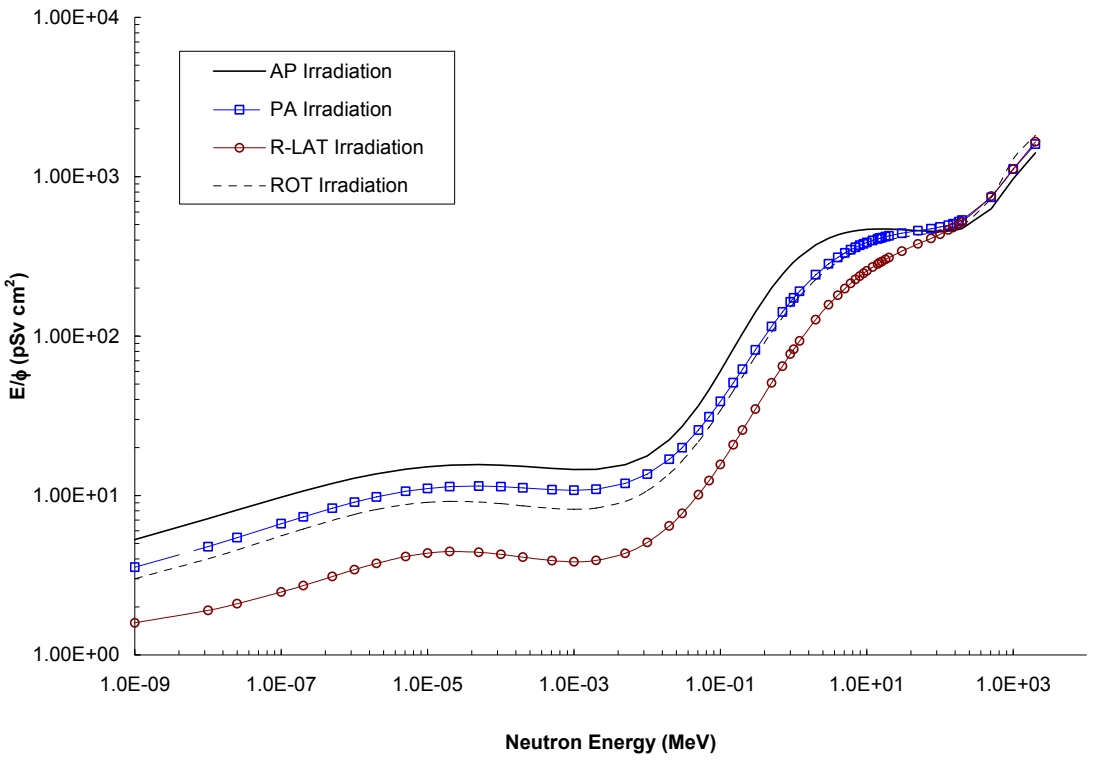

Figure 80. Neutron Fluence-to-Effective Dose Conversion Coefficients. Reprinted from [79].

Table 85. Neutron Fluence-to-Effective Dose Conversion Coefficients. Reprinted from [79].

ENERGY [MeV]	AP [pSv-cm^2]	PA [pSv-cm^2]	R-LAT [pSv-cm^2]	ROT [pSv-cm^2]
1.00E-09	5.3	3.5	1.6	3.0
1.00E-08	7.2	4.8	1.9	4.0
2.50E-08	8.1	5.4	2.1	4.6
1.00E-07	9.8	6.7	2.5	5.6
2.00E-07	10.7	7.3	2.7	6.2
5.00E-07	11.9	8.3	3.1	7.0
1.00E-06	12.8	9.1	3.4	7.6
2.00E-06	13.7	9.8	3.7	8.2
5.00E-06	14.6	10.6	4.1	8.8
1.00E-05	15.2	11.1	4.3	9.1
2.00E-05	15.5	11.4	4.4	9.2
5.00E-05	15.6	11.5	4.4	9.1
1.00E-04	15.5	11.4	4.3	8.9
2.00E-04	15.2	11.2	4.1	8.6
5.00E-04	14.8	10.9	3.9	8.3
1.00E-03	14.6	10.8	3.8	8.2
2.00E-03	14.6	10.9	3.9	8.3
5.00E-03	15.6	11.9	4.3	9.2
1.00E-02	17.7	13.6	5.1	10.7
2.00E-02	22.4	16.9	6.4	13.7
3.00E-02	27	20	8	16
5.00E-02	37	26	10	22
7.00E-02	46	31	12	27
1.00E-01	60	39	16	34
1.50E-01	83	51	21	45
2.00E-01	104	62	26	56
3.00E-01	142	82	35	75
5.00E-01	201	115	51	106
7.00E-01	244	142	65	131
9.00E-01	277	164	77	152
1.00E+00	291	173	83	161
1.20E+00	314	191	93	178
2.00E+00	373	242	127	226
3.00E+00	411	284	157	265
4.00E+00	431	311	180	292
5.00E+00	444	332	199	311
6.00E+00	452	348	214	326
7.00E+00	458	360	227	338
8.00E+00	462	370	238	348
9.00E+00	465	379	247	357
1.00E+01	466	386	256	364
1.20E+01	469	398	271	375
1.40E+01	470	407	283	384
1.50E+01	470	411	288	387
1.60E+01	470	414	293	391
1.80E+01	470	420	303	396
2.00E+01	469	425	311	401
3.00E+01	466	442	341	417

Table 86. Neutron Effective Dose (AP) Data at 10 meters.

Orientation from Beam Centerline	Off-Axis Angle	Φ_{TOTAL} [neutrons/cm^2/source e$^-$]	E (AP) [Sv]	δE (AP) [Sv]	E (AP) [Sv/μC]	δE (AP) [Sv/μC]	E Dose-Weighted Average Energy [MeV]
Beam LEFT	-45	5.06E-12	4.29E-22	2E-24	2.68E-09	1E-11	1.55
Beam LEFT	-30	6.83E-12	4.75E-22	1E-24	2.96E-09	8E-12	1.36
Beam LEFT	-20	7.17E-12	4.78E-22	2E-24	2.99E-09	1E-11	1.36
Beam LEFT	-10	7.18E-12	4.86E-22	1E-24	3.03E-09	9E-12	1.37
Beam LEFT	-5	7.17E-12	4.97E-22	3E-24	3.10E-09	2E-11	1.36
Beam LEFT	-2	7.26E-12	5.12E-22	6E-24	3.19E-09	4E-11	1.34
Beam LEFT	-1	7.39E-12	5.77E-22	3E-24	3.60E-09	2E-11	1.49
Beam LEFT	-0.5	7.77E-12	7.01E-22	4E-24	4.37E-09	2E-11	1.74
Beam CENTER	0	8.18E-12	8.70E-22	4E-24	5.43E-09	2E-11	2.11
Beam RIGHT	0.5	7.71E-12	6.99E-22	2E-24	4.36E-09	2E-11	1.73
Beam RIGHT	1	7.36E-12	5.81E-22	3E-24	3.63E-09	2E-11	1.48
Beam RIGHT	2	7.23E-12	5.30E-22	6E-24	3.31E-09	4E-11	1.37
Beam RIGHT	5	7.15E-12	4.98E-22	2E-24	3.11E-09	1E-11	1.37
Beam RIGHT	10	7.13E-12	4.87E-22	1E-24	3.04E-09	8E-12	1.37
Beam RIGHT	20	7.17E-12	4.80E-22	2E-24	3.00E-09	1E-11	1.37
Beam RIGHT	30	6.86E-12	4.75E-22	2E-24	2.96E-09	1E-11	1.37
Beam RIGHT	45	5.04E-12	4.26E-22	1E-24	2.66E-09	8E-12	1.54

Table 87. Neutron Effective Dose (AP) Data at 25 meters.

Orientation from Beam Centerline	Off-Axis Angle	Φ_{TOTAL} [neutrons/cm^2/source e$^-$]	E (AP) [Sv]	δE (AP) [Sv]	E (AP) [Sv/μC]	δE (AP) [Sv/μC]	E Dose-Weighted Average Energy [MeV]
Beam LEFT	-45	4.75E-13	5.21E-23	2E-25	3.25E-10	1E-12	1.42
Beam LEFT	-30	7.95E-13	6.24E-23	4E-25	3.89E-10	3E-12	1.41
Beam LEFT	-20	9.21E-13	6.48E-23	3E-25	4.04E-10	2E-12	1.38
Beam LEFT	-10	9.62E-13	6.59E-23	2E-24	4.11E-10	1E-11	1.38
Beam LEFT	-5	9.55E-13	6.80E-23	8E-25	4.24E-10	5E-12	1.28
Beam LEFT	-2	9.44E-13	6.90E-23	7E-25	4.31E-10	5E-12	1.42
Beam LEFT	-1	9.59E-13	7.78E-23	3E-25	4.85E-10	2E-12	1.52
Beam LEFT	-0.5	1.00E-12	9.35E-23	4E-25	5.84E-10	2E-12	1.72
Beam CENTER	0	1.07E-12	1.17E-22	5E-25	7.30E-10	3E-12	2.17
Beam RIGHT	0.5	1.02E-12	9.69E-23	8E-25	6.05E-10	5E-12	1.90
Beam RIGHT	1	9.67E-13	7.82E-23	5E-25	4.88E-10	3E-12	1.54
Beam RIGHT	2	9.40E-13	6.87E-23	3E-25	4.29E-10	2E-12	1.41
Beam RIGHT	5	9.63E-13	7.36E-23	2E-24	4.60E-10	1E-11	1.34
Beam RIGHT	10	9.35E-13	6.58E-23	9E-25	4.10E-10	5E-12	1.39
Beam RIGHT	20	9.11E-13	6.53E-23	3E-25	4.08E-10	2E-12	1.38
Beam RIGHT	30	7.88E-13	6.25E-23	4E-25	3.90E-10	2E-12	1.41
Beam RIGHT	45	5.00E-13	6.02E-23	3E-24	3.76E-10	2E-11	1.63

Table 88. Neutron Effective Dose (AP) Data at 50 meters.

Orientation from Beam Centerline	Off-Axis Angle	Φ_{TOTAL} [neutrons/cm^2/source e$^-$]	E (AP) [Sv]	δE (AP) [Sv]	E (AP) [Sv/μC]	δE (AP) [Sv/μC]	E Dose-Weighted Average Energy [MeV]
Beam LEFT	-45	5.03E-14	8.91E-24	1E-25	5.56E-11	6E-13	1.82
Beam LEFT	-30	9.74E-14	1.16E-23	2E-25	7.22E-11	1E-12	1.58
Beam LEFT	-20	1.14E-13	1.19E-23	1E-25	7.40E-11	7E-13	1.51
Beam LEFT	-10	1.26E-13	1.27E-23	1E-25	7.91E-11	9E-13	1.61
Beam LEFT	-5	1.27E-13	1.26E-23	1E-25	7.88E-11	6E-13	1.51
Beam LEFT	-2	1.28E-13	1.32E-23	1E-25	8.21E-11	6E-13	1.59
Beam LEFT	-1	1.36E-13	1.52E-23	1E-25	9.49E-11	9E-13	1.73
Beam LEFT	-0.5	1.47E-13	1.92E-23	3E-25	1.20E-10	2E-12	2.11
Beam CENTER	0	1.69E-13	2.73E-23	1E-24	1.70E-10	6E-12	2.56
Beam RIGHT	0.5	1.56E-13	1.94E-23	1E-24	1.21E-10	7E-12	2.04
Beam RIGHT	1	1.37E-13	1.54E-23	2E-25	9.58E-11	1E-12	1.74
Beam RIGHT	2	1.29E-13	1.31E-23	1E-25	8.15E-11	7E-13	1.56
Beam RIGHT	5	1.29E-13	1.26E-23	1E-25	7.84E-11	9E-13	1.49
Beam RIGHT	10	1.24E-13	1.23E-23	1E-25	7.67E-11	6E-13	1.50
Beam RIGHT	20	1.15E-13	1.18E-23	1E-25	7.37E-11	8E-13	1.52
Beam RIGHT	30	9.54E-14	1.13E-23	1E-25	7.06E-11	7E-13	1.57
Beam RIGHT	45	5.01E-14	8.75E-24	6E-26	5.46E-11	4E-13	1.79

Table 89. Neutron Effective Dose (AP) Data at 100 meters.

Orientation from Beam Centerline	Off-Axis Angle	Φ_{TOTAL} [neutrons/cm^2/source e$^-$]	E (AP) [Sv]	δE (AP) [Sv]	E (AP) [Sv/μC]	δE (AP) [Sv/μC]	E Dose-Weighted Average Energy [MeV]
Beam LEFT	-45	3.94E-15	1.09E-24	2E-26	6.81E-12	1E-13	2.00
Beam LEFT	-30	6.88E-15	1.52E-24	3E-26	9.49E-12	2E-13	1.84
Beam LEFT	-20	8.24E-15	1.63E-24	3E-26	1.02E-11	2E-13	1.74
Beam LEFT	-10	9.03E-15	1.73E-24	2E-26	1.08E-11	1E-13	1.69
Beam LEFT	-5	9.54E-15	1.80E-24	4E-26	1.12E-11	2E-13	1.73
Beam LEFT	-2	9.87E-15	1.94E-24	2E-26	1.21E-11	1E-13	1.79
Beam LEFT	-1	1.13E-14	2.39E-24	3E-26	1.49E-11	2E-13	2.01
Beam LEFT	-0.5	1.36E-14	3.28E-24	1E-25	2.05E-11	6E-13	2.35
Beam CENTER	0	1.81E-14	5.07E-24	4E-25	3.16E-11	2E-12	3.35
Beam RIGHT	0.5	1.45E-14	3.52E-24	2E-25	2.20E-11	1E-12	2.41
Beam RIGHT	1	1.24E-14	2.45E-24	2E-25	1.53E-11	1E-12	2.04
Beam RIGHT	2	1.04E-14	2.01E-24	4E-26	1.26E-11	2E-13	1.85
Beam RIGHT	5	9.64E-15	1.83E-24	3E-26	1.14E-11	2E-13	1.75
Beam RIGHT	10	9.40E-15	1.77E-24	3E-26	1.10E-11	2E-13	1.71
Beam RIGHT	20	8.11E-15	1.63E-24	2E-26	1.02E-11	1E-13	1.74
Beam RIGHT	30	6.90E-15	1.48E-24	3E-26	9.26E-12	2E-13	1.78
Beam RIGHT	45	4.04E-15	1.10E-24	4E-26	6.88E-12	3E-13	2.01

Table 90. Neutron Effective Dose (AP) Data at 120 meters.

Orientation from Beam Centerline	Off-Axis Angle	Φ_{TOTAL} [neutrons/cm^2/source e$^-$]	E (AP) [Sv]	δE (AP) [Sv]	E (AP) [Sv/μC]	δE (AP) [Sv/μC]	E Dose-Weighted Average Energy [MeV]
Beam LEFT	-45	1.92E-15	5.70E-25	7E-27	3.56E-12	5E-14	2.08
Beam LEFT	-30	3.24E-15	8.11E-25	1E-26	5.06E-12	9E-14	1.80
Beam LEFT	-20	3.91E-15	8.99E-25	1E-26	5.61E-12	9E-14	1.74
Beam LEFT	-10	4.40E-15	1.01E-24	2E-26	6.27E-12	1E-13	1.83
Beam LEFT	-5	4.80E-15	1.06E-24	4E-26	6.62E-12	3E-13	1.79
Beam LEFT	-2	5.06E-15	1.18E-24	2E-26	7.34E-12	1E-13	1.96
Beam LEFT	-1	5.85E-15	1.44E-24	3E-26	8.96E-12	2E-13	2.12
Beam LEFT	-0.5	6.96E-15	1.84E-24	4E-26	1.15E-11	3E-13	2.42
Beam CENTER	0	9.33E-15	2.81E-24	2E-25	1.75E-11	1E-12	2.94
Beam RIGHT	0.5	7.04E-15	1.90E-24	5E-26	1.18E-11	3E-13	2.52
Beam RIGHT	1	5.93E-15	1.47E-24	4E-26	9.14E-12	2E-13	2.15
Beam RIGHT	2	5.22E-15	1.18E-24	3E-26	7.39E-12	2E-13	1.93
Beam RIGHT	5	4.80E-15	1.07E-24	2E-26	6.65E-12	1E-13	1.84
Beam RIGHT	10	4.61E-15	9.94E-25	3E-26	6.20E-12	2E-13	1.81
Beam RIGHT	20	4.36E-15	9.47E-25	5E-26	5.91E-12	3E-13	1.75
Beam RIGHT	30	3.43E-15	8.27E-25	3E-26	5.16E-12	2E-13	1.81
Beam RIGHT	45	1.98E-15	5.80E-25	2E-26	3.62E-12	1E-13	2.09

Table 91. Neutron Effective Dose (AP) Data at 170 meters.

Orientation from Beam Centerline	Off-Axis Angle	Φ_{TOTAL} [neutrons/cm^2/source e$^-$]	E (AP) [Sv]	δE (AP) [Sv]	E (AP) [Sv/μC]	δE (AP) [Sv/μC]	E Dose-Weighted Average Energy [MeV]
Beam LEFT	-45	4.60E-16	1.50E-25	2E-27	9.38E-13	1E-14	2.30
Beam LEFT	-30	8.39E-16	2.36E-25	1E-26	1.47E-12	7E-14	1.73
Beam LEFT	-20	9.62E-16	2.71E-25	8E-27	1.69E-12	5E-14	1.88
Beam LEFT	-10	1.22E-15	3.11E-25	4E-26	1.94E-12	3E-13	2.06
Beam LEFT	-5	1.39E-15	3.79E-25	3E-26	2.37E-12	2E-13	2.34
Beam LEFT	-2	1.42E-15	3.97E-25	1E-26	2.48E-12	7E-14	2.20
Beam LEFT	-1	1.95E-15	5.54E-25	4E-26	3.46E-12	3E-13	2.55
Beam LEFT	-0.5	2.72E-15	8.46E-25	6E-26	5.28E-12	4E-13	2.87
Beam CENTER	0	3.92E-15	1.35E-24	1E-25	8.44E-12	7E-13	3.71
Beam RIGHT	0.5	2.90E-15	9.36E-25	7E-26	5.84E-12	4E-13	3.32
Beam RIGHT	1	2.02E-15	5.78E-25	4E-26	3.61E-12	3E-13	2.80
Beam RIGHT	2	1.47E-15	4.16E-25	2E-26	2.59E-12	1E-13	2.56
Beam RIGHT	5	1.18E-15	3.21E-25	8E-27	2.00E-12	5E-14	2.07
Beam RIGHT	10	1.07E-15	2.95E-25	5E-27	1.84E-12	3E-14	1.99
Beam RIGHT	20	1.02E-15	2.89E-25	1E-26	1.81E-12	8E-14	1.93
Beam RIGHT	30	9.65E-16	2.70E-25	4E-26	1.69E-12	2E-13	1.84
Beam RIGHT	45	4.63E-16	1.50E-25	3E-27	9.39E-13	2E-14	2.26

5.5.4 Total Effective Dose Calculations

The total effective dose for similar irradiation geometries were calculated by summing the individual constituents (photon, electron and neutron) at downfield distances of 10, 25, 50, 100, 120 and 170 meters. Total effective dose for the AP, PA and R-LAT irradiation geometries were calculated. The contribution from electrons at far off-axis distances are not reported since calculating electron fluences at those locations was computationally expensive. Therefore, the total effective dose is only reported (both in tabular and graphical form) at locations where electron fluence data were available. The total effective doses (AP) calculated for the PITAS prototype, as well as the relative contribution from each constituent, are given in Table 92 through Table 97 and shown in Figure 81 through Figure 86. All additional total effective dose data are reported in Appendix K.

Table 92. Total Effective Dose (AP) Data at 10 meters.

Orientation from Beam Centerline	Off-Axis Angle	E (AP) [Sv]	δE (AP) [Sv]	E (AP) [Sv/μC]	δE (AP) [Sv/μC]	% photon	% electron	% neutron
Beam LEFT	-5	1.04E-20	5E-22	6.51E-08	3E-09	31.3%	63.9%	4.8%
Beam LEFT	-2	3.39E-20	8E-22	2.11E-07	5E-09	19.0%	79.5%	1.5%
Beam LEFT	-1	9.22E-20	1E-21	5.76E-07	7E-09	18.5%	80.8%	0.6%
Beam LEFT	-0.5	8.03E-18	2E-20	5.01E-05	1E-07	99.99%	0.0%	0.01%
Beam CENTER	0	7.95E-17	7E-20	4.96E-04	4E-07	99.4%	0.6%	0.001%
Beam RIGHT	0.5	8.03E-18	2E-20	5.01E-05	1E-07	99.99%	0.0%	0.01%
Beam RIGHT	1	9.14E-20	7E-22	5.70E-07	4E-09	19.4%	79.9%	0.6%
Beam RIGHT	2	3.40E-20	8E-22	2.12E-07	5E-09	19.6%	78.8%	1.6%
Beam RIGHT	5	9.89E-21	4E-22	6.17E-08	2E-09	35.0%	60.0%	5.0%

Table 93. Total Effective Dose (AP) Data at 25 meters.

Orientation from Beam Centerline	Off-Axis Angle	E (AP) [Sv]	δE (AP) [Sv]	E (AP) [Sv/μC]	δE (AP) [Sv/μC]	% photon	% electron	% neutron
Beam LEFT	-2	7.55E-21	1E-22	4.71E-08	7E-10	18.8%	80.3%	0.91%
Beam LEFT	-1	2.28E-20	3E-22	1.42E-07	2E-09	16.5%	83.1%	0.34%
Beam LEFT	-0.5	1.46E-18	3E-21	9.10E-06	2E-08	95.4%	4.6%	0.006%
Beam CENTER	0	1.18E-17	9E-21	7.39E-05	6E-08	98.4%	1.6%	0.001%
Beam RIGHT	0.5	1.46E-18	2E-21	9.09E-06	2E-08	95.4%	4.6%	0.007%
Beam RIGHT	1	2.24E-20	2E-22	1.40E-07	1E-09	16.6%	83.1%	0.35%
Beam RIGHT	2	7.95E-21	2E-22	4.96E-08	1E-09	18.1%	81.1%	0.86%

Table 94. Total Effective Dose (AP) Data at 50 meters.

Orientation from Beam Centerline	Off-Axis Angle	E (AP) [Sv]	δE (AP) [Sv]	E (AP) [Sv/μC]	δE (AP) [Sv/μC]	% photon	% electron	% neutron
Beam LEFT	-2	2.45E-21	9E-23	1.53E-08	5E-10	20.2%	79.3%	0.54%
Beam LEFT	-1	7.46E-21	1E-22	4.66E-08	9E-10	16.3%	83.5%	0.20%
Beam LEFT	-0.5	3.56E-19	6E-22	2.22E-06	4E-09	93.3%	6.7%	0.005%
Beam CENTER	0	2.73E-18	2E-21	1.70E-05	1E-08	97.2%	2.8%	0.001%
Beam RIGHT	0.5	3.56E-19	8E-22	2.22E-06	5E-09	93.3%	6.7%	0.005%
Beam RIGHT	1	7.50E-21	2E-22	4.68E-08	9E-10	16.6%	83.2%	0.20%
Beam RIGHT	2	2.47E-21	9E-23	1.54E-08	5E-10	19.8%	79.7%	0.53%

Table 95. Total Effective Dose (AP) Data at 100 meters.

Orientation from Beam Centerline	Off-Axis Angle	E (AP) [Sv]	δE (AP) [Sv]	E (AP) [Sv/μC]	δE (AP) [Sv/μC]	% photon	% electron	% neutron
Beam LEFT	-2	6.41E-22	3E-23	4.00E-09	2E-10	27.5%	72.2%	0.30%
Beam LEFT	-1	2.23E-21	6E-23	1.39E-08	4E-10	18.9%	81.0%	0.11%
Beam LEFT	-0.5	8.03E-20	2E-22	5.01E-07	1E-09	90.2%	9.8%	0.004%
Beam CENTER	0	5.89E-19	5E-22	3.67E-06	3E-09	95.5%	4.5%	0.001%
Beam RIGHT	0.5	8.02E-20	2E-22	5.01E-07	1E-09	90.4%	9.6%	0.004%
Beam RIGHT	1	2.22E-21	6E-23	1.39E-08	4E-10	19.0%	80.9%	0.11%
Beam RIGHT	2	6.45E-22	3E-23	4.03E-09	2E-10	27.9%	71.8%	0.31%

Table 96. Total Effective Dose (AP) Data at 120 meters.

Orientation from Beam Centerline	Off-Axis Angle	E (AP) [Sv]	δE (AP) [Sv]	E (AP) [Sv/μC]	δE (AP) [Sv/μC]	% photon	% electron	% neutron
Beam LEFT	-2	4.38E-22	2E-23	2.73E-09	2E-10	30.6%	69.1%	0.27%
Beam LEFT	-1	1.55E-21	5E-23	9.68E-09	3E-10	19.6%	80.3%	0.09%
Beam LEFT	-0.5	5.32E-20	2E-22	3.32E-07	2E-09	89.4%	10.6%	0.003%
Beam CENTER	0	3.86E-19	6E-22	2.41E-06	4E-09	95.0%	5.0%	0.001%
Beam RIGHT	0.5	5.32E-20	2E-22	3.32E-07	1E-09	89.5%	10.5%	0.004%
Beam RIGHT	1	1.58E-21	1E-22	9.87E-09	6E-10	21.6%	78.3%	0.09%
Beam RIGHT	2	4.31E-22	2E-23	2.69E-09	2E-10	30.9%	68.9%	0.27%

Table 97. Total Effective Dose (AP) Data at 170 meters.

Orientation from Beam Centerline	Off-Axis Angle	E (AP) [Sv]	δE (AP) [Sv]	E (AP) [Sv/μC]	δE (AP) [Sv/μC]	% photon	% electron	% neutron
Beam LEFT	-1	7.53E-22	6E-23	4.70E-09	4E-10	23.4%	76.5%	0.07%
Beam LEFT	-0.5	2.34E-20	2E-22	1.46E-07	1E-09	87.6%	12.4%	0.004%
Beam CENTER	0	1.68E-19	3E-22	1.05E-06	2E-09	93.4%	6.6%	0.001%
Beam RIGHT	0.5	2.34E-20	1E-22	1.46E-07	9E-10	87.5%	12.5%	0.004%
Beam RIGHT	1	7.48E-22	6E-23	4.67E-09	4E-10	22.9%	77.0%	0.08%

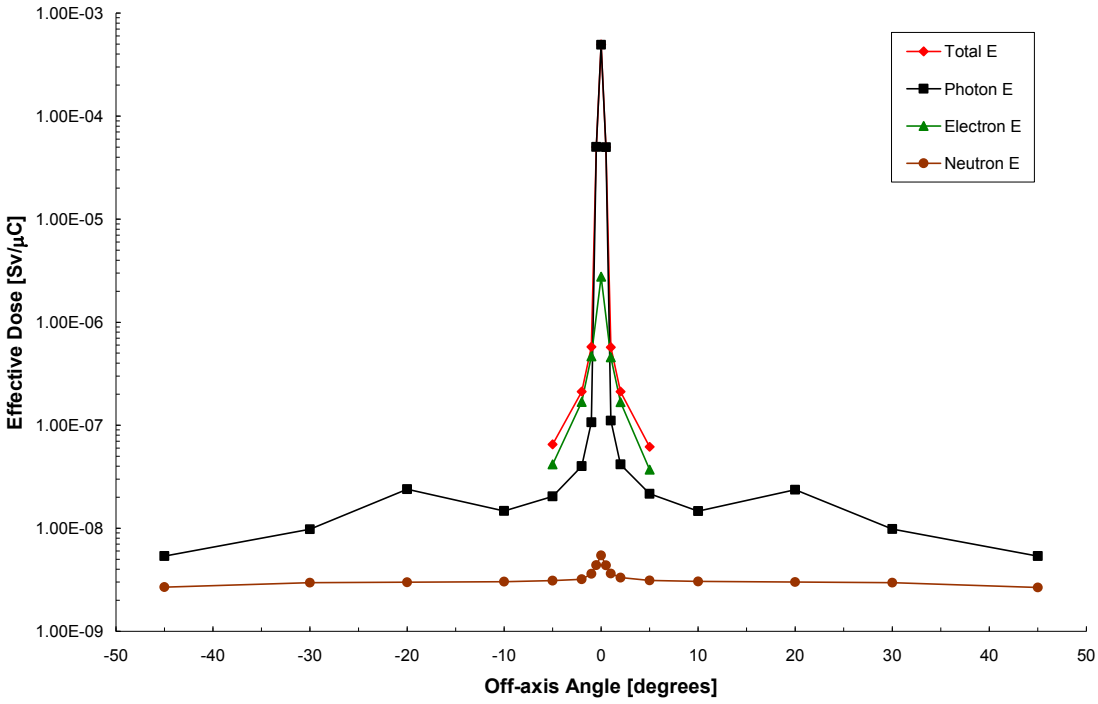

Figure 81. Total Effective Dose (AP) Data at 10 meters.

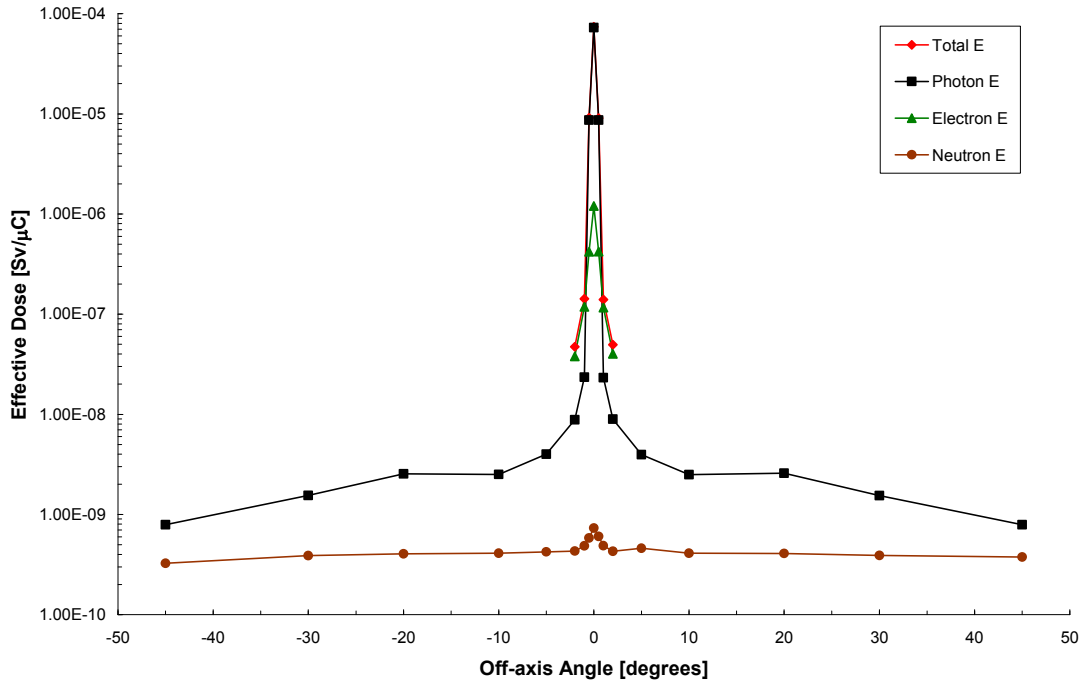

Figure 82. Total Effective Dose (AP) Data at 25 meters.

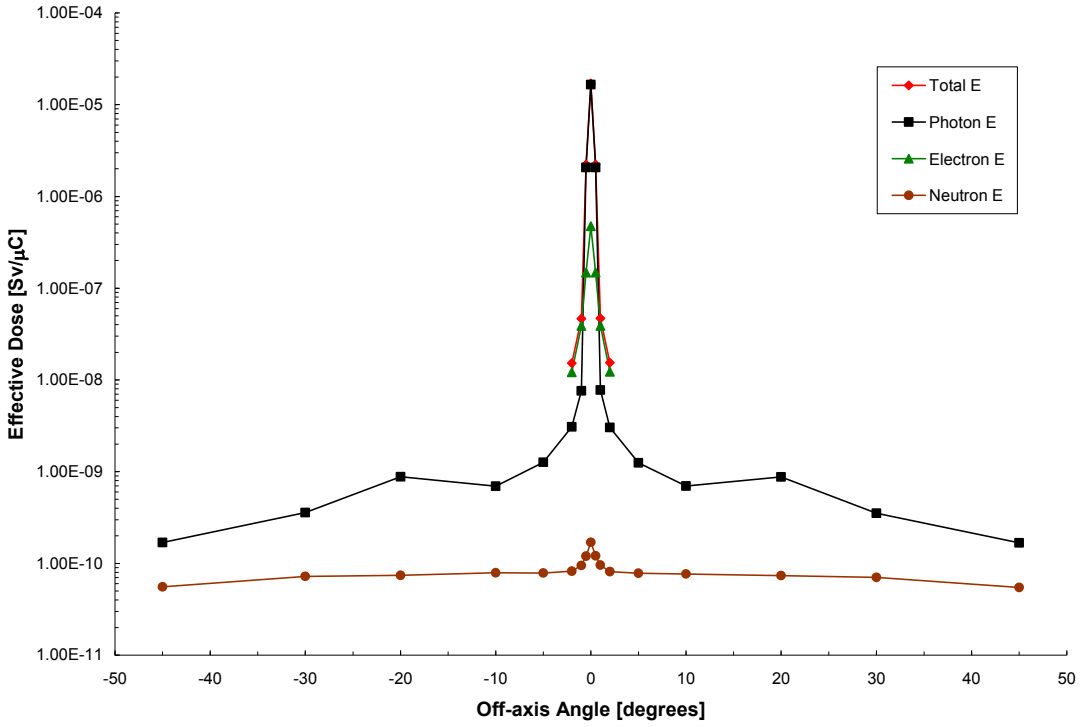

Figure 83. Total Effective Dose (AP) Data at 50 meters.

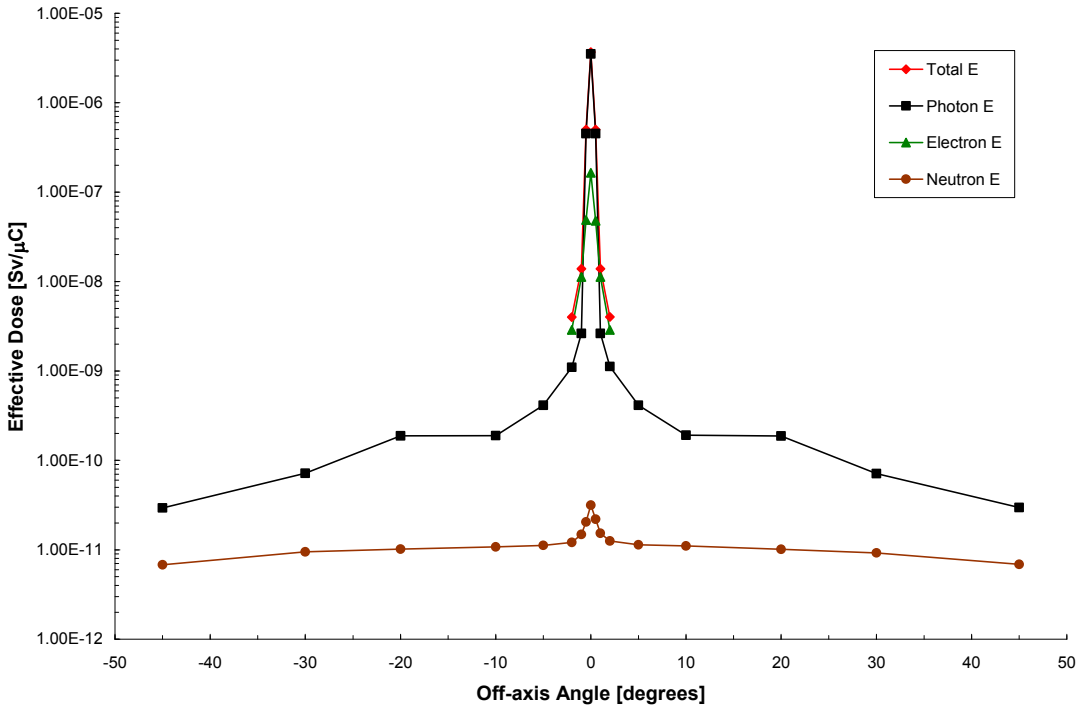

Figure 84. Total Effective Dose (AP) Data at 100 meters.

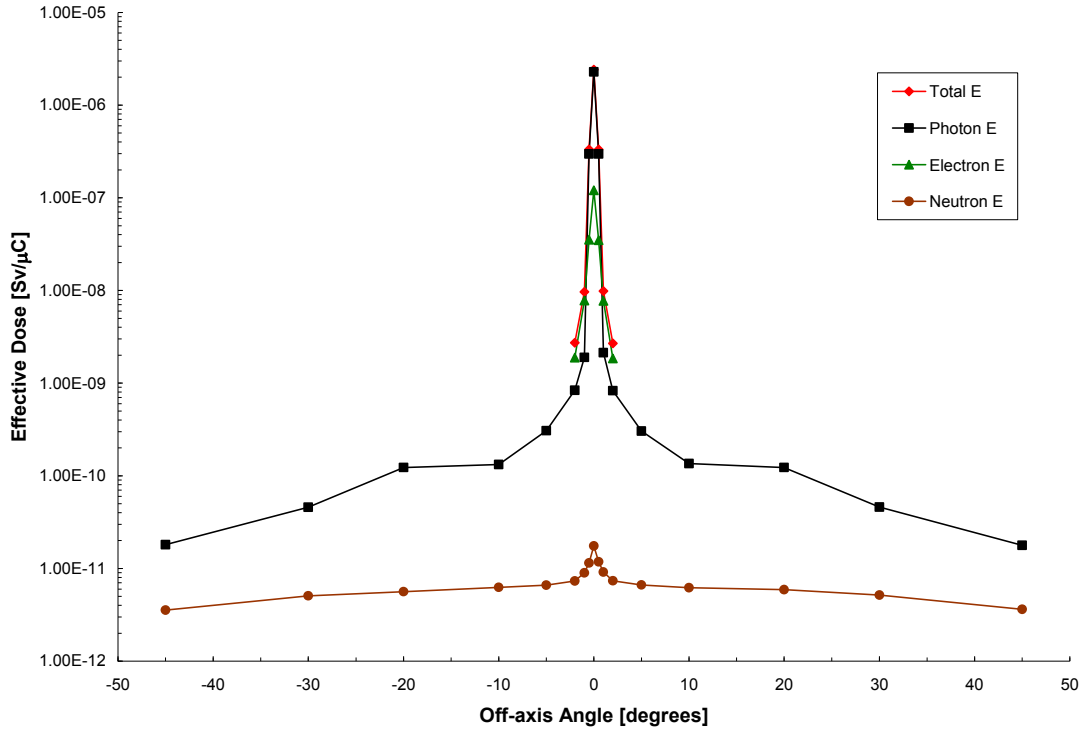

Figure 85. Total Effective Dose (AP) Data at 120 meters.

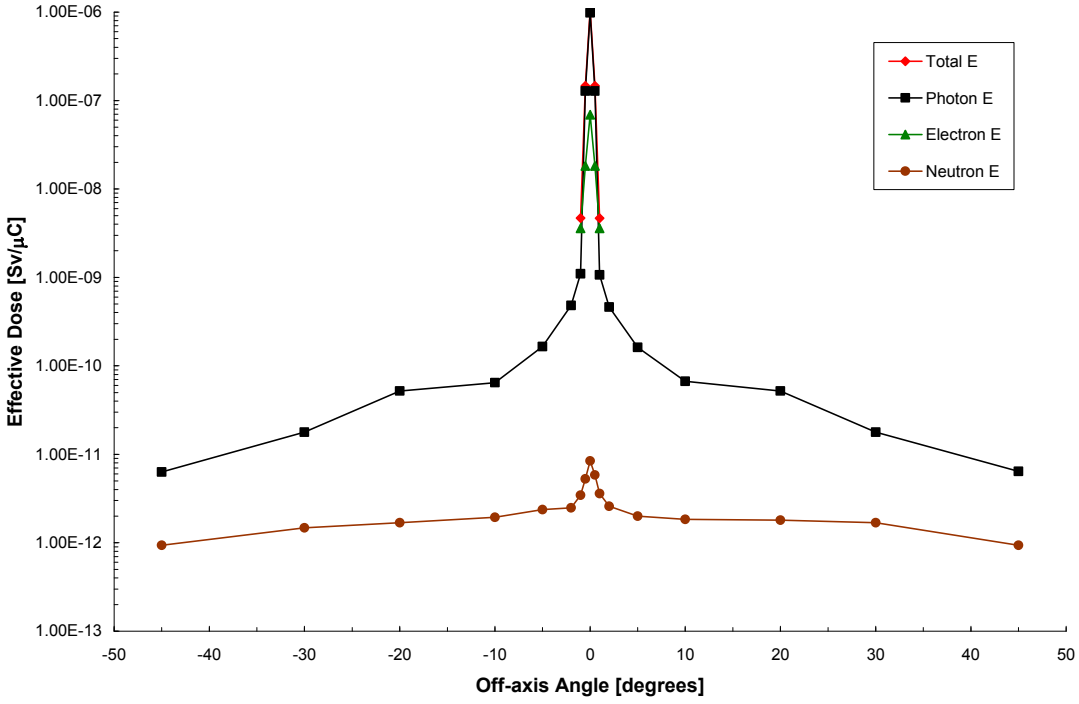

Figure 86. Total Effective Dose (AP) Data at 170 meters.

5.6 Ambient Dose Equivalent Calculations

The ambient dose equivalent is the operational quantity which can be directly related to measurements. The ambient dose equivalent for photons, electrons and neutrons was calculated at all downfield and off-axis locations, as reported for previous calculations. The following subsections will describe the specifics of these calculations.

5.6.1 Photon Ambient Dose Equivalent Calculations

The relationship between the ambient dose equivalent and the effective dose was described in Chapter 2. This relationship is such that H*(10) should bound (be greater than) E. If this is not the case, then a greater penetrating depth should be used to calculate the ambient dose equivalent (i.e., H*(15) or greater). It was important to perform these calculations since ICRP Publication 74 reports that up to 10 MeV the ambient dose equivalent always overestimates the effective dose (i.e. $E/H^*(10)<1$). This ratio ranged from 0.75 to 0.92 for the AP geometry and 0.48 to 0.85 for the ROT geometry. Therefore, the ambient dose equivalent provides an overestimate of the effective dose exceeding 15% for a wide range of photon energies and irradiation geometries [20].

The data reported in ICRP Publication 74 for photons only covers up to 10 MeV which is reasonable since that is the energy regime seen widely in most radiation protection scenarios, specifically at a nuclear power facility. The present work adds a new set of challenges since photon energies up to 25 MeV are typically observed. So an analysis of the relationship at photon energies exceeding 10 MeV was warranted. In an effort to be consistent with ICRP Publication 74, the comparison was made between effective dose

and ambient dose equivalent by taking the quotient of E or H*(d) to air kerma free-in-air which provides units of Sv/Gy [20]. Although these are ambiguous units, the ICRP used this relationship, so for comparative purposes the same is reported herein.

Published air kerma factors only extend to 10 MeV, therefore, a new set of kerma factors was generated. These factors used the same methodology previously described in Section 5.2 using mass energy–absorption coefficient data obtained from Seltzer [74]. A summary of the calculated air kerma factors is given in Table 98 and shown in Figure 87.

The conversion coefficients for the effective dose and ambient dose equivalent, H*(10) as well as the ratio of E/H*(10) as a function of energy (up to 25 MeV) are shown in Figure 88 and Figure 89, respectively. A discontinuity exists in the H*(10) above 1 MeV. This stems from the manner in which H*(10) was calculated in the present work utilizing the in vacuo assumption in lieu of the air-scattered assumption as discussed in Chapter 3. The effect of this is shown in Figure 88 where the H*(10) data from ICRP Publication 74 continues to bound E above 1 MeV whereas the H*(10) data from the present work falls off at approximately 1 MeV. Unlike the data reported in ICRP Publication 74 [20], the ratios of E(AP) to H*(10) range from 0.91 at 1 MeV to 4.94 at 25 MeV. Similarly, the ratios of E(ROT) to H*(10) range from 0.72 at 1 MeV to 5.45 at 25 MeV.

Table 98. Calculated Air Kerma Factors.

Photon Energy [MeV]	Kerma Factor (pGy-cm^2)
0.01	7.6
0.015	3.2
0.02	1.7
0.03	0.74
0.04	0.44
0.05	0.33
0.06	0.29
0.08	0.31
0.1	0.37
0.15	0.60
0.2	0.86
0.3	1.4
0.4	1.9
0.5	2.4
0.6	2.8
0.8	3.7
1	4.5
1.5	6.1
2	7.5
3	10
4	12
5	14
6	16
8	20
10	23
15	33
20	42
30	61

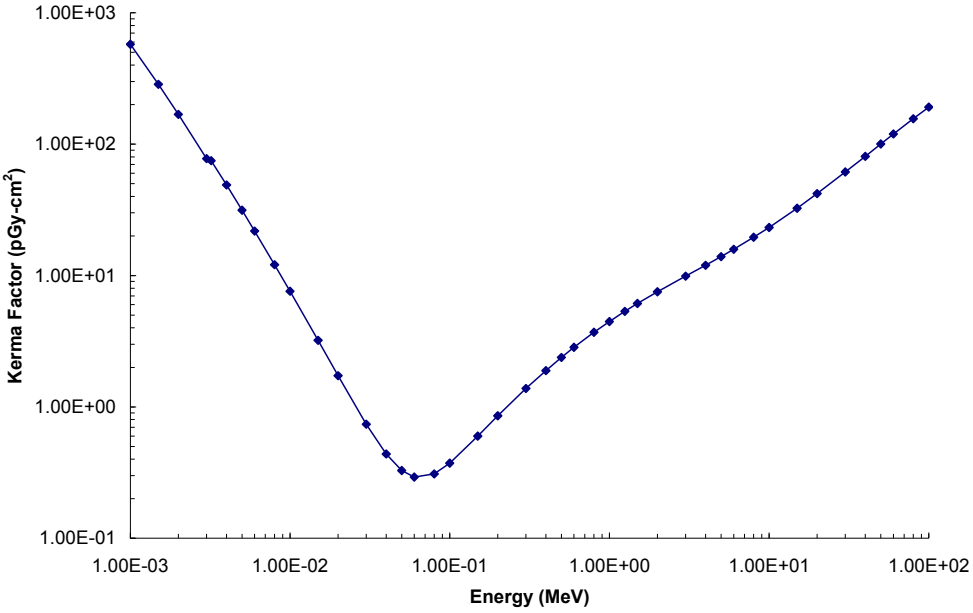

Figure 87. Calculated Air Kerma Factors.

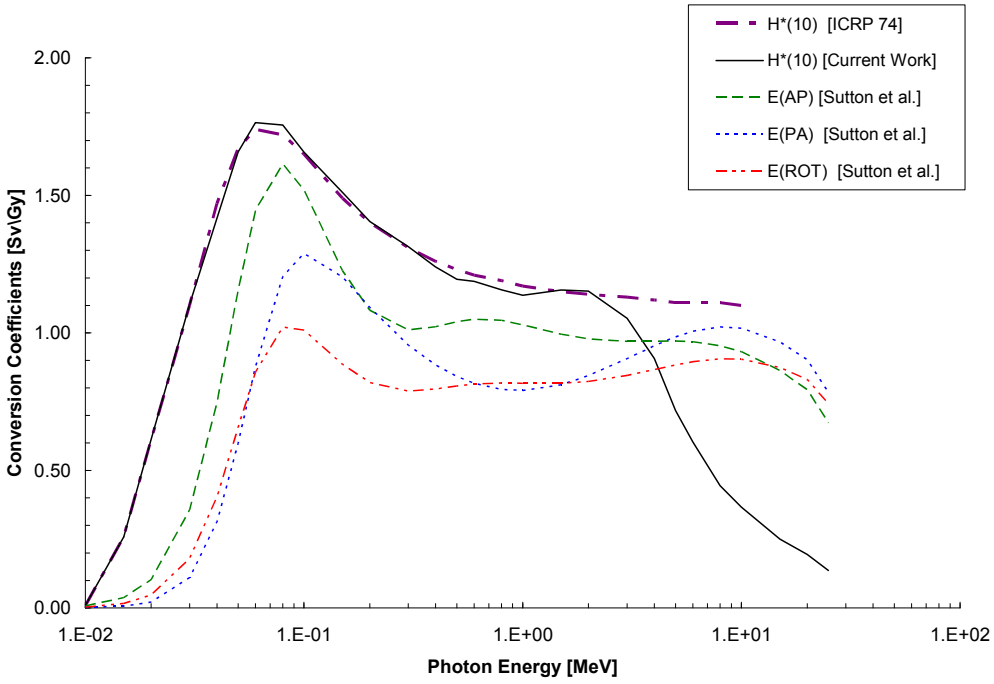

Figure 88. Comparison of Photon Ambient Dose Equivalent, H*(10) and Effective Dose, E Conversion Coefficients (> 10 MeV). Effective Dose data reprinted from [79].

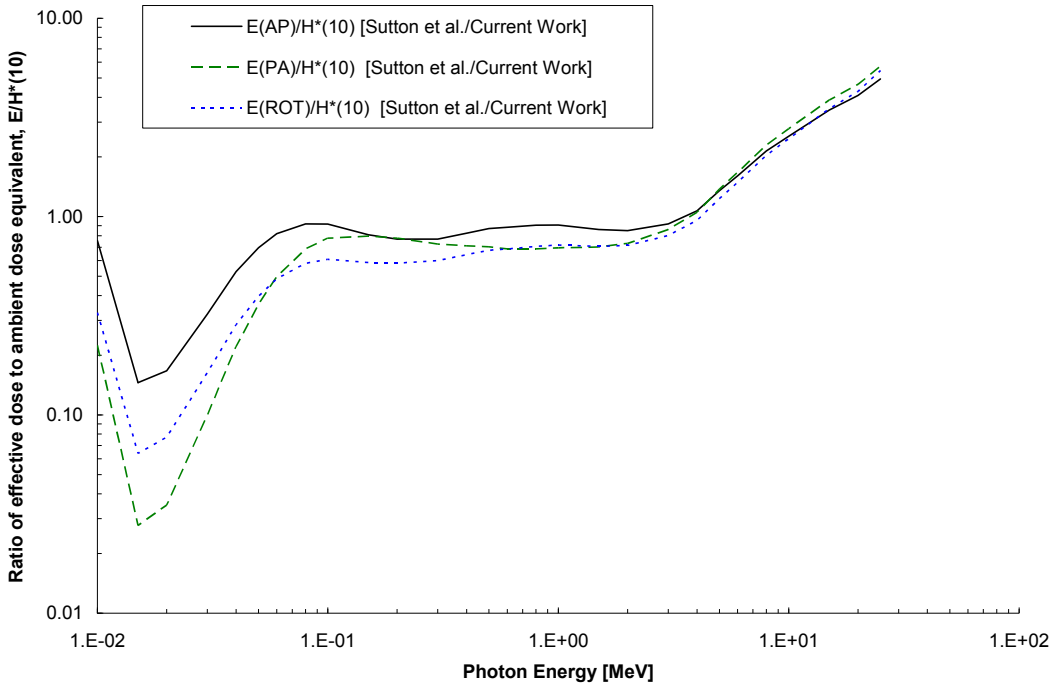

Figure 89. Ratio of E/H*(10) Conversion Coefficients for Various Irradiation Geometries (>10 MeV). Effective dose data reprinted from [79].

In order to see the effect at greater penetrating depths, the same plots were generated using the H*(40) conversion coefficients generated in the initial stages of the present work. The conversion coefficients for the effective dose and ambient dose equivalent, H*(40) as well as the ratio of E/H*(40) as a function of energy (up to 25 MeV) are shown in Figure 90 and Figure 91, respectively. Although a drop-off still exists, it is observed at 10 MeV versus 1 MeV as in the H*(10) case.

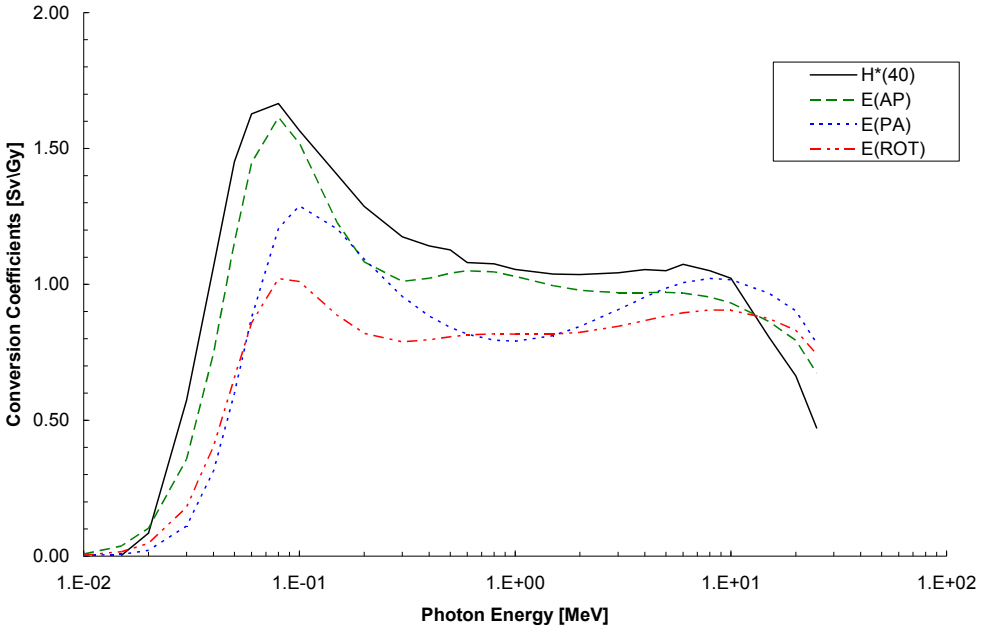

Figure 90. Comparison of Photon Ambient Dose Equivalent, H*(40) and Effective Dose, E Conversion Coefficients (>10 MeV).

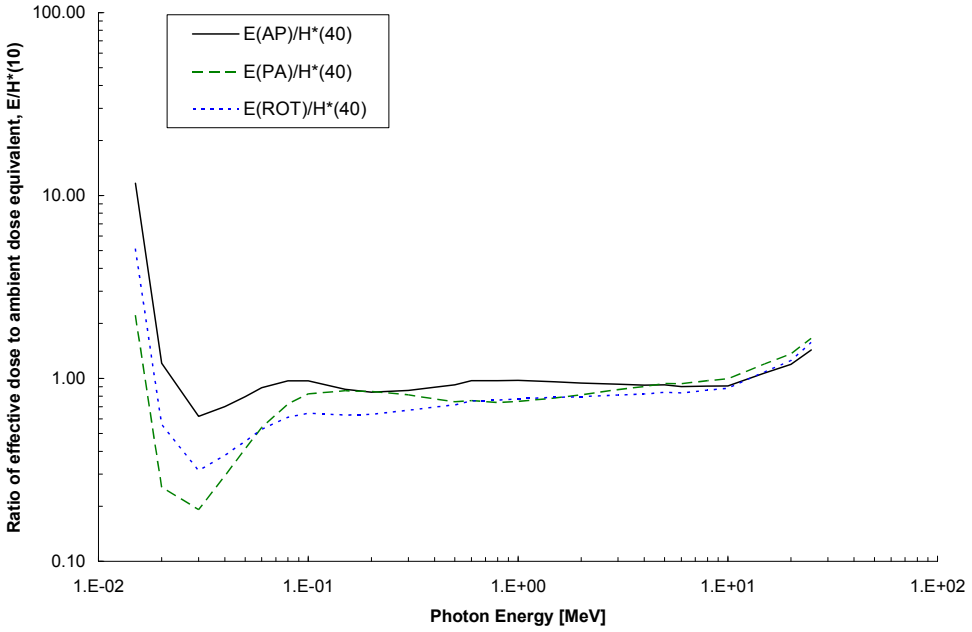

Figure 91. Ratio of E/H*(40) Conversion Coefficients for Various Irradiation Geometries (>10 MeV).

With an understanding of the relationship between H*(d) and E established, the photon fluence-to-ambient dose equivalent conversion coefficients calculated in the initial stages of the present work and discussed in Chapter 3, were used to calculate the ambient dose equivalent at 10 meters using the coefficients of the five depths in the ICRU sphere, H*(10), H*(15), H*(20), H*(30), and H*(40). This study was performed to see the depth at which E is bounded by H*(d). The coefficients were folded with the photon fluences calculated with MCNP5 at 17 angular locations, as previously discussed. The H*(d) data were compared to the E data reported in Section 5.5, for the detector located at 0 degrees (beam centerline) at a downfield distance of 10 meters. A summary of the data are given in Table 99 and Table 100.

Figure 92 shows the graphical relationship between E and H*(d) at all five penetrating depths. Note that H*(d) does not bound E until a depth of 30 mm is reached. H*(40) is the bounding case for all effective dose irradiation geometries (error bars are present yet difficult to see). Another representation of the relationship between H*(d) and E at 10 meters for all off-axis distances is shown in Figure 93. The entire set of data for H*(15), H*(20) and H*(30) are reported in Appendix L.

Table 99. Ambient Dose Equivalent Data at 10 meters (0 degrees).

H*(10) [Sv/μC]	δH*(10) [Sv/μC]	H*(15) [Sv/μC]	δH*(15) [Sv/μC]	H*(20) [Sv/μC]	δH*(20) [Sv/μC]	H*(30) [Sv/μC]	δH*(30) [Sv/μC]	H*(40) [Sv/μC]	δH*(40) [Sv/μC]
3.02E-04	3E-07	3.68E-04	3E-07	4.19E-04	3E-07	4.73E-04	3E-07	5.05E-04	3E-07

Table 100. Effective Dose Data at 10 meters (0 degrees).

E (AP) [Sv/μC]	δE(AP) [Sv/μC]	E (PA) [Sv/μC]	δE(PA) [Sv/μC]	E (R-LAT) [Sv/μC]	δE(R-LAT) [Sv/μC]	E (ROT) [Sv/μC]	δE(ROT) [Sv/μC]
4.93E-04	4E-06	5.09E-04	4E-06	4.46E-04	3E-06	4.65E-04	4E-06

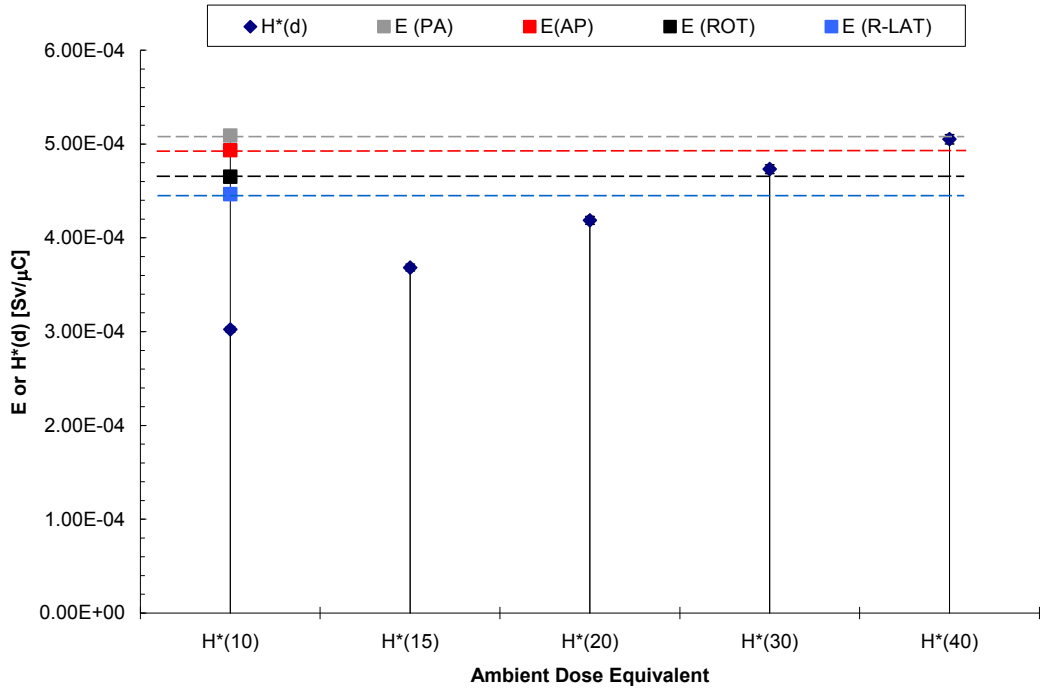

Figure 92. Comparison of H*(d) and E at 10 meters (0 degrees).
(The error bars are smaller than the size of the symbols).

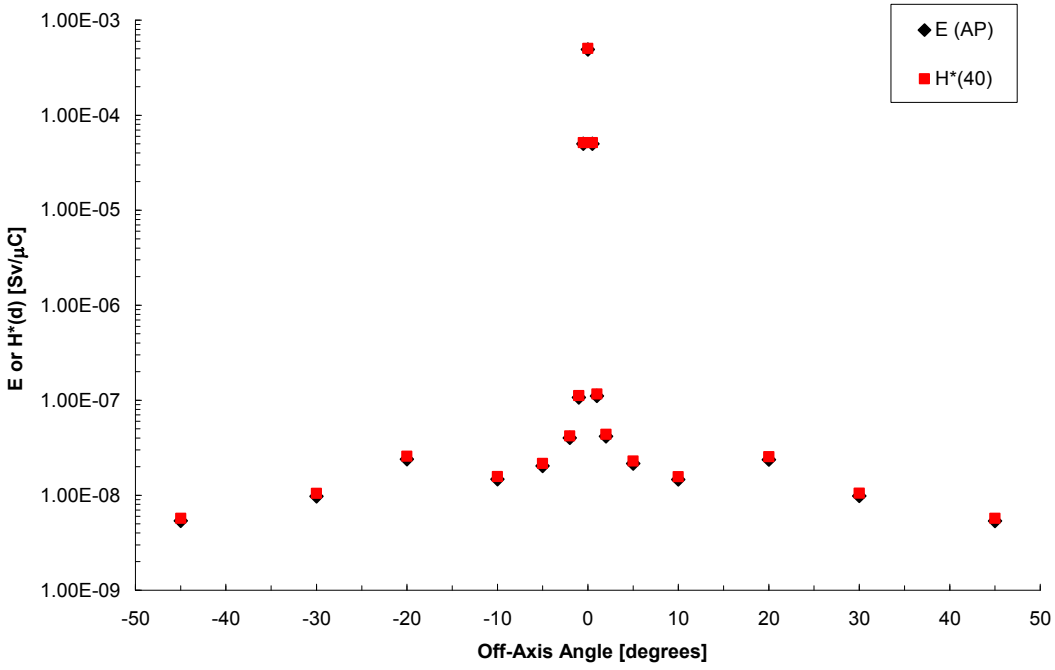

Figure 93. Comparison of H*(d) and E at 10 meters.
(The error bars are smaller than the size of the symbols).

Although H*(40) was the bounding condition over effective dose, the conversion coefficients for H*(10) calculated using the kerma approximation still exceed those for H*(40). At photon energies less than 0.03 MeV the difference ranges from 48 % to 99% and above 20 MeV, which is the energy regime of interest for the present work, the difference ranges from 40% to 50%. With this being the case, H*(10) (based on the kerma approximation) will be used in some situations to calculate the total ambient dose equivalent. This will be discussed in a later subsection. The percent difference between the conversion coefficients for H*(10) based on the kerma approximation and those for H*(40) is shown in Figure 94.

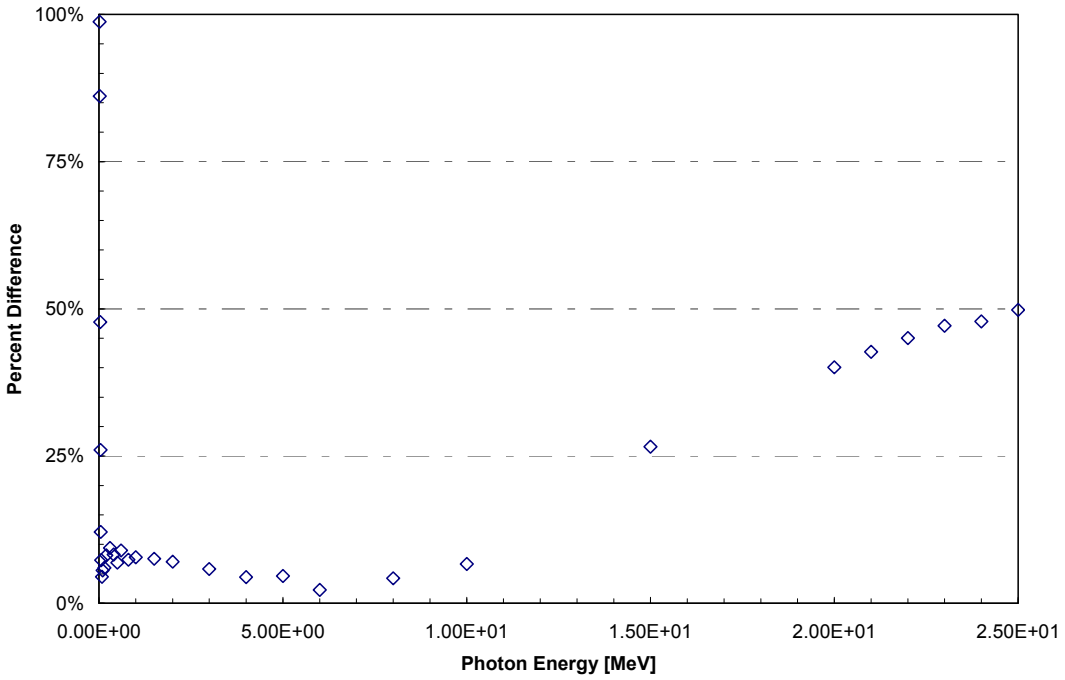

Figure 94. Percent Difference Between Fluence-to-Dose Conversion Coefficients for H*(10) (from Kerma Approximation) and H*(40).

With the bounding relationship of H*(40) established, the ambient dose equivalent at downfield distances of 25, 50, 100, 120 and 170 meters were calculated. For completeness, H*(10), H*(10) based on the kerma approximation and H*(40) were calculated for the PITAS prototype for all downfield distances and off-axis locations. Data are given in Table 101 through Table 118 and shown in Figure 95 through Figure 97.

Table 101. Photon Ambient Dose Equivalent, H*(10) Data at 10 meters.

Orientation from Beam Centerline	Off-Axis Angle	Φ_{TOTAL} [photons/cm^2/source e$^-$]	H*(10) [Sv]	δH*(10) [Sv]	H*(10) [Sv/μC]	δH*(10) [Sv/μC]	H*(10) Dose-Weighted Average Energy [MeV]
Beam LEFT	-45	1.80E-10	9.11E-22	5E-24	5.68E-09	3E-11	2.06
Beam LEFT	-30	3.00E-10	1.59E-21	1E-23	9.92E-09	9E-11	2.40
Beam LEFT	-20	5.22E-10	3.34E-21	4E-23	2.09E-08	2E-10	3.30
Beam LEFT	-10	4.58E-10	2.33E-21	5E-23	1.45E-08	3E-10	2.41
Beam LEFT	-5	5.83E-10	2.98E-21	8E-23	1.86E-08	5E-10	2.67
Beam LEFT	-2	9.91E-10	5.27E-21	2E-22	3.29E-08	1E-09	3.10
Beam LEFT	-1	2.20E-09	1.29E-20	4E-22	8.08E-08	2E-09	3.58
Beam LEFT	-0.5	6.28E-07	4.87E-18	1E-20	3.04E-05	7E-08	4.78
Beam CENTER	0	6.48E-06	4.84E-17	4E-20	3.02E-04	3E-07	4.72
Beam RIGHT	0.5	6.27E-07	4.87E-18	1E-20	3.04E-05	7E-08	4.78
Beam RIGHT	1	2.26E-09	1.35E-20	2E-22	8.41E-08	1E-09	3.57
Beam RIGHT	2	1.01E-09	5.45E-21	1E-22	3.40E-08	7E-10	3.13
Beam RIGHT	5	6.06E-10	3.14E-21	1E-22	1.96E-08	8E-10	2.71
Beam RIGHT	10	4.64E-10	2.34E-21	4E-23	1.46E-08	3E-10	2.37
Beam RIGHT	20	5.15E-10	3.30E-21	2E-23	2.06E-08	2E-10	3.31
Beam RIGHT	30	3.03E-10	1.60E-21	1E-23	9.97E-09	9E-11	2.41
Beam RIGHT	45	1.82E-10	9.11E-22	7E-24	5.68E-09	4E-11	2.04

Table 102. Photon Ambient Dose Equivalent, H*(10) based on Kerma Approximation at 10 meters.

Orientation from Beam Centerline	Off-Axis Angle	Φ_{TOTAL} [photons/cm^2/source e$^-$]	H*(10)$_{Kerma}$ [Sv]	δH*(10)$_{Kerma}$ [Sv]	H*(10)$_{Kerma}$ [Sv/μC]	δH*(10)$_{Kerma}$ [Sv/μC]	H*(10)$_{Kerma}$ - Weighted Average Energy [MeV]
Beam LEFT	-45	1.80E-10	9.81E-22	6E-24	6.12E-09	4E-11	2.33
Beam LEFT	-30	3.00E-10	1.79E-21	2E-23	1.12E-08	1E-10	2.78
Beam LEFT	-20	5.22E-10	4.40E-21	5E-23	2.75E-08	3E-10	4.06
Beam LEFT	-10	4.58E-10	2.70E-21	5E-23	1.68E-08	3E-10	2.96
Beam LEFT	-5	5.83E-10	3.78E-21	1E-22	2.36E-08	6E-10	3.64
Beam LEFT	-2	9.91E-10	7.52E-21	2E-22	4.69E-08	1E-09	4.44
Beam LEFT	-1	2.20E-09	2.01E-20	6E-22	1.25E-07	4E-09	5.01
Beam LEFT	-0.5	6.28E-07	9.65E-18	2E-20	6.02E-05	1E-07	6.38
Beam CENTER	0	6.48E-06	9.51E-17	9E-20	5.94E-04	5E-07	6.54
Beam RIGHT	0.5	6.27E-07	9.64E-18	2E-20	6.02E-05	1E-07	6.39
Beam RIGHT	1	2.26E-09	2.09E-20	3E-22	1.30E-07	2E-09	5.01
Beam RIGHT	2	1.01E-09	7.80E-21	2E-22	4.87E-08	1E-09	4.48
Beam RIGHT	5	6.06E-10	4.00E-21	2E-22	2.50E-08	1E-09	3.70
Beam RIGHT	10	4.64E-10	2.69E-21	5E-23	1.68E-08	3E-10	2.87
Beam RIGHT	20	5.15E-10	4.36E-21	3E-23	2.72E-08	2E-10	4.08
Beam RIGHT	30	3.03E-10	1.80E-21	2E-23	1.12E-08	1E-10	2.79
Beam RIGHT	45	1.82E-10	9.82E-22	7E-24	6.13E-09	4E-11	2.32

Table 103. Photon Ambient Dose Equivalent, H*(40) Data at 10 meters.

Orientation from Beam Centerline	Off-Axis Angle	Φ_{TOTAL} [photons/cm^2/source e$^-$]	H*(40) [Sv]	δH*(40) [Sv]	H*(40) [Sv/μC]	δH*(40) [Sv/μC]	H*(40) Dose-Weighted Average Energy [MeV]
Beam LEFT	-45	1.80E-10	9.16E-22	5E-24	5.72E-09	3E-11	2.35
Beam LEFT	-30	3.00E-10	1.67E-21	2E-23	1.04E-08	1E-10	2.80
Beam LEFT	-20	5.22E-10	4.12E-21	5E-23	2.57E-08	3E-10	4.04
Beam LEFT	-10	4.58E-10	2.52E-21	5E-23	1.57E-08	3E-10	2.96
Beam LEFT	-5	5.83E-10	3.47E-21	9E-23	2.16E-08	6E-10	3.55
Beam LEFT	-2	9.91E-10	6.75E-21	2E-22	4.21E-08	1E-09	4.27
Beam LEFT	-1	2.20E-09	1.79E-20	5E-22	1.12E-07	3E-09	4.82
Beam LEFT	-0.5	6.28E-07	8.25E-18	2E-20	5.15E-05	1E-07	6.10
Beam CENTER	0	6.48E-06	8.09E-17	7E-20	5.05E-04	5E-07	6.17
Beam RIGHT	0.5	6.27E-07	8.24E-18	2E-20	5.15E-05	1E-07	6.11
Beam RIGHT	1	2.26E-09	1.86E-20	3E-22	1.16E-07	2E-09	4.81
Beam RIGHT	2	1.01E-09	7.01E-21	2E-22	4.37E-08	9E-10	4.30
Beam RIGHT	5	6.06E-10	3.67E-21	1E-22	2.29E-08	9E-10	3.61
Beam RIGHT	10	4.64E-10	2.51E-21	5E-23	1.56E-08	3E-10	2.88
Beam RIGHT	20	5.15E-10	4.07E-21	3E-23	2.54E-08	2E-10	4.06
Beam RIGHT	30	3.03E-10	1.69E-21	2E-23	1.05E-08	9E-11	2.81
Beam RIGHT	45	1.82E-10	9.16E-22	7E-24	5.72E-09	4E-11	2.34

Table 104. Photon Ambient Dose Equivalent, H*(10) Data at 25 meters.

Orientation from Beam Centerline	Off-Axis Angle	Φ_{TOTAL} [photons/cm^2/source e$^-$]	H*(10) [Sv]	δH*(10) [Sv]	H*(10) [Sv/μC]	δH*(10) [Sv/μC]	H*(10) Dose-Weighted Average Energy [MeV]
Beam LEFT	-45	2.54E-11	1.34E-22	1E-24	8.36E-10	7E-12	2.09
Beam LEFT	-30	4.56E-11	2.52E-22	2E-24	1.57E-09	1E-11	2.42
Beam LEFT	-20	7.12E-11	3.99E-22	3E-24	2.49E-09	2E-11	2.58
Beam LEFT	-10	7.77E-11	4.03E-22	5E-24	2.52E-09	3E-11	2.36
Beam LEFT	-5	1.13E-10	5.88E-22	9E-24	3.67E-09	6E-11	2.65
Beam LEFT	-2	2.27E-10	1.19E-21	3E-23	7.44E-09	2E-10	3.01
Beam LEFT	-1	5.15E-10	2.95E-21	9E-23	1.84E-08	6E-10	3.45
Beam LEFT	-0.5	1.06E-07	8.34E-19	2E-21	5.20E-06	9E-09	4.84
Beam CENTER	0	9.26E-07	7.04E-18	6E-21	4.40E-05	4E-08	4.80
Beam RIGHT	0.5	1.06E-07	8.33E-19	1E-21	5.20E-06	9E-09	4.84
Beam RIGHT	1	4.97E-10	2.88E-21	6E-23	1.80E-08	4E-10	3.46
Beam RIGHT	2	2.28E-10	1.20E-21	5E-23	7.51E-09	3E-10	3.03
Beam RIGHT	5	1.12E-10	5.82E-22	2E-23	3.63E-09	1E-10	2.65
Beam RIGHT	10	7.77E-11	4.02E-22	5E-24	2.51E-09	3E-11	2.35
Beam RIGHT	20	7.33E-11	4.05E-22	6E-24	2.53E-09	4E-11	2.57
Beam RIGHT	30	4.52E-11	2.51E-22	2E-24	1.57E-09	1E-11	2.42
Beam RIGHT	45	2.54E-11	1.34E-22	1E-24	8.37E-10	6E-12	2.08

Table 105. Photon Ambient Dose Equivalent, H*(10) based on Kerma Approximation at 25 meters.

Orientation from Beam Centerline	Off-Axis Angle	Φ_{TOTAL} [photons/cm^2/source e$^-$]	H*(10)$_{Kerma}$ [Sv]	δH*(10)$_{Kerma}$ [Sv]	H*(10)$_{Kerma}$ [Sv/μC]	δH*(10)$_{Kerma}$ [Sv/μC]	H*(10)$_{Kerma}$ - Weighted Average Energy [MeV]
Beam LEFT	-45	2.54E-11	1.45E-22	1E-24	9.03E-10	8E-12	2.37
Beam LEFT	-30	4.56E-11	2.84E-22	2E-24	1.77E-09	1E-11	2.80
Beam LEFT	-20	7.12E-11	4.66E-22	4E-24	2.91E-09	2E-11	3.09
Beam LEFT	-10	7.77E-11	4.62E-22	6E-24	2.88E-09	4E-11	2.86
Beam LEFT	-5	1.13E-10	7.41E-22	1E-23	4.62E-09	7E-11	3.60
Beam LEFT	-2	2.27E-10	1.66E-21	5E-23	1.03E-08	3E-10	4.27
Beam LEFT	-1	5.15E-10	4.42E-21	1E-22	2.76E-08	9E-10	4.81
Beam LEFT	-0.5	1.06E-07	1.67E-18	3E-21	1.04E-05	2E-08	6.45
Beam CENTER	0	9.26E-07	1.40E-17	1E-20	8.76E-05	7E-08	6.62
Beam RIGHT	0.5	1.06E-07	1.67E-18	3E-21	1.04E-05	2E-08	6.45
Beam RIGHT	1	4.97E-10	4.35E-21	9E-23	2.72E-08	6E-10	4.84
Beam RIGHT	2	2.28E-10	1.68E-21	7E-23	1.05E-08	5E-10	4.30
Beam RIGHT	5	1.12E-10	7.33E-22	2E-23	4.58E-09	1E-10	3.60
Beam RIGHT	10	7.77E-11	4.59E-22	5E-24	2.87E-09	3E-11	2.84
Beam RIGHT	20	7.33E-11	4.73E-22	7E-24	2.95E-09	4E-11	3.07
Beam RIGHT	30	4.52E-11	2.83E-22	2E-24	1.76E-09	1E-11	2.80
Beam RIGHT	45	2.54E-11	1.45E-22	1E-24	9.02E-10	6E-12	2.35

Table 106. Photon Ambient Dose Equivalent, H*(40) Data at 25 meters.

Orientation from Beam Centerline	Off-Axis Angle	Φ_{TOTAL} [photons/cm^2/source e$^-$]	H*(40) [Sv]	δH*(40) [Sv]	H*(40) [Sv/μC]	δH*(40) [Sv/μC]	H*(40) Dose-Weighted Average Energy [MeV]
Beam LEFT	-45	2.54E-11	1.35E-22	1E-24	8.43E-10	7E-12	2.39
Beam LEFT	-30	4.56E-11	2.66E-22	2E-24	1.66E-09	1E-11	2.82
Beam LEFT	-20	7.12E-11	4.36E-22	3E-24	2.72E-09	2E-11	3.10
Beam LEFT	-10	7.77E-11	4.31E-22	5E-24	2.69E-09	3E-11	2.87
Beam LEFT	-5	1.13E-10	6.80E-22	1E-23	4.25E-09	7E-11	3.52
Beam LEFT	-2	2.27E-10	1.49E-21	4E-23	9.32E-09	3E-10	4.12
Beam LEFT	-1	5.15E-10	3.97E-21	1E-22	2.48E-08	8E-10	4.64
Beam LEFT	-0.5	1.06E-07	1.43E-18	3E-21	8.90E-06	2E-08	6.16
Beam CENTER	0	9.26E-07	1.19E-17	1E-20	7.43E-05	6E-08	6.24
Beam RIGHT	0.5	1.06E-07	1.42E-18	2E-21	8.89E-06	2E-08	6.16
Beam RIGHT	1	4.97E-10	3.90E-21	8E-23	2.44E-08	5E-10	4.67
Beam RIGHT	2	2.28E-10	1.51E-21	7E-23	9.45E-09	4E-10	4.15
Beam RIGHT	5	1.12E-10	6.74E-22	2E-23	4.20E-09	1E-10	3.52
Beam RIGHT	10	7.77E-11	4.29E-22	5E-24	2.67E-09	3E-11	2.85
Beam RIGHT	20	7.33E-11	4.42E-22	6E-24	2.76E-09	4E-11	3.08
Beam RIGHT	30	4.52E-11	2.65E-22	2E-24	1.65E-09	1E-11	2.82
Beam RIGHT	45	2.54E-11	1.35E-22	1E-24	8.42E-10	6E-12	2.37

Table 107. Photon Ambient Dose Equivalent, H*(10) Data at 50 meters.

Orientation from Beam Centerline	Off-Axis Angle	Φ_{TOTAL} [photons/cm^2/source e$^-$]	H*(10) [Sv]	δH*(10) [Sv]	H*(10) [Sv/μC]	δH*(10) [Sv/μC]	H*(10) Dose-Weighted Average Energy [MeV]
Beam LEFT	-45	5.22E-12	2.85E-23	6E-25	1.78E-10	4E-12	2.13
Beam LEFT	-30	1.02E-11	5.79E-23	7E-25	3.62E-10	4E-12	2.45
Beam LEFT	-20	1.90E-11	1.23E-22	2E-24	7.70E-10	1E-11	3.25
Beam LEFT	-10	2.14E-11	1.11E-22	2E-24	6.92E-10	1E-11	2.36
Beam LEFT	-5	3.58E-11	1.86E-22	4E-24	1.16E-09	2E-11	2.66
Beam LEFT	-2	7.73E-11	4.16E-22	8E-24	2.60E-09	5E-11	3.03
Beam LEFT	-1	1.64E-10	9.59E-22	1E-23	5.99E-09	9E-11	3.42
Beam LEFT	-0.5	2.45E-08	1.96E-19	3E-22	1.22E-06	2E-09	4.94
Beam CENTER	0	2.01E-07	1.57E-18	1E-21	9.81E-06	7E-09	4.93
Beam RIGHT	0.5	2.46E-08	1.96E-19	5E-22	1.22E-06	3E-09	4.94
Beam RIGHT	1	1.74E-10	9.92E-22	4E-23	6.19E-09	3E-10	3.36
Beam RIGHT	2	7.59E-11	4.11E-22	8E-24	2.56E-09	5E-11	3.04
Beam RIGHT	5	3.51E-11	1.83E-22	3E-24	1.14E-09	2E-11	2.68
Beam RIGHT	10	2.17E-11	1.12E-22	2E-24	6.97E-10	1E-11	2.35
Beam RIGHT	20	1.99E-11	1.24E-22	6E-24	7.72E-10	4E-11	3.20
Beam RIGHT	30	1.01E-11	5.71E-23	8E-25	3.56E-10	5E-12	2.46
Beam RIGHT	45	5.13E-12	2.82E-23	4E-25	1.76E-10	3E-12	2.14

Table 108. Photon Ambient Dose Equivalent, H*(10) based on Kerma Approximation at 50 meters.

Orientation from Beam Centerline	Off-Axis Angle	Φ_{TOTAL} [photons/cm^2/source e$^-$]	H*(10)$_{Kerma}$ [Sv]	δH*(10)$_{Kerma}$ [Sv]	H*(10)$_{Kerma}$ [Sv/μC]	δH*(10)$_{Kerma}$ [Sv/μC]	H*(10)$_{Kerma}$ - Weighted Average Energy [MeV]
Beam LEFT	-45	5.22E-12	3.08E-23	6E-25	1.92E-10	4E-12	2.41
Beam LEFT	-30	1.02E-11	6.55E-23	8E-25	4.09E-10	5E-12	2.84
Beam LEFT	-20	1.90E-11	1.62E-22	2E-24	1.01E-09	2E-11	4.02
Beam LEFT	-10	2.14E-11	1.27E-22	2E-24	7.93E-10	1E-11	2.87
Beam LEFT	-5	3.58E-11	2.34E-22	5E-24	1.46E-09	3E-11	3.59
Beam LEFT	-2	7.73E-11	5.76E-22	1E-23	3.59E-09	7E-11	4.25
Beam LEFT	-1	1.64E-10	1.43E-21	2E-23	8.91E-09	1E-10	4.76
Beam LEFT	-0.5	2.45E-08	4.00E-19	7E-22	2.50E-06	4E-09	6.54
Beam CENTER	0	2.01E-07	3.20E-18	2E-21	2.00E-05	1E-08	6.73
Beam RIGHT	0.5	2.46E-08	4.00E-19	9E-22	2.50E-06	6E-09	6.53
Beam RIGHT	1	1.74E-10	1.46E-21	6E-23	9.11E-09	4E-10	4.68
Beam RIGHT	2	7.59E-11	5.68E-22	1E-23	3.54E-09	7E-11	4.25
Beam RIGHT	5	3.51E-11	2.31E-22	4E-24	1.44E-09	3E-11	3.61
Beam RIGHT	10	2.17E-11	1.28E-22	2E-24	7.99E-10	1E-11	2.86
Beam RIGHT	20	1.99E-11	1.62E-22	8E-24	1.01E-09	5E-11	3.98
Beam RIGHT	30	1.01E-11	6.47E-23	9E-25	4.04E-10	6E-12	2.86
Beam RIGHT	45	5.13E-12	3.06E-23	5E-25	1.91E-10	3E-12	2.43

Table 109. Photon Ambient Dose Equivalent, H*(40) Data at 50 meters.

Orientation from Beam Centerline	Off-Axis Angle	Φ_{TOTAL} [photons/cm^2/source e$^-$]	H*(40) [Sv]	δH*(40) [Sv]	H*(40) [Sv/μC]	δH*(40) [Sv/μC]	H*(40) Dose-Weighted Average Energy [MeV]
Beam LEFT	-45	5.22E-12	2.88E-23	6E-25	1.80E-10	4E-12	2.43
Beam LEFT	-30	1.02E-11	6.14E-23	8E-25	3.83E-10	5E-12	2.86
Beam LEFT	-20	1.90E-11	1.51E-22	2E-24	9.44E-10	1E-11	4.00
Beam LEFT	-10	2.14E-11	1.19E-22	2E-24	7.41E-10	1E-11	2.88
Beam LEFT	-5	3.58E-11	2.15E-22	4E-24	1.34E-09	3E-11	3.51
Beam LEFT	-2	7.73E-11	5.22E-22	1E-23	3.25E-09	6E-11	4.12
Beam LEFT	-1	1.64E-10	1.28E-21	2E-23	8.02E-09	1E-10	4.60
Beam LEFT	-0.5	2.45E-08	3.40E-19	6E-22	2.12E-06	4E-09	6.25
Beam CENTER	0	2.01E-07	2.71E-18	2E-21	1.69E-05	1E-08	6.35
Beam RIGHT	0.5	2.46E-08	3.40E-19	8E-22	2.12E-06	5E-09	6.25
Beam RIGHT	1	1.74E-10	1.31E-21	6E-23	8.20E-09	4E-10	4.53
Beam RIGHT	2	7.59E-11	5.15E-22	1E-23	3.21E-09	7E-11	4.12
Beam RIGHT	5	3.51E-11	2.13E-22	4E-24	1.33E-09	2E-11	3.54
Beam RIGHT	10	2.17E-11	1.19E-22	2E-24	7.45E-10	1E-11	2.87
Beam RIGHT	20	1.99E-11	1.51E-22	7E-24	9.42E-10	4E-11	3.96
Beam RIGHT	30	1.01E-11	6.06E-23	8E-25	3.78E-10	5E-12	2.88
Beam RIGHT	45	5.13E-12	2.86E-23	4E-25	1.78E-10	3E-12	2.45

Table 110. Photon Ambient Dose Equivalent, H*(10) Data at 100 meters.

Orientation from Beam Centerline	Off-Axis Angle	Φ_{TOTAL} [photons/cm^2/source e$^-$]	H*(10) [Sv]	δH*(10) [Sv]	H*(10) [Sv/μC]	δH*(10) [Sv/μC]	H*(10) Dose-Weighted Average Energy [MeV]
Beam LEFT	-45	8.16E-13	4.89E-24	5E-26	3.05E-11	3E-13	2.28
Beam LEFT	-30	1.94E-12	1.15E-23	1E-25	7.19E-11	8E-13	2.52
Beam LEFT	-20	3.98E-12	2.64E-23	3E-25	1.65E-10	2E-12	3.27
Beam LEFT	-10	5.66E-12	2.99E-23	5E-25	1.87E-10	3E-12	2.42
Beam LEFT	-5	1.14E-11	5.99E-23	2E-24	3.74E-10	1E-11	2.73
Beam LEFT	-2	2.73E-11	1.49E-22	4E-24	9.27E-10	2E-11	3.06
Beam LEFT	-1	5.90E-11	3.37E-22	1E-23	2.10E-09	9E-11	3.33
Beam LEFT	-0.5	5.02E-09	4.13E-20	6E-23	2.58E-07	4E-10	5.14
Beam CENTER	0	3.95E-08	3.21E-19	2E-22	2.01E-06	1E-09	5.16
Beam RIGHT	0.5	5.02E-09	4.14E-20	7E-23	2.58E-07	4E-10	5.14
Beam RIGHT	1	5.95E-11	3.36E-22	1E-23	2.10E-09	9E-11	3.35
Beam RIGHT	2	2.84E-11	1.52E-22	6E-24	9.49E-10	4E-11	3.03
Beam RIGHT	5	1.16E-11	6.01E-23	2E-24	3.75E-10	1E-11	2.72
Beam RIGHT	10	5.75E-12	3.03E-23	6E-25	1.89E-10	4E-12	2.41
Beam RIGHT	20	3.95E-12	2.62E-23	2E-25	1.64E-10	1E-12	3.26
Beam RIGHT	30	1.91E-12	1.13E-23	1E-25	7.08E-11	7E-13	2.54
Beam RIGHT	45	8.30E-13	4.95E-24	1E-25	3.09E-11	7E-13	2.28

Table 111. Photon Ambient Dose Equivalent, H*(10) based on Kerma Approximation at 100 meters.

Orientation from Beam Centerline	Off-Axis Angle	Φ_{TOTAL} [photons/cm^2/source e$^-$]	H*(10)$_{Kerma}$ [Sv]	δH*(10)$_{Kerma}$ [Sv]	H*(10)$_{Kerma}$ [Sv/μC]	δH*(10)$_{Kerma}$ [Sv/μC]	H*(10)$_{Kerma}$ - Weighted Average Energy [MeV]
Beam LEFT	-45	8.16E-13	5.37E-24	6E-26	3.35E-11	4E-13	2.60
Beam LEFT	-30	1.94E-12	1.31E-23	1E-25	8.20E-11	9E-13	2.93
Beam LEFT	-20	3.98E-12	3.47E-23	4E-25	2.17E-10	2E-12	4.05
Beam LEFT	-10	5.66E-12	3.47E-23	5E-25	2.17E-10	3E-12	2.96
Beam LEFT	-5	1.14E-11	7.63E-23	2E-24	4.76E-10	1E-11	3.67
Beam LEFT	-2	2.73E-11	2.06E-22	5E-24	1.28E-09	3E-11	4.26
Beam LEFT	-1	5.90E-11	4.93E-22	2E-23	3.08E-09	1E-10	4.64
Beam LEFT	-0.5	5.02E-09	8.75E-20	1E-22	5.46E-07	8E-10	6.70
Beam CENTER	0	3.95E-08	6.80E-19	5E-22	4.25E-06	3E-09	6.92
Beam RIGHT	0.5	5.02E-09	8.76E-20	1E-22	5.47E-07	9E-10	6.70
Beam RIGHT	1	5.95E-11	4.94E-22	2E-23	3.08E-09	1E-10	4.67
Beam RIGHT	2	2.84E-11	2.10E-22	9E-24	1.31E-09	5E-11	4.23
Beam RIGHT	5	1.16E-11	7.64E-23	2E-24	4.77E-10	2E-11	3.66
Beam RIGHT	10	5.75E-12	3.51E-23	7E-25	2.19E-10	4E-12	2.93
Beam RIGHT	20	3.95E-12	3.45E-23	3E-25	2.15E-10	2E-12	4.05
Beam RIGHT	30	1.91E-12	1.30E-23	1E-25	8.10E-11	8E-13	2.96
Beam RIGHT	45	8.30E-13	5.43E-24	1E-25	3.39E-11	7E-13	2.60

Table 112. Photon Ambient Dose Equivalent, H*(40) Data at 100 meters.

Orientation from Beam Centerline	Off-Axis Angle	Φ_{TOTAL} [photons/cm^2/source e$^-$]	H*(40) [Sv]	δH*(40) [Sv]	H*(40) [Sv/μC]	δH*(40) [Sv/μC]	H*(40) Dose-Weighted Average Energy [MeV]
Beam LEFT	-45	8.16E-13	5.03E-24	5E-26	3.14E-11	3E-13	2.61
Beam LEFT	-30	1.94E-12	1.23E-23	1E-25	7.68E-11	9E-13	2.94
Beam LEFT	-20	3.98E-12	3.24E-23	4E-25	2.02E-10	2E-12	4.03
Beam LEFT	-10	5.66E-12	3.24E-23	5E-25	2.02E-10	3E-12	2.97
Beam LEFT	-5	1.14E-11	7.02E-23	2E-24	4.38E-10	1E-11	3.60
Beam LEFT	-2	2.73E-11	1.87E-22	5E-24	1.16E-09	3E-11	4.13
Beam LEFT	-1	5.90E-11	4.44E-22	2E-23	2.77E-09	1E-10	4.49
Beam LEFT	-0.5	5.02E-09	7.40E-20	1E-22	4.62E-07	7E-10	6.42
Beam CENTER	0	3.95E-08	5.73E-19	4E-22	3.57E-06	3E-09	6.55
Beam RIGHT	0.5	5.02E-09	7.41E-20	1E-22	4.62E-07	7E-10	6.41
Beam RIGHT	1	5.95E-11	4.45E-22	2E-23	2.78E-09	1E-10	4.53
Beam RIGHT	2	2.84E-11	1.90E-22	8E-24	1.19E-09	5E-11	4.11
Beam RIGHT	5	1.16E-11	7.03E-23	2E-24	4.39E-10	1E-11	3.59
Beam RIGHT	10	5.75E-12	3.27E-23	7E-25	2.04E-10	4E-12	2.94
Beam RIGHT	20	3.95E-12	3.23E-23	2E-25	2.01E-10	2E-12	4.02
Beam RIGHT	30	1.91E-12	1.22E-23	1E-25	7.60E-11	8E-13	2.97
Beam RIGHT	45	8.30E-13	5.08E-24	1E-25	3.17E-11	7E-13	2.62

Table 113. Photon Ambient Dose Equivalent, H*(10) Data at 120 meters.

Orientation from Beam Centerline	Off-Axis Angle	Φ_{TOTAL} [photons/cm^2/source e$^-$]	H*(10) [Sv]	δH*(10) [Sv]	H*(10) [Sv/μC]	δH*(10) [Sv/μC]	H*(10) Dose-Weighted Average Energy [MeV]
Beam LEFT	-45	4.78E-13	2.98E-24	4E-26	1.86E-11	2E-13	2.34
Beam LEFT	-30	1.21E-12	7.29E-24	1E-25	4.55E-11	7E-13	2.53
Beam LEFT	-20	2.56E-12	1.71E-23	2E-25	1.07E-10	1E-12	3.26
Beam LEFT	-10	3.90E-12	2.09E-23	3E-25	1.31E-10	2E-12	2.44
Beam LEFT	-5	8.56E-12	4.45E-23	1E-24	2.77E-10	9E-12	2.74
Beam LEFT	-2	2.05E-11	1.12E-22	4E-24	7.00E-10	2E-11	3.11
Beam LEFT	-1	4.03E-11	2.40E-22	5E-24	1.50E-09	3E-11	3.43
Beam LEFT	-0.5	3.23E-09	2.68E-20	1E-22	1.67E-07	8E-10	5.21
Beam CENTER	0	2.51E-08	2.07E-19	3E-22	1.29E-06	2E-09	5.25
Beam RIGHT	0.5	3.23E-09	2.68E-20	5E-23	1.67E-07	3E-10	5.21
Beam RIGHT	1	5.61E-11	2.84E-22	7E-23	1.78E-09	4E-10	3.07
Beam RIGHT	2	2.06E-11	1.11E-22	4E-24	6.95E-10	3E-11	3.07
Beam RIGHT	5	8.28E-12	4.38E-23	1E-24	2.73E-10	8E-12	2.80
Beam RIGHT	10	3.91E-12	2.13E-23	5E-25	1.33E-10	3E-12	2.47
Beam RIGHT	20	2.56E-12	1.71E-23	2E-25	1.06E-10	1E-12	3.28
Beam RIGHT	30	1.22E-12	7.31E-24	2E-25	4.56E-11	1E-12	2.54
Beam RIGHT	45	4.65E-13	2.93E-24	2E-26	1.83E-11	2E-13	2.34

Table 114. Photon Ambient Dose Equivalent, H*(10) based on Kerma Approximation at 120 meters.

Orientation from Beam Centerline	Off-Axis Angle	Φ_{TOTAL} [photons/cm^2/source e$^-$]	H*(10)$_{Kerma}$ [Sv]	δH*(10)$_{Kerma}$ [Sv]	H*(10)$_{Kerma}$ [Sv/μC]	δH*(10)$_{Kerma}$ [Sv/μC]	H*(10)$_{Kerma}$ - Weighted Average Energy [MeV]
Beam LEFT	-45	4.78E-13	3.30E-24	4E-26	2.06E-11	3E-13	2.69
Beam LEFT	-30	1.21E-12	8.34E-24	1E-25	5.21E-11	8E-13	2.96
Beam LEFT	-20	2.56E-12	2.26E-23	2E-25	1.41E-10	1E-12	4.05
Beam LEFT	-10	3.90E-12	2.43E-23	4E-25	1.52E-10	2E-12	2.97
Beam LEFT	-5	8.56E-12	5.67E-23	2E-24	3.54E-10	1E-11	3.68
Beam LEFT	-2	2.05E-11	1.56E-22	5E-24	9.76E-10	3E-11	4.32
Beam LEFT	-1	4.03E-11	3.56E-22	8E-24	2.22E-09	5E-11	4.74
Beam LEFT	-0.5	3.23E-09	5.75E-20	3E-22	3.59E-07	2E-09	6.75
Beam CENTER	0	2.51E-08	4.44E-19	6E-22	2.77E-06	4E-09	6.99
Beam RIGHT	0.5	3.23E-09	5.75E-20	1E-22	3.59E-07	7E-10	6.75
Beam RIGHT	1	5.61E-11	4.00E-22	1E-22	2.49E-09	6E-10	4.34
Beam RIGHT	2	2.06E-11	1.55E-22	6E-24	9.68E-10	4E-11	4.29
Beam RIGHT	5	8.28E-12	5.63E-23	2E-24	3.51E-10	1E-11	3.75
Beam RIGHT	10	3.91E-12	2.48E-23	5E-25	1.55E-10	3E-12	3.01
Beam RIGHT	20	2.56E-12	2.26E-23	3E-25	1.41E-10	2E-12	4.08
Beam RIGHT	30	1.22E-12	8.39E-24	2E-25	5.23E-11	2E-12	2.97
Beam RIGHT	45	4.65E-13	3.24E-24	3E-26	2.02E-11	2E-13	2.68

Table 115. Photon Ambient Dose Equivalent, H*(40) Data at 120 meters.

Orientation from Beam Centerline	Off-Axis Angle	Φ_{TOTAL} [photons/cm^2/source e$^-$]	H*(40) [Sv]	δH*(40) [Sv]	H*(40) [Sv/μC]	δH*(40) [Sv/μC]	H*(40) Dose-Weighted Average Energy [MeV]
Beam LEFT	-45	4.78E-13	3.08E-24	4E-26	1.93E-11	2E-13	2.71
Beam LEFT	-30	1.21E-12	7.82E-24	1E-25	4.88E-11	7E-13	2.97
Beam LEFT	-20	2.56E-12	2.11E-23	2E-25	1.32E-10	1E-12	4.03
Beam LEFT	-10	3.90E-12	2.27E-23	4E-25	1.42E-10	2E-12	2.98
Beam LEFT	-5	8.56E-12	5.22E-23	2E-24	3.26E-10	1E-11	3.62
Beam LEFT	-2	2.05E-11	1.42E-22	4E-24	8.85E-10	3E-11	4.19
Beam LEFT	-1	4.03E-11	3.21E-22	7E-24	2.00E-09	4E-11	4.59
Beam LEFT	-0.5	3.23E-09	4.85E-20	2E-22	3.03E-07	1E-09	6.47
Beam CENTER	0	2.51E-08	3.73E-19	5E-22	2.33E-06	3E-09	6.62
Beam RIGHT	0.5	3.23E-09	4.86E-20	1E-22	3.03E-07	6E-10	6.47
Beam RIGHT	1	5.61E-11	3.60E-22	9E-23	2.25E-09	5E-10	4.21
Beam RIGHT	2	2.06E-11	1.41E-22	5E-24	8.77E-10	3E-11	4.16
Beam RIGHT	5	8.28E-12	5.19E-23	2E-24	3.24E-10	9E-12	3.69
Beam RIGHT	10	3.91E-12	2.32E-23	5E-25	1.45E-10	3E-12	3.02
Beam RIGHT	20	2.56E-12	2.11E-23	3E-25	1.31E-10	2E-12	4.06
Beam RIGHT	30	1.22E-12	7.86E-24	2E-25	4.90E-11	1E-12	2.99
Beam RIGHT	45	4.65E-13	3.03E-24	3E-26	1.89E-11	2E-13	2.69

Table 116. Photon Ambient Dose Equivalent, H*(10) Data at 170 meters.

Orientation from Beam Centerline	Off-Axis Angle	Φ_{TOTAL} [photons/cm^2/source e$^-$]	H*(10) [Sv]	δH*(10) [Sv]	H*(10) [Sv/μC]	δH*(10) [Sv/μC]	H*(10) Dose-Weighted Average Energy [MeV]
Beam LEFT	-45	1.51E-13	1.03E-24	1E-26	6.41E-12	7E-14	2.49
Beam LEFT	-30	4.32E-13	2.82E-24	5E-26	1.76E-11	3E-13	2.64
Beam LEFT	-20	1.06E-12	7.20E-24	1E-25	4.49E-11	8E-13	3.31
Beam LEFT	-10	1.77E-12	1.01E-23	1E-25	6.29E-11	9E-13	2.54
Beam LEFT	-5	4.25E-12	2.35E-23	9E-25	1.47E-10	5E-12	2.89
Beam LEFT	-2	1.16E-11	6.39E-23	3E-24	3.99E-10	2E-11	3.16
Beam LEFT	-1	2.45E-11	1.39E-22	7E-24	8.65E-10	4E-11	3.44
Beam LEFT	-0.5	1.33E-09	1.12E-20	3E-23	7.00E-08	2E-10	5.39
Beam CENTER	0	1.01E-08	8.54E-20	9E-23	5.33E-07	6E-10	5.45
Beam RIGHT	0.5	1.32E-09	1.12E-20	2E-23	6.99E-08	1E-10	5.39
Beam RIGHT	1	2.28E-11	1.34E-22	5E-24	8.36E-10	3E-11	3.47
Beam RIGHT	2	1.06E-11	6.09E-23	2E-24	3.80E-10	9E-12	3.23
Beam RIGHT	5	4.08E-12	2.29E-23	5E-25	1.43E-10	3E-12	2.90
Beam RIGHT	10	1.92E-12	1.05E-23	6E-25	6.55E-11	3E-12	2.49
Beam RIGHT	20	1.03E-12	7.18E-24	8E-26	4.48E-11	5E-13	3.33
Beam RIGHT	30	4.35E-13	2.81E-24	3E-26	1.76E-11	2E-13	2.64
Beam RIGHT	45	1.58E-13	1.05E-24	2E-26	6.54E-12	1E-13	2.45

Table 117. Photon Ambient Dose Equivalent, H*(10) based on Kerma Approximation at 170 meters.

Orientation from Beam Centerline	Off-Axis Angle	Φ_{TOTAL} [photons/cm^2/source e$^-$]	H*(10)$_{Kerma}$ [Sv]	δH*(10)$_{Kerma}$ [Sv]	H*(10)$_{Kerma}$ [Sv/μC]	δH*(10)$_{Kerma}$ [Sv/μC]	H*(10)$_{Kerma}$ - Weighted Average Energy [MeV]
Beam LEFT	-45	1.51E-13	1.15E-24	1E-26	7.19E-12	8E-14	2.85
Beam LEFT	-30	4.32E-13	3.26E-24	5E-26	2.03E-11	3E-13	3.08
Beam LEFT	-20	1.06E-12	9.56E-24	2E-25	5.97E-11	1E-12	4.11
Beam LEFT	-10	1.77E-12	1.19E-23	2E-25	7.40E-11	1E-12	3.10
Beam LEFT	-5	4.25E-12	3.06E-23	1E-24	1.91E-10	7E-12	3.87
Beam LEFT	-2	1.16E-11	9.01E-23	4E-24	5.62E-10	2E-11	4.38
Beam LEFT	-1	2.45E-11	2.06E-22	1E-23	1.29E-09	6E-11	4.76
Beam LEFT	-0.5	1.33E-09	2.49E-20	6E-23	1.55E-07	4E-10	6.90
Beam CENTER	0	1.01E-08	1.90E-19	2E-22	1.19E-06	1E-09	7.16
Beam RIGHT	0.5	1.32E-09	2.48E-20	5E-23	1.55E-07	3E-10	6.90
Beam RIGHT	1	2.28E-11	2.00E-22	7E-24	1.25E-09	4E-11	4.80
Beam RIGHT	2	1.06E-11	8.66E-23	2E-24	5.40E-10	1E-11	4.46
Beam RIGHT	5	4.08E-12	2.99E-23	6E-25	1.86E-10	4E-12	3.88
Beam RIGHT	10	1.92E-12	1.23E-23	7E-25	7.67E-11	4E-12	3.04
Beam RIGHT	20	1.03E-12	9.55E-24	1E-25	5.96E-11	7E-13	4.13
Beam RIGHT	30	4.35E-13	3.25E-24	4E-26	2.03E-11	2E-13	3.08
Beam RIGHT	45	1.58E-13	1.17E-24	2E-26	7.31E-12	1E-13	2.81

Table 118. Photon Ambient Dose Equivalent, H*(40) Data at 170 meters.

Orientation from Beam Centerline	Off-Axis Angle	Φ_{TOTAL} [photons/cm^2/source e$^-$]	H*(40) [Sv]	δH*(40) [Sv]	H*(40) [Sv/μC]	δH*(40) [Sv/μC]	H*(40) Dose-Weighted Average Energy [MeV]
Beam LEFT	-45	1.51E-13	1.08E-24	1E-26	6.74E-12	8E-14	2.86
Beam LEFT	-30	4.32E-13	3.06E-24	5E-26	1.91E-11	3E-13	3.10
Beam LEFT	-20	1.06E-12	8.93E-24	2E-25	5.57E-11	1E-12	4.09
Beam LEFT	-10	1.77E-12	1.11E-23	2E-25	6.91E-11	1E-12	3.11
Beam LEFT	-5	4.25E-12	2.82E-23	1E-24	1.76E-10	7E-12	3.80
Beam LEFT	-2	1.16E-11	8.18E-23	3E-24	5.10E-10	2E-11	4.26
Beam LEFT	-1	2.45E-11	1.86E-22	9E-24	1.16E-09	6E-11	4.61
Beam LEFT	-0.5	1.33E-09	2.09E-20	5E-23	1.30E-07	3E-10	6.62
Beam CENTER	0	1.01E-08	1.59E-19	2E-22	9.92E-07	1E-09	6.78
Beam RIGHT	0.5	1.32E-09	2.09E-20	4E-23	1.30E-07	2E-10	6.62
Beam RIGHT	1	2.28E-11	1.80E-22	6E-24	1.13E-09	4E-11	4.64
Beam RIGHT	2	1.06E-11	7.86E-23	2E-24	4.90E-10	1E-11	4.33
Beam RIGHT	5	4.08E-12	2.75E-23	6E-25	1.72E-10	4E-12	3.81
Beam RIGHT	10	1.92E-12	1.15E-23	6E-25	7.17E-11	4E-12	3.05
Beam RIGHT	20	1.03E-12	8.92E-24	1E-25	5.56E-11	6E-13	4.10
Beam RIGHT	30	4.35E-13	3.05E-24	3E-26	1.91E-11	2E-13	3.10
Beam RIGHT	45	1.58E-13	1.10E-24	2E-26	6.85E-12	1E-13	2.82

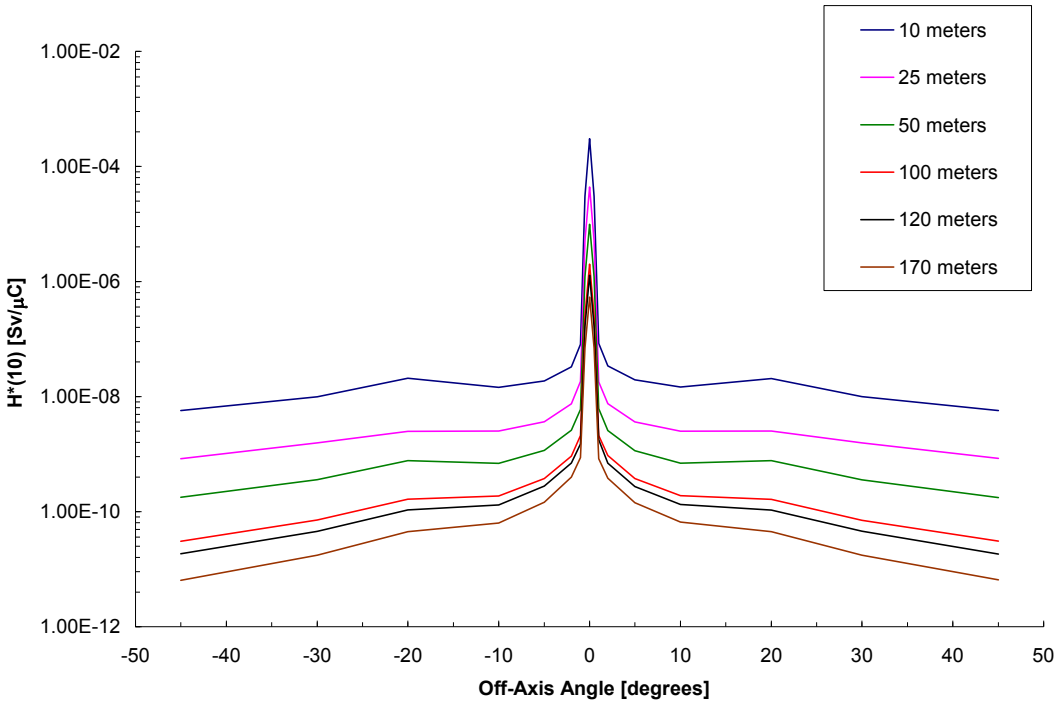

Figure 95. Photon Ambient Dose Equivalent H*(10) at all Downfield Distances.

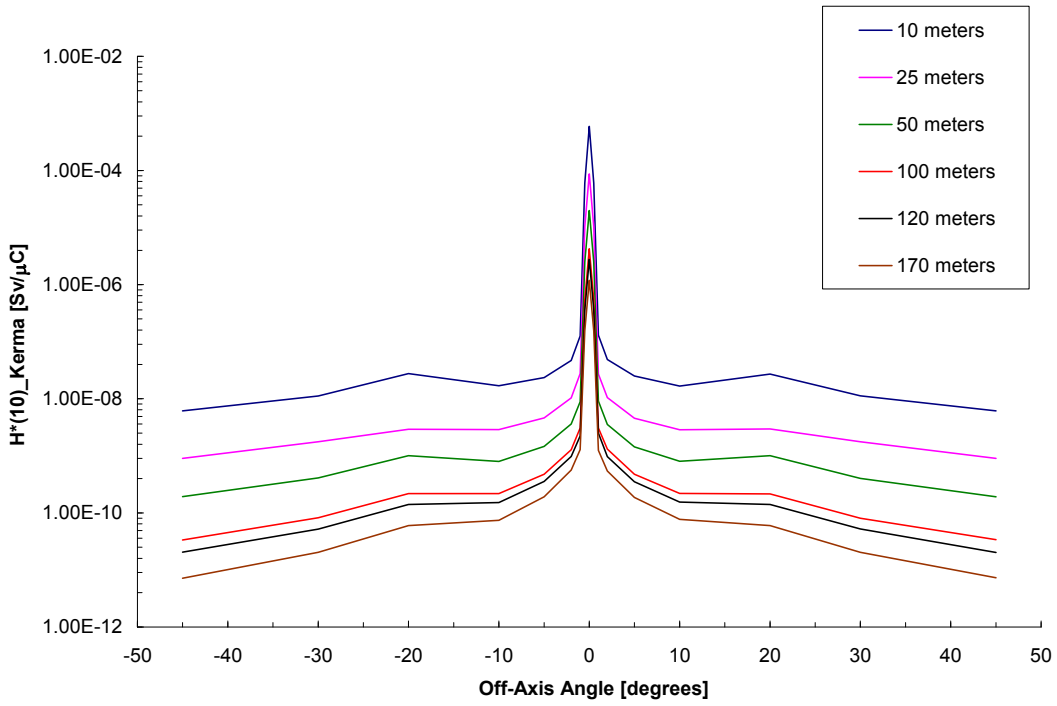

Figure 96. Photon Ambient Dose Equivalent H*(10) Based on Kerma Approximation at all Downfield Distances.

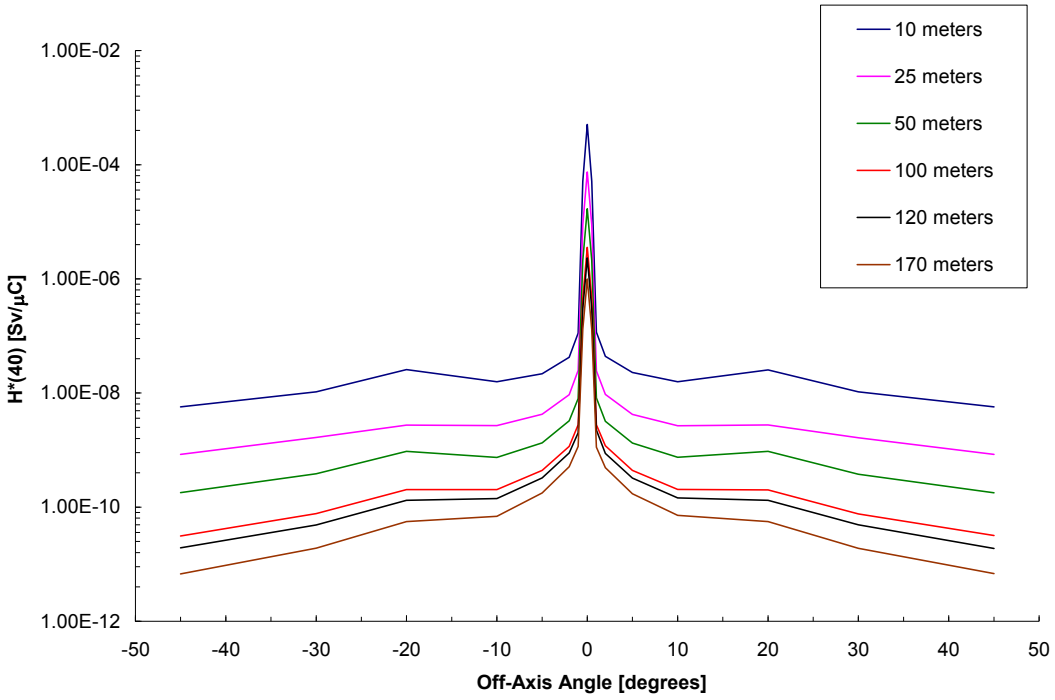

Figure 97. Photon Ambient Dose Equivalent H*(40) at all Downfield Distances.

5.6.2 Electron Ambient Dose Equivalent Calculations

The electron fluence-to-ambient dose equivalent conversion coefficients discussed in Chapter 3 were used to calculate the ambient dose equivalent at downfield distances of 10, 25, 50, 100, 120 and 170 meters. These coefficients were folded with the electron fluences calculated with MCNP5 at seven angular locations (only five angular locations were calculated at 170 meters), as previously discussed. Although the H*(10) for electrons bounds the E for electrons, for completeness ambient dose equivalent data were calculated for both penetration depths thus H*(10) and H*(40).

Electron ambient dose equivalents, H*(10) and H*(40) calculated for the PITAS prototype are given in Table 119 through Table 130. No graphical information is reported due to the paucity of fluence data and thus a lack of structure in the electron dose profile.

Table 119. Electron Ambient Dose Equivalent, H*(10) at 10 meters.

Orientation from Beam Centerline	Off-Axis Angle	Φ_{TOTAL} [electrons/cm^2/source e$^-$]	H*(10) [Sv]	δH*(10) [Sv]	H*(10) [Sv/μC]	δH*(10) [Sv/μC]	H*(10) Dose-Weighted Average Energy [MeV]
Beam LEFT	-5	8.73E-11	2.32E-20	2E-21	1.45E-07	1E-08	6.39
Beam LEFT	-2	3.17E-10	8.75E-20	3E-21	5.46E-07	2E-08	6.95
Beam LEFT	-1	8.27E-10	2.29E-19	3E-21	1.43E-06	2E-08	7.37
Beam CENTER	0	4.54E-09	1.30E-18	3E-21	8.09E-06	2E-08	7.81
Beam RIGHT	1	8.14E-10	2.25E-19	2E-21	1.41E-06	1E-08	7.34
Beam RIGHT	2	3.15E-10	8.62E-20	2E-21	5.38E-07	1E-08	6.98
Beam RIGHT	5	7.97E-11	2.06E-20	1E-21	1.29E-07	8E-09	6.14

Table 120. Electron Ambient Dose Equivalent, H*(40) at 10 meters.

Orientation from Beam Centerline	Off-Axis Angle	Φ_{TOTAL} [electrons/cm^2/source e$^-$]	H*(40) [Sv]	δH*(40) [Sv]	H*(40) [Sv/μC]	δH*(40) [Sv/μC]	H*(40) Dose-Weighted Average Energy [MeV]
Beam LEFT	-5	8.73E-11	4.95E-21	4E-22	3.09E-08	2E-09	12.7
Beam LEFT	-2	3.17E-10	2.26E-20	7E-22	1.41E-07	4E-09	12.9
Beam LEFT	-1	8.27E-10	6.67E-20	9E-22	4.16E-07	6E-09	13.8
Beam CENTER	0	4.54E-09	4.24E-19	9E-22	2.65E-06	6E-09	13.9
Beam RIGHT	1	8.14E-10	6.49E-20	5E-22	4.05E-07	3E-09	13.7
Beam RIGHT	2	3.15E-10	2.22E-20	6E-22	1.39E-07	4E-09	13.1
Beam RIGHT	5	7.97E-11	3.52E-21	2E-22	2.20E-08	1E-09	12.9

Table 121. Electron Ambient Dose Equivalent, H*(10) at 25 meters.

Orientation from Beam Centerline	Off-Axis Angle	Φ_{TOTAL} [electrons/cm^2/source e$^-$]	H*(10) [Sv]	δH*(10) [Sv]	H*(10) [Sv/μC]	δH*(10) [Sv/μC]	H*(10) Dose-Weighted Average Energy [MeV]
Beam LEFT	-2	7.59E-11	2.02E-20	4E-22	1.26E-07	2E-09	6.68
Beam LEFT	-1	2.23E-10	6.05E-20	8E-22	3.77E-07	5E-09	7.05
Beam LEFT	-0.5	7.37E-10	2.07E-19	1E-21	1.29E-06	8E-09	7.41
Beam CENTER	0	2.00E-09	5.69E-19	2E-21	3.55E-06	1E-08	7.74
Beam RIGHT	0.5	7.37E-10	2.06E-19	1E-21	1.29E-06	9E-09	7.43
Beam RIGHT	1	2.20E-10	6.00E-20	7E-22	3.74E-07	4E-09	6.94
Beam RIGHT	2	7.85E-11	2.07E-20	7E-22	1.29E-07	4E-09	6.84

Table 122. Electron Ambient Dose Equivalent, H*(40) at 25 meters.

Orientation from Beam Centerline	Off-Axis Angle	Φ_{TOTAL} [electrons/cm^2/source e$^-$]	H*(40) [Sv]	δH*(40) [Sv]	H*(40) [Sv/μC]	δH*(40) [Sv/μC]	H*(40) Dose-Weighted Average Energy [MeV]
Beam LEFT	-2	7.59E-11	4.73E-21	8E-23	2.95E-08	5E-10	13.3
Beam LEFT	-1	2.23E-10	1.62E-20	2E-22	1.01E-07	1E-09	13.5
Beam LEFT	-0.5	7.37E-10	6.10E-20	4E-22	3.80E-07	2E-09	13.7
Beam CENTER	0	2.00E-09	1.83E-19	6E-22	1.14E-06	4E-09	13.9
Beam RIGHT	0.5	7.37E-10	6.06E-20	4E-22	3.78E-07	3E-09	13.7
Beam RIGHT	1	2.20E-10	1.53E-20	2E-22	9.55E-08	1E-09	13.4
Beam RIGHT	2	7.85E-11	5.14E-21	2E-22	3.21E-08	1E-09	13.4

Table 123. Electron Ambient Dose Equivalent, H*(10) at 50 meters.

Orientation from Beam Centerline	Off-Axis Angle	Φ_{TOTAL} [electrons/cm^2/source e$^-$]	H*(10) [Sv]	δH*(10) [Sv]	H*(10) [Sv/μC]	δH*(10) [Sv/μC]	H*(10) Dose-Weighted Average Energy [MeV]
Beam LEFT	-2	2.51E-11	6.75E-21	3E-22	4.21E-08	2E-09	6.45
Beam LEFT	-1	7.74E-11	2.10E-20	5E-22	1.31E-07	3E-09	6.63
Beam LEFT	-0.5	2.69E-10	7.51E-20	7E-22	4.69E-07	4E-09	7.18
Beam CENTER	0	8.00E-10	2.27E-19	1E-21	1.41E-06	7E-09	7.64
Beam RIGHT	0.5	2.66E-10	7.42E-20	7E-22	4.63E-07	4E-09	7.22
Beam RIGHT	1	7.65E-11	2.05E-20	5E-22	1.28E-07	3E-09	6.69
Beam RIGHT	2	2.57E-11	6.81E-21	3E-22	4.25E-08	2E-09	6.33

Table 124. Electron Ambient Dose Equivalent, H*(40) at 50 meters.

Orientation from Beam Centerline	Off-Axis Angle	Φ_{TOTAL} [electrons/cm^2/source e$^-$]	H*(40) [Sv]	δH*(40) [Sv]	H*(40) [Sv/μC]	δH*(40) [Sv/μC]	H*(40) Dose-Weighted Average Energy [MeV]
Beam LEFT	-2	2.51E-11	1.44E-21	6E-23	9.02E-09	4E-10	12.8
Beam LEFT	-1	7.74E-11	4.69E-21	1E-22	2.93E-08	7E-10	13.2
Beam LEFT	-0.5	2.69E-10	2.06E-20	2E-22	1.29E-07	1E-09	13.5
Beam CENTER	0	8.00E-10	7.12E-20	4E-22	4.44E-07	2E-09	13.8
Beam RIGHT	0.5	2.66E-10	2.04E-20	2E-22	1.28E-07	1E-09	13.6
Beam RIGHT	1	7.65E-11	4.65E-21	1E-22	2.90E-08	7E-10	13.5
Beam RIGHT	2	2.57E-11	1.30E-21	6E-23	8.10E-09	4E-10	13.1

Table 125. Electron Ambient Dose Equivalent, H*(10) at 100 meters.

Orientation from Beam Centerline	Off-Axis Angle	Φ_{TOTAL} [electrons/cm^2/source e$^-$]	H*(10) [Sv]	δH*(10) [Sv]	H*(10) [Sv/μC]	δH*(10) [Sv/μC]	H*(10) Dose-Weighted Average Energy [MeV]
Beam LEFT	-2	6.46E-12	1.75E-21	1E-22	1.09E-08	7E-10	5.89
Beam LEFT	-1	2.36E-11	6.28E-21	2E-22	3.92E-08	1E-09	6.32
Beam LEFT	-0.5	9.13E-11	2.55E-20	5E-22	1.59E-07	3E-09	6.97
Beam CENTER	0	2.85E-10	8.04E-20	7E-22	5.02E-07	4E-09	7.49
Beam RIGHT	0.5	8.96E-11	2.47E-20	4E-22	1.54E-07	2E-09	6.99
Beam RIGHT	1	2.35E-11	6.37E-21	2E-22	3.98E-08	1E-09	6.27
Beam RIGHT	2	6.46E-12	1.75E-21	1E-22	1.09E-08	7E-10	5.89

Table 126. Electron Ambient Dose Equivalent, H*(40) at 100 meters.

Orientation from Beam Centerline	Off-Axis Angle	Φ_{TOTAL} [electrons/cm^2/source e$^-$]	H*(40) [Sv]	δH*(40) [Sv]	H*(40) [Sv/μC]	δH*(40) [Sv/μC]	H*(40) Dose-Weighted Average Energy [MeV]
Beam LEFT	-2	6.46E-12	2.64E-22	2E-23	1.65E-09	1E-10	12.6
Beam LEFT	-1	2.36E-11	1.25E-21	4E-23	7.79E-09	2E-10	13.1
Beam LEFT	-0.5	9.13E-11	6.49E-21	1E-22	4.05E-08	7E-10	13.5
Beam CENTER	0	2.85E-10	2.44E-20	2E-22	1.52E-07	1E-09	13.7
Beam RIGHT	0.5	8.96E-11	6.42E-21	9E-23	4.01E-08	6E-10	13.5
Beam RIGHT	1	2.35E-11	1.21E-21	4E-23	7.53E-09	2E-10	13.1
Beam RIGHT	2	6.46E-12	2.64E-22	2E-23	1.65E-09	1E-10	12.6

Table 127. Electron Ambient Dose Equivalent, H*(10) at 120 meters.

Orientation from Beam Centerline	Off-Axis Angle	Φ_{TOTAL} [electrons/cm^2/source e$^-$]	H*(10) [Sv]	δH*(10) [Sv]	H*(10) [Sv/μC]	δH*(10) [Sv/μC]	H*(10) Dose-Weighted Average Energy [MeV]
Beam LEFT	-2	4.51E-12	1.11E-21	9E-23	6.93E-09	6E-10	5.78
Beam LEFT	-1	1.59E-11	4.25E-21	2E-22	2.65E-08	1E-09	6.50
Beam LEFT	-0.5	6.52E-11	1.80E-20	4E-22	1.12E-07	2E-09	7.04
Beam CENTER	0	2.10E-10	5.95E-20	7E-22	3.71E-07	4E-09	7.41
Beam RIGHT	0.5	6.52E-11	1.81E-20	4E-22	1.13E-07	3E-09	6.94
Beam RIGHT	1	1.67E-11	4.37E-21	2E-22	2.73E-08	1E-09	6.22
Beam RIGHT	2	4.36E-12	1.08E-21	9E-23	6.76E-09	5E-10	5.91

Table 128. Electron Ambient Dose Equivalent, H*(40) at 120 meters.

Orientation from Beam Centerline	Off-Axis Angle	Φ_{TOTAL} [electrons/cm^2/source e$^-$]	H*(40) [Sv]	δH*(40) [Sv]	H*(40) [Sv/μC]	δH*(40) [Sv/μC]	H*(40) Dose-Weighted Average Energy [MeV]
Beam LEFT	-2	4.51E-12	1.80E-22	1E-23	1.12E-09	9E-11	13.0
Beam LEFT	-1	1.59E-11	8.92E-22	4E-23	5.57E-09	2E-10	13.0
Beam LEFT	-0.5	6.52E-11	4.66E-21	1E-22	2.91E-08	6E-10	13.6
Beam CENTER	0	2.10E-10	1.75E-20	2E-22	1.09E-07	1E-09	13.7
Beam RIGHT	0.5	6.52E-11	4.52E-21	1E-22	2.82E-08	7E-10	13.4
Beam RIGHT	1	1.67E-11	8.18E-22	3E-23	5.10E-09	2E-10	13.0
Beam RIGHT	2	4.36E-12	1.91E-22	2E-23	1.19E-09	1E-10	13.2

Table 129. Electron Ambient Dose Equivalent, H*(10) at 170 meters.

Orientation from Beam Centerline	Off-Axis Angle	Φ_{TOTAL} [electrons/cm^2/source e$^-$]	H*(10) [Sv]	δH*(10) [Sv]	H*(10) [Sv/μC]	δH*(10) [Sv/μC]	H*(10) Dose-Weighted Average Energy [MeV]
Beam LEFT	-1	7.95E-12	2.10E-21	2E-22	1.31E-08	1E-09	6.10
Beam LEFT	-0.5	3.26E-11	9.14E-21	4E-22	5.71E-08	3E-09	7.16
Beam CENTER	0	1.17E-10	3.42E-20	9E-22	2.13E-07	6E-09	7.53
Beam RIGHT	0.5	3.26E-11	9.14E-21	4E-22	5.71E-08	3E-09	7.16
Beam RIGHT	1	7.95E-12	2.10E-21	2E-22	1.31E-08	1E-09	6.10

Table 130. Electron Ambient Dose Equivalent, H*(40) at 170 meters.

Orientation from Beam Centerline	Off-Axis Angle	Φ_{TOTAL} [electrons/cm^2/source e$^-$]	H*(40) [Sv]	δH*(40) [Sv]	H*(40) [Sv/μC]	δH*(40) [Sv/μC]	H*(40) Dose-Weighted Average Energy [MeV]
Beam LEFT	-1	7.95E-12	3.84E-22	4E-23	2.40E-09	2E-10	13.0
Beam LEFT	-0.5	3.26E-11	2.42E-21	1E-22	1.51E-08	7E-10	13.6
Beam CENTER	0	1.17E-10	1.04E-20	3E-22	6.52E-08	2E-09	13.5
Beam RIGHT	0.5	3.26E-11	2.42E-21	1E-22	1.51E-08	7E-10	13.6
Beam RIGHT	1	7.95E-12	3.84E-22	4E-23	2.40E-09	2E-10	13.0

5.6.3 Neutron Ambient Dose Equivalent Calculations

The neutron fluence-to-ambient dose equivalent conversion coefficients discussed in Chapter 3 were used to calculate the ambient dose equivalent at downfield distances of 10, 25, 50, 100, 120 and 170 meters. These coefficients were folded with the neutron fluences calculated with MCNP5 at 17 angular locations, as previously discussed. In general, the neutron field beyond a few meters of the system is nearly background. In all cases, H*(10) for neutrons bounds the E for neutrons, therefore only H*(10) was calculated for neutrons. This makes sense since the kerma approximation is good for neutrons $\leq$ 20 MeV at 1cm.

Neutron ambient dose equivalent data calculated for the PITAS prototype are given in Table 131 through Table 136. No graphical information is reported due to the paucity of neutrons beyond a few meters of the system thus a visually uninteresting structure in the neutron dose profile exists.

Table 131. Neutron Ambient Dose Equivalent, H*(10) at 10 meters.

Orientation from Beam Centerline	Off-Axis Angle	Φ_{TOTAL} [neutrons/cm^2/source e$^-$]	H*(10) [Sv]	δH*(10) [Sv]	H*(10) [Sv/μC]	δH*(10) [Sv/μC]	H*(10) Dose-Weighted Average Energy [MeV]
Beam LEFT	-45	5.06E-12	5.48E-22	3E-24	3.42E-09	2E-11	1.37
Beam LEFT	-30	6.83E-12	6.14E-22	2E-24	3.83E-09	1E-11	1.22
Beam LEFT	-20	7.17E-12	6.17E-22	2E-24	3.85E-09	1E-11	1.21
Beam LEFT	-10	7.18E-12	6.28E-22	2E-24	3.92E-09	1E-11	1.22
Beam LEFT	-5	7.17E-12	6.42E-22	4E-24	4.01E-09	2E-11	1.22
Beam LEFT	-2	7.26E-12	6.60E-22	8E-24	4.12E-09	5E-11	1.19
Beam LEFT	-1	7.39E-12	7.38E-22	4E-24	4.61E-09	3E-11	1.32
Beam LEFT	-0.5	7.77E-12	8.77E-22	5E-24	5.47E-09	3E-11	1.53
Beam CENTER	0	8.18E-12	1.06E-21	4E-24	6.59E-09	3E-11	1.84
Beam RIGHT	0.5	7.71E-12	8.77E-22	3E-24	5.47E-09	2E-11	1.52
Beam RIGHT	1	7.36E-12	7.45E-22	3E-24	4.65E-09	2E-11	1.32
Beam RIGHT	2	7.23E-12	6.89E-22	8E-24	4.30E-09	5E-11	1.22
Beam RIGHT	5	7.15E-12	6.45E-22	2E-24	4.02E-09	1E-11	1.22
Beam RIGHT	10	7.13E-12	6.29E-22	2E-24	3.92E-09	1E-11	1.22
Beam RIGHT	20	7.17E-12	6.20E-22	3E-24	3.87E-09	2E-11	1.21
Beam RIGHT	30	6.86E-12	6.14E-22	3E-24	3.83E-09	2E-11	1.22
Beam RIGHT	45	5.04E-12	5.44E-22	2E-24	3.39E-09	1E-11	1.36

Table 132. Neutron Ambient Dose Equivalent, H*(10) at 25 meters.

Orientation from Beam Centerline	Off-Axis Angle	Φ_{TOTAL} [neutrons/cm^2/source e$^-$]	H*(10) [Sv]	δH*(10) [Sv]	H*(10) [Sv/μC]	δH*(10) [Sv/μC]	H*(10) Dose-Weighted Average Energy [MeV]
Beam LEFT	-45	4.75E-13	6.63E-23	3E-25	4.14E-10	2E-12	1.26
Beam LEFT	-30	7.95E-13	8.06E-23	5E-25	5.03E-10	3E-12	1.25
Beam LEFT	-20	9.21E-13	8.35E-23	4E-25	5.21E-10	3E-12	1.23
Beam LEFT	-10	9.62E-13	8.49E-23	2E-24	5.30E-10	1E-11	1.23
Beam LEFT	-5	9.55E-13	8.77E-23	1E-24	5.47E-10	7E-12	1.13
Beam LEFT	-2	9.44E-13	8.88E-23	1E-24	5.54E-10	6E-12	1.26
Beam LEFT	-1	9.59E-13	9.91E-23	4E-25	6.19E-10	2E-12	1.35
Beam LEFT	-0.5	1.00E-12	1.17E-22	5E-25	7.28E-10	3E-12	1.52
Beam CENTER	0	1.07E-12	1.41E-22	6E-25	8.80E-10	4E-12	1.89
Beam RIGHT	0.5	1.02E-12	1.20E-22	1E-24	7.47E-10	6E-12	1.65
Beam RIGHT	1	9.67E-13	9.96E-23	7E-25	6.21E-10	4E-12	1.37
Beam RIGHT	2	9.40E-13	8.85E-23	4E-25	5.52E-10	2E-12	1.26
Beam RIGHT	5	9.63E-13	9.62E-23	3E-24	6.01E-10	2E-11	1.20
Beam RIGHT	10	9.35E-13	8.48E-23	1E-24	5.30E-10	7E-12	1.23
Beam RIGHT	20	9.11E-13	8.45E-23	4E-25	5.27E-10	3E-12	1.23
Beam RIGHT	30	7.88E-13	8.09E-23	5E-25	5.05E-10	3E-12	1.25
Beam RIGHT	45	5.00E-13	7.62E-23	4E-24	4.76E-10	2E-11	1.47

Table 133. Neutron Ambient Dose Equivalent, H*(10) at 50 meters.

Orientation from Beam Centerline	Off-Axis Angle	Φ_{TOTAL} [neutrons/cm^2/source e$^-$]	H*(10) [Sv]	δH*(10) [Sv]	H*(10) [Sv/μC]	δH*(10) [Sv/μC]	H*(10) Dose-Weighted Average Energy [MeV]
Beam LEFT	-45	5.03E-14	1.13E-23	1E-25	7.03E-11	8E-13	1.60
Beam LEFT	-30	9.74E-14	1.49E-23	2E-25	9.28E-11	1E-12	1.41
Beam LEFT	-20	1.14E-13	1.53E-23	2E-25	9.56E-11	9E-13	1.34
Beam LEFT	-10	1.26E-13	1.63E-23	2E-25	1.01E-10	1E-12	1.41
Beam LEFT	-5	1.27E-13	1.63E-23	1E-25	1.02E-10	8E-13	1.34
Beam LEFT	-2	1.28E-13	1.69E-23	1E-25	1.05E-10	8E-13	1.40
Beam LEFT	-1	1.36E-13	1.92E-23	2E-25	1.20E-10	1E-12	1.51
Beam LEFT	-0.5	1.47E-13	2.34E-23	3E-25	1.46E-10	2E-12	1.81
Beam CENTER	0	1.69E-13	3.20E-23	1E-24	2.00E-10	7E-12	2.23
Beam RIGHT	0.5	1.56E-13	2.39E-23	1E-24	1.49E-10	9E-12	1.77
Beam RIGHT	1	1.37E-13	1.94E-23	2E-25	1.21E-10	1E-12	1.52
Beam RIGHT	2	1.29E-13	1.68E-23	1E-25	1.05E-10	9E-13	1.38
Beam RIGHT	5	1.29E-13	1.62E-23	2E-25	1.01E-10	1E-12	1.33
Beam RIGHT	10	1.24E-13	1.59E-23	1E-25	9.91E-11	8E-13	1.33
Beam RIGHT	20	1.15E-13	1.52E-23	2E-25	9.50E-11	1E-12	1.34
Beam RIGHT	30	9.54E-14	1.46E-23	1E-25	9.08E-11	9E-13	1.39
Beam RIGHT	45	5.01E-14	1.10E-23	8E-26	6.89E-11	5E-13	1.58

Table 134. Neutron Ambient Dose Equivalent, H*(10) at 100 meters.

Orientation from Beam Centerline	Off-Axis Angle	Φ_{TOTAL} [neutrons/cm^2/source e$^-$]	H*(10) [Sv]	δH*(10) [Sv]	H*(10) [Sv/μC]	δH*(10) [Sv/μC]	H*(10) Dose-Weighted Average Energy [MeV]
Beam LEFT	-45	3.94E-15	1.35E-24	2E-26	8.41E-12	1E-13	1.78
Beam LEFT	-30	6.88E-15	1.93E-24	3E-26	1.20E-11	2E-13	1.62
Beam LEFT	-20	8.24E-15	2.09E-24	4E-26	1.30E-11	2E-13	1.53
Beam LEFT	-10	9.03E-15	2.20E-24	3E-26	1.37E-11	2E-13	1.49
Beam LEFT	-5	9.54E-15	2.29E-24	5E-26	1.43E-11	3E-13	1.52
Beam LEFT	-2	9.87E-15	2.46E-24	3E-26	1.53E-11	2E-13	1.57
Beam LEFT	-1	1.13E-14	2.95E-24	4E-26	1.84E-11	3E-13	1.75
Beam LEFT	-0.5	1.36E-14	3.88E-24	1E-25	2.42E-11	7E-13	2.03
Beam CENTER	0	1.81E-14	5.66E-24	4E-25	3.53E-11	3E-12	2.93
Beam RIGHT	0.5	1.45E-14	4.21E-24	2E-25	2.63E-11	1E-12	2.10
Beam RIGHT	1	1.24E-14	3.04E-24	2E-25	1.90E-11	1E-12	1.78
Beam RIGHT	2	1.04E-14	2.54E-24	4E-26	1.59E-11	3E-13	1.62
Beam RIGHT	5	9.64E-15	2.33E-24	4E-26	1.45E-11	2E-13	1.54
Beam RIGHT	10	9.40E-15	2.26E-24	4E-26	1.41E-11	2E-13	1.51
Beam RIGHT	20	8.11E-15	2.08E-24	3E-26	1.30E-11	2E-13	1.53
Beam RIGHT	30	6.90E-15	1.88E-24	3E-26	1.18E-11	2E-13	1.57
Beam RIGHT	45	4.04E-15	1.36E-24	5E-26	8.46E-12	3E-13	1.80

Table 135. Neutron Ambient Dose Equivalent, H*(10) at 120 meters.

Orientation from Beam Centerline	Off-Axis Angle	Φ_{TOTAL} [neutrons/cm^2/source e$^-$]	H*(10) [Sv]	δH*(10) [Sv]	H*(10) [Sv/μC]	δH*(10) [Sv/μC]	H*(10) Dose-Weighted Average Energy [MeV]
Beam LEFT	-45	1.92E-15	6.94E-25	9E-27	4.33E-12	6E-14	1.84
Beam LEFT	-30	3.24E-15	1.02E-24	2E-26	6.38E-12	1E-13	1.59
Beam LEFT	-20	3.91E-15	1.14E-24	2E-26	7.09E-12	1E-13	1.51
Beam LEFT	-10	4.40E-15	1.27E-24	2E-26	7.95E-12	1E-13	1.62
Beam LEFT	-5	4.80E-15	1.35E-24	5E-26	8.43E-12	3E-13	1.58
Beam LEFT	-2	5.06E-15	1.47E-24	3E-26	9.18E-12	2E-13	1.70
Beam LEFT	-1	5.85E-15	1.76E-24	4E-26	1.10E-11	2E-13	1.85
Beam LEFT	-0.5	6.96E-15	2.17E-24	5E-26	1.36E-11	3E-13	2.12
Beam CENTER	0	9.33E-15	3.16E-24	2E-25	1.97E-11	1E-12	2.62
Beam RIGHT	0.5	7.04E-15	2.24E-24	5E-26	1.40E-11	3E-13	2.21
Beam RIGHT	1	5.93E-15	1.79E-24	4E-26	1.12E-11	3E-13	1.88
Beam RIGHT	2	5.22E-15	1.49E-24	3E-26	9.29E-12	2E-13	1.68
Beam RIGHT	5	4.80E-15	1.35E-24	3E-26	8.41E-12	2E-13	1.62
Beam RIGHT	10	4.61E-15	1.26E-24	4E-26	7.87E-12	2E-13	1.59
Beam RIGHT	20	4.36E-15	1.21E-24	7E-26	7.55E-12	4E-13	1.53
Beam RIGHT	30	3.43E-15	1.05E-24	4E-26	6.54E-12	2E-13	1.60
Beam RIGHT	45	1.98E-15	7.08E-25	2E-26	4.42E-12	1E-13	1.86

Table 136. Neutron Ambient Dose Equivalent, H*(10) at 170 meters.

Orientation from Beam Centerline	Off-Axis Angle	Φ_{TOTAL} [neutrons/cm^2/source e$^-$]	H*(10) [Sv]	δH*(10) [Sv]	H*(10) [Sv/μC]	δH*(10) [Sv/μC]	H*(10) Dose-Weighted Average Energy [MeV]
Beam LEFT	-45	4.60E-16	1.78E-25	2E-27	1.11E-12	2E-14	2.06
Beam LEFT	-30	8.39E-16	2.92E-25	1E-26	1.82E-12	9E-14	1.50
Beam LEFT	-20	9.62E-16	3.35E-25	9E-27	2.09E-12	6E-14	1.65
Beam LEFT	-10	1.22E-15	3.88E-25	5E-26	2.42E-12	3E-13	1.82
Beam LEFT	-5	1.39E-15	4.71E-25	4E-26	2.94E-12	3E-13	2.08
Beam LEFT	-2	1.42E-15	4.81E-25	1E-26	3.00E-12	8E-14	1.94
Beam LEFT	-1	1.95E-15	6.50E-25	5E-26	4.06E-12	3E-13	2.23
Beam LEFT	-0.5	2.72E-15	9.51E-25	7E-26	5.93E-12	4E-13	2.55
Beam CENTER	0	3.92E-15	1.45E-24	1E-25	9.04E-12	7E-13	3.32
Beam RIGHT	0.5	2.90E-15	1.04E-24	8E-26	6.50E-12	5E-13	2.92
Beam RIGHT	1	2.02E-15	6.74E-25	5E-26	4.21E-12	3E-13	2.44
Beam RIGHT	2	1.47E-15	5.00E-25	3E-26	3.12E-12	2E-13	2.23
Beam RIGHT	5	1.18E-15	3.97E-25	1E-26	2.48E-12	6E-14	1.81
Beam RIGHT	10	1.07E-15	3.66E-25	7E-27	2.28E-12	4E-14	1.76
Beam RIGHT	20	1.02E-15	3.60E-25	2E-26	2.25E-12	9E-14	1.72
Beam RIGHT	30	9.65E-16	3.42E-25	4E-26	2.14E-12	3E-13	1.62
Beam RIGHT	45	4.63E-16	1.79E-25	3E-27	1.12E-12	2E-14	2.03

5.6.4 Total Ambient Dose Equivalent Calculations

The total ambient dose equivalent, H*(d) was calculated by summing the individual constituents (photon, electron and neutron) at downfield distances of 10, 25, 50, 100, 120 and 170 meters. The definition of H*(d) dictates that the dose equivalents from the constituent particles be computed at the same depth in the ICRU sphere even though different depths for different constituent particles may bound the effective dose (i.e. H*(40) for photons and H*(10) for electrons, as is the case in the present work).

Since H*(40) was the bounding condition for photons, the total ambient dose equivalent should be calculated by summing the H*(40) data. Two irregularities in the data need to be addressed. First, the contribution from electrons at far off-axis angles were not computed since calculating electron fluences at those locations was computationally expensive. Therefore, the contribution of electrons to the total H*(d) beyond 5 degrees (and -5 degrees) was not determined in the present work. Secondly, H*(40) conversion coefficients for neutrons in the energy regime of interest, were not available.

So, in order to calculate the total ambient dose equivalent, a few assumptions were made. The first assumption is that since H*(40) data for neutrons were not available, coupled with the fact that the neutron fluence is low and the fact that neutron contribution to the dose equivalent is inconsequential, the neutron component will be ignored in this calculation. The second assumption is that H*(10) for photons by the kerma approximation is the correct quantity to use at locations where no electron fluence data exist. So, close to the beam centerline where data exists, the total H*(d) will be

computed using H*(40) for both photons and electrons. This value will be denoted as Total H*(40). At off-axis locations where no electron data were calculated, the H*(d) will be computed only from H*(10) for photons based on the kerma approximation. This value will be denoted as Total H*(10)-Kerma Approximation.

The total ambient dose equivalent calculated for the PITAS prototype is given in Table 137 through Table 142 and shown in Figure 98 through Figure 103. In order to provide clarity, colors were used to show how data were calculated. Total H*(40) is represented with a blue line and circle data symbol. Total H*(10)-Kerma Approximation is represented by a green line with a filled diamond symbol. Photon H*(40) is represented by an unfilled black square. Electron H*(10) is represented by a red line with a filled triangle.

Table 137. Total Ambient Dose Equivalent at 10 meters.

Orientation from Beam Centerline	Off-Axis Angle	Total H*(40) [Sv/μC]	δH*(40) [Sv/μC]	Total $H^*(10)_{Kerma\ Approx}$ [Sv/μC]	$\delta H^*(10)_{Kerma\ Approx}$ [Sv/μC]
Beam LEFT	-45			6.12E-09	4E-11
Beam LEFT	-30			1.12E-08	1E-10
Beam LEFT	-20			2.75E-08	3E-10
Beam LEFT	-10			1.68E-08	3E-10
Beam LEFT	-5	5.25E-08	2E-09		
Beam LEFT	-2	1.83E-07	5E-09		
Beam LEFT	-1	5.28E-07	6E-09		
Beam LEFT	-0.5	6.02E-05	1E-07		
Beam CENTER	0	5.08E-04	5E-07		
Beam RIGHT	0.5	6.02E-05	1E-07		
Beam RIGHT	1	5.21E-07	4E-09		
Beam RIGHT	2	1.83E-07	4E-09		
Beam RIGHT	5	4.49E-08	2E-09		
Beam RIGHT	10			1.68E-08	3E-10
Beam RIGHT	20			2.72E-08	2E-10
Beam RIGHT	30			1.12E-08	1E-10
Beam RIGHT	45			6.13E-09	4E-11

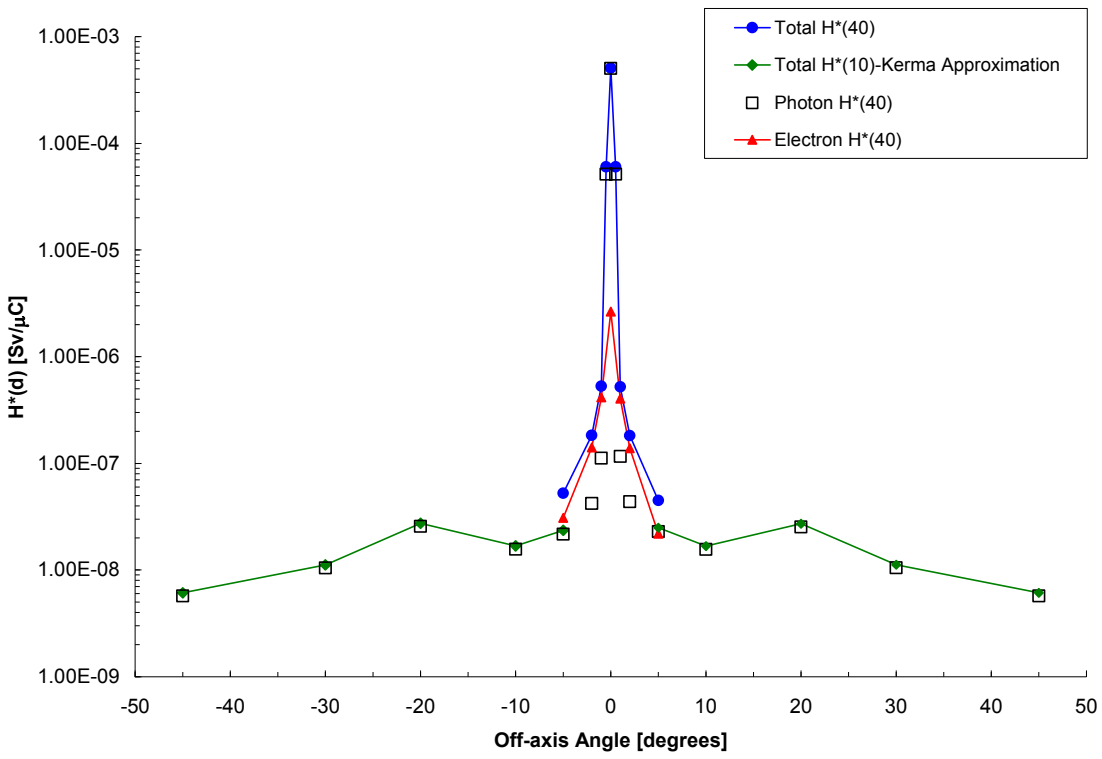

Figure 98. Total Ambient Dose Equivalent at 10 meters.

Table 138. Total Ambient Dose Equivalent at 25 meters.

Orientation from Beam Centerline	Off-Axis Angle	Total H*(40) [Sv/μC]	δH*(40) [Sv/μC]	Total $H^*(10)_{Kerma\ Approx}$ [Sv/μC]	$\delta H^*(10)_{Kerma\ Approx}$ [Sv/μC]
Beam LEFT	-45			9.03E-10	8E-12
Beam LEFT	-30			1.77E-09	1E-11
Beam LEFT	-20			2.91E-09	2E-11
Beam LEFT	-10			2.88E-09	4E-11
Beam LEFT	-5			4.62E-09	7E-11
Beam LEFT	-2	3.88E-08	6E-10		
Beam LEFT	-1	1.26E-07	2E-09		
Beam LEFT	-0.5	9.28E-06	2E-08		
Beam CENTER	0	7.55E-05	6E-08		
Beam RIGHT	0.5	9.27E-06	2E-08		
Beam RIGHT	1	1.20E-07	1E-09		
Beam RIGHT	2	4.15E-08	1E-09		
Beam RIGHT	5			4.58E-09	1E-10
Beam RIGHT	10			2.87E-09	3E-11
Beam RIGHT	20			2.95E-09	4E-11
Beam RIGHT	30			1.76E-09	1E-11
Beam RIGHT	45			9.02E-10	6E-12

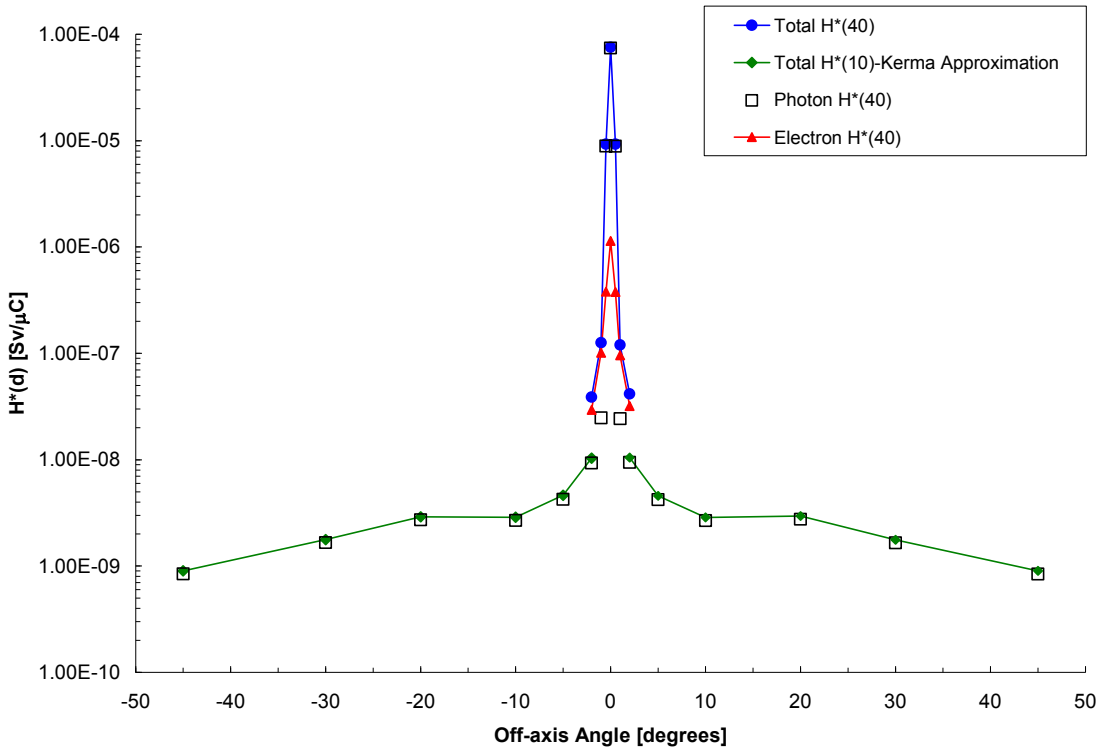

Figure 99. Total Ambient Dose Equivalent at 25 meters.

Table 139. Total Ambient Dose Equivalent at 50 meters.

Orientation from Beam Centerline	Off-Axis Angle	Total H*(40) [Sv/μC]	δH*(40) [Sv/μC]	Total $H^*(10)_{Kerma\ Approx}$ [Sv/μC]	$\delta H^*(10)_{Kerma\ Approx}$ [Sv/μC]
Beam LEFT	-45			1.92E-10	4E-12
Beam LEFT	-30			4.09E-10	5E-12
Beam LEFT	-20			1.01E-09	2E-11
Beam LEFT	-10			7.93E-10	1E-11
Beam LEFT	-5			1.46E-09	3E-11
Beam LEFT	-2	1.26E-08	4E-10		
Beam LEFT	-1	3.82E-08	7E-10		
Beam LEFT	-0.5	2.63E-06	4E-09		
Beam CENTER	0	2.04E-05	1E-08		
Beam RIGHT	0.5	2.63E-06	6E-09		
Beam RIGHT	1	3.81E-08	8E-10		
Beam RIGHT	2	1.16E-08	4E-10		
Beam RIGHT	5			1.44E-09	3E-11
Beam RIGHT	10			7.99E-10	1E-11
Beam RIGHT	20			1.01E-09	5E-11
Beam RIGHT	30			4.04E-10	6E-12
Beam RIGHT	45			1.91E-10	3E-12

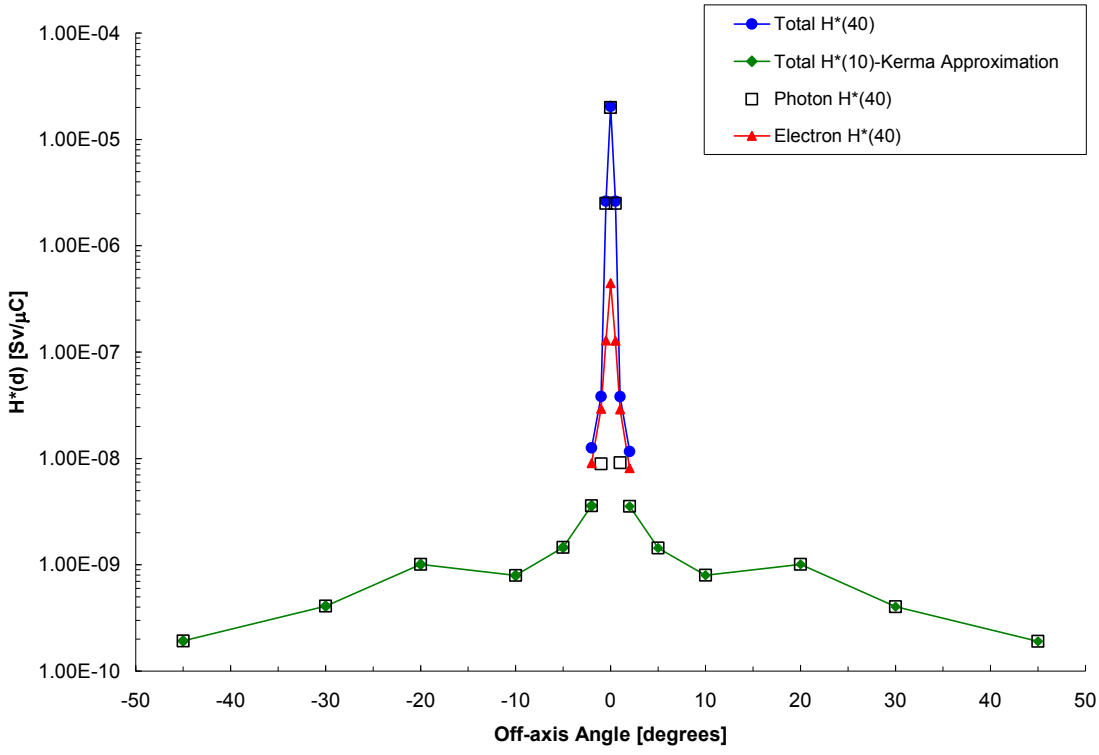

Figure 100. Total Ambient Dose Equivalent at 50 meters.

Table 140. Total Ambient Dose Equivalent at 100 meters.

Orientation from Beam Centerline	Off-Axis Angle	Total H*(40) [Sv/μC]	δH*(40) [Sv/μC]	Total $H^*(10)_{Kerma\ Approx}$ [Sv/μC]	$\delta H^*(10)_{Kerma\ Approx}$ [Sv/μC]
Beam LEFT	-45			3.35E-11	4E-13
Beam LEFT	-30			8.20E-11	9E-13
Beam LEFT	-20			2.17E-10	2E-12
Beam LEFT	-10			2.17E-10	3E-12
Beam LEFT	-5			4.76E-10	1E-11
Beam LEFT	-2	2.81E-09	1E-10		
Beam LEFT	-1	1.06E-08	3E-10		
Beam LEFT	-0.5	5.03E-07	1E-09		
Beam CENTER	0	3.73E-06	3E-09		
Beam RIGHT	0.5	5.02E-07	9E-10		
Beam RIGHT	1	1.03E-08	3E-10		
Beam RIGHT	2	2.84E-09	1E-10		
Beam RIGHT	5			4.77E-10	2E-11
Beam RIGHT	10			2.19E-10	4E-12
Beam RIGHT	20			2.15E-10	2E-12
Beam RIGHT	30			8.10E-11	8E-13
Beam RIGHT	45			3.39E-11	7E-13

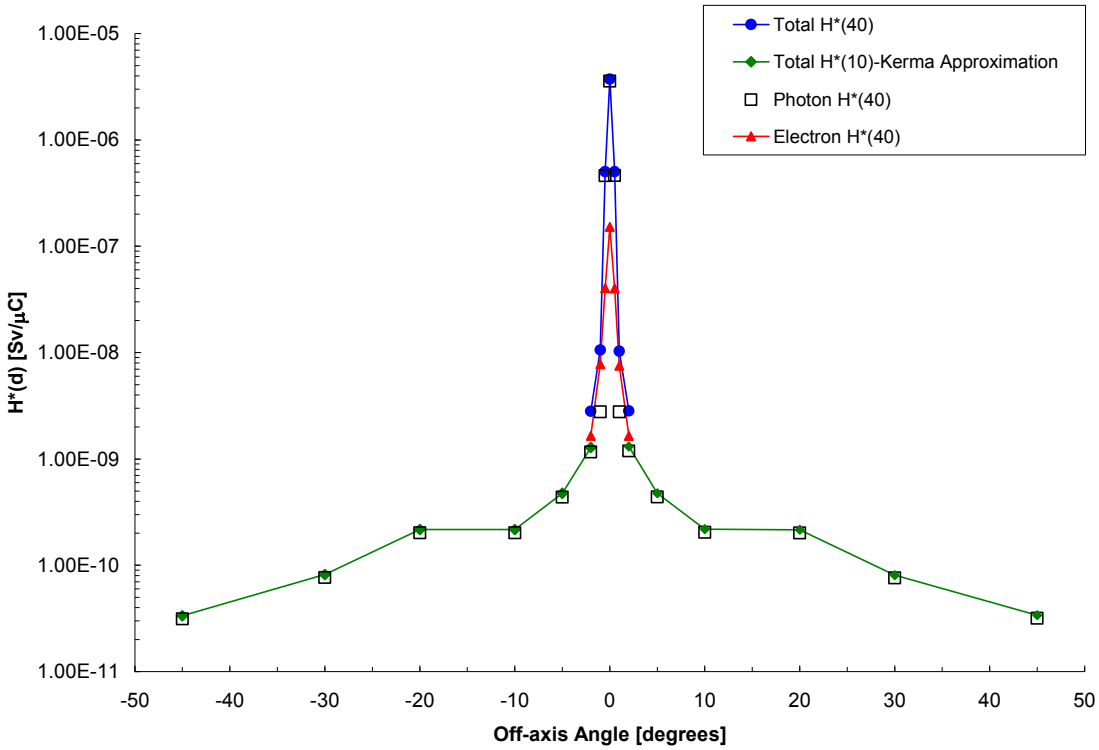

Figure 101. Total Ambient Dose Equiavlent at 100 meters.

Table 141. Total Ambient Dose Equivalent at 120 meters.

Orientation from Beam Centerline	Off-Axis Angle	Total H*(40) [Sv/μC]	δH*(40) [Sv/μC]	Total $H^*(10)_{Kerma\ Approx}$ [Sv/μC]	$\delta H^*(10)_{Kerma\ Approx}$ [Sv/μC]
Beam LEFT	-45			2.06E-11	3E-13
Beam LEFT	-30			5.21E-11	8E-13
Beam LEFT	-20			1.41E-10	1E-12
Beam LEFT	-10			1.52E-10	2E-12
Beam LEFT	-5			3.54E-10	1E-11
Beam LEFT	-2	2.01E-09	9E-11		
Beam LEFT	-1	7.57E-09	2E-10		
Beam LEFT	-0.5	3.32E-07	2E-09		
Beam CENTER	0	2.44E-06	4E-09		
Beam RIGHT	0.5	3.31E-07	9E-10		
Beam RIGHT	1	7.35E-09	6E-10		
Beam RIGHT	2	2.07E-09	1E-10		
Beam RIGHT	5			3.51E-10	1E-11
Beam RIGHT	10			1.55E-10	3E-12
Beam RIGHT	20			1.41E-10	2E-12
Beam RIGHT	30			5.23E-11	2E-12
Beam RIGHT	45			2.02E-11	2E-13

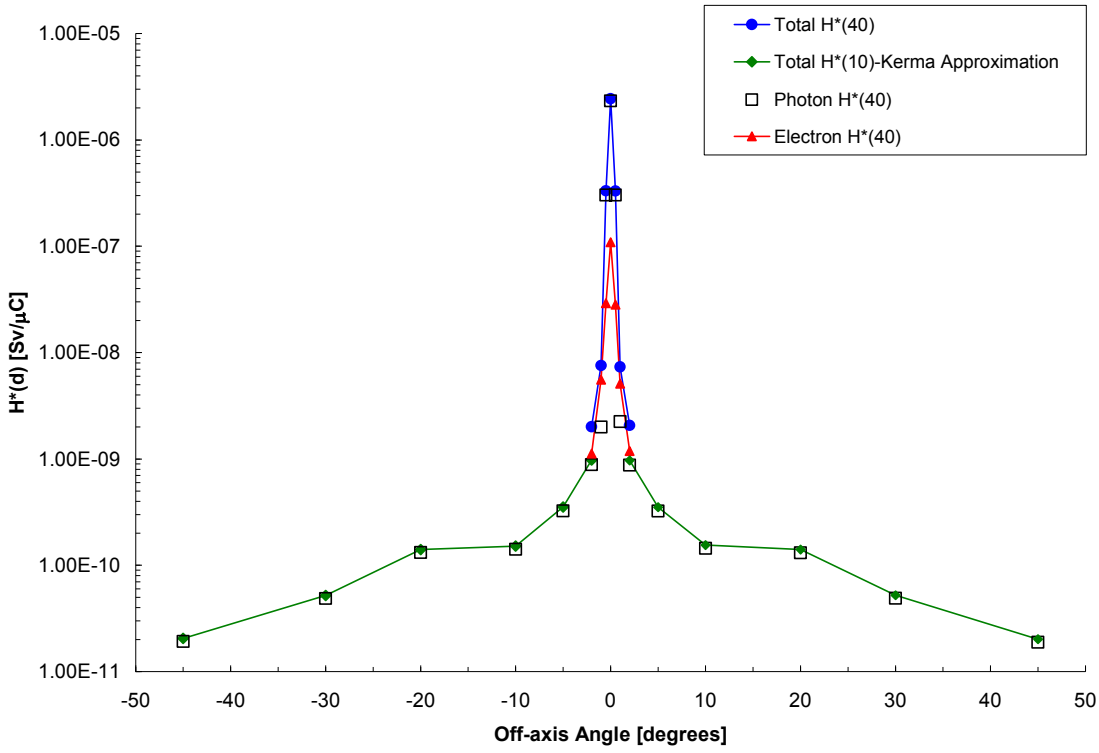

Figure 102. Total Ambient Dose Equivalent at 120 meters.

Table 142. Total Ambient Dose Equivalent at 170 meters.

Orientation from Beam Centerline	Off-Axis Angle	Total H*(40) [Sv/μC]	δH*(40) [Sv/μC]	Total $H^*(10)_{Kerma\ Approx}$ [Sv/μC]	$\delta H^*(10)_{Kerma\ Approx}$ [Sv/μC]
Beam LEFT	-45			7.19E-12	8E-14
Beam LEFT	-30			2.03E-11	3E-13
Beam LEFT	-20			5.97E-11	1E-12
Beam LEFT	-10			7.40E-11	1E-12
Beam LEFT	-5			1.91E-10	7E-12
Beam LEFT	-2			5.62E-10	2E-11
Beam LEFT	-1	3.56E-09	2E-10		
Beam LEFT	-0.5	1.46E-07	8E-10		
Beam CENTER	0	1.06E-06	2E-09		
Beam RIGHT	0.5	1.45E-07	8E-10		
Beam RIGHT	1	3.52E-09	2E-10		
Beam RIGHT	2			5.40E-10	1E-11
Beam RIGHT	5			1.86E-10	4E-12
Beam RIGHT	10			7.67E-11	4E-12
Beam RIGHT	20			5.96E-11	7E-13
Beam RIGHT	30			2.03E-11	2E-13
Beam RIGHT	45			7.31E-12	1E-13

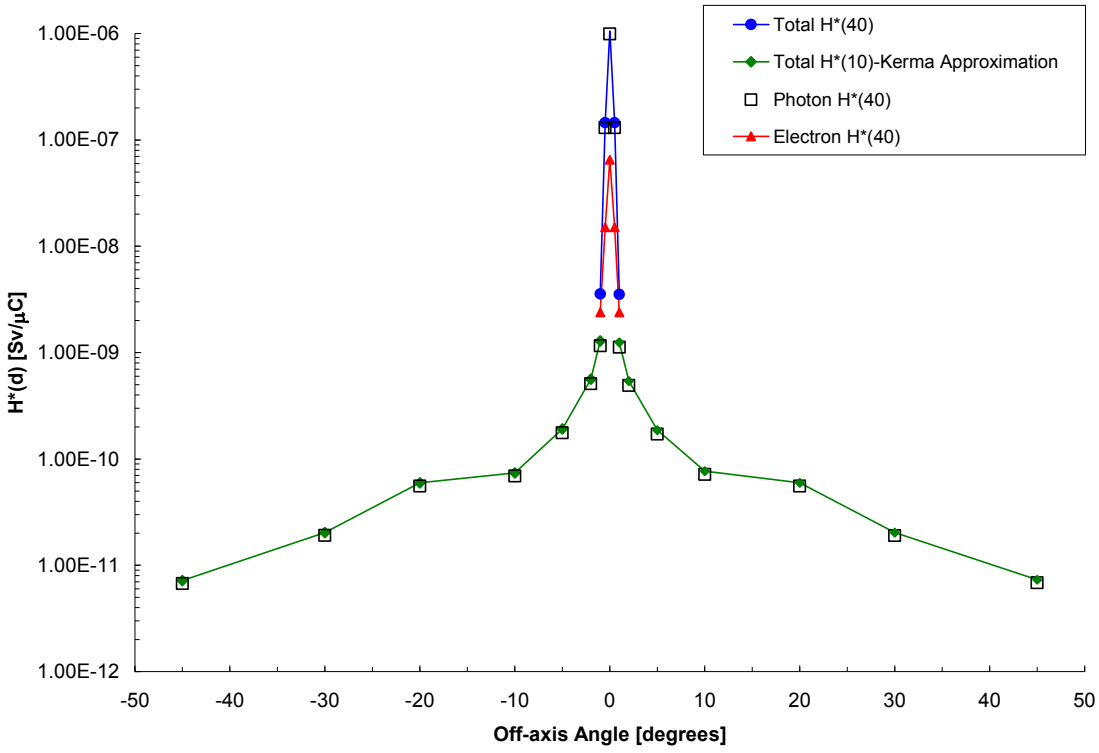

Figure 103. Total Ambient Dose Equiavlent at 170 meters.

5.7 Photon Air Kerma Calculations

Photon air kerma was calculated for all downfield and off-axis distances utilizing the air kerma factors previously reported. This was accomplished by folding the air kerma factors with the MCNP5 calculated fluences. For brevity, all photon air kerma data are reported in Appendix M.

5.8 Special Photon Dose Driver Calculations

In order to gain insight into the components of the PITAS prototype which drive the dose, several parameterized calculations were performed. In order to simplify the extensive number of perturbations that could be presented, only data for H*(10) are reported since any conversion coefficient sets could be folded with the fluences calculated. The results for these calculations at a downfield distance of 10 meters are reported in Figure 104 through Figure 109. The special calculations performed include the following:

1. The H*(10) calculations were repeated in vacuo to ascertain the affect of air scatter;
2. The density of the lead in the collimator was reduced by 10% in order to ascertain the affect of a non-homogenous lead mixture. This calculation was run both in air and in vacuo;
3. The effect of low energy photons was studied by placing a 0.50 cm-thick lead disk over the beam exit hole in the collimator (i.e. beam filtering);
4. The effect of the beam on the downfield dose was explored by making the collimator shielding a region of zero importance which in MCNP5 parlance

means that all photons are killed and only the contribution directly from the beam is tallied;

5. The effect of the collimator on the downfield dose was explored by placing a disk of zero importance over the beam exit hole in the collimator which in MCNP5 parlance means that all photons from the primary beam are killed and only the contribution directly from the collimator is tallied.

The effect of air scatter versus in vacuo was studied by simply changing the air to a void in the MCNP5 model. As excepted the air-scattered dose was higher than the in vacuo dose. On the primary beam axis very little change (less than 1%) was observed, however, at off-axis angles between 1 and 10 degrees, the difference was as high as 37%. At further off-axis angles, 20 to 45 degrees, the differences averaged approximately 11%. The data calculated for the air scatter H*(10) versus the in vacuo H*(10) are shown in Figure 104.

The fidelity of the collimator portion of the model depends on the accurate modeling of several aspects from physical dimensions to material compositions and densities. Densities and material compositions play a major role as they dictate the effective atomic number which in turn dictates the attenuation coefficients and thus the cross section sets utilized. This dependence in photon transport is significant as the attenuation coefficient is key to the equations of the physics employed. There must be a good deal of certainty in the densities used as slight variations, especially high atomic number materials in photon problems, will significantly effect the calculations. With all of this in mind, in all

models of the PITAS prototype it was assumed that the density of the lead used to fabricate the collimator was standard (i.e. 11.344 g/cm^3) and was homogeneous within the actual assembly. If this assumption is not true then the calculations of dose could be influenced. Therefore, the lead density in the standard model of the prototype system was reduced by 10% to study this effect.

The effect of this reduction in density was significant as the H*(10) calculated both with and without the reduction increased the dose vividly, depending on off-axis location. At the beam centerline, the increase was less than 1%, whereas between 1 and 10 degrees the increased differences ranged from 10 to 30%. At far off-axis angles, the increased differences exceeded 37%. This study showed that a straightforward assumption such as a material density can have a relatively considerable impact on the simulations performed. Likewise, a slightly higher density could potentially change the calculations in the opposite direction, however, this perturbation was not studied as the trend would hold. The data calculated for the lead reduction in the collimator calculation are shown in Figure 106.

The effect of attenuating the low energy bremsstrahlung which tend to drive the dose was studied. This was accomplished by changing the standard model to include covering the beam exit hole with a small lead disk (0.5 cm thick) of standard density (i.e. 11.344 g/cm^3). A desired outcome was to determine if this simple approach could noticeably reduce doses within a few degrees of the beam centerline. The differences at beam centerline were notable as the H*(10) was reduced by 35% from -0.5 to 0.5 degrees.

Beyond 0.50 degrees, H*(10) was increased by roughly 1% to 16%. The data for this attenuation study are shown in Figure 107.

The final set of perturbation studies performed focused on the effect of the collimator dose as well as the beam dose on the overall system dose. These studies were performed by using an MCNP5 approach where particles are "killed" by the computation when they reach certain regions (cells) within the model. The first model was based on the model of the standard prototype and all elements of the collimator were made a region of zero importance for photons. Therefore, once a photon reached these cells, it was killed. The effect of this model was to tally only the contribution from the beam itself. In the second model, the opposite was computed where the beam "tube" was made a region of zero importance and the remainder of the collimator was not changed. Therefore, any photons forced down the collimator were killed. The effect of this model was to tally only the contribution from the collimator itself.

The data for these two simulations are shown in Figure 108. The H*(10) observed from the beam only was as expected, highly-collimated and forward peaked. The H*(10) from the collimator was interesting as it was found that at angles greater than 5 (or -5) degrees, the collimator-only dose tends to drive the dose from the entire system. Of course this approach is slightly skewed as the model forced the photons to be transported in a specific manner which may not really reflect physical reality. However, a good deal of insight can be obtained from this straightforward study. In order to ascertain the relative proportion of the beam and collimator to the complete prototype system, a ratio of these

data was computed and plotted as shown in Figure 109. Note that beyond 5 (-5) degrees, the ratio of the H*(10) from the collimator to the complete system is greater than 96%, whereas below 5 (-5) degrees it ranges from 53% down to less than 0.04%. The opposite case holds for the ratio of the beam to the complete system where a steep reduction is seen at locations greater than 5 (-5) degrees. In order to provide some additional clarity, these data are given in Table 143.

The results for these insightful calculations at 25 meters through 170 meters are reported in Appendix N. Only graphical data are reported so that insight can be gained into the shape of the associated dose profiles under the different simulation conditions.

Table 143. H*(10) Data Calculated for Beam-only and Collimator-only Comparisons to the Complete System at 10 meters.

Orientation from Beam Centerline	Off-Axis Angle	Δ H*(10) (System - Beam only) [Sv/μC]	Ratio H*(10) Beam Only : Complete System [Sv/μC]	Δ H*(10) (System - Collimator only) [Sv/μC]	Ratio H*(10) Collimator Only : Complete System [Sv/μC]	Δ H*(10) (Collimator only-Beam only) [Sv/μC]
Beam LEFT	-45	5.63E-09	0.01	6.31E-11	0.99	5.56E-09
Beam LEFT	-30	9.69E-09	0.02	2.23E-10	0.98	9.47E-09
Beam LEFT	-20	2.02E-08	0.03	9.58E-10	0.95	1.93E-08
Beam LEFT	-10	1.22E-08	0.16	3.38E-09	0.77	8.78E-09
Beam LEFT	-5	1.21E-08	0.35	8.30E-09	0.55	3.82E-09
Beam LEFT	-2	1.22E-08	0.63	2.35E-08	0.29	1.13E-08
Beam LEFT	-1	2.42E-08	0.70	6.94E-08	0.14	4.52E-08
Beam LEFT	-0.5	1.16E-06	0.96	3.04E-05	0.0004	2.92E-05
Beam CENTER	0	5.92E-08	1.00	3.02E-04	0.00003	3.02E-04
Beam RIGHT	0.5	1.12E-06	0.96	3.04E-05	0.0004	2.92E-05
Beam RIGHT	1	2.69E-08	0.68	7.26E-08	0.14	4.57E-08
Beam RIGHT	2	1.35E-08	0.60	2.45E-08	0.28	1.10E-08
Beam RIGHT	5	1.29E-08	0.34	9.27E-09	0.53	3.61E-09
Beam RIGHT	10	1.22E-08	0.17	3.45E-09	0.76	8.76E-09
Beam RIGHT	20	1.99E-08	0.03	8.19E-10	0.96	1.91E-08
Beam RIGHT	30	9.75E-09	0.02	3.81E-10	0.96	9.37E-09
Beam RIGHT	45	5.63E-09	0.01	8.53E-11	0.98	5.54E-09

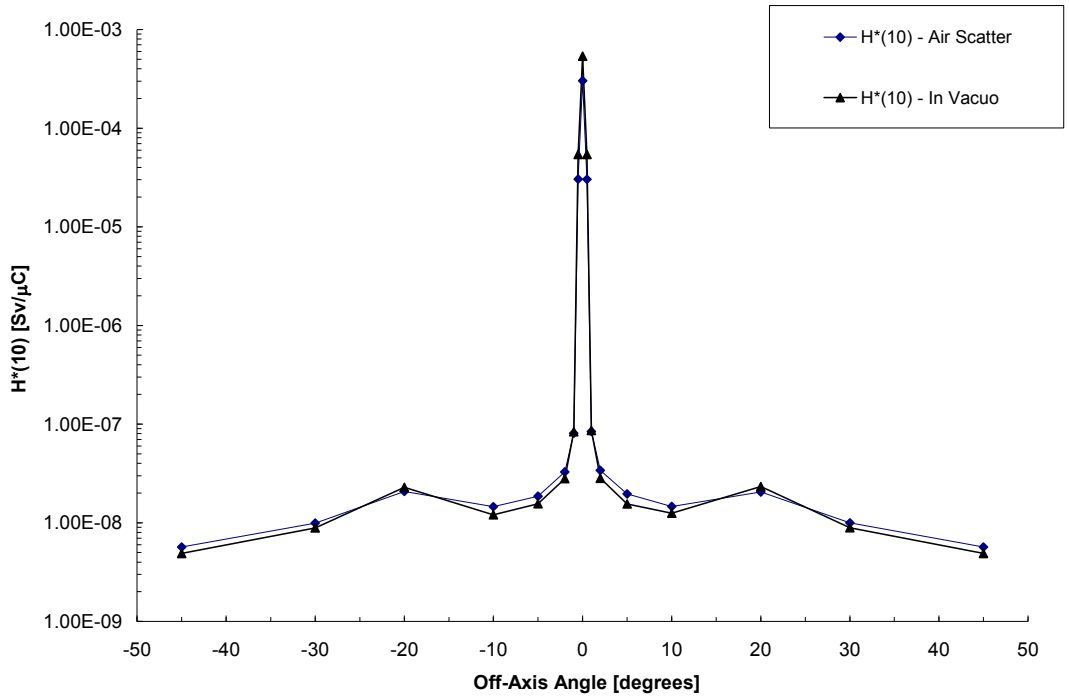

Figure 104. Comparison of H*(10) in Air and In Vacuo for the System at 10 meters.

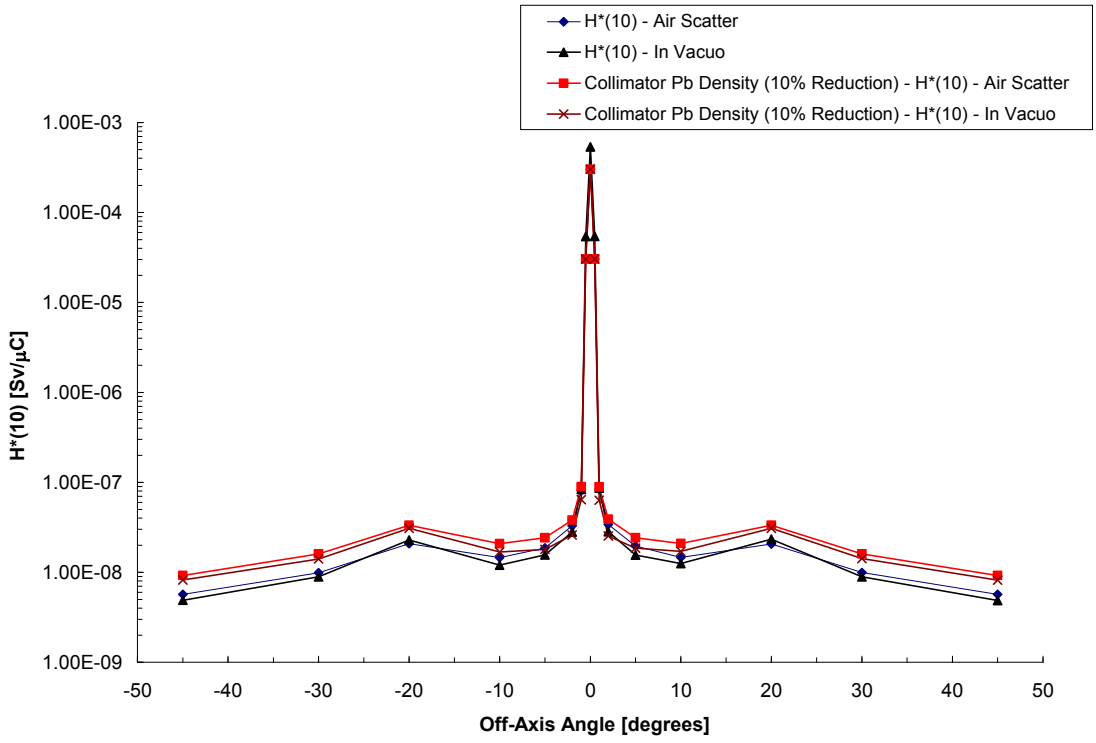

Figure 105. Comparison of H*(10) in Air, In Vacuo, with a Pb Density Reduction of 10% in the Collimator (in Air), and with a Density Reduction of 10% in the Collimator (in Vacuo) at 10 meters.

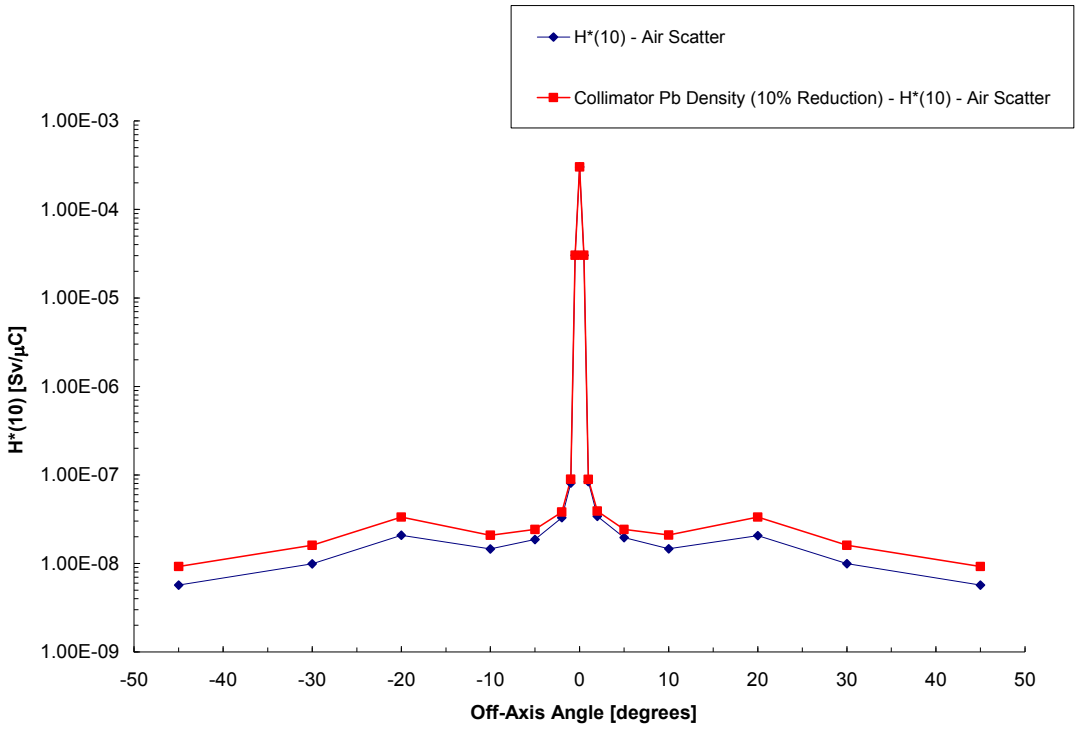

Figure 106. Comparison of H*(10) for the System (in Air) and H*(10) with a Pb Density Reduction of 10% in the Collimator (in Air) at 10 meters.

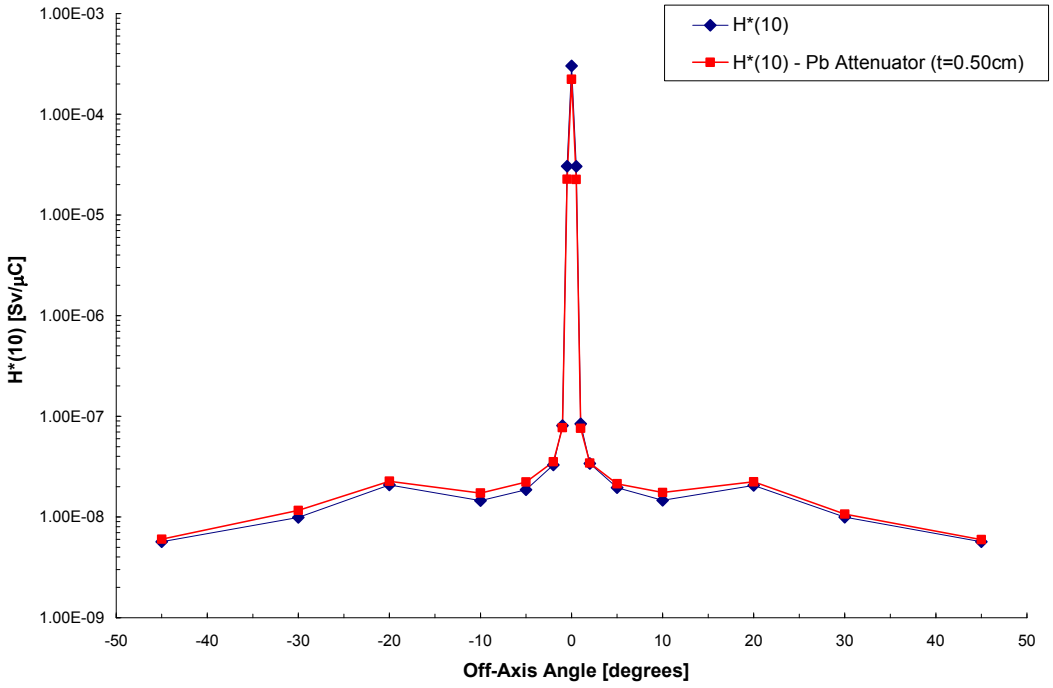

Figure 107. Comparison of H*(10) for the System (in Air) and the System with a Pb Attenuator (t=0.50 cm) in the Beam Line (in Air) at 10 meters.

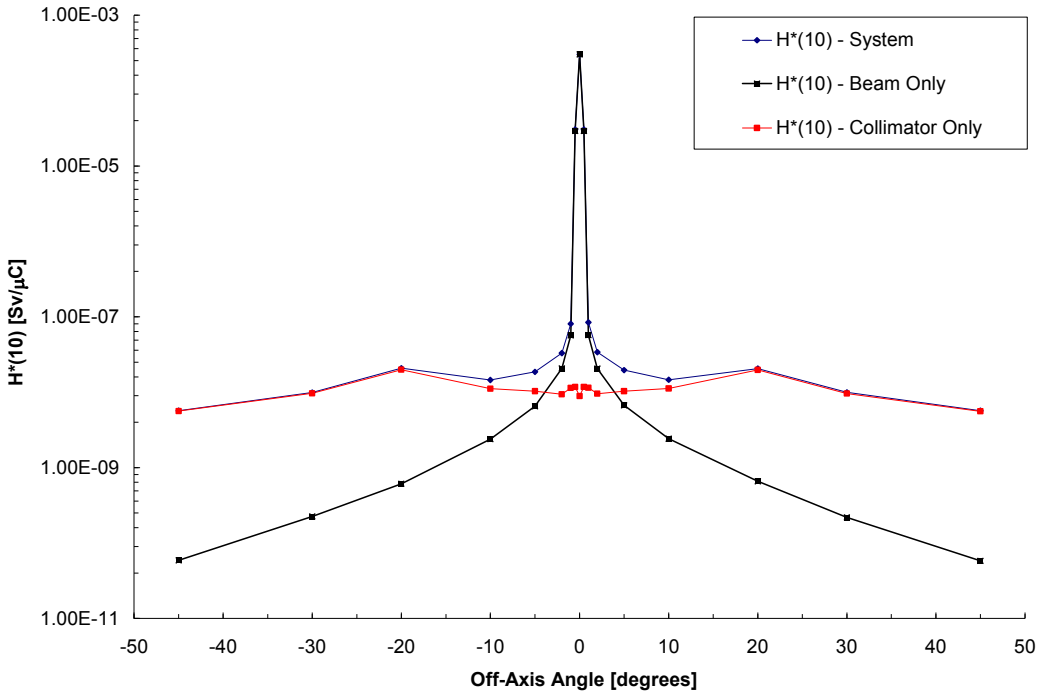

Figure 108. Comparison of H*(10) for the System (in Air), the Beam Only Contribution, and the Collimator Only Contribution at 10 meters.

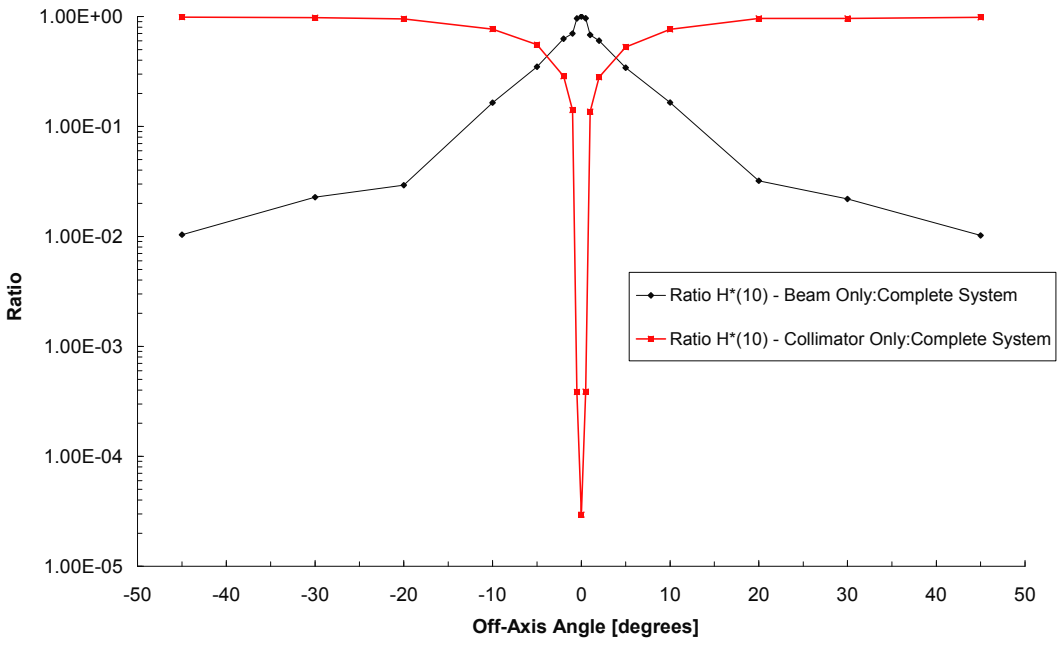

Figure 109. Ratio of H*(10) for the Beam Only to the System (in Air) and the Collimator Only to the System (in Air) at 10 meters.

5.9 RADCAL Model RC1800 Build-up Calculation

In order to determine the effect of dose build-up when using the RADCAL Model RC1800 ion chamber to measure absorbed dose within the primary beam, a set a calculations were performed to compute the ratio of absorbed dose as a function of wall material thickness (build-up). This model included a RADCAL Model RC1800 ion chamber placed at the beam centerline at downfield distances of 1 meter, 50 meters and 100 meters. The absorbed dose inside the detector gas (air) was calculated using an energy deposition tally (MCNP5 *f8). The first model included only the ion chamber followed by successive models each time adding 1-cm of polycarbonate material. A total of eight runs were performed for a total thickness of 7-cm of build-up material. From these data, the ratio of the absorbed dose in the ion chamber gas only to the absorbed dose in the ion chamber gas with each thickness of build-up material, was calculated.

As expected, the dose maximum was found at 4-cm of build-up material which is consistent with a similar calculation for build-up using the PMMA phantom, as previously reported. These data now provide a computed instrument build-up factor to correct in-beam measurements with the RADCAL Model RC1800 ion chamber, should it be necessary. These factors are 2.51, 2.67 and 2.79 for 1 meter, 50 meters and 100 meters, respectively. The average of all downfield distances is 2.66. A summary of these data is given in Table 144 and shown in Figure 110. Note that the build-up thickness reported is the total thickness between the ion chamber gas (air) and the ambient air.

Table 144. RADCAL Model RC1800 Dose Build-up Response at 1 meter, 50 meters and 100 meters.

1 meter Response	Build-up Thickness [cm]	D [Gy]	δD [Gy]	D [Gy/μC]	δD [Gy/μC]	$D_{Ion\ Chamber}/D_{max}$
RADCAL Ion Chamber only	0.330	3.72E-21	7E-23	2.32E-08	4.2E-10	1.00
RADCAL Ion Chamber + 1cm Build-up	1.330	7.26E-21	1E-22	4.53E-08	8.2E-10	1.95
RADCAL Ion Chamber + 2cm Build-up	2.330	8.51E-21	1E-22	5.31E-08	8.2E-10	2.29
RADCAL Ion Chamber + 3cm Build-up	3.330	8.81E-21	1E-22	5.50E-08	8.2E-10	2.37
RADCAL Ion Chamber + 4cm Build-up	4.330	9.33E-21	1E-22	5.82E-08	7.9E-10	2.51
RADCAL Ion Chamber + 5cm Build-up	5.330	9.14E-21	1E-22	5.70E-08	8.0E-10	2.46
RADCAL Ion Chamber + 6cm Build-up	6.330	9.28E-21	1E-22	5.79E-08	7.7E-10	2.49
RADCAL Ion Chamber + 7cm Build-up	7.330	8.87E-21	1E-22	5.53E-08	7.9E-10	2.38
50 meter Response	**Build-up Thickness [cm]**	**D [Gy]**	**δD [Gy]**	**D [Gy/μC]**	**δD [Gy/μC]**	$D_{Ion\ Chamber}/D_{max}$
RADCAL Ion Chamber only	0.330	3.89E-21	7E-23	2.43E-08	4.5E-10	1.00
RADCAL Ion Chamber + 1cm Build-up	1.330	7.94E-21	1E-22	4.96E-08	8.9E-10	2.04
RADCAL Ion Chamber + 2cm Build-up	2.330	9.37E-21	1E-22	5.85E-08	8.9E-10	2.41
RADCAL Ion Chamber + 3cm Build-up	3.330	9.84E-21	1E-22	6.14E-08	8.8E-10	2.53
RADCAL Ion Chamber + 4cm Build-up	4.330	1.04E-20	1E-22	6.49E-08	8.4E-10	2.67
RADCAL Ion Chamber + 5cm Build-up	5.330	1.02E-20	1E-22	6.34E-08	8.6E-10	2.61
RADCAL Ion Chamber + 6cm Build-up	6.330	1.04E-20	1E-22	6.47E-08	8.3E-10	2.66
RADCAL Ion Chamber + 7cm Build-up	7.330	9.99E-21	1E-22	6.23E-08	8.5E-10	2.57
100 meter Response	**Build-up Thickness [cm]**	**D [Gy]**	**δD [Gy]**	**D [Gy/μC]**	**δD [Gy/μC]**	$D_{Ion\ Chamber}/D_{max}$
RADCAL Ion Chamber only	0.330	4.01E-21	8E-23	2.50E-08	4.8E-10	1.00
RADCAL Ion Chamber + 1cm Build-up	1.330	8.43E-21	2E-22	5.26E-08	9.4E-10	2.10
RADCAL Ion Chamber + 2cm Build-up	2.330	1.01E-20	1E-22	6.28E-08	9.4E-10	2.51
RADCAL Ion Chamber + 3cm Build-up	3.330	1.06E-20	1E-22	6.62E-08	9.3E-10	2.65
RADCAL Ion Chamber + 4cm Build-up	4.330	1.12E-20	1E-22	6.97E-08	9.1E-10	2.79
RADCAL Ion Chamber + 5cm Build-up	5.330	1.11E-20	1E-22	6.92E-08	9.1E-10	2.77
RADCAL Ion Chamber + 6cm Build-up	6.330	1.12E-20	1E-22	6.99E-08	8.9E-10	2.80
RADCAL Ion Chamber + 7cm Build-up	7.330	1.09E-20	1E-22	6.81E-08	9.0E-10	2.72

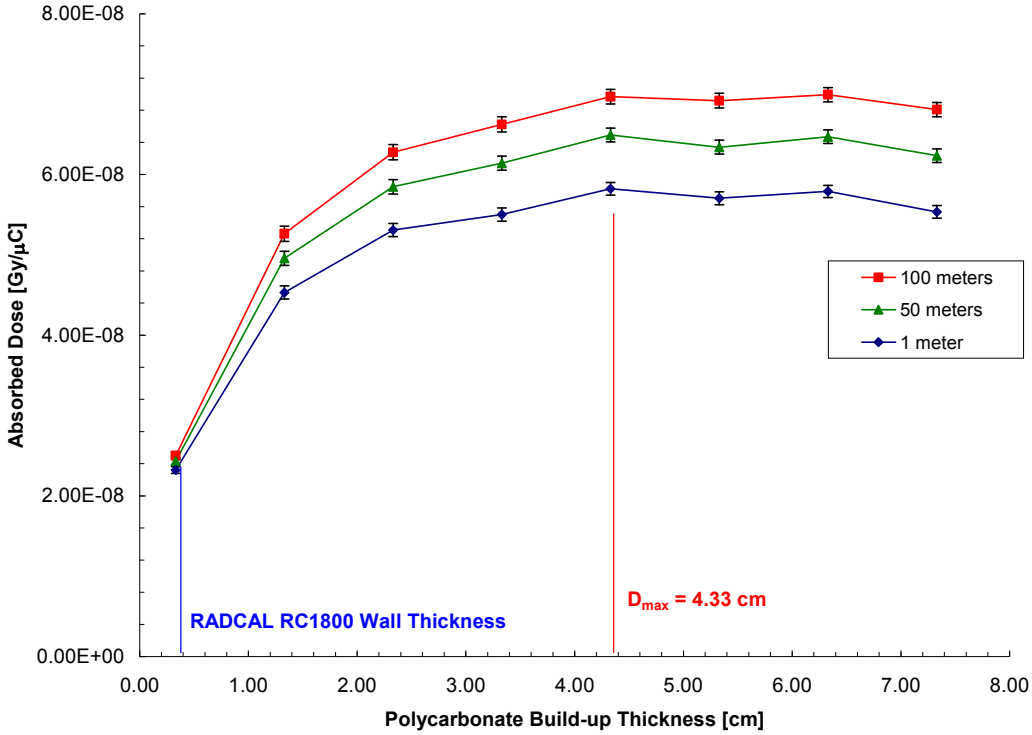

Figure 110. RADCAL Model RC1800 Dose Build-up Response.

CHAPTER 6

COMPARISON OF CALCULATED AND EXPERIMENTAL RESULTS

The following chapter contains comparisons between calculated and experimental results. These comparisons are shown graphically and percent differences provided, where appropriate. Comparisons are made between the beam energy measurements and calculations, the beam profile measurements and calculations, the downfield dose measurements and ambient dose equivalent calculations, and the system absorbed dose measurements and calculations. For all calculations, the statistical uncertainty is shown unless the error bars are smaller than the symbols. The error bars shown for experimental data are the total relative uncertainties propagated as explained in Appendix B.

6.1 Beam Energy Measurement – Calculation Comparison

The absorbed dose measurement used to assess the electron beam energy are compared with the computational results in Figure 111. A plot of the percent difference between the calculations in measurements as a function of lead thickness is shown in Figure 112. The results match to within 20% for both the absorbed dose and kerma calculation at 25 MeV. The 24 MeV kerma calculation matches slightly better with the highest percent difference at approximately 13%. The result of this experiment show that within an

uncertainty of 13-19%, the energy of the electron beam is near 24-25 MeV, which is at the nominal voltage of the prototype system. So the remainder of the calculations that were performed at 25 MeV should yield the best results.

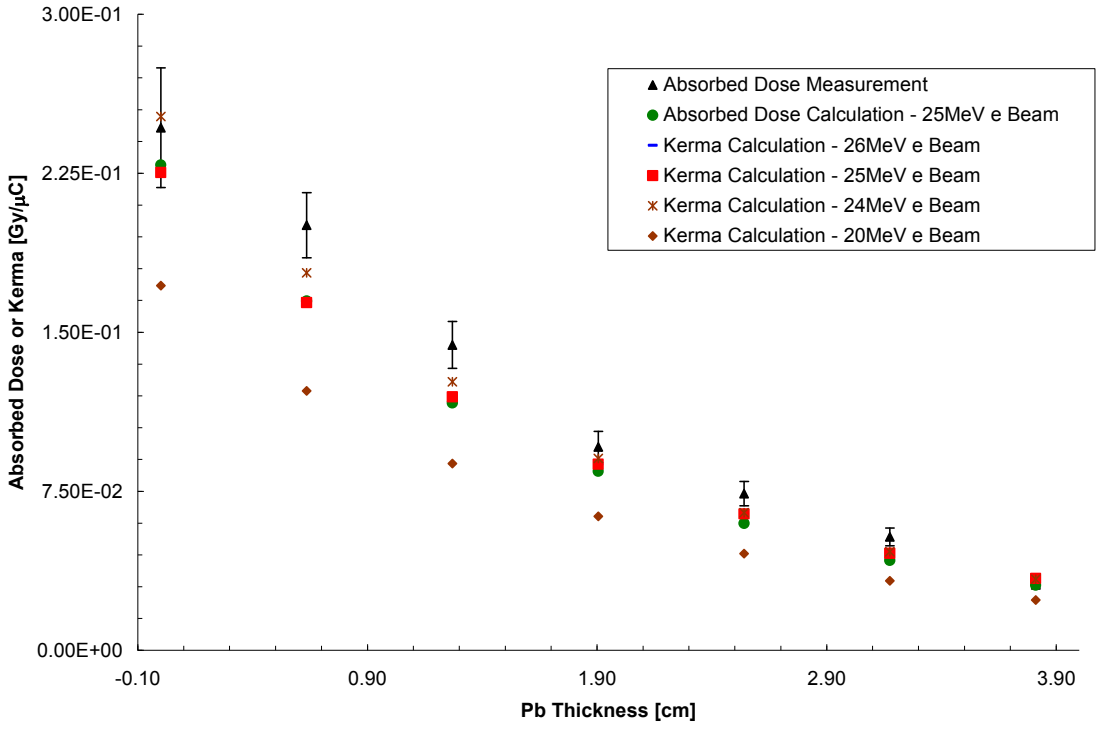

Figure 111. Experimental Absorbed Dose in a Virtual Water Phantom Compared with Calculated Absorbed Dose and Kerma.

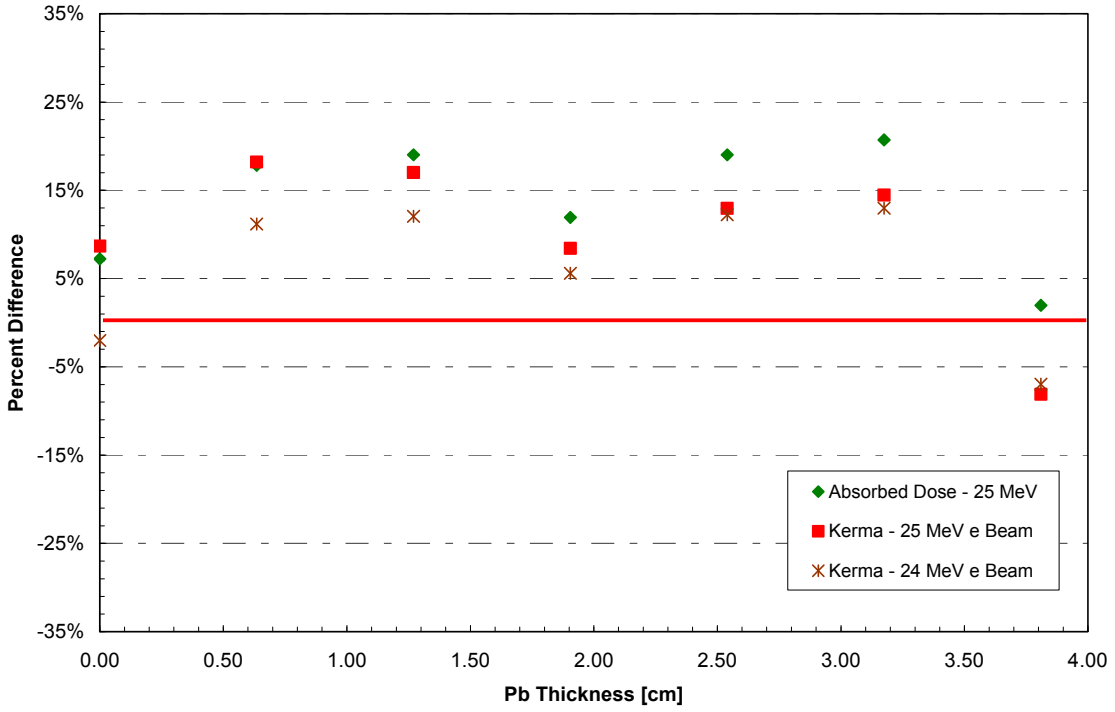

Figure 112. Percent Difference Between Experiment & Calculation of Absorbed Dose in Virtual Water Phantom Used for Beam Energy Assessment.

6.2 Beam Profile Measurement – Calculation Comparison

The size and shape of the photon beam was predicted using the solid angle defined by the collimator. The predicted geometric size was then overlayed on the measured beam profile as reported in Chapter 4. A set of simulations was performed at 8, 30 and 50 meters, to predict the beam profile. A comparison of all three data sets is prudent in order to cross-compare methodologies. Therefore a graphical analyses, keeping the scale of the plots intact, are shown in Figure 113 through Figure 115. The contour plot (developed from measurements) and the dashed circle (developed from geometric calculations) are overlayed upon a plot of the beam profile (from the beam profile simulations). The results from the 30 meter data are poor. This stems from the fact that a

larger array should have been used for the measurement and maybe misaligned OSL dosimeters. The smaller array created a problem with sampling the entire beam and therefore an overall poor estimate of the beam profile.

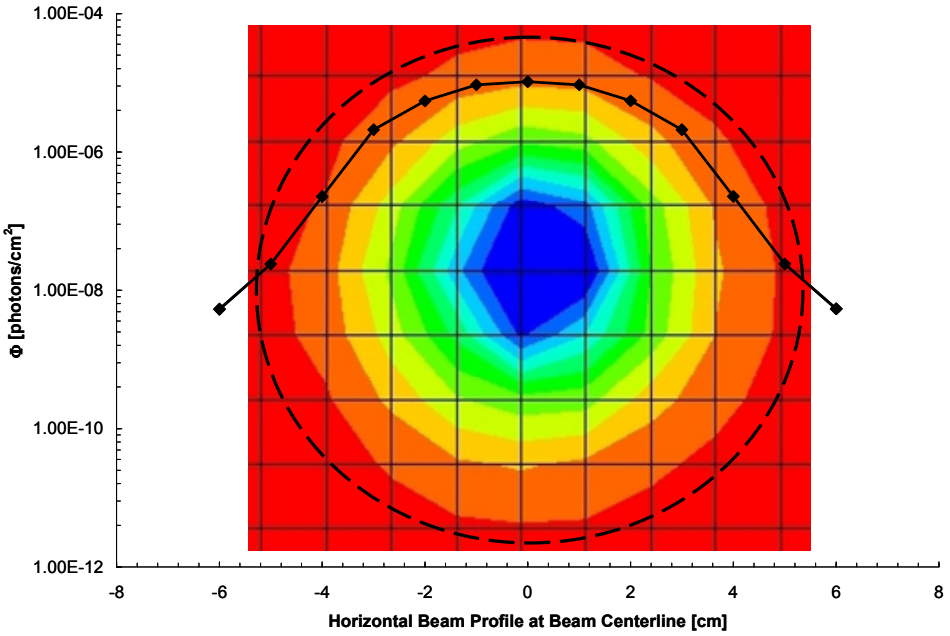

Figure 113. Comparison of Beam Profile Measurements and Calculations at 8 meters. The dashed circle represent the solid angle calculation and the parabolic line are the MCNP calculated data.

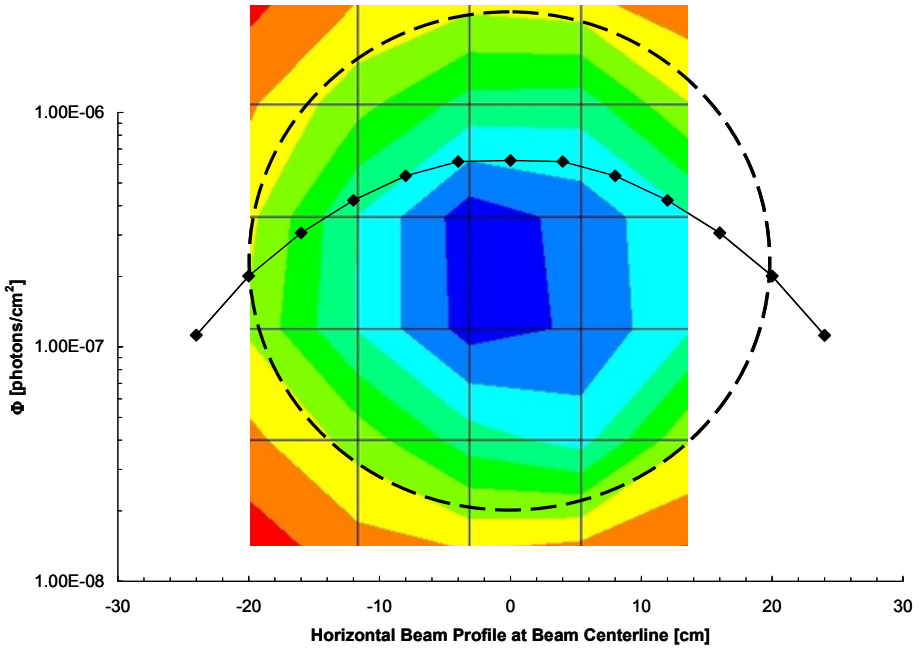

Figure 114. Comparison of Beam Profile Measurements and Calculations at 30 meters. The dashed circle represent the solid angle calculation and the parabolic line are the MCNP calculated data.

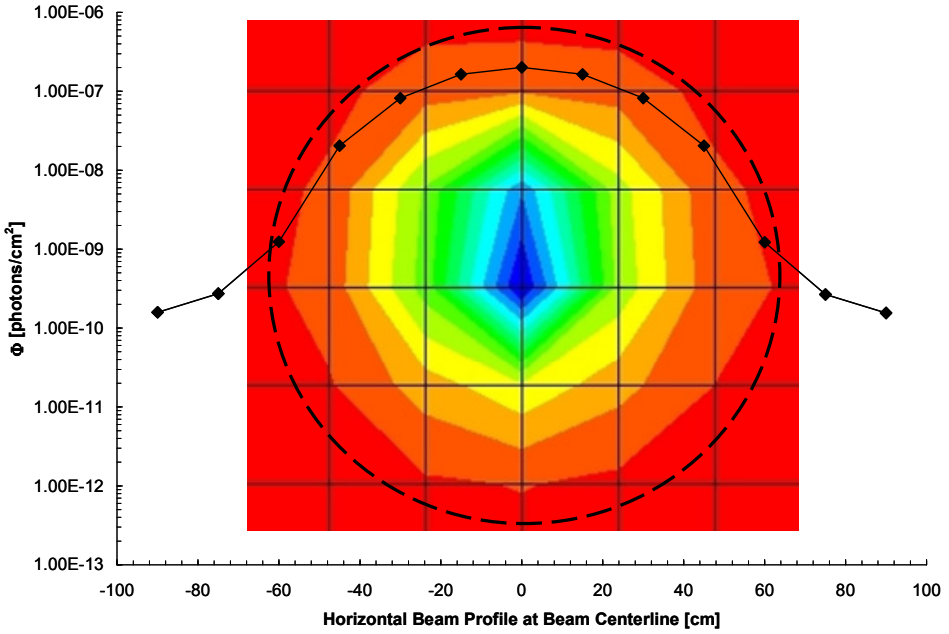

Figure 115. Comparison of Beam Profile Measurements and Calculations at 50 meters. The dashed circle represent the solid angle calculation and the parabolic line are the MCNP calculated data

6.3 Downfield Absorbed Dose Measurement – Calculation Comparison

The downfield absorbed dose measurements are compared with the ambient dose equivalent, H*(d) calculations (both H*(40) and H*(10) based on the kerma approximation) using the logic developed in Chapter 5. The results at downfield distances of 10, 25, 50, 100 and 170 meters are shown in Figure 116 through Figure 121.

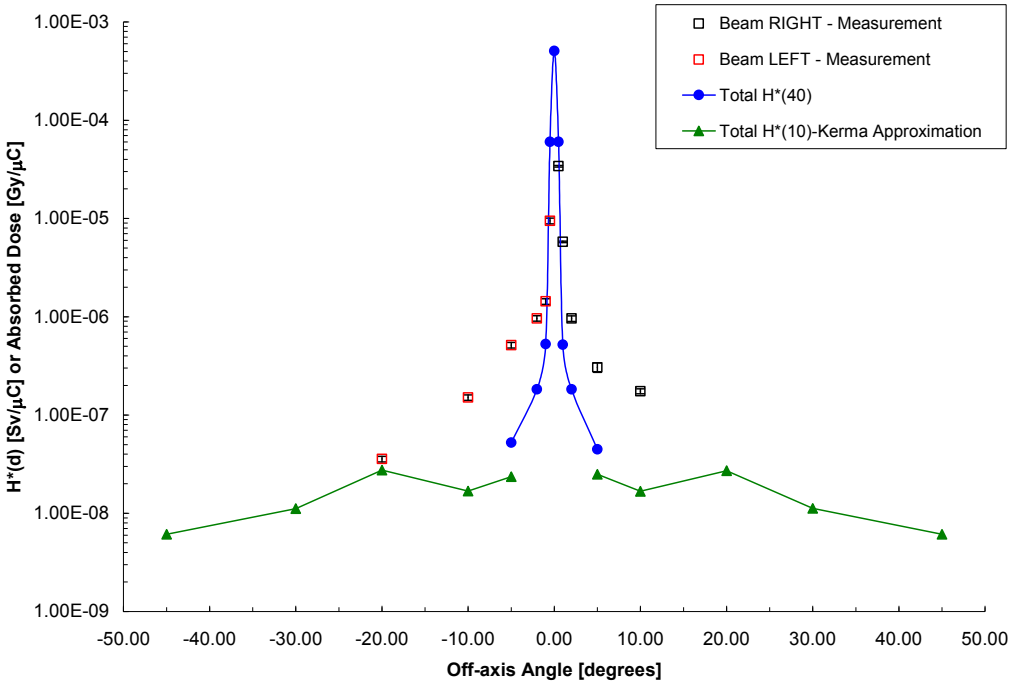

Figure 116. Experimental Downfield Absorbed Dose Measurements (made with RADCAL Model RC1800) Compared with the Calculated Total Ambient Dose Equivalent, H*(d) at 10 meters. (The error bars are smaller than the size of the symbols).

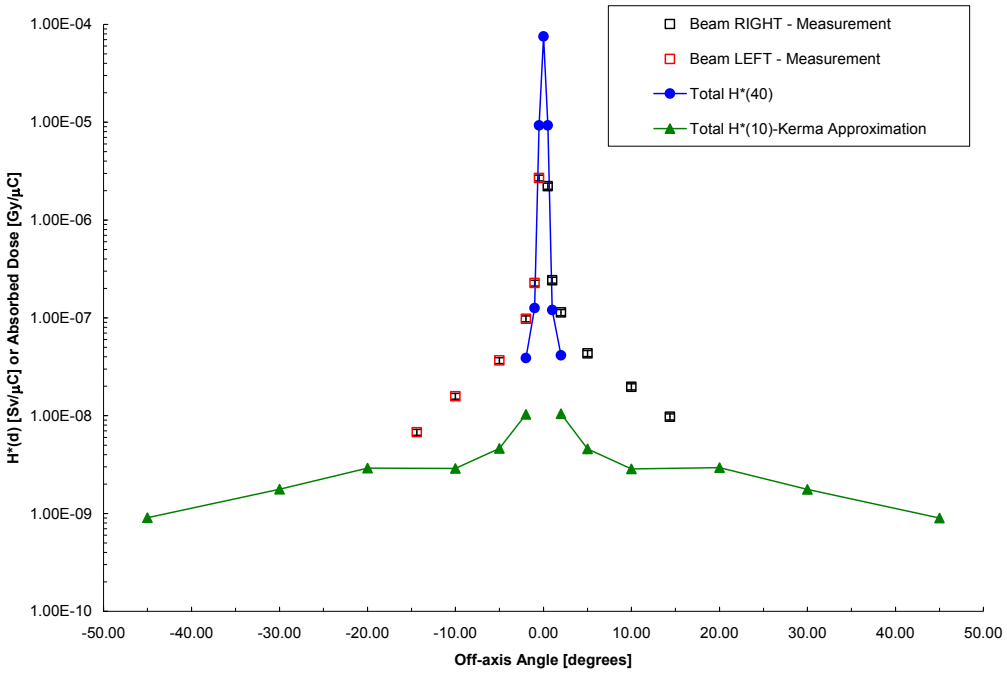

Figure 117. Experimental Downfield Absorbed Dose Measurements (made with RADCAL Model RC1800) Compared with the Calculated Total Ambient Dose Equivalent, H*(d) at 25 meters. (The error bars are smaller than the size of the symbols).

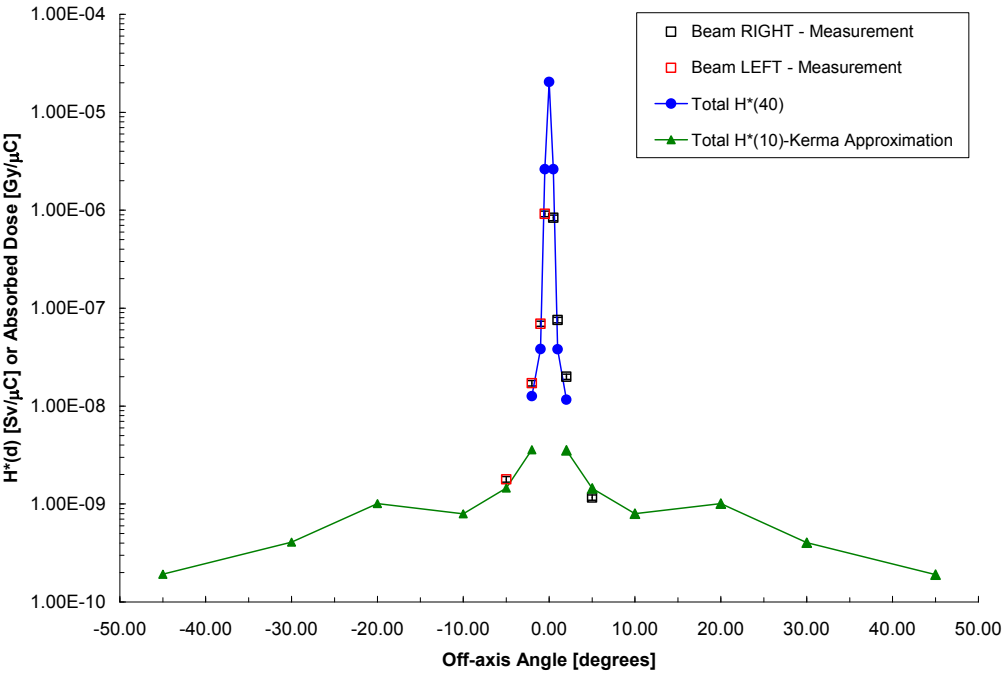

Figure 118. Experimental Downfield Absorbed Dose Measurements (made with RADCAL Model RC1800) Compared with the Calculated Total Ambient Dose Equivalent, H*(d) at 50 meters. (The error bars are smaller than the size of the symbols).

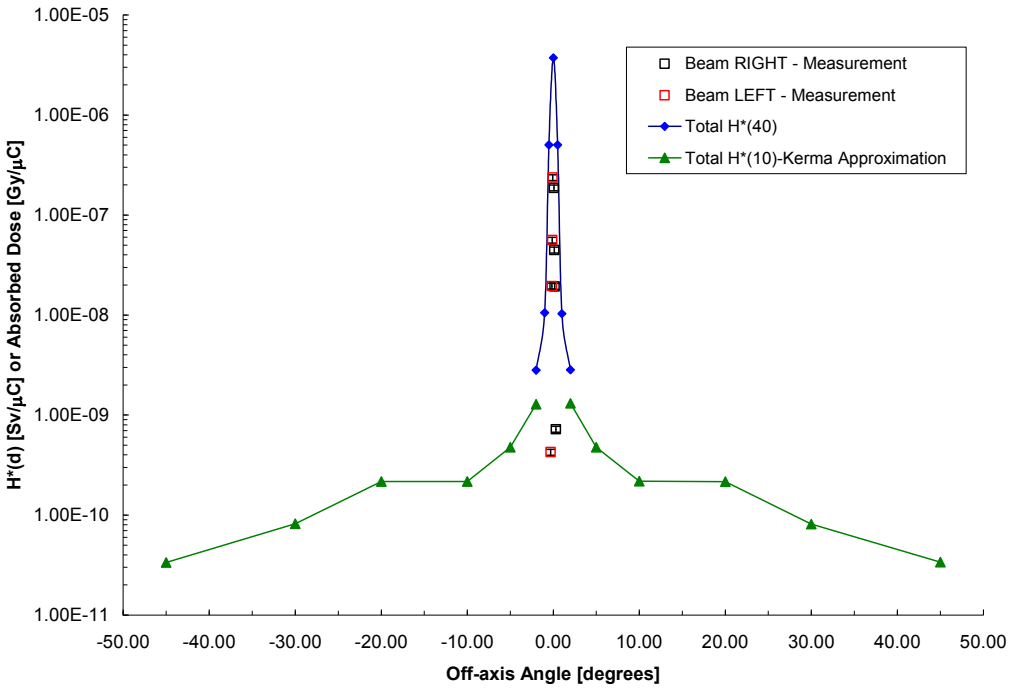

Figure 119. Experimental Downfield Absorbed Dose Measurements (made with RADCAL Model RC1800) Compared with the Calculated Total Ambient Dose Equivalent, H*(d) at 100 meters. (The error bars are smaller than the size of the symbols).

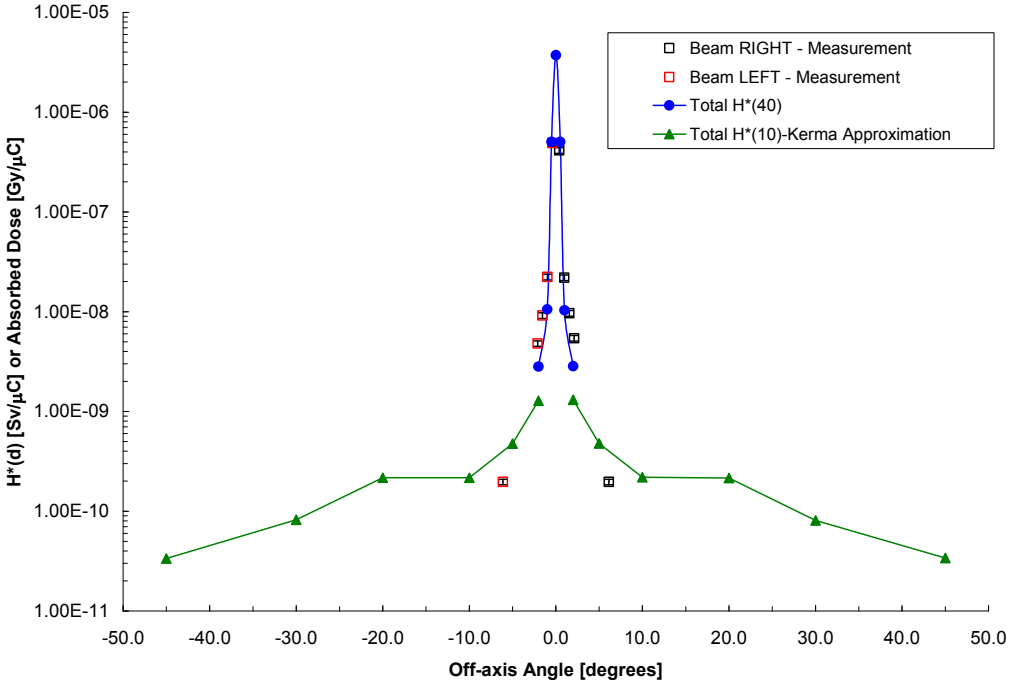

Figure 120. Experimental Downfield Absorbed Dose Measurements (made with Far West Model 1055 Chipmunk) Compared with the Calculated Total Ambient Dose Equivalent, H*(d) at 100 meters. (The error bars are smaller than the size of the symbols).

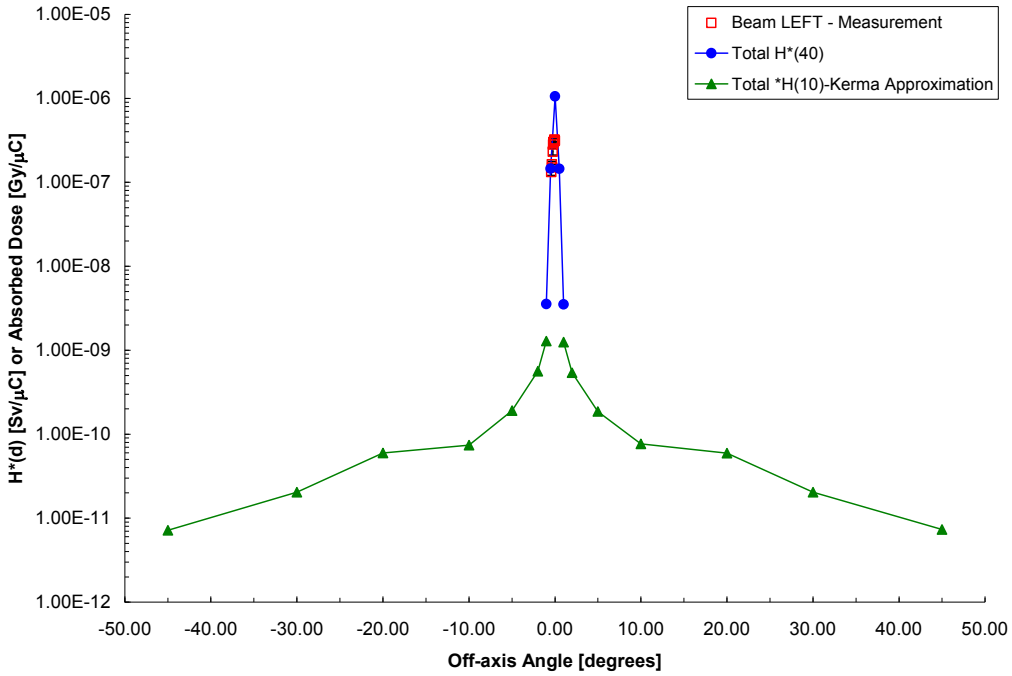

Figure 121. Experimental Downfield Absorbed Dose Measurements (made with RADCAL Model RC1800) Compared with the Calculated Total Ambient Dose Equivalent, H*(d) at 170 meters. (The error bars are smaller than the size of the symbols).

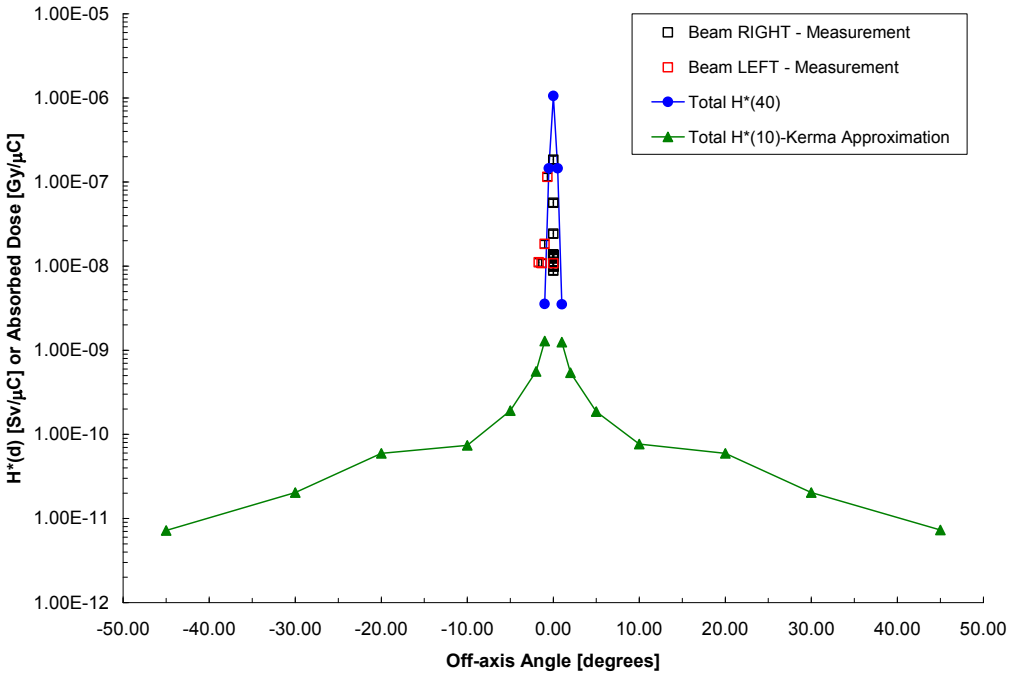

Figure 122. Experimental Downfield Absorbed Dose Measurements (made with Far West Model 1055 Chipmunk) Compared with the Calculated Total Ambient Dose Equivalent, H*(d) at 170 meters. (The error bars are smaller than the size of the symbols).

Overall, agreement to a first order was achieved between the measurements and calculations. The difference becomes less significant further downfield. At closer downfield distances, there is a larger disparity between the measured and calculated data. A few hypotheses exist for the differences in data sets. First, as reported in Chapter 5, the models of the system for downfield absorbed dose and system dose calculations did not include the entire facility and associated intricacies of the physical reality. The actual experimental facilities contain several specific characteristics (i.e. some walls, a roof awning, other structures) which have the potential to skew empirical results. These scattering sources provide additional error in measurement data. Unless these are added to the simulations with complete fidelity, there will potentially be a mismatch in measurement data versus computational data. This is a potentially large reason for a difference in data sets.

Second, errors exhibited at greater downfield distances could be attributed to the targeting of the prototype coupled with error in positioning. As discussed in Chapter 4, for some measurement sets the system was in a non-fixed position. At times, the ion chambers were moving relative the beam, therefore, potentially a major cause of error. It is unclear how to fully characterize this error without doing a series of measurements in both a fixed and non-fixed configuration and then use these data to perform a sensitivity analysis.

The third hypothesis is that a non-uniform field may exist within the beam. This means that at closer downfield distances the variation in a cross-sectional slice of the beam is

greater than at greater downfield distances. It seems that much of this effect can be attributed to the large amount of secondary radiations, especially electrons, which are generated as a result of the beam interacting in the air and the subsequent air-scatter contribution.

The fourth hypothesis is that the simulations exhibit an effect such that the gradient of the dose within the ion chamber is broadened as the distance increases. In other words, the dose is averaged over a larger space which leads to an overall lowering of the dose. This is seen in a comparison of point tally fluence data versus volume averaged fluence data. For a point detector tally, MCNP5 calculates the fluence at a very specific point in space. Depending on the geometry and orientation of the beam, small changes can lead to very large or very small differences in the calculated fluences, and thus doses. This is especially apparent when considering the dose over the volume with same dimensions as the ion chamber used in the measurements for the present work.

In order to test this hypothesis, an MCNP5 model was created to look at the effect of this change over small distances. In this calculation, 12 photon fluence point detector tallies were arrayed in a 3 x 4 matrix with the same dimensions as a RADCAL Model RC1800 ion chamber. The matrix was repeated three times in the model with one matrix on the beam centerline (Center Detector), one matrix off-axis to the right of the beam centerline (Right Detector) and one matrix off-axis to the left of the beam centerline (Left Detector). These matrices of point detectors were used to calculate the photon H*(10) at 10 meters and at 100 meters. The only difference in the two models was the downfield distance so

the same spacing in the matrix was kept at each downfield location. A summary of the locations used in the matrices is provided in Table 145.

Table 145. Summary of Detector Locations in Each Matrix.

Left Detector			Center Detector			Right Detector		
X [cm]	Y [cm]	Z [cm]	X [cm]	Y [cm]	Z [cm]	X [cm]	Y [cm]	Z [cm]
-27.6	-8.5	1000, 10000	-6.9	-8.5	1000, 10000	13.8	-8.5	1000, 10000
-27.6	-2.83	1000, 10000	-6.9	-2.83	1000, 10000	13.8	-2.83	1000, 10000
-27.6	2.83	1000, 10000	-6.9	2.83	1000, 10000	13.8	2.83	1000, 10000
-27.6	8.5	1000, 10000	-6.9	8.5	1000, 10000	13.8	8.5	1000, 10000
-20.7	8.5	1000, 10000	0	-8.5	1000, 10000	20.7	-8.5	1000, 10000
-20.7	-8.5	1000, 10000	0	-2.83	1000, 10000	20.7	-2.83	1000, 10000
-20.7	-2.83	1000, 10000	0	2.83	1000, 10000	20.7	2.83	1000, 10000
-20.7	2.83	1000, 10000	0	8.5	1000, 10000	20.7	8.5	1000, 10000
-13.8	-8.5	1000, 10000	6.9	-8.5	1000, 10000	27.6	-8.5	1000, 10000
-13.8	-2.83	1000, 10000	6.9	-2.83	1000, 10000	27.6	-2.83	1000, 10000
-13.8	2.83	1000, 10000	6.9	2.83	1000, 10000	27.6	2.83	1000, 10000
-13.8	8.5	1000, 10000	6.9	8.5	1000, 10000	27.6	8.5	1000, 10000

The results of the H*(10) calculations as well as the gradient in H*(10) from the beam centerline (away from the beam) at 10 meters and 100 meters are given in Table 146 and Table 147 and Table 148 and Table 149, respectively. These data were also plotted as contour plots to show the visual change in dose and are shown in Figure 123 through Figure 128. Note the steep variation in gradient at 10 meters versus 100 meters. All data are reported in units of Sv/μA.

There is a dramatic difference in the variation in the gradient at 10 meters versus 100 meters which supports the hypothesis that the gradient of the dose in the ion chamber is broadened over large downfield distances and off-axis angles. The extent to which this effect has on the measurements remains for future work. However, this effect should be

noted and taken into account in future system simulations where a sensitivity analysis can be performed to ascertain the overall effect on calculating dose equivalents.

Table 146. Summary of H*(10) in each Detector Location at 10 meters.

Left Detector			Center Detector			Right Detector		
X [cm]	Y [cm]	H*(10) [Sv/μC]	X [cm]	Y [cm]	H*(10) [Sv/μC]	X [cm]	Y [cm]	H*(10) [Sv/μC]
-27.6	-8.5	4.07E-08	-6.9	-8.5	2.90E-06	13.8	-8.5	1.06E-07
-27.6	-2.83	4.24E-08	-6.9	-2.83	6.62E-05	13.8	-2.83	2.79E-07
-27.6	2.83	4.21E-08	-6.9	2.83	6.60E-05	13.8	2.83	2.75E-07
-27.6	8.5	4.01E-08	-6.9	8.5	2.90E-06	13.8	8.5	1.05E-07
-20.7	8.5	5.40E-08	0	-8.5	3.61E-05	20.7	-8.5	5.18E-08
-20.7	-8.5	5.90E-08	0	-2.83	2.58E-04	20.7	-2.83	5.65E-08
-20.7	-2.83	5.83E-08	0	2.83	2.58E-04	20.7	2.83	5.67E-08
-20.7	2.83	5.23E-08	0	8.5	3.60E-05	20.7	8.5	5.18E-08
-13.8	-8.5	1.12E-07	6.9	-8.5	2.89E-06	27.6	-8.5	3.95E-08
-13.8	-2.83	2.75E-07	6.9	-2.83	6.61E-05	27.6	-2.83	4.09E-08
-13.8	2.83	2.75E-07	6.9	2.83	6.60E-05	27.6	2.83	4.06E-08
-13.8	8.5	1.06E-07	6.9	8.5	2.90E-06	27.6	8.5	3.90E-08

Table 147. Summary of Gradient in H*(10) from Beam Centerline at 10 meters.

Left Detector			Center Detector			Right Detector		
62.0%	50.6%	0.0%	92.0%	0.0%	91.9%	0.0%	50.9%	62.9%
84.7%	78.8%	0.0%	74.4%	0.0%	74.4%	0.0%	79.4%	85.2%
84.6%	78.6%	0.0%	74.4%	0.0%	74.4%	0.0%	79.8%	85.4%
63.5%	51.6%	0.0%	91.9%	0.0%	92.0%	0.0%	51.1%	62.7%

Table 148. Summary of H*(10) in each Detector Location at 100 meters.

Left Detector			Center Detector			Right Detector		
X [cm]	Y [cm]	H*(10) [Sv/μC]	X [cm]	Y [cm]	H*(10) [Sv/μC]	X [cm]	Y [cm]	H*(10) [Sv/μC]
-27.6	-8.5	1.66E-06	-6.9	-8.5	1.99E-06	13.8	-8.5	1.95E-06
-27.6	-2.83	1.69E-06	-6.9	-2.83	2.00E-06	13.8	-2.83	1.98E-06
-27.6	2.83	1.69E-06	-6.9	2.83	2.00E-06	13.8	2.83	1.98E-06
-27.6	8.5	1.66E-06	-6.9	8.5	1.99E-06	13.8	8.5	1.95E-06
-20.7	8.5	1.83E-06	0	-8.5	2.00E-06	20.7	-8.5	1.83E-06
-20.7	-8.5	1.86E-06	0	-2.83	2.00E-06	20.7	-2.83	1.87E-06
-20.7	-2.83	1.86E-06	0	2.83	2.00E-06	20.7	2.83	1.86E-06
-20.7	2.83	1.83E-06	0	8.5	2.00E-06	20.7	8.5	1.83E-06
-13.8	-8.5	1.96E-06	6.9	-8.5	1.99E-06	27.6	-8.5	1.66E-06
-13.8	-2.83	1.98E-06	6.9	-2.83	2.00E-06	27.6	-2.83	1.69E-06
-13.8	2.83	1.98E-06	6.9	2.83	2.00E-06	27.6	2.83	1.69E-06
-13.8	8.5	1.95E-06	6.9	8.5	1.99E-06	27.6	8.5	1.66E-06

Table 149. Summary of Gradient in H*(10) from Beam Centerline at 100 meters.

Left Detector			Center Detector			Right Detector		
14.8%	6.4%	0.0%	0.22%	0.0%	0.22%	0.0%	6.4%	14.9%
14.3%	5.7%	0.0%	0.29%	0.0%	0.27%	0.0%	5.7%	14.4%
14.4%	5.8%	0.0%	0.28%	0.0%	0.28%	0.0%	5.7%	14.4%
14.9%	6.5%	0.0%	0.21%	0.0%	0.21%	0.0%	6.2%	14.9%

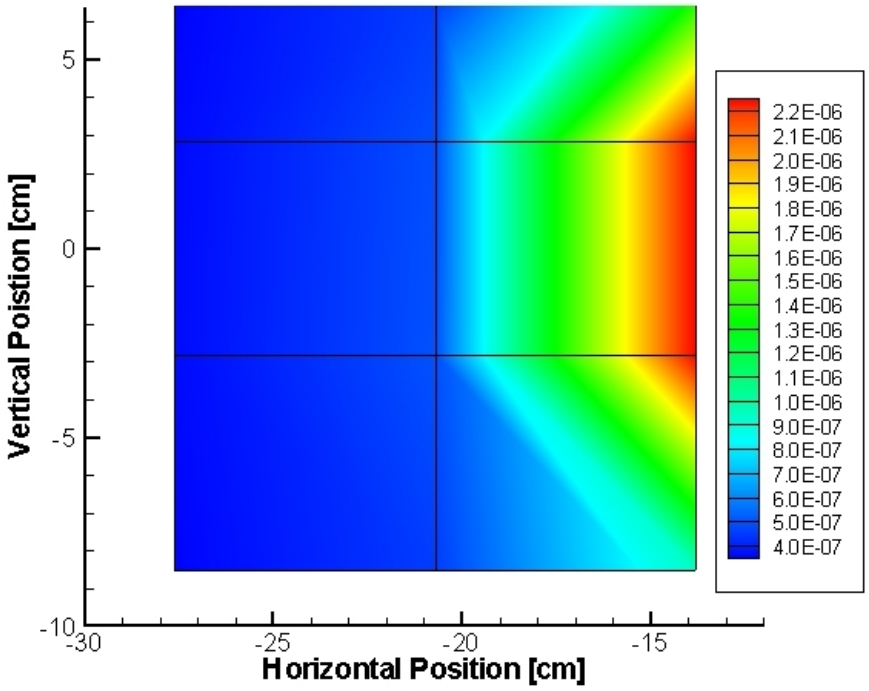

Figure 123. H*(10) Dose Gradient in Left Detector (left of beam centerline) at 10 meters.

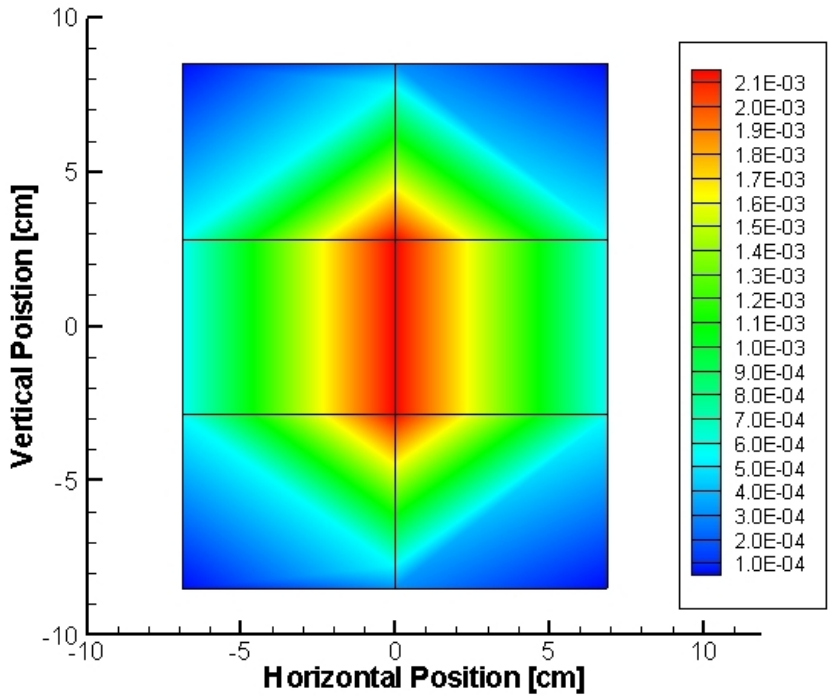

Figure 124. H*(10) Dose Gradient in Center Detector (beam centerline) at 10 meters.

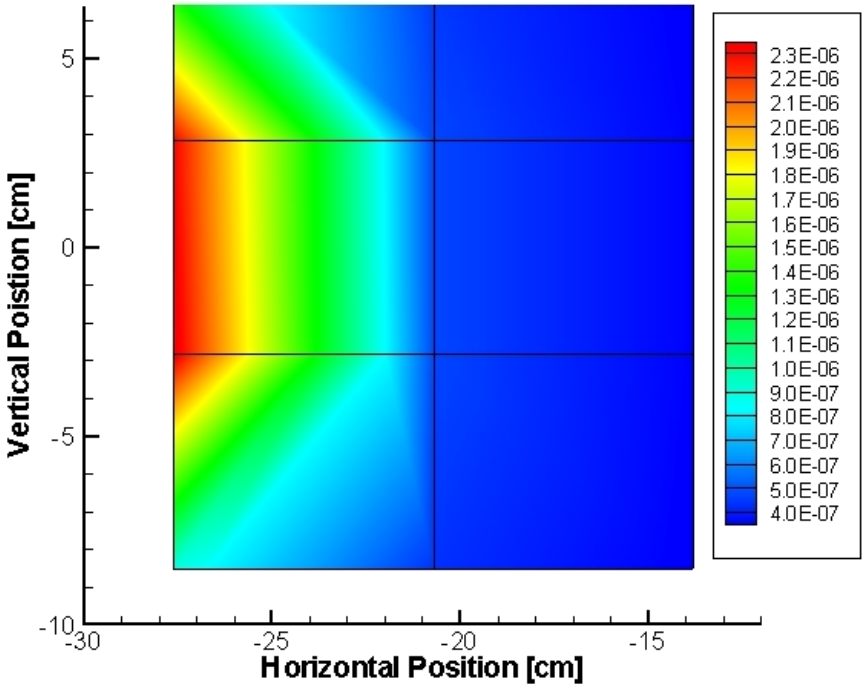

Figure 125. H*(10) Dose Gradient in Right Detector (right of beam centerline) at 10 meters.

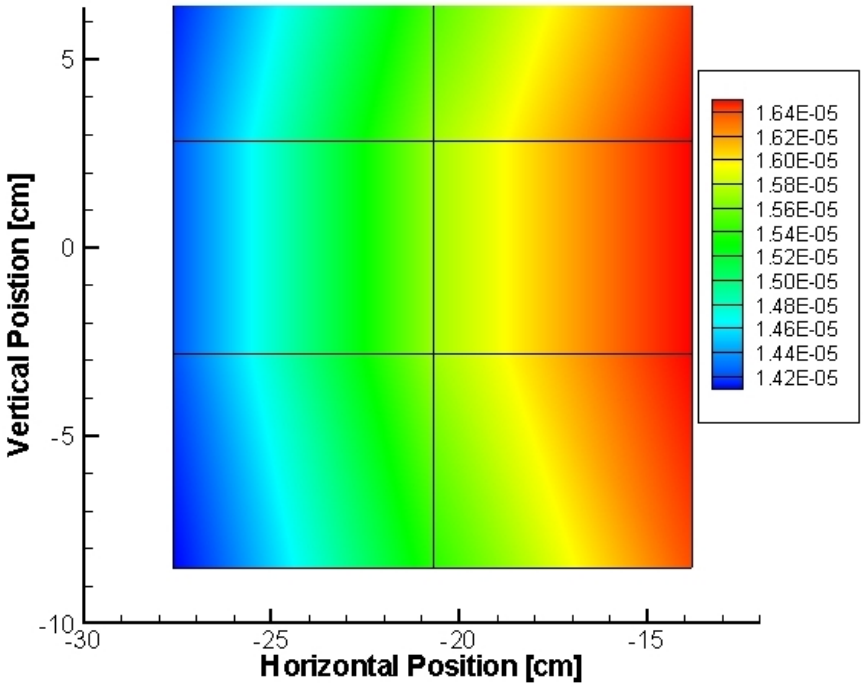

Figure 126. H*(10) Dose Gradient in Left Detector (left of beam centerline) at 100 meters.

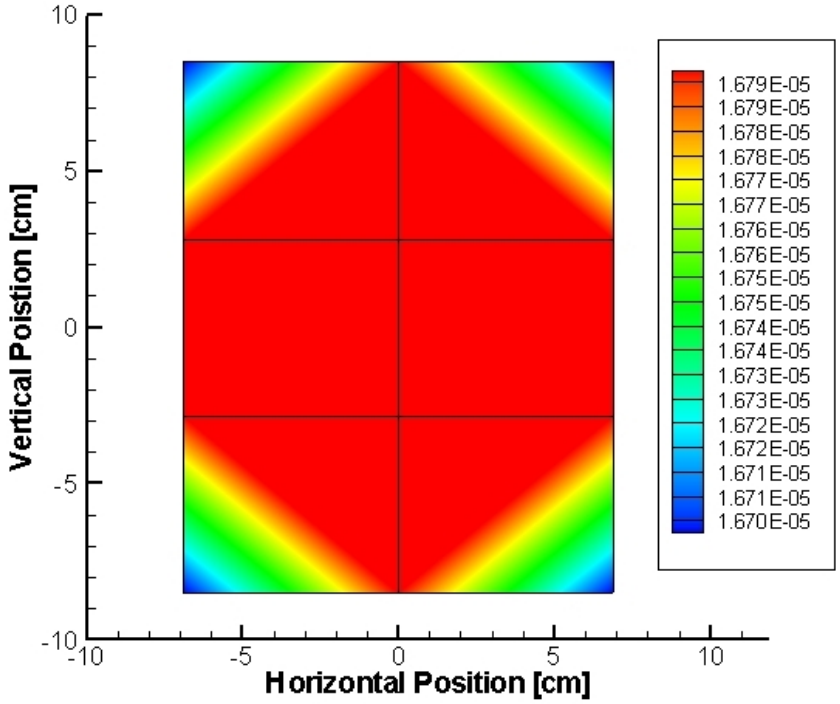

Figure 127. H*(10) Dose Gradient in Center Detector (beam centerline) at 100 meters.

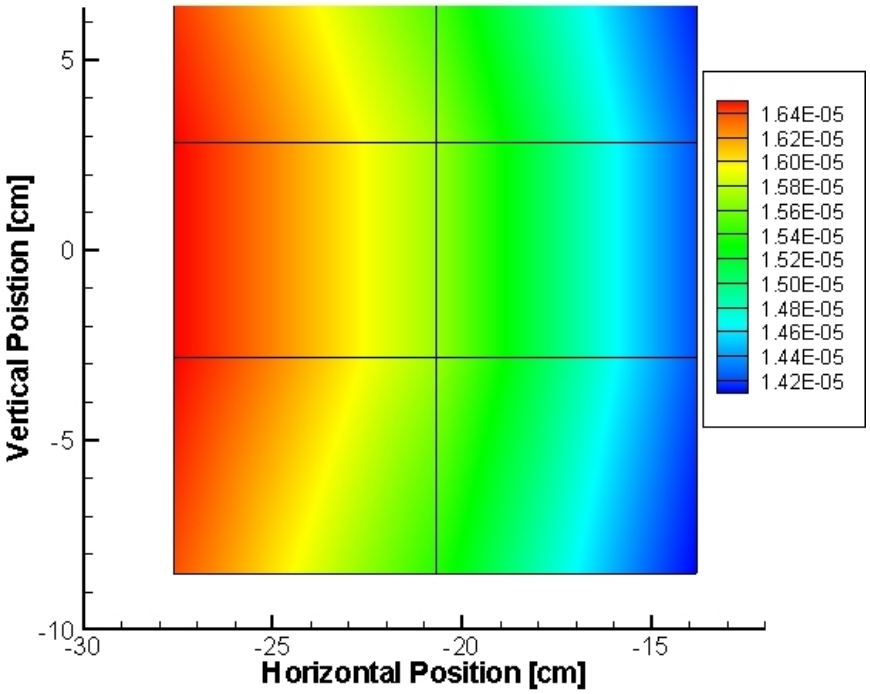

Figure 128. H*(10) Dose Gradient in Right Detector (right of beam centerline) at 100 meters.

Another hypothesis for the underestimate of the calculations versus the measurements is related to the influence of the interface between the air and the ion chamber. The key driver in this theory is the size of the ion chamber relative to the range of secondary electrons. The magnitude of the interface effects depend on the extent of the difference in the mass energy-absorption coefficients of the high-energy photons and in the mass stopping power of the electrons between the air and the ion chamber. Bragg-Gray cavity theory generally holds for dosimeters which are small compared to the range of the directly ionizing particles. A discontinuity exists when these ranges are much larger such as those seen in the present work. Gray evaluated the mass stopping power ratio for the situation in which the dimensions of the dosimeter were small compared with the electron range. Gray assumed that the electron spectrum set up in the medium was not modified

in crossing the dosimeter and that the number of electrons generated within the dosimeter itself was negligible. These assumptions limit the theory to very small dosimeters [83].

Following the work of Gray, the Spencer-Attix theory was introduced and then modified to account for the interface effects. Terms were added to the expression which accounted for the attenuation of the electrons entering the dosimeter from the medium and the build-up of electrons within the dosimeter. These two terms eliminated both of Gray's assumptions and led to the general theory of cavity ionization. Burlin proved experimentally that the general theory breaks down if the dimensions of an ion chamber are increased by an order of magnitude thus invoking the use of condensed state dosimeters (i.e. Fricke dosimeter, TLD, etc.) [83]. He does conclude that the general theory of cavity is applicable across all dosimeter sizes but variations do exist [83].

Since the size of the ion chambers employed in the present work is small in comparison to the very extensive measurement space, it is believed that these interface effects are present. The extent to which this effect has on the measurements was not fully developed and remains for future work. However, much of this work can be accomplished through simulations which should explore the spatial effects of the secondary electron ranges at various measurement locations. Then, through the employment of the various cavity ionization theories, a rigorous analysis can be completed.

Another hypothesis for the difference between measurement data and model data stems from the special dose driver calculations. The effective of slight changes to material

compositions and densities have a significant effect as discussed with the Pb density reduction study. The entire suite of models designed for the present work assumed textbook densities and material compositions for system components. It is possible that variations in these values and inhomogeneities can change the outcome of radiation transport computations and thus change calculated dosimetry quantities. It is therefore desirable that the sensitivity of these perturbations be explored.

A final observation from the data takes note of the high electron fluences calculated directly off the central axis of the primary beam. In the total effective dose and total ambient dose equivalent calculations, the electron dose is the dose driver at off-axis angles ranging from 0.50 to 2 degrees. It was not completely clear why this is the case so an additional calculation was performed to provide some insight as to why this phenomenon was observed. A simulation was performed to determine the electron fluence directly in front of the PITAS prototype.

In this model, a 0.5-cm thick disk slightly larger than the diameter of the collimator was placed 1 meter in front of the collimator at the central axis of the beam. The disk was used as a tally volume for electrons. The spectrum generated from this model is shown in Figure 129. The relative error of the calculation, 3.8%, is higher than most reported in the present work, but is reasonable for electron transport.

It is noteworthy that the electron fluence coming off the collimator (i.e. the electrons that are not absorbed in the converter or collimator material) is quite high. In fact, the flux-

weighted average electron energy is on the order of 5.5 MeV. The range of a 5.5 MeV electron in air is roughly 23 meters. Moreover, a calculation of the flux-weighted average ranges of the calculated electron spectra on the beam centerline (0 degrees) at downfield distances of 1 meter, 10 meters and 100 meters were roughly 32 meters, 30 meters and 28 meters, respectively. Therefore, it seems reasonable that such a large component of the total dose equivalent is contributed by electrons.

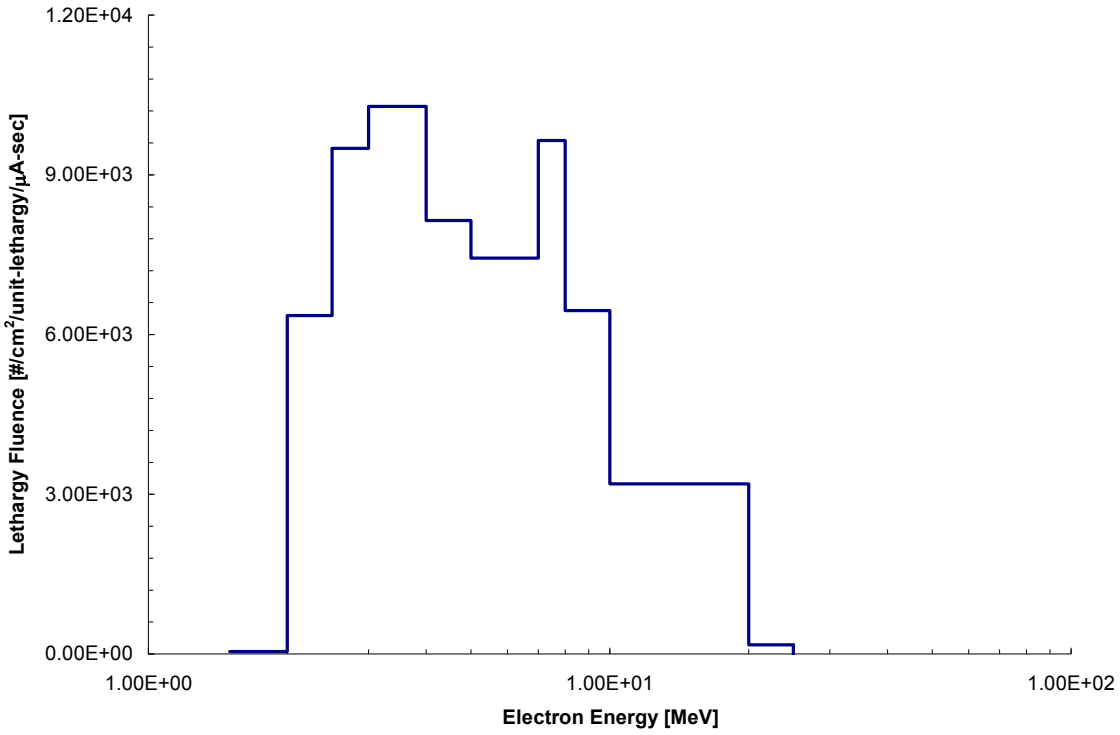

Figure 129. Electron Spectrum at Beam Centerline at a Downfield Distance of 1 meter.

CHAPTER 7

CONCLUSIONS AND RECOMMENDATIONS

An extensive effort was undertaken to computationally characterize and measure the spatial, temporal and energy emission of air-scattered photons, electrons and neutrons generated near a highly-collimated bremsstrahlung-based source in an outdoor environment. The objective was to determine the dose equivalents at both long standoff distances and in the vicinity of a prototype system.

This work yielded a set of fluence-to-ambient dose equivalent conversion coefficients for both photons and electrons through 25 MeV. Photon ambient dose equivalent conversion coefficients were calculated for depths of 10 mm, 15 mm, 20 mm, 30 mm, and 40 mm in the ICRU sphere. The H*(10) data compared well with published data [20]. The dose contribution below 1 MeV decreases with depth. However, above 3 MeV, the dose contribution increases quite steadily with depth and energy. Note that the H*(10) calculated using the kerma approximation greatly overestimates the dose above 3 MeV.

Electron ambient dose equivalent conversion coefficients were calculated for depths of 10 mm, 15 mm, 20 mm, 30 mm, and 40 mm in the ICRU sphere. The electron ambient dose equivalent dose conversion factors compared well with published data [38, 39]. The dose equivalent grows to a maximum at 4 MeV and then levels out since the stopping

power is then fairly constant with energy. The conversion coefficients for the 10 mm depth remain constant above about 8 MeV, a mean value of (312 ± 2.75) pSv-cm^2, and for the 15 mm depth above about 10 MeV a mean value of (315 ± 3.25) pSv-cm^2. The 20 mm and 30 mm cases are constant above about 20 MeV, a mean value on the order of (320 ± 3) pSv-cm^2. A comparison to Ferrari and Pelliccioni's data show good agreement [38]. Much like the data calculated for the present work, above about 8 MeV, the energy deposition is constant. Comparison to Roger's data show a less than 8% difference in dose equivalent between 3 MeV and 30 MeV [39].

An extensive set of system simulations was performed to model a prototype high-energy bremsstrahlung-based accelerator system to obtain photon, electron and neutron fluence spectra. These fluence data were folded with the calculated ambient dose equivalent conversion coefficients, air kerma factors as well as effective dose conversion coefficients. This yielded an entire data set of dose data for several downfield and off-axis distances.

A set of integral air-scatter measurements for accelerator-generated primary and secondary radiations (photon and neutron) were performed, in an outdoor environment, around the prototype system in order to provide a comparative data set from which to determine the total dose equivalent both in the beam (on-axis) and outside of the beam (off-axis). Measurements were performed at a variety of locations under multiple weather and terrain conditions. Overall, agreement to a first order was achieved between the measurements and calculations. The difference becomes less significant further

downfield. At closer downfield distances, there is a larger disparity between the measured and calculated data. Measurements to assess the beam energy of the prototype were performed and compare to within 13 – 20% of the predicted values.

A key task in this work was to develop a methodology to assess the radiation dose surrounding a high-energy bremsstrahlung-based accelerator system for national defense applications. This work provides a large library of data which can be used as a point of departure for future work. A fit of key data at each downfield distance and off-axis angle is presented in Appendix O. This fit provides a predictive metric for using the data presented herein. The use of a Monte Carlo radiation transport code (MCNP5) was critical to this work. A degree of confidence now exists that one can analytically predict the dose equivalents around a highly-collimated bremsstrahlung source using the methods outlined herein.

The following is a summary of key recommendations from the present work. First, the results of this work showed that the neutrons fluences at downfield distances were near background levels and can be considered insignificant. Therefore, the dose equivalent from neutrons is not a factor in the total dose equivalent from the PITAS prototype system. The neutron field measured during system measurements was such that adequately designed and engineered shielding could mitigate this field.

The second recommendation is that computed electron fluences within a few degrees of the centerline of the primary beam are higher than one would expect. These electron

fluences are a significant contribution to the total ambient dose equivalent at these off-axis locations. A substantial fraction of these electrons come directly from the system via leakage from the collimator assembly. From a radiation protection standpoint, this dose contribution can be mitigated by future study of the bremsstrahlung conversion process in the converter assembly and subsequent electron transport in the air.

The third recommendation is to use ensure that when using fluence-to-ambient dose equivalent conversion coefficients, the same depth in the ICRU sphere, where effective dose is bounding, should be utilized. As shown in the present work for the prototype studied, the H*(40) conversion coefficients should be employed when both electron and photon fluences can be computed. If computing electron fluence is not feasible, then it is appropriate to utilize the photon H*(10) (based on the kerma approximation) conversion coefficients to estimate the total ambient dose equivalent.

The fourth recommendation is that the dose equivalent received by a person standing downfield of the system while operating is not significant unless the person is standing directly in the primary beam. At a downfield distance of 25 meters at beam centerline (0 degrees), the total ambient dose equivalent received by a person after one (1) hour, assuming an average beam current of 8.4 μA, would be approximately 2.4 Sv (240 rem). If the same person was to move just 2 degrees off-axis, the total ambient dose equivalent received under the same operating conditions would be 4.2 $x10^{-3}$ Sv (0.42 rem). At 10 degrees off-axis, the total ambient dose equivalent received drops to 8.7 x 10^{-5} Sv (8.7 mrem).

Likewise, if the person were to move downfield of the system to 100 meters and stand at beam centerline (0 degrees) for one hour, assuming an average beam current of 8.4 μA, the total ambient dose equivalent would be approximately 0.11 Sv (11 rem). If the same person was to move just 2 degrees off-axis, the total ambient dose equivalent received under the same operating conditions would be 8.6 $x10^{-5}$ Sv (8.6 mrem). At 10 degrees off-axis, the total ambient dose equivalent received drops to 6.6 μSv (0.66 mrem). Overall, unless standing directly in the primary beam, the total ambient dose equivalent received by a person is not significant.

CHAPTER 8

FUTURE WORK

Several areas of future work exist both experimentally and computationally in order to improve this research. From an experimental standpoint, additional measurements should be performed to further confirm the beam energy measurements. Additional measurements should be performed using two additional attenuating materials. The present work involved using several sheets of lead, a high atomic number attenuator. The additional materials used should be a low atomic number material, such as aluminum and a medium atomic number material, such as copper. These additional measurement sets along with updating the models, should provide a higher fidelity answer to the question of beam energy.

The calculations showed that a large electron fluence is present downfield of the PITAS prototype. The reason for this fluence is unclear as most electrons should be stopped in the converter and collimator material. In order to confirm the calculated fluences and provide further insight, an electron measurement utilizing a magnet to determine the total electron leakage in front of the collimator, should be performed. This measurement should be performed at various downfield and off-axis distances to acquire the measured electron spectrum. These data should then be compared and reconciled with the

calculations to determine if the MCNP5 models and subsequent fluence calculations are correct

An additional question which should be explored is the issue surrounding the use of a build-up cap for in-beam or near-beam measurements at close downfield distances. Another measurement set using various thicknesses of tissue equivalent build-up materials should be employed to ensure that the correct build-up on the ion chamber wall is being considered. The challenge will be logistically as specially designed build-up caps would need to be fabricated. A comparative analysis of these data would lead to resolution in the concern over build-up near the beam at close downfield distances.

From a computational standpoint, several sets of simulations should be performed to answer some remaining questions. First, a more thorough model of the experimental facility used in measurement applications should be created. A major consideration in this is the tradeoff between the fidelity of modeling the physical reality and the ability of the Monte Carlo code to converge on a statistically significant answer in a manageable period of time. Some thought should go into the creation of these models and how to best capitalize on computing resources. One approach is to create a model which includes the facility and system to a high fidelity and use this model only to create a spatial and energy-dependent source term. The source term can then be used in more simplistic models to calculate the quantities of interest (i.e. particle fluence and energy deposition). This source term model may take a significant amount of time to create and run but the idea is then that subsequent models would be much easier to create and run.

The source definition used in all MCNP5 simulations was a 25 MeV monoenergetic electron beam. In reality, it is highly unlikely that the electron beam consistently at 25 MeV and thus not really monoenergetic. The dynamics of the beam parameters coupled with system oscillations and the cyclic nature of accelerators would lead one to believe that the beam probably exhibits some slight variations. In order to compensate for this in computations, a Gaussian electron energy distribution should be used. This would allow for slight variations in the beam and lead to a more realistic model of the physical system.

The model used in the present work assumed that the electron beam, which was modeled as a pencil beam, is directly inline with the collimator. This implies that the maximum amount of bremsstrahlung photons (i.e. a maximum of bremsstrahlung photons are created) always make it down the collimator. In reality, this may not be the case. The beam could drift or actually encompass a larger area then was sampled in the simulations. This could potentially change the solutions obtained in the computations. The physical cause of this could be the fact that in some cases, the beam is off center (i.e. it wanders or strays due to system perturbations) or the beam size may actually be larger than the "perfect" pencil beam used in the simulations. Therefore, a set of calculations should be performed to determine the effect of perturbations in beam size and alignment on dose calculations. A simulation plan would have to be developed in order to ensure that the best perturbation conditions are selected as this could lead to numerous models and excessive study, which may not be warranted.

The correctness and reliability of the calculated ambient dose equivalent conversion coefficients is highly certain. This is due to the large amount of published data which provide a basis for comparison. However, the calculation of fluence (photon, electron and neutron) is less certain since a comparative data set was not available. Therefore, one recommended approach is to utilize a different radiation transport code, such as the EGSnrc code [86] to confirm electron fluence calculations. In this approach, a benchmark exercise could be performed using the electron fluence data reported in the present work along with data calculated with the EGSnrc code compared to the measured electron fluences (from the measurement previously recommended). This research is prudent as it would provide a great deal of insight and a path for follow-on study.

A computational assessment of the large electron fluences observed slightly off-axis should be performed. This assessment should include a variation in the physics models used in MCNP5 and other codes (i.e. EGSnrc) [86] in order to assess their effect on calculated electron fluences. In addition, different cross section sets should be utilized to determine the best approach to the problem. Overall, these additional simulations should provide insight as to why electrons tended to drive the dose at 0.5 to 2 degrees off-axis.

Since the dose gradient in the volume of the ion chamber was so dramatic at various downfield distances and locations, a computational assessment of the effect of this dose gradient should be performed. One approach is to use additional point detectors in the fluence calculations. In the present work, only one detector at each off-axis distance was used. The effect of using only one detector was reported in Chapter 6. Additional point

detectors should be employed and the data averaged to acquire a better estimate of the associated particle fluences in the ion chamber. The number of detectors would be driven by the cross-sectional volume of the ion chamber "seen" by the photon beam at the various locations. This study would be very advantageous as it would provide insight as to the effect of the large dose gradients calculated downfield.

In order to consistently calculate the total ambient dose equivalent, a set of neutron fluence-to-ambient dose equivalent conversion coefficients at additional depths in the ICRU sphere (i.e. 15 mm, 20 mm, 30 mm, and 40 mm) should be computed. These calculations should be executed both with and without the kerma approximation. This will provide an entire set of conversion coefficients which can then be used under all conditions for calculation of the ambient dose equivalent.

APPENDIX A

GLOSSARY OF TERMS AND DEFINITIONS OF QUANTITIES

Absorbed Dose

The absorbed dose, D, is defined as the quotient of the mean energy imparted by ionizing radiation to matter in a specified volume element and the mass of the matter in the volume.

$$D = \frac{d\bar{\varepsilon}}{dm} \tag{A.1}$$

The unit for absorbed dose is the gray (Gy), which is equal to one joule per kilogram.

Ambient Dose Equivalent

The ambient dose equivalent, *H*(d),* at a point in a radiation field is the dose equivalent that would be produced by the corresponding expanded and aligned field in the ICRU sphere at a depth, *d*, on the radius opposing the direction of the aligned field. The recommended value of d is 10 mm for penetrating radiation and 0.07 mm for low penetrating radiation.

The unit of ambient dose equivalent is sievert (Sv) which is equal to one joule per kilogram [24].

Directional Dose Equivalent

Directional dose equivalent, *H'(d)*, at a point in a radiation field is the dose equivalent that would be produced by the corresponding field in the ICRU sphere at depth, *d*, on a radius in a specified direction, Ω. The recommended value of d is 10 mm for penetrating radiation and 0.07 mm for low-penetrating radiation.

The unit of directional dose equivalent is sievert (Sv) which is equal to one joule per kilogram [24].

Dose Equivalent

The dose equivalent, H, at a point is given by

$$H = \int Q(L) \frac{dD}{dL} dL \tag{A.2}$$

where *Q(L)* is the quality factor for particles with linear energy transfer, *L*, and *dD/dL* is absorbed dose between linear energy transfer, *L*, and *L* + *dL* at the point.

The unit for dose equivalent is the sievert (Sv), which is equal to one joule per kilogram [27].

Effective Dose

The effective dose, *E*, is the summation of the equivalent doses in tissues or organs, H_T, each multiplied by the appropriate tissue weighting factor, w_T

$$E = \sum_T w_T \, H_T \tag{A.3}$$

The unit for effective dose is the sievert (Sv), which is equal to one joule per kilogram [77].

Energy Imparted

The energy imparted, ε, by ionizing radiation to matter in a volume, is

$$\varepsilon = R_{in} - R_{out} + \sum Q \tag{A.4}$$

where R_{in} is the radiant energy incident on the volume, i.e., the sum of the energies (excluding rest energies) of all those charged and uncharged ionizing particles which enter the volume, R_{out} is the radiant energy emerging from the volume, i.e., the sum of the energies (excluding rest energies) of all those charged and uncharged ionizing particles which leave the volume, and ΣQ is the sum of all charges of the rest mass energy of nuclei and elementary particles in any interactions which occur in the volume. The expectation value of energy imparted is termed the mean energy imparted, ε.

The units for energy imparted are joules [6].

Expanded and Aligned Field

An expanded radiation field is defined as a hypothetical field where the fluence and its angular and energy distributions have the same value throughout the volume of interest as that in the actual field at the point of reference. An expanded and aligned field is a hypothetical field where the flounce and its energy distribution are the same as an expanded field, but the fluence is unidirectional [20].

Fluence

The fluence, Φ, is the quotient of dN by da, where dN is the number of particles incident on a sphere of cross-sectional area da, thus

$$\Phi = \frac{dN}{da} \tag{A.7}$$

The units for fluence are number of particles per square meter.

ICRU Sphere

The ICRU sphere [35] is a 30-cm diameter tissue-equivalent sphere with a density of 1 g/cm^3 and a mass composition of 76.2% oxygen, 11.1% carbon, 10.1% hydrogen and 2.6% nitrogen.

Kerma

Kerma is the quotient of dE_{tr} by dm, where dE_{tr} is the sum of the initial kinetic energies of all charged ionizing particles liberated by uncharged ionizing particles in a volume element of mass, dm,

$$K = \frac{dE_{tr}}{dm} \tag{A.8}$$

The unit of kerma is the gray (Gy), which is equal to one joule per kilogram [6].

Linear Energy Transfer (LET)

The linear energy transfer or linear collision stopping power [6], L, of a material, for a charged particle is the quotient of dE by dl, where dE is the mean energy lost by the particle due to collisions with electrons, in travesrsing a distance, dl,

$$L = \frac{dE}{dl} \tag{A.9}$$

Linear Stopping Power

The linear stopping power [6] is the energy loss of a charged particle per unit distance in a medium. The linear stopping power, S, is equal to the sum of the collisional stopping power, S_{col} and the radiative stopping power, S_{rad}

$$S = \left(\frac{dE}{dl}\right)_{col} + \left(\frac{dE}{dl}\right)_{rad} \tag{A.10}$$

Quality Factor

The quality factor is a function, Q, of unrestricted linear energy transfer, L, in water. The quality factor is used in operational quantities to weigh the absorbed dose for biological effectiveness of the radiation type producing it. Unlike the radiation weighting factors used for protection quantities, the quality factor is applied to the absorbed dose from charged particles at the point of interaction. It is obtained by assuming that the stopping power of the charged particle in water is numerically equal to L in the appropriate $Q(L)$-L relationship as specified by the ICRP [77].

Radiation Weighting Factor

Radiation weighting factors are used to reflect the higher relative biological effectiveness (RBE) of high LET particles such as neutrons, protons, and alphas. The radiation weighting factor, w_R, related to RBE and only indirectly related to L, the linear energy transfer in water. The radiation weighting factor is determined by the radiation incident on the body and is applied to the mean absorbed dose over the organ or tissue of interest [77].

Tissue Weighting Factor

Tissue weighting factors are defined by the ICRP to account for the relative stochastic detriment resulting from exposure of different tissues and organs to ionizing radiation [77].

APPENDIX B

TEST FOR DATA POINT OUTLIERS

Measured data taken over multiple repeated runs, were analyzed to determine if an individual data point was an outlier. To determine outliers, Grubb's Test was applied to the data. Grubb's test is simply a calculation to find the critical value Z such that

$$Z = \frac{|mean - n_i|}{\sigma} \tag{B.1}$$

where n is the i^{th} data point within the data set and σ is the standard deviation of the set of n. The outlier test checks to determine if the critical value is greater than the P value. If the critical value is greater than P, then that data point is an outlier. If the critical value is less than P, then the data point is not an outlier. P is approximated by

$$P = \sqrt{\frac{N(N-2)Z^2}{(N-1)^2 - NZ^2}} \tag{B.2}$$

where N is the number of values in the sample set and Z is the calculated using (B.1) for the suspected outlier. A set of tabulated P values exists and are given in Table B-1.

Table B-1. Critical Z Values for Grubbs Test.

N	Critical Z
3	1.15
4	1.48
5	1.71
6	1.89
7	2.02
8	2.13
9	2.21
10	2.29

Further information concerning Grubb's Test is found in Igelwicz and Hoaglin [84].

APPENDIX C

ESTIMATION AND PROPAGATION OF ERRORS

C.1 General Formalism

The standard convention for reporting the error associated with measurements was utilized in the present work. Every attempt was made to report measured values along with their inherent absolute uncertainty of the form

$$(x \pm \delta x) \tag{C.1}$$

where x is the measured value in the appropriate units and δx is the absolute uncertainty in the measurement of x in the same appropriate units. It follows that the relative uncertainty (or the precision) of the measurement will be

$$\frac{\delta x}{|x|} \tag{C.2}$$

and is a dimensionless quantity. In the present work, measurements will be reported using the above standard notation with all experimental uncertainties reported to one significant figure.

The measurements reported contain two distinct steps to obtaining a viable solution. First, one or more quantities are measured directly (i.e. ionization charge or temperature) and secondly, using these values, a quantity of interest is calculated (i.e. absorbed dose). In the same respect, the estimation of the error associated with the final calculated quantity follows two steps. First, an estimation of the uncertainties in the directly measured quantities is made and second these uncertainties are propagated through the calculations to determine an uncertainty in the final solution. Throughout the present

work, various direct quantities $x,\ldots,w$ with uncertainties $\delta x,\ldots, \delta w$ are used to calculate specific quantities q. The uncertainties in $x,\ldots,w$ propagate through the calculation to cause an uncertainty in q. The evaluation of the propagation of errors follows certain rules depending on the arithmetic process being utilized in the final calculation as given by Taylor [85].

For sums and differences, if the calculation is of the order

$$q = x + \ldots + z - (u + \ldots + w) \tag{C.3}$$

then the propagation of errors is (provided all errors are independent and random),

$$\delta q = \sqrt{(\delta x)^2 + \ldots + (\delta z)^2 + (\delta u)^2 + \ldots + (\delta w)^2} \ . \tag{C.4}$$

For products and quotients, if the calculation is of the order

$$q = \frac{x \times \ldots \times z}{u \times \ldots \times w} \tag{C.5}$$

then the propagation of errors is (provided all errors are independent and random),

$$\frac{\delta q}{|q|} = \sqrt{\left(\frac{\delta x}{x}\right)^2 + \cdots + \left(\frac{\delta z}{z}\right)^2 + \left(\frac{\delta u}{u}\right)^2 + \cdots + \left(\frac{\delta w}{w}\right)^2} \ . \tag{C.6}$$

For a function of one variable, if the calculation is of the order

$$q = q(x) \tag{C.7}$$

then the propagation of errors is,

$$\delta q = \left|\frac{dq}{dx}\right| \delta x \ . \tag{C.8}$$

In general, if the calculation is of the order

$$q = q(x, \ldots, z) \tag{C.9}$$

(any function of x,…z,) then the propagation of errors is (provided all errors are independent and random),

$$\delta q = \sqrt{\left(\frac{\partial q}{\partial x}\delta x\right)^2 + \cdots + \left(\frac{\partial q}{\partial z}\delta z\right)^2}\,. \tag{C.10}$$

C.2 Absolute Uncertainty Data

Estimation of the relative uncertainty of all measurements relied on an established value for the absolute uncertainty. When possible, these data were obtained from manufacturer's documentation or from calibration data. Absolute uncertainty data used in arriving at relative uncertainties are shown in Table C-1.

Table C-1. Absolute Uncertainty Data and Sources.

Measured Quantity	**Instrument Used**	**Absolute Uncertainty**	**Source**
Temperature	Omega iBTX Probe	0.8 °C	iBTX User's Guide [54]
Temperature	Keithley Model 6517 Type-K Thermocouple	0.3% Rdg °C	Keithley Model 6517 Manual [53]
Barometric Pressure	Omega iBTX Probe	1.50 mm Hg	iBTX User's Guide [54]
Relative Humidity	Keithley Model 6517 Relative Humidity Probe	0.3% Rdg %RH	Keithley Model 6517 Manual [53]
Ionization Charge	Keithley Model 6517 Electrometer	0.3% Rdg C	Keithley Model 6517 Manual [53]
Downfield Distance	Tape Measure Laser Range Finder	30.48 cm	Experimental Assumption
Off-axis Distance	Tape Measure	1.27 cm	Experimental Assumption
Instrument Height	Tape Measure	1.27 cm	Experimental Assumption
Ionization	RADCAL Model RC1800	8.00E2 Gy/C	RADCAL Calibration
Ionization	Far West Model 1055	2.40E4 R/C	Far West Calibration

APPENIDIX D

NEUTRON MEASUREMENT BSS DATA

PITAS --- Neutron Measurements --- Location A
Start: Maxwellian (T=1.4 MeV)

RESPONSE MATRIX	UNFOLD CODE	MAXWELL TEMP,SHAPE	CALIB. FACTOR	SMOOTH FACTOR	PER CENT ERROR	NO. OF ITERATIONS
UTA4	SPUN	.70, .80	1.0000	.0000	2.0653	1000

DETECTORS	MEASURED COUNTS	CALCULATED COUNTS	PERCENT DIFFERENCE
bare	916541.000	913049.300	-.381
2 inch	1814894.000	1849469.000	1.905
3 inch	3277316.000	3170305.000	-3.265
5 inch	4526937.000	4660319.000	2.946
8 inch	3649250.000	3630768.000	-.506
10 inch	2535359.000	2481719.000	-2.116
12 inch	1558882.000	1580970.000	1.417

TOTAL FLUENCE= 2.875E+07 NEUTRONS/CM2
AVE ENERGY(LESS TH)= 1.082E+00 MEV
DOSE= 5.461E-02 RAD
DOSE EQUIVALENT= 4.574E-01 REM
QUALITY FACTOR= 8.376 REM/RAD
NRL TLD RESPONSE= 3.929 REM/REM(CF-252)
"HANKINS"TLD RESPONSE= 4.921 REM/REM(CF-252)
NEUTRAK RESPONSE= .854 REM/REM(CF-252)
NTA RESPONSE= .852 REM/REM(CF-252)
ANPDR-70 RESPONSE= 1.034 REM/REM(CF-252)

BIN NO.	ENERGY MAX (MEV)	FLUENCE NEUT/CM2	FLUENCE N/CM2/LETH	DOSE (RAD)	DOSE EQV. (REM)	DOSE EQV. (% OF TOTAL)
1	4.140E-07	5.339E+06	3.302E+06	2.808E-03	6.145E-03	1.343E+00
2	6.826E-07	9.665E+04	4.451E+05	5.884E-05	1.191E-04	2.603E-02
3	1.445E-06	1.526E+05	4.684E+05	9.420E-05	1.913E-04	4.182E-02
4	3.059E-06	1.743E+05	5.352E+05	1.069E-04	2.169E-04	4.741E-02
5	6.476E-06	2.105E+05	6.464E+05	1.278E-04	2.583E-04	5.647E-02
6	1.371E-05	2.641E+05	8.108E+05	1.587E-04	3.198E-04	6.992E-02
7	2.902E-05	3.378E+05	1.037E+06	2.017E-04	4.037E-04	8.825E-02
8	6.144E-05	4.328E+05	1.329E+06	2.570E-04	5.103E-04	1.116E-01
9	1.301E-04	5.431E+05	1.667E+06	3.200E-04	6.306E-04	1.378E-01
10	2.754E-04	6.557E+05	2.013E+06	3.736E-04	7.364E-04	1.610E-01
11	5.929E-04	7.874E+05	2.364E+06	4.303E-04	8.504E-04	1.859E-01
12	1.234E-03	8.322E+05	2.614E+06	4.370E-04	8.655E-04	1.892E-01
13	2.613E-03	9.031E+05	2.772E+06	4.650E-04	9.211E-04	2.014E-01
14	5.531E-03	9.245E+05	2.839E+06	4.699E-04	9.319E-04	2.037E-01
15	1.171E-02	9.042E+05	2.776E+06	4.556E-04	9.124E-04	1.995E-01
16	2.479E-02	8.579E+05	2.634E+06	4.829E-04	1.299E-03	2.839E-01
17	5.247E-02	7.919E+05	2.432E+06	5.258E-04	2.128E-03	4.652E-01
18	1.111E-01	7.317E+05	2.246E+06	5.742E-04	3.494E-03	7.638E-01
19	2.237E-01	7.202E+05	2.370E+06	7.476E-04	5.977E-03	1.307E+00
20	4.508E-01	1.077E+06	3.539E+06	1.566E-03	1.525E-02	3.334E+00
21	9.072E-01	2.697E+06	8.880E+06	6.052E-03	6.449E-02	1.410E+01
22	1.872E+00	4.582E+06	1.456E+07	1.561E-02	1.606E-01	3.512E+01
23	3.679E+00	3.350E+06	1.142E+07	1.414E-02	1.338E-01	2.925E+01
24	7.408E+00	1.196E+06	3.935E+06	6.911E-03	4.870E-02	1.065E+01
25	1.492E+01	1.748E+05	5.747E+05	1.157E-03	7.184E-03	1.571E+00
26	2.581E+01	1.008E+04	4.236E+04	9.171E-05	4.391E-04	9.600E-02

PITAS --- Neutron Measurements --- Location A
Start: NBS Cf-252

RESPONSE MATRIX	UNFOLD CODE	MAXWELL TEMP,SHAPE	CALIB. FACTOR	SMOOTH FACTOR	PER CENT ERROR	NO. OF ITERATIONS
UTA4	SPUN	.00, .80	1.0000	.0000	2.3721	1000

DETECTORS	MEASURED COUNTS	CALCULATED COUNTS	PERCENT DIFFERENCE
bare	916541.000	912669.700	-.422
2 inch	1814894.000	1854183.000	2.165
3 inch	3277316.000	3155188.000	-3.726
5 inch	4526937.000	4679190.000	3.363
8 inch	3649250.000	3626357.000	-.627
10 inch	2535359.000	2473106.000	-2.455
12 inch	1558882.000	1585437.000	1.703

TOTAL FLUENCE= 2.871E+07 NEUTRONS/CM2
AVE ENERGY(LESS TH)= 1.081E+00 MEV
DOSE= 5.466E-02 RAD
DOSE EQUIVALENT= 4.558E-01 REM
QUALITY FACTOR= 8.339 REM/RAD
NRL TLD RESPONSE= 3.845 REM/REM(CF-252)
"HANKINS"TLD RESPONSE= 5.211 REM/REM(CF-252)
NEUTRAK RESPONSE= .906 REM/REM(CF-252)
NTA RESPONSE= .864 REM/REM(CF-252)
ANPDR-70 RESPONSE= 1.033 REM/REM(CF-252)

BIN NO.	ENERGY MAX (MEV)	FLUENCE NEUT/CM2	FLUENCE N/CM2/LETH	DOSE (RAD)	DOSE EQV. (REM)	DOSE EQV. (% OF TOTAL)
1	4.140E-07	5.120E+06	3.166E+06	2.693E-03	5.893E-03	1.293E+00
2	6.826E-07	6.656E+04	3.065E+05	4.052E-05	8.200E-05	1.799E-02
3	1.445E-06	2.108E+05	6.472E+05	1.302E-04	2.643E-04	5.800E-02
4	3.059E-06	2.924E+05	8.977E+05	1.794E-04	3.637E-04	7.980E-02
5	6.476E-06	3.804E+05	1.168E+06	2.309E-04	4.668E-04	1.024E-01
6	1.371E-05	4.550E+05	1.397E+06	2.734E-04	5.510E-04	1.209E-01
7	2.902E-05	5.024E+05	1.543E+06	2.999E-04	6.003E-04	1.317E-01
8	6.144E-05	5.295E+05	1.626E+06	3.144E-04	6.243E-04	1.370E-01
9	1.301E-04	5.443E+05	1.670E+06	3.207E-04	6.319E-04	1.386E-01
10	2.754E-04	5.408E+05	1.660E+06	3.081E-04	6.073E-04	1.332E-01
11	5.929E-04	5.715E+05	1.716E+06	3.123E-04	6.172E-04	1.354E-01
12	1.234E-03	5.366E+05	1.686E+06	2.818E-04	5.581E-04	1.224E-01
13	2.613E-03	5.904E+05	1.812E+06	3.040E-04	6.022E-04	1.321E-01
14	5.531E-03	6.489E+05	1.992E+06	3.298E-04	6.541E-04	1.435E-01
15	1.171E-02	7.249E+04	2.225E+05	3.653E-05	7.314E-05	1.605E-02
16	2.479E-02	8.150E+05	2.502E+06	4.587E-04	1.234E-03	2.707E-01
17	5.247E-02	8.697E+05	2.671E+06	5.774E-04	2.337E-03	5.127E-01
18	1.111E-01	8.996E+05	2.761E+06	7.059E-04	4.296E-03	9.425E-01
19	2.237E-01	1.557E+06	5.124E+06	1.617E-03	1.293E-02	2.836E+00
20	4.508E-01	3.030E+06	9.958E+06	4.406E-03	4.291E-02	9.414E+00
21	9.072E-01	1.376E+06	4.531E+06	3.088E-03	3.290E-02	7.219E+00
22	1.872E+00	3.668E+06	1.166E+07	1.249E-02	1.286E-01	2.822E+01
23	3.679E+00	3.962E+06	1.350E+07	1.672E-02	1.583E-01	3.473E+01
24	7.408E+00	1.380E+06	4.540E+06	7.973E-03	5.619E-02	1.233E+01
25	1.492E+01	8.449E+04	2.779E+05	5.595E-04	3.474E-03	7.621E-01
26	2.581E+01	3.097E+02	1.301E+03	2.817E-06	1.349E-05	2.959E-03

PITAS --- Neutron Measurements --- Location A
Start: Cf-252 Room Return

RESPONSE MATRIX	UNFOLD CODE	MAXWELL TEMP,SHAPE	CALIB. FACTOR	SMOOTH FACTOR	PER CENT ERROR	NO. OF ITERATIONS
UTA4	SPUN	.00, .80	1.0000	.0000	1.8821	1000

DETECTORS	MEASURED COUNTS	CALCULATED COUNTS	PERCENT DIFFERENCE
bare	916541.000	913151.500	-.370
2 inch	1814894.000	1847502.000	1.797
3 inch	3277316.000	3178825.000	-3.005
5 inch	4526937.000	4647445.000	2.662
8 inch	3649250.000	3629757.000	-.534
10 inch	2535359.000	2488807.000	-1.836
12 inch	1558882.000	1578939.000	1.287

TOTAL FLUENCE= 2.865E+07 NEUTRONS/CM2
AVE ENERGY(LESS TH)= 9.646E-01 MEV
DOSE= 5.297E-02 RAD
DOSE EQUIVALENT= 4.528E-01 REM
QUALITY FACTOR= 8.548 REM/RAD
NRL TLD RESPONSE= 4.002 REM/REM(CF-252)
"HANKINS"TLD RESPONSE= 4.858 REM/REM(CF-252)
NEUTRAK RESPONSE= .842 REM/REM(CF-252)
NTA RESPONSE= .825 REM/REM(CF-252)
ANPDR-70 RESPONSE= 1.082 REM/REM(CF-252)

BIN NO.	ENERGY MAX (MEV)	FLUENCE NEUT/CM2	FLUENCE N/CM2/LETH	DOSE (RAD)	DOSE EQV. (REM)	DOSE EQV. (% OF TOTAL)
1	4.140E-07	5.459E+06	3.376E+06	2.872E-03	6.284E-03	1.388E+00
2	6.826E-07	3.909E+04	1.800E+05	2.380E-05	4.815E-05	1.064E-02
3	1.445E-06	1.013E+05	3.111E+05	6.258E-05	1.271E-04	2.807E-02
4	3.059E-06	1.283E+05	3.940E+05	7.873E-05	1.596E-04	3.526E-02
5	6.476E-06	1.610E+05	4.943E+05	9.772E-05	1.975E-04	4.363E-02
6	1.371E-05	2.145E+05	6.586E+05	1.289E-04	2.598E-04	5.737E-02
7	2.902E-05	2.885E+05	8.859E+05	1.722E-04	3.447E-04	7.614E-02
8	6.144E-05	4.789E+05	1.470E+06	2.843E-04	5.647E-04	1.247E-01
9	1.301E-04	5.993E+05	1.839E+06	3.531E-04	6.957E-04	1.537E-01
10	2.754E-04	7.117E+05	2.185E+06	4.055E-04	7.992E-04	1.765E-01
11	5.929E-04	8.617E+05	2.588E+06	4.709E-04	9.307E-04	2.055E-01
12	1.234E-03	8.514E+05	2.674E+06	4.470E-04	8.854E-04	1.956E-01
13	2.613E-03	9.185E+05	2.819E+06	4.729E-04	9.369E-04	2.069E-01
14	5.531E-03	1.045E+06	3.208E+06	5.310E-04	1.053E-03	2.325E-01
15	1.171E-02	1.041E+06	3.197E+06	5.248E-04	1.051E-03	2.321E-01
16	2.479E-02	9.305E+05	2.857E+06	5.238E-04	1.409E-03	3.112E-01
17	5.247E-02	7.832E+05	2.405E+06	5.200E-04	2.104E-03	4.648E-01
18	1.111E-01	6.132E+05	1.882E+06	4.812E-04	2.928E-03	6.467E-01
19	2.237E-01	8.844E+05	2.910E+06	9.180E-04	7.339E-03	1.621E+00
20	4.508E-01	8.798E+05	2.891E+06	1.279E-03	1.246E-02	2.751E+00
21	9.072E-01	1.945E+06	6.405E+06	4.365E-03	4.651E-02	1.027E+01
22	1.872E+00	4.651E+06	1.478E+07	1.584E-02	1.631E-01	3.601E+01
23	3.679E+00	4.581E+06	1.561E+07	1.933E-02	1.830E-01	4.042E+01
24	7.408E+00	4.819E+05	1.585E+06	2.784E-03	1.962E-02	4.334E+00
25	1.492E+01	1.047E+02	3.444E+02	6.935E-07	4.305E-06	9.509E-04
26	2.581E+01	7.631E-01	3.206E+00	6.942E-09	3.324E-08	7.342E-06

PITAS --- Neutron Measurements --- Location A
Start: Equal Lethargy

RESPONSE MATRIX	UNFOLD CODE	MAXWELL TEMP,SHAPE	CALIB. FACTOR	SMOOTH FACTOR	PER CENT ERROR	NO. OF ITERATIONS
UTA4	SPUN	.00, .80	1.0000	.0000	2.4086	1000

DETECTORS	MEASURED COUNTS	CALCULATED COUNTS	PERCENT DIFFERENCE
bare	916541.000	912737.300	-.415
2 inch	1814894.000	1853875.000	2.148
3 inch	3277316.000	3153875.000	-3.767
5 inch	4526937.000	4683311.000	3.454
8 inch	3649250.000	3630290.000	-.520
10 inch	2535359.000	2470068.000	-2.575
12 inch	1558882.000	1584981.000	1.674

TOTAL FLUENCE= 2.900E+07 NEUTRONS/CM2
AVE ENERGY(LESS TH)= 1.340E+00 MEV
DOSE= 5.707E-02 RAD
DOSE EQUIVALENT= 4.687E-01 REM
QUALITY FACTOR= 8.213 REM/RAD
NRL TLD RESPONSE= 3.766 REM/REM(CF-252)
"HANKINS"TLD RESPONSE= 5.102 REM/REM(CF-252)
NEUTRAK RESPONSE= .841 REM/REM(CF-252)
NTA RESPONSE= .870 REM/REM(CF-252)
ANPDR-70 RESPONSE= .990 REM/REM(CF-252)

BIN NO.	ENERGY MAX (MEV)	FLUENCE NEUT/CM2	FLUENCE N/CM2/LETH	DOSE (RAD)	DOSE EQV. (REM)	DOSE EQV. (% OF TOTAL)
1	4.140E-07	5.058E+06	3.128E+06	2.660E-03	5.822E-03	1.242E+00
2	6.826E-07	2.166E+05	9.973E+05	1.319E-04	2.668E-04	5.692E-02
3	1.445E-06	3.003E+05	9.219E+05	1.854E-04	3.765E-04	8.033E-02
4	3.059E-06	2.939E+05	9.024E+05	1.803E-04	3.656E-04	7.800E-02
5	6.476E-06	3.053E+05	9.373E+05	1.853E-04	3.746E-04	7.992E-02
6	1.371E-05	3.319E+05	1.019E+06	1.994E-04	4.019E-04	8.574E-02
7	2.902E-05	3.727E+05	1.144E+06	2.225E-04	4.454E-04	9.501E-02
8	6.144E-05	4.264E+05	1.309E+06	2.532E-04	5.027E-04	1.072E-01
9	1.301E-04	4.878E+05	1.497E+06	2.874E-04	5.664E-04	1.208E-01
10	2.754E-04	5.484E+05	1.684E+06	3.125E-04	6.159E-04	1.314E-01
11	5.929E-04	6.259E+05	1.880E+06	3.421E-04	6.760E-04	1.442E-01
12	1.234E-03	6.434E+05	2.021E+06	3.379E-04	6.691E-04	1.428E-01
13	2.613E-03	6.941E+05	2.130E+06	3.574E-04	7.080E-04	1.510E-01
14	5.531E-03	7.215E+05	2.216E+06	3.668E-04	7.273E-04	1.552E-01
15	1.171E-02	7.330E+05	2.250E+06	3.694E-04	7.396E-04	1.578E-01
16	2.479E-02	7.409E+05	2.275E+06	4.171E-04	1.122E-03	2.393E-01
17	5.247E-02	7.515E+05	2.308E+06	4.989E-04	2.019E-03	4.308E-01
18	1.111E-01	8.019E+05	2.461E+06	6.292E-04	3.829E-03	8.169E-01
19	2.237E-01	9.732E+05	3.202E+06	1.010E-03	8.077E-03	1.723E+00
20	4.508E-01	1.787E+06	5.871E+06	2.598E-03	2.530E-02	5.398E+00
21	9.072E-01	3.652E+06	1.202E+07	8.195E-03	8.732E-02	1.863E+01
22	1.872E+00	3.113E+06	9.895E+06	1.060E-02	1.091E-01	2.328E+01
23	3.679E+00	3.580E+06	1.220E+07	1.511E-02	1.430E-01	3.051E+01
24	7.408E+00	7.878E+05	2.592E+06	4.552E-03	3.208E-02	6.844E+00
25	1.492E+01	1.035E+06	3.403E+06	6.852E-03	4.254E-02	9.074E+00
26	2.581E+01	2.387E+04	1.003E+05	2.172E-04	1.040E-03	2.218E-01

PITAS --- Neutron Measurements --- Location B
Start: Maxwellian (T=1.4 MeV)

RESPONSE MATRIX	UNFOLD CODE	MAXWELL TEMP,SHAPE	CALIB. FACTOR	SMOOTH FACTOR	PER CENT ERROR	NO. OF ITERATIONS
UTA4	SPUN	.20, .80	1.0000	.0000	11.4893	1000

DETECTORS	MEASURED COUNTS	CALCULATED COUNTS	PERCENT DIFFERENCE
bare	114505.000	113612.700	-.779
2 inch	255835.000	255677.900	-.061
3 inch	413316.000	454697.400	10.012
5 inch	643754.000	490055.900	-23.875
8 inch	170248.000	194840.100	14.445
10 inch	86866.000	91074.020	4.844
12 inch	48376.000	46157.770	-4.585

TOTAL FLUENCE= 3.018E+06 NEUTRONS/CM2
AVE ENERGY(LESS TH)= 5.231E-01 MEV
DOSE= 2.367E-03 RAD
DOSE EQUIVALENT= 8.896E-03 REM
QUALITY FACTOR= 3.758 REM/RAD
NRL TLD RESPONSE= 28.205 REM/REM(CF-252)
"HANKINS"TLD RESPONSE= 31.740 REM/REM(CF-252)
NEUTRAK RESPONSE= .672 REM/REM(CF-252)
NTA RESPONSE= .894 REM/REM(CF-252)
ANPDR-70 RESPONSE= .843 REM/REM(CF-252)

BIN NO.	ENERGY MAX (MEV)	FLUENCE NEUT/CM2	FLUENCE N/CM2/LETH	DOSE (RAD)	DOSE EQV. (REM)	DOSE EQV. (% OF TOTAL)
1	4.140E-07	7.244E+05	4.480E+05	3.810E-04	8.338E-04	9.372E+00
2	6.826E-07	1.478E+03	6.806E+03	8.999E-07	1.821E-06	2.047E-02
3	1.445E-06	1.244E+03	3.818E+03	7.679E-07	1.559E-06	1.753E-02
4	3.059E-06	8.775E+02	2.694E+03	5.383E-07	1.092E-06	1.227E-02
5	6.476E-06	8.743E+02	2.684E+03	5.307E-07	1.073E-06	1.206E-02
6	1.371E-05	1.217E+03	3.737E+03	7.313E-07	1.474E-06	1.657E-02
7	2.902E-05	2.226E+03	6.835E+03	1.329E-06	2.660E-06	2.990E-02
8	6.144E-05	4.997E+03	1.534E+04	2.967E-06	5.892E-06	6.623E-02
9	1.301E-04	1.237E+04	3.797E+04	7.290E-06	1.436E-05	1.615E-01
10	2.754E-04	3.170E+04	9.733E+04	1.806E-05	3.560E-05	4.002E-01
11	5.929E-04	7.802E+04	2.343E+05	4.264E-05	8.426E-05	9.471E-01
12	1.234E-03	1.600E+05	5.026E+05	8.400E-05	1.664E-04	1.870E+00
13	2.613E-03	2.937E+05	9.015E+05	1.512E-04	2.996E-04	3.368E+00
14	5.531E-03	4.231E+05	1.299E+06	2.151E-04	4.265E-04	4.795E+00
15	1.171E-02	4.924E+05	1.512E+06	2.481E-04	4.969E-04	5.585E+00
16	2.479E-02	4.073E+05	1.250E+06	2.293E-04	6.167E-04	6.932E+00
17	5.247E-02	2.127E+05	6.530E+05	1.412E-04	5.714E-04	6.423E+00
18	1.111E-01	4.296E+04	1.319E+05	3.371E-05	2.051E-04	2.306E+00
19	2.237E-01	1.600E+03	5.265E+03	1.661E-06	1.328E-05	1.493E-01
20	4.508E-01	1.155E+01	3.795E+01	1.679E-08	1.635E-07	1.838E-03
21	9.072E-01	3.305E-01	1.088E+00	7.417E-10	7.903E-09	8.884E-05
22	1.872E+00	2.124E+00	6.751E+00	7.234E-09	7.446E-08	8.371E-04
23	3.679E+00	2.282E+02	7.776E+02	9.628E-07	9.115E-06	1.025E-01
24	7.408E+00	3.010E+04	9.903E+04	1.739E-04	1.226E-03	1.378E+01
25	1.492E+01	9.129E+04	3.002E+05	6.045E-04	3.753E-03	4.219E+01
26	2.581E+01	2.947E+03	1.238E+04	2.681E-05	1.284E-04	1.443E+00

PITAS --- Neutron Measurements --- Location B
Start: NBS Cf-252

RESPONSE MATRIX	UNFOLD CODE	MAXWELL TEMP,SHAPE	CALIB. FACTOR	SMOOTH FACTOR	PER CENT ERROR	NO. OF ITERATIONS
UTA4	SPUN	.00, .80	1.0000	.0000	11.4673	1000

DETECTORS	MEASURED COUNTS	CALCULATED COUNTS	PERCENT DIFFERENCE
bare	114505.000	113636.300	-.759
2 inch	255835.000	255758.500	-.030
3 inch	413316.000	453795.000	9.794
5 inch	643754.000	489934.900	-23.894
8 inch	170248.000	194998.600	14.538
10 inch	86866.000	90983.000	4.739
12 inch	48376.000	46253.040	-4.388

TOTAL FLUENCE= 3.021E+06 NEUTRONS/CM2
AVE ENERGY(LESS TH)= 5.949E-01 MEV
DOSE= 2.445E-03 RAD
DOSE EQUIVALENT= 9.379E-03 REM
QUALITY FACTOR= 3.835 REM/RAD
NRL TLD RESPONSE= 26.607 REM/REM(CF-252)
"HANKINS"TLD RESPONSE= 30.465 REM/REM(CF-252)
NEUTRAK RESPONSE= .580 REM/REM(CF-252)
NTA RESPONSE= .852 REM/REM(CF-252)
ANPDR-70 RESPONSE= .804 REM/REM(CF-252)

BIN NO.	ENERGY MAX (MEV)	FLUENCE NEUT/CM2	FLUENCE N/CM2/LETH	DOSE (RAD)	DOSE EQV. (REM)	DOSE EQV. (% OF TOTAL)
1	4.140E-07	7.220E+05	4.465E+05	3.798E-04	8.310E-04	8.860E+00
2	6.826E-07	7.121E+02	3.279E+03	4.335E-07	8.773E-07	9.353E-03
3	1.445E-06	1.393E+03	4.278E+03	8.605E-07	1.747E-06	1.863E-02
4	3.059E-06	1.391E+03	4.271E+03	8.535E-07	1.731E-06	1.845E-02
5	6.476E-06	1.702E+03	5.224E+03	1.033E-06	2.088E-06	2.226E-02
6	1.371E-05	2.521E+03	7.740E+03	1.515E-06	3.053E-06	3.255E-02
7	2.902E-05	4.354E+03	1.337E+04	2.599E-06	5.203E-06	5.547E-02
8	6.144E-05	8.642E+03	2.653E+04	5.131E-06	1.019E-05	1.086E-01
9	1.301E-04	1.852E+04	5.685E+04	1.091E-05	2.150E-05	2.293E-01
10	2.754E-04	4.075E+04	1.251E+05	2.322E-05	4.576E-05	4.879E-01
11	5.929E-04	9.108E+04	2.735E+05	4.977E-05	9.836E-05	1.049E+00
12	1.234E-03	1.695E+05	5.323E+05	8.898E-05	1.762E-04	1.879E+00
13	2.613E-03	3.185E+05	9.775E+05	1.640E-04	3.249E-04	3.464E+00
14	5.531E-03	4.905E+05	1.506E+06	2.493E-04	4.944E-04	5.272E+00
15	1.171E-02	6.375E+04	1.957E+05	3.212E-05	6.433E-05	6.858E-01
16	2.479E-02	5.886E+05	1.807E+06	3.313E-04	8.911E-04	9.501E+00
17	5.247E-02	3.121E+05	9.585E+05	2.072E-04	8.387E-04	8.942E+00
18	1.111E-01	5.402E+04	1.658E+05	4.239E-05	2.579E-04	2.750E+00
19	2.237E-01	2.080E+03	6.843E+03	2.159E-06	1.726E-05	1.840E-01
20	4.508E-01	1.071E+01	3.518E+01	1.557E-08	1.516E-07	1.616E-03
21	9.072E-01	4.019E-02	1.323E-01	9.018E-11	9.608E-10	1.024E-05
22	1.872E+00	1.518E-01	4.826E-01	5.171E-10	5.323E-09	5.675E-05
23	3.679E+00	1.828E+01	6.229E+01	7.713E-08	7.302E-07	7.785E-03
24	7.408E+00	6.058E+03	1.993E+04	3.501E-05	2.467E-04	2.630E+00
25	1.492E+01	1.207E+05	3.968E+05	7.990E-04	4.960E-03	5.288E+01
26	2.581E+01	1.960E+03	8.234E+03	1.783E-05	8.537E-05	9.102E-01

PITAS --- Neutron Measurements --- Location B
Start: NBS Cf-252 Room Return

RESPONSE MATRIX	UNFOLD CODE	MAXWELL TEMP,SHAPE	CALIB. FACTOR	SMOOTH FACTOR	PER CENT ERROR	NO. OF ITERATIONS
UTA4	SPUN	.00, .80	1.0000	.0000	11.7288	1000

DETECTORS	MEASURED COUNTS	CALCULATED COUNTS	PERCENT DIFFERENCE
bare	114505.000	113637.000	-.758
2 inch	255835.000	255718.900	-.045
3 inch	413316.000	454034.000	9.852
5 inch	643754.000	488804.600	-24.070
8 inch	170248.000	195700.300	14.950
10 inch	86866.000	91751.640	5.624
12 inch	48376.000	45689.740	-5.553

TOTAL FLUENCE= 2.985E+06 NEUTRONS/CM2
AVE ENERGY(LESS TH)= 2.732E-01 MEV
DOSE= 2.163E-03 RAD
DOSE EQUIVALENT= 7.970E-03 REM
QUALITY FACTOR= 3.685 REM/RAD
NRL TLD RESPONSE= 31.458 REM/REM(CF-252)
"HANKINS"TLD RESPONSE= 35.259 REM/REM(CF-252)
NEUTRAK RESPONSE= .920 REM/REM(CF-252)
NTA RESPONSE= .946 REM/REM(CF-252)
ANPDR-70 RESPONSE= 1.044 REM/REM(CF-252)

BIN NO.	ENERGY MAX (MEV)	FLUENCE NEUT/CM2	FLUENCE N/CM2/LETH	DOSE (RAD)	DOSE EQV. (REM)	DOSE EQV. (% OF TOTAL)
1	4.140E-07	7.259E+05	4.489E+05	3.818E-04	8.355E-04	1.048E+01
2	6.826E-07	3.643E+02	1.678E+03	2.218E-07	4.488E-07	5.632E-03
3	1.445E-06	5.681E+02	1.744E+03	3.508E-07	7.124E-07	8.938E-03
4	3.059E-06	4.998E+02	1.535E+03	3.067E-07	6.218E-07	7.802E-03
5	6.476E-06	5.665E+02	1.739E+03	3.438E-07	6.950E-07	8.721E-03
6	1.371E-05	8.936E+02	2.743E+03	5.369E-07	1.082E-06	1.358E-02
7	2.902E-05	1.790E+03	5.497E+03	1.069E-06	2.139E-06	2.684E-02
8	6.144E-05	5.321E+03	1.633E+04	3.159E-06	6.273E-06	7.871E-02
9	1.301E-04	1.323E+04	4.061E+04	7.795E-06	1.536E-05	1.927E-01
10	2.754E-04	3.327E+04	1.022E+05	1.896E-05	3.736E-05	4.688E-01
11	5.929E-04	8.195E+04	2.461E+05	4.478E-05	8.850E-05	1.110E+00
12	1.234E-03	1.557E+05	4.892E+05	8.177E-05	1.619E-04	2.032E+00
13	2.613E-03	2.816E+05	8.641E+05	1.450E-04	2.872E-04	3.603E+00
14	5.531E-03	4.465E+05	1.371E+06	2.269E-04	4.501E-04	5.647E+00
15	1.171E-02	5.232E+05	1.606E+06	2.636E-04	5.279E-04	6.624E+00
16	2.479E-02	3.982E+05	1.222E+06	2.241E-04	6.028E-04	7.564E+00
17	5.247E-02	1.799E+05	5.526E+05	1.195E-04	4.835E-04	6.067E+00
18	1.111E-01	2.831E+04	8.689E+04	2.221E-05	1.352E-04	1.696E+00
19	2.237E-01	1.490E+03	4.902E+03	1.546E-06	1.236E-05	1.551E-01
20	4.508E-01	8.797E+00	2.891E+01	1.279E-08	1.246E-07	1.563E-03
21	9.072E-01	3.531E-01	1.163E+00	7.924E-10	8.443E-09	1.059E-04
22	1.872E+00	3.486E+00	1.108E+01	1.187E-08	1.222E-07	1.534E-03
23	3.679E+00	7.258E+02	2.473E+03	3.063E-06	2.899E-05	3.638E-01
24	7.408E+00	9.753E+04	3.208E+05	5.635E-04	3.971E-03	4.983E+01
25	1.492E+01	7.518E+03	2.472E+04	4.978E-05	3.091E-04	3.878E+00
26	2.581E+01	2.467E+02	1.036E+03	2.244E-06	1.075E-05	1.348E-01

PITAS --- Neutron Measurements --- Location B
Start: Equal Lethargy

RESPONSE MATRIX	UNFOLD CODE	MAXWELL TEMP,SHAPE	CALIB. FACTOR	SMOOTH FACTOR	PER CENT ERROR	NO. OF ITERATIONS
UTA4	SPUN	.00, .80	1.0000	.0000	11.3811	1000

DETECTORS	MEASURED COUNTS	CALCULATED COUNTS	PERCENT DIFFERENCE
bare	114505.000	113711.400	-.693
2 inch	255835.000	255083.300	-.294
3 inch	413316.000	454709.900	10.015
5 inch	643754.000	491246.800	-23.690
8 inch	170248.000	194693.800	14.359
10 inch	86866.000	90802.770	4.532
12 inch	48376.000	46330.250	-4.229

TOTAL FLUENCE= 3.040E+06 NEUTRONS/CM2
AVE ENERGY(LESS TH)= 6.812E-01 MEV
DOSE= 2.502E-03 RAD
DOSE EQUIVALENT= 9.438E-03 REM
QUALITY FACTOR= 3.771 REM/RAD
NRL TLD RESPONSE= 26.597 REM/REM(CF-252)
"HANKINS"TLD RESPONSE= 29.881 REM/REM(CF-252)
NEUTRAK RESPONSE= .561 REM/REM(CF-252)
NTA RESPONSE= .864 REM/REM(CF-252)
ANPDR-70 RESPONSE= .748 REM/REM(CF-252)

BIN NO.	ENERGY MAX (MEV)	FLUENCE NEUT/CM2	FLUENCE N/CM2/LETH	DOSE (RAD)	DOSE EQV. (REM)	DOSE EQV. (% OF TOTAL)
1	4.140E-07	7.256E+05	4.487E+05	3.817E-04	8.352E-04	8.849E+00
2	6.826E-07	1.784E+03	8.215E+03	1.086E-06	2.198E-06	2.329E-02
3	1.445E-06	1.449E+03	4.447E+03	8.945E-07	1.816E-06	1.925E-02
4	3.059E-06	9.728E+02	2.987E+03	5.968E-07	1.210E-06	1.282E-02
5	6.476E-06	9.211E+02	2.828E+03	5.591E-07	1.130E-06	1.197E-02
6	1.371E-05	1.220E+03	3.746E+03	7.330E-07	1.477E-06	1.565E-02
7	2.902E-05	2.137E+03	6.562E+03	1.276E-06	2.554E-06	2.706E-02
8	6.144E-05	4.645E+03	1.426E+04	2.758E-06	5.477E-06	5.803E-02
9	1.301E-04	1.128E+04	3.462E+04	6.646E-06	1.309E-05	1.387E-01
10	2.754E-04	2.874E+04	8.825E+04	1.638E-05	3.228E-05	3.420E-01
11	5.929E-04	7.125E+04	2.139E+05	3.894E-05	7.694E-05	8.153E-01
12	1.234E-03	1.491E+05	4.684E+05	7.829E-05	1.551E-04	1.643E+00
13	2.613E-03	2.823E+05	8.665E+05	1.454E-04	2.880E-04	3.051E+00
14	5.531E-03	4.214E+05	1.294E+06	2.142E-04	4.248E-04	4.501E+00
15	1.171E-02	5.092E+05	1.563E+06	2.566E-04	5.138E-04	5.444E+00
16	2.479E-02	4.310E+05	1.323E+06	2.426E-04	6.525E-04	6.914E+00
17	5.247E-02	2.199E+05	6.754E+05	1.460E-04	5.910E-04	6.262E+00
18	1.111E-01	3.949E+04	1.212E+05	3.099E-05	1.886E-04	1.998E+00
19	2.237E-01	1.124E+03	3.697E+03	1.166E-06	9.325E-06	9.881E-02
20	4.508E-01	4.477E+00	1.471E+01	6.509E-09	6.339E-08	6.717E-04
21	9.072E-01	2.898E-02	9.543E-02	6.504E-11	6.930E-10	7.343E-06
22	1.872E+00	1.644E-02	5.224E-02	5.598E-11	5.762E-10	6.105E-06
23	3.679E+00	1.451E+00	4.946E+00	6.124E-09	5.798E-08	6.143E-04
24	7.408E+00	2.734E+02	8.993E+02	1.580E-06	1.113E-05	1.179E-01
25	1.492E+01	1.231E+05	4.050E+05	8.154E-04	5.062E-03	5.364E+01
26	2.581E+01	1.304E+04	5.478E+04	1.186E-04	5.680E-04	6.018E+00

PITAS --- Neutron Measurement --- Location C
Start: Maxwellian (T=1.4 MeV)

RESPONSE MATRIX	UNFOLD CODE	MAXWELL TEMP,SHAPE	CALIB. FACTOR	SMOOTH FACTOR	PER CENT ERROR	NO. OF ITERATIONS
UTA4	SPUN	.20, .80	1.0000	.0000	19.9819	1000

DETECTORS	MEASURED COUNTS	CALCULATED COUNTS	PERCENT DIFFERENCE
bare	2240144.000	2170842.000	-3.094
2 inch	3970780.000	4314874.000	8.666
3 inch	6373502.000	6522884.000	2.344
5 inch	8854312.000	5891831.000	-33.458
8 inch	1468682.000	2024802.000	37.865
10 inch	948829.000	832018.500	-12.311
12 inch	335185.000	335144.700	-.012

TOTAL FLUENCE= 3.930E+07 NEUTRONS/CM2
AVE ENERGY(LESS TH)= 5.658E-02 MEV
DOSE= 2.190E-02 RAD
DOSE EQUIVALENT= 5.142E-02 REM
QUALITY FACTOR= 2.348 REM/RAD
NRL TLD RESPONSE= 71.552 REM/REM(CF-252)
"HANKINS"TLD RESPONSE= 76.925 REM/REM(CF-252)
NEUTRAK RESPONSE= .260 REM/REM(CF-252)
NTA RESPONSE= .283 REM/REM(CF-252)
ANPDR-70 RESPONSE= 1.290 REM/REM(CF-252)

BIN NO.	ENERGY MAX (MEV)	FLUENCE NEUT/CM2	FLUENCE N/CM2/LETH	DOSE (RAD)	DOSE EQV. (REM)	DOSE EQV. (% OF TOTAL)
1	4.140E-07	1.375E+07	8.500E+06	7.230E-03	1.582E-02	3.077E+01
2	6.826E-07	7.674E+02	3.534E+03	4.672E-07	9.454E-07	1.839E-03
3	1.445E-06	1.022E+03	3.137E+03	6.309E-07	1.281E-06	2.491E-03
4	3.059E-06	1.558E+03	4.784E+03	9.559E-07	1.938E-06	3.769E-03
5	6.476E-06	3.742E+03	1.149E+04	2.271E-06	4.591E-06	8.928E-03
6	1.371E-05	1.249E+04	3.833E+04	7.502E-06	1.512E-05	2.940E-02
7	2.902E-05	4.942E+04	1.517E+05	2.950E-05	5.906E-05	1.148E-01
8	6.144E-05	2.000E+05	6.139E+05	1.187E-04	2.358E-04	4.585E-01
9	1.301E-04	6.957E+05	2.135E+06	4.099E-04	8.077E-04	1.571E+00
10	2.754E-04	1.934E+06	5.939E+06	1.102E-03	2.172E-03	4.224E+00
11	5.929E-04	4.063E+06	1.220E+07	2.220E-03	4.388E-03	8.533E+00
12	1.234E-03	5.630E+06	1.769E+07	2.956E-03	5.855E-03	1.139E+01
13	2.613E-03	5.946E+06	1.825E+07	3.062E-03	6.065E-03	1.179E+01
14	5.531E-03	4.099E+06	1.259E+07	2.084E-03	4.132E-03	8.036E+00
15	1.171E-02	2.016E+06	6.187E+06	1.016E-03	2.034E-03	3.955E+00
16	2.479E-02	5.946E+05	1.825E+06	3.347E-04	9.002E-04	1.750E+00
17	5.247E-02	9.267E+04	2.846E+05	6.152E-05	2.490E-04	4.842E-01
18	1.111E-01	4.593E+03	1.410E+04	3.604E-06	2.193E-05	4.264E-02
19	2.237E-01	6.273E+01	2.064E+02	6.512E-08	5.206E-07	1.012E-03
20	4.508E-01	8.239E-01	2.707E+00	1.198E-09	1.167E-08	2.269E-05
21	9.072E-01	4.292E-01	1.413E+00	9.632E-10	1.026E-08	1.996E-05
22	1.872E+00	4.447E+01	1.413E+02	1.515E-07	1.559E-06	3.032E-03
23	3.679E+00	6.480E+03	2.209E+04	2.735E-05	2.589E-04	5.034E-01
24	7.408E+00	1.520E+05	5.000E+05	8.782E-04	6.189E-03	1.203E+01
25	1.492E+01	5.284E+04	1.738E+05	3.499E-04	2.172E-03	4.224E+00
26	2.581E+01	8.507E+02	3.574E+03	7.739E-06	3.706E-05	7.206E-02

PITAS --- Neutron Measurement --- Location C
Start: NBS Cf-252

RESPONSE MATRIX	UNFOLD CODE	MAXWELL TEMP,SHAPE	CALIB. FACTOR	SMOOTH FACTOR	PER CENT ERROR	NO. OF ITERATIONS
UTA4	SPUN	.00, .80	1.0000	.0000	19.9422	1000

DETECTORS	MEASURED COUNTS	CALCULATED COUNTS	PERCENT DIFFERENCE
bare	2240144.000	2169686.000	-3.145
2 inch	3970780.000	4319520.000	8.783
3 inch	6373502.000	6526435.000	2.400
5 inch	8854312.000	5887972.000	-33.502
8 inch	1468682.000	2020792.000	37.592
10 inch	948829.000	830546.100	-12.466
12 inch	335185.000	336320.000	.339

TOTAL FLUENCE= 3.932E+07 NEUTRONS/CM2
AVE ENERGY(LESS TH)= 8.876E-02 MEV
DOSE= 2.224E-02 RAD
DOSE EQUIVALENT= 5.312E-02 REM
QUALITY FACTOR= 2.389 REM/RAD
NRL TLD RESPONSE= 69.353 REM/REM(CF-252)
"HANKINS"TLD RESPONSE= 74.696 REM/REM(CF-252)
NEUTRAK RESPONSE= .225 REM/REM(CF-252)
NTA RESPONSE= .295 REM/REM(CF-252)
ANPDR-70 RESPONSE= 1.236 REM/REM(CF-252)

BIN NO.	ENERGY MAX (MEV)	FLUENCE NEUT/CM2	FLUENCE N/CM2/LETH	DOSE (RAD)	DOSE EQV. (REM)	DOSE EQV. (% OF TOTAL)
1	4.140E-07	1.372E+07	8.488E+06	7.219E-03	1.580E-02	2.974E+01
2	6.826E-07	6.314E+02	2.907E+03	3.844E-07	7.778E-07	1.464E-03
3	1.445E-06	1.529E+03	4.695E+03	9.443E-07	1.918E-06	3.610E-03
4	3.059E-06	2.589E+03	7.950E+03	1.589E-06	3.221E-06	6.064E-03
5	6.476E-06	6.332E+03	1.944E+04	3.844E-06	7.770E-06	1.463E-02
6	1.371E-05	1.979E+04	6.077E+04	1.189E-05	2.397E-05	4.512E-02
7	2.902E-05	6.906E+04	2.121E+05	4.123E-05	8.252E-05	1.553E-01
8	6.144E-05	2.432E+05	7.466E+05	1.444E-04	2.867E-04	5.398E-01
9	1.301E-04	7.519E+05	2.308E+06	4.430E-04	8.729E-04	1.643E+00
10	2.754E-04	1.900E+06	5.835E+06	1.083E-03	2.134E-03	4.017E+00
11	5.929E-04	3.919E+06	1.177E+07	2.142E-03	4.232E-03	7.967E+00
12	1.234E-03	5.375E+06	1.688E+07	2.822E-03	5.590E-03	1.052E+01
13	2.613E-03	6.354E+06	1.950E+07	3.272E-03	6.481E-03	1.220E+01
14	5.531E-03	5.119E+06	1.572E+07	2.602E-03	5.160E-03	9.713E+00
15	1.171E-02	3.062E+05	9.399E+05	1.543E-04	3.089E-04	5.815E-01
16	2.479E-02	1.091E+06	3.348E+06	6.139E-04	1.651E-03	3.108E+00
17	5.247E-02	1.853E+05	5.690E+05	1.230E-04	4.978E-04	9.371E-01
18	1.111E-01	8.284E+03	2.543E+04	6.501E-06	3.956E-05	7.446E-02
19	2.237E-01	1.142E+02	3.757E+02	1.185E-07	9.477E-07	1.784E-03
20	4.508E-01	9.865E-01	3.242E+00	1.434E-09	1.397E-08	2.630E-05
21	9.072E-01	7.471E-02	2.460E-01	1.676E-10	1.786E-09	3.362E-06
22	1.872E+00	4.960E+00	1.577E+01	1.690E-08	1.739E-07	3.274E-04
23	3.679E+00	9.375E+02	3.195E+03	3.956E-06	3.745E-05	7.050E-02
24	7.408E+00	6.618E+04	2.177E+05	3.824E-04	2.695E-03	5.073E+00
25	1.492E+01	1.740E+05	5.723E+05	1.152E-03	7.154E-03	1.347E+01
26	2.581E+01	1.451E+03	6.098E+03	1.320E-05	6.322E-05	1.190E-01

PITAS --- Neutron Measurement --- Location C
Start: NBS Cf-252 Room Return

RESPONSE MATRIX	UNFOLD CODE	MAXWELL TEMP,SHAPE	CALIB. FACTOR	SMOOTH FACTOR	PER CENT ERROR	NO. OF ITERATIONS
UTA4	SPUN	.00, .80	1.0000	.0000	20.0068	1000

DETECTORS	MEASURED COUNTS	CALCULATED COUNTS	PERCENT DIFFERENCE
bare	2240144.000	2171144.000	-3.080
2 inch	3970780.000	4314100.000	8.646
3 inch	6373502.000	6520790.000	2.311
5 inch	8854312.000	5892468.000	-33.451
8 inch	1468682.000	2026690.000	37.994
10 inch	948829.000	832701.200	-12.239
12 inch	335185.000	334579.100	-.181

TOTAL FLUENCE= 3.929E+07 NEUTRONS/CM2
AVE ENERGY(LESS TH)= 4.234E-02 MEV
DOSE= 2.177E-02 RAD
DOSE EQUIVALENT= 5.081E-02 REM
QUALITY FACTOR= 2.334 REM/RAD
NRL TLD RESPONSE= 72.337 REM/REM(CF-252)
"HANKINS"TLD RESPONSE= 78.075 REM/REM(CF-252)
NEUTRAK RESPONSE= .273 REM/REM(CF-252)
NTA RESPONSE= .276 REM/REM(CF-252)
ANPDR-70 RESPONSE= 1.316 REM/REM(CF-252)

BIN NO.	ENERGY MAX (MEV)	FLUENCE NEUT/CM2	FLUENCE N/CM2/LETH	DOSE (RAD)	DOSE EQV. (REM)	DOSE EQV. (% OF TOTAL)
1	4.140E-07	1.374E+07	8.500E+06	7.230E-03	1.582E-02	3.113E+01
2	6.826E-07	4.334E+02	1.996E+03	2.638E-07	5.339E-07	1.051E-03
3	1.445E-06	8.915E+02	2.737E+03	5.505E-07	1.118E-06	2.200E-03
4	3.059E-06	1.407E+03	4.319E+03	8.631E-07	1.750E-06	3.444E-03
5	6.476E-06	3.291E+03	1.010E+04	1.998E-06	4.038E-06	7.946E-03
6	1.371E-05	1.101E+04	3.380E+04	6.614E-06	1.333E-05	2.624E-02
7	2.902E-05	4.360E+04	1.339E+05	2.603E-05	5.210E-05	1.025E-01
8	6.144E-05	2.199E+05	6.751E+05	1.306E-04	2.593E-04	5.102E-01
9	1.301E-04	7.410E+05	2.274E+06	4.366E-04	8.603E-04	1.693E+00
10	2.754E-04	1.986E+06	6.099E+06	1.132E-03	2.231E-03	4.390E+00
11	5.929E-04	4.159E+06	1.249E+07	2.273E-03	4.492E-03	8.840E+00
12	1.234E-03	5.364E+06	1.685E+07	2.817E-03	5.579E-03	1.098E+01
13	2.613E-03	5.634E+06	1.729E+07	2.901E-03	5.747E-03	1.131E+01
14	5.531E-03	4.328E+06	1.329E+07	2.200E-03	4.362E-03	8.585E+00
15	1.171E-02	2.171E+06	6.664E+06	1.094E-03	2.190E-03	4.311E+00
16	2.479E-02	5.958E+05	1.829E+06	3.354E-04	9.020E-04	1.775E+00
17	5.247E-02	8.087E+04	2.483E+05	5.369E-05	2.173E-04	4.276E-01
18	1.111E-01	3.111E+03	9.550E+03	2.441E-06	1.486E-05	2.924E-02
19	2.237E-01	5.915E+01	1.946E+02	6.139E-08	4.908E-07	9.660E-04
20	4.508E-01	5.745E-01	1.888E+00	8.354E-10	8.135E-09	1.601E-05
21	9.072E-01	3.555E-01	1.171E+00	7.978E-10	8.500E-09	1.673E-05
22	1.872E+00	4.415E+01	1.403E+02	1.504E-07	1.548E-06	3.046E-03
23	3.679E+00	9.801E+03	3.340E+04	4.136E-05	3.916E-04	7.706E-01
24	7.408E+00	1.870E+05	6.152E+05	1.080E-03	7.614E-03	1.498E+01
25	1.492E+01	1.410E+03	4.637E+03	9.337E-06	5.797E-05	1.141E-01
26	2.581E+01	2.226E+01	9.351E+01	2.025E-07	9.695E-07	1.908E-03

PITAS --- Neutron Measurement --- Location C
Start: Equal Lethargy

RESPONSE MATRIX	UNFOLD CODE	MAXWELL TEMP,SHAPE	CALIB. FACTOR	SMOOTH FACTOR	PER CENT ERROR	NO. OF ITERATIONS
UTA4	SPUN	.00, .80	1.0000	.0000	19.9225	1000

DETECTORS	MEASURED COUNTS	CALCULATED COUNTS	PERCENT DIFFERENCE
bare	2240144.000	2171160.000	-3.079
2 inch	3970780.000	4313458.000	8.630
3 inch	6373502.000	6522878.000	2.344
5 inch	8854312.000	5891006.000	-33.467
8 inch	1468682.000	2020553.000	37.576
10 inch	948829.000	830092.900	-12.514
12 inch	335185.000	336898.700	.511

TOTAL FLUENCE= 3.938E+07 NEUTRONS/CM2
AVE ENERGY(LESS TH)= 1.167E-01 MEV
DOSE= 2.244E-02 RAD
DOSE EQUIVALENT= 5.371E-02 REM
QUALITY FACTOR= 2.393 REM/RAD
NRL TLD RESPONSE= 68.568 REM/REM(CF-252)
"HANKINS"TLD RESPONSE= 73.510 REM/REM(CF-252)
NEUTRAK RESPONSE= .198 REM/REM(CF-252)
NTA RESPONSE= .301 REM/REM(CF-252)
ANPDR-70 RESPONSE= 1.192 REM/REM(CF-252)

BIN NO.	ENERGY MAX (MEV)	FLUENCE NEUT/CM2	FLUENCE N/CM2/LETH	DOSE (RAD)	DOSE EQV. (REM)	DOSE EQV. (% OF TOTAL)
1	4.140E-07	1.375E+07	8.504E+06	7.233E-03	1.583E-02	2.947E+01
2	6.826E-07	1.613E+03	7.426E+03	9.818E-07	1.987E-06	3.700E-03
3	1.445E-06	1.734E+03	5.323E+03	1.071E-06	2.174E-06	4.048E-03
4	3.059E-06	2.157E+03	6.624E+03	1.324E-06	2.684E-06	4.997E-03
5	6.476E-06	4.448E+03	1.366E+04	2.700E-06	5.458E-06	1.016E-02
6	1.371E-05	1.334E+04	4.096E+04	8.016E-06	1.616E-05	3.008E-02
7	2.902E-05	4.946E+04	1.519E+05	2.953E-05	5.910E-05	1.101E-01
8	6.144E-05	1.941E+05	5.959E+05	1.152E-04	2.289E-04	4.261E-01
9	1.301E-04	6.706E+05	2.058E+06	3.951E-04	7.785E-04	1.450E+00
10	2.754E-04	1.880E+06	5.772E+06	1.071E-03	2.111E-03	3.931E+00
11	5.929E-04	4.012E+06	1.205E+07	2.192E-03	4.333E-03	8.068E+00
12	1.234E-03	5.656E+06	1.777E+07	2.970E-03	5.882E-03	1.095E+01
13	2.613E-03	6.052E+06	1.857E+07	3.116E-03	6.173E-03	1.149E+01
14	5.531E-03	4.173E+06	1.281E+07	2.121E-03	4.207E-03	7.833E+00
15	1.171E-02	2.015E+06	6.185E+06	1.015E-03	2.033E-03	3.785E+00
16	2.479E-02	5.585E+05	1.715E+06	3.144E-04	8.456E-04	1.575E+00
17	5.247E-02	7.455E+04	2.290E+05	4.950E-05	2.003E-04	3.730E-01
18	1.111E-01	2.638E+03	8.096E+03	2.070E-06	1.260E-05	2.345E-02
19	2.237E-01	1.977E+01	6.505E+01	2.052E-08	1.641E-07	3.055E-04
20	4.508E-01	9.189E-02	3.020E-01	1.336E-10	1.301E-09	2.423E-06
21	9.072E-01	8.926E-03	2.939E-02	2.003E-11	2.134E-10	3.974E-07
22	1.872E+00	1.221E-01	3.882E-01	4.160E-10	4.282E-09	7.973E-06
23	3.679E+00	3.074E+01	1.048E+02	1.297E-07	1.228E-06	2.286E-03
24	7.408E+00	2.449E+03	8.058E+03	1.415E-05	9.974E-05	1.857E-01
25	1.492E+01	2.484E+05	8.171E+05	1.645E-03	1.021E-02	1.902E+01
26	2.581E+01	1.541E+04	6.474E+04	1.402E-04	6.712E-04	1.250E+00

APPENIDIX E

CALCULATED PHOTON SPECTRA

The photon spectra calculated for all downfield distances are reported as lethargy fluence. For scaling purposes, spectra from the detectors at 0 and 0.5 degrees are presented on one plot and spectra from 1 through 45 degrees are presented on an additional plot. Additionally, the relative lethargy fluences are reported for the standard system prototype.

Fluences are reported for the following calculation scenarios:

1. PITAS prototype in air (lethargy fluence and relative lethargy fluence);
2. PITAS prototype in vacuo (lethargy fluence);
3. PITAS prototype with collimator Pb reduction by 10% in air (lethargy fluence);
4. PITAS prototype with Pb disk (t=0.50cm) attenuator in air (lethargy fluence);
5. PITAS prototype collimator only in air (lethargy fluence);
6. PITAS prototype beam only in air (lethargy fluence).

Data for 10 meters are shown in Figure E-1 through Figure E-14. Data for 25 meters are shown in Figure E-15 through Figure E-28. Data for 50 meters are shown in Figure E-29 through Figure E-42. Data for 100 meters are shown in Figure E-43 through Figure E-56. Data for 120 meters are shown in Figure E-57 through Figure E-70. Data for 170 meters are shown in Figure E-71 through Figure E-84.

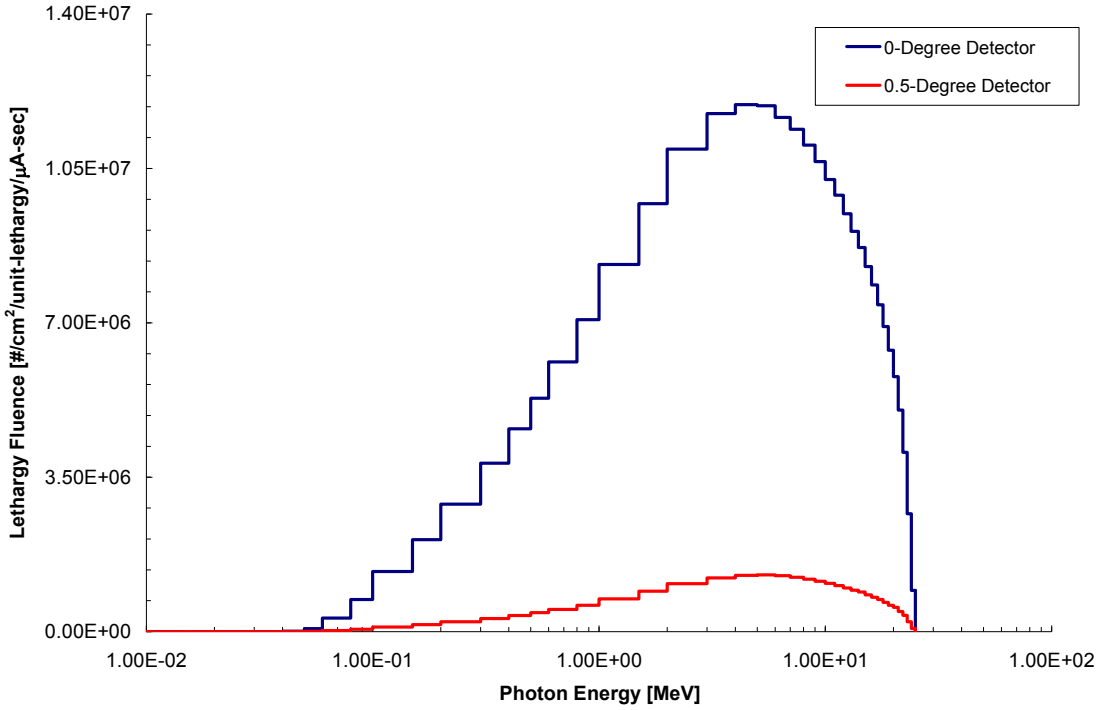

Figure E-1. Photon Spectrum (0 to 0.5 degree detectors) at 10 meters for the System in Air.

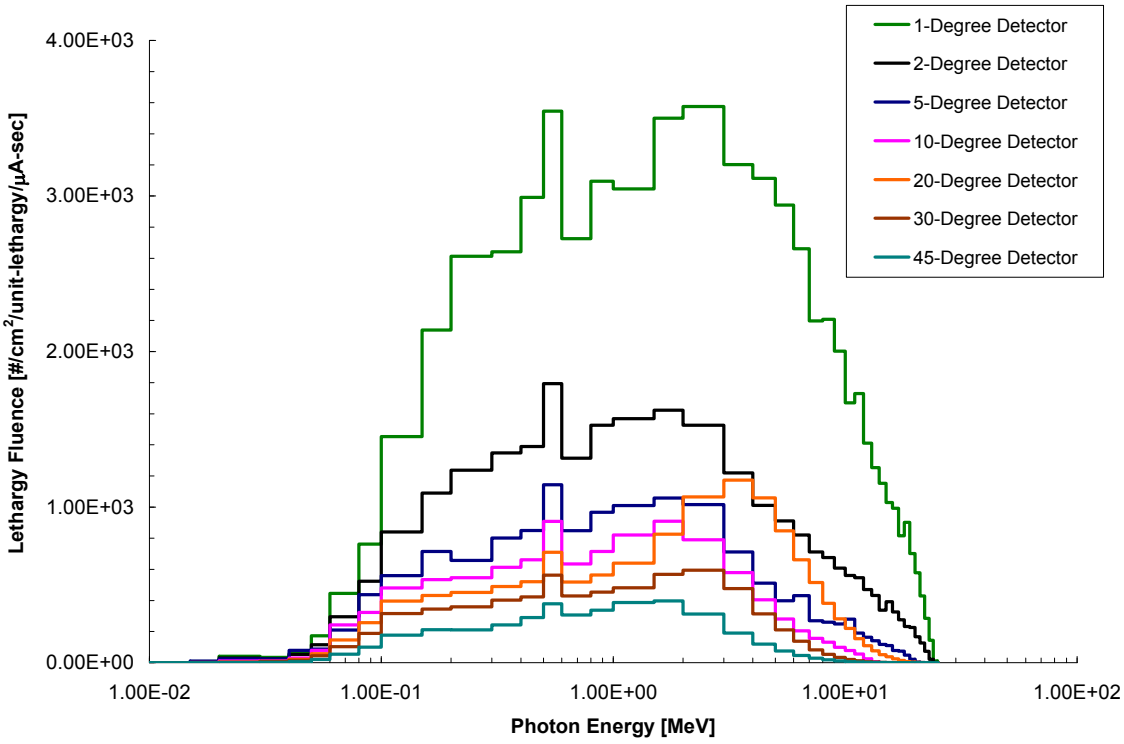

Figure E-2. Photon Spectrum (1 to 45 degree detectors) at 10 meters for the System in Air.

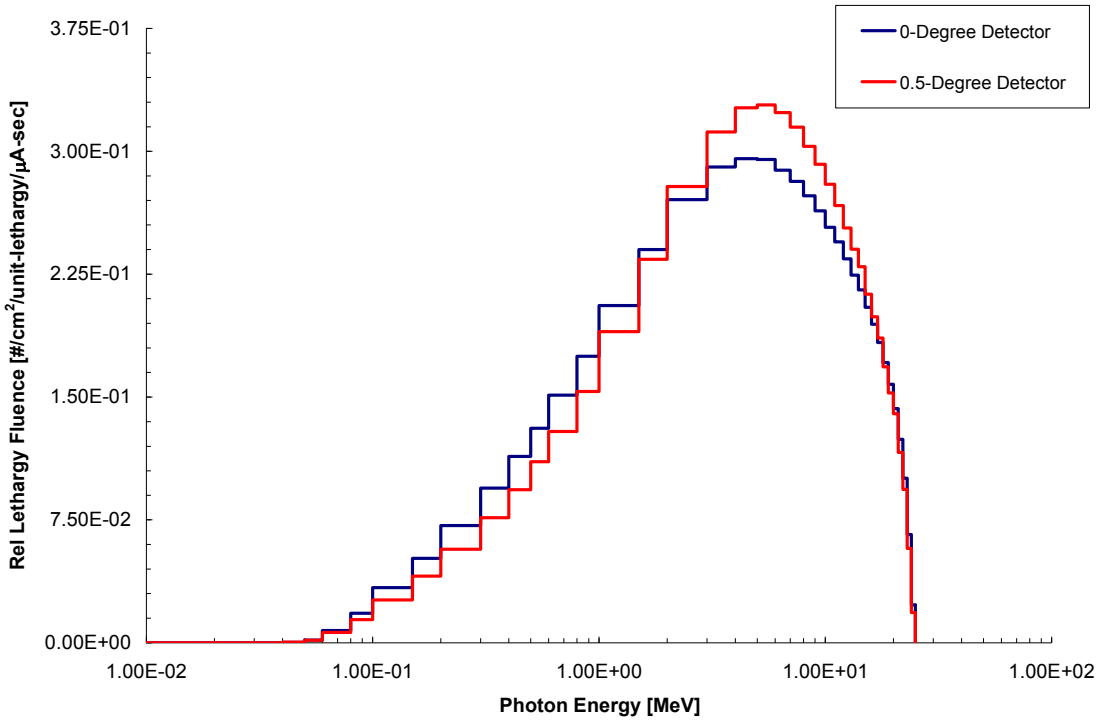

Figure E-3. Relative Photon Spectrum (0 to 0.5 degree detectors) at 10 meters for the System in Air.

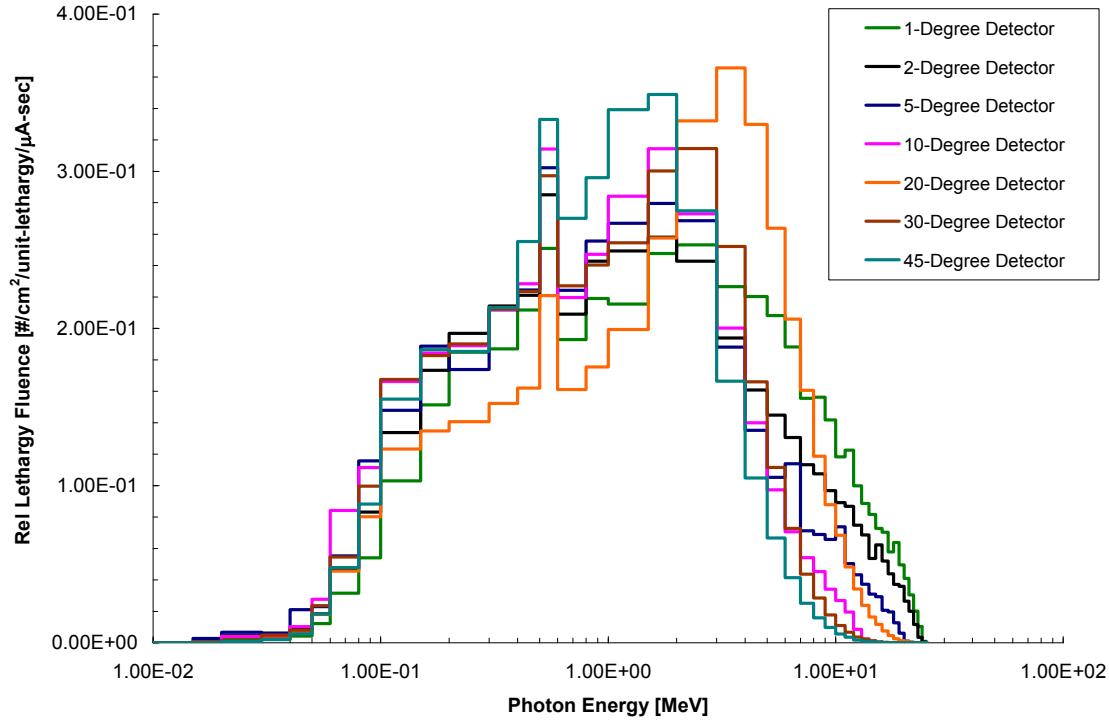

Figure E-4. Relative Photon Spectrum (1 to 45 degree detectors) at 10 meters for the System in Air.

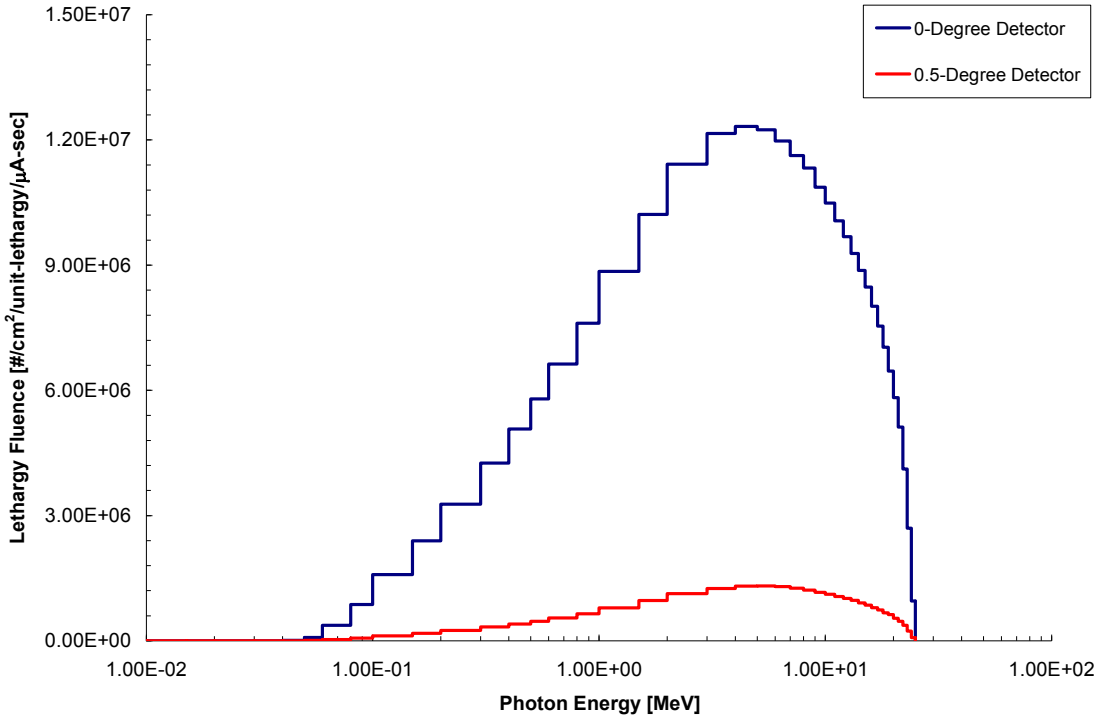

Figure E-5. Photon Spectrum (0 to 0.5 degree detectors) at 10 meters for the System in Vacuo.

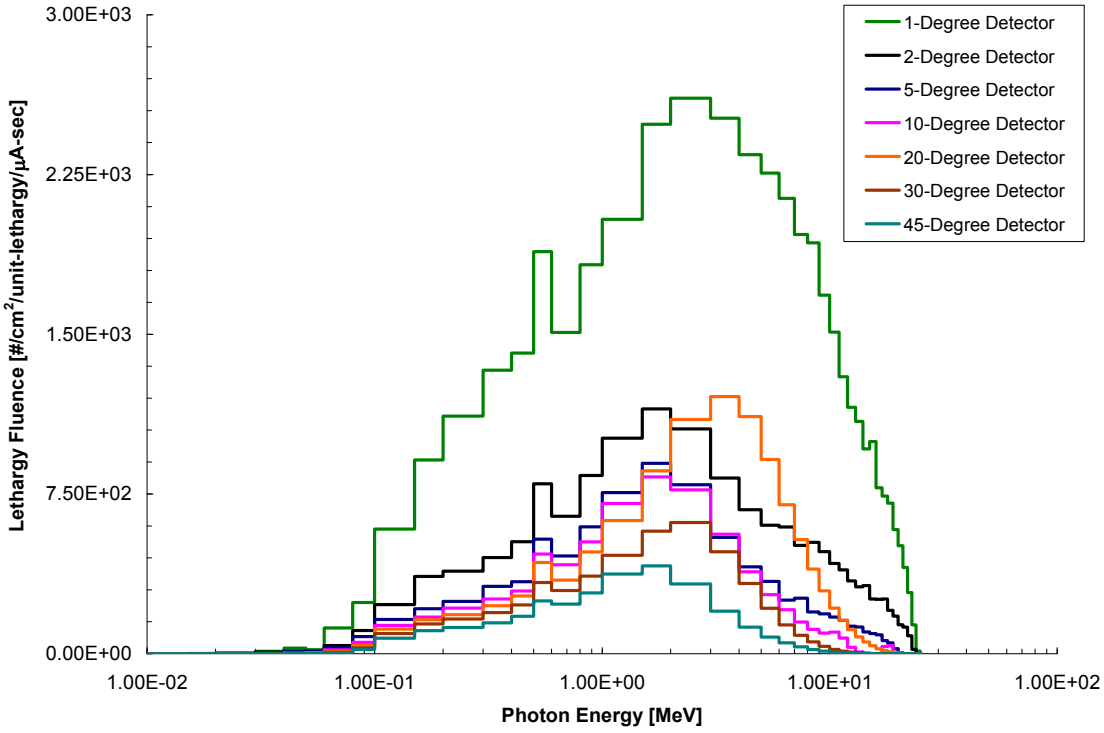

Figure E-6. Photon Spectrum (1 to 45 degree detectors) at 10 meters for the System in Vacuo.

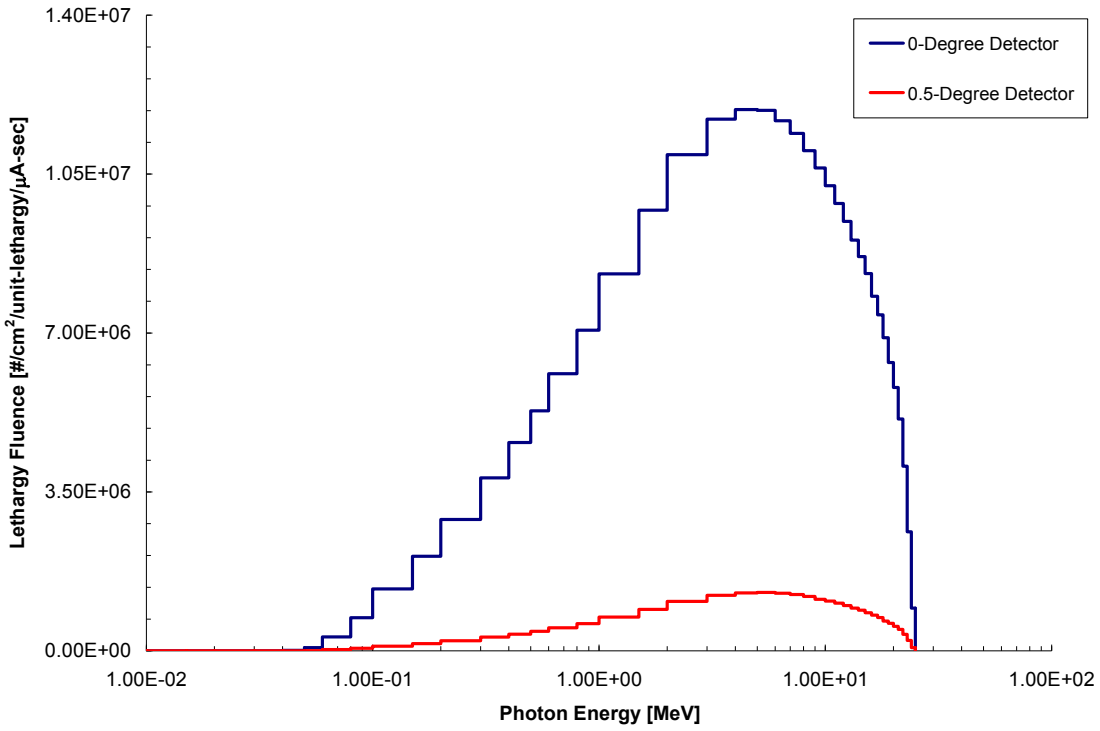

Figure E-7. Photon Spectrum (0 to 0.5 degree detectors) at 10 meters for the System (in Air) with a Pb Density Reduction of 10% in the Collimator.

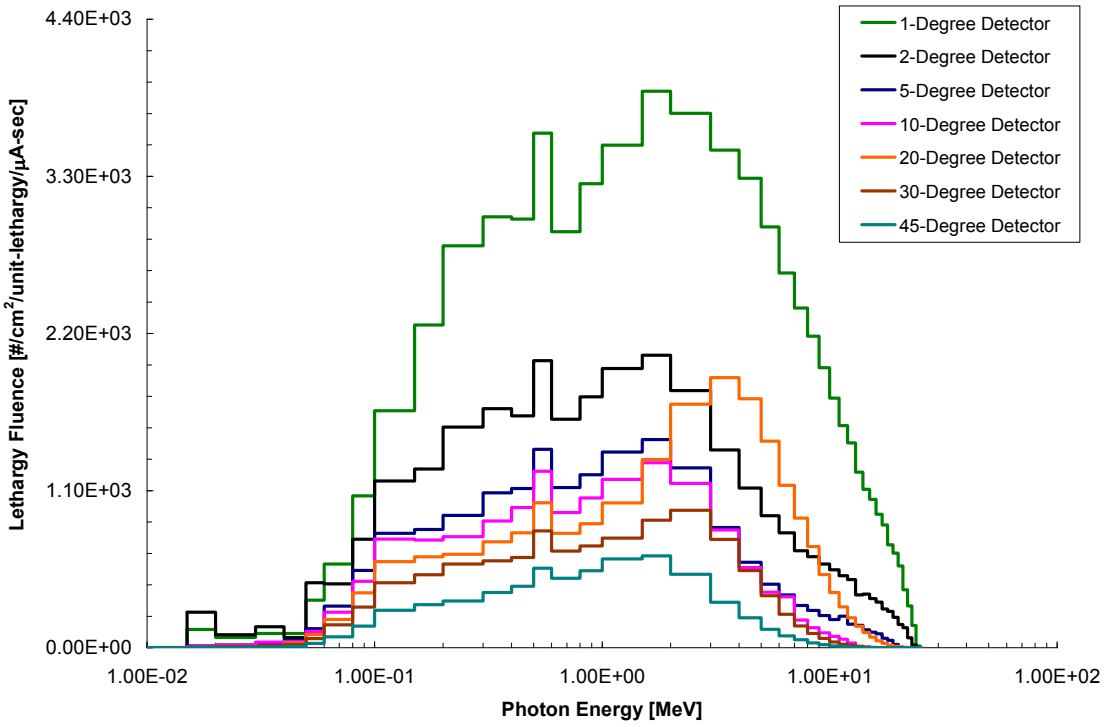

Figure E-8. Photon Spectrum (1 to 45 degree detectors) at 10 meters for the System (in Air) with a Pb Density Reduction of 10% in the Collimator.

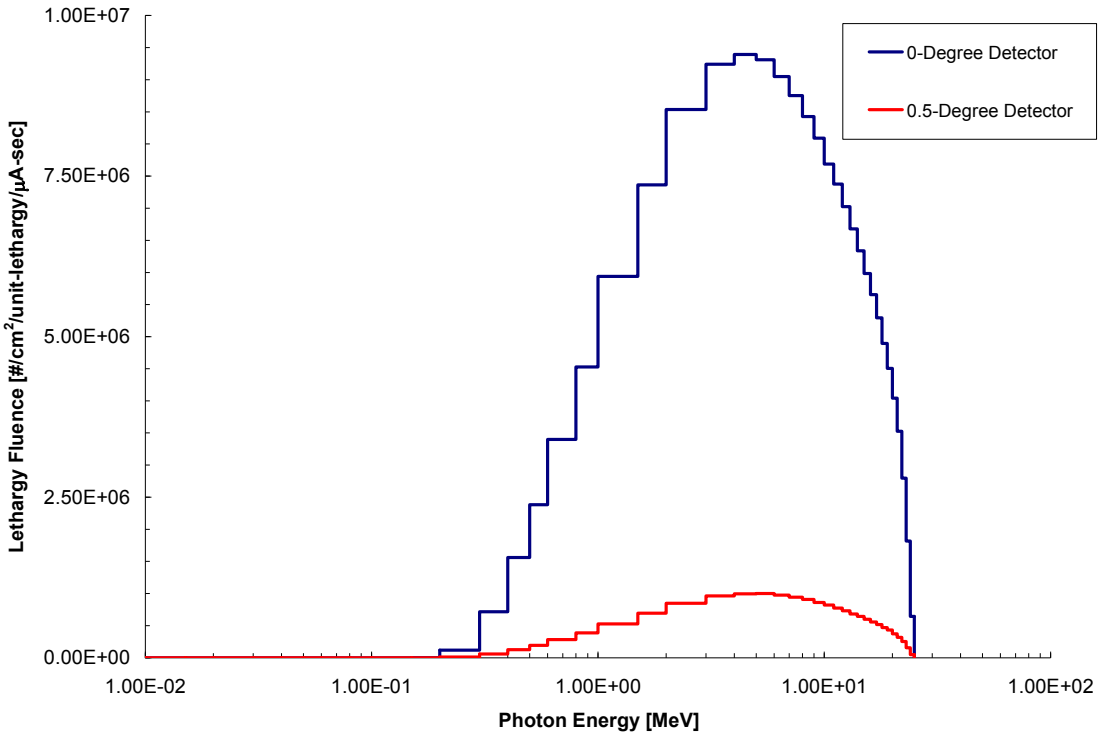

Figure E-9. Photon Spectrum (0 to 0.5 degree detectors) at 10 meters for the System (in Air) with a Pb Attenuator (t=0.50 cm) in the Beam Line.

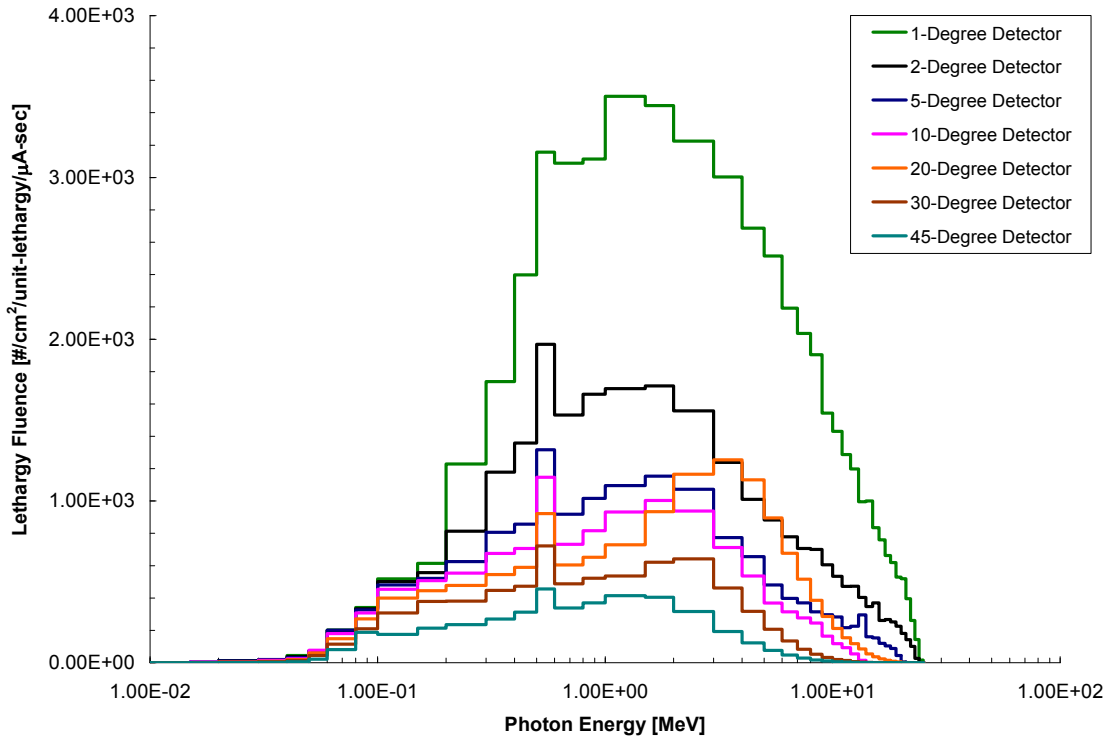

Figure E-10. Photon Spectrum (1 to 45 degree detectors) at 10 meters for the System (in Air) with a Pb Attenuator (t=0.50 cm) in the Beam Line.

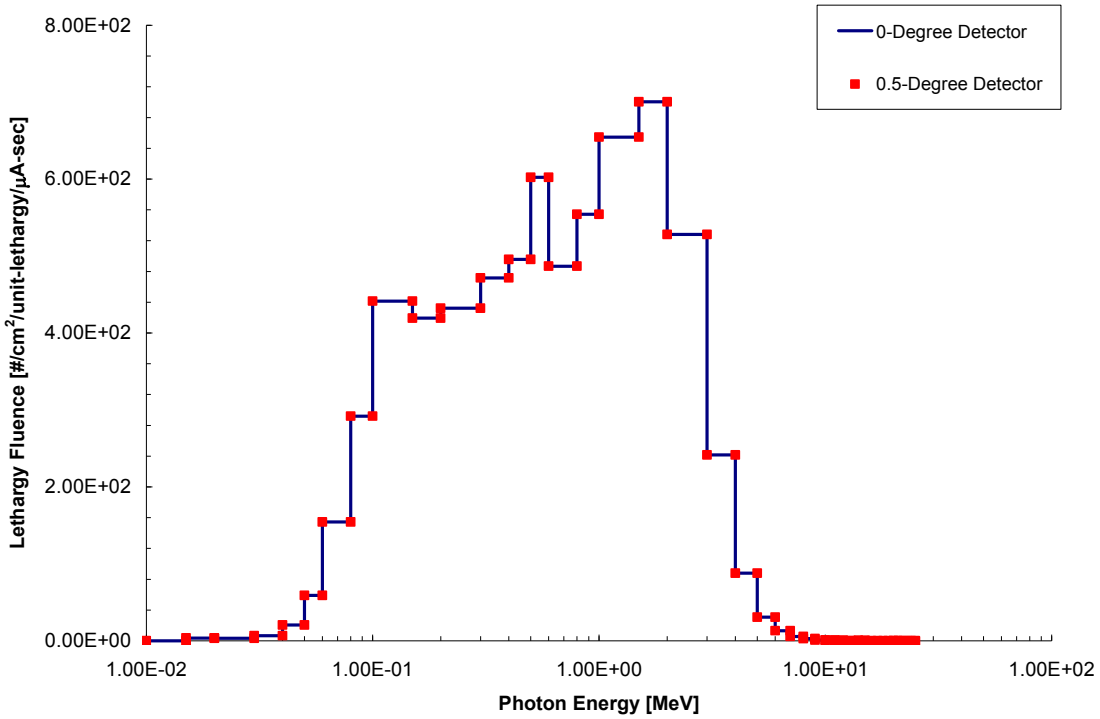

Figure E-11. Photon Spectrum (0 to 0.5 degree detectors) at 10 meters for the Collimator Only Contribution (in Air).

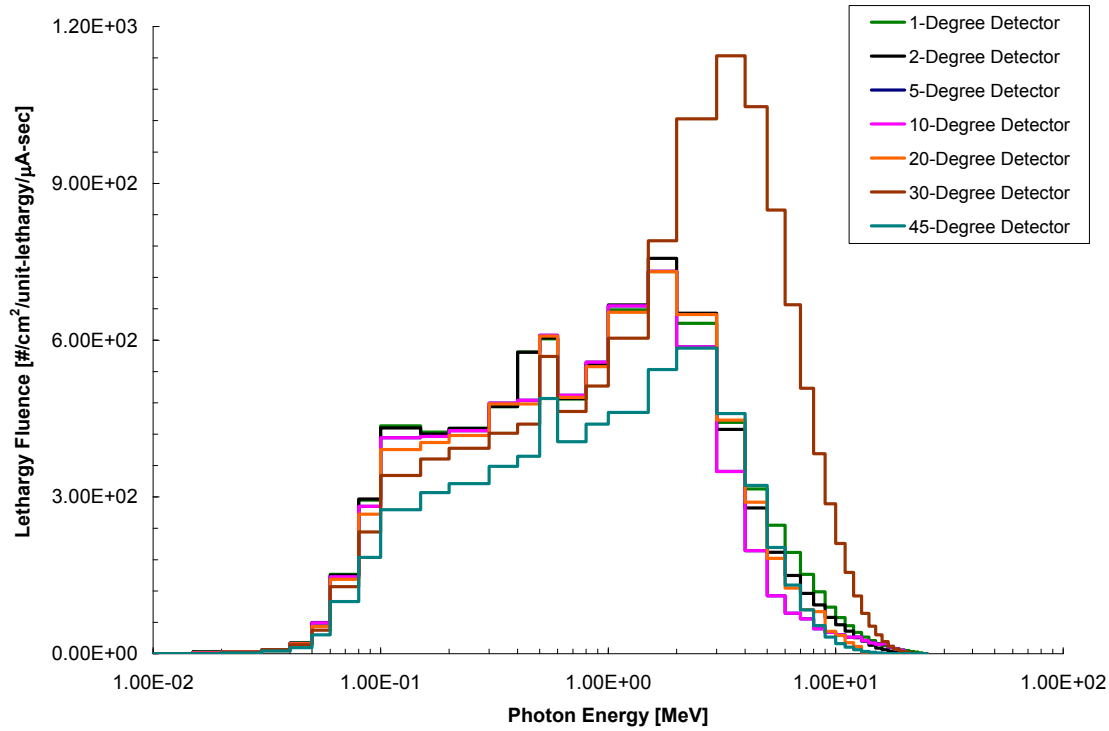

Figure E-12. Photon Spectrum (1 to 45 degree detectors) at 10 meters for the Collimator Only Contribution (in Air).

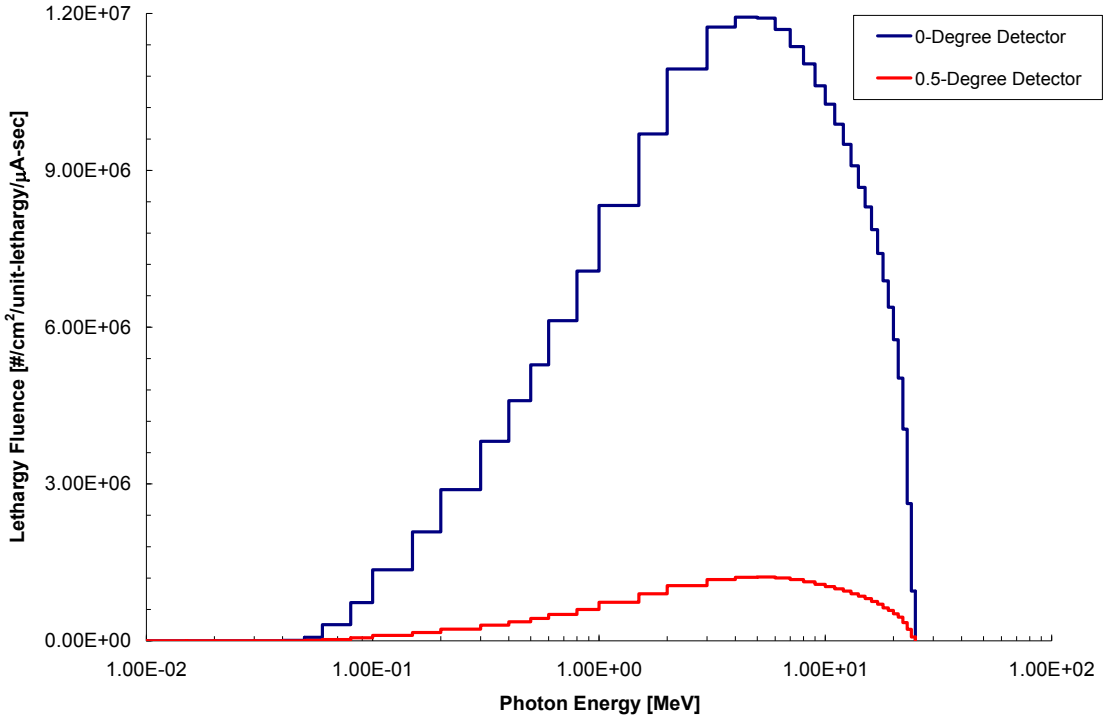

Figure E-13. Photon Spectrum (0 to 0.5 degree detectors) at 10 meters for the Beam Only Contribution (in Air).

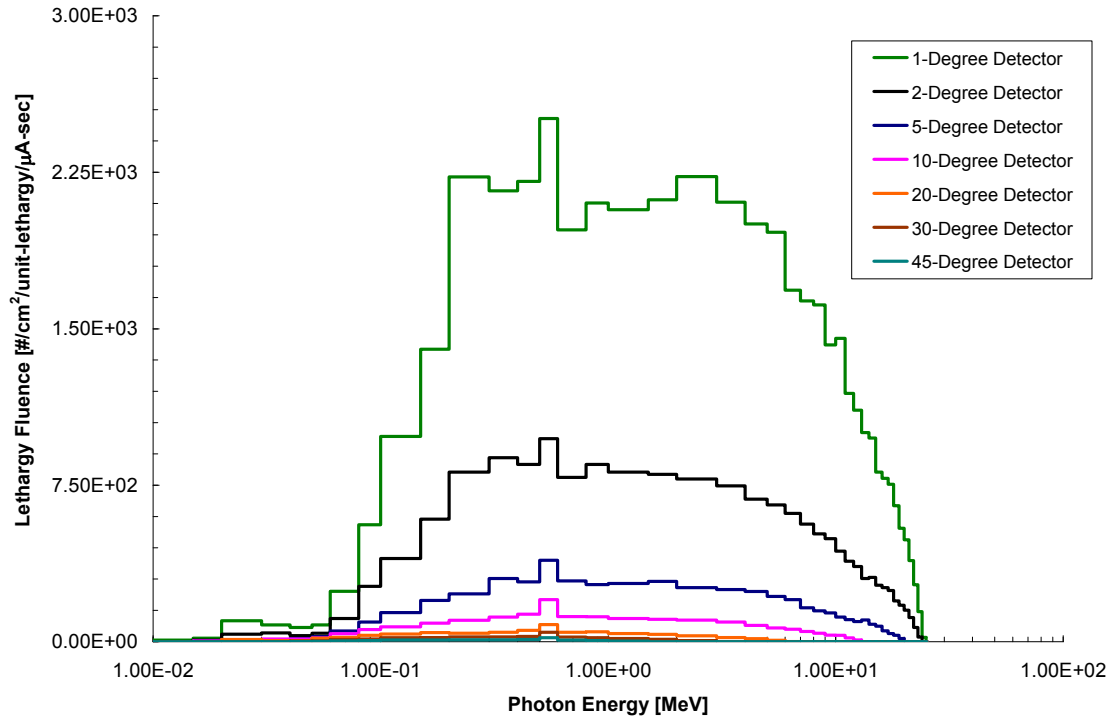

Figure E-14. Photon Spectrum (1 to 45 degree detectors) at 10 meters for the Beam Only Contribution (in Air).

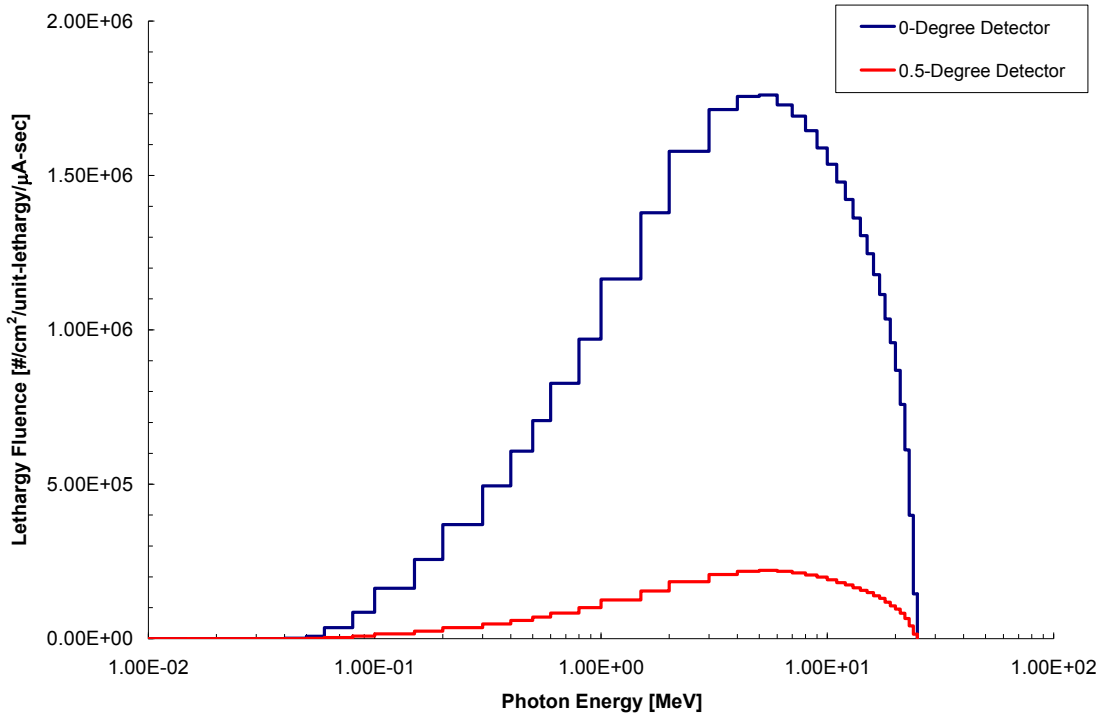

Figure E-15. Photon Spectrum (0 to 0.5 degree detectors) at 25 meters for the System in Air.

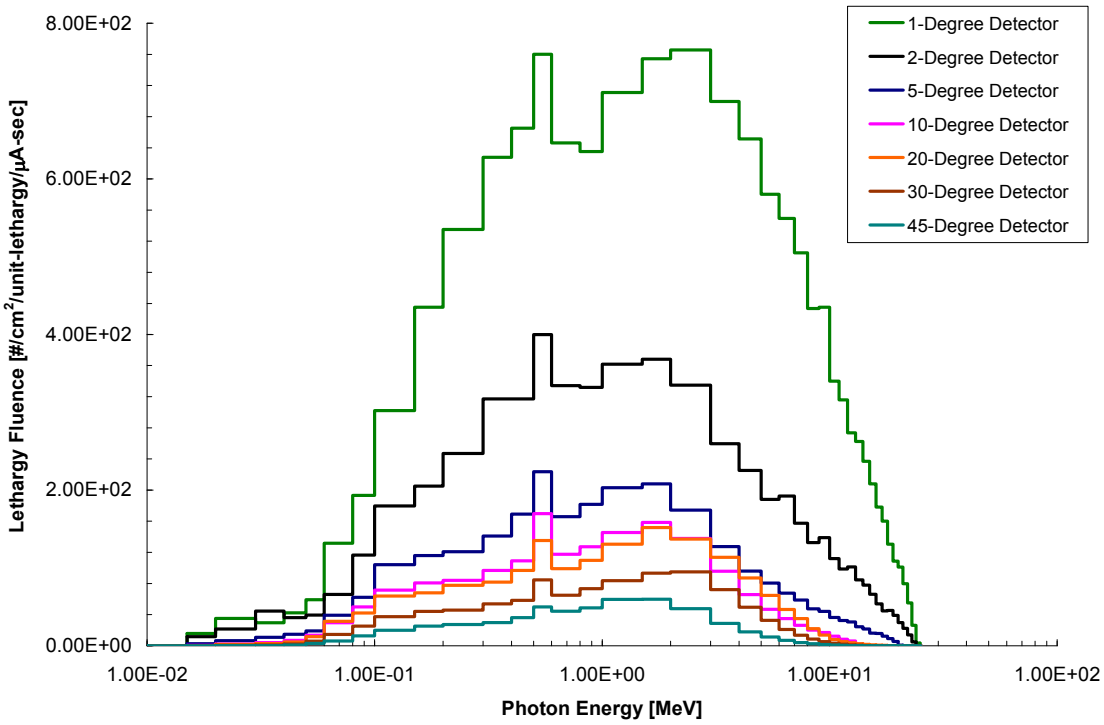

Figure E-16. Photon Spectrum (1 to 45 degree detectors) at 25 meters for the System in Air.

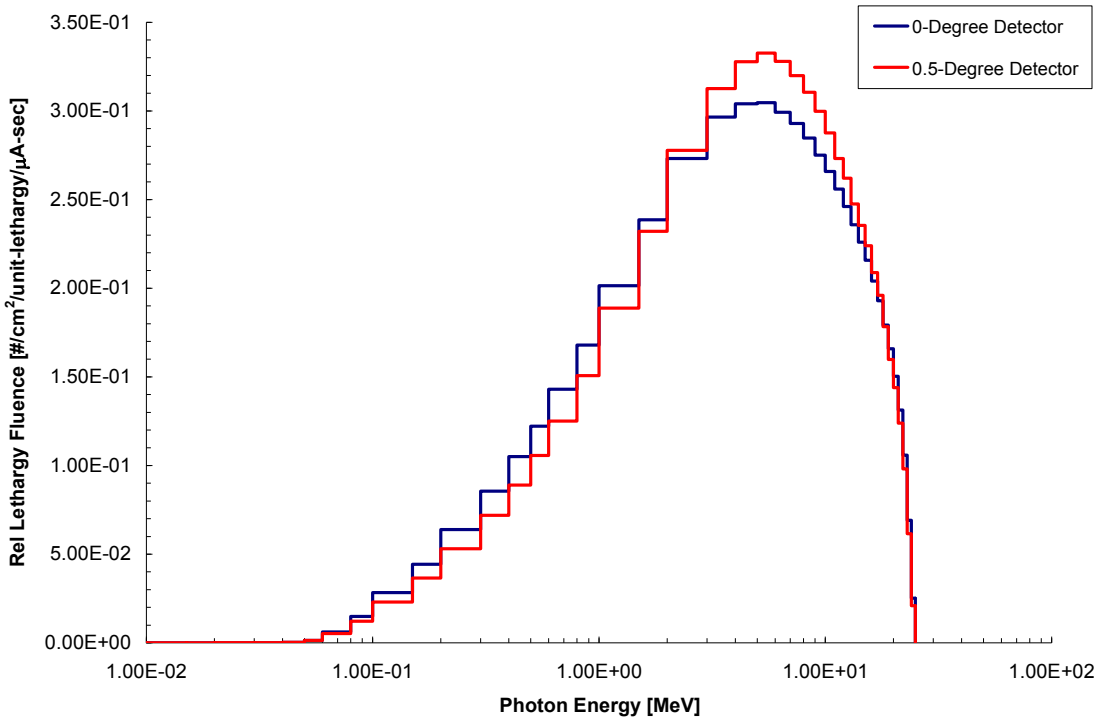

Figure E-17. Relative Photon Spectrum (0 to 0.5 degree detectors) at 25 meters for the System in Air.

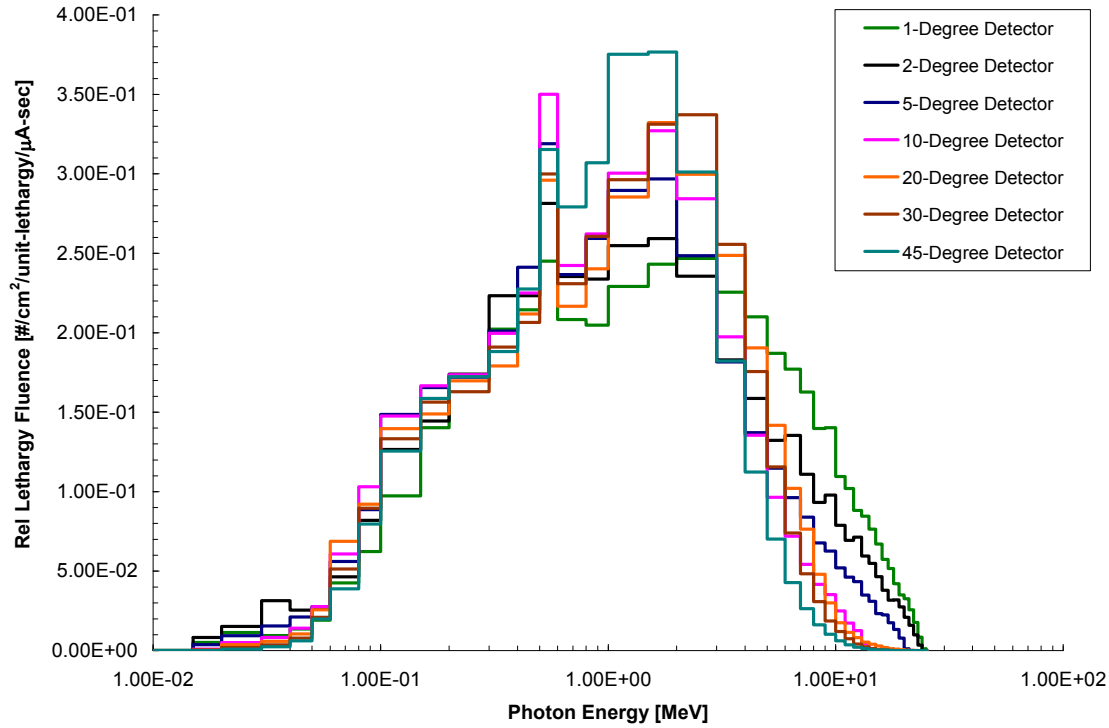

Figure E-18. Relative Photon Spectrum (1 to 45 degree detectors) at 25 meters for the System in Air.

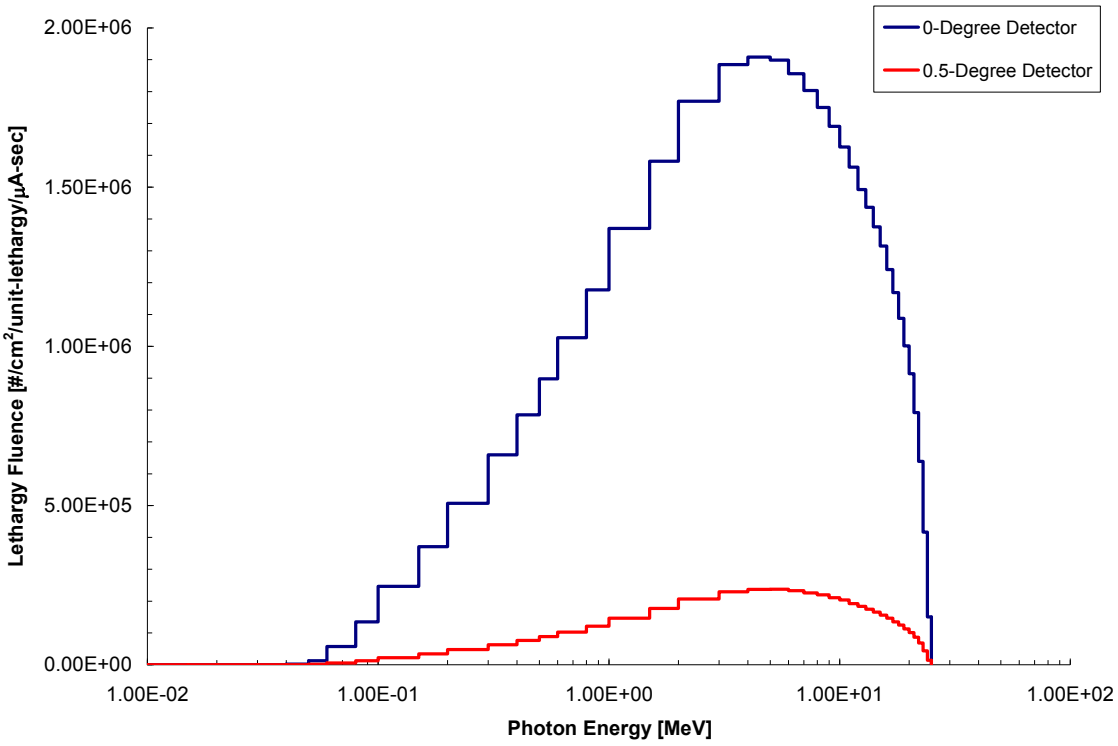

Figure E-19. Photon Spectrum (0 to 0.5 degree detectors) at 25 meters for the System in Vacuo.

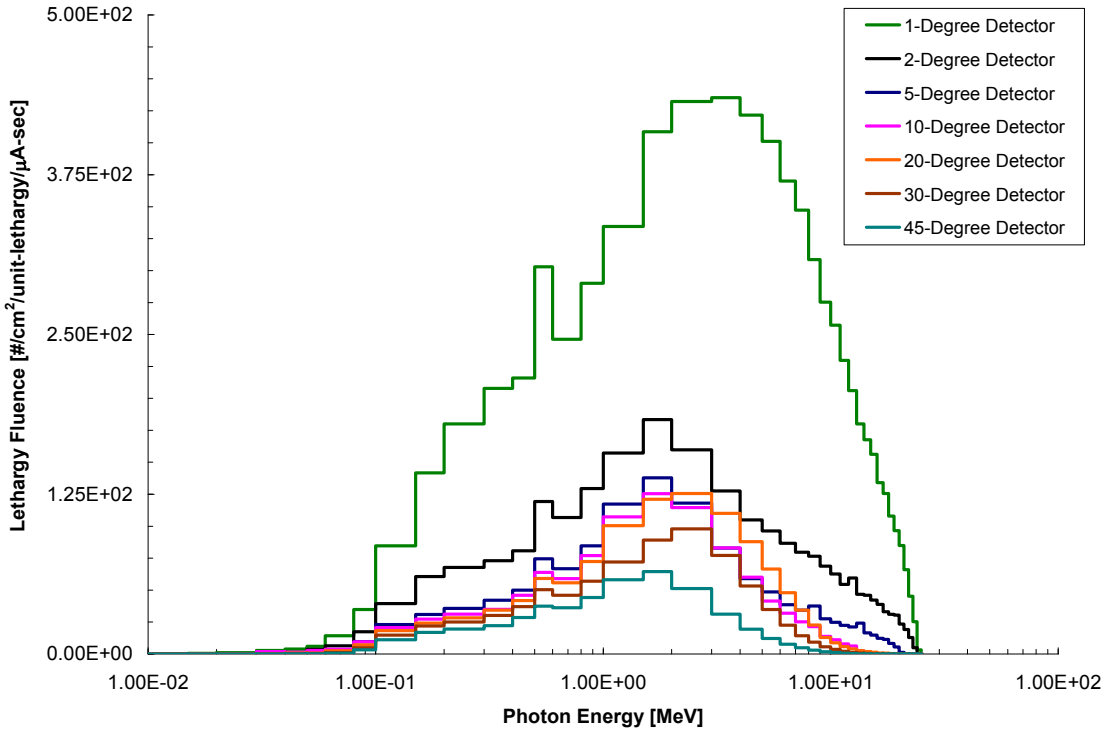

Figure E-20. Photon Spectrum (1 to 45 degree detectors) at 25 meters for the System in Vacuo.

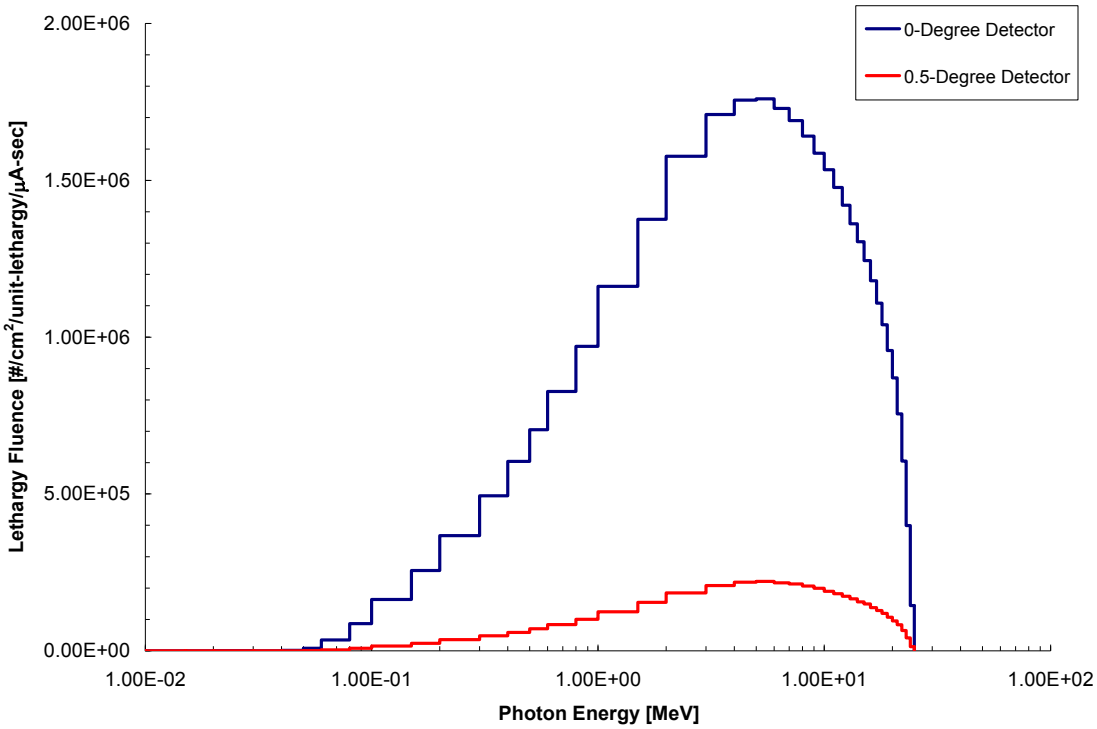

Figure E-21. Photon Spectrum (0 to 0.5 degree detectors) at 25 meters for the System (in Air) with a Pb Density Reduction of 10% in the Collimator.

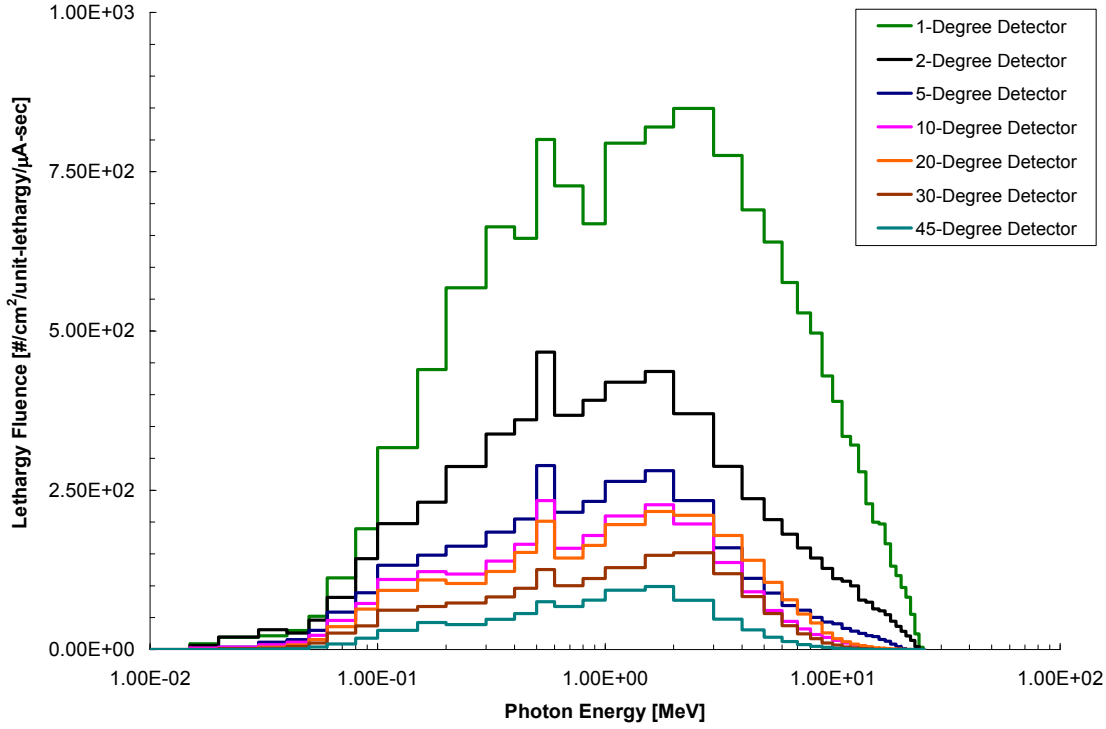

Figure E-22. Photon Spectrum (1 to 45 degree detectors) at 25 meters for the System (in Air) with a Pb Density Reduction of 10% in the Collimator.

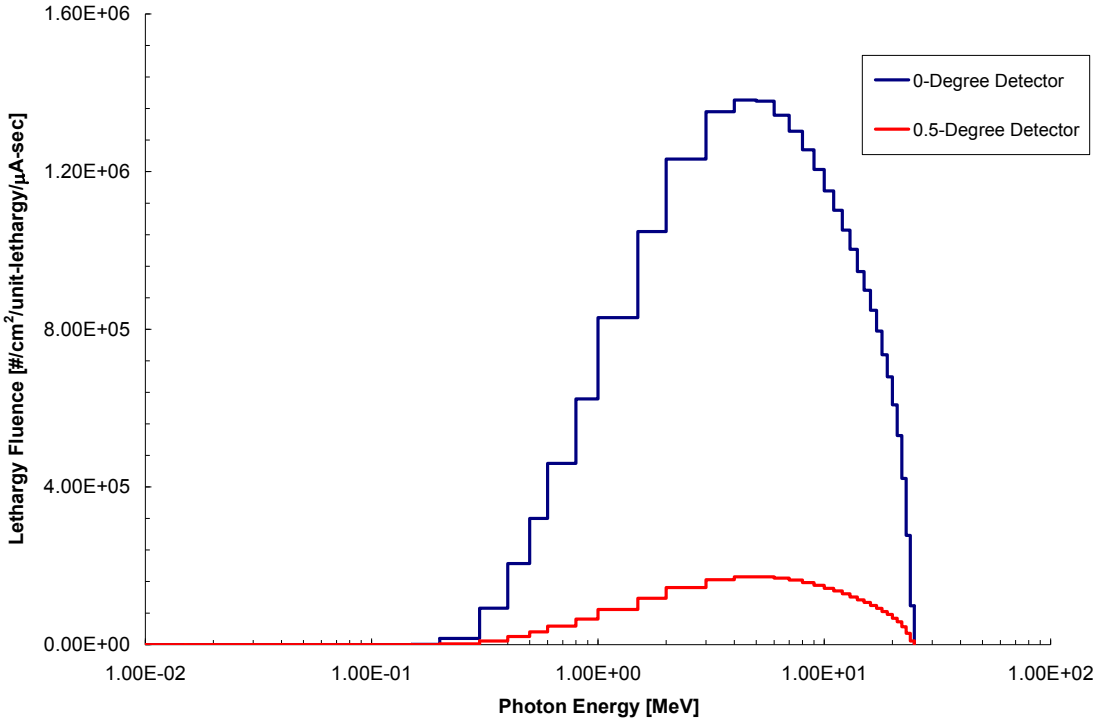

Figure E-23. Photon Spectrum (0 to 0.5 degree detectors) at 25 meters for the System (in Air) with a Pb Attenuator (t=0.50 cm) in the Beam Line.

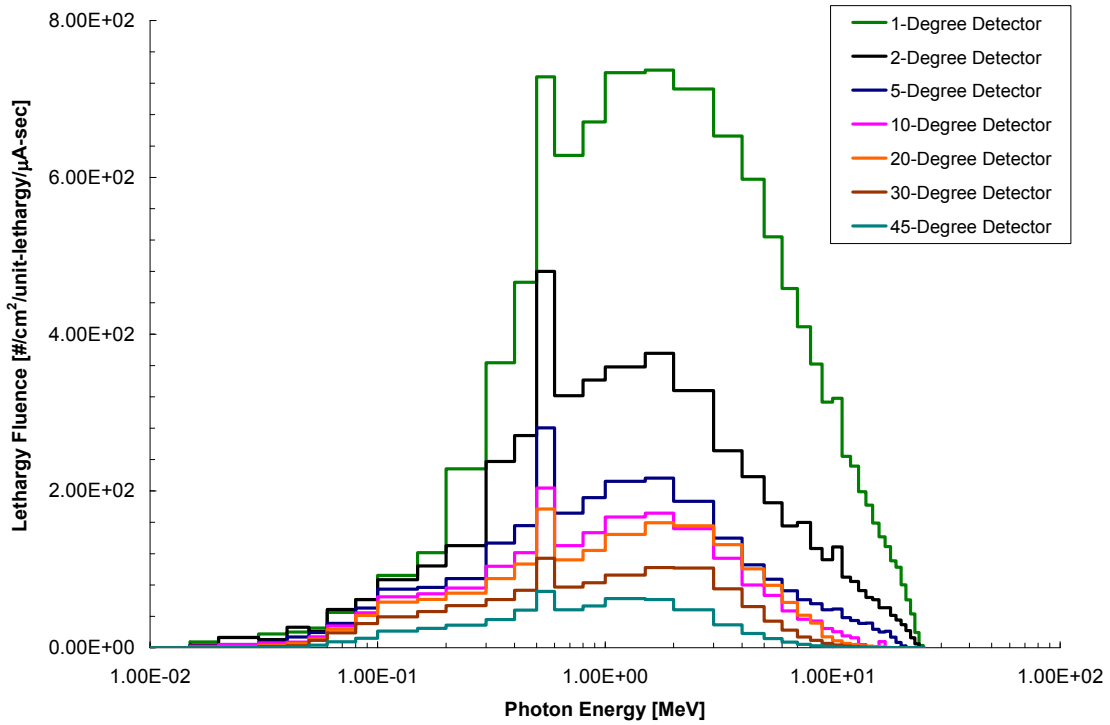

Figure E-24. Photon Spectrum (1 to 45 degree detectors) at 25 meters for the System (in Air) with a Pb Attenuator (t=0.50 cm) in the Beam Line.

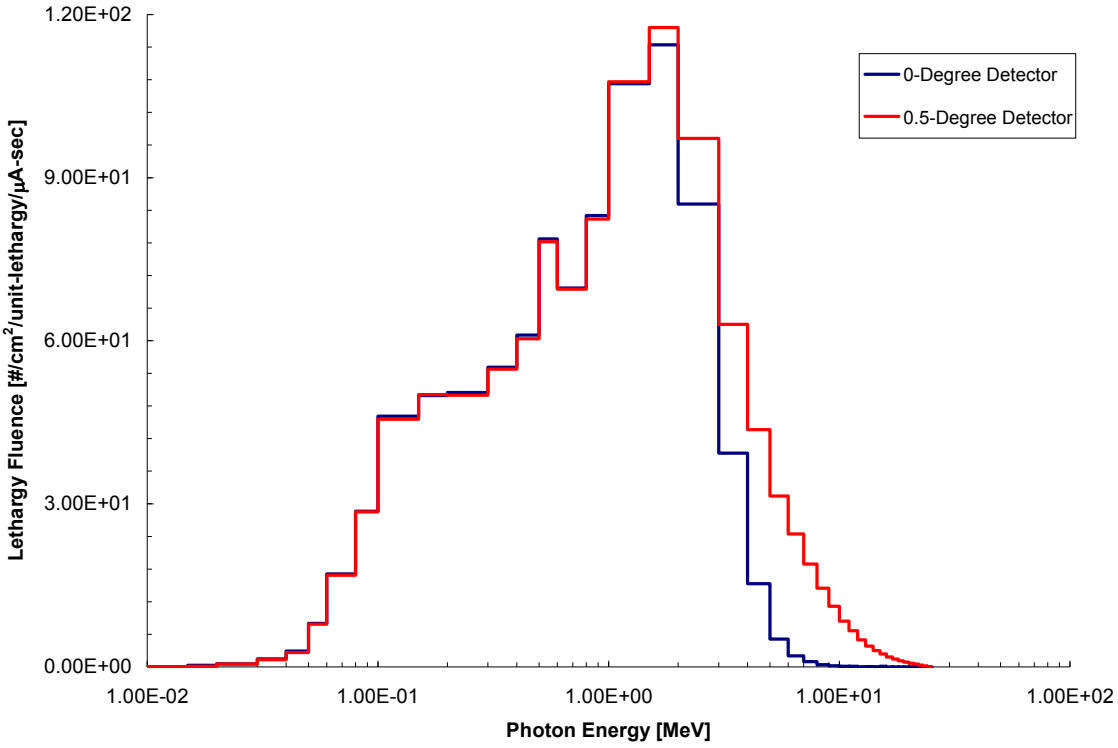

Figure E-25. Photon Spectrum (0 to 0.5 degree detectors) at 25 meters for the Collimator Only Contribution (in Air).

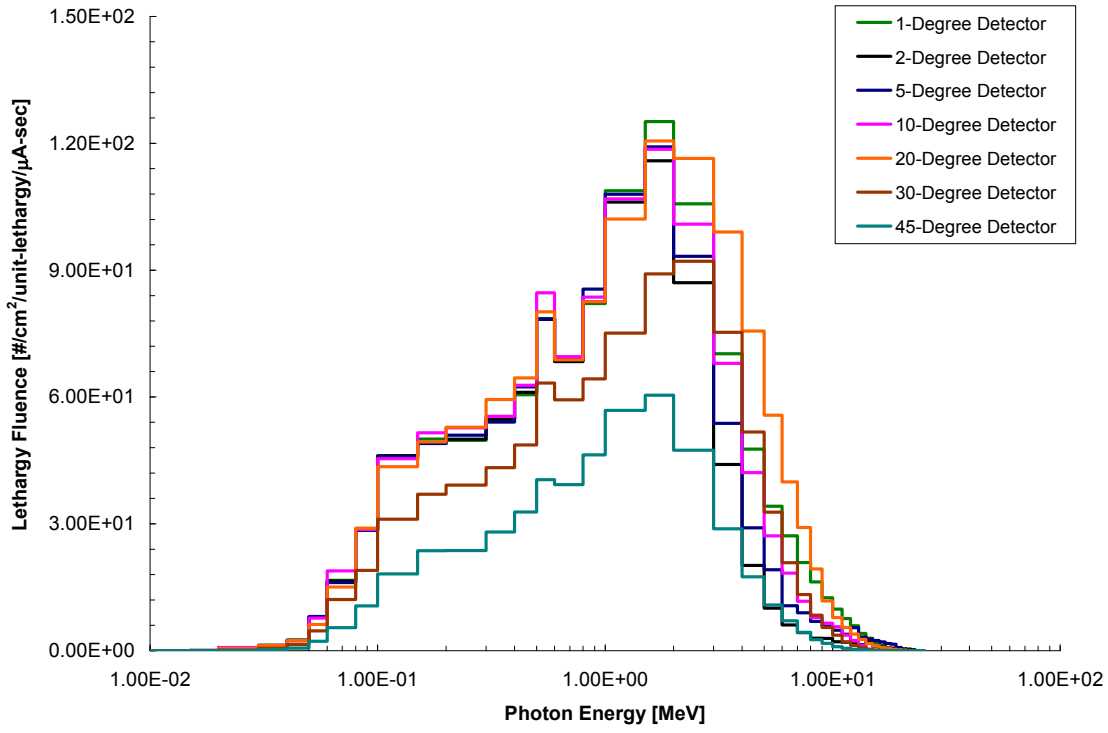

Figure E-26. Photon Spectrum (1 to 45 degree detectors) at 25 meters for the Collimator Only Contribution (in Air).

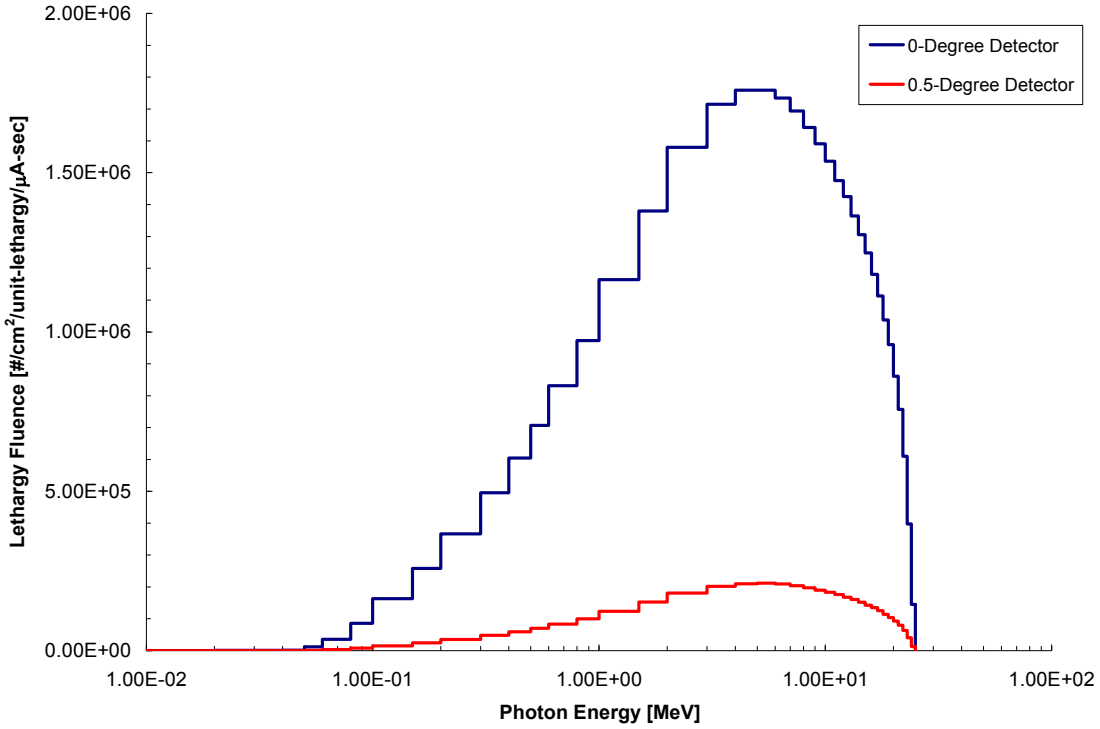

Figure E-27. Photon Spectrum (0 to 0.5 degree detectors) at 25 meters for the Beam Only Contribution (in Air).

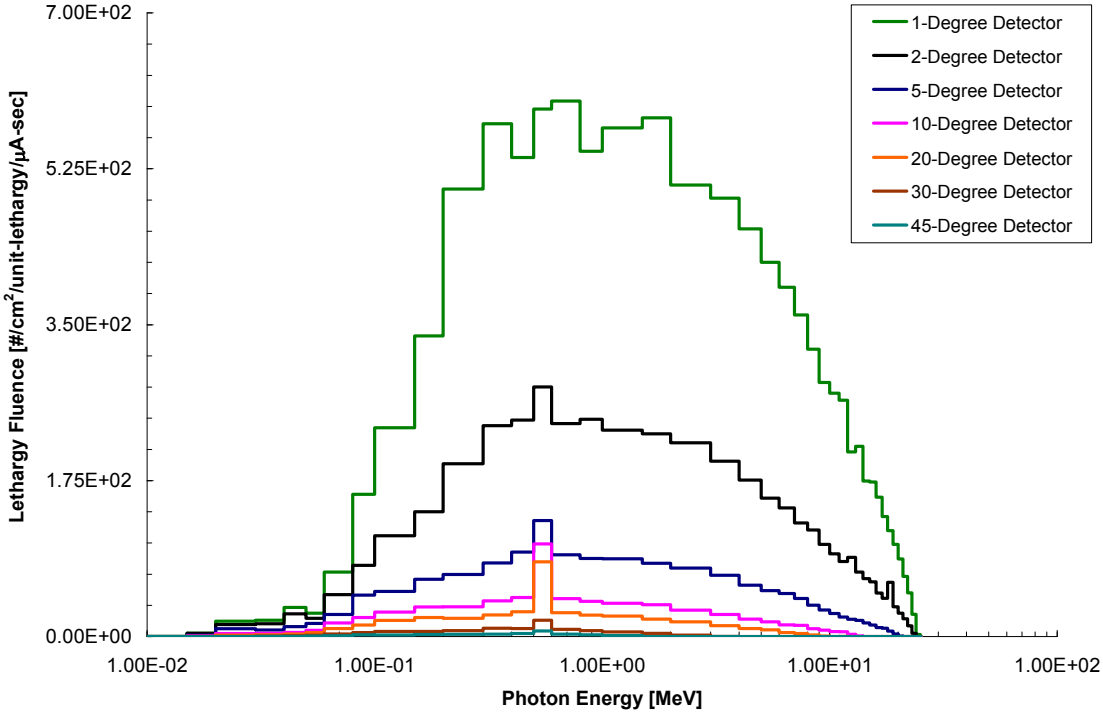

Figure E-28. Photon Spectrum (1 to 45 degree detectors) at 25 meters for the Beam Only Contribution (in Air).

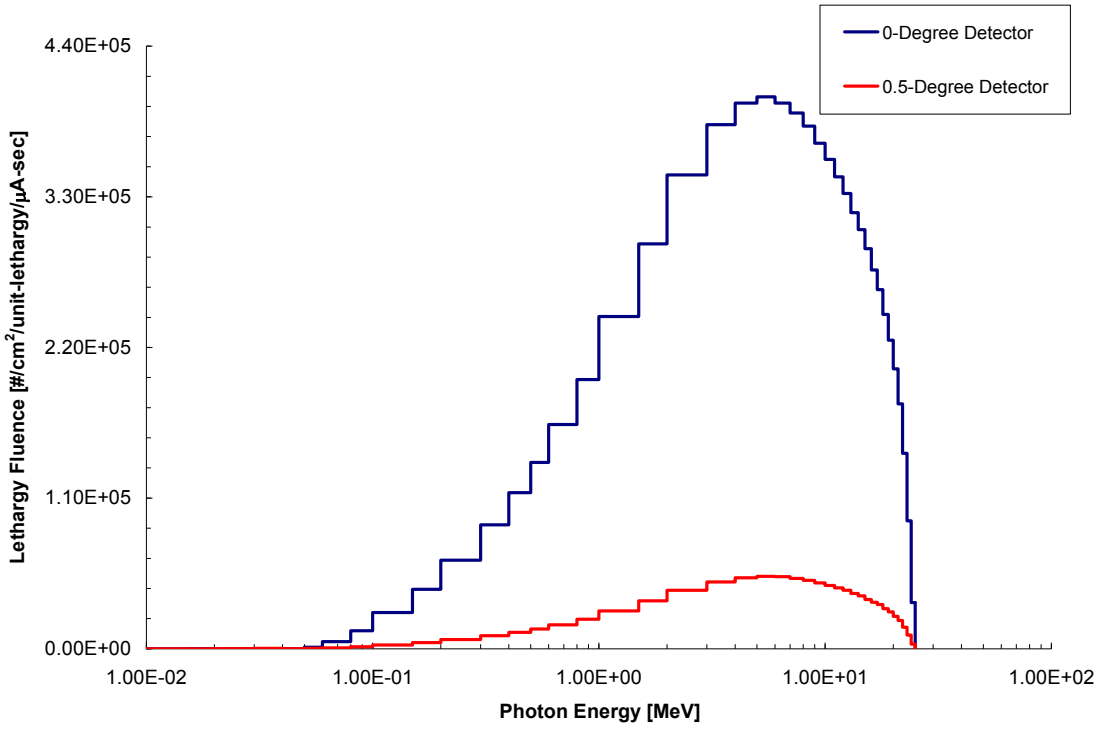

Figure E-29. Photon Spectrum (0 to 0.5 degree detectors) at 50 meters for the System in Air.

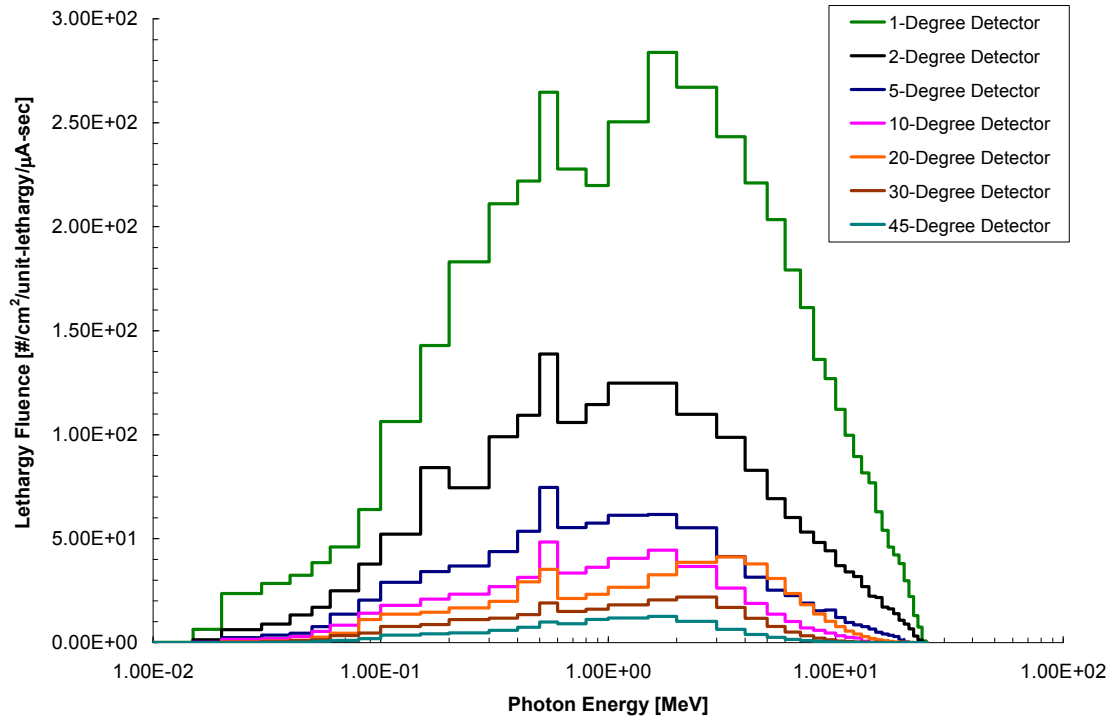

Figure E-30. Photon Spectrum (1 to 45 degree detectors) at 50 meters for the System in Air.

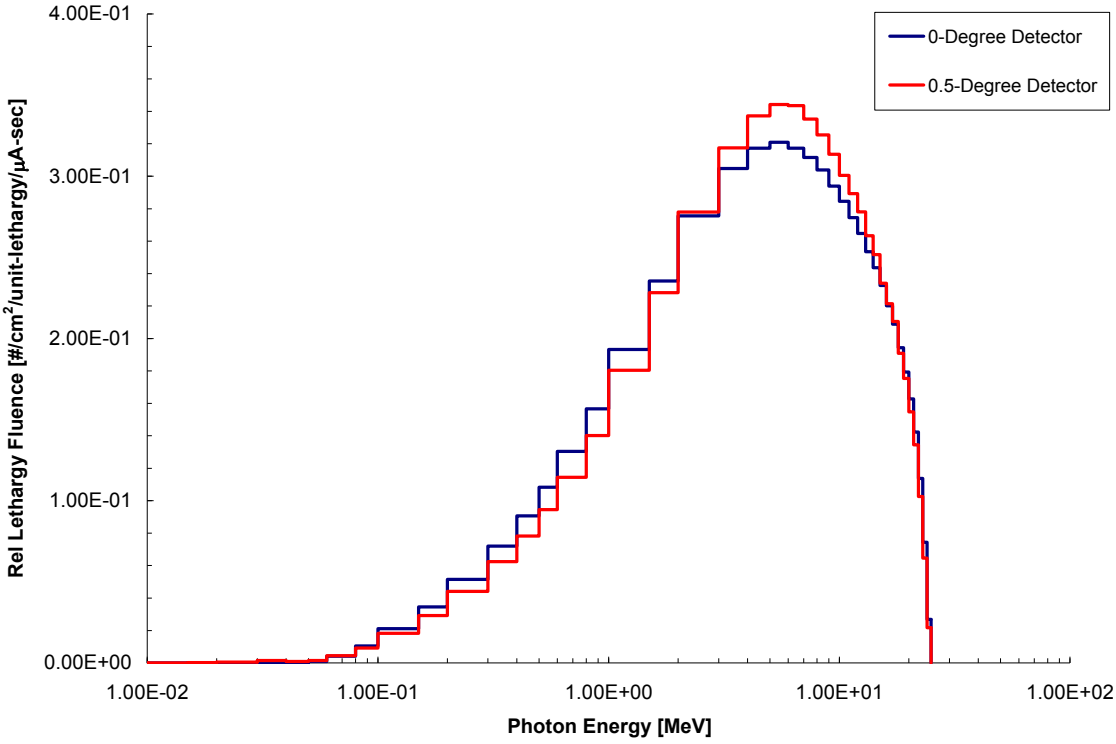

Figure E-31. Relative Photon Spectrum (0 to 0.5 degree detectors) at 50 meters for the System in Air.

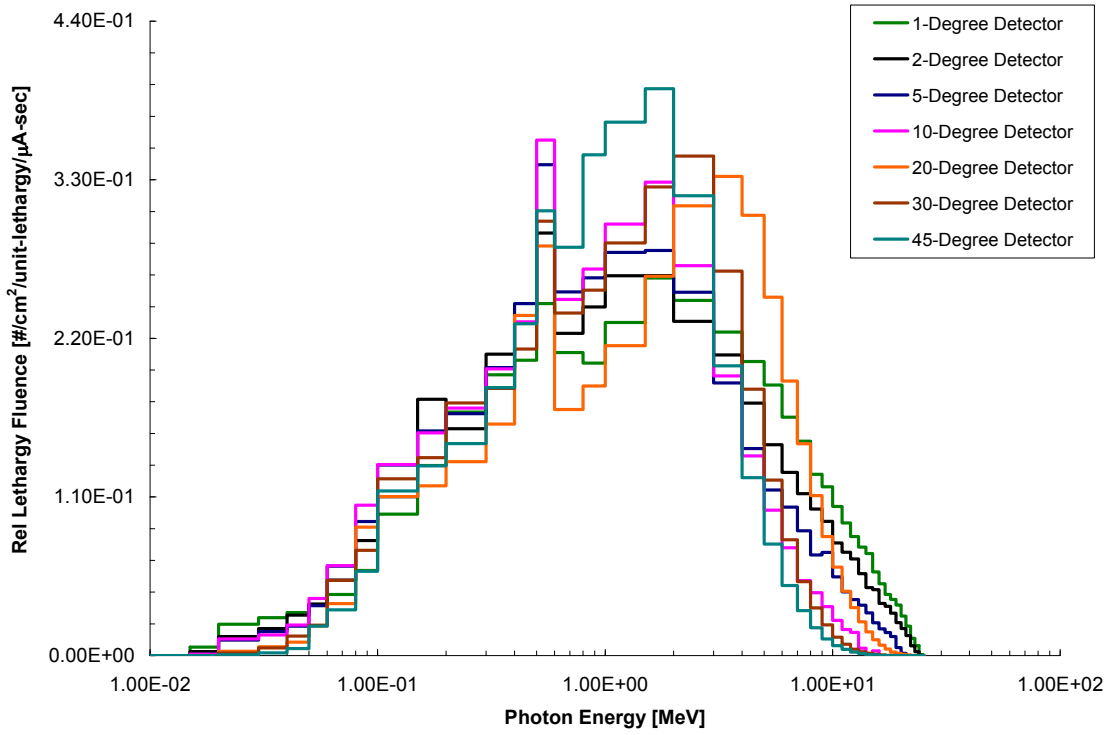

Figure E-32. Relative Photon Spectrum (1 to 45 degree detectors) at 50 meters for the System in Air.

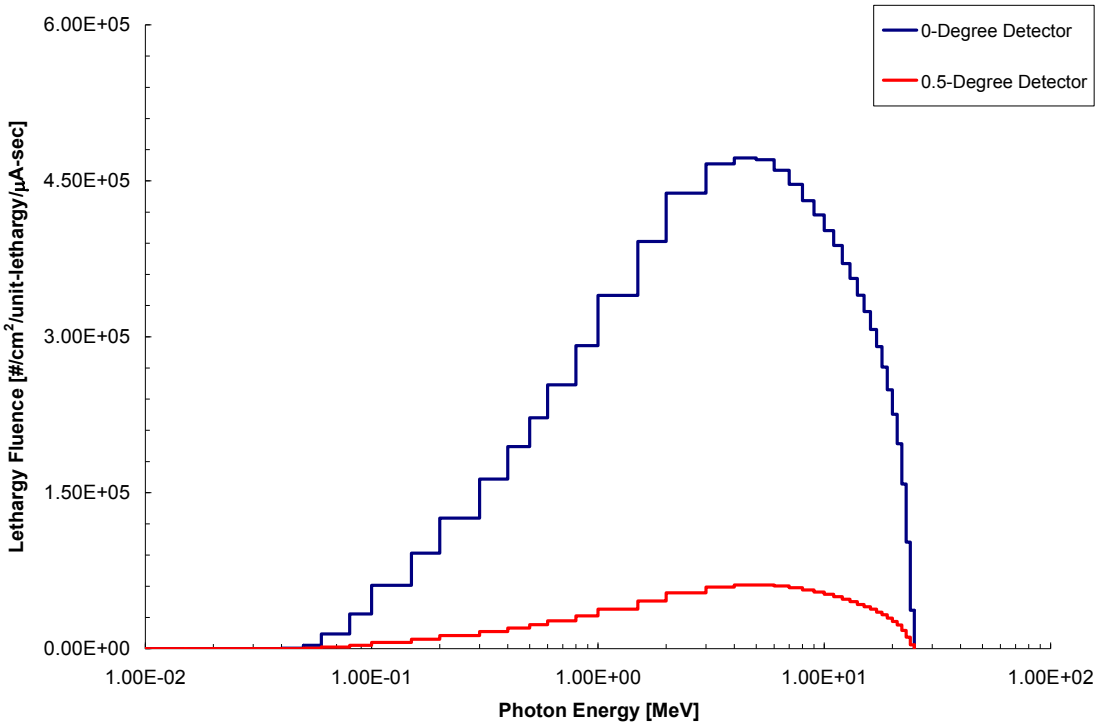

Figure E-33. Photon Spectrum (0 to 0.5 degree detectors) at 50 meters for the System in Vacuo.

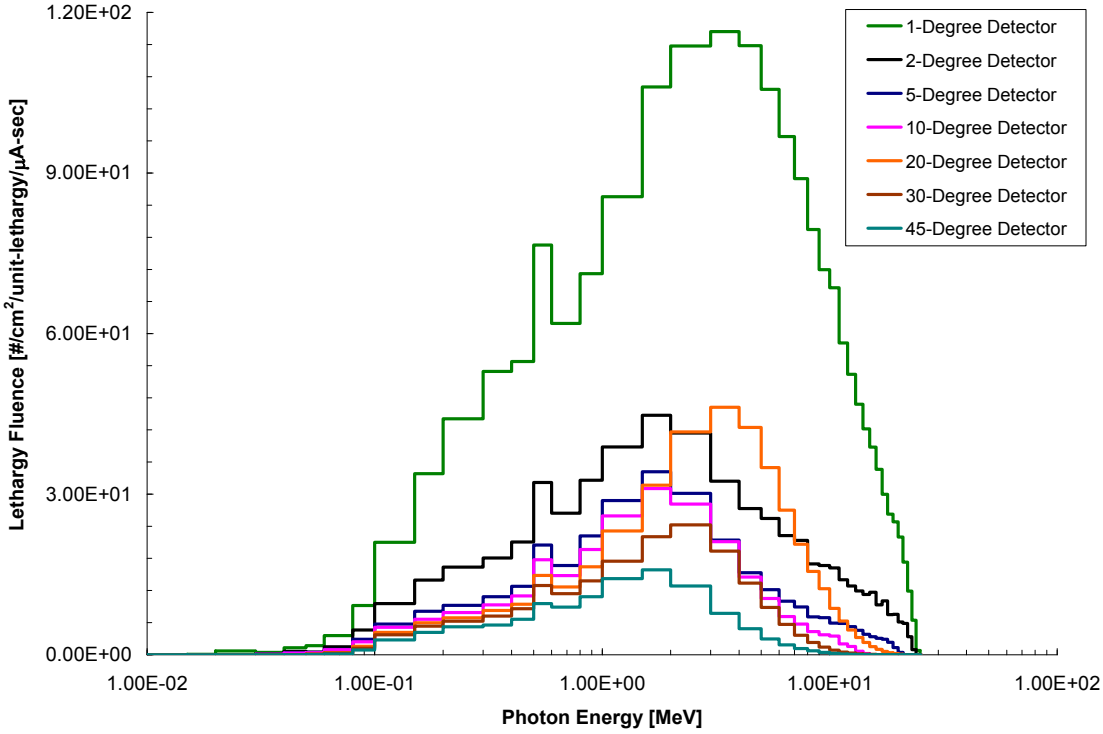

Figure E-34. Photon Spectrum (1 to 45 degree detectors) at 50 meters for the System in Vacuo.

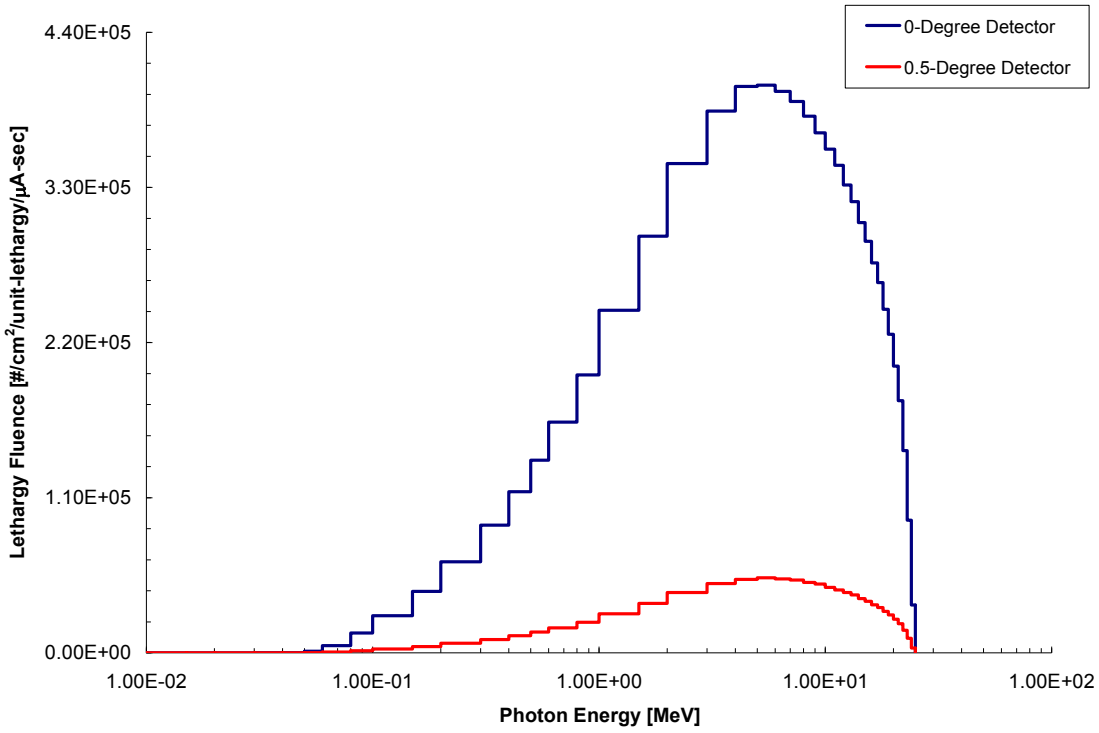

Figure E-35. Photon Spectrum (0 to 0.5 degree detectors) at 50 meters for the System (in Air) with a Pb Density Reduction of 10% in the Collimator.

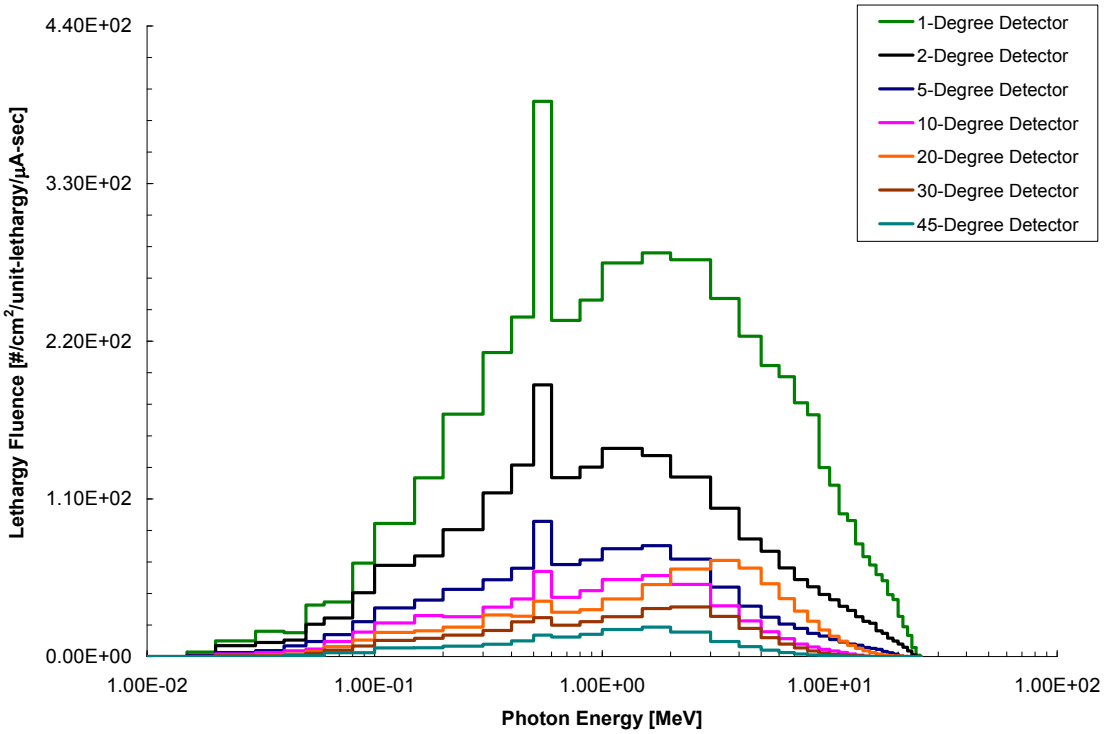

Figure E-36. Photon Spectrum (1 to 45 degree detectors) at 50 meters for the System (in Air) with a Pb Density Reduction of 10% in the Collimator.

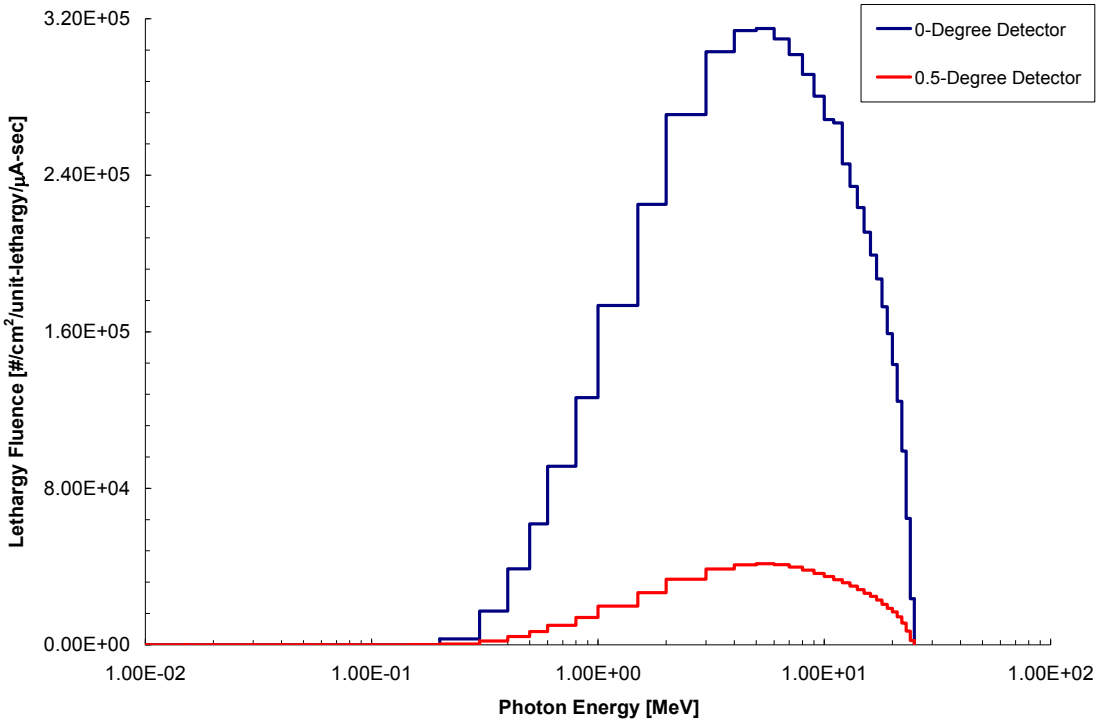

Figure E-37. Photon Spectrum (0 to 0.5 degree detectors) at 50 meters for the System (in Air) with a Pb Attenuator (t=0.50 cm) in the Beam Line.

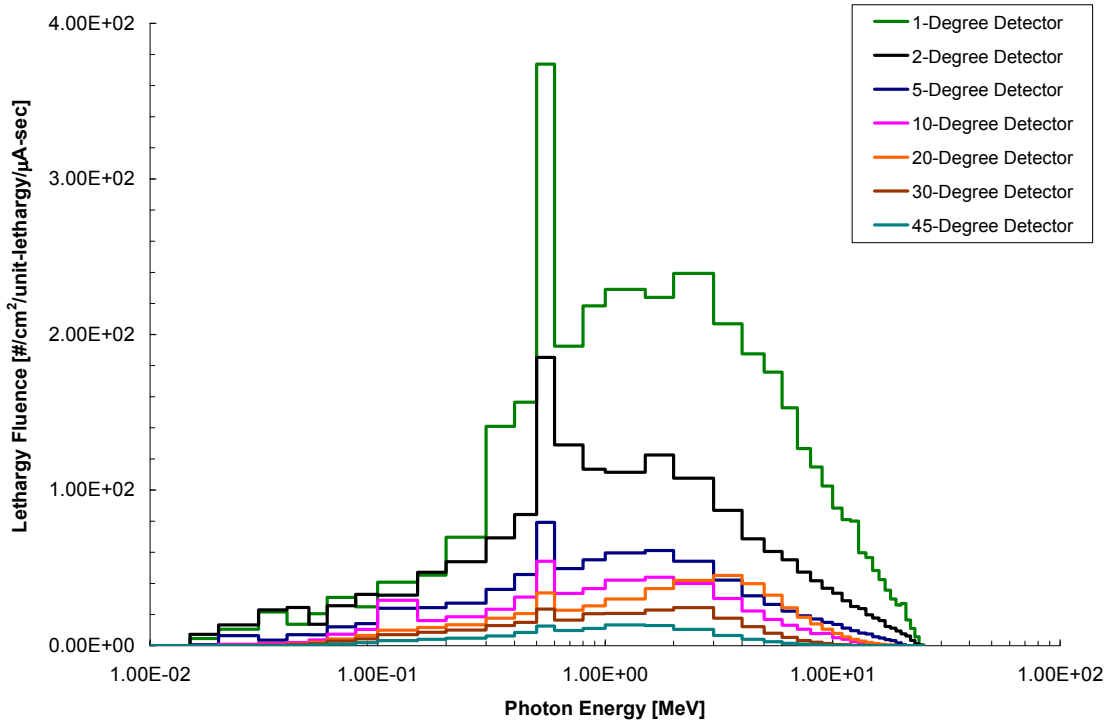

Figure E-38. Photon Spectrum (1 to 45 degree detectors) at 50 meters for the System (in Air) with a Pb Attenuator (t=0.50 cm) in the Beam Line.

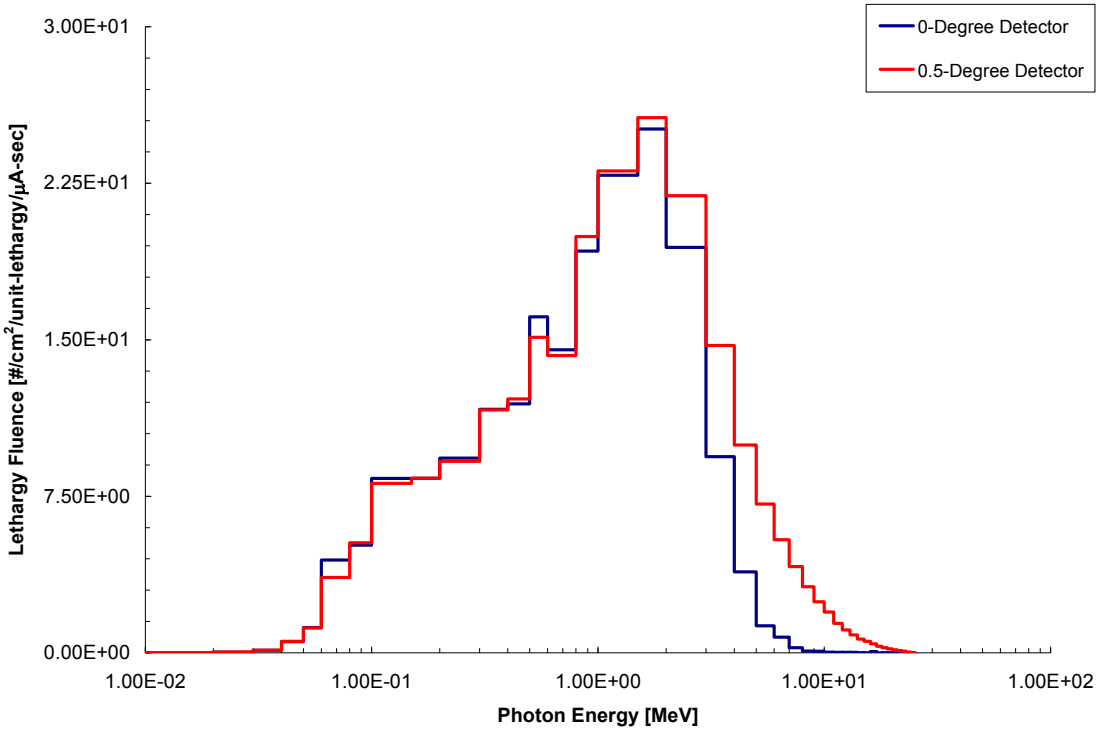

Figure E-39. Photon Spectrum (0 to 0.5 degree detectors) at 50 meters for the Collimator Only Contribution (in Air).

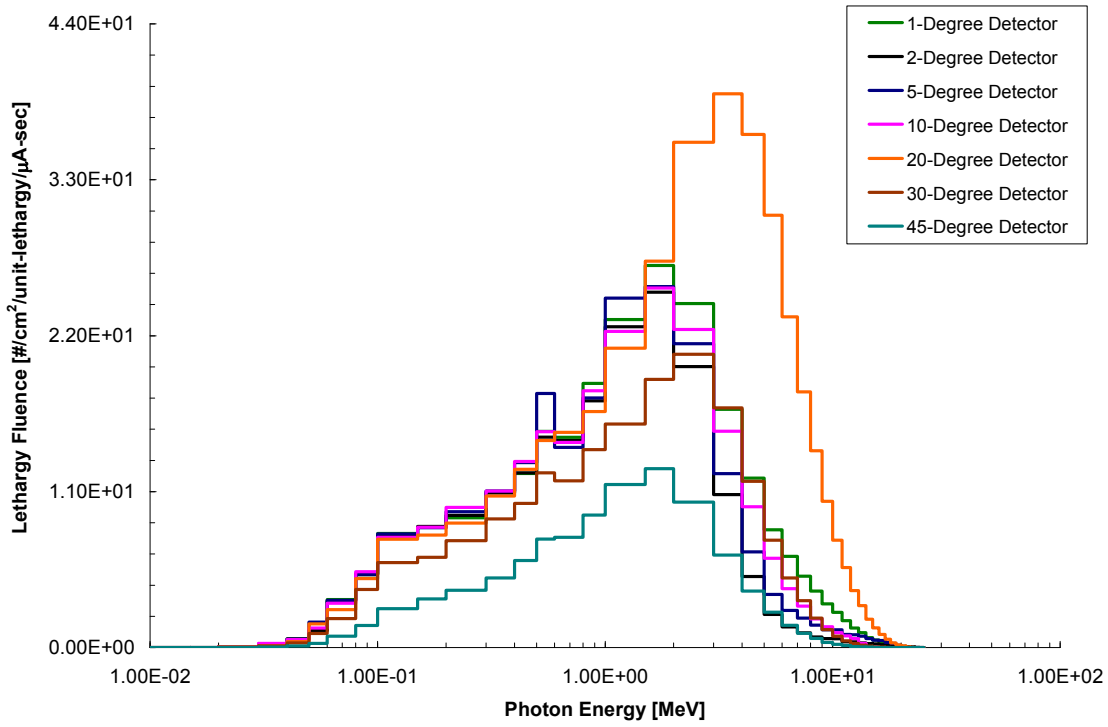

Figure E-40. Photon Spectrum (1 to 45 degree detectors) at 50 meters for the Collimator Only Contribution (in Air).

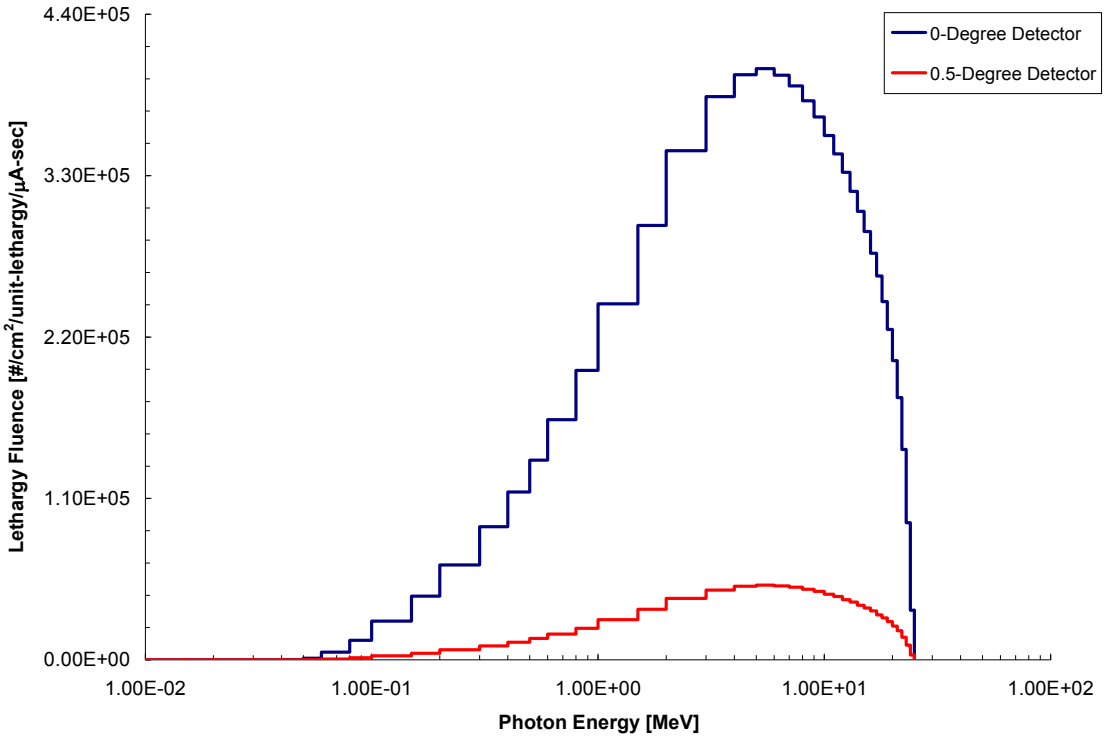

Figure E-41. Photon Spectrum (0 to 0.5 degree detectors) at 50 meters for the Beam Only Contribution (in Air).

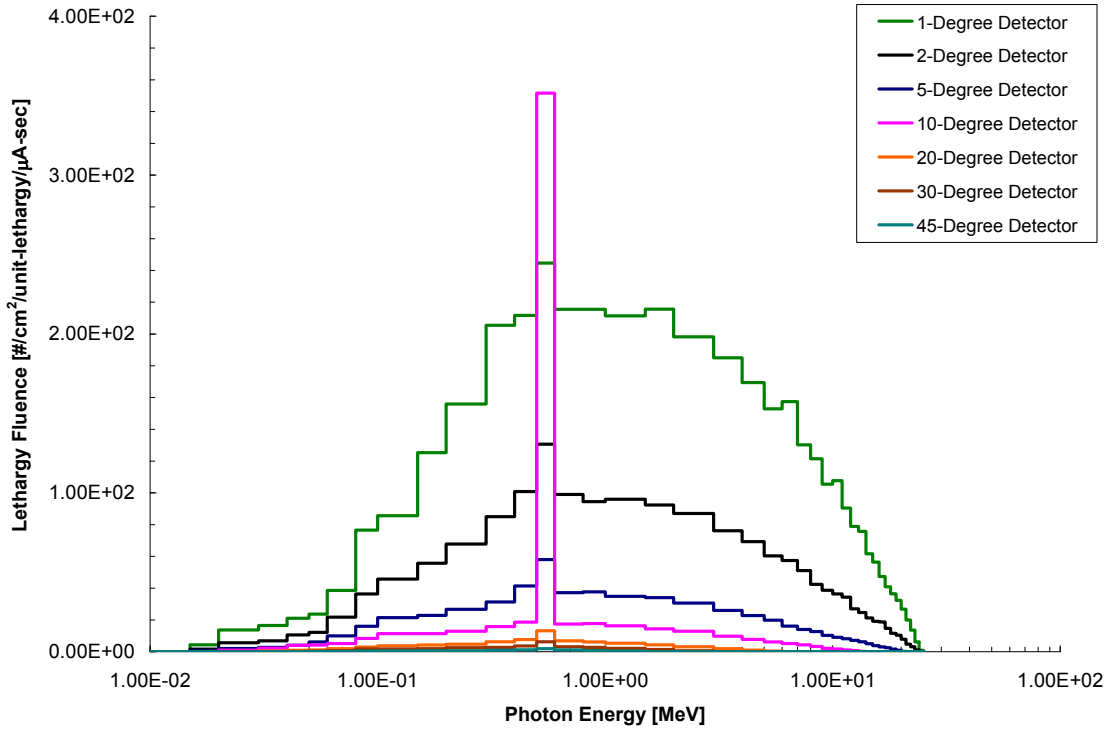

Figure E-42. Photon Spectrum (1 to 45 degree detectors) at 50 meters for the Beam Only Contribution (in Air).

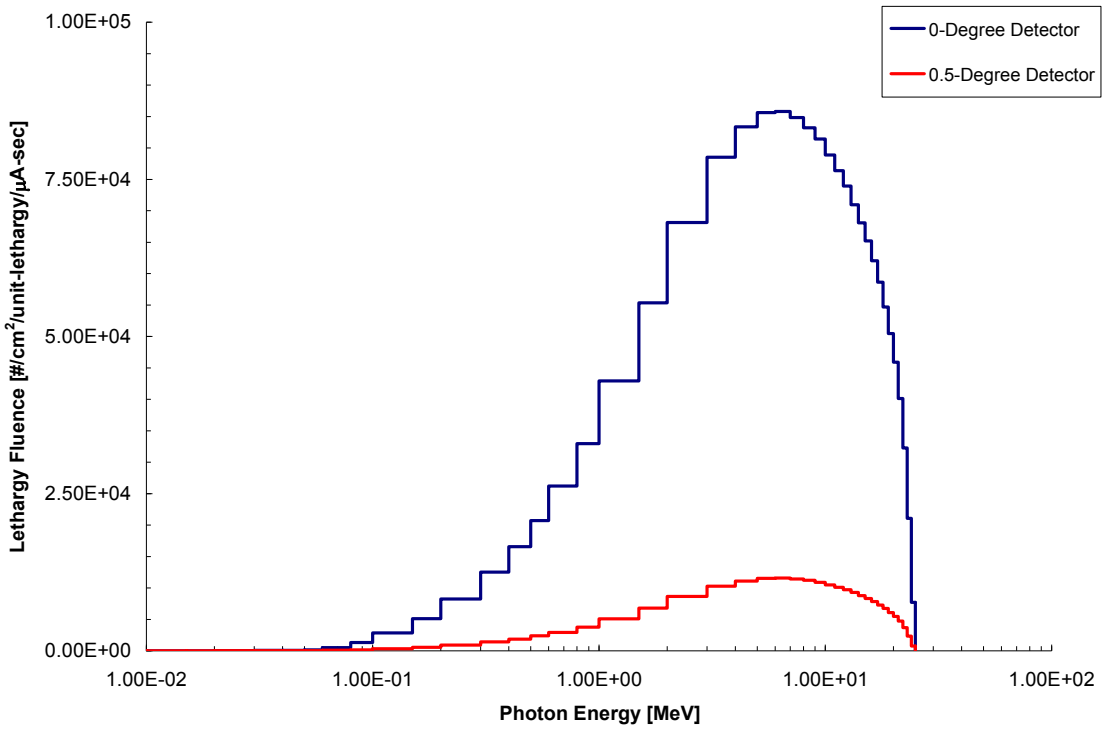

Figure E-43. Photon Spectrum (0 to 0.5 degree detectors) at 100 meters for the System in Air.

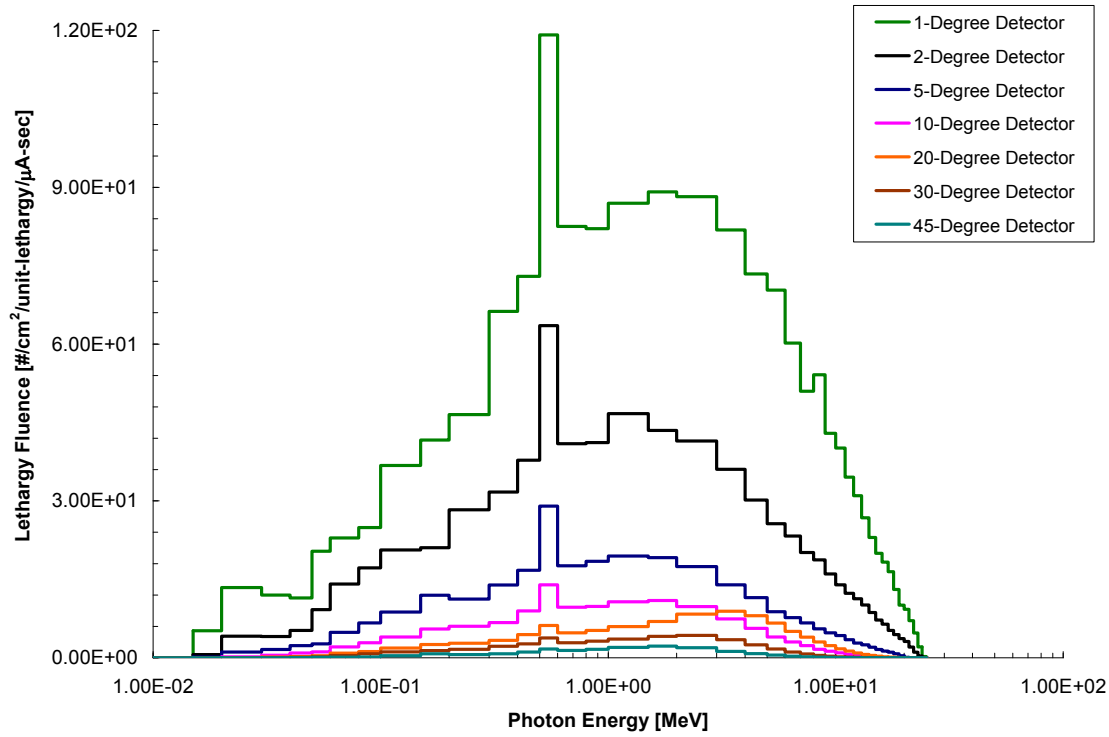

Figure E-44. Photon Spectrum (1 to 45 degree detectors) at 100 meters for the System in Air.

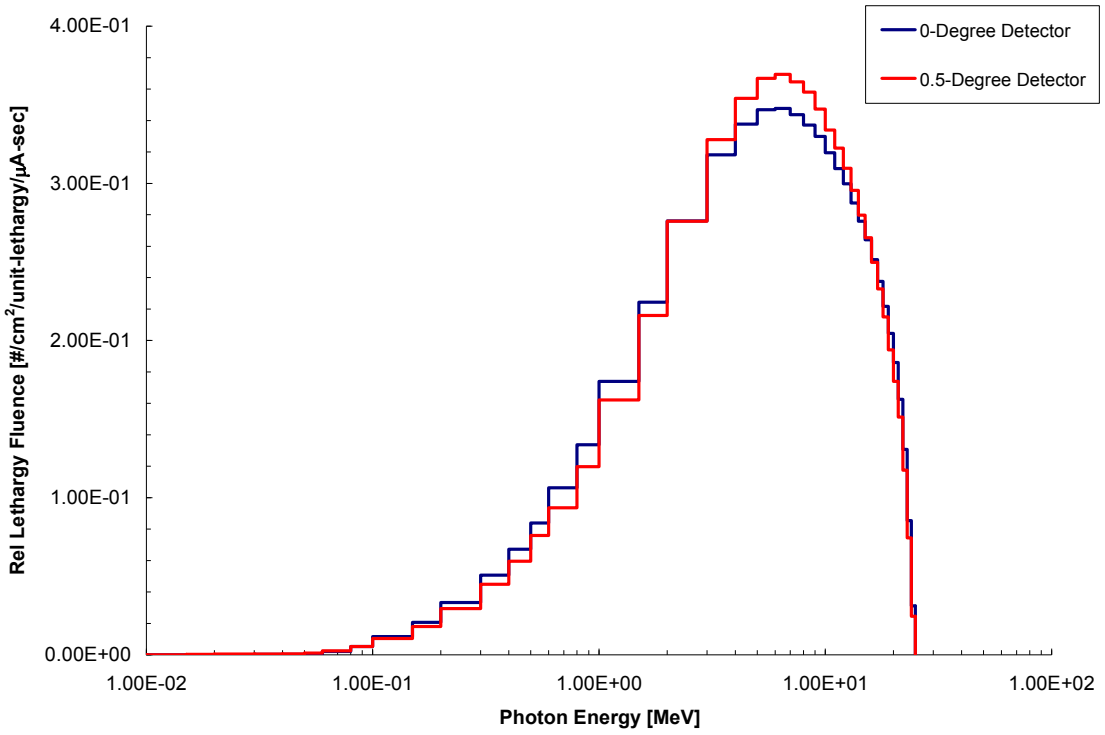

Figure E-45. Relative Photon Spectrum (0 to 0.5 degree detectors) at 100 meters for the System in Air.

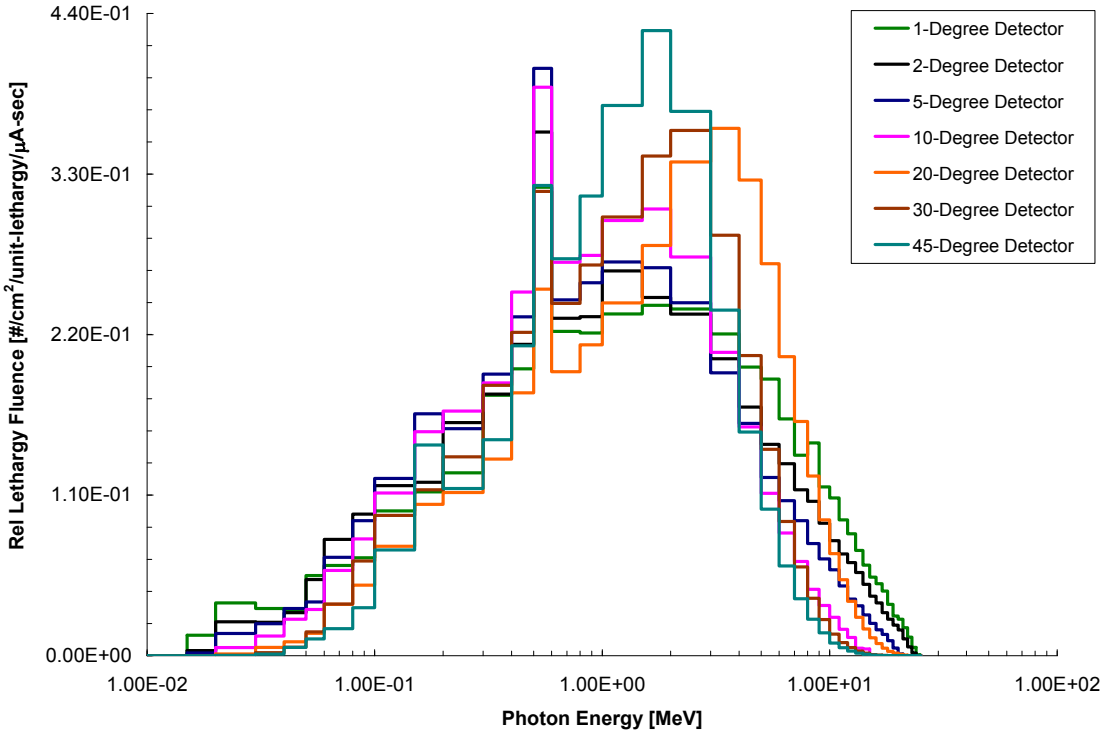

Figure E-46. Relative Photon Spectrum (1 to 45 degree detectors) at 100 meters for the System in Air.

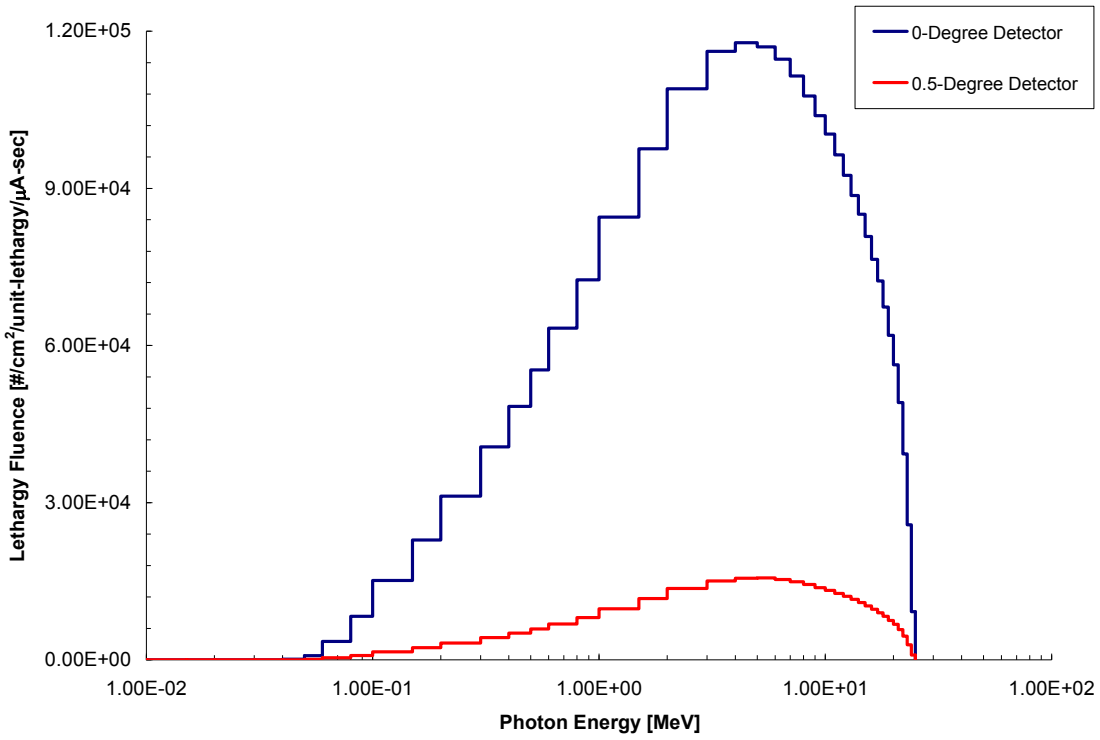

Figure E-47. Photon Spectrum (0 to 0.5 degree detectors) at 100 meters for the System in Vacuo.

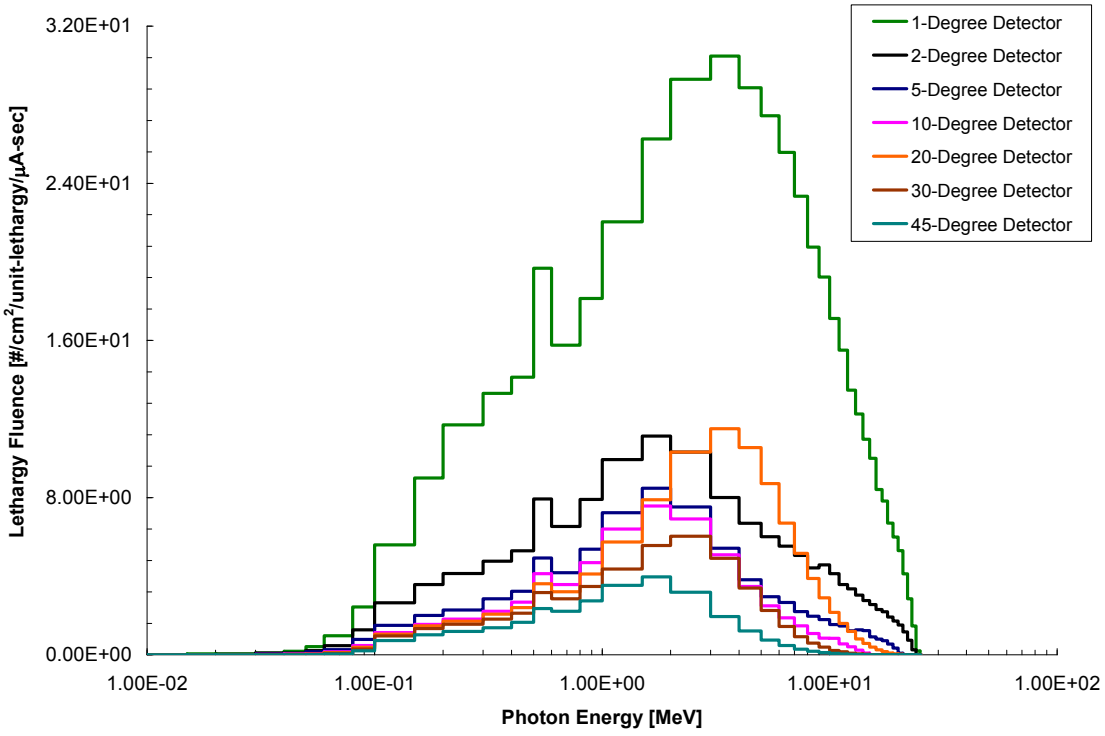

Figure E-48. Photon Spectrum (1 to 45 degree detectors) at 100 meters for the System in Vacuo.

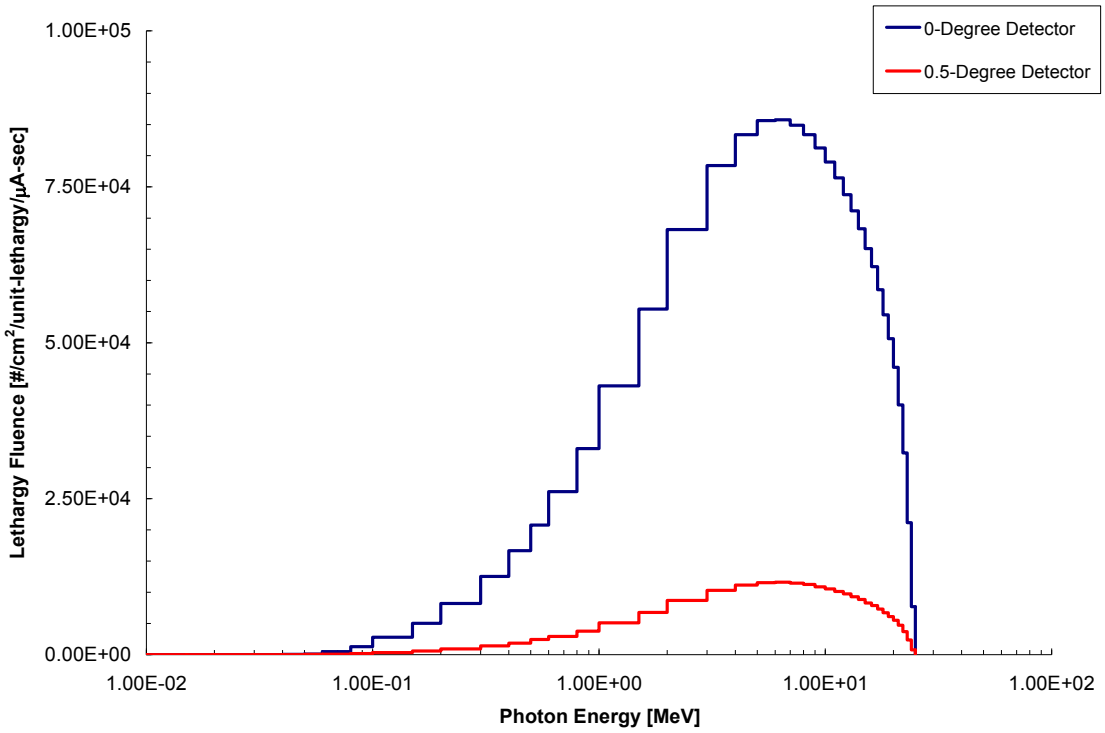

Figure E-49. Photon Spectrum (0 to 0.5 degree detectors) at 100 meters for the System (in Air) with a Pb Density Reduction of 10% in the Collimator.

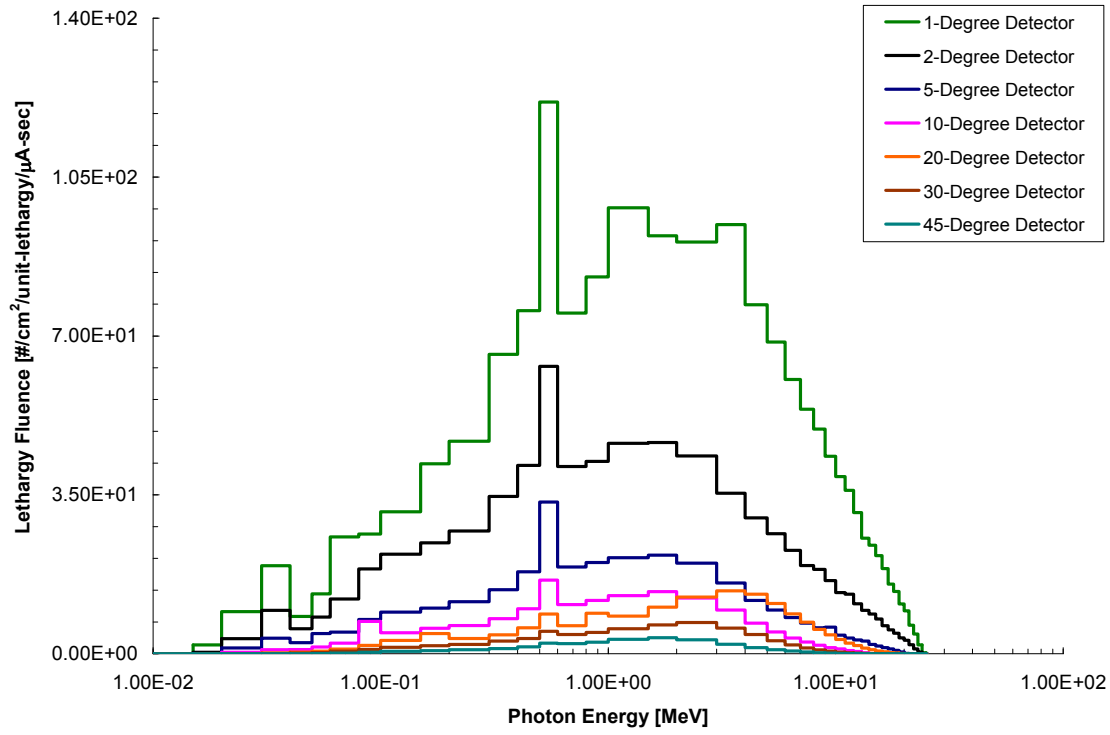

Figure E-50. Photon Spectrum (1 to 45 degree detectors) at 100 meters for the System (in Air) with a Pb Density Reduction of 10% in the Collimator.

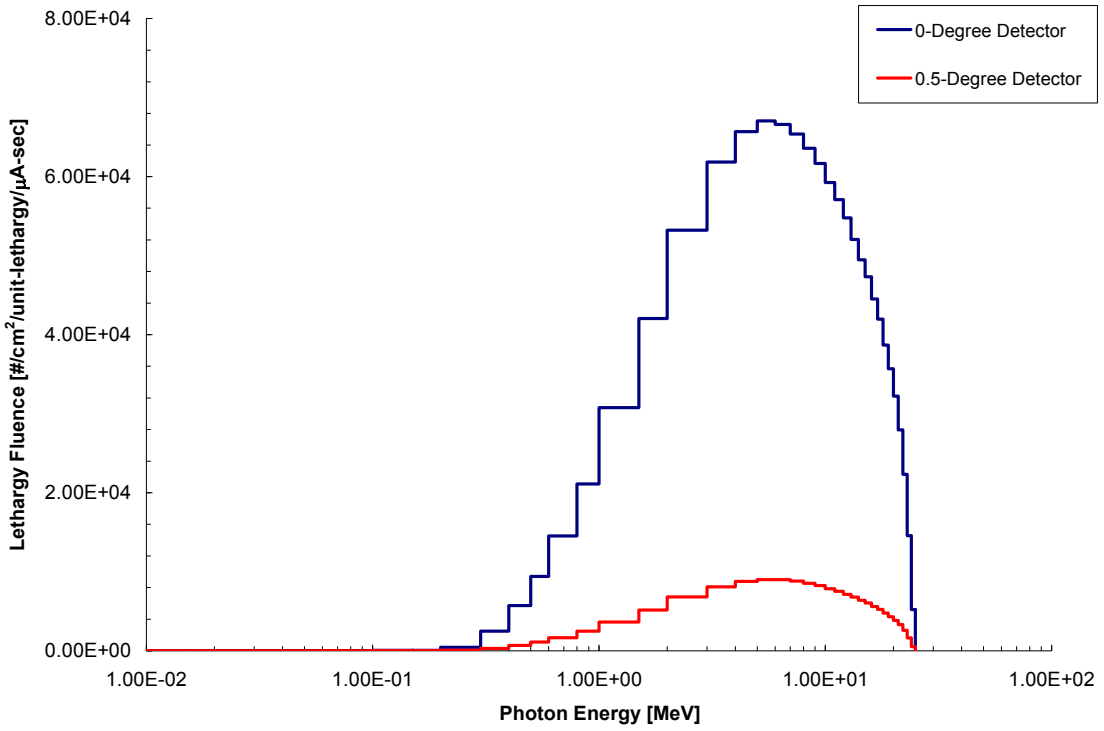

Figure E-51. Photon Spectrum (0 to 0.5 degree detectors) at 100 meters for the System (in Air) with a Pb Attenuator (t=0.50 cm) in the Beam Line.

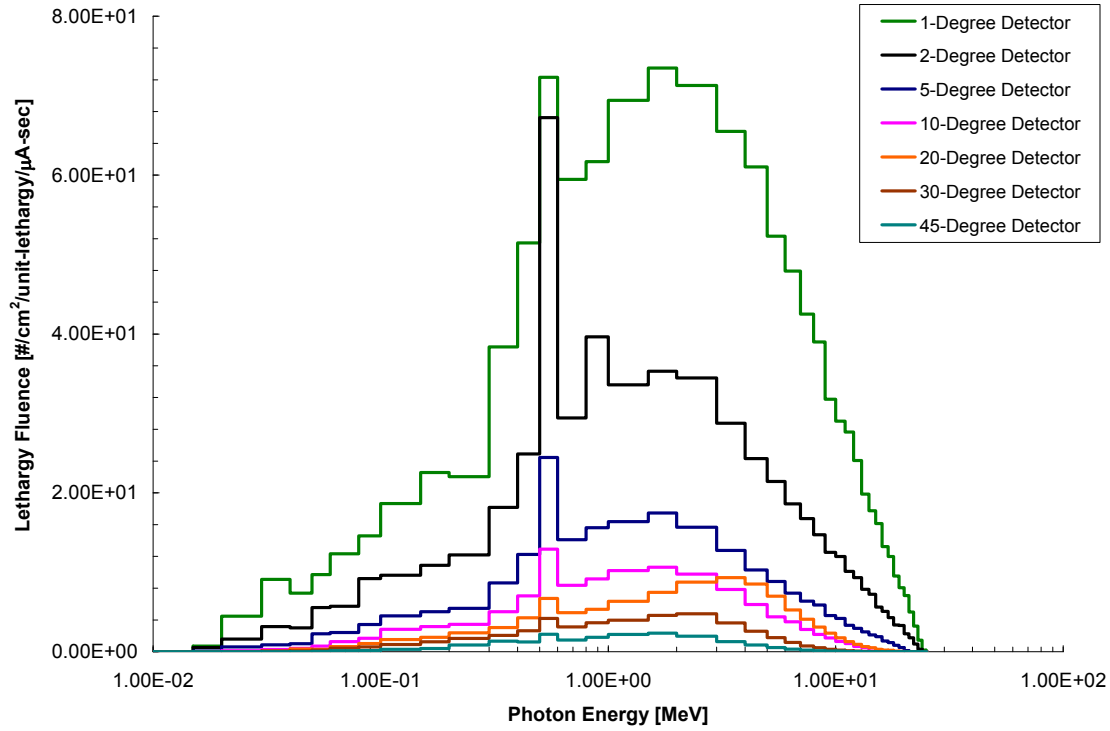

Figure E-52. Photon Spectrum (1 to 45 degree detectors) at 100 meters for the System (in Air) with a Pb Attenuator (t=0.50 cm) in the Beam Line.

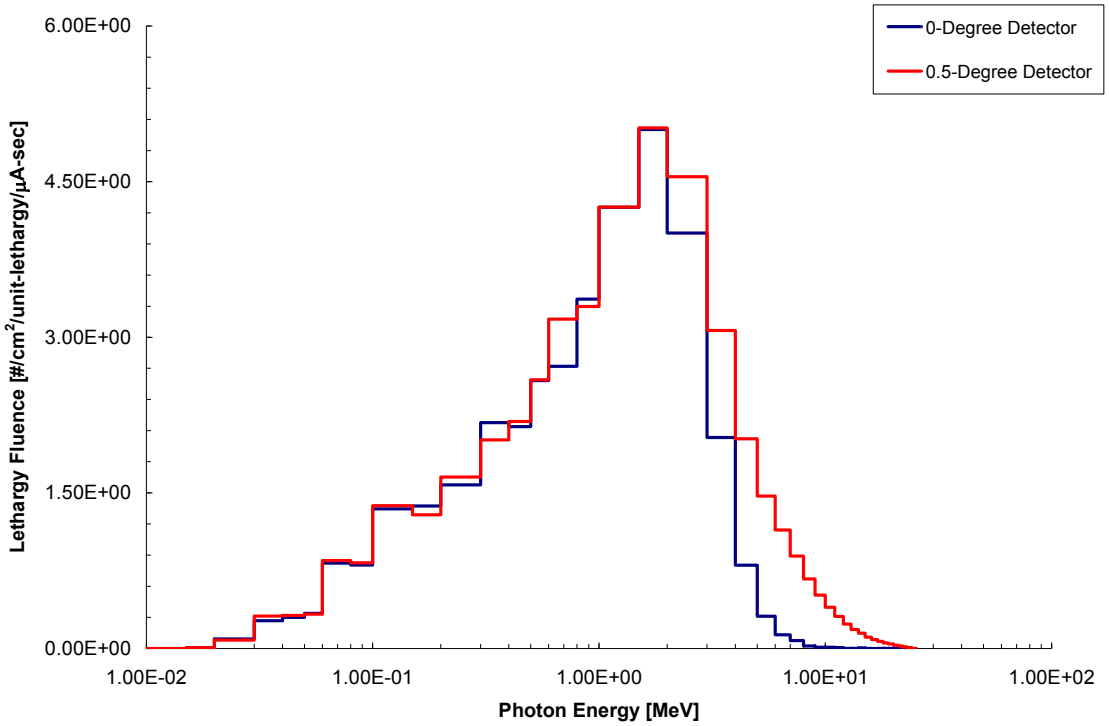

Figure E-53. Photon Spectrum (0 to 0.5 degree detectors) at 100 meters for the Collimator Only Contribution (in Air).

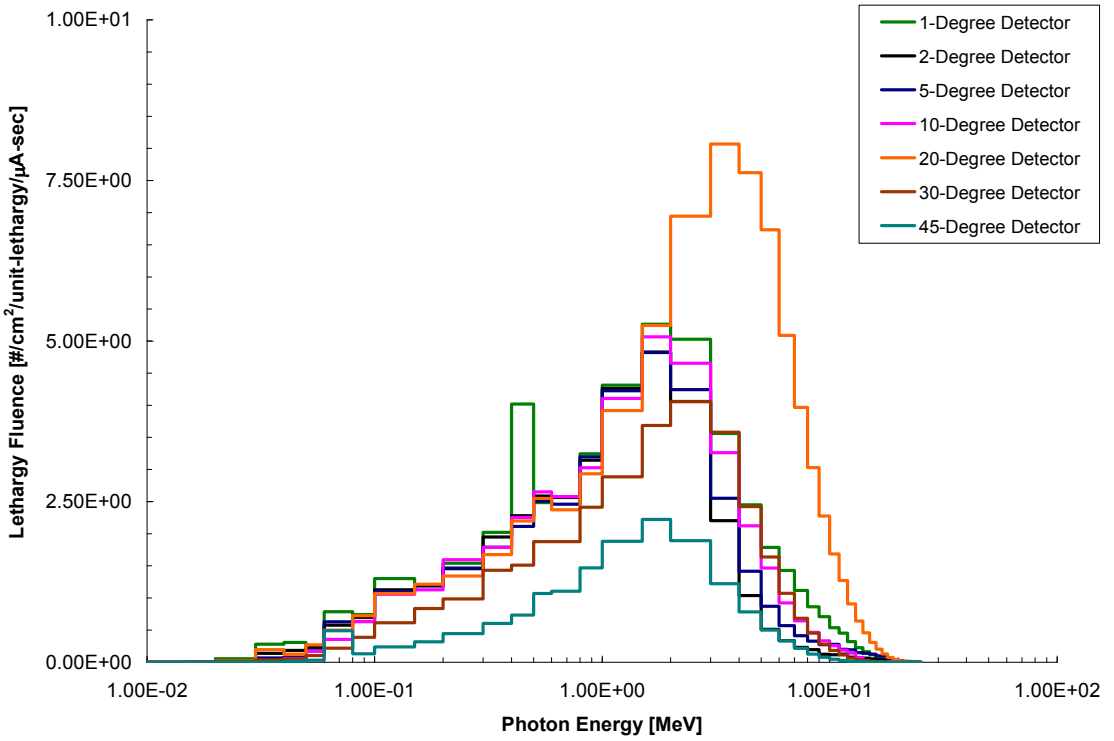

Figure E-54. Photon Spectrum (1 to 45 degree detectors) at 100 meters for the Collimator Only Contribution (in Air).

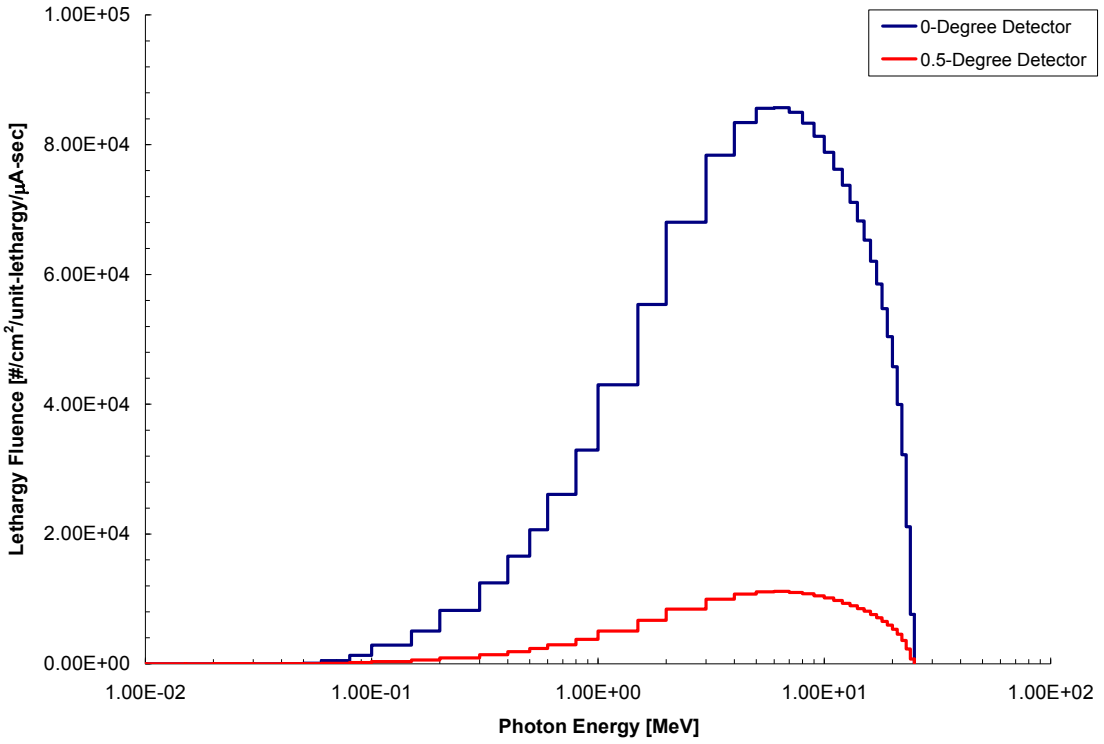

Figure E-55. Photon Spectrum (0 to 0.5 degree detectors) at 100 meters for the Beam Only Contribution (in Air).

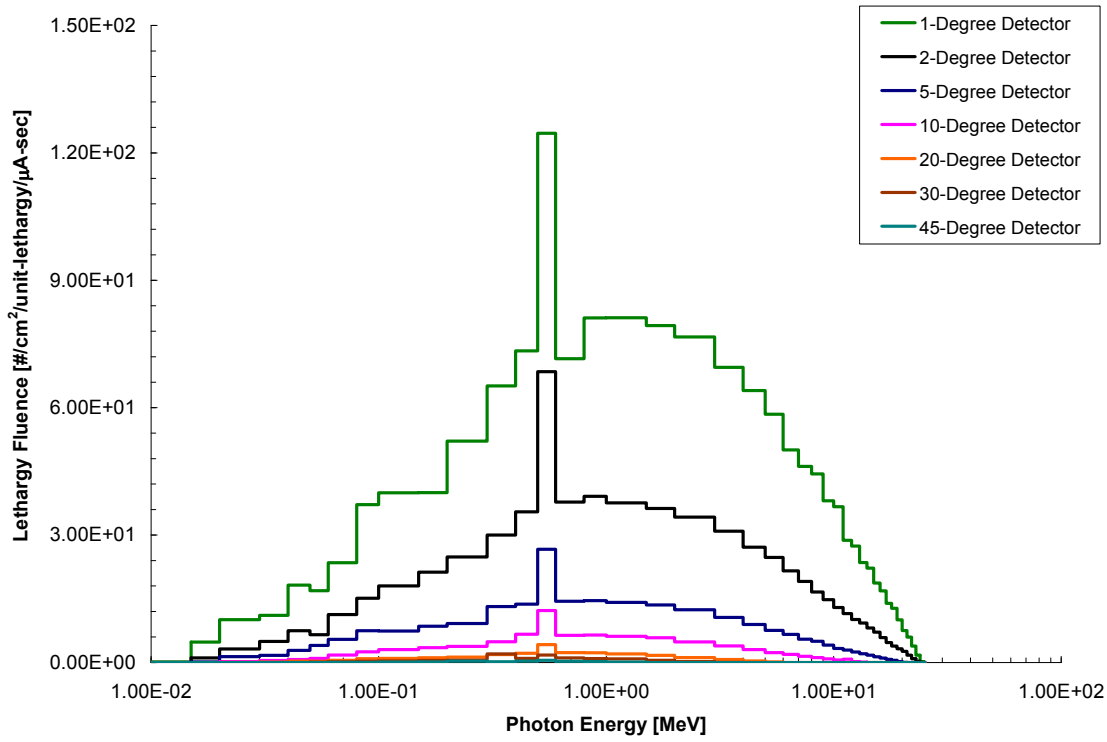

Figure E-56. Photon Spectrum (1 to 45 degree detectors) at 100 meters for the Beam Only Contribution (in Air).

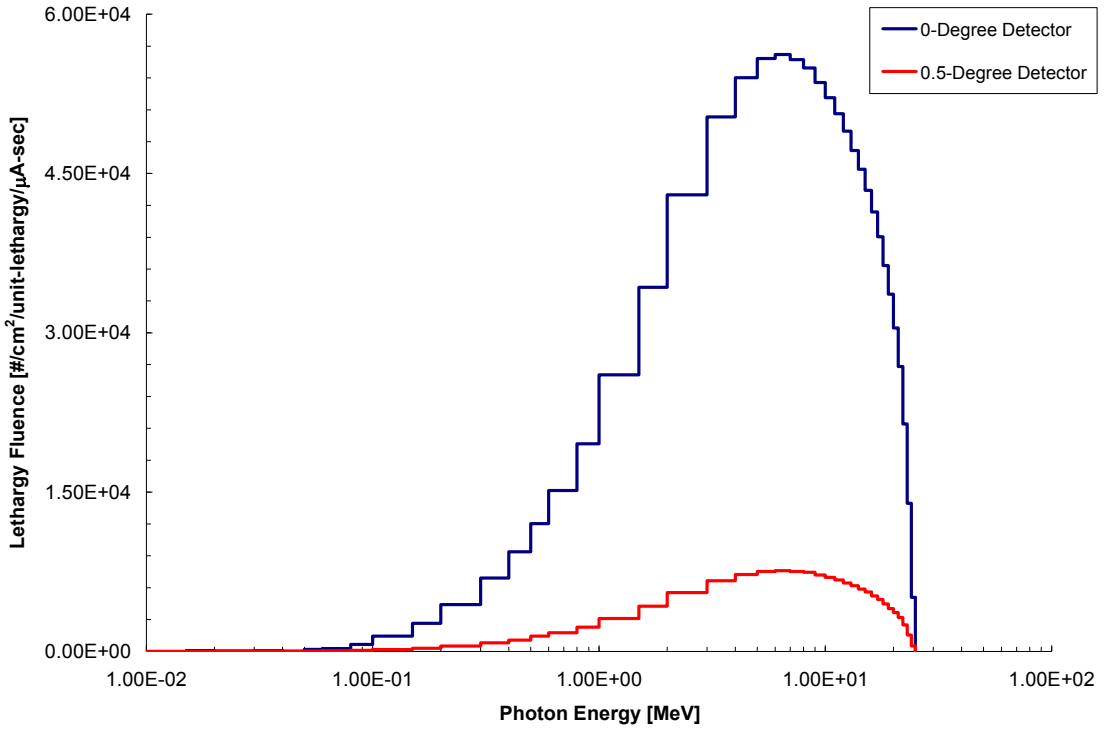

Figure E-57. Photon Spectrum (0 to 0.5 degree detectors) at 120 meters for the System in Air.

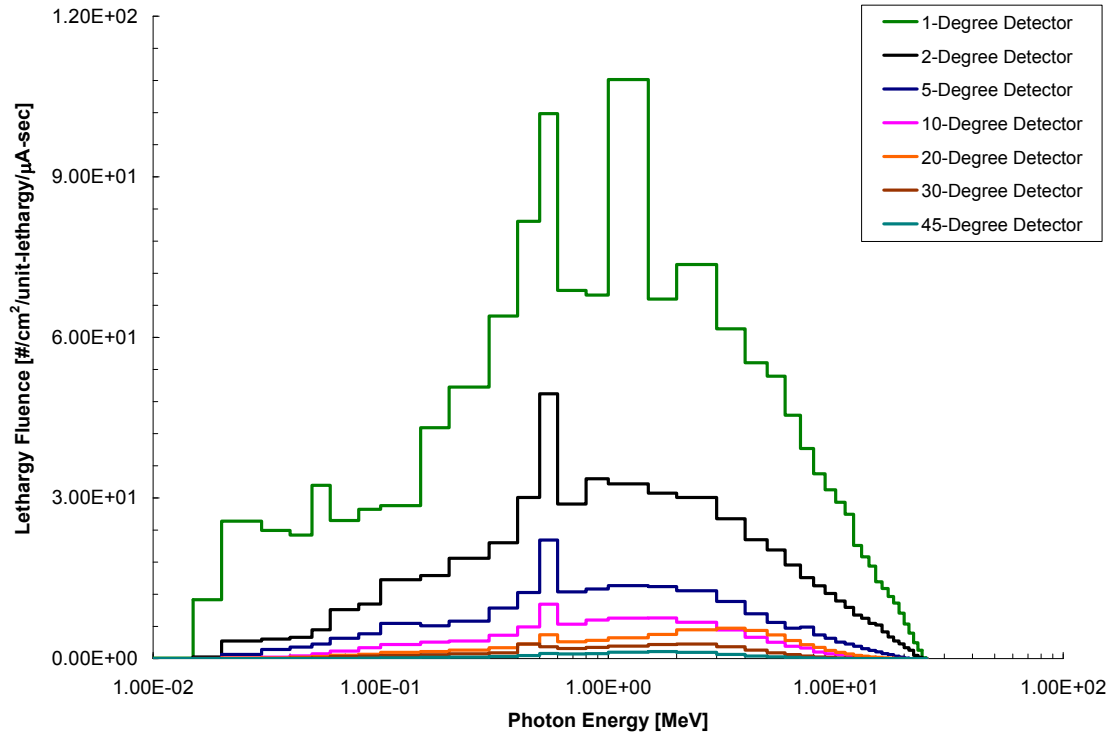

Figure E-58. Photon Spectrum (1 to 45 degree detectors) at 120 meters for the System in Air.

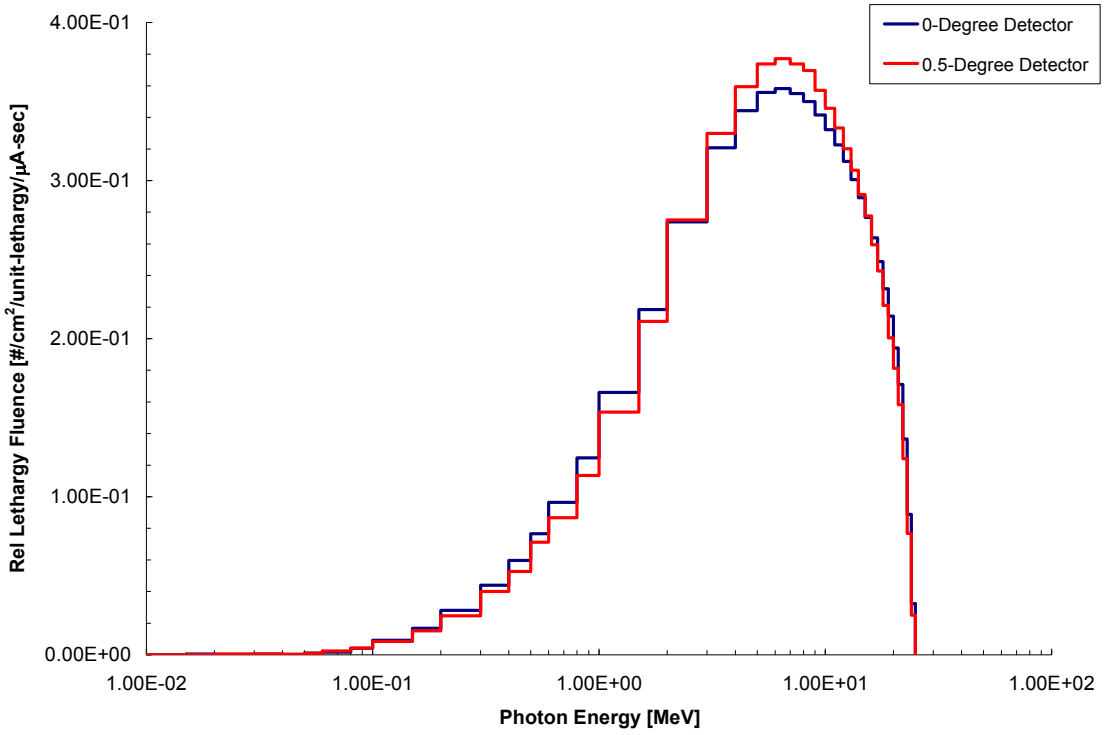

Figure E-59. Relative Photon Spectrum (0 to 0.5 degree detectors) at 120 meters for the System in Air.

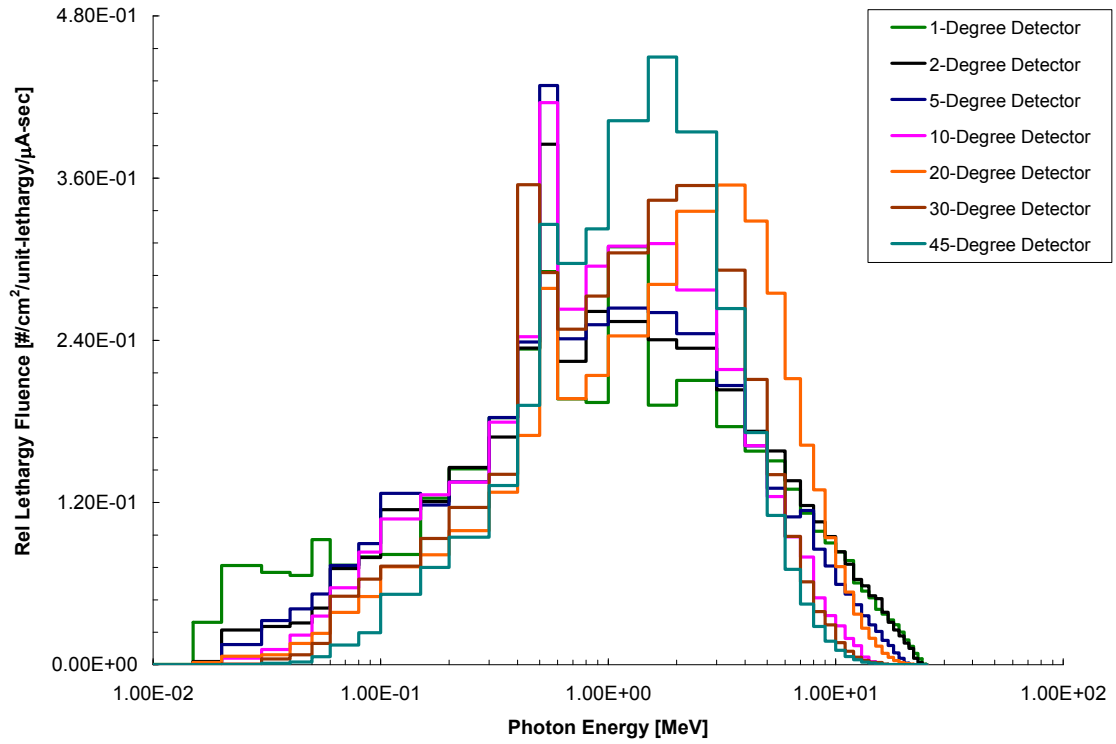

Figure E-60. Relative Photon Spectrum (1 to 45 degree detectors) at 120 meters for the System in Air.

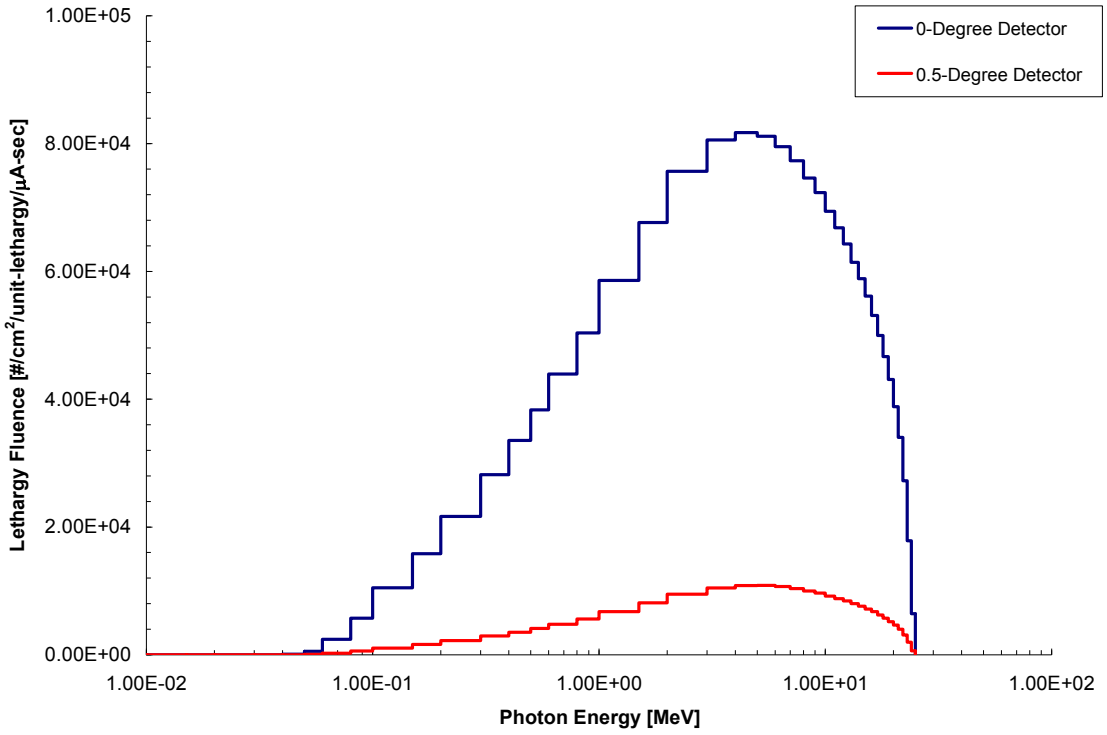

Figure E-61. Photon Spectrum (0 to 0.5 degree detectors) at 120 meters for the System in Vacuo.

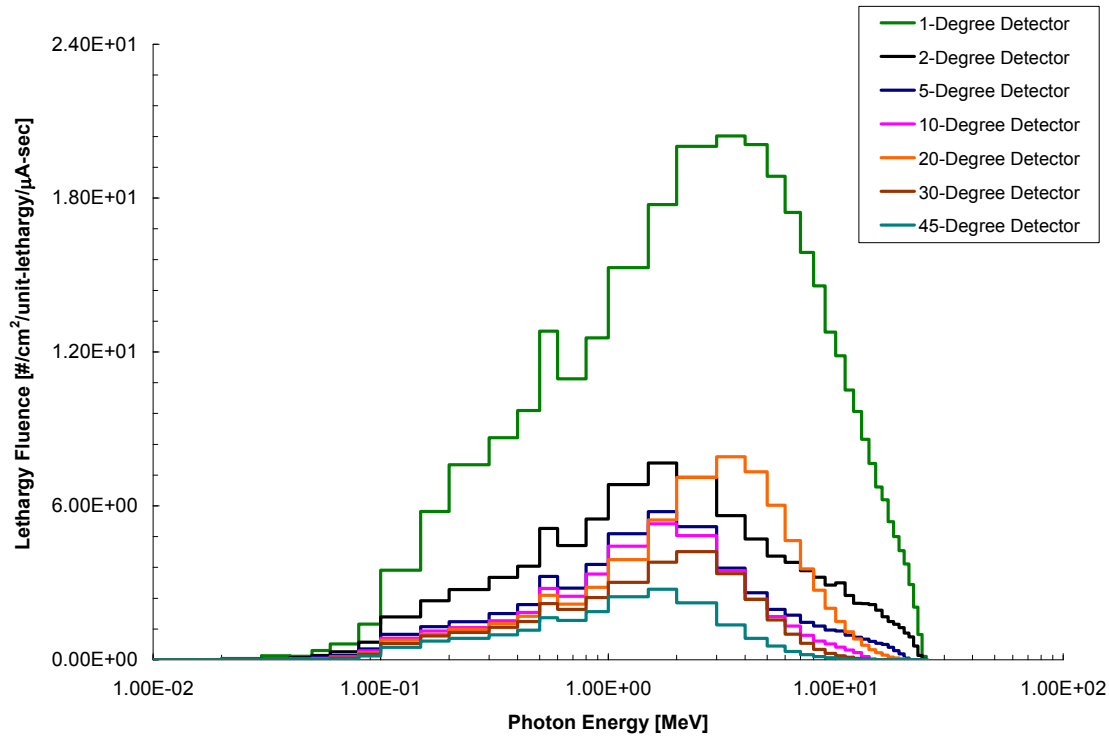

Figure E-62. Photon Spectrum (1 to 45 degree detectors) at 120 meters for the System in Vacuo.

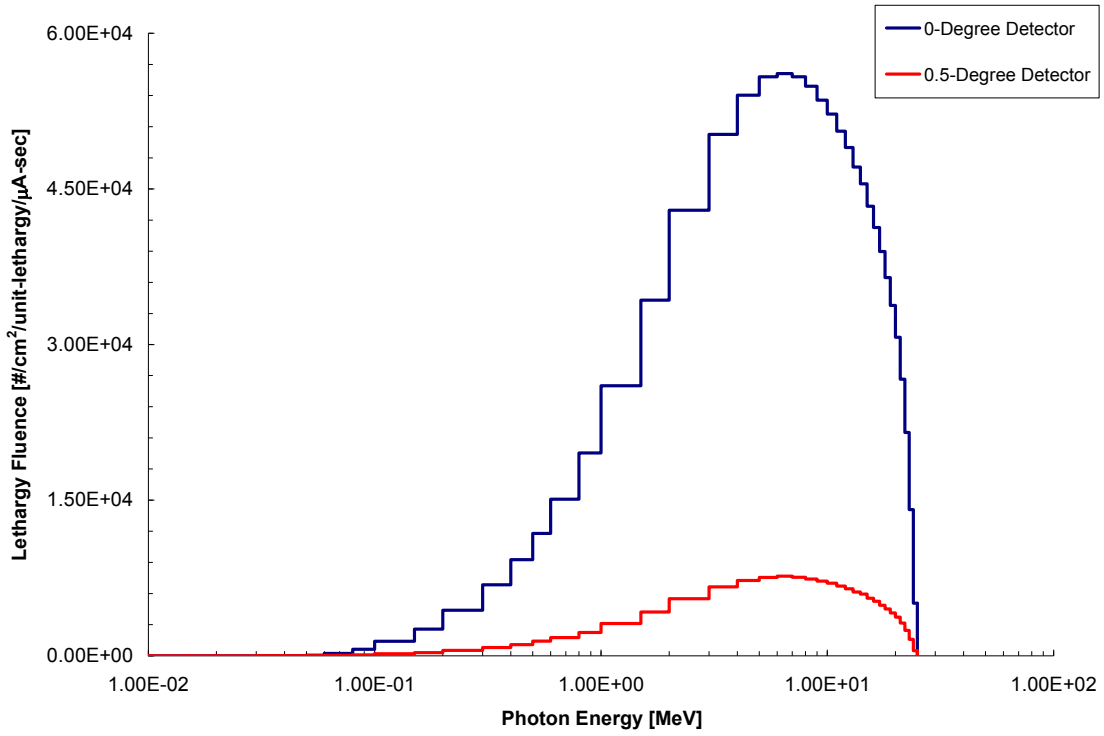

Figure E-63. Photon Spectrum (0 to 0.5 degree detectors) at 120 meters for the System (in Air) with a Pb Density Reduction of 10% in the Collimator.

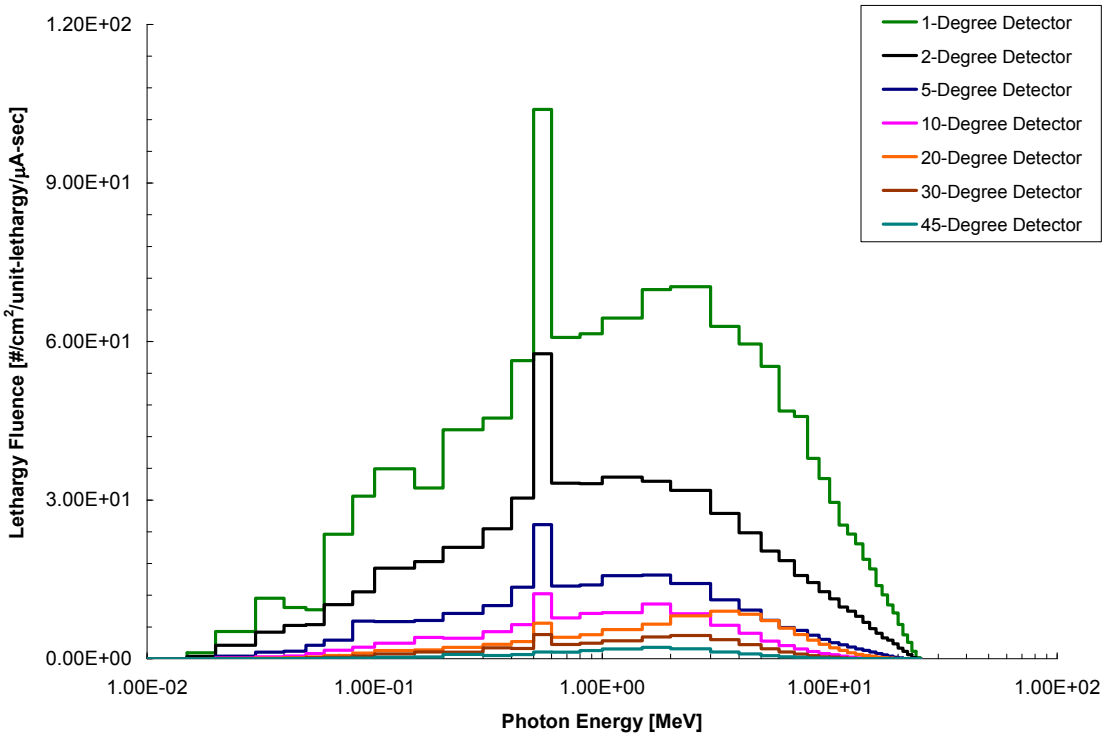

Figure E-64. Photon Spectrum (1 to 45 degree detectors) at 120 meters for the System (in Air) with a Pb Density Reduction of 10% in the Collimator.

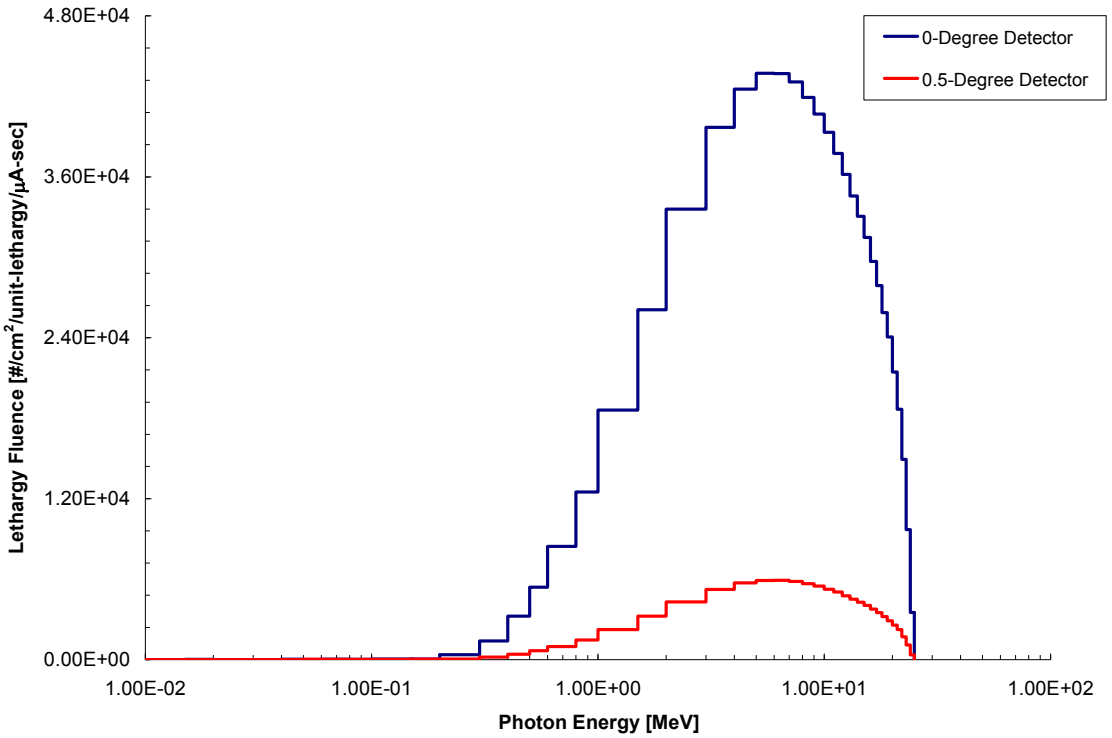

Figure E-65. Photon Spectrum (0 to 0.5 degree detectors) at 120 meters for the System (in Air) with a Pb Attenuator (t=0.50 cm) in the Beam Line.

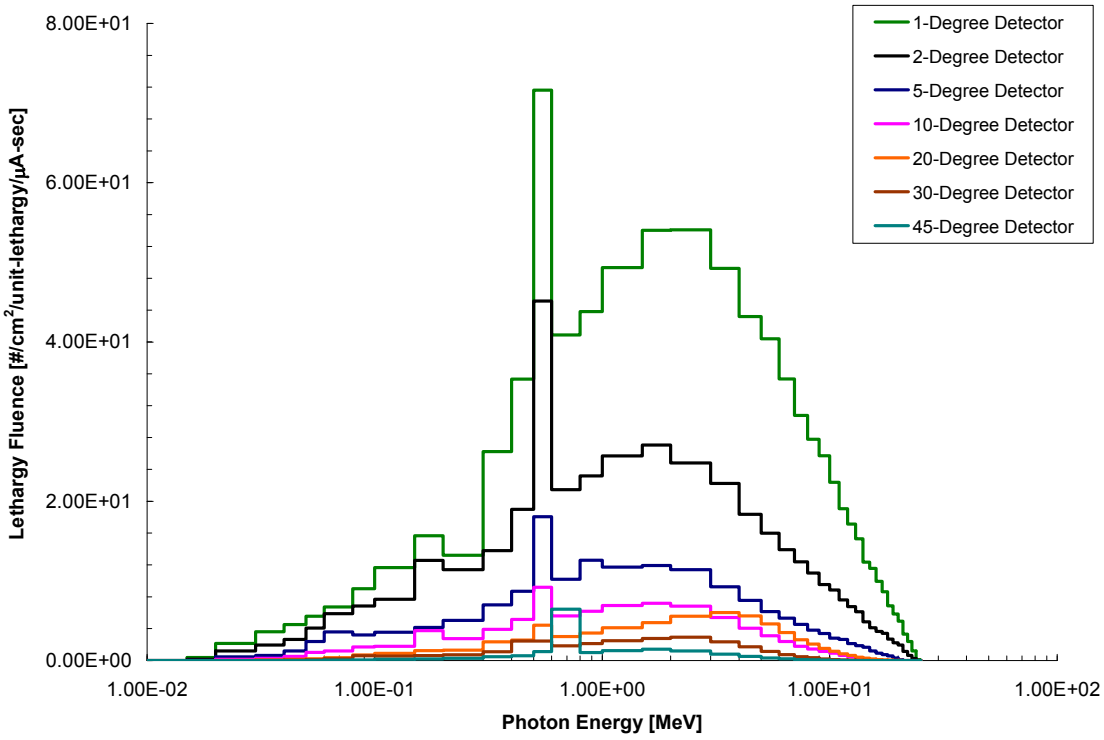

Figure E-66. Photon Spectrum (1 to 45 degree detectors) at 120 meters for the System (in Air) with a Pb Attenuator (t=0.50 cm) in the Beam Line.

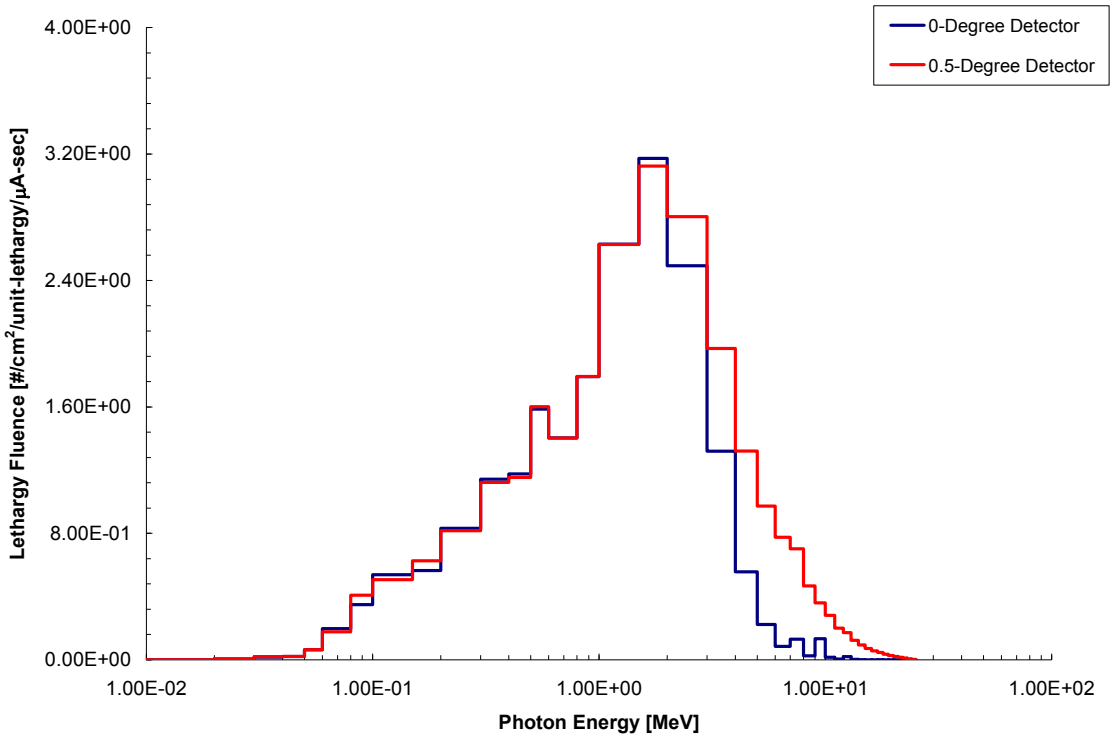

Figure E-67. Photon Spectrum (0 to 0.5 degree detectors) at 120 meters for the Collimator Only Contribution (in Air).

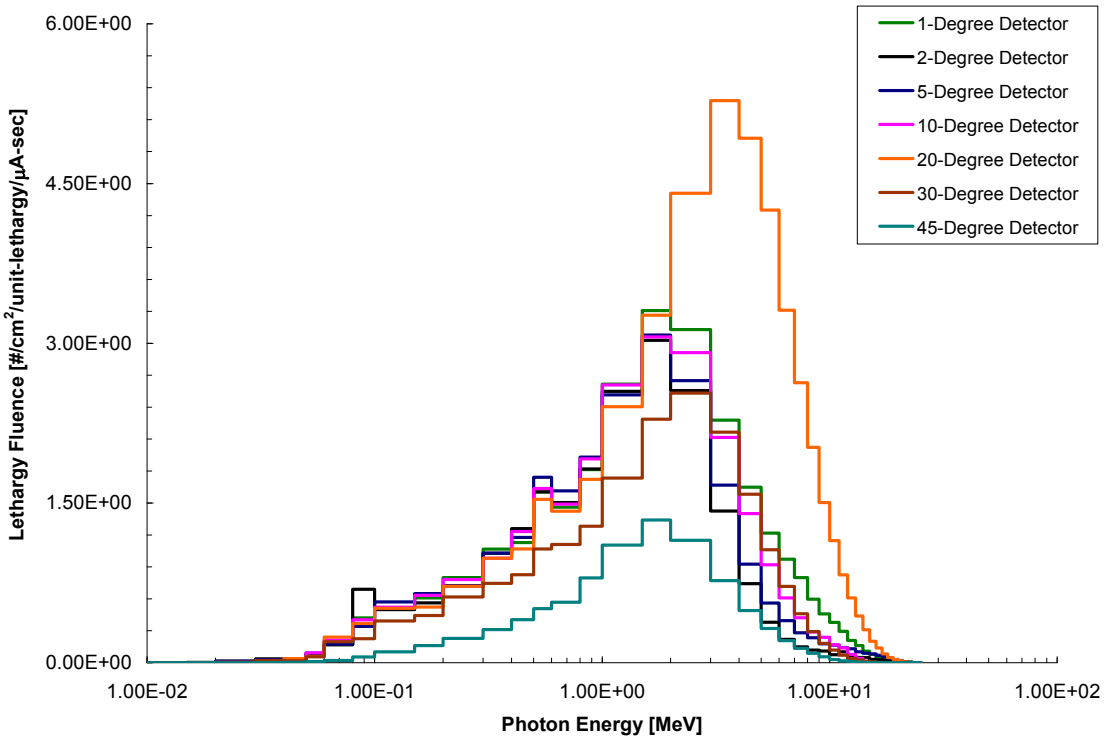

Figure E-68. Photon Spectrum (1 to 45 degree detectors) at 120 meters for the Collimator Only Contribution (in Air).

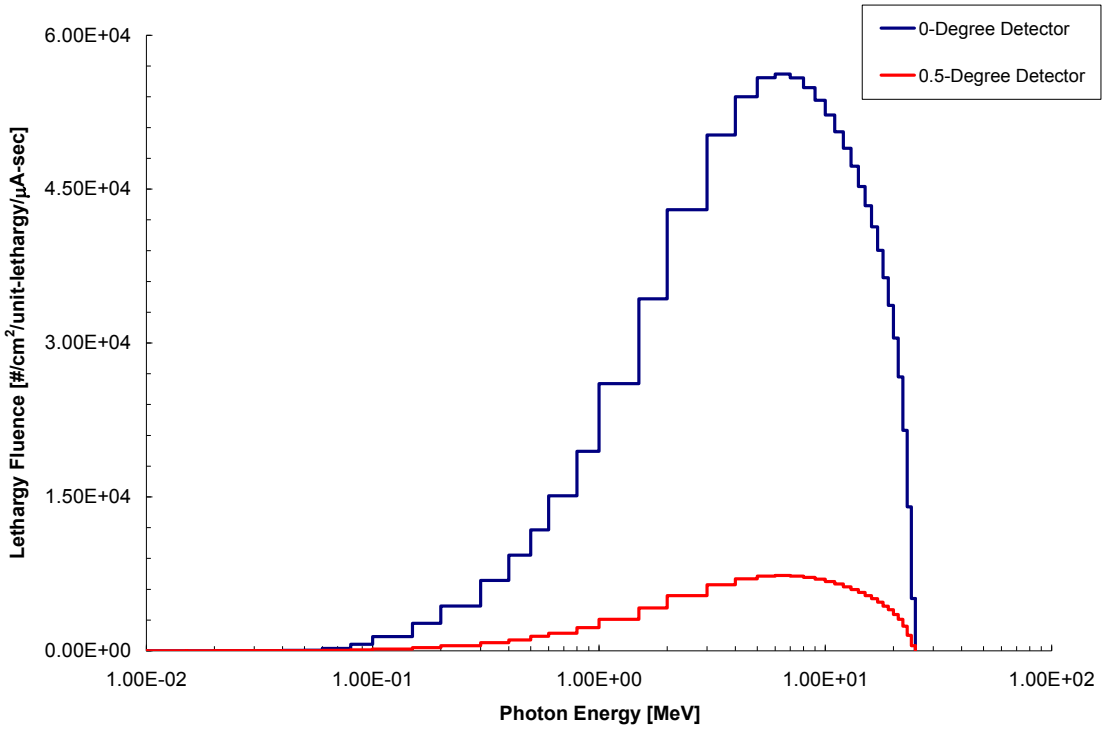

Figure E-69. Photon Spectrum (0 to 0.5 degree detectors) at 120 meters for the Beam Only Contribution (in Air).

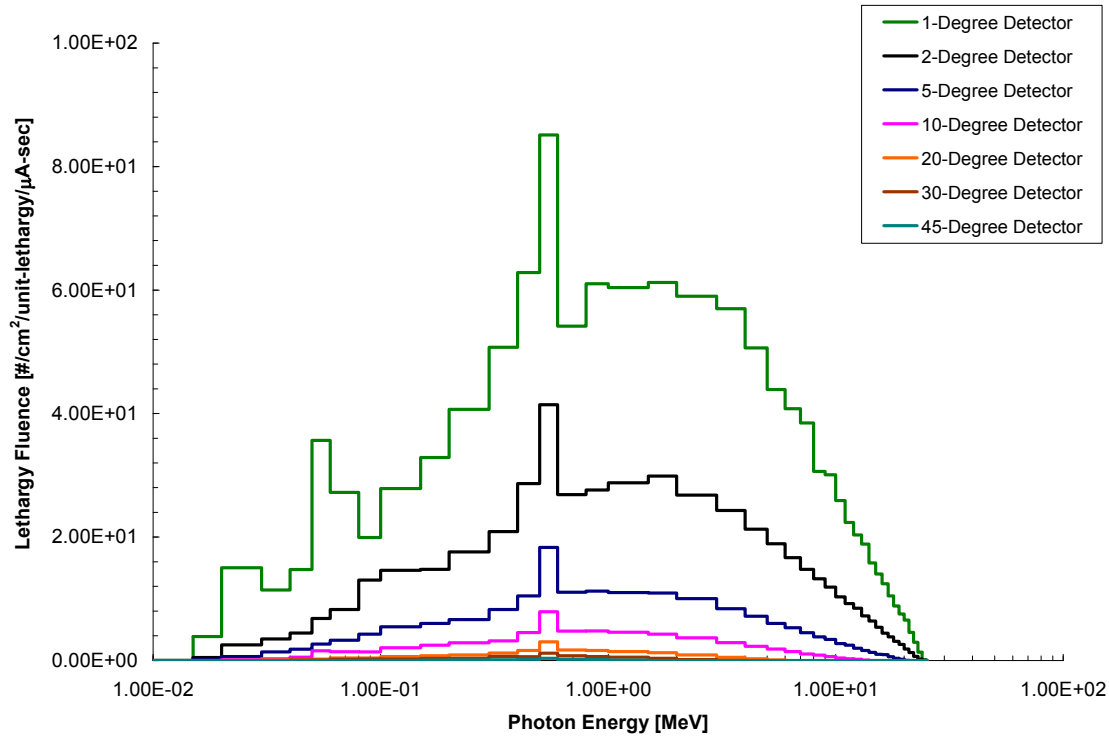

Figure E-70. Photon Spectrum (1 to 45 degree detectors) at 120 meters for the Beam Only Contribution (in Air).

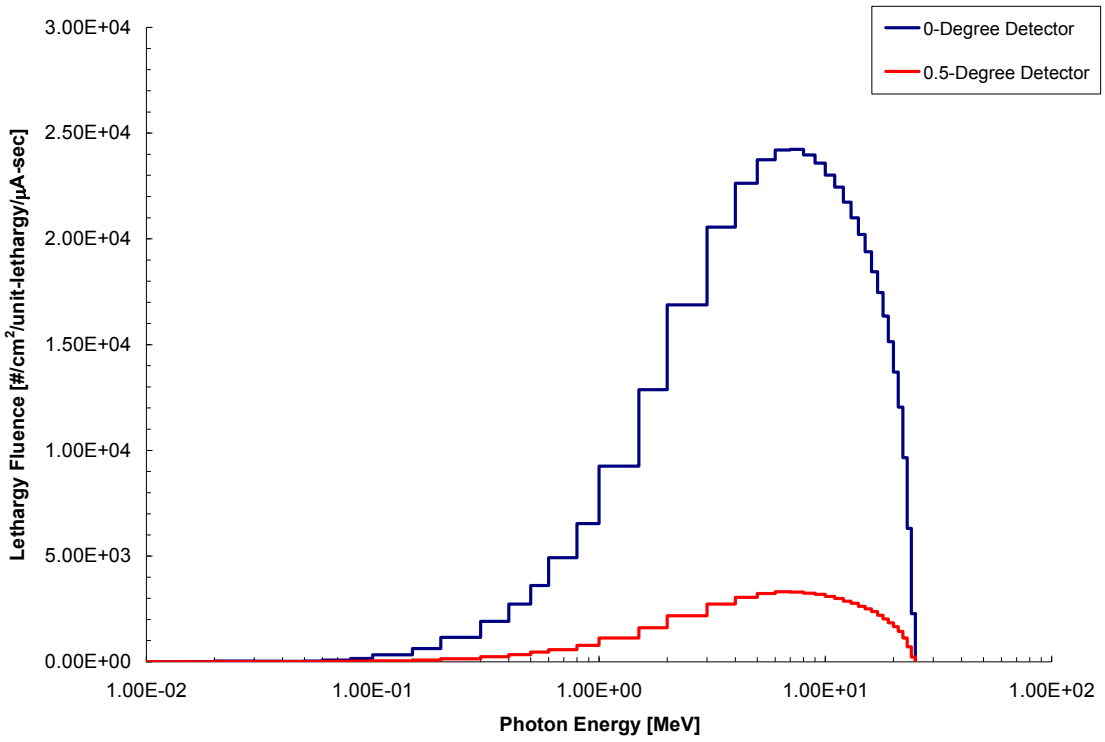

Figure E-71. Photon Spectrum (0 to 0.5 degree detectors) at 170 meters for the System in Air.

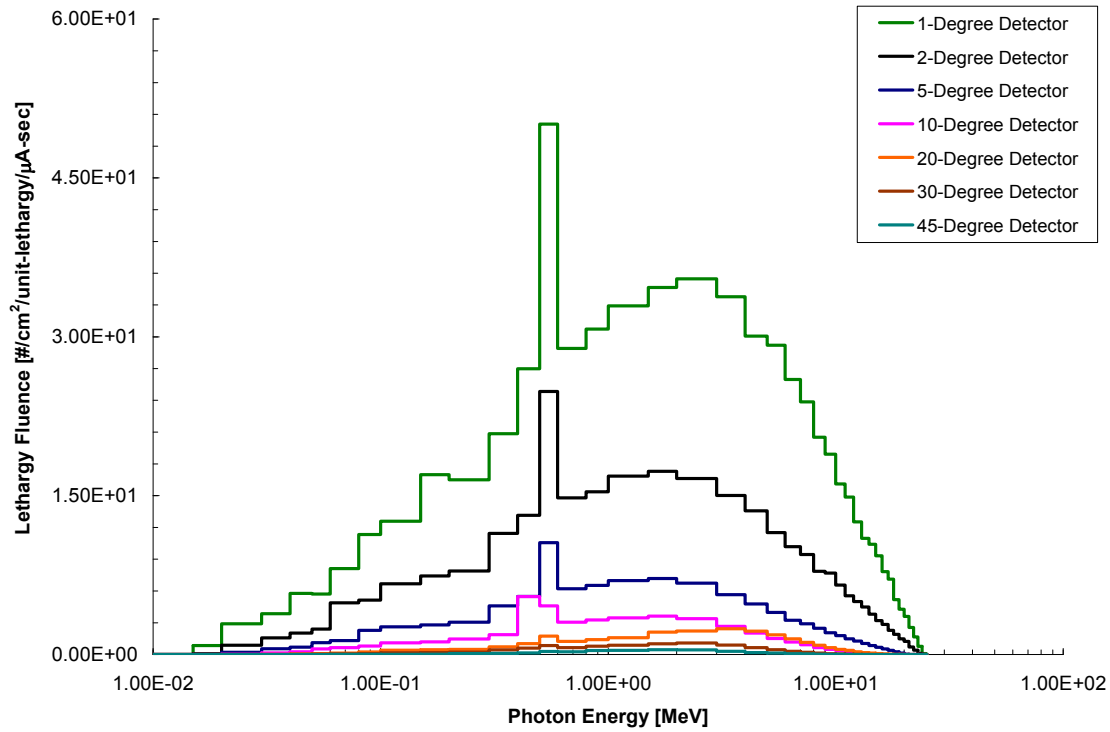

Figure E-72. Photon Spectrum (1 to 45 degree detectors) at 170 meters for the System in Air.

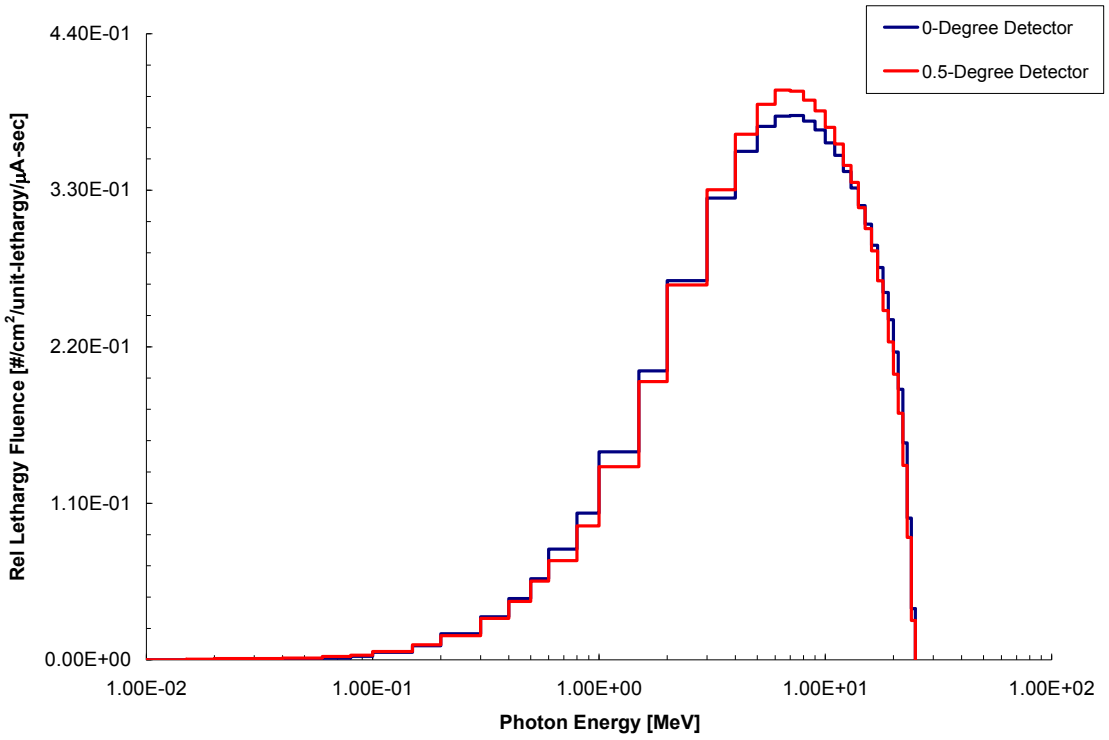

Figure E-73. Relative Photon Spectrum (0 to 0.5 degree detectors) at 170 meters for the System in Air.

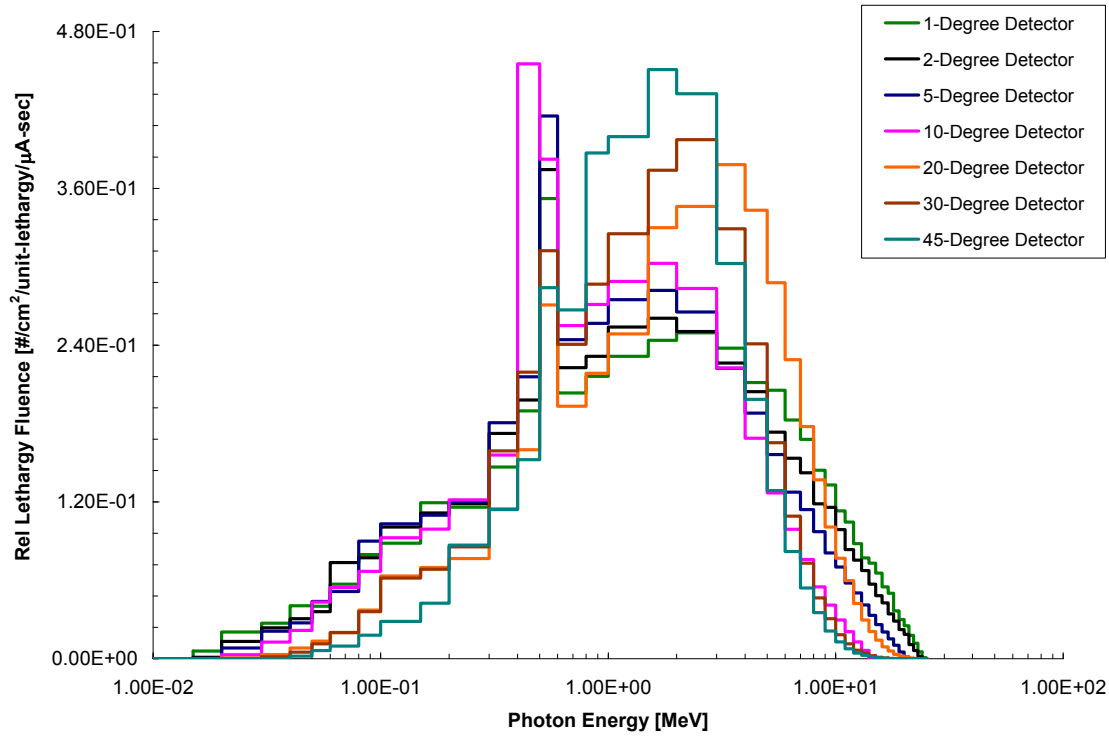

Figure E-74. Relative Photon Spectrum (1 to 45 degree detectors) at 170 meters for the System in Air.

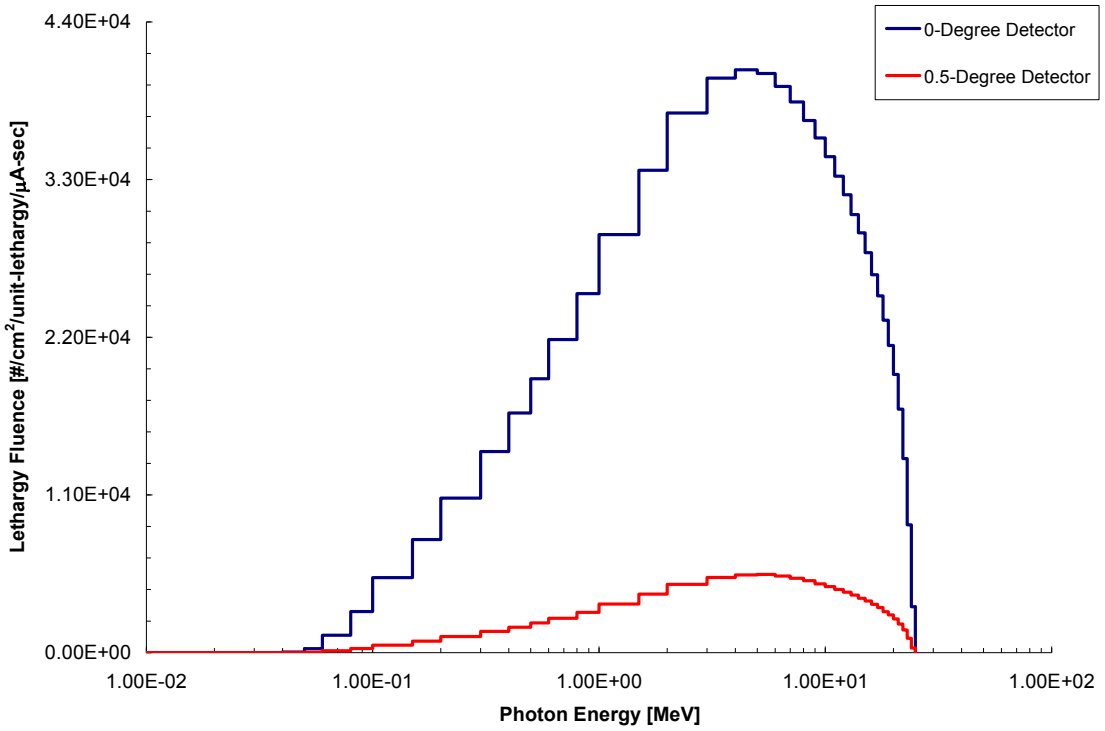

Figure E-75. Photon Spectrum (0 to 0.5 degree detectors) at 170 meters for the System in Vacuo.

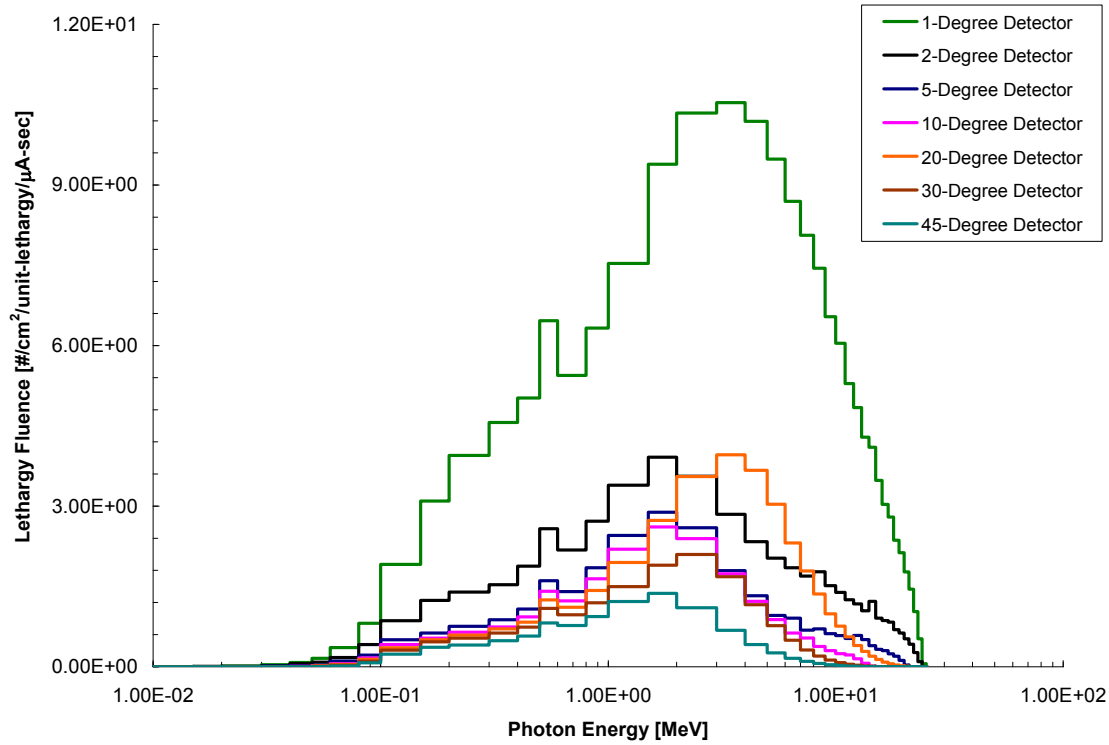

Figure E-76. Photon Spectrum (1 to 45 degree detectors) at 170 meters for the System in Vacuo.

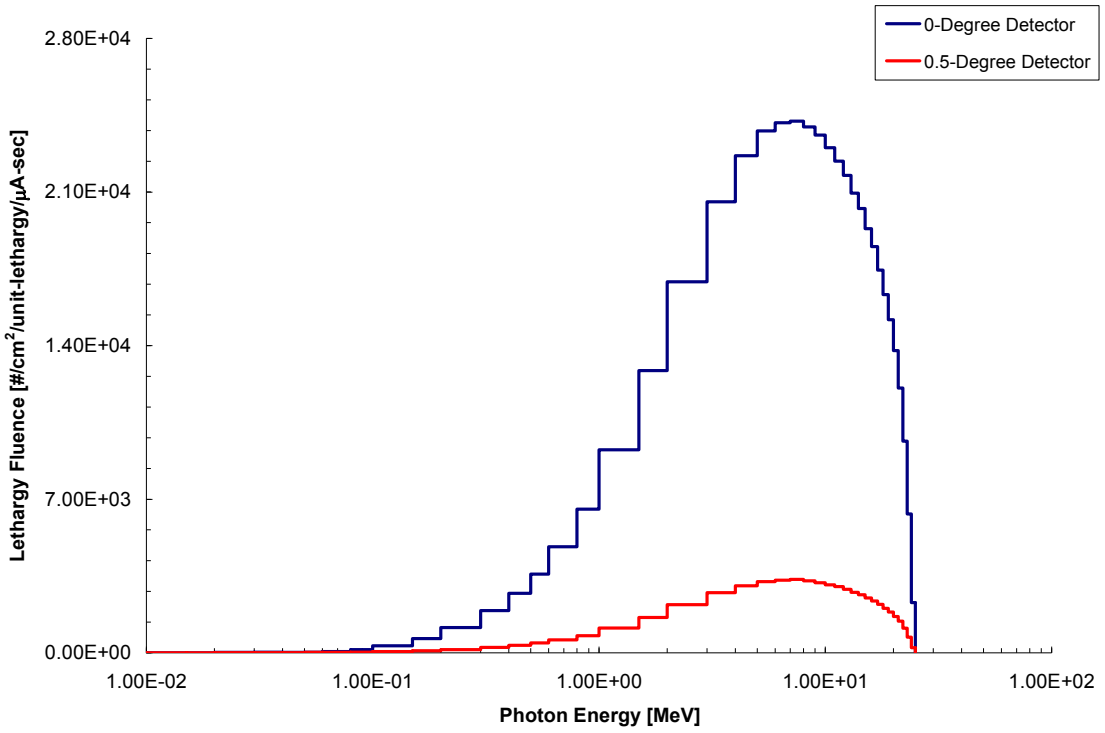

Figure E-77. Photon Spectrum (0 to 0.5 degree detectors) at 170 meters for the System (in Air) with a Pb Density Reduction of 10% in the Collimator.

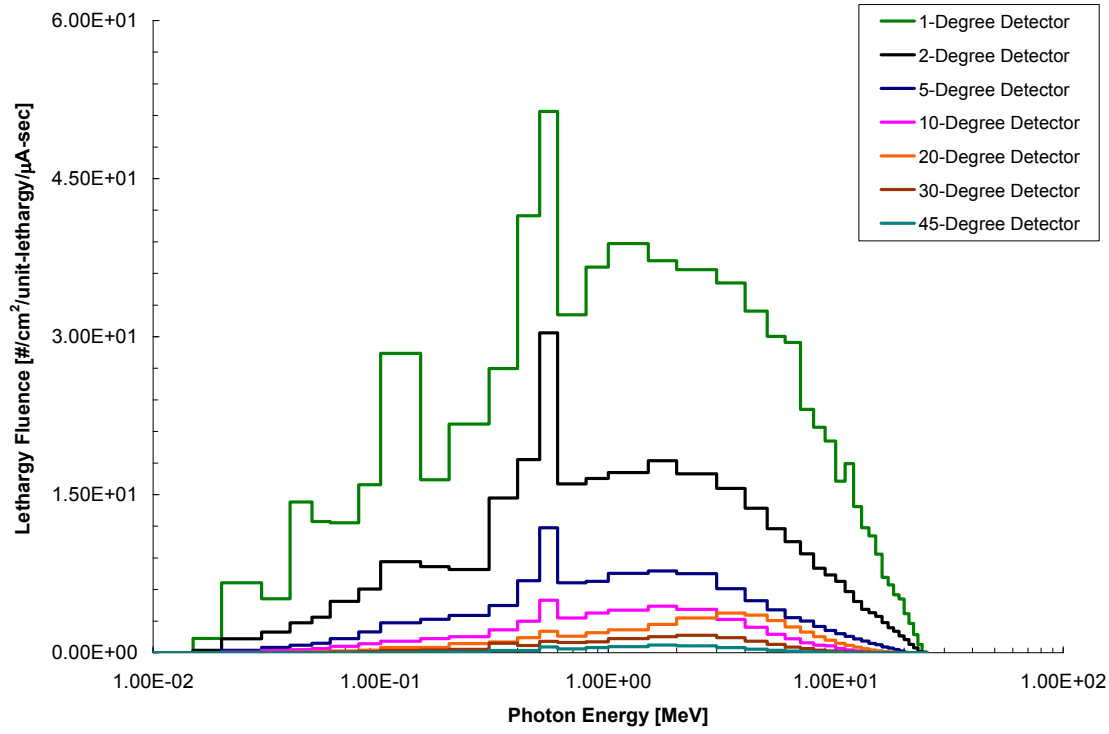

Figure E-78. Photon Spectrum (1 to 45 degree detectors) at 170 meters for the System (in Air) with a Pb Density Reduction of 10% in the Collimator.

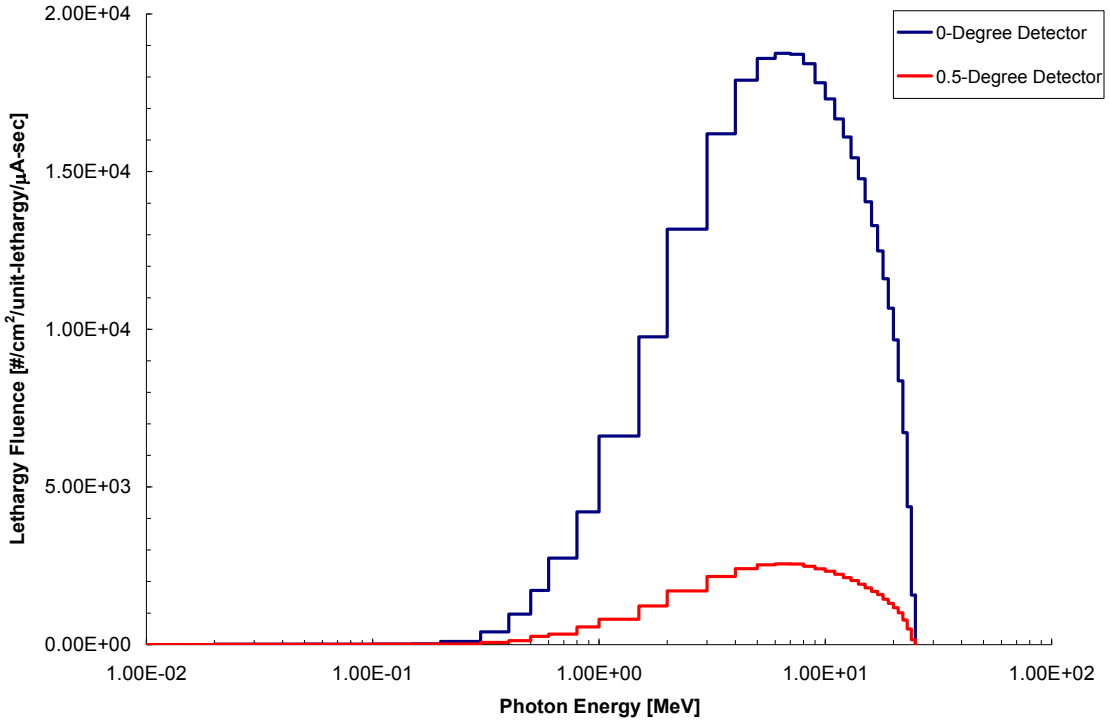

FigureE-79. Photon Spectrum (0 to 0.5 degree detectors) at 170 meters for the System (in Air) with a Pb Attenuator (t=0.50 cm) in the Beam Line.

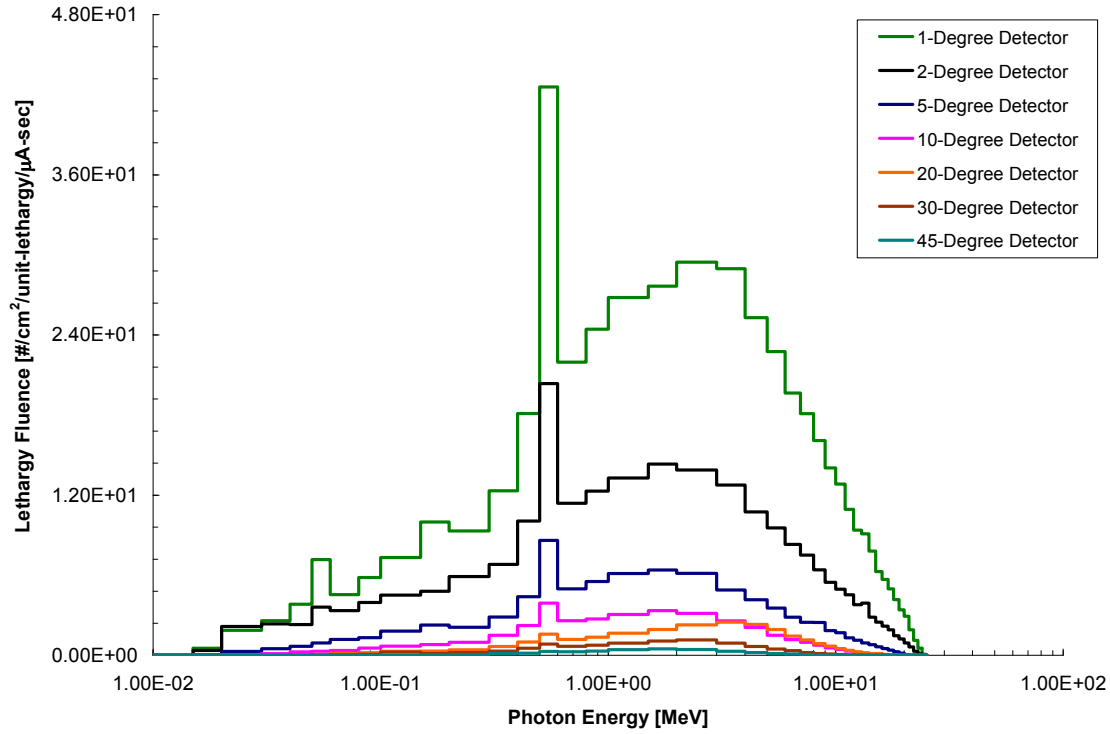

Figure E-80. Photon Spectrum (1 to 45 degree detectors) at 170 meters for the System (in Air) with a Pb Attenuator (t=0.50 cm) in the Beam Line.

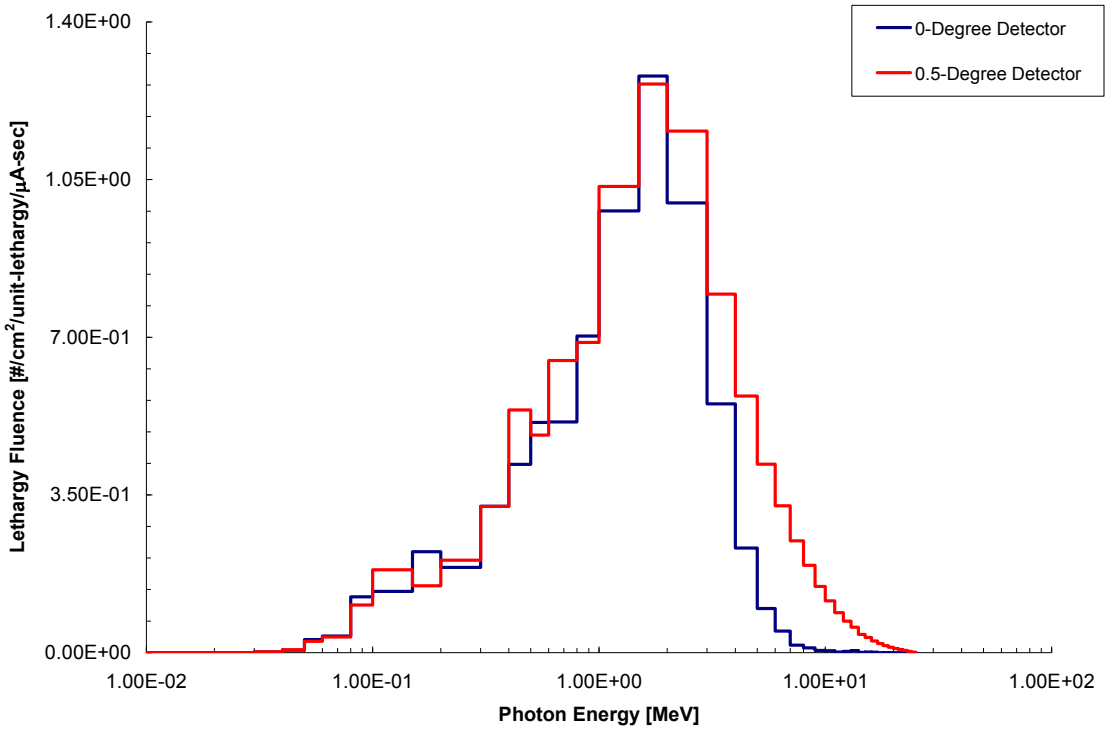

Figure E-81. Photon Spectrum (0 to 0.5 degree detectors) at 170 meters for the Collimator Only Contribution (in Air).

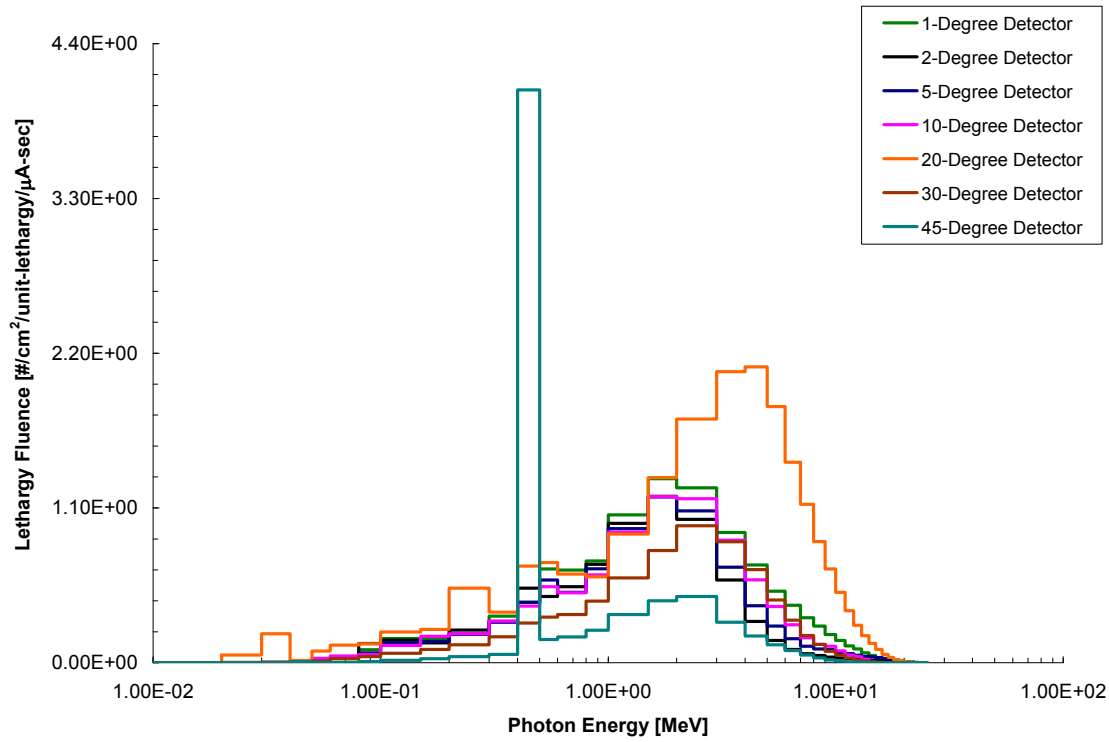

Figure E-82. Photon Spectrum (1 to 45 degree detectors) at 170 meters for the Collimator Only Contribution (in Air).

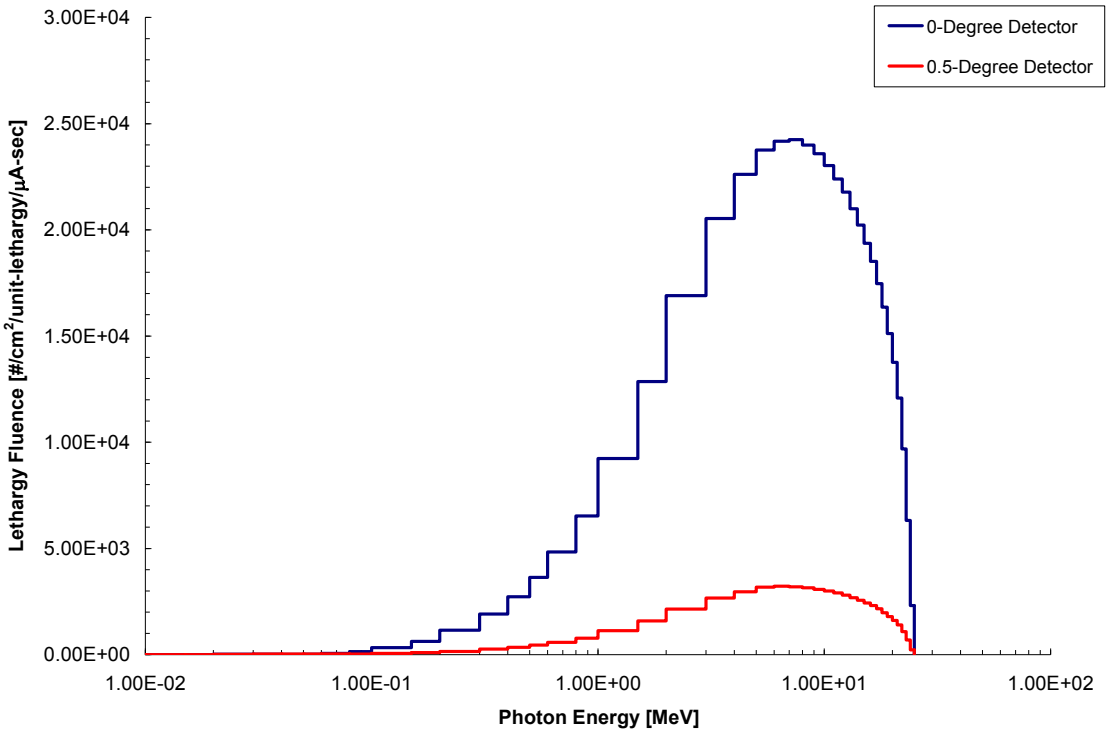

Figure E-83. Photon Spectrum (0 to 0.5 degree detectors) at 170 meters for the Beam Only Contribution (in Air).

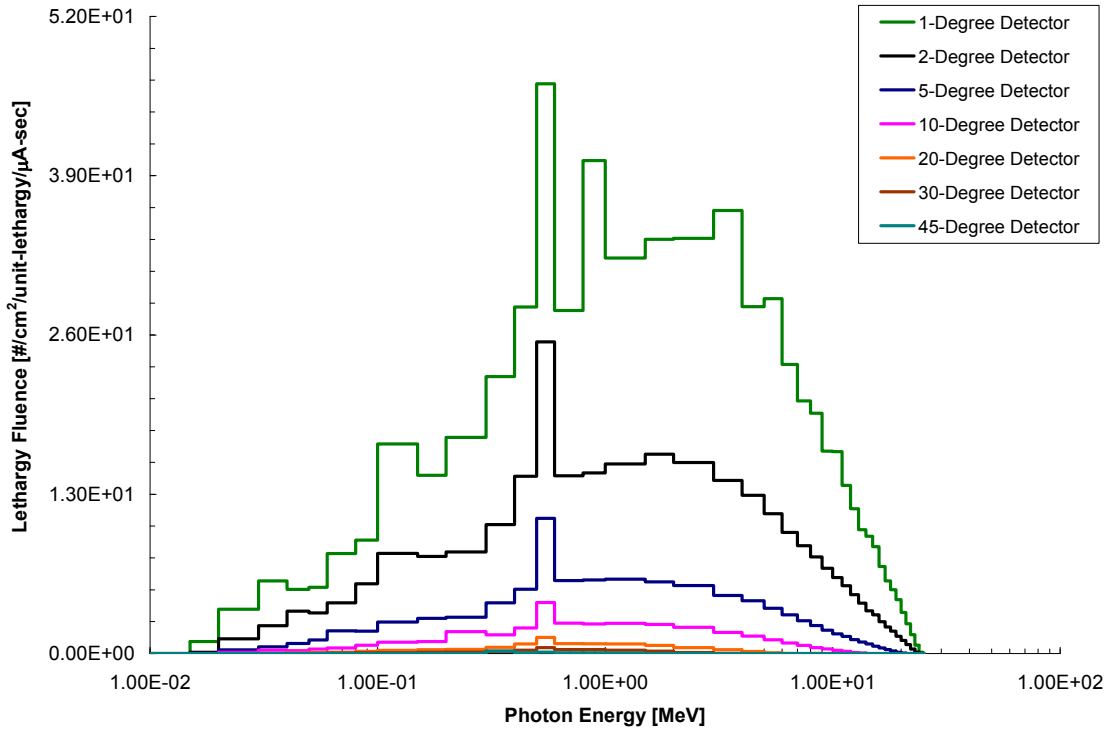

Figure E-84. Photon Spectrum (1 to 45 degree detectors) at 170 meters for the Beam Only Contribution (in Air).

APPENIDIX F

CALCULATED ELECTRON SPECTRA

The electron spectra calculated for all downfield distances are reported as lethargy fluence. For scaling purposes, spectra from the detector at 0 degrees are presented on one plot and spectra from all other detectors are presented on an additional plot. Additionally, the relative lethargy fluences are reported for the standard system prototype.

Fluences are reported for the following calculation scenarios:

1. PITAS prototype in air (lethargy fluence and relative lethargy fluence);

Data for 10 meters are shown in Figure F-1 through Figure F-4. Data for 25 meters are shown in Figure F-5 through Figure F-8. Data for 50 meters are shown in Figure F-9 through Figure F-12. Data for 100 meters are shown in Figure F-13 through Figure F-16. Data for 120 meters are shown in Figure F-17 through Figure F-20. Data for 170 meters are shown in Figure F-21 through Figure F-24.

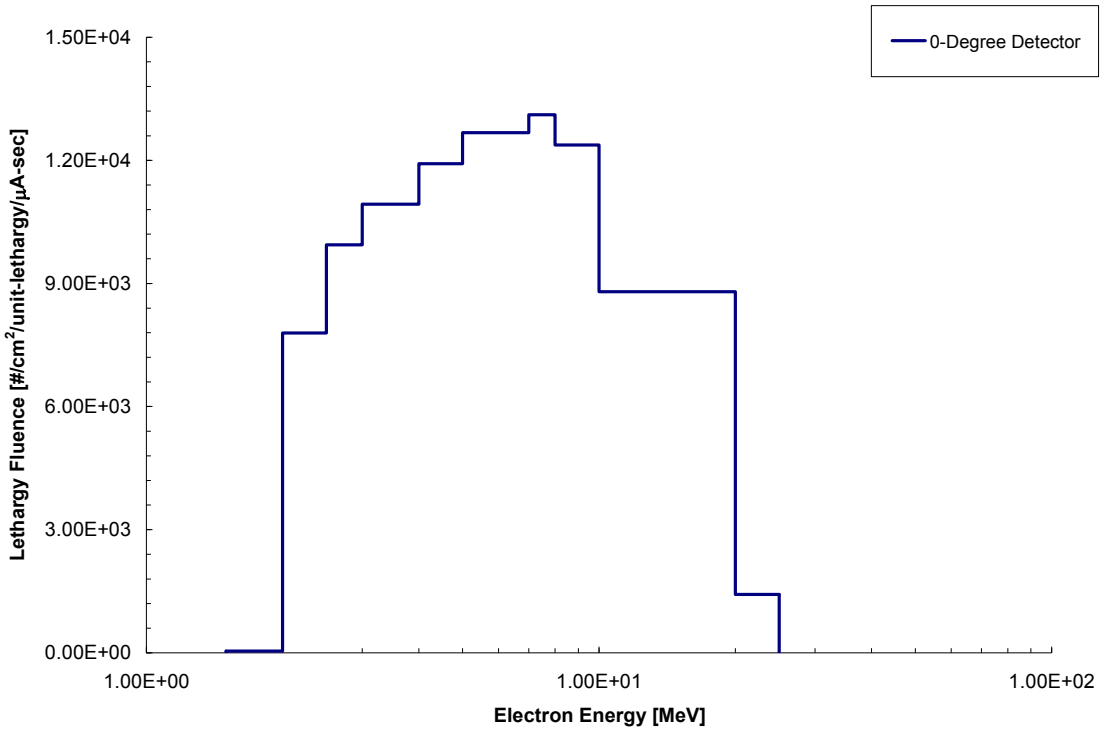

Figure F-1. Electron Spectrum (0 degree detector) at 10 meters for the System in Air.

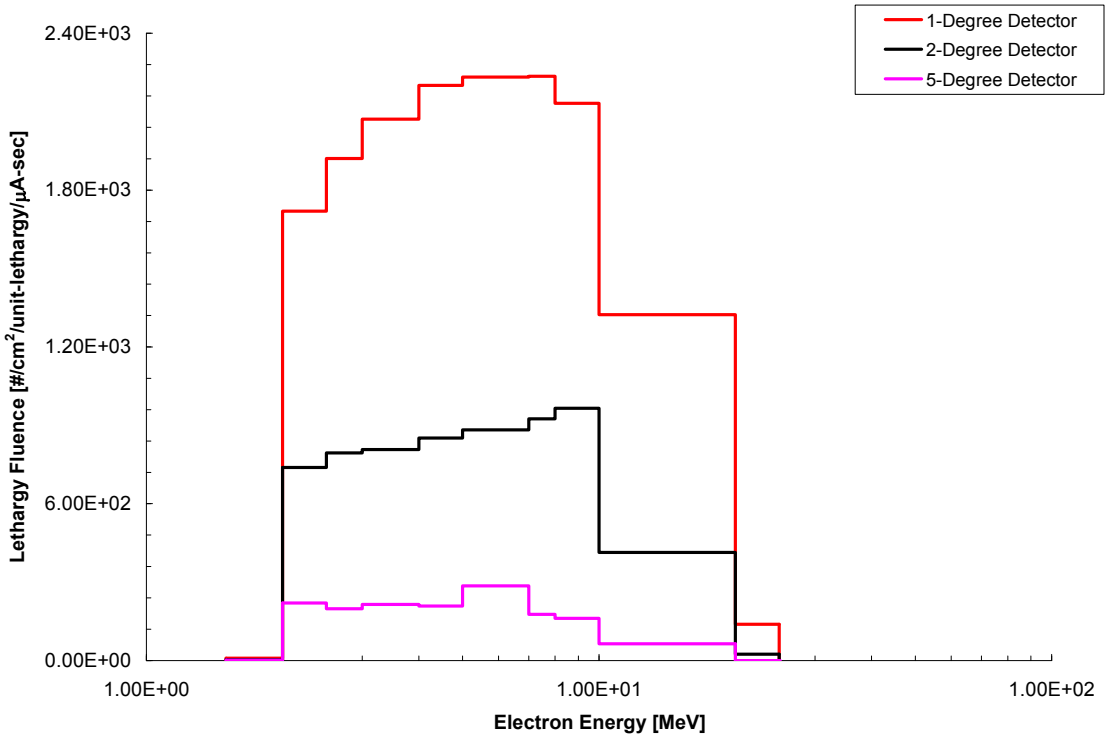

Figure F-2. Electron Spectrum (1 to 5 degree detectors) at 10 meters for the System in Air.

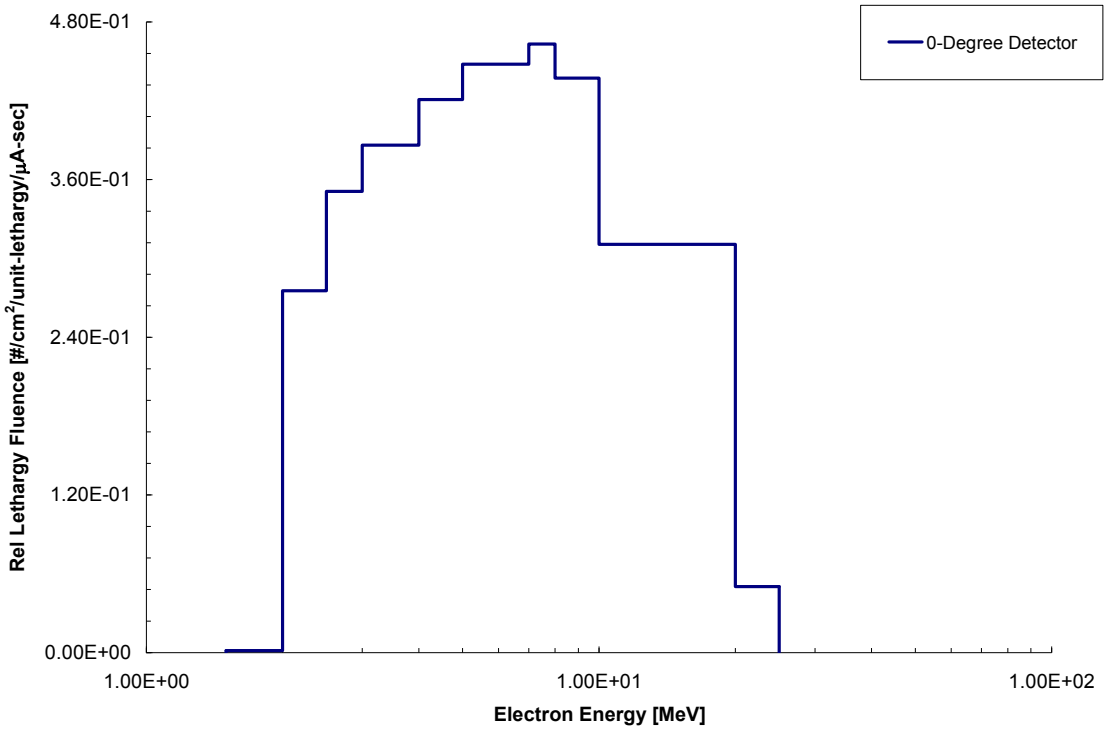

Figure F-3. Relative Electron Spectrum (0 degree detector) at 10 meters for the System in Air.

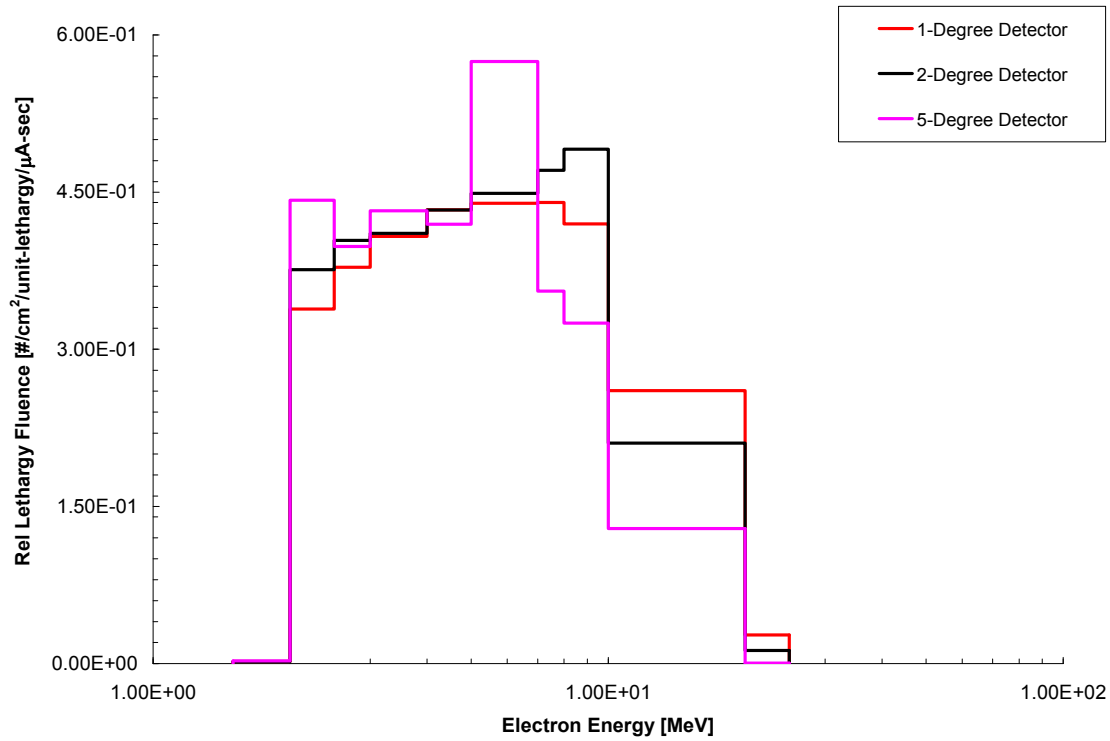

Figure F-4. Relative Electron Spectrum (1 to 5 degree detectors) at 10 meters for the System in Air.

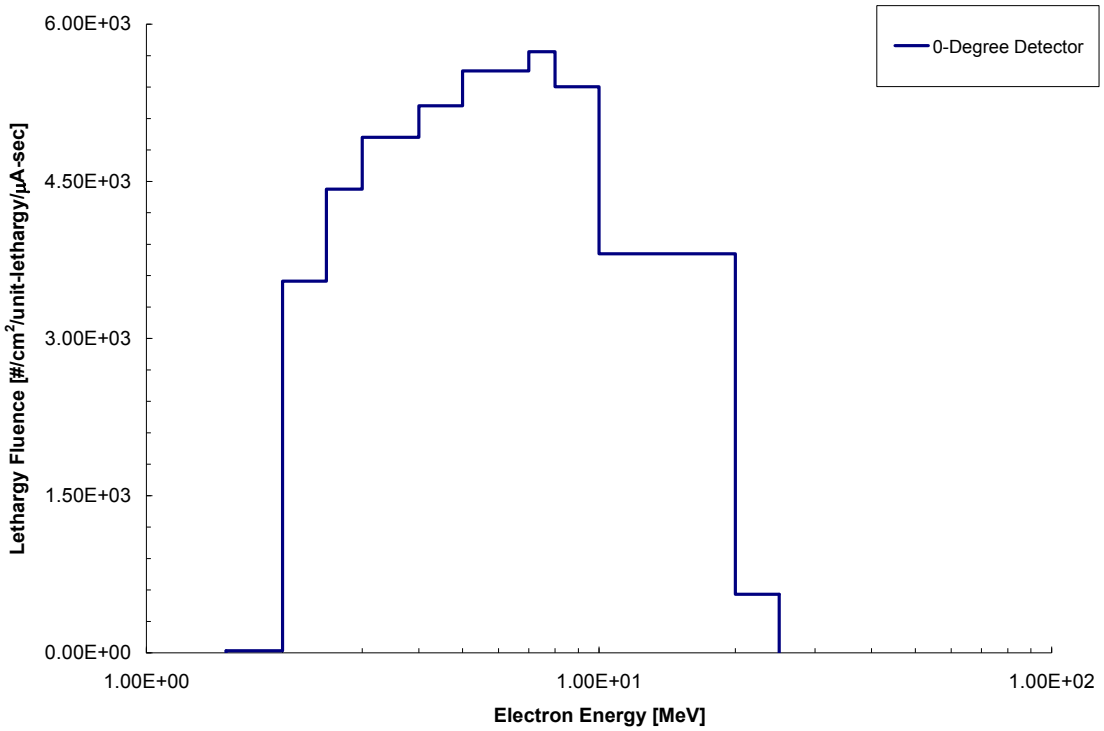

Figure F-5. Electron Spectrum (0 degree detector) at 25 meters for the System in Air.

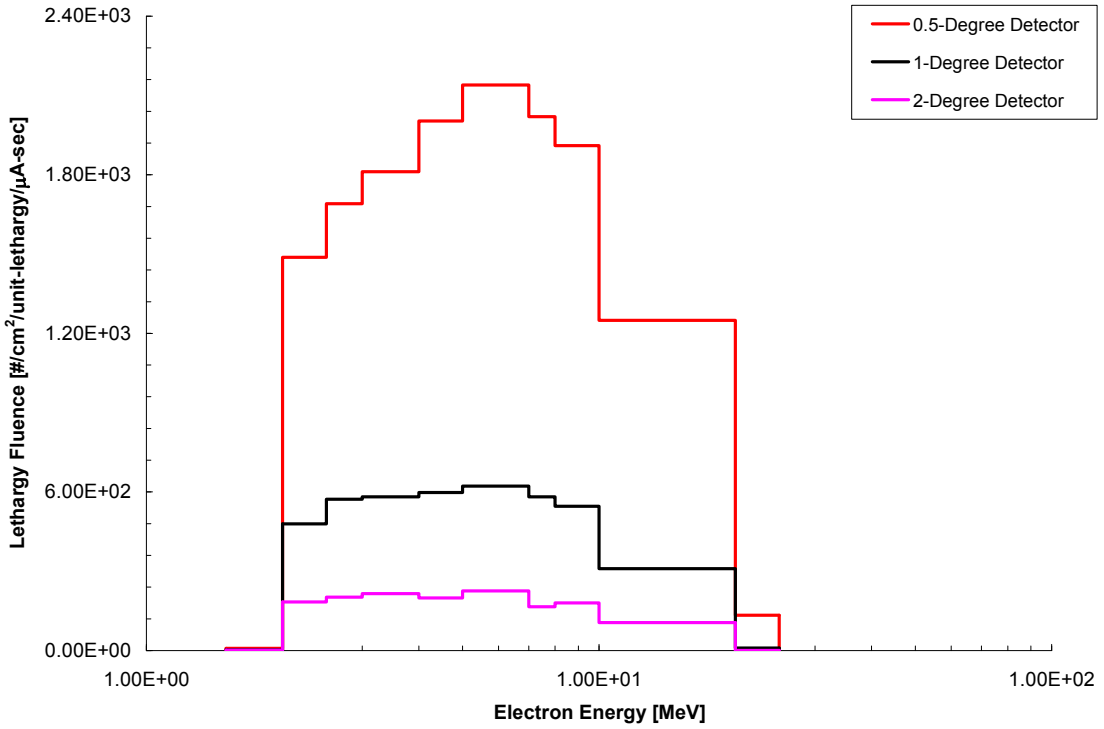

Figure F-6. Electron Spectrum (0.5 to 2 degree detectors) at 25 meters for the System in Air.

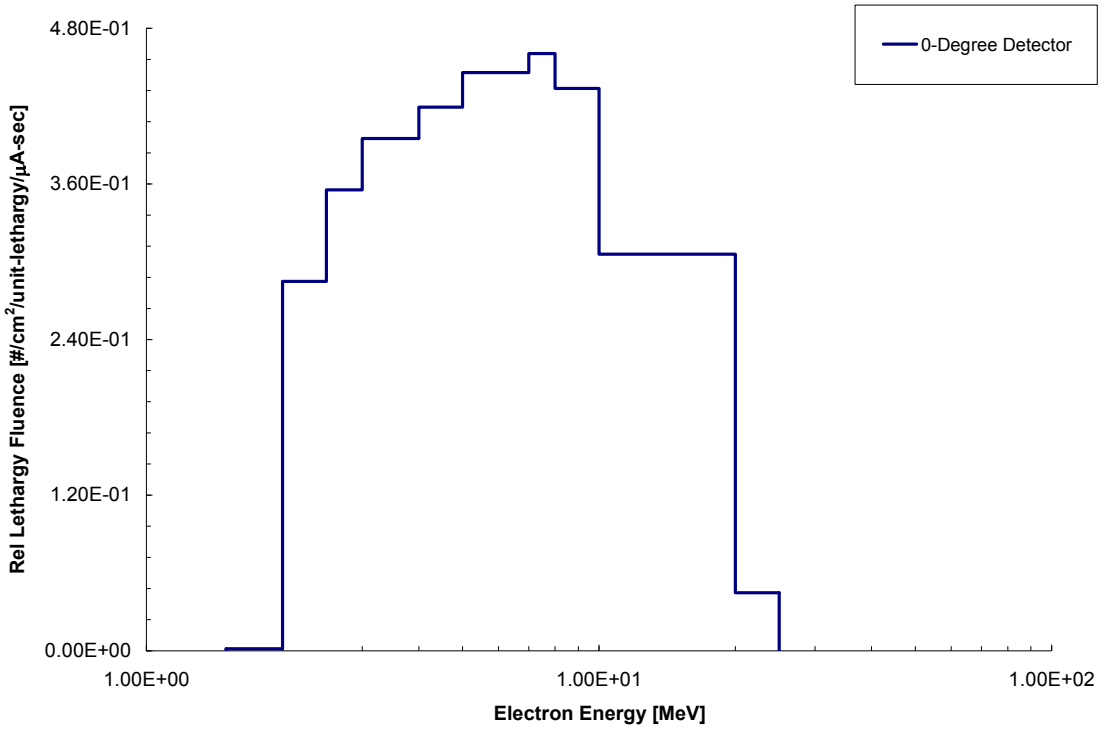

Figure F-7. Relative Electron Spectrum (0 degree detector) at 25 meters for the System in Air.

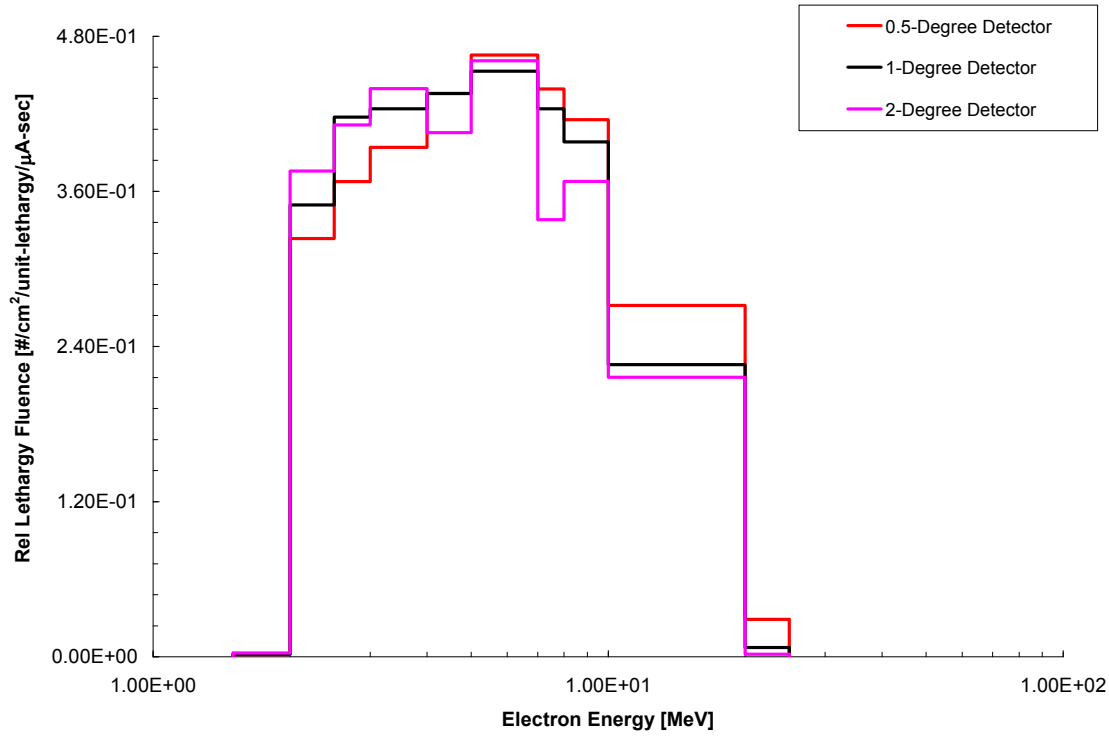

Figure F-8. Relative Electron Spectrum (0.5 to 2 degree detectors) at 25 meters for the System in Air.

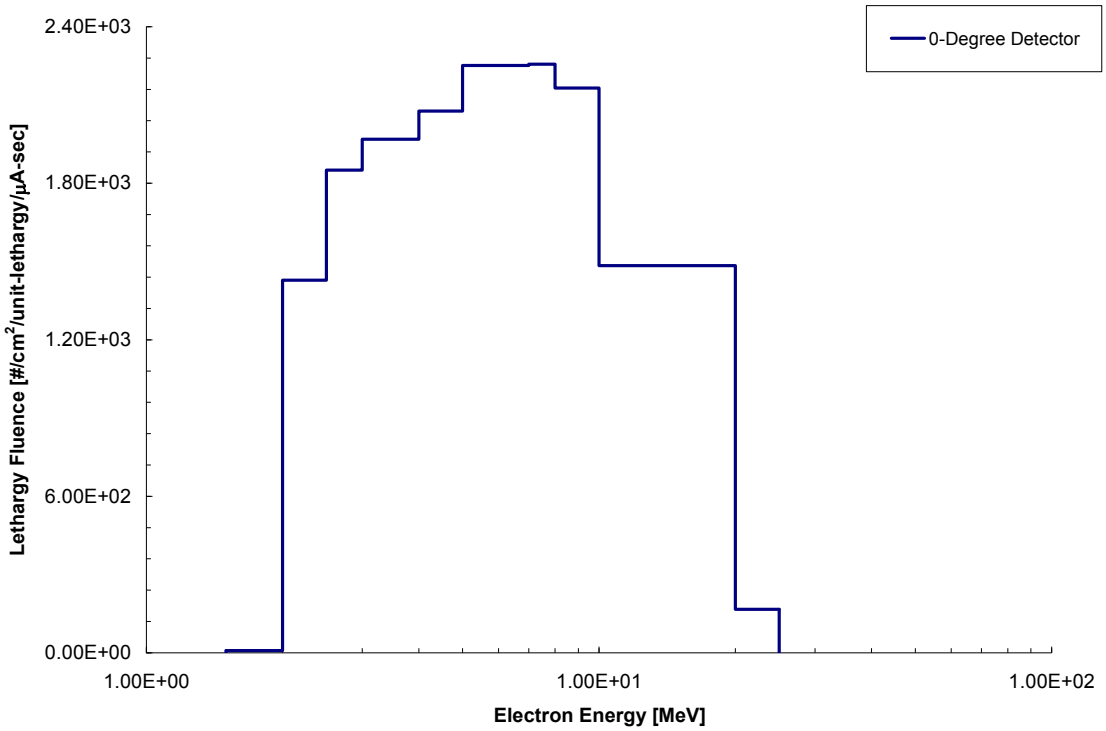

Figure F-9. Electron Spectrum (0 degree detector) at 50 meters for the System in Air.

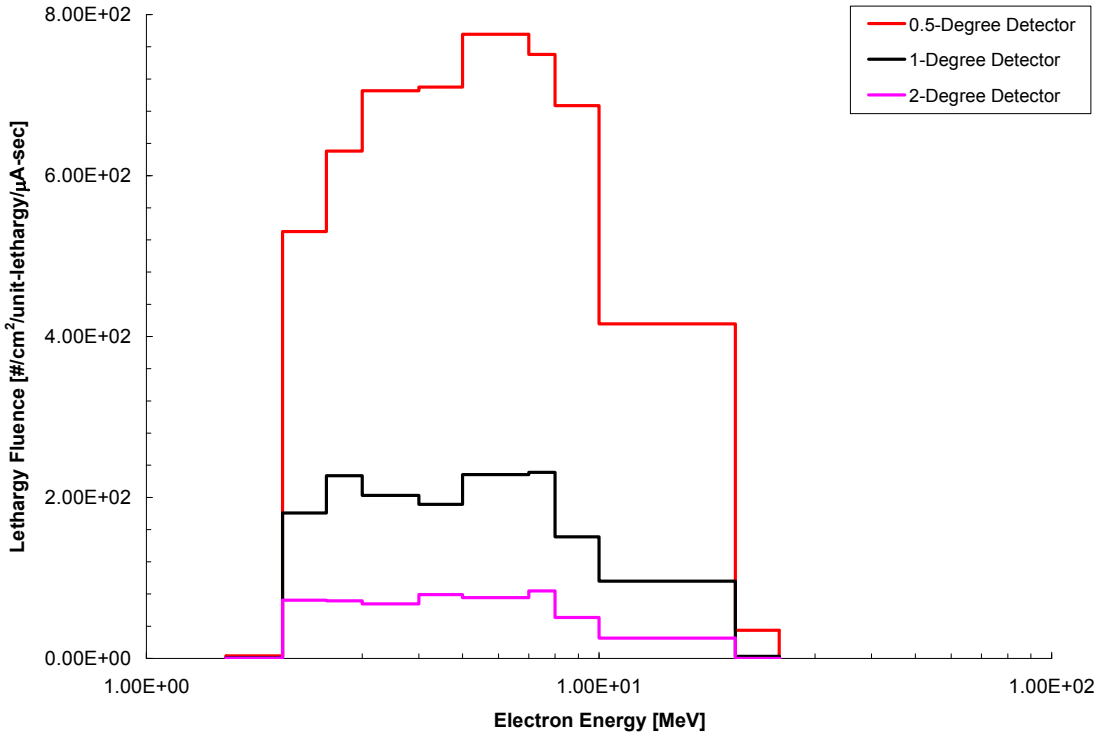

Figure F-10. Electron Spectrum (0.5 to 2 degree detectors) at 50 meters for the System in Air.

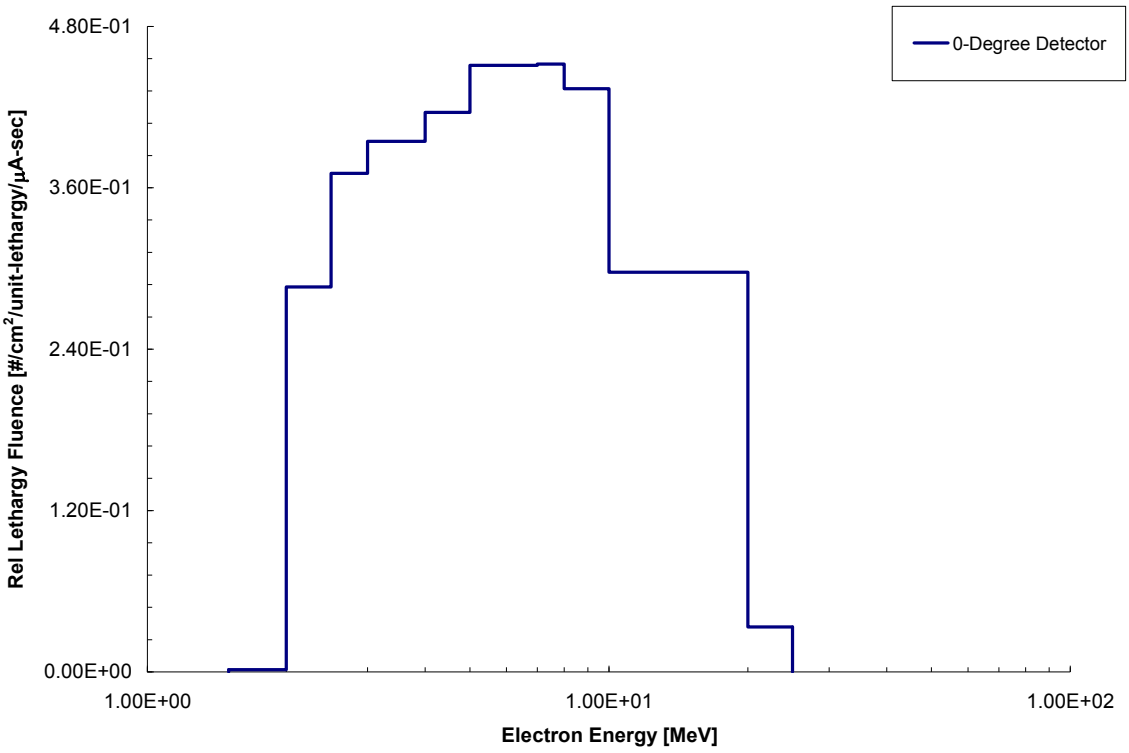

Figure F-11. Relative Electron Spectrum (0 degree detector) at 50 meters for the System in Air.

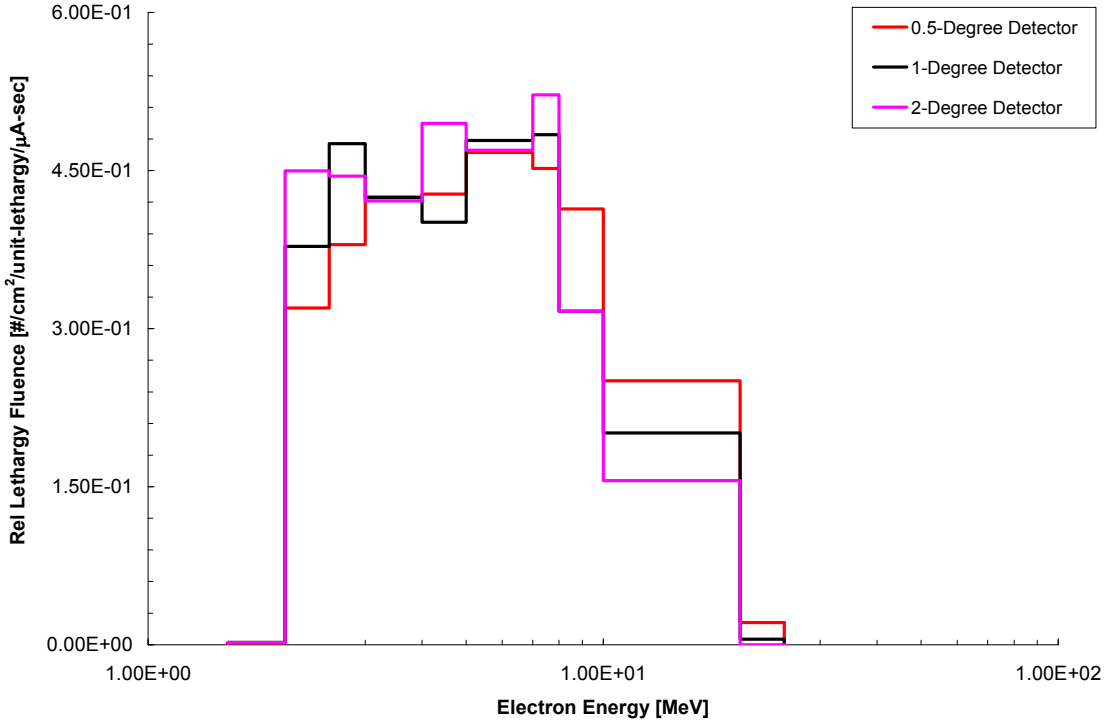

Figure F-12. Relative Electron Spectrum (0.5 to 2 degree detectors) at 50 meters for the System in Air.

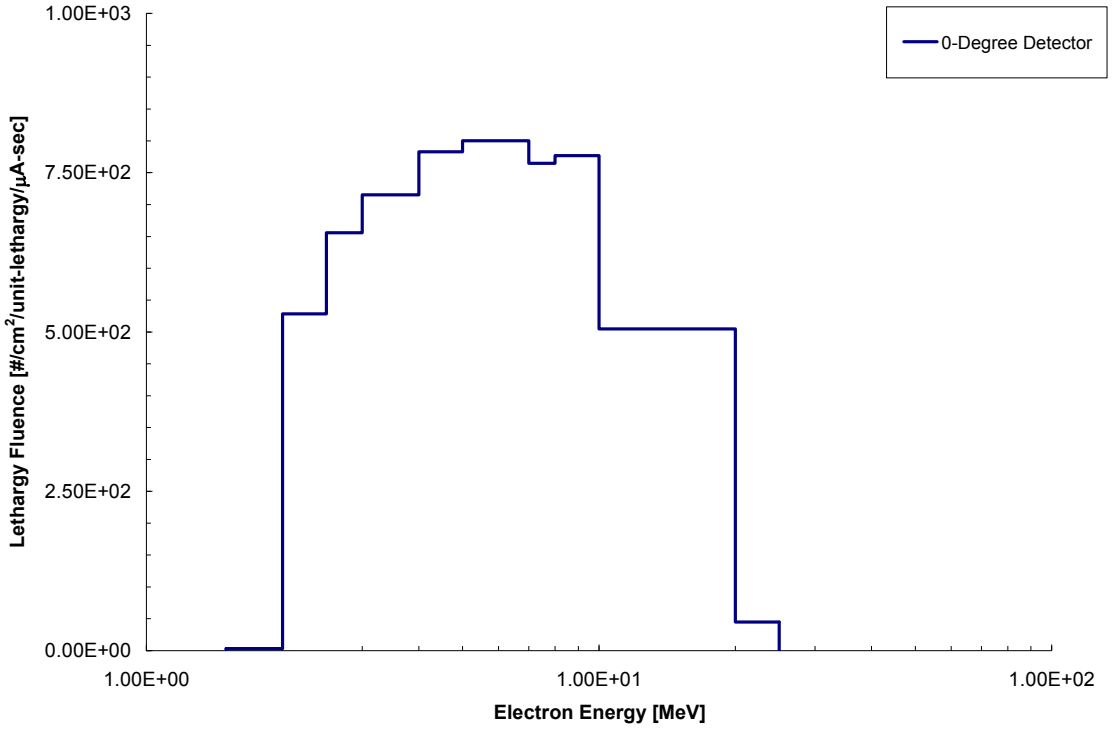

Figure F-13. Electron Spectrum (0 degree detector) at 100 meters for the System in Air.

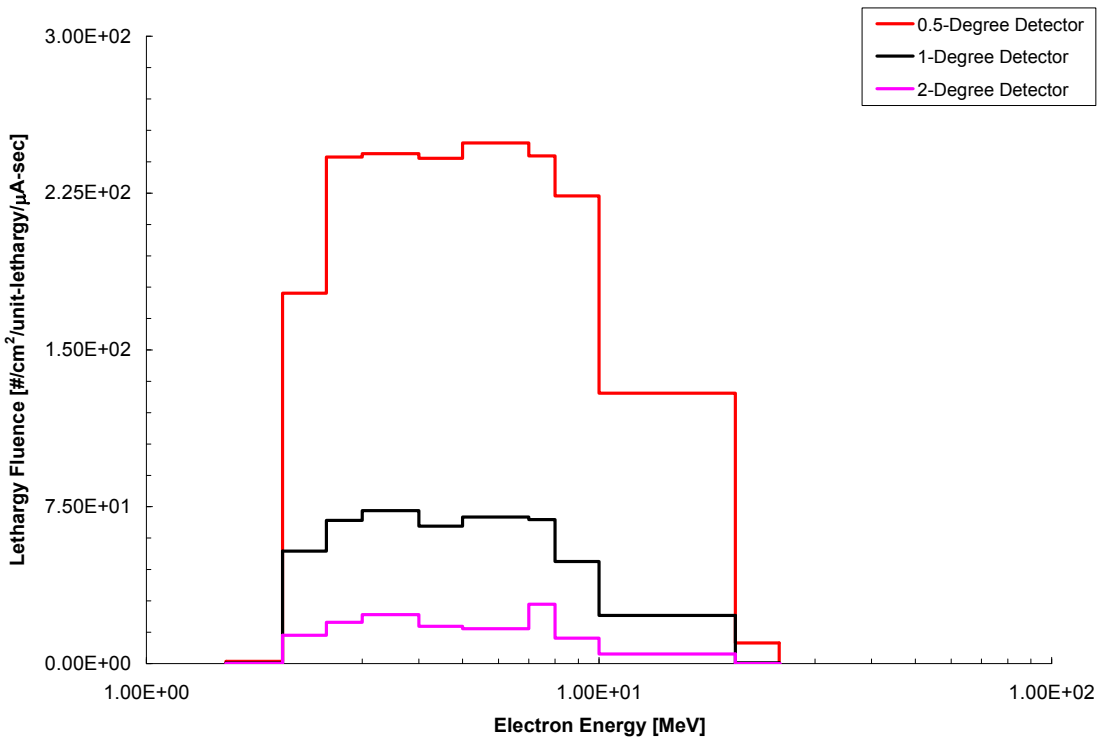

Figure F-14. Electron Spectrum (0.5 to 2 degree detectors) at 100 meters for the System in Air.

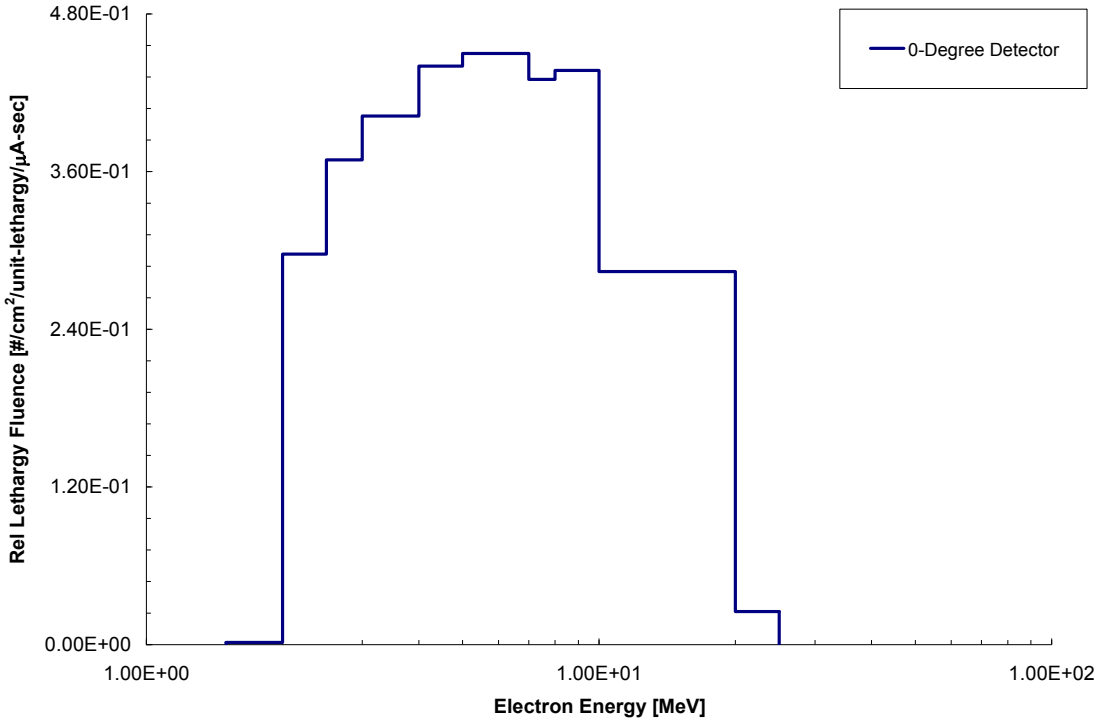

Figure F-15. Relative Electron Spectrum (0 degree detector) at 100 meters for the System in Air.

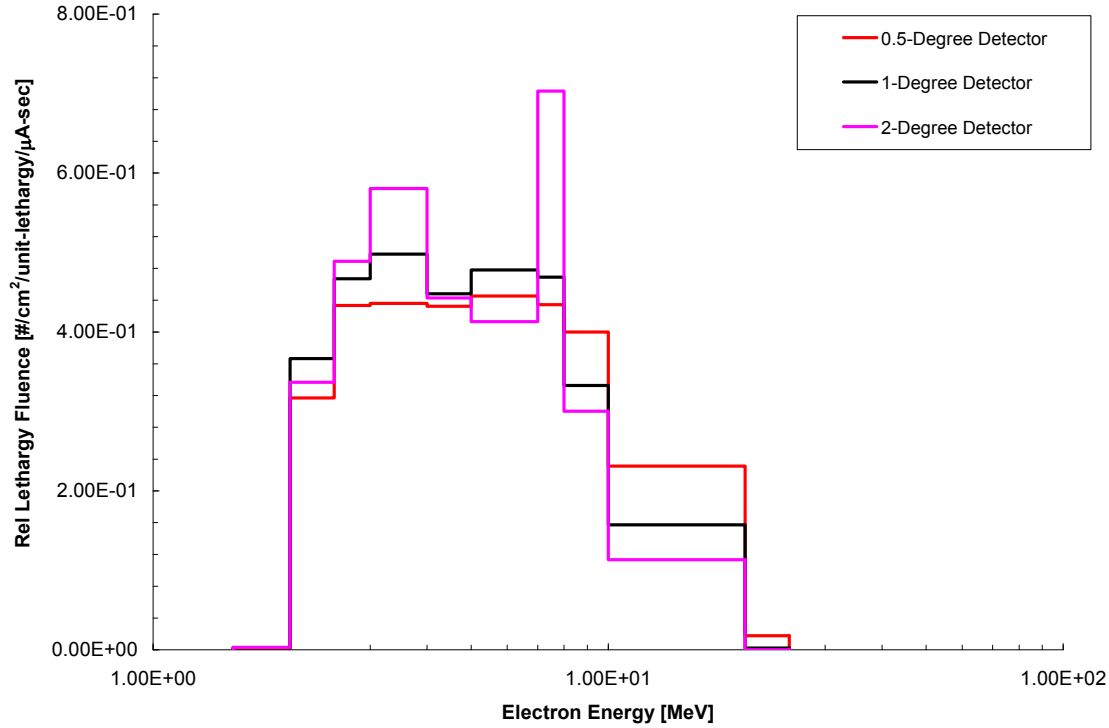

Figure F-16. Relative Electron Spectrum (0.5 to 2 degree detectors) at 100 meters for the System in Air.

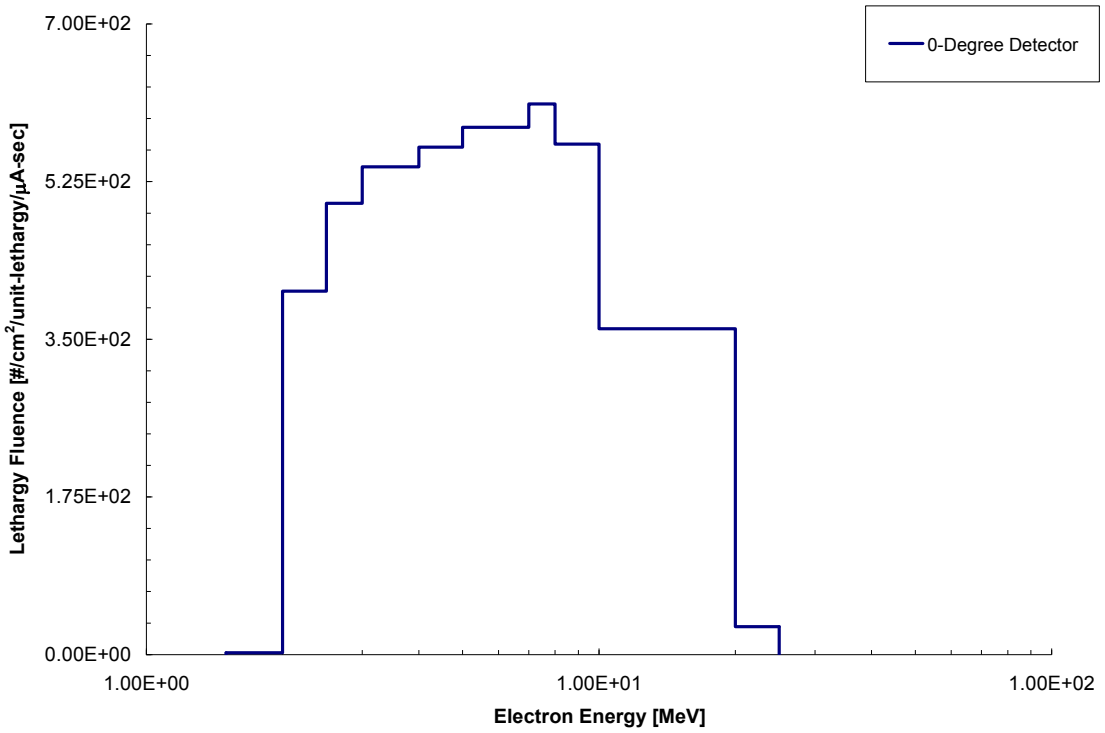

Figure F-17. Electron Spectrum (0 degree detector) at 120 meters for the System in Air.

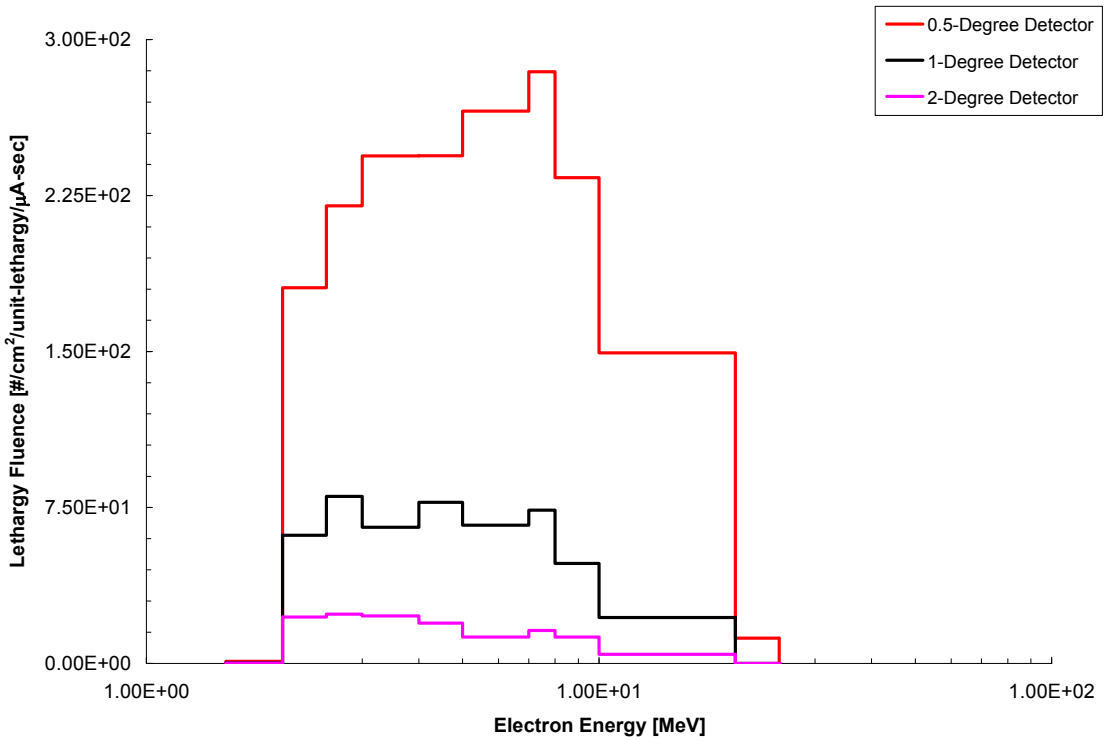

Figure F-18. Electron Spectrum (0.5 to 2 degree detectors) at 120 meters for the System in Air.

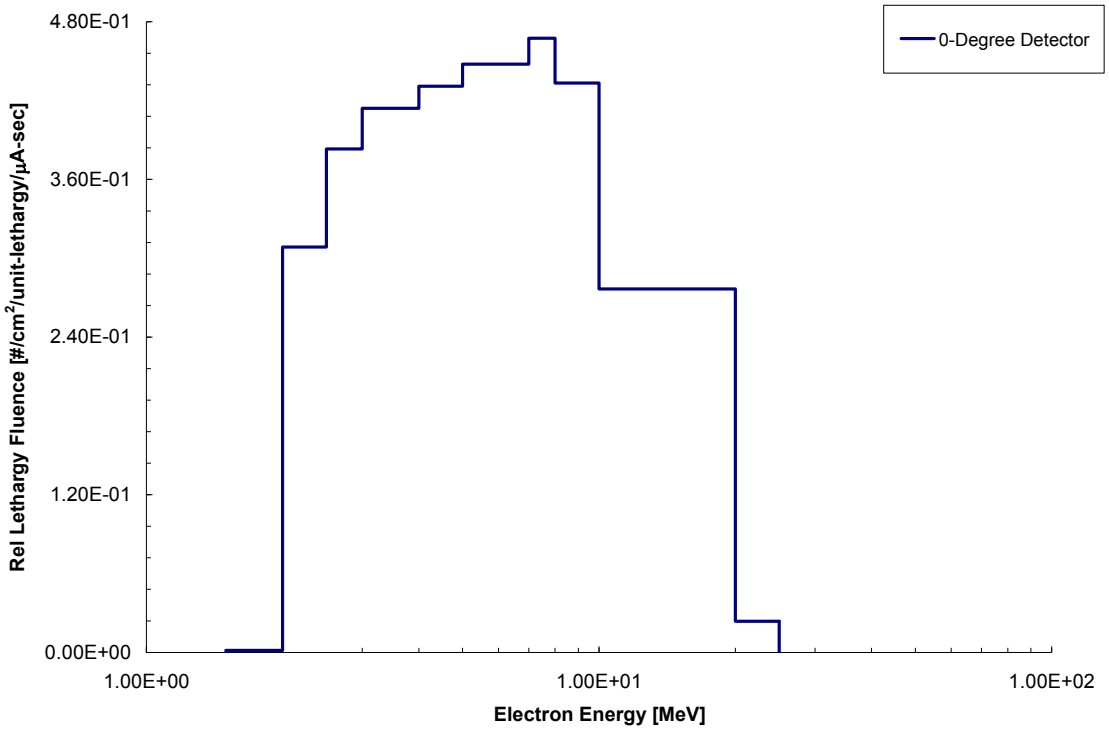

Figure F-19. Relative Electron Spectrum (0 degree detector) at 120 meters for the System in Air.

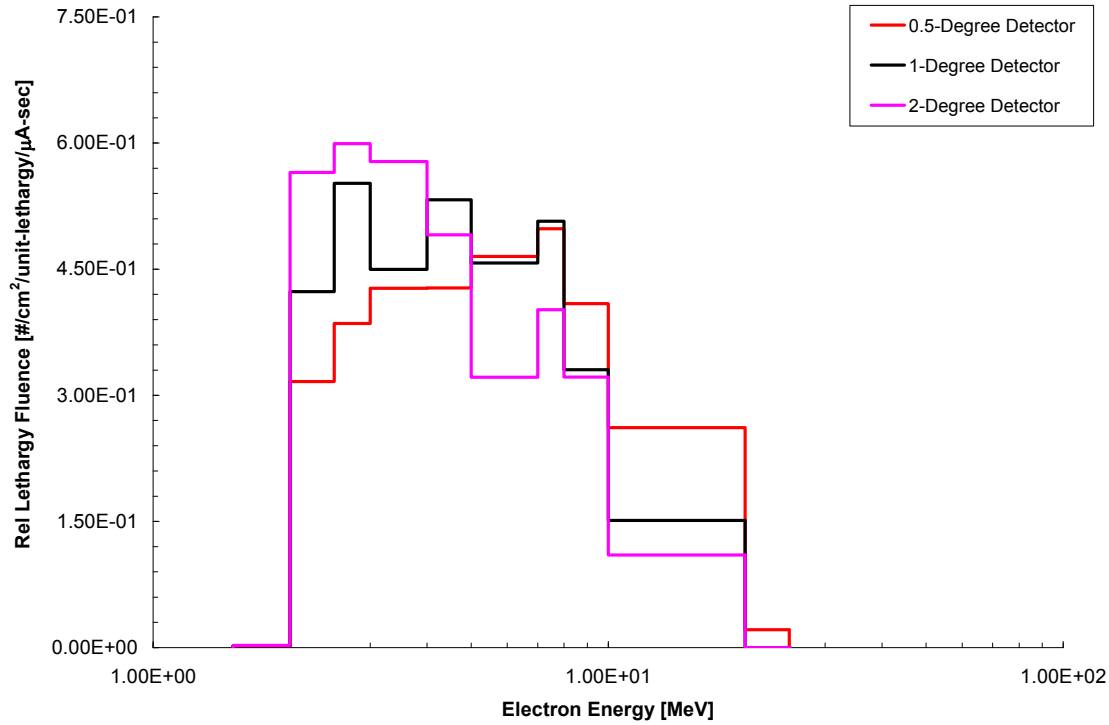

Figure F-20. Relative Electron Spectrum (0.5 to 2 degree detectors) at 120 meters for the System in Air.

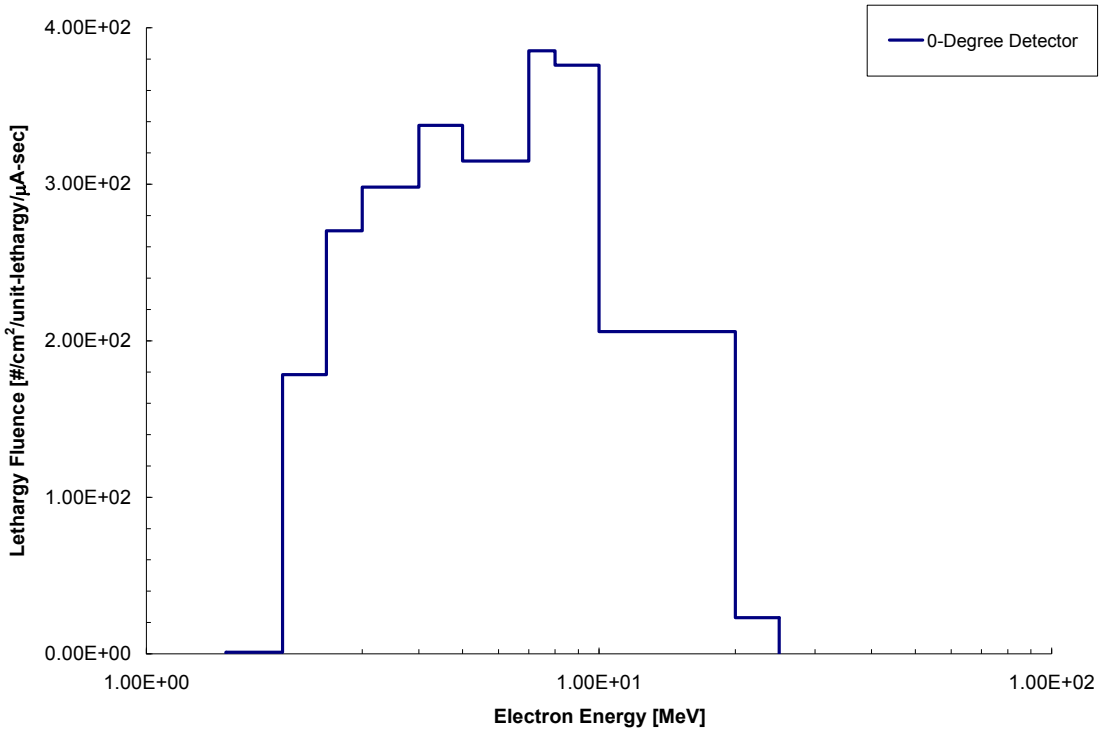

Figure F-21. Electron Spectrum (0 degree detector) at 170 meters for the System in Air.

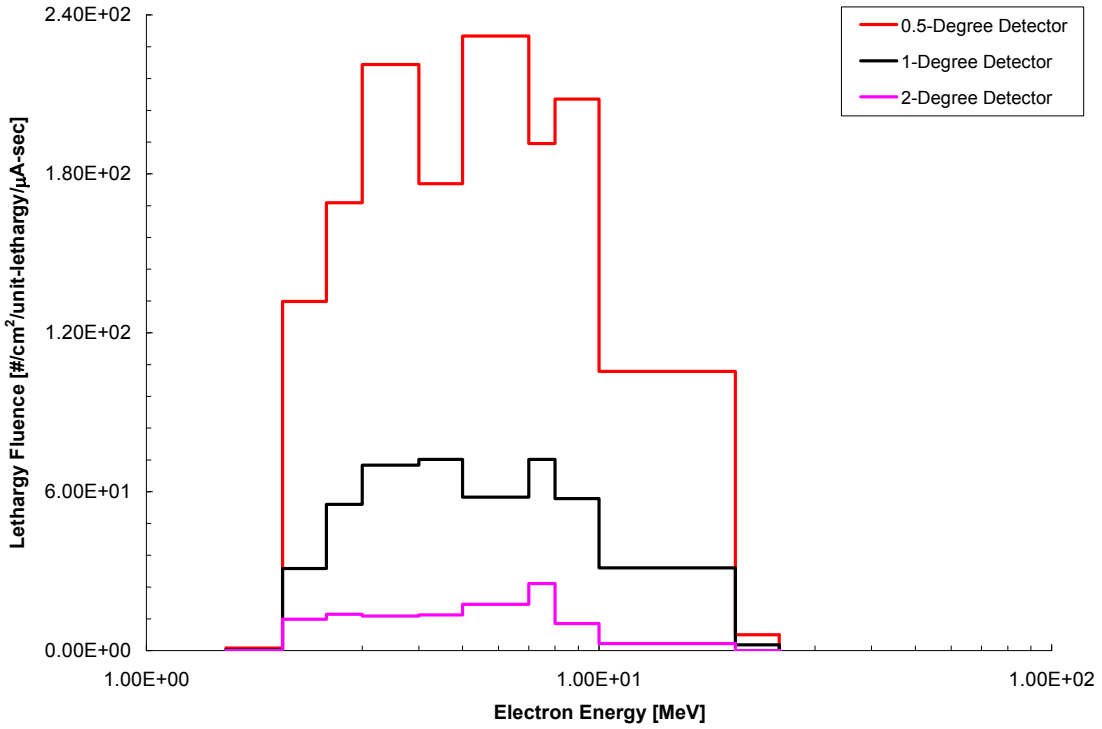

Figure F-22. Electron Spectrum (0.5 to 2 degree detectors) at 170 meters for the System in Air.

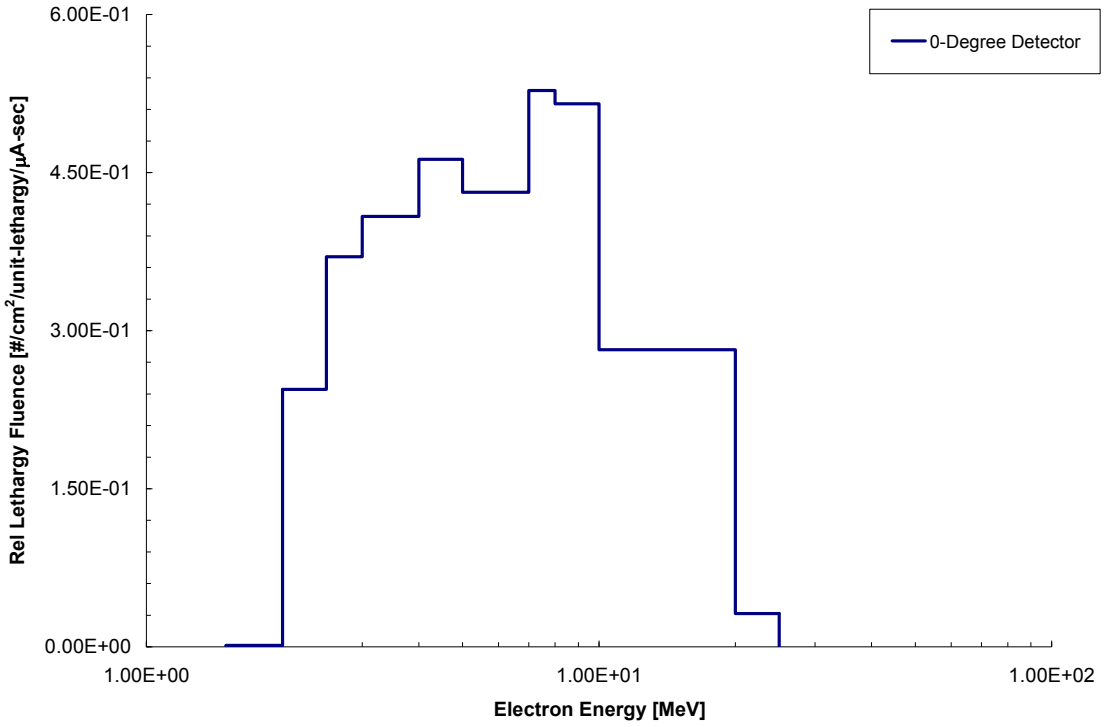

Figure F-23. Relative Electron Spectrum (0 degree detector) at 170 meters for the System in Air.

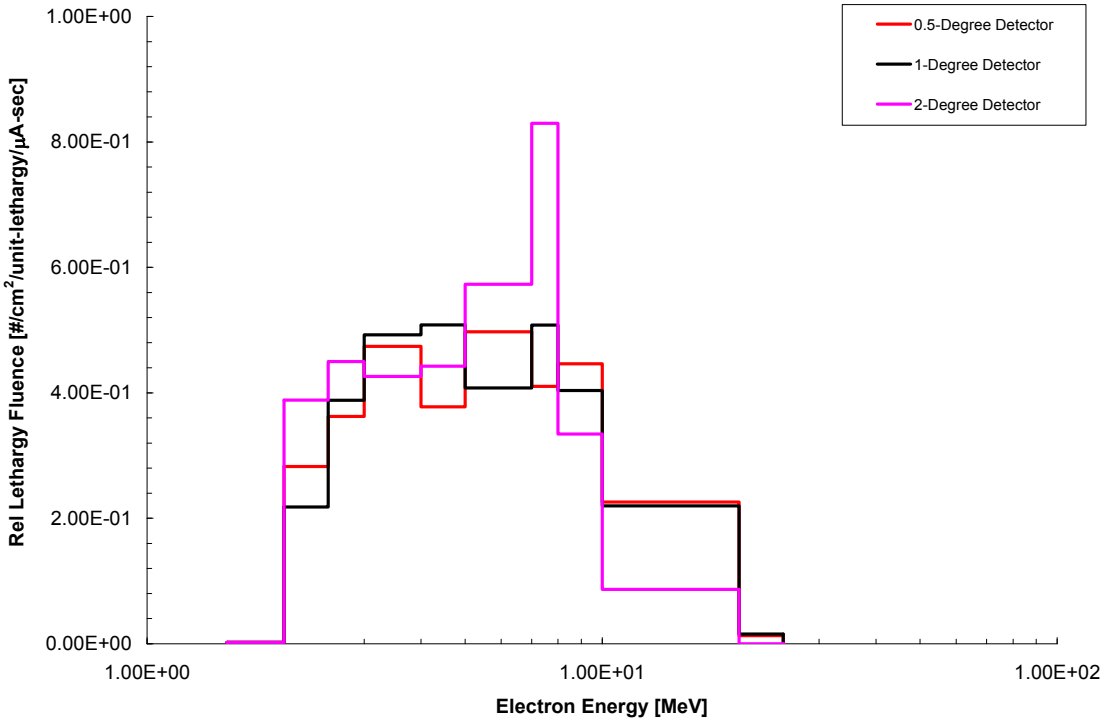

Figure F-24. Relative Electron Spectrum (0.5 to 2 degree detectors) at 170 meters for the System in Air.

APPENIDIX G

CALCULATED NEUTRON SPECTRA

The neutron spectra calculated for all downfield distances are reported as lethargy fluence. For scaling purposes, spectra from the detectors at 0 and 0.5 degrees are presented on one plot and spectra from 1 through 45 degrees are presented on an additional plot. Additionally, the relative lethargy fluences are reported for the standard system prototype.

Fluences are reported for the following calculation scenarios:

1. PITAS prototype in air (lethargy fluence and relative lethargy fluence);

Data for 10 meters are shown in Figure G-1 through Figure G-4. Data for 25 meters are shown in Figure G-5 through Figure G-8. Data for 50 meters are shown in Figure G-9 through Figure G-12. Data for 100 meters are shown in Figure G-13 through Figure G-16. Data for 120 meters are shown in Figure G-17 through Figure G-20. Data for 170 meters are shown in Figure G-21 through Figure G-24.

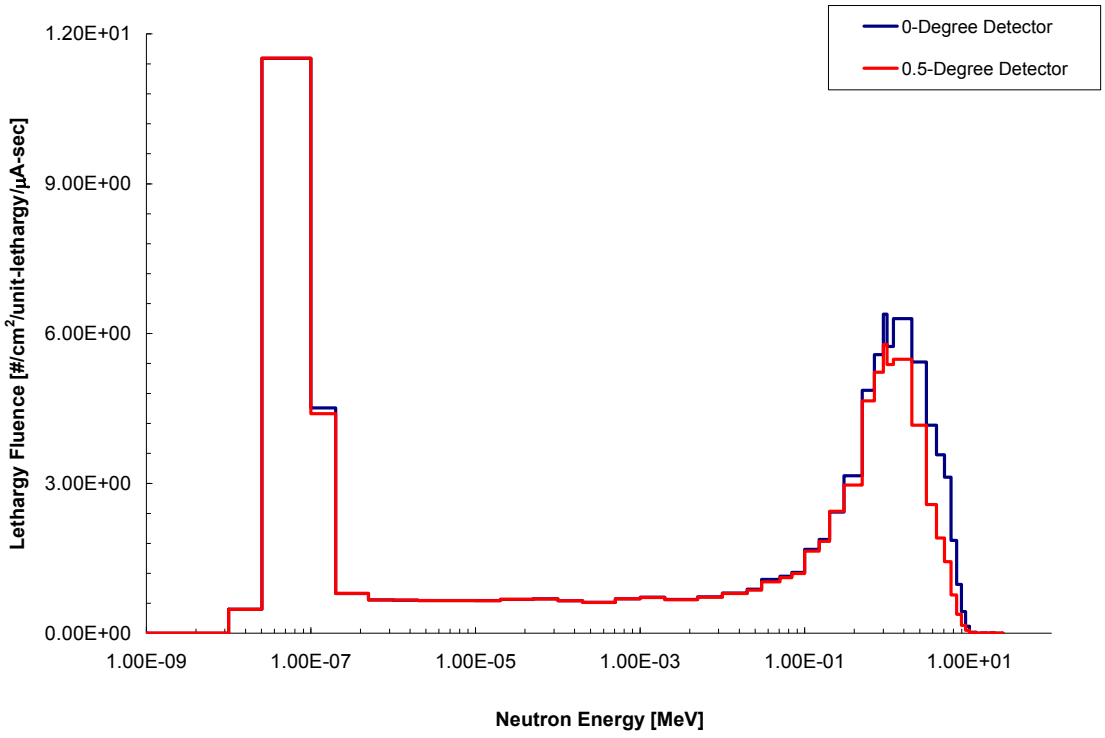

Figure G-1. Neutron Spectrum (0 and 0.5 degree detector) at 10 meters for the System in Air.

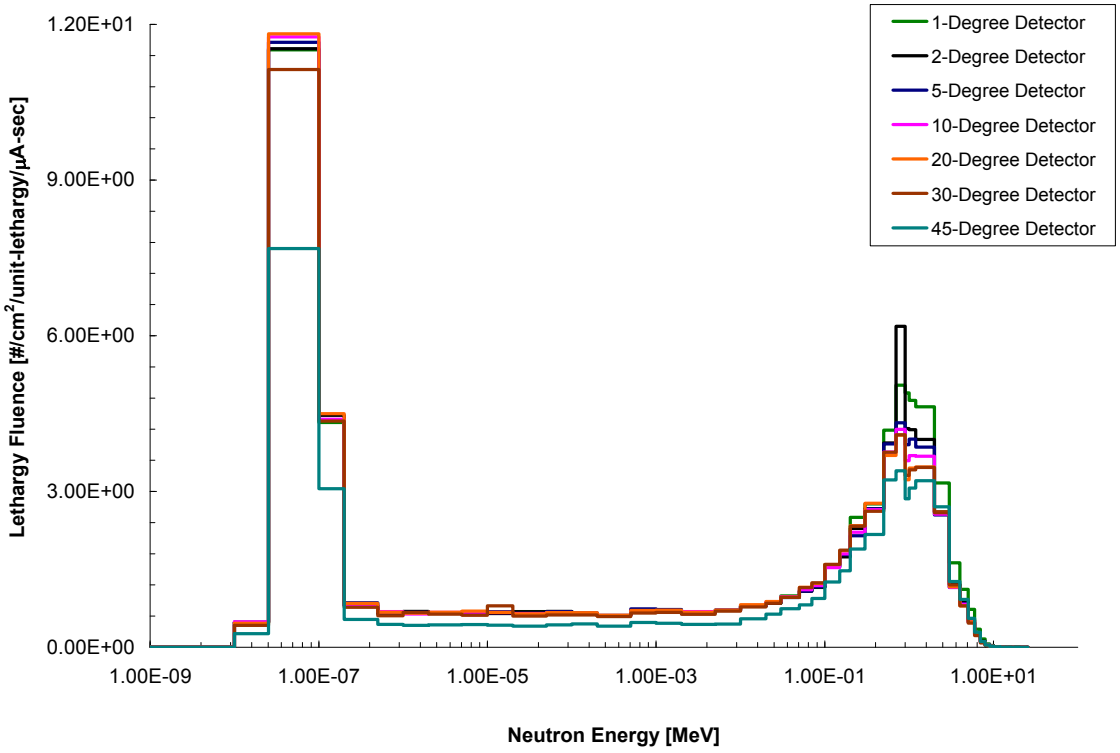

Figure G-2. Neutron Spectrum (1 to 45 degree detectors) at 10 meters for the System in Air.

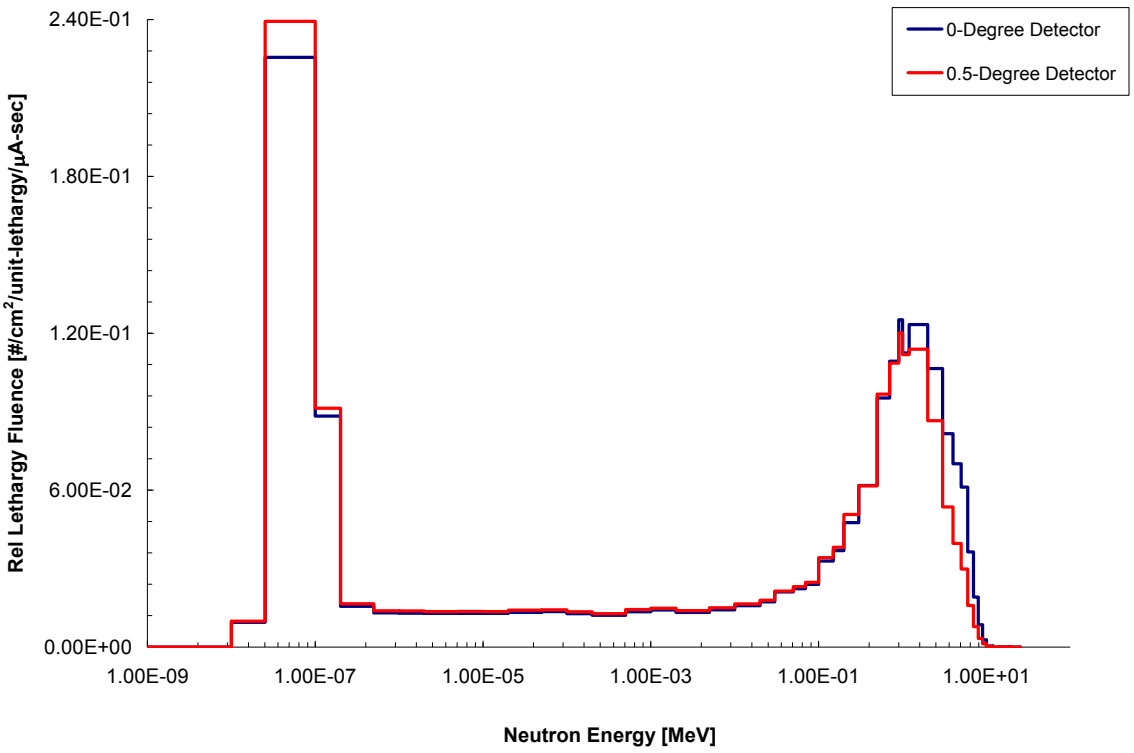

Figure G-3. Relative Neutron Spectrum (0 and 0.5 degree detector) at 10 meters for the System in Air.

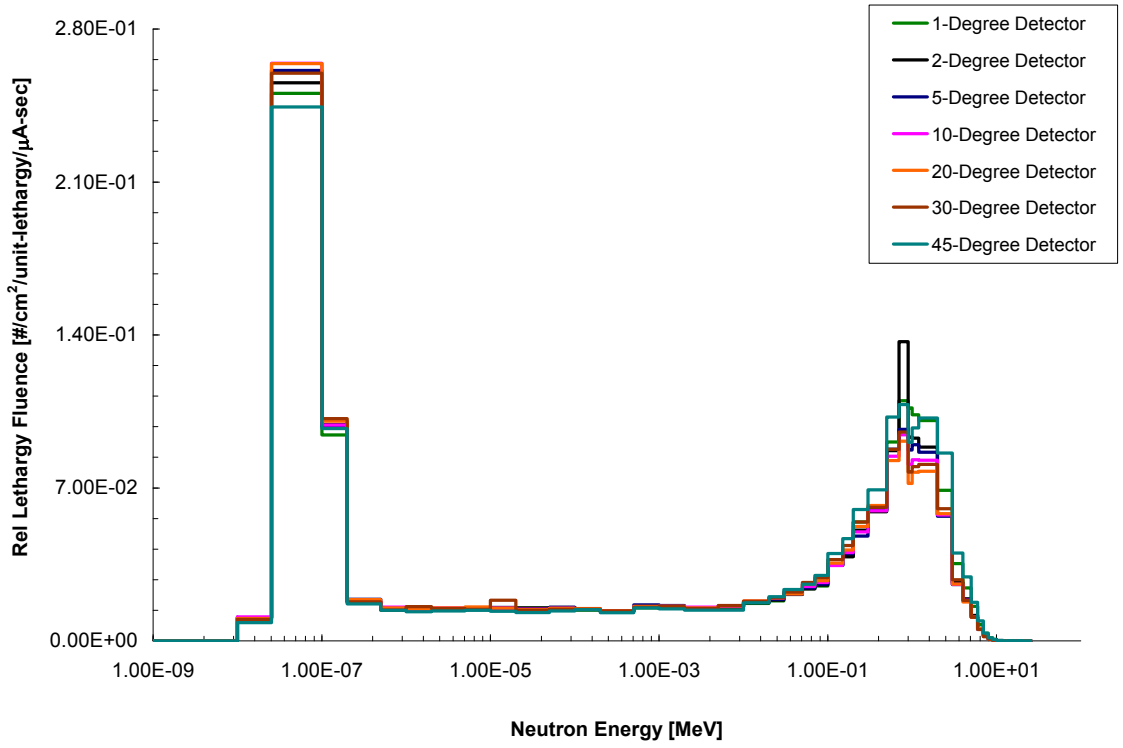

Figure G-4. Relative Neutron Spectrum (1 to 45 degree detectors) at 10 meters for the System in Air.

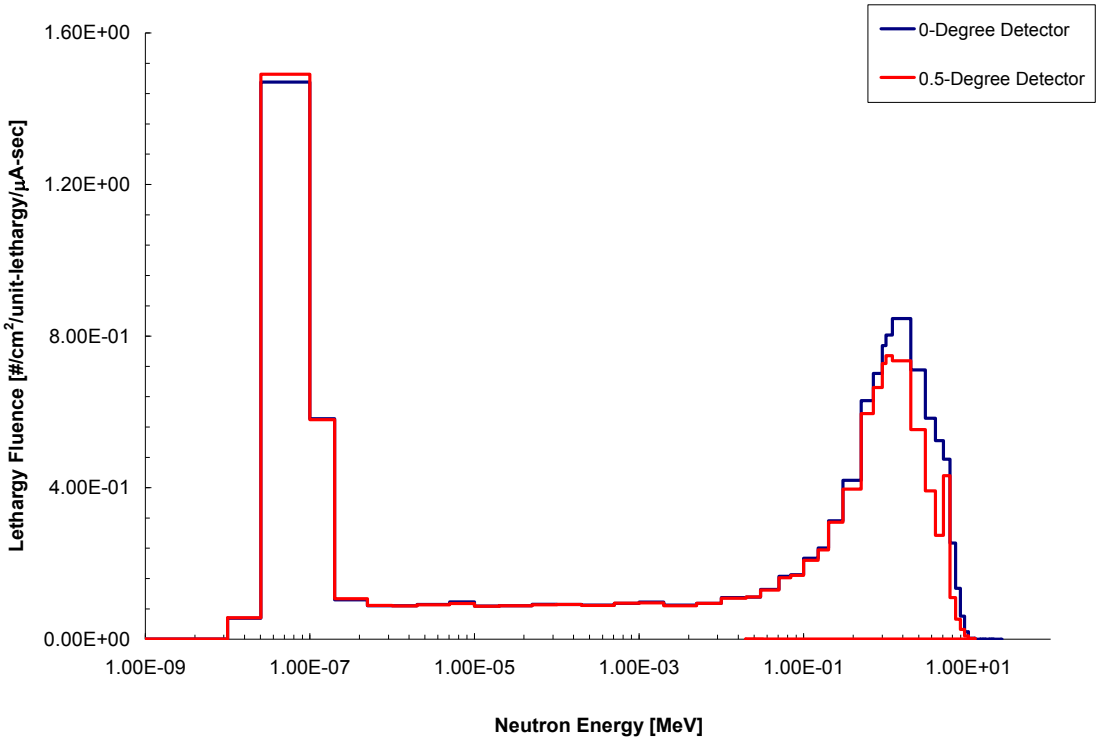

Figure G-5. Neutron Spectrum (0 and 0.5 degree detector) at 25 meters for the System in Air.

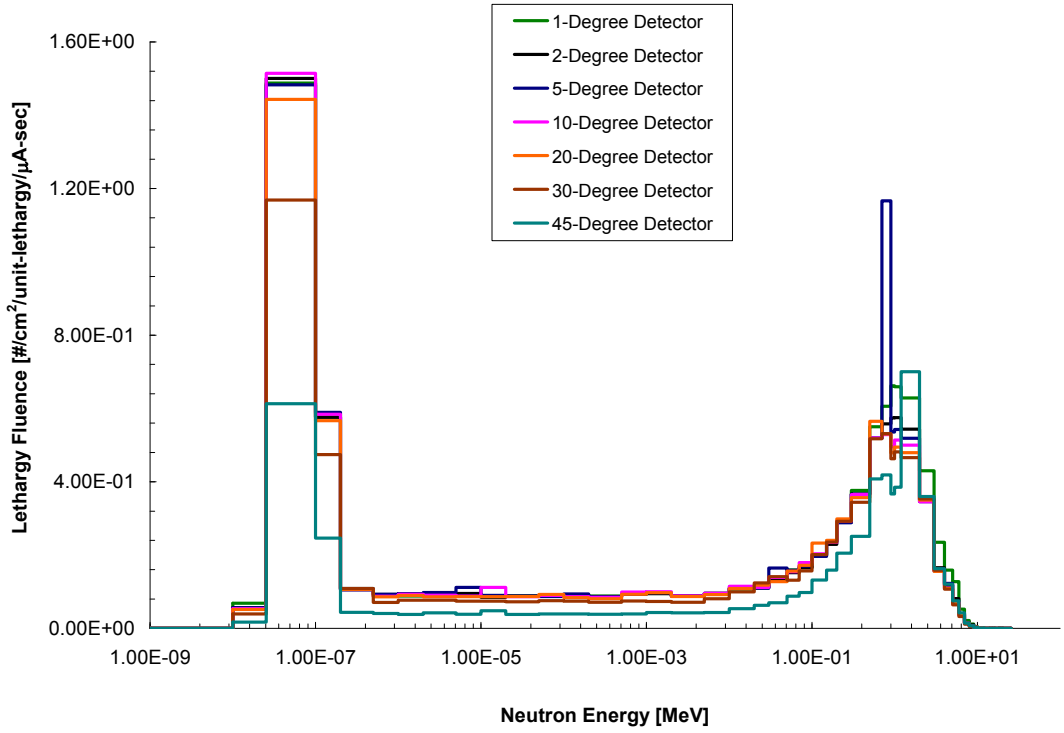

Figure G-6. Neutron Spectrum (1 to 45 degree detectors) at 25 meters for the System in Air.

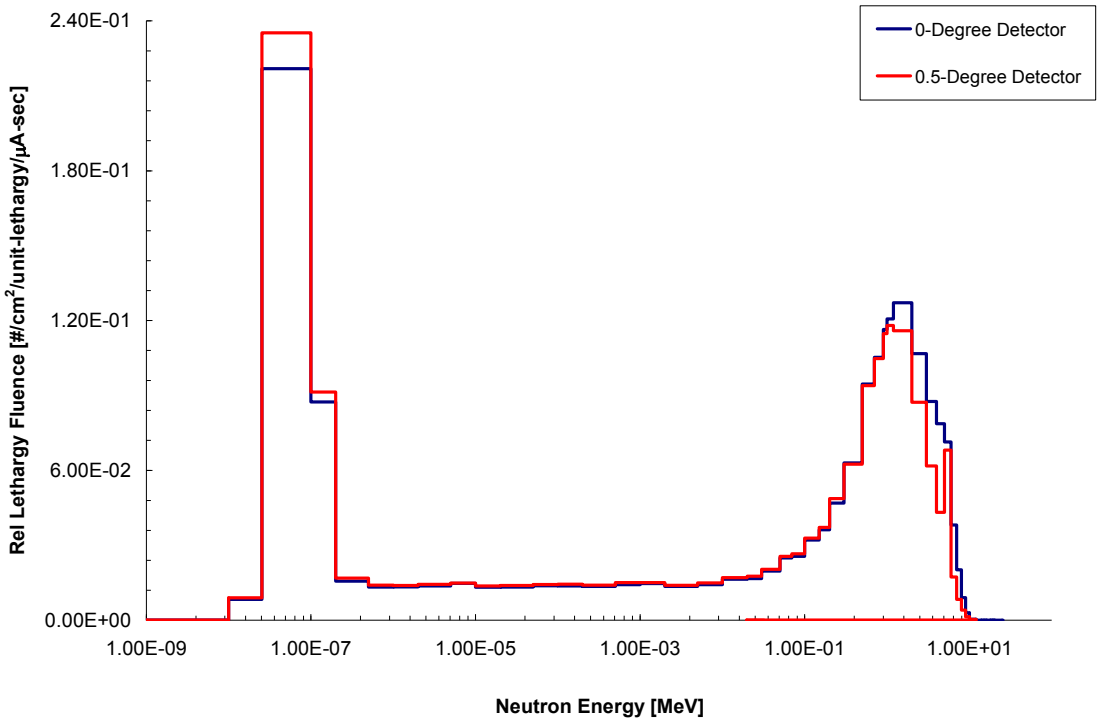

Figure G-7. Relative Neutron Spectrum (0 and 0.5 degree detector) at 25 meters for the System in Air.

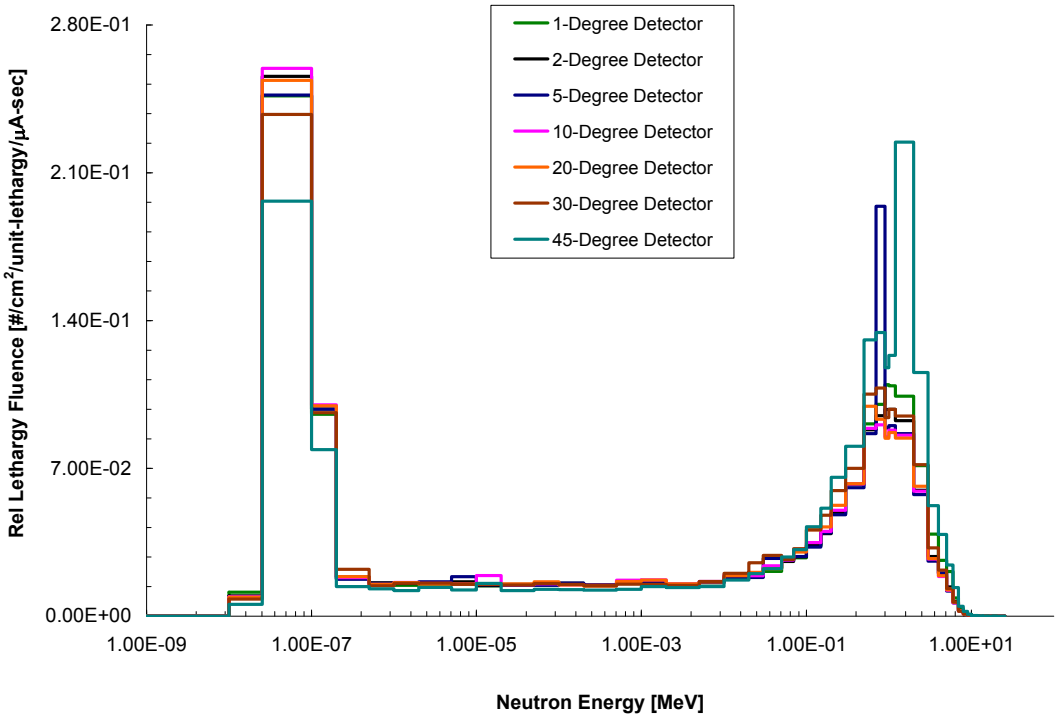

Figure G-8. Relative Neutron Spectrum (1 to 45 degree detectors) at 25 meters for the System in Air.

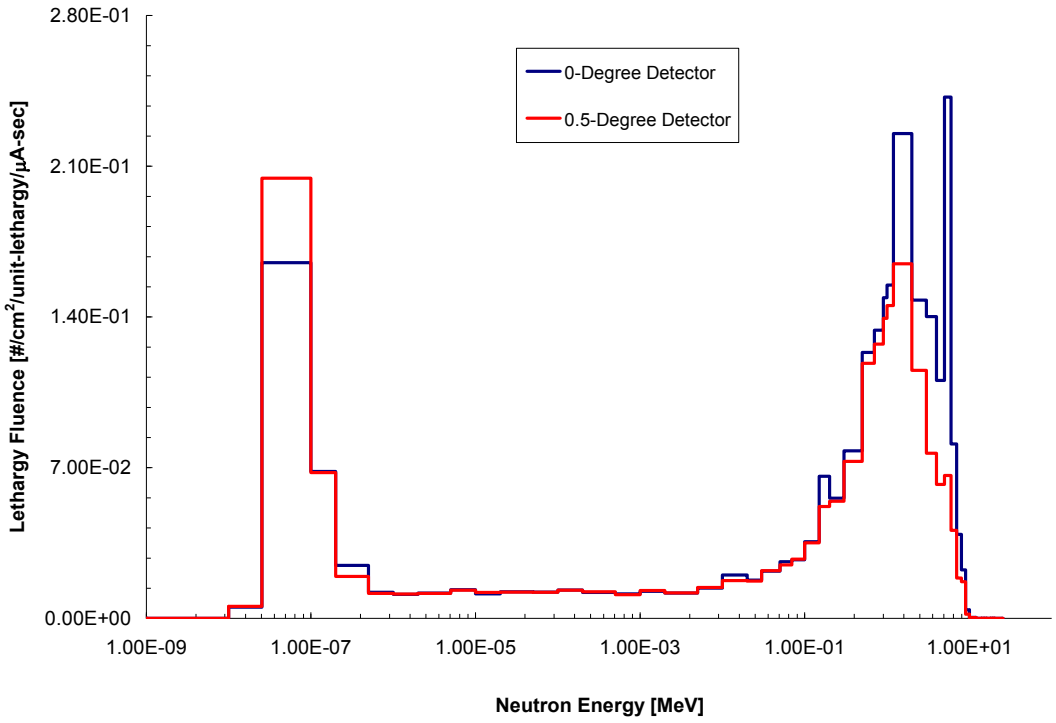

Figure G-9. Neutron Spectrum (0 and 0.5 degree detector) at 50 meters for the System in Air.

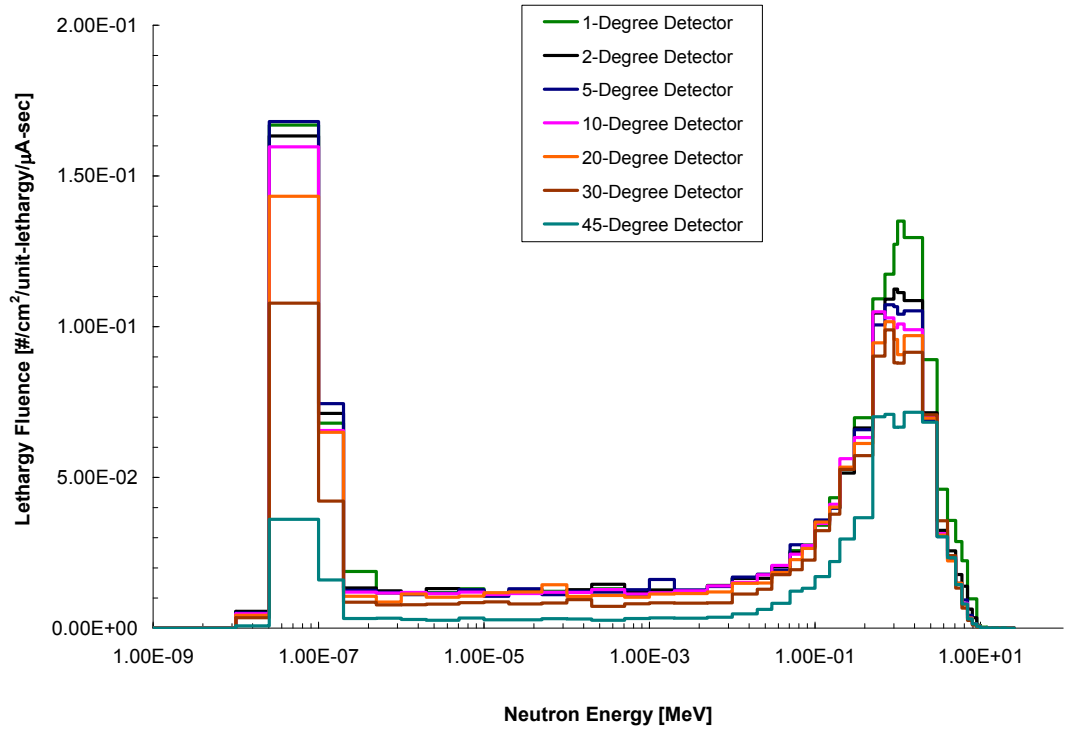

Figure G-10. Neutron Spectrum (1 to 45 degree detectors) at 50 meters for the System in Air.

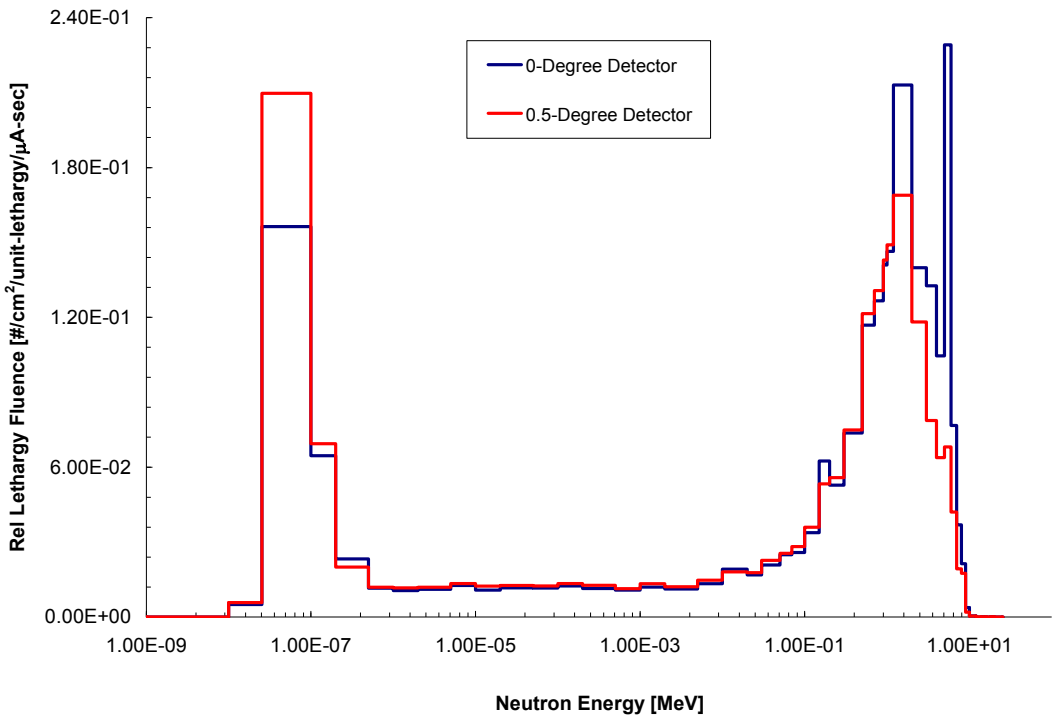

Figure G-11. Relative Neutron Spectrum (0 and 0.5 degree detector) at 50 meters for the System in Air.

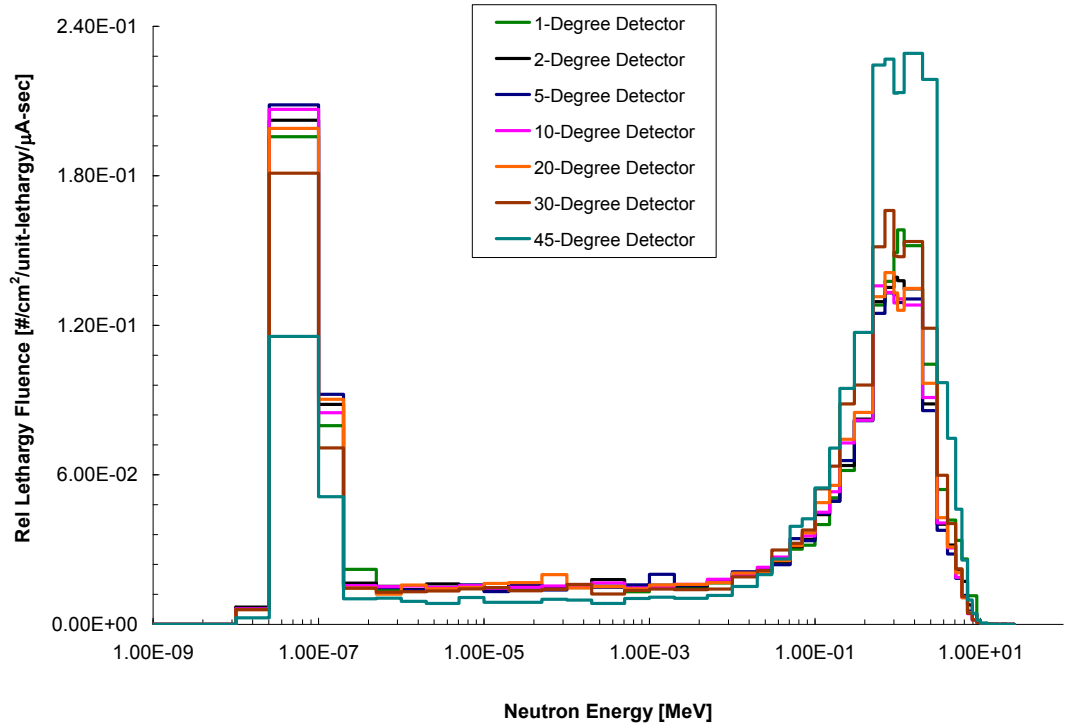

Figure G-12. Relative Neutron Spectrum (1 to 45 degree detectors) at 50 meters for the System in Air.

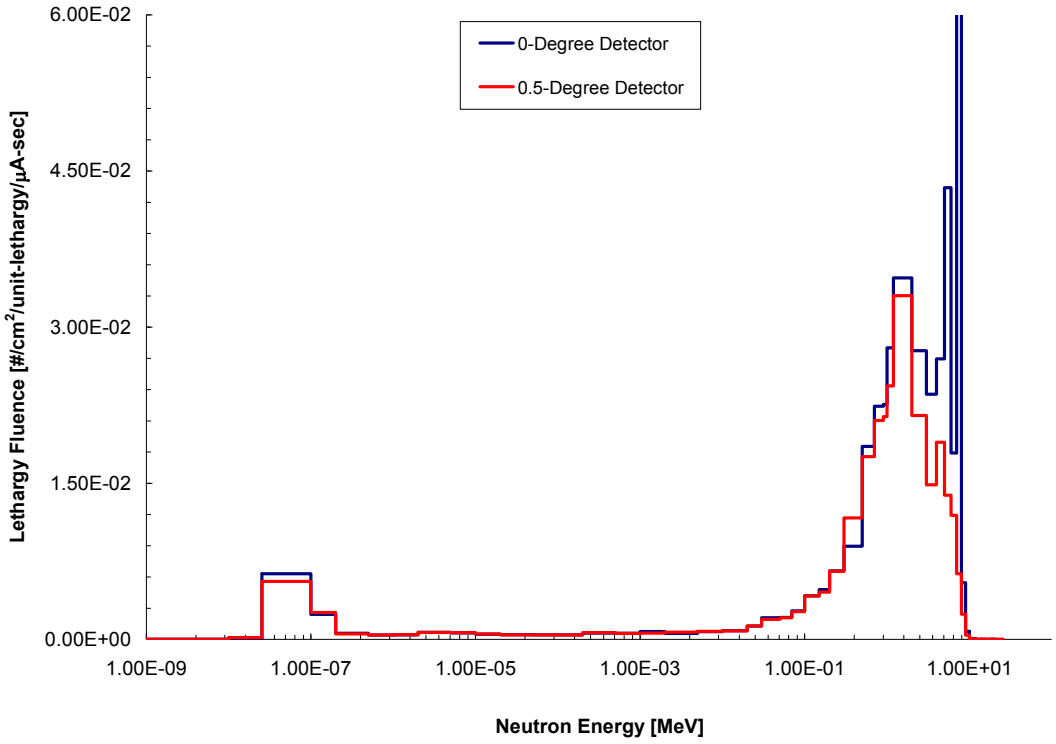

Figure G-13. Neutron Spectrum (0 and 0.5 degree detector) at 100 meters for the System in Air.

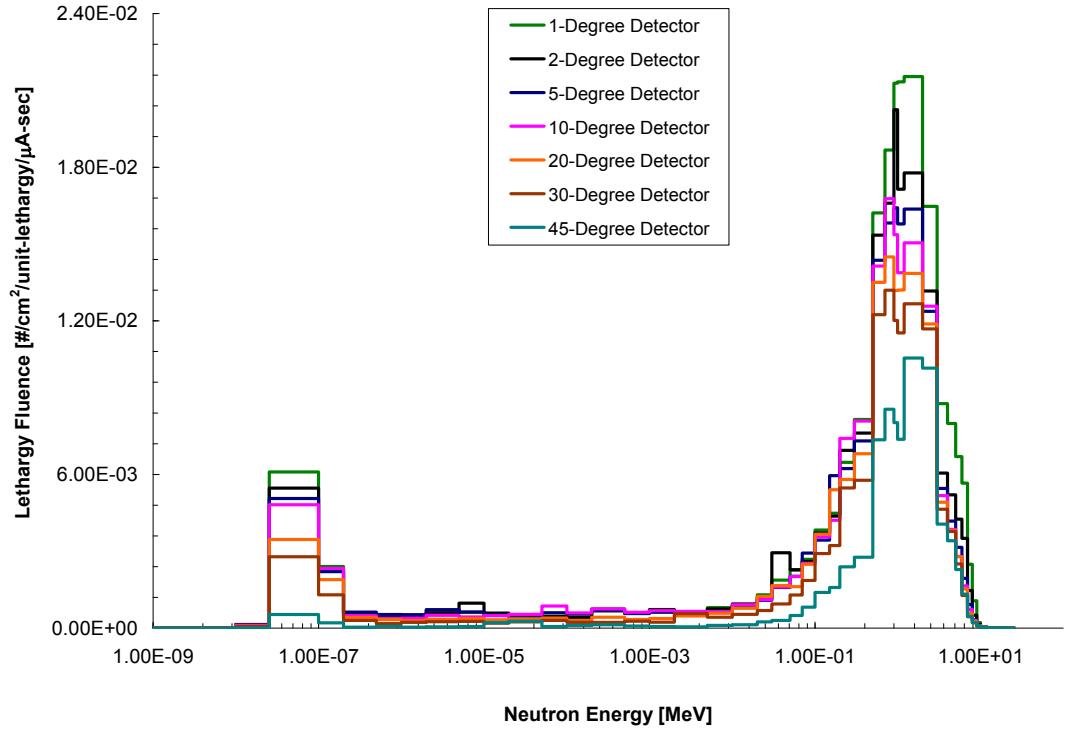

Figure G-14. Neutron Spectrum (1 to 45 degree detectors) at 100 meters for the System in Air.

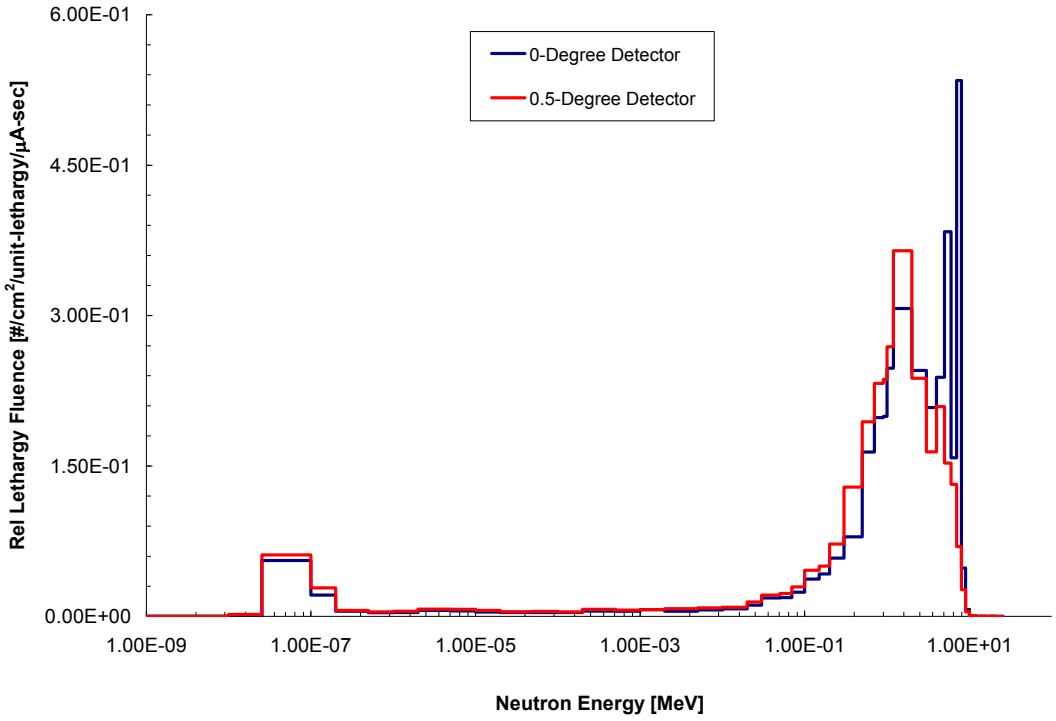

Figure G-15. Relative Neutron Spectrum (0 and 0.5 degree detector) at 100 meters for the System in Air.

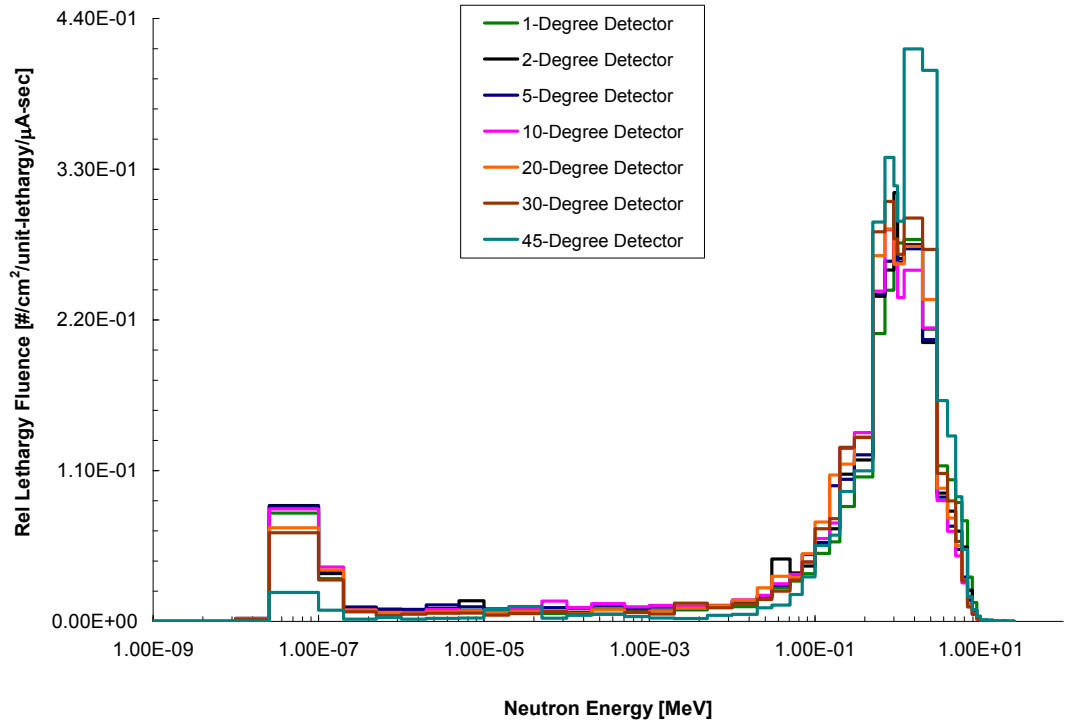

Figure G-16. Relative Neutron Spectrum (1 to 45 degree detectors) at 100 meters for the System in Air.

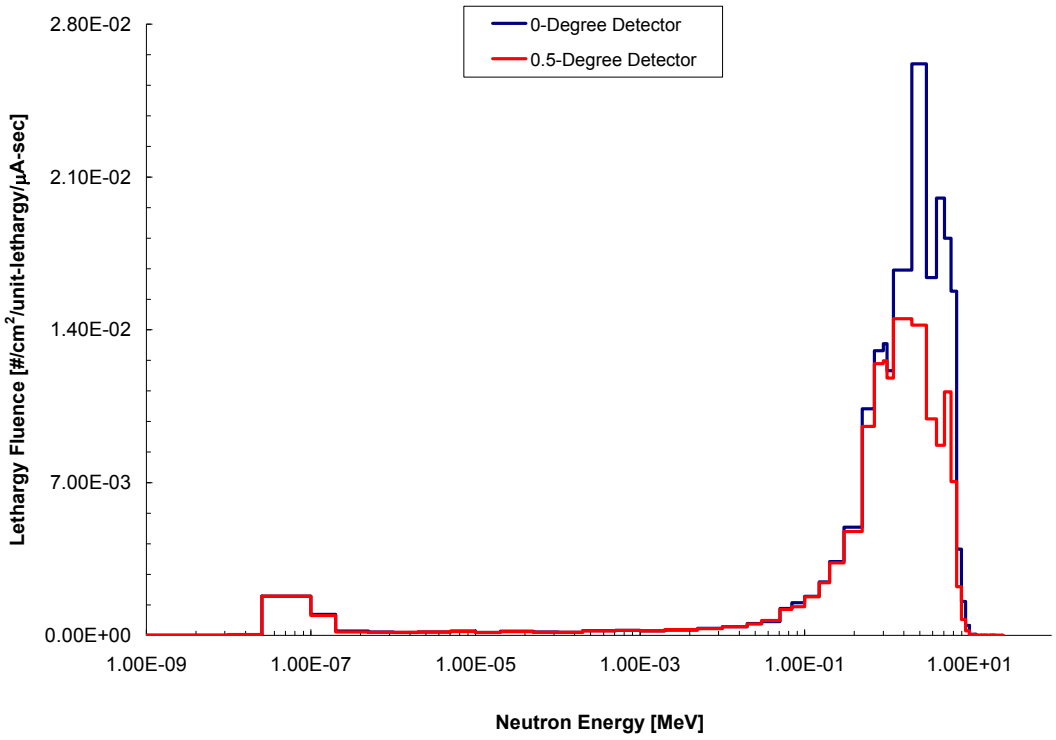

Figure G-17. Neutron Spectrum (0 and 0.5 degree detector) at 120 meters for the System in Air.

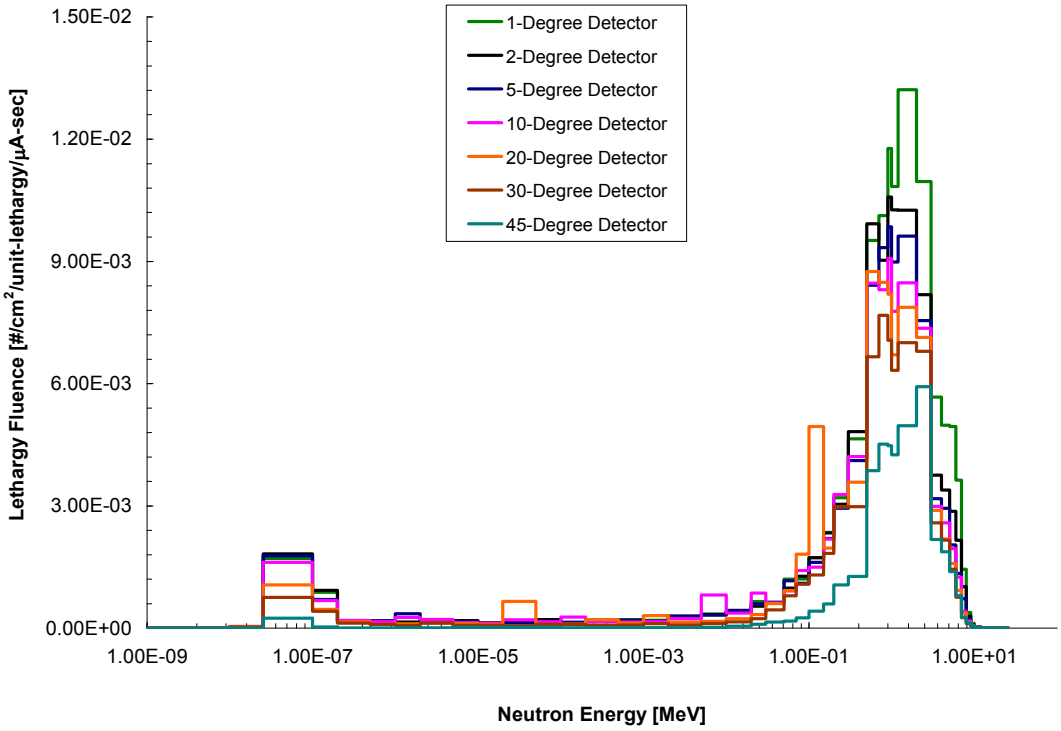

Figure G-18. Neutron Spectrum (1 to 45 degree detectors) at 120 meters for the System in Air.

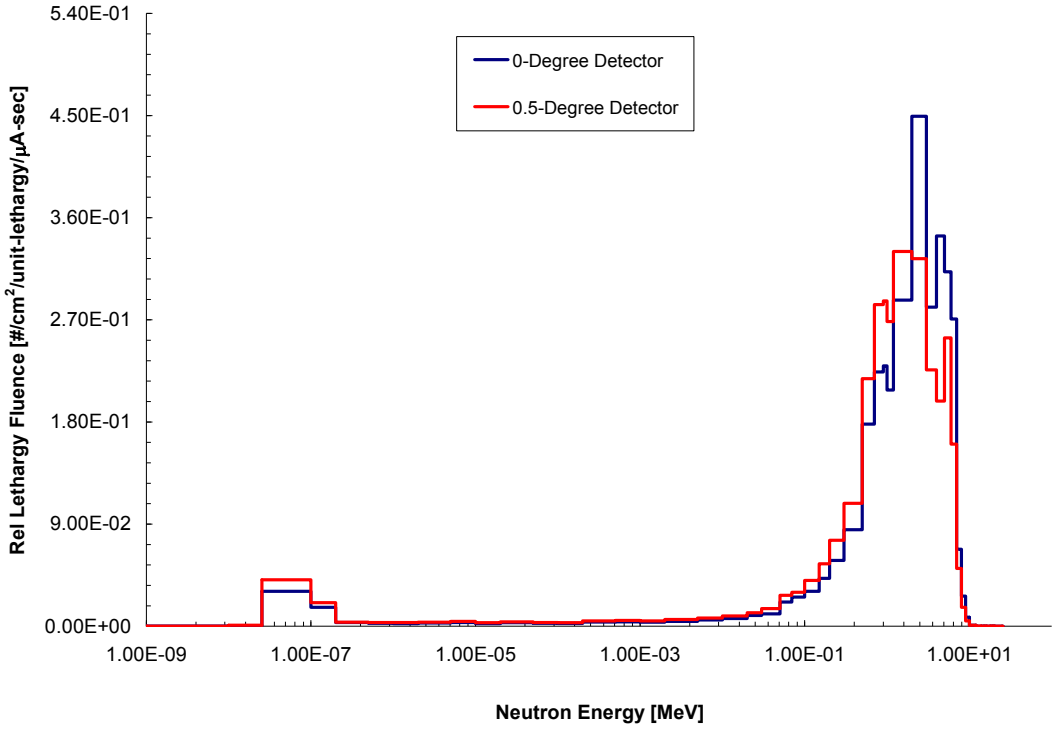

Figure G-19. Relative Neutron Spectrum (0 and 0.5 degree detector) at 120 meters for the System in Air.

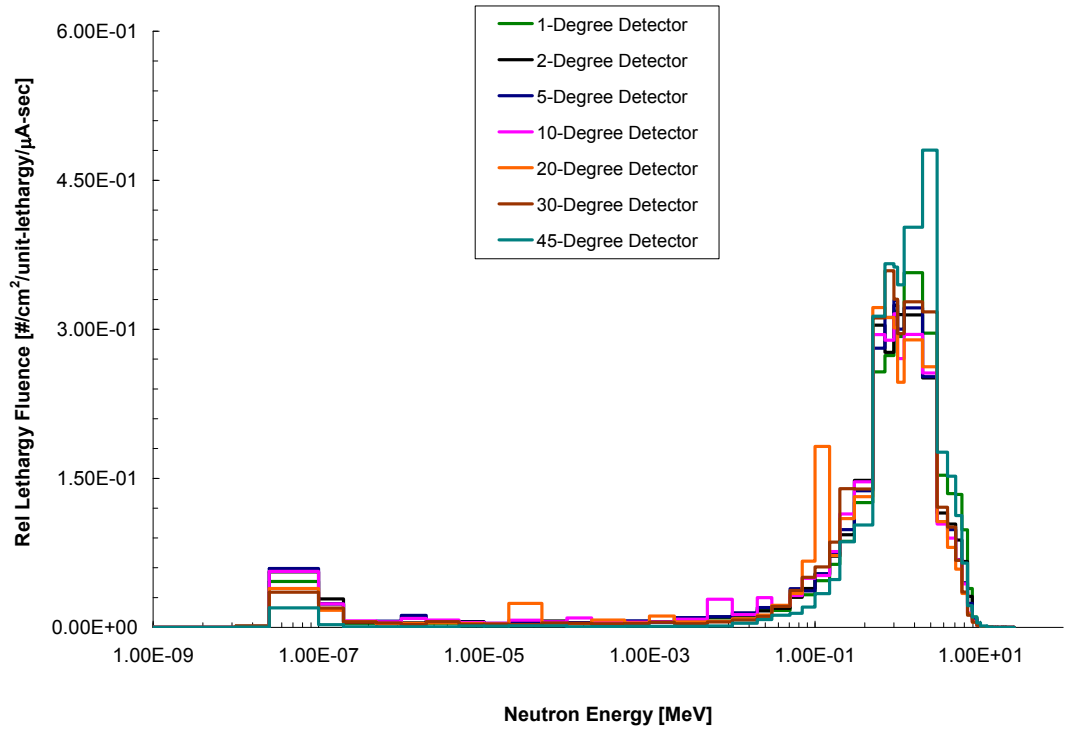

Figure G-20. Relative Neutron Spectrum (1 to 45 degree detectors) at 120 meters for the System in Air.

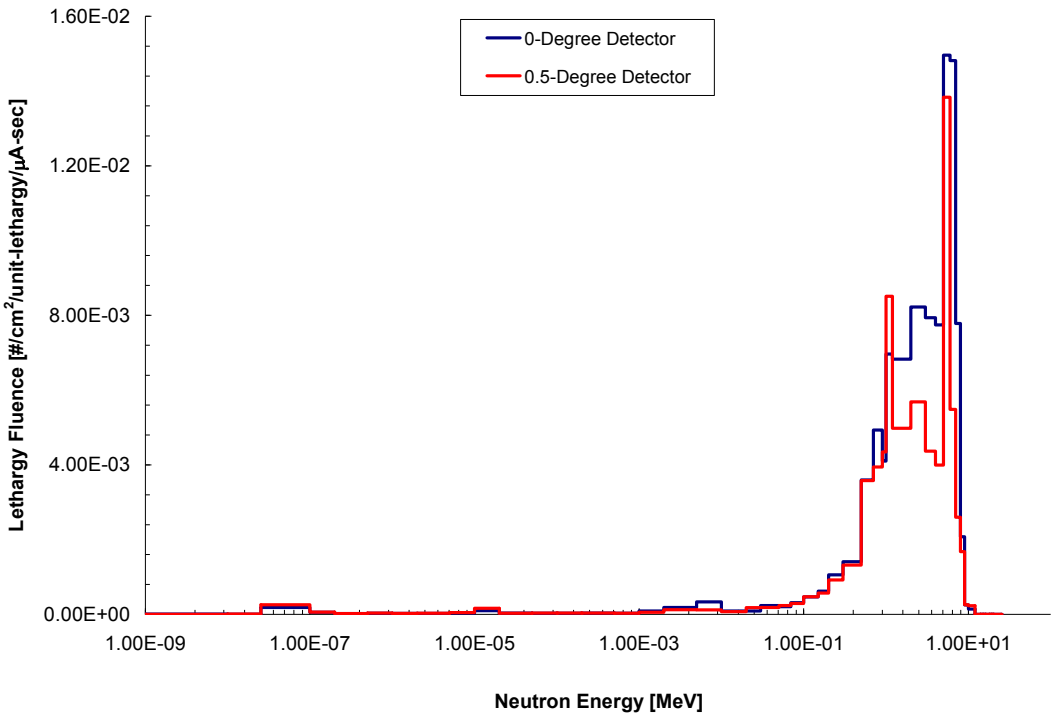

Figure G-21. Neutron Spectrum (0 and 0.5 degree detector) at 170 meters for the System in Air.

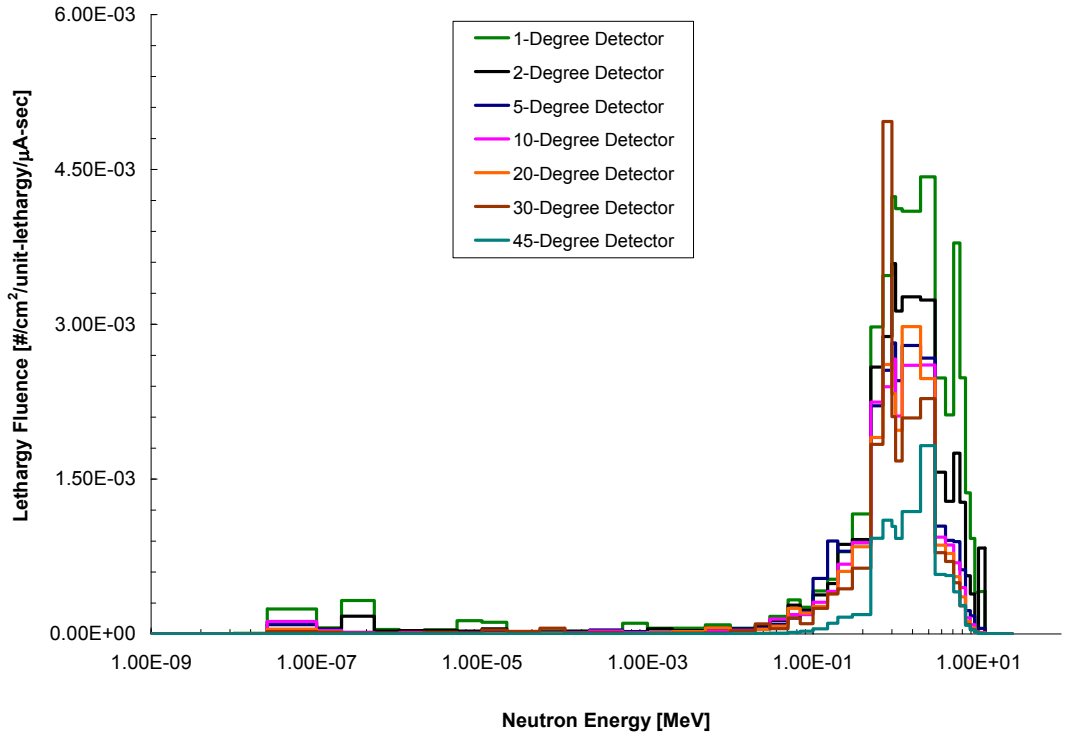

Figure G-22. Neutron Spectrum (1 to 45 degree detectors) at 170 meters for the System in Air.

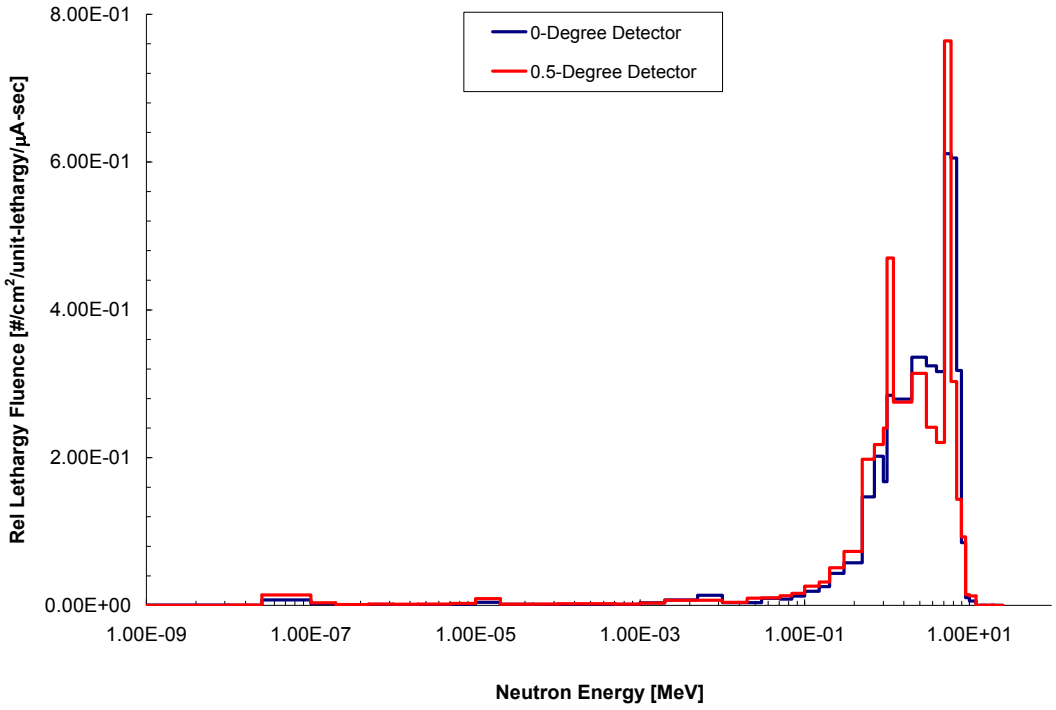

Figure G-23. Relative Neutron Spectrum (0 and 0.5 degree detector) at 170 meters for the System in Air.

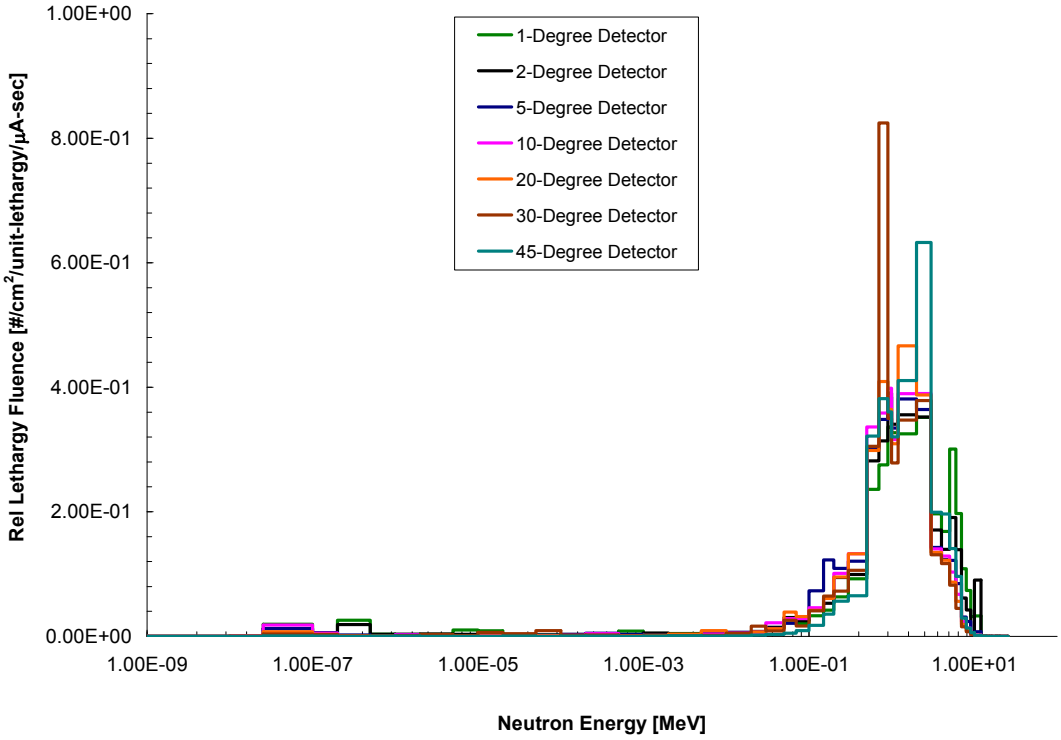

Figure G-24. Relative Neutron Spectrum (1 to 45 degree detectors) at 170 meters for the System in Air.

APPENIDIX H

PHOTON EFFECTIVE DOSE (PA, R-LAT, ROT) DATA

Table H-1. Photon Effective Dose (PA) Data at 10 meters.

Orientation from Beam Centerline	Off-Axis Angle	Φ_{TOTAL} [photons/cm^2/source e$^-$]	E (PA) [Sv]	δE (PA) [Sv]	E (PA) [Sv/μC]	δE (PA) [Sv/μC]	E Dose-Weighted Average Energy [MeV]
Beam LEFT	-45	1.80E-10	7.60E-22	4E-24	4.74E-09	3E-11	2.48
Beam LEFT	-30	3.00E-10	1.42E-21	1E-23	8.86E-09	8E-11	2.95
Beam LEFT	-20	5.22E-10	3.68E-21	4E-23	2.30E-08	3E-10	4.26
Beam LEFT	-10	4.58E-10	2.15E-21	4E-23	1.34E-08	3E-10	3.17
Beam LEFT	-5	5.83E-10	3.05E-21	8E-23	1.90E-08	5E-10	3.90
Beam LEFT	-2	9.91E-10	6.19E-21	2E-22	3.86E-08	1E-09	4.76
Beam LEFT	-1	2.20E-09	1.69E-20	5E-22	1.05E-07	3E-09	5.30
Beam LEFT	-0.5	6.28E-07	8.31E-18	2E-20	5.19E-05	1E-07	6.59
Beam CENTER	0	6.48E-06	8.16E-17	7E-20	5.09E-04	5E-07	6.56
Beam RIGHT	0.5	6.27E-07	8.31E-18	2E-20	5.19E-05	1E-07	6.60
Beam RIGHT	1	2.26E-09	1.75E-20	3E-22	1.09E-07	2E-09	5.29
Beam RIGHT	2	1.01E-09	6.44E-21	1E-22	4.02E-08	9E-10	4.78
Beam RIGHT	5	6.06E-10	3.24E-21	1E-22	2.02E-08	8E-10	3.95
Beam RIGHT	10	4.64E-10	2.13E-21	4E-23	1.33E-08	2E-10	3.07
Beam RIGHT	20	5.15E-10	3.64E-21	3E-23	2.27E-08	2E-10	4.28
Beam RIGHT	30	3.03E-10	1.43E-21	1E-23	8.93E-09	8E-11	2.97
Beam RIGHT	45	1.82E-10	7.60E-22	6E-24	4.74E-09	3E-11	2.47

Table H-2. Photon Effective Dose (R-LAT) Data at 10 meters.

Orientation from Beam Centerline	Off-Axis Angle	Φ_{TOTAL} [photons/cm^2/source e$^-$]	E (R-LAT) [Sv]	δE (R-LAT) [Sv]	E (R-LAT) [Sv/μC]	δE (R-LAT) [Sv/μC]	E Dose-Weighted Average Energy [MeV]
Beam LEFT	-45	1.80E-10	5.92E-22	3E-24	3.70E-09	2E-11	2.62
Beam LEFT	-30	3.00E-10	1.13E-21	1E-23	7.03E-09	6E-11	3.10
Beam LEFT	-20	5.22E-10	3.04E-21	3E-23	1.90E-08	2E-10	4.42
Beam LEFT	-10	4.58E-10	1.71E-21	3E-23	1.07E-08	2E-10	3.36
Beam LEFT	-5	5.83E-10	2.47E-21	6E-23	1.54E-08	4E-10	4.15
Beam LEFT	-2	9.91E-10	5.15E-21	2E-22	3.21E-08	1E-09	5.05
Beam LEFT	-1	2.20E-09	1.43E-20	4E-22	8.90E-08	2E-09	5.56
Beam LEFT	-0.5	6.28E-07	7.30E-18	2E-20	4.55E-05	1E-07	6.78
Beam CENTER	0	6.48E-06	7.15E-17	6E-20	4.46E-04	4E-07	6.77
Beam RIGHT	0.5	6.27E-07	7.30E-18	2E-20	4.55E-05	1E-07	6.78
Beam RIGHT	1	2.26E-09	1.48E-20	2E-22	9.24E-08	1E-09	5.54
Beam RIGHT	2	1.01E-09	5.36E-21	1E-22	3.34E-08	7E-10	5.07
Beam RIGHT	5	6.06E-10	2.63E-21	1E-22	1.64E-08	7E-10	4.21
Beam RIGHT	10	4.64E-10	1.69E-21	3E-23	1.05E-08	2E-10	3.25
Beam RIGHT	20	5.15E-10	3.01E-21	2E-23	1.88E-08	1E-10	4.44
Beam RIGHT	30	3.03E-10	1.13E-21	1E-23	7.08E-09	6E-11	3.12
Beam RIGHT	45	1.82E-10	5.92E-22	4E-24	3.69E-09	3E-11	2.61

Table H-3. Photon Effective Dose (ROT) Data at 10 meters.

Orientation from Beam Centerline	Off-Axis Angle	Φ_{TOTAL} [photons/cm^2/source e$^-$]	E (ROT) [Sv]	δE (ROT) [Sv]	E (ROT) [Sv/μC]	δE (ROT) [Sv/μC]	E Dose-Weighted Average Energy [MeV]
Beam LEFT	-45	1.80E-10	7.22E-22	4E-24	4.51E-09	3E-11	2.43
Beam LEFT	-30	3.00E-10	1.33E-21	1E-23	8.32E-09	8E-11	2.90
Beam LEFT	-20	5.22E-10	3.39E-21	4E-23	2.12E-08	2E-10	4.19
Beam LEFT	-10	4.58E-10	2.01E-21	4E-23	1.26E-08	3E-10	3.10
Beam LEFT	-5	5.83E-10	2.84E-21	7E-23	1.78E-08	5E-10	3.81
Beam LEFT	-2	9.91E-10	5.73E-21	2E-22	3.57E-08	1E-09	4.67
Beam LEFT	-1	2.20E-09	1.55E-20	4E-22	9.68E-08	3E-09	5.23
Beam LEFT	-0.5	6.28E-07	7.58E-18	2E-20	4.73E-05	1E-07	6.54
Beam CENTER	0	6.48E-06	7.45E-17	7E-20	4.65E-04	4E-07	6.51
Beam RIGHT	0.5	6.27E-07	7.58E-18	2E-20	4.73E-05	1E-07	6.55
Beam RIGHT	1	2.26E-09	1.61E-20	3E-22	1.00E-07	2E-09	5.21
Beam RIGHT	2	1.01E-09	5.95E-21	1E-22	3.72E-08	8E-10	4.70
Beam RIGHT	5	6.06E-10	3.02E-21	1E-22	1.88E-08	8E-10	3.87
Beam RIGHT	10	4.64E-10	2.00E-21	4E-23	1.25E-08	2E-10	3.01
Beam RIGHT	20	5.15E-10	3.36E-21	2E-23	2.10E-08	2E-10	4.21
Beam RIGHT	30	3.03E-10	1.34E-21	1E-23	8.38E-09	8E-11	2.91
Beam RIGHT	45	1.82E-10	7.22E-22	5E-24	4.50E-09	3E-11	2.42

Table H-4. Photon Effective Dose (PA) Data at 25 meters.

Orientation from Beam Centerline	Off-Axis Angle	Φ_{TOTAL} [photons/cm^2/source e$^-$]	E (PA) [Sv]	δE (PA) [Sv]	E (PA) [Sv/μC]	δE (PA) [Sv/μC]	E Dose-Weighted Average Energy [MeV]
Beam LEFT	-45	2.54E-11	1.12E-22	1E-24	7.00E-10	6E-12	2.52
Beam LEFT	-30	4.56E-11	2.25E-22	2E-24	1.41E-09	1E-11	2.98
Beam LEFT	-20	7.12E-11	3.74E-22	3E-24	2.34E-09	2E-11	3.29
Beam LEFT	-10	7.77E-11	3.66E-22	5E-24	2.28E-09	3E-11	3.06
Beam LEFT	-5	1.13E-10	5.97E-22	9E-24	3.73E-09	6E-11	3.86
Beam LEFT	-2	2.27E-10	1.36E-21	4E-23	8.47E-09	2E-10	4.58
Beam LEFT	-1	5.15E-10	3.69E-21	1E-22	2.31E-08	7E-10	5.09
Beam LEFT	-0.5	1.06E-07	1.44E-18	3E-21	9.00E-06	2E-08	6.65
Beam CENTER	0	9.26E-07	1.20E-17	1E-20	7.52E-05	6E-08	6.63
Beam RIGHT	0.5	1.06E-07	1.44E-18	2E-21	8.99E-06	2E-08	6.65
Beam RIGHT	1	4.97E-10	3.64E-21	8E-23	2.27E-08	5E-10	5.13
Beam RIGHT	2	2.28E-10	1.38E-21	6E-23	8.59E-09	4E-10	4.61
Beam RIGHT	5	1.12E-10	5.91E-22	2E-23	3.69E-09	1E-10	3.85
Beam RIGHT	10	7.77E-11	3.63E-22	4E-24	2.27E-09	3E-11	3.04
Beam RIGHT	20	7.33E-11	3.79E-22	5E-24	2.37E-09	3E-11	3.27
Beam RIGHT	30	4.52E-11	2.24E-22	1E-24	1.40E-09	9E-12	2.98
Beam RIGHT	45	2.54E-11	1.12E-22	8E-25	6.99E-10	5E-12	2.50

Table H-5. Photon Effective Dose (R-LAT) Data at 25 meters.

Orientation from Beam Centerline	Off-Axis Angle	Φ_{TOTAL} [photons/cm^2/source e$^-$]	E (R-LAT) [Sv]	δE (R-LAT) [Sv]	E (R-LAT) [Sv/μC]	δE (R-LAT) [Sv/μC]	E Dose-Weighted Average Energy [MeV]
Beam LEFT	-45	2.54E-11	8.77E-23	8E-25	5.48E-10	5E-12	2.65
Beam LEFT	-30	4.56E-11	1.79E-22	1E-24	1.12E-09	9E-12	3.12
Beam LEFT	-20	7.12E-11	3.00E-22	2E-24	1.87E-09	1E-11	3.45
Beam LEFT	-10	7.77E-11	2.90E-22	4E-24	1.81E-09	2E-11	3.24
Beam LEFT	-5	1.13E-10	4.84E-22	8E-24	3.02E-09	5E-11	4.11
Beam LEFT	-2	2.27E-10	1.12E-21	3E-23	7.00E-09	2E-10	4.86
Beam LEFT	-1	5.15E-10	3.11E-21	1E-22	1.94E-08	6E-10	5.35
Beam LEFT	-0.5	1.06E-07	1.27E-18	2E-21	7.91E-06	1E-08	6.83
Beam CENTER	0	9.26E-07	1.06E-17	8E-21	6.61E-05	5E-08	6.82
Beam RIGHT	0.5	1.06E-07	1.27E-18	2E-21	7.90E-06	1E-08	6.83
Beam RIGHT	1	4.97E-10	3.06E-21	7E-23	1.91E-08	4E-10	5.39
Beam RIGHT	2	2.28E-10	1.14E-21	5E-23	7.11E-09	3E-10	4.88
Beam RIGHT	5	1.12E-10	4.79E-22	1E-23	2.99E-09	9E-11	4.10
Beam RIGHT	10	7.77E-11	2.88E-22	3E-24	1.80E-09	2E-11	3.22
Beam RIGHT	20	7.33E-11	3.04E-22	4E-24	1.90E-09	3E-11	3.44
Beam RIGHT	30	4.52E-11	1.78E-22	1E-24	1.11E-09	7E-12	3.12
Beam RIGHT	45	2.54E-11	8.76E-23	6E-25	5.47E-10	4E-12	2.64

Table H-6. Photon Effective Dose (ROT) Data at 25 meters.

Orientation from Beam Centerline	Off-Axis Angle	Φ_{TOTAL} [photons/cm^2/source e$^-$]	E (ROT) [Sv]	δE (ROT) [Sv]	E (ROT) [Sv/μC]	δE (ROT) [Sv/μC]	E Dose-Weighted Average Energy [MeV]
Beam LEFT	-45	2.54E-11	1.07E-22	9E-25	6.66E-10	6E-12	2.47
Beam LEFT	-30	4.56E-11	2.12E-22	2E-24	1.32E-09	1E-11	2.92
Beam LEFT	-20	7.12E-11	3.51E-22	3E-24	2.19E-09	2E-11	3.22
Beam LEFT	-10	7.77E-11	3.44E-22	4E-24	2.15E-09	3E-11	3.00
Beam LEFT	-5	1.13E-10	5.58E-22	9E-24	3.48E-09	5E-11	3.77
Beam LEFT	-2	2.27E-10	1.26E-21	3E-23	7.85E-09	2E-10	4.49
Beam LEFT	-1	5.15E-10	3.40E-21	1E-22	2.12E-08	7E-10	5.02
Beam LEFT	-0.5	1.06E-07	1.31E-18	2E-21	8.20E-06	1E-08	6.60
Beam CENTER	0	9.26E-07	1.10E-17	9E-21	6.86E-05	5E-08	6.58
Beam RIGHT	0.5	1.06E-07	1.31E-18	2E-21	8.19E-06	1E-08	6.60
Beam RIGHT	1	4.97E-10	3.35E-21	7E-23	2.09E-08	5E-10	5.05
Beam RIGHT	2	2.28E-10	1.28E-21	6E-23	7.96E-09	4E-10	4.52
Beam RIGHT	5	1.12E-10	5.52E-22	2E-23	3.44E-09	1E-10	3.77
Beam RIGHT	10	7.77E-11	3.42E-22	4E-24	2.13E-09	2E-11	2.98
Beam RIGHT	20	7.33E-11	3.55E-22	5E-24	2.22E-09	3E-11	3.21
Beam RIGHT	30	4.52E-11	2.11E-22	1E-24	1.32E-09	9E-12	2.92
Beam RIGHT	45	2.54E-11	1.07E-22	8E-25	6.65E-10	5E-12	2.45

Table H-7. Photon Effective Dose (PA) Data at 50 meters.

Orientation from Beam Centerline	Off-Axis Angle	Φ_{TOTAL} [photons/cm^2/source e$^-$]	E (PA) [Sv]	δE (PA) [Sv]	E (PA) [Sv/μC]	δE (PA) [Sv/μC]	E Dose-Weighted Average Energy [MeV]
Beam LEFT	-45	5.22E-12	2.39E-23	5E-25	1.49E-10	3E-12	2.57
Beam LEFT	-30	1.02E-11	5.21E-23	6E-25	3.25E-10	4E-12	3.02
Beam LEFT	-20	1.90E-11	1.35E-22	2E-24	8.42E-10	1E-11	4.23
Beam LEFT	-10	2.14E-11	1.01E-22	2E-24	6.28E-10	1E-11	3.08
Beam LEFT	-5	3.58E-11	1.89E-22	4E-24	1.18E-09	2E-11	3.84
Beam LEFT	-2	7.73E-11	4.73E-22	9E-24	2.95E-09	6E-11	4.55
Beam LEFT	-1	1.64E-10	1.19E-21	2E-23	7.44E-09	1E-10	5.04
Beam LEFT	-0.5	2.45E-08	3.46E-19	6E-22	2.16E-06	4E-09	6.73
Beam CENTER	0	2.01E-07	2.75E-18	2E-21	1.72E-05	1E-08	6.72
Beam RIGHT	0.5	2.46E-08	3.46E-19	8E-22	2.16E-06	5E-09	6.73
Beam RIGHT	1	1.74E-10	1.21E-21	5E-23	7.58E-09	3E-10	4.97
Beam RIGHT	2	7.59E-11	4.66E-22	1E-23	2.91E-09	6E-11	4.55
Beam RIGHT	5	3.51E-11	1.86E-22	3E-24	1.16E-09	2E-11	3.87
Beam RIGHT	10	2.17E-11	1.01E-22	2E-24	6.32E-10	1E-11	3.08
Beam RIGHT	20	1.98E-11	1.34E-22	6E-24	8.39E-10	4E-11	4.19
Beam RIGHT	30	1.01E-11	5.15E-23	7E-25	3.21E-10	4E-12	3.04
Beam RIGHT	45	5.13E-12	2.38E-23	4E-25	1.48E-10	2E-12	2.58

Table H-8. Photon Effective Dose (R-LAT) Data at 50 meters.

Orientation from Beam Centerline	Off-Axis Angle	Φ_{TOTAL} [photons/cm^2/source e$^-$]	E (R-LAT) [Sv]	δE (R-LAT) [Sv]	E (R-LAT) [Sv/μC]	δE (R-LAT) [Sv/μC]	E Dose-Weighted Average Energy [MeV]
Beam LEFT	-45	5.22E-12	1.88E-23	4E-25	1.17E-10	2E-12	2.70
Beam LEFT	-30	1.02E-11	4.15E-23	5E-25	2.59E-10	3E-12	3.16
Beam LEFT	-20	1.90E-11	1.11E-22	2E-24	6.95E-10	1E-11	4.39
Beam LEFT	-10	2.14E-11	7.99E-23	1E-24	4.99E-10	8E-12	3.25
Beam LEFT	-5	3.58E-11	1.53E-22	3E-24	9.54E-10	2E-11	4.09
Beam LEFT	-2	7.73E-11	3.91E-22	8E-24	2.44E-09	5E-11	4.82
Beam LEFT	-1	1.64E-10	1.00E-21	2E-23	6.25E-09	9E-11	5.30
Beam LEFT	-0.5	2.45E-08	3.05E-19	5E-22	1.90E-06	3E-09	6.91
Beam CENTER	0	2.01E-07	2.42E-18	2E-21	1.51E-05	1E-08	6.91
Beam RIGHT	0.5	2.46E-08	3.05E-19	7E-22	1.90E-06	4E-09	6.90
Beam RIGHT	1	1.74E-10	1.02E-21	4E-23	6.35E-09	3E-10	5.23
Beam RIGHT	2	7.59E-11	3.86E-22	8E-24	2.41E-09	5E-11	4.82
Beam RIGHT	5	3.51E-11	1.51E-22	3E-24	9.44E-10	2E-11	4.11
Beam RIGHT	10	2.17E-11	8.04E-23	1E-24	5.02E-10	9E-12	3.26
Beam RIGHT	20	1.98E-11	1.11E-22	5E-24	6.91E-10	3E-11	4.36
Beam RIGHT	30	1.01E-11	4.10E-23	6E-25	2.56E-10	4E-12	3.18
Beam RIGHT	45	5.13E-12	1.87E-23	3E-25	1.17E-10	2E-12	2.71

Table H-9. Photon Effective Dose (ROT) Data at 50 meters.

Orientation from Beam Centerline	Off-Axis Angle	Φ_{TOTAL} [photons/cm^2/source e$^-$]	E (ROT) [Sv]	δE (ROT) [Sv]	E (ROT) [Sv/μC]	δE (ROT) [Sv/μC]	E Dose-Weighted Average Energy [MeV]
Beam LEFT	-45	5.22E-12	2.28E-23	5E-25	1.42E-10	3E-12	2.52
Beam LEFT	-30	1.02E-11	4.91E-23	6E-25	3.06E-10	4E-12	2.95
Beam LEFT	-20	1.90E-11	1.25E-22	2E-24	7.78E-10	1E-11	4.15
Beam LEFT	-10	2.14E-11	9.47E-23	1E-24	5.91E-10	9E-12	3.01
Beam LEFT	-5	3.58E-11	1.76E-22	4E-24	1.10E-09	2E-11	3.76
Beam LEFT	-2	7.73E-11	4.38E-22	9E-24	2.73E-09	5E-11	4.46
Beam LEFT	-1	1.64E-10	1.10E-21	2E-23	6.85E-09	1E-10	4.96
Beam LEFT	-0.5	2.45E-08	3.15E-19	5E-22	1.97E-06	3E-09	6.69
Beam CENTER	0	2.01E-07	2.51E-18	2E-21	1.57E-05	1E-08	6.68
Beam RIGHT	0.5	2.46E-08	3.15E-19	7E-22	1.97E-06	5E-09	6.69
Beam RIGHT	1	1.74E-10	1.12E-21	5E-23	6.99E-09	3E-10	4.89
Beam RIGHT	2	7.59E-11	4.32E-22	9E-24	2.70E-09	6E-11	4.46
Beam RIGHT	5	3.51E-11	1.74E-22	3E-24	1.09E-09	2E-11	3.78
Beam RIGHT	10	2.17E-11	9.54E-23	2E-24	5.95E-10	1E-11	3.01
Beam RIGHT	20	1.98E-11	1.24E-22	6E-24	7.75E-10	4E-11	4.12
Beam RIGHT	30	1.01E-11	4.84E-23	7E-25	3.02E-10	4E-12	2.98
Beam RIGHT	45	5.13E-12	2.26E-23	3E-25	1.41E-10	2E-12	2.53

Table H-10. Photon Effective Dose (PA) Data at 100 meters.

Orientation from Beam Centerline	Off-Axis Angle	Φ_{TOTAL} [photons/cm^2/source e$^-$]	E (PA) [Sv]	δE (PA) [Sv]	E (PA) [Sv/μC]	δE (PA) [Sv/μC]	E Dose-Weighted Average Energy [MeV]
Beam LEFT	-45	8.16E-13	4.21E-24	4E-26	2.63E-11	3E-13	2.76
Beam LEFT	-30	1.94E-12	1.05E-23	1E-25	6.55E-11	7E-13	3.11
Beam LEFT	-20	3.98E-12	2.89E-23	3E-25	1.81E-10	2E-12	4.26
Beam LEFT	-10	5.66E-12	2.76E-23	4E-25	1.72E-10	3E-12	3.18
Beam LEFT	-5	1.14E-11	6.17E-23	2E-24	3.85E-10	1E-11	3.93
Beam LEFT	-2	2.73E-11	1.69E-22	4E-24	1.05E-09	3E-11	4.55
Beam LEFT	-1	5.90E-11	4.09E-22	2E-23	2.56E-09	1E-10	4.94
Beam LEFT	-0.5	5.02E-09	7.58E-20	1E-22	4.73E-07	7E-10	6.88
Beam CENTER	0	3.95E-08	5.88E-19	4E-22	3.67E-06	3E-09	6.89
Beam RIGHT	0.5	5.02E-09	7.59E-20	1E-22	4.73E-07	8E-10	6.88
Beam RIGHT	1	5.95E-11	4.11E-22	2E-23	2.56E-09	1E-10	4.97
Beam RIGHT	2	2.84E-11	1.72E-22	7E-24	1.07E-09	4E-11	4.53
Beam RIGHT	5	1.16E-11	6.18E-23	2E-24	3.86E-10	1E-11	3.92
Beam RIGHT	10	5.75E-12	2.78E-23	6E-25	1.74E-10	3E-12	3.15
Beam RIGHT	20	3.95E-12	2.88E-23	2E-25	1.80E-10	1E-12	4.25
Beam RIGHT	30	1.91E-12	1.04E-23	1E-25	6.48E-11	7E-13	3.14
Beam RIGHT	45	8.30E-13	4.26E-24	9E-26	2.66E-11	6E-13	2.76

Table H-11. Photon Effective Dose (R-LAT) Data at 100 meters.

Orientation from Beam Centerline	Off-Axis Angle	Φ_{TOTAL} [photons/cm^2/source e$^-$]	E (R-LAT) [Sv]	δE (R-LAT) [Sv]	E (R-LAT) [Sv/μC]	δE (R-LAT) [Sv/μC]	E Dose-Weighted Average Energy [MeV]
Beam LEFT	-45	8.16E-13	3.34E-24	4E-26	2.08E-11	2E-13	2.88
Beam LEFT	-30	1.94E-12	8.39E-24	9E-26	5.24E-11	6E-13	3.25
Beam LEFT	-20	3.98E-12	2.39E-23	3E-25	1.49E-10	2E-12	4.42
Beam LEFT	-10	5.66E-12	2.20E-23	3E-25	1.37E-10	2E-12	3.36
Beam LEFT	-5	1.14E-11	5.02E-23	1E-24	3.13E-10	8E-12	4.17
Beam LEFT	-2	2.73E-11	1.40E-22	3E-24	8.73E-10	2E-11	4.82
Beam LEFT	-1	5.90E-11	3.43E-22	1E-23	2.14E-09	9E-11	5.19
Beam LEFT	-0.5	5.02E-09	6.71E-20	1E-22	4.19E-07	6E-10	7.04
Beam CENTER	0	3.95E-08	5.20E-19	4E-22	3.25E-06	2E-09	7.06
Beam RIGHT	0.5	5.02E-09	6.71E-20	1E-22	4.19E-07	7E-10	7.04
Beam RIGHT	1	5.95E-11	3.44E-22	1E-23	2.15E-09	9E-11	5.23
Beam RIGHT	2	2.84E-11	1.42E-22	6E-24	8.88E-10	4E-11	4.80
Beam RIGHT	5	1.16E-11	5.02E-23	2E-24	3.13E-10	1E-11	4.16
Beam RIGHT	10	5.75E-12	2.22E-23	4E-25	1.38E-10	3E-12	3.33
Beam RIGHT	20	3.95E-12	2.38E-23	2E-25	1.49E-10	1E-12	4.42
Beam RIGHT	30	1.91E-12	8.31E-24	9E-26	5.19E-11	5E-13	3.28
Beam RIGHT	45	8.30E-13	3.38E-24	7E-26	2.11E-11	5E-13	2.89

Table H-12. Photon Effective Dose (ROT) Data at 100 meters.

Orientation from Beam Centerline	Off-Axis Angle	Φ_{TOTAL} [photons/cm^2/source e$^-$]	E (ROT) [Sv]	δE (ROT) [Sv]	E (ROT) [Sv/μC]	δE (ROT) [Sv/μC]	E Dose-Weighted Average Energy [MeV]
Beam LEFT	-45	8.16E-13	4.00E-24	4E-26	2.50E-11	3E-13	2.69
Beam LEFT	-30	1.94E-12	9.87E-24	1E-25	6.16E-11	7E-13	3.04
Beam LEFT	-20	3.98E-12	2.67E-23	3E-25	1.67E-10	2E-12	4.18
Beam LEFT	-10	5.66E-12	2.59E-23	4E-25	1.62E-10	2E-12	3.10
Beam LEFT	-5	1.14E-11	5.76E-23	1E-24	3.59E-10	9E-12	3.84
Beam LEFT	-2	2.73E-11	1.57E-22	4E-24	9.77E-10	2E-11	4.46
Beam LEFT	-1	5.90E-11	3.78E-22	2E-23	2.36E-09	1E-10	4.85
Beam LEFT	-0.5	5.02E-09	6.90E-20	1E-22	4.31E-07	6E-10	6.85
Beam CENTER	0	3.95E-08	5.35E-19	4E-22	3.34E-06	2E-09	6.85
Beam RIGHT	0.5	5.02E-09	6.90E-20	1E-22	4.31E-07	7E-10	6.84
Beam RIGHT	1	5.95E-11	3.79E-22	2E-23	2.36E-09	1E-10	4.88
Beam RIGHT	2	2.84E-11	1.60E-22	7E-24	9.96E-10	4E-11	4.44
Beam RIGHT	5	1.16E-11	5.76E-23	2E-24	3.60E-10	1E-11	3.83
Beam RIGHT	10	5.75E-12	2.62E-23	5E-25	1.63E-10	3E-12	3.08
Beam RIGHT	20	3.95E-12	2.66E-23	2E-25	1.66E-10	1E-12	4.18
Beam RIGHT	30	1.91E-12	9.76E-24	1E-25	6.09E-11	6E-13	3.07
Beam RIGHT	45	8.30E-13	4.05E-24	9E-26	2.53E-11	6E-13	2.70

Table H-13. Photon Effective Dose (PA) Data at 120 meters.

Orientation from Beam Centerline	Off-Axis Angle	Φ_{TOTAL} [photons/cm^2/source e$^-$]	E (PA) [Sv]	δE (PA) [Sv]	E (PA) [Sv/μC]	δE (PA) [Sv/μC]	E Dose-Weighted Average Energy [MeV]
Beam LEFT	-45	4.78E-13	2.60E-24	3E-26	1.62E-11	2E-13	2.86
Beam LEFT	-30	1.21E-12	6.66E-24	1E-25	4.16E-11	6E-13	3.14
Beam LEFT	-20	2.56E-12	1.88E-23	2E-25	1.17E-10	1E-12	4.26
Beam LEFT	-10	3.90E-12	1.93E-23	3E-25	1.21E-10	2E-12	3.18
Beam LEFT	-5	8.56E-12	4.59E-23	1E-24	2.87E-10	9E-12	3.94
Beam LEFT	-2	2.05E-11	1.29E-22	4E-24	8.03E-10	3E-11	4.61
Beam LEFT	-1	4.03E-11	2.97E-22	6E-24	1.85E-09	4E-11	5.03
Beam LEFT	-0.5	3.23E-09	4.98E-20	2E-22	3.11E-07	1E-09	6.93
Beam CENTER	0	2.51E-08	3.84E-19	5E-22	2.40E-06	3E-09	6.95
Beam RIGHT	0.5	3.23E-09	4.99E-20	1E-22	3.11E-07	6E-10	6.93
Beam RIGHT	1	5.61E-11	3.27E-22	8E-23	2.04E-09	5E-10	4.66
Beam RIGHT	2	2.06E-11	1.27E-22	5E-24	7.95E-10	3E-11	4.59
Beam RIGHT	5	8.28E-12	4.57E-23	1E-24	2.85E-10	8E-12	4.02
Beam RIGHT	10	3.91E-12	1.98E-23	4E-25	1.23E-10	3E-12	3.23
Beam RIGHT	20	2.56E-12	1.88E-23	3E-25	1.17E-10	2E-12	4.29
Beam RIGHT	30	1.22E-12	6.70E-24	2E-25	4.18E-11	1E-12	3.16
Beam RIGHT	45	4.65E-13	2.55E-24	2E-26	1.59E-11	1E-13	2.84

Table H-14. Photon Effective Dose (R-LAT) Data at 120 meters.

Orientation from Beam Centerline	Off-Axis Angle	Φ_{TOTAL} [photons/cm^2/source e$^-$]	E (R-LAT) [Sv]	δE (R-LAT) [Sv]	E (R-LAT) [Sv/μC]	δE (R-LAT) [Sv/μC]	E Dose-Weighted Average Energy [MeV]
Beam LEFT	-45	4.78E-13	2.07E-24	3E-26	1.29E-11	2E-13	2.98
Beam LEFT	-30	1.21E-12	5.34E-24	8E-26	3.33E-11	5E-13	3.28
Beam LEFT	-20	2.56E-12	1.56E-23	2E-25	9.72E-11	1E-12	4.42
Beam LEFT	-10	3.90E-12	1.54E-23	2E-25	9.61E-11	2E-12	3.36
Beam LEFT	-5	8.56E-12	3.73E-23	1E-24	2.33E-10	8E-12	4.18
Beam LEFT	-2	2.05E-11	1.07E-22	3E-24	6.66E-10	2E-11	4.87
Beam LEFT	-1	4.03E-11	2.49E-22	5E-24	1.56E-09	3E-11	5.27
Beam LEFT	-0.5	3.23E-09	4.41E-20	2E-22	2.76E-07	1E-09	7.09
Beam CENTER	0	2.51E-08	3.40E-19	5E-22	2.12E-06	3E-09	7.12
Beam RIGHT	0.5	3.23E-09	4.42E-20	9E-23	2.76E-07	6E-10	7.09
Beam RIGHT	1	5.61E-11	2.71E-22	7E-23	1.69E-09	4E-10	4.93
Beam RIGHT	2	2.06E-11	1.06E-22	4E-24	6.59E-10	2E-11	4.85
Beam RIGHT	5	8.28E-12	3.73E-23	1E-24	2.33E-10	7E-12	4.26
Beam RIGHT	10	3.91E-12	1.58E-23	3E-25	9.85E-11	2E-12	3.41
Beam RIGHT	20	2.56E-12	1.56E-23	2E-25	9.72E-11	1E-12	4.45
Beam RIGHT	30	1.22E-12	5.37E-24	2E-25	3.35E-11	1E-12	3.30
Beam RIGHT	45	4.65E-13	2.03E-24	2E-26	1.27E-11	1E-13	2.96

Table H-15. Photon Effective Dose (ROT) Data at 120 meters.

Orientation from Beam Centerline	Off-Axis Angle	Φ_{TOTAL} [photons/cm^2/source e$^-$]	E (ROT) [Sv]	δE (ROT) [Sv]	E (ROT) [Sv/μC]	δE (ROT) [Sv/μC]	E Dose-Weighted Average Energy [MeV]
Beam LEFT	-45	4.78E-13	2.47E-24	3E-26	1.54E-11	2E-13	2.79
Beam LEFT	-30	1.21E-12	6.27E-24	9E-26	3.91E-11	6E-13	3.07
Beam LEFT	-20	2.56E-12	1.74E-23	2E-25	1.09E-10	1E-12	4.18
Beam LEFT	-10	3.90E-12	1.82E-23	3E-25	1.13E-10	2E-12	3.11
Beam LEFT	-5	8.56E-12	4.28E-23	1E-24	2.67E-10	9E-12	3.85
Beam LEFT	-2	2.05E-11	1.19E-22	4E-24	7.44E-10	2E-11	4.52
Beam LEFT	-1	4.03E-11	2.74E-22	6E-24	1.71E-09	4E-11	4.94
Beam LEFT	-0.5	3.23E-09	4.53E-20	2E-22	2.83E-07	1E-09	6.89
Beam CENTER	0	2.51E-08	3.50E-19	5E-22	2.18E-06	3E-09	6.92
Beam RIGHT	0.5	3.23E-09	4.54E-20	9E-23	2.83E-07	6E-10	6.90
Beam RIGHT	1	5.61E-11	3.03E-22	7E-23	1.89E-09	5E-10	4.57
Beam RIGHT	2	2.06E-11	1.18E-22	4E-24	7.37E-10	3E-11	4.50
Beam RIGHT	5	8.28E-12	4.26E-23	1E-24	2.66E-10	8E-12	3.93
Beam RIGHT	10	3.91E-12	1.86E-23	4E-25	1.16E-10	2E-12	3.15
Beam RIGHT	20	2.56E-12	1.74E-23	2E-25	1.09E-10	1E-12	4.21
Beam RIGHT	30	1.22E-12	6.30E-24	2E-25	3.93E-11	1E-12	3.09
Beam RIGHT	45	4.65E-13	2.42E-24	2E-26	1.51E-11	1E-13	2.77

Table H-16. Photon Effective Dose (PA) Data at 170 meters.

Orientation from Beam Centerline	Off-Axis Angle	Φ_{TOTAL} [photons/cm^2/source e$^-$]	E (PA) [Sv]	δE (PA) [Sv]	E (PA) [Sv/μC]	δE (PA) [Sv/μC]	E Dose-Weighted Average Energy [MeV]
Beam LEFT	-45	1.51E-13	9.15E-25	1E-26	5.71E-12	7E-14	3.01
Beam LEFT	-30	4.32E-13	2.62E-24	4E-26	1.63E-11	3E-13	3.27
Beam LEFT	-20	1.06E-12	7.99E-24	1E-25	4.98E-11	9E-13	4.32
Beam LEFT	-10	1.77E-12	9.48E-24	1E-25	5.92E-11	9E-13	3.32
Beam LEFT	-5	4.25E-12	2.50E-23	9E-25	1.56E-10	6E-12	4.13
Beam LEFT	-2	1.16E-11	7.44E-23	3E-24	4.64E-10	2E-11	4.67
Beam LEFT	-1	2.45E-11	1.72E-22	8E-24	1.07E-09	5E-11	5.04
Beam LEFT	-0.5	1.33E-09	2.16E-20	5E-23	1.35E-07	3E-10	7.07
Beam CENTER	0	1.01E-08	1.65E-19	2E-22	1.03E-06	1E-09	7.10
Beam RIGHT	0.5	1.32E-09	2.16E-20	4E-23	1.35E-07	3E-10	7.07
Beam RIGHT	1	2.28E-11	1.67E-22	6E-24	1.04E-09	4E-11	5.08
Beam RIGHT	2	1.06E-11	7.17E-23	2E-24	4.48E-10	1E-11	4.74
Beam RIGHT	5	4.08E-12	2.44E-23	5E-25	1.52E-10	3E-12	4.13
Beam RIGHT	10	1.92E-12	9.81E-24	5E-25	6.12E-11	3E-12	3.27
Beam RIGHT	20	1.03E-12	7.98E-24	9E-26	4.98E-11	5E-13	4.34
Beam RIGHT	30	4.35E-13	2.62E-24	3E-26	1.63E-11	2E-13	3.27
Beam RIGHT	45	1.58E-13	9.28E-25	2E-26	5.79E-12	1E-13	2.98

Table H-17. Photon Effective Dose (R-LAT) Data at 170 meters.

Orientation from Beam Centerline	Off-Axis Angle	Φ_{TOTAL} [photons/cm^2/source e$^-$]	E (R-LAT) [Sv]	δE (R-LAT) [Sv]	E (R-LAT) [Sv/μC]	δE (R-LAT) [Sv/μC]	E Dose-Weighted Average Energy [MeV]
Beam LEFT	-45	1.51E-13	7.34E-25	8E-27	4.58E-12	5E-14	3.12
Beam LEFT	-30	4.32E-13	2.11E-24	4E-26	1.32E-11	2E-13	3.40
Beam LEFT	-20	1.06E-12	6.62E-24	1E-25	4.13E-11	7E-13	4.48
Beam LEFT	-10	1.77E-12	7.61E-24	1E-25	4.75E-11	7E-13	3.49
Beam LEFT	-5	4.25E-12	2.05E-23	8E-25	1.28E-10	5E-12	4.36
Beam LEFT	-2	1.16E-11	6.18E-23	2E-24	3.85E-10	2E-11	4.93
Beam LEFT	-1	2.45E-11	1.45E-22	7E-24	9.02E-10	4E-11	5.29
Beam LEFT	-0.5	1.33E-09	1.92E-20	5E-23	1.20E-07	3E-10	7.21
Beam CENTER	0	1.01E-08	1.47E-19	2E-22	9.16E-07	1E-09	7.25
Beam RIGHT	0.5	1.32E-09	1.92E-20	4E-23	1.20E-07	2E-10	7.21
Beam RIGHT	1	2.28E-11	1.41E-22	5E-24	8.78E-10	3E-11	5.32
Beam RIGHT	2	1.06E-11	5.98E-23	1E-24	3.73E-10	9E-12	4.99
Beam RIGHT	5	4.08E-12	2.00E-23	4E-25	1.25E-10	3E-12	4.36
Beam RIGHT	10	1.92E-12	7.84E-24	4E-25	4.90E-11	3E-12	3.44
Beam RIGHT	20	1.03E-12	6.62E-24	7E-26	4.13E-11	5E-13	4.49
Beam RIGHT	30	4.35E-13	2.11E-24	2E-26	1.32E-11	1E-13	3.40
Beam RIGHT	45	1.58E-13	7.44E-25	1E-26	4.64E-12	9E-14	3.09

Table H-18. Photon Effective Dose (ROT) Data at 170 meters.

Orientation from Beam Centerline	Off-Axis Angle	Φ_{TOTAL} [photons/cm^2/source e$^-$]	E (ROT) [Sv]	δE (ROT) [Sv]	E (ROT) [Sv/μC]	δE (ROT) [Sv/μC]	E Dose-Weighted Average Energy [MeV]
Beam LEFT	-45	1.51E-13	8.67E-25	1E-26	5.41E-12	6E-14	2.94
Beam LEFT	-30	4.32E-13	2.46E-24	4E-26	1.54E-11	3E-13	3.19
Beam LEFT	-20	1.06E-12	7.38E-24	1E-25	4.61E-11	8E-13	4.24
Beam LEFT	-10	1.77E-12	8.91E-24	1E-25	5.56E-11	8E-13	3.24
Beam LEFT	-5	4.25E-12	2.33E-23	9E-25	1.45E-10	5E-12	4.04
Beam LEFT	-2	1.16E-11	6.88E-23	3E-24	4.30E-10	2E-11	4.58
Beam LEFT	-1	2.45E-11	1.59E-22	8E-24	9.90E-10	5E-11	4.96
Beam LEFT	-0.5	1.33E-09	1.96E-20	5E-23	1.23E-07	3E-10	7.04
Beam CENTER	0	1.01E-08	1.50E-19	2E-22	9.37E-07	1E-09	7.06
Beam RIGHT	0.5	1.32E-09	1.96E-20	4E-23	1.22E-07	2E-10	7.04
Beam RIGHT	1	2.28E-11	1.54E-22	5E-24	9.62E-10	3E-11	4.99
Beam RIGHT	2	1.06E-11	6.63E-23	2E-24	4.14E-10	1E-11	4.65
Beam RIGHT	5	4.08E-12	2.27E-23	5E-25	1.42E-10	3E-12	4.04
Beam RIGHT	10	1.92E-12	9.21E-24	5E-25	5.75E-11	3E-12	3.19
Beam RIGHT	20	1.03E-12	7.38E-24	8E-26	4.60E-11	5E-13	4.25
Beam RIGHT	30	4.35E-13	2.46E-24	3E-26	1.54E-11	2E-13	3.19
Beam RIGHT	45	1.58E-13	8.81E-25	2E-26	5.50E-12	1E-13	2.90

APPENIDIX I

ELECTRON EFFECTIVE DOSE (PA, R-LAT, ISO) DATA

Table I-1. Electron Effective Dose (PA) Data at 10 meters.

Orientation from Beam Centerline	Off-Axis Angle	Φ_{TOTAL} [electrons/cm^2/source e$^-$]	E (PA) [Sv]	δE (PA) [Sv]	E (PA) [Sv/μC]	δE (PA) [Sv/μC]
Beam LEFT	-5	8.73E-11	1.64E-21	1E-22	1.02E-08	8E-10
Beam LEFT	-2	3.17E-10	7.08E-21	2E-22	4.42E-08	1E-09
Beam LEFT	-1	8.27E-10	2.13E-20	3E-22	1.33E-07	2E-09
Beam CENTER	0	4.54E-09	1.32E-19	3E-22	8.27E-07	2E-09
Beam RIGHT	1	8.14E-10	2.07E-20	2E-22	1.29E-07	1E-09
Beam RIGHT	2	3.15E-10	7.13E-21	2E-22	4.45E-08	1E-09
Beam RIGHT	5	7.97E-11	1.40E-21	9E-23	8.71E-09	5E-10

Table I-2. Electron Effective Dose (R-LAT) Data at 10 meters.

Orientation from Beam Centerline	Off-Axis Angle	Φ_{TOTAL} [electrons/cm^2/source e$^-$]	E (R-LAT) [Sv]	δE (R-LAT) [Sv]	E (R-LAT) [Sv/μC]	δE (R-LAT) [Sv/μC]
Beam LEFT	-5	8.73E-11	1.10E-21	9E-23	6.88E-09	5E-10
Beam LEFT	-2	3.17E-10	4.62E-21	1E-22	2.89E-08	9E-10
Beam LEFT	-1	8.27E-10	1.38E-20	2E-22	8.59E-08	1E-09
Beam CENTER	0	4.54E-09	8.46E-20	2E-22	5.28E-07	1E-09
Beam RIGHT	1	8.14E-10	1.34E-20	1E-22	8.37E-08	7E-10
Beam RIGHT	2	3.15E-10	4.66E-21	1E-22	2.91E-08	8E-10
Beam RIGHT	5	7.97E-11	9.44E-22	6E-23	5.89E-09	4E-10

Table I-3. Electron Effective Dose (ISO) Data at 10 meters.

Orientation from Beam Centerline	Off-Axis Angle	Φ_{TOTAL} [electrons/cm^2/source e$^-$]	E (ISO) [Sv]	δE (ISO) [Sv]	E (ISO) [Sv/μC]	δE (ISO) [Sv/μC]
Beam LEFT	-5	8.73E-11	2.25E-21	2E-22	1.40E-08	1E-09
Beam LEFT	-2	3.17E-10	9.25E-21	3E-22	5.77E-08	2E-09
Beam LEFT	-1	8.27E-10	2.63E-20	4E-22	1.64E-07	2E-09
Beam CENTER	0	4.54E-09	1.58E-19	3E-22	9.88E-07	2E-09
Beam RIGHT	1	8.14E-10	2.57E-20	2E-22	1.61E-07	1E-09
Beam RIGHT	2	3.15E-10	9.24E-21	3E-22	5.77E-08	2E-09
Beam RIGHT	5	7.97E-11	1.97E-21	1E-22	1.23E-08	8E-10

Table I-4. Electron Effective Dose (PA) Data at 25 meters.

Orientation from Beam Centerline	Off-Axis Angle	Φ_{TOTAL} [electrons/cm^2/source e$^-$]	E (PA) [Sv]	δE (PA) [Sv]	E (PA) [Sv/μC]	δE (PA) [Sv/μC]
Beam LEFT	-2	7.59E-11	1.57E-21	3E-23	9.81E-09	2E-10
Beam LEFT	-1	2.23E-10	5.18E-21	7E-23	3.23E-08	4E-10
Beam LEFT	-0.5	7.37E-10	1.93E-20	1E-22	1.20E-07	8E-10
Beam CENTER	0	2.00E-09	5.73E-20	2E-22	3.57E-07	1E-09
Beam RIGHT	0.5	7.37E-10	1.94E-20	1E-22	1.21E-07	8E-10
Beam RIGHT	1	2.20E-10	5.01E-21	6E-23	3.13E-08	4E-10
Beam RIGHT	2	7.85E-11	1.70E-21	6E-23	1.06E-08	3E-10

Table I-5. Electron Effective Dose (R-LAT) Data at 25 meters.

Orientation from Beam Centerline	Off-Axis Angle	Φ_{TOTAL} [electrons/cm^2/source e$^-$]	E (R-LAT) [Sv]	δE (R-LAT) [Sv]	E (R-LAT) [Sv/μC]	δE (R-LAT) [Sv/μC]
Beam LEFT	-2	7.59E-11	1.05E-21	2E-23	6.52E-09	1E-10
Beam LEFT	-1	2.23E-10	3.40E-21	4E-23	2.12E-08	3E-10
Beam LEFT	-0.5	7.37E-10	1.25E-20	8E-23	7.78E-08	5E-10
Beam CENTER	0	2.00E-09	3.66E-20	1E-22	2.29E-07	8E-10
Beam RIGHT	0.5	7.37E-10	1.25E-20	8E-23	7.79E-08	5E-10
Beam RIGHT	1	2.20E-10	3.28E-21	4E-23	2.05E-08	2E-10
Beam RIGHT	2	7.85E-11	1.13E-21	4E-23	7.03E-09	2E-10

Table I-6. Electron Effective Dose (ISO) Data at 25 meters.

Orientation from Beam Centerline	Off-Axis Angle	Φ_{TOTAL} [electrons/cm^2/source e$^-$]	E (ISO) [Sv]	δE (ISO) [Sv]	E (ISO) [Sv/μC]	δE (ISO) [Sv/μC]
Beam LEFT	-2	7.59E-11	2.08E-21	4E-23	1.30E-08	2E-10
Beam LEFT	-1	2.23E-10	6.60E-21	9E-23	4.12E-08	5E-10
Beam LEFT	-0.5	7.37E-10	2.38E-20	2E-22	1.48E-07	1E-09
Beam CENTER	0	2.00E-09	6.88E-20	2E-22	4.29E-07	2E-09
Beam RIGHT	0.5	7.37E-10	2.39E-20	2E-22	1.49E-07	1E-09
Beam RIGHT	1	2.20E-10	6.45E-21	7E-23	4.02E-08	5E-10
Beam RIGHT	2	7.85E-11	2.22E-21	7E-23	1.39E-08	5E-10

Table I-7. Electron Effective Dose (PA) Data at 50 meters.

Orientation from Beam Centerline	Off-Axis Angle	Φ_{TOTAL} [electrons/cm^2/source e$^-$]	E (PA) [Sv]	δE (PA) [Sv]	E (PA) [Sv/μC]	δE (PA) [Sv/μC]
Beam LEFT	-2	2.51E-11	4.81E-22	2E-23	3.00E-09	1E-10
Beam LEFT	-1	7.74E-11	1.60E-21	4E-23	1.00E-08	2E-10
Beam LEFT	-0.5	2.69E-10	6.57E-21	6E-23	4.10E-08	4E-10
Beam CENTER	0	8.00E-10	2.23E-20	1E-22	1.39E-07	7E-10
Beam RIGHT	0.5	2.66E-10	6.61E-21	6E-23	4.13E-08	4E-10
Beam RIGHT	1	7.65E-11	1.63E-21	4E-23	1.02E-08	2E-10
Beam RIGHT	2	2.57E-11	4.80E-22	2E-23	3.00E-09	1E-10

Table I-8. Electron Effective Dose (R-LAT) Data at 50 meters.

Orientation from Beam Centerline	Off-Axis Angle	Φ_{TOTAL} [electrons/cm^2/source e$^-$]	E (R-LAT) [Sv]	δE (R-LAT) [Sv]	E (R-LAT) [Sv/μC]	δE (R-LAT) [Sv/μC]
Beam LEFT	-2	2.51E-11	3.22E-22	1E-23	2.01E-09	9E-11
Beam LEFT	-1	7.74E-11	1.06E-21	2E-23	6.64E-09	1E-10
Beam LEFT	-0.5	2.69E-10	4.27E-21	4E-23	2.67E-08	3E-10
Beam CENTER	0	8.00E-10	1.43E-20	7E-23	8.91E-08	4E-10
Beam RIGHT	0.5	2.66E-10	4.29E-21	4E-23	2.68E-08	3E-10
Beam RIGHT	1	7.65E-11	1.08E-21	2E-23	6.72E-09	2E-10
Beam RIGHT	2	2.57E-11	3.23E-22	1E-23	2.01E-09	9E-11

Table I-9. Electron Effective Dose (ISO) Data at 50 meters.

Orientation from Beam Centerline	Off-Axis Angle	Φ_{TOTAL} [electrons/cm^2/source e$^-$]	E (ISO) [Sv]	δE (ISO) [Sv]	E (ISO) [Sv/μC]	δE (ISO) [Sv/μC]
Beam LEFT	-2	2.51E-11	6.56E-22	3E-23	4.10E-09	2E-10
Beam LEFT	-1	7.74E-11	2.13E-21	5E-23	1.33E-08	3E-10
Beam LEFT	-0.5	2.69E-10	8.29E-21	8E-23	5.17E-08	5E-10
Beam CENTER	0	8.00E-10	2.70E-20	1E-22	1.69E-07	8E-10
Beam RIGHT	0.5	2.66E-10	8.30E-21	8E-23	5.18E-08	5E-10
Beam RIGHT	1	7.65E-11	2.14E-21	5E-23	1.34E-08	3E-10
Beam RIGHT	2	2.57E-11	6.61E-22	3E-23	4.13E-09	2E-10

Table I-10. Electron Effective Dose (PA) Data at 100 meters.

Orientation from Beam Centerline	Off-Axis Angle	Φ_{TOTAL} [electrons/cm^2/source e$^-$]	E (PA) [Sv]	δE (PA) [Sv]	E (PA) [Sv/μC]	δE (PA) [Sv/μC]
Beam LEFT	-2	6.46E-12	1.06E-22	7E-24	6.59E-10	4E-11
Beam LEFT	-1	2.36E-11	4.44E-22	1E-23	2.77E-09	8E-11
Beam LEFT	-0.5	9.13E-11	2.14E-21	4E-23	1.34E-08	2E-10
Beam CENTER	0	2.85E-10	7.63E-21	6E-23	4.76E-08	4E-10
Beam RIGHT	0.5	8.96E-11	2.10E-21	3E-23	1.31E-08	2E-10
Beam RIGHT	1	2.35E-11	4.42E-22	1E-23	2.76E-09	8E-11
Beam RIGHT	2	6.46E-12	1.06E-22	7E-24	6.59E-10	4E-11

Table I-11. Electron Effective Dose (R-LAT) Data at 100 meters.

Orientation from Beam Centerline	Off-Axis Angle	Φ_{TOTAL} [electrons/cm^2/source e$^-$]	E (R-LAT) [Sv]	δE (R-LAT) [Sv]	E (R-LAT) [Sv/μC]	δE (R-LAT) [Sv/μC]
Beam LEFT	-2	6.46E-12	7.23E-23	5E-24	4.51E-10	3E-11
Beam LEFT	-1	2.36E-11	2.98E-22	9E-24	1.86E-09	6E-11
Beam LEFT	-0.5	9.13E-11	1.40E-21	3E-23	8.72E-09	2E-10
Beam CENTER	0	2.85E-10	4.91E-21	4E-23	3.06E-08	3E-10
Beam RIGHT	0.5	8.96E-11	1.37E-21	2E-23	8.55E-09	1E-10
Beam RIGHT	1	2.35E-11	2.97E-22	9E-24	1.85E-09	6E-11
Beam RIGHT	2	6.46E-12	7.23E-23	5E-24	4.51E-10	3E-11

Table I-12. Electron Effective Dose (ISO) Data at 100 meters.

Orientation from Beam Centerline	Off-Axis Angle	Φ_{TOTAL} [electrons/cm^2/source e$^-$]	E (ISO) [Sv]	δE (ISO) [Sv]	E (ISO) [Sv/μC]	δE (ISO) [Sv/μC]
Beam LEFT	-2	6.46E-12	1.53E-22	1E-23	9.53E-10	6E-11
Beam LEFT	-1	2.36E-11	6.08E-22	2E-23	3.79E-09	1E-10
Beam LEFT	-0.5	9.13E-11	2.73E-21	5E-23	1.70E-08	3E-10
Beam CENTER	0	2.85E-10	9.36E-21	8E-23	5.84E-08	5E-10
Beam RIGHT	0.5	8.96E-11	2.67E-21	4E-23	1.67E-08	2E-10
Beam RIGHT	1	2.35E-11	6.06E-22	2E-23	3.78E-09	1E-10
Beam RIGHT	2	6.46E-12	1.53E-22	1E-23	9.53E-10	6E-11

Table I-13. Electron Effective Dose (PA) Data at 120 meters.

Orientation from Beam Centerline	Off-Axis Angle	Φ_{TOTAL} [electrons/cm^2/source e$^-$]	E (PA) [Sv]	δE (PA) [Sv]	E (PA) [Sv/μC]	δE (PA) [Sv/μC]
Beam LEFT	-2	4.51E-12	6.88E-23	6E-24	4.30E-10	3E-11
Beam LEFT	-1	1.59E-11	3.11E-22	1E-23	1.94E-09	8E-11
Beam LEFT	-0.5	6.52E-11	1.55E-21	3E-23	9.64E-09	2E-10
Beam CENTER	0	2.10E-10	5.53E-21	7E-23	3.45E-08	4E-10
Beam RIGHT	0.5	6.52E-11	1.51E-21	4E-23	9.40E-09	2E-10
Beam RIGHT	1	1.67E-11	2.99E-22	1E-23	1.87E-09	8E-11
Beam RIGHT	2	4.36E-12	6.94E-23	6E-24	4.33E-10	3E-11

Table I-14. Electron Effective Dose (R-LAT) Data at 120 meters.

Orientation from Beam Centerline	Off-Axis Angle	Φ_{TOTAL} [electrons/cm^2/source e$^-$]	E (R-LAT) [Sv]	δE (R-LAT) [Sv]	E (R-LAT) [Sv/μC]	δE (R-LAT) [Sv/μC]
Beam LEFT	-2	4.51E-12	4.83E-23	4E-24	3.02E-10	2E-11
Beam LEFT	-1	1.59E-11	2.08E-22	9E-24	1.30E-09	5E-11
Beam LEFT	-0.5	6.52E-11	1.01E-21	2E-23	6.29E-09	1E-10
Beam CENTER	0	2.10E-10	3.57E-21	4E-23	2.23E-08	3E-10
Beam RIGHT	0.5	6.52E-11	9.84E-22	2E-23	6.14E-09	1E-10
Beam RIGHT	1	1.67E-11	2.03E-22	8E-24	1.27E-09	5E-11
Beam RIGHT	2	4.36E-12	4.84E-23	4E-24	3.02E-10	2E-11

Table I-15. Electron Effective Dose (ISO) Data at 120 meters.

Orientation from Beam Centerline	Off-Axis Angle	Φ_{TOTAL} [electrons/cm^2/source e$^-$]	E (ISO) [Sv]	δE (ISO) [Sv]	E (ISO) [Sv/μC]	δE (ISO) [Sv/μC]
Beam LEFT	-2	4.51E-12	1.00E-22	8E-24	6.25E-10	5E-11
Beam LEFT	-1	1.59E-11	4.22E-22	2E-23	2.63E-09	1E-10
Beam LEFT	-0.5	6.52E-11	1.96E-21	4E-23	1.23E-08	3E-10
Beam CENTER	0	2.10E-10	6.82E-21	8E-23	4.26E-08	5E-10
Beam RIGHT	0.5	6.52E-11	1.94E-21	5E-23	1.21E-08	3E-10
Beam RIGHT	1	1.67E-11	4.16E-22	2E-23	2.59E-09	1E-10
Beam RIGHT	2	4.36E-12	9.90E-23	8E-24	6.18E-10	5E-11

Table I-16. Electron Effective Dose (PA) Data at 170 meters.

Orientation from Beam Centerline	Off-Axis Angle	Φ_{TOTAL} [electrons/cm^2/source e$^-$]	E (PA) [Sv]	δE (PA) [Sv]	E (PA) [Sv/μC]	δE (PA) [Sv/μC]
Beam LEFT	-1	7.95E-12	1.38E-22	1E-23	8.62E-10	8E-11
Beam LEFT	-0.5	3.26E-11	8.08E-22	4E-23	5.04E-09	2E-10
Beam CENTER	0	1.17E-10	3.21E-21	8E-23	2.00E-08	5E-10
Beam RIGHT	0.5	3.26E-11	8.08E-22	4E-23	5.04E-09	2E-10
Beam RIGHT	1	7.95E-12	1.38E-22	1E-23	8.62E-10	8E-11

Table I-17. Electron Effective Dose (R-LAT) Data at 170 meters.

Orientation from Beam Centerline	Off-Axis Angle	Φ_{TOTAL} [electrons/cm^2/source e$^-$]	E (R-LAT) [Sv]	δE (R-LAT) [Sv]	E (R-LAT) [Sv/μC]	δE (R-LAT) [Sv/μC]
Beam LEFT	-1	7.95E-12	9.44E-23	9E-24	5.89E-10	6E-11
Beam LEFT	-0.5	3.26E-11	5.23E-22	3E-23	3.26E-09	2E-10
Beam CENTER	0	1.17E-10	2.06E-21	5E-23	1.28E-08	3E-10
Beam RIGHT	0.5	3.26E-11	5.23E-22	3E-23	3.26E-09	2E-10
Beam RIGHT	1	7.95E-12	9.44E-23	9E-24	5.89E-10	6E-11

Table I-18. Electron Effective Dose (ISO) Data at 170 meters.

Orientation from Beam Centerline	Off-Axis Angle	Φ_{TOTAL} [electrons/cm^2/source e$^-$]	E (ISO) [Sv]	δE (ISO) [Sv]	E (ISO) [Sv/μC]	δE (ISO) [Sv/μC]
Beam LEFT	-1	7.95E-12	1.93E-22	2E-23	1.20E-09	1E-10
Beam LEFT	-0.5	3.26E-11	1.02E-21	5E-23	6.36E-09	3E-10
Beam CENTER	0	1.17E-10	3.93E-21	1E-22	2.45E-08	6E-10
Beam RIGHT	0.5	3.26E-11	1.02E-21	5E-23	6.36E-09	3E-10
Beam RIGHT	1	7.95E-12	1.93E-22	2E-23	1.20E-09	1E-10

APPENIDIX J

NEUTRON EFFECTIVE DOSE (PA, R-LAT, ROT) DATA

Table J-1. Neutron Effective Dose (PA) Data at 10 meters.

Orientation from Beam Centerline	Off-Axis Angle	Φ_{TOTAL} [neutrons/cm^2/source e$^-$]	E (PA) [Sv]	δE (PA) [Sv]	E (PA) [Sv/μC]	δE (PA) [Sv/μC]	E Dose-Weighted Average Energy [MeV]
Beam LEFT	-45	5.06E-12	2.73E-22	1E-24	1.71E-09	9E-12	1.63
Beam LEFT	-30	6.83E-12	3.01E-22	8E-25	1.88E-09	5E-12	1.42
Beam LEFT	-20	7.17E-12	3.04E-22	1E-24	1.90E-09	6E-12	1.43
Beam LEFT	-10	7.18E-12	3.09E-22	9E-25	1.93E-09	6E-12	1.43
Beam LEFT	-5	7.17E-12	3.15E-22	2E-24	1.97E-09	1E-11	1.43
Beam LEFT	-2	7.26E-12	3.25E-22	4E-24	2.03E-09	3E-11	1.41
Beam LEFT	-1	7.39E-12	3.68E-22	2E-24	2.30E-09	1E-11	1.56
Beam LEFT	-0.5	7.77E-12	4.51E-22	3E-24	2.81E-09	2E-11	1.85
Beam CENTER	0	8.18E-12	5.69E-22	2E-24	3.55E-09	1E-11	2.25
Beam RIGHT	0.5	7.71E-12	4.49E-22	2E-24	2.80E-09	1E-11	1.83
Beam RIGHT	1	7.36E-12	3.70E-22	2E-24	2.31E-09	1E-11	1.56
Beam RIGHT	2	7.23E-12	3.36E-22	4E-24	2.09E-09	2E-11	1.43
Beam RIGHT	5	7.15E-12	3.16E-22	1E-24	1.97E-09	7E-12	1.43
Beam RIGHT	10	7.13E-12	3.09E-22	8E-25	1.93E-09	5E-12	1.43
Beam RIGHT	20	7.17E-12	3.05E-22	1E-24	1.90E-09	9E-12	1.43
Beam RIGHT	30	6.86E-12	3.02E-22	1E-24	1.88E-09	8E-12	1.43
Beam RIGHT	45	5.04E-12	2.71E-22	9E-25	1.69E-09	5E-12	1.62

Table J-2. Neutron Effective Dose (R-LAT) Data at 10 meters.

Orientation from Beam Centerline	Off-Axis Angle	Φ_{TOTAL} [neutrons/cm^2/source e$^-$]	E (R-LAT) [Sv]	δE (R-LAT) [Sv]	E (R-LAT) [Sv/μC]	δE (R-LAT) [Sv/μC]	E Dose-Weighted Average Energy [MeV]
Beam LEFT	-45	5.06E-12	1.34E-22	7E-25	8.35E-10	5E-12	1.80
Beam LEFT	-30	6.83E-12	1.45E-22	4E-25	9.03E-10	2E-12	1.59
Beam LEFT	-20	7.17E-12	1.46E-22	5E-25	9.11E-10	3E-12	1.60
Beam LEFT	-10	7.18E-12	1.48E-22	4E-25	9.26E-10	3E-12	1.59
Beam LEFT	-5	7.17E-12	1.52E-22	9E-25	9.46E-10	6E-12	1.59
Beam LEFT	-2	7.26E-12	1.57E-22	2E-24	9.77E-10	1E-11	1.56
Beam LEFT	-1	7.39E-12	1.79E-22	1E-24	1.12E-09	6E-12	1.73
Beam LEFT	-0.5	7.77E-12	2.24E-22	1E-24	1.40E-09	8E-12	2.04
Beam CENTER	0	8.18E-12	2.91E-22	1E-24	1.82E-09	7E-12	2.48
Beam RIGHT	0.5	7.71E-12	2.23E-22	8E-25	1.39E-09	5E-12	2.02
Beam RIGHT	1	7.36E-12	1.80E-22	8E-25	1.12E-09	5E-12	1.72
Beam RIGHT	2	7.23E-12	1.62E-22	2E-24	1.01E-09	1E-11	1.58
Beam RIGHT	5	7.15E-12	1.52E-22	5E-25	9.49E-10	3E-12	1.59
Beam RIGHT	10	7.13E-12	1.49E-22	4E-25	9.27E-10	2E-12	1.60
Beam RIGHT	20	7.17E-12	1.46E-22	7E-25	9.14E-10	4E-12	1.59
Beam RIGHT	30	6.86E-12	1.45E-22	6E-25	9.05E-10	4E-12	1.59
Beam RIGHT	45	5.04E-12	1.33E-22	4E-25	8.29E-10	3E-12	1.79

Table J-3. Neutron Effective Dose (ROT) Data at 10 meters.

Orientation from Beam Centerline	Off-Axis Angle	Φ_{TOTAL} [neutrons/cm^2/source e$^-$]	E (ROT) [Sv]	δE (ROT) [Sv]	E (ROT) [Sv/μC]	δE (ROT) [Sv/μC]	E Dose-Weighted Average Energy [MeV]
Beam LEFT	-45	5.06E-12	2.51E-22	1E-24	1.57E-09	8E-12	1.65
Beam LEFT	-30	6.83E-12	2.75E-22	7E-25	1.72E-09	4E-12	1.46
Beam LEFT	-20	7.17E-12	2.78E-22	9E-25	1.73E-09	6E-12	1.46
Beam LEFT	-10	7.18E-12	2.82E-22	8E-25	1.76E-09	5E-12	1.46
Beam LEFT	-5	7.17E-12	2.88E-22	2E-24	1.80E-09	1E-11	1.46
Beam LEFT	-2	7.26E-12	2.97E-22	4E-24	1.85E-09	2E-11	1.43
Beam LEFT	-1	7.39E-12	3.37E-22	2E-24	2.10E-09	1E-11	1.59
Beam LEFT	-0.5	7.77E-12	4.15E-22	2E-24	2.59E-09	1E-11	1.88
Beam CENTER	0	8.18E-12	5.25E-22	2E-24	3.28E-09	1E-11	2.28
Beam RIGHT	0.5	7.71E-12	4.13E-22	1E-24	2.58E-09	9E-12	1.86
Beam RIGHT	1	7.36E-12	3.39E-22	1E-24	2.11E-09	9E-12	1.59
Beam RIGHT	2	7.23E-12	3.07E-22	3E-24	1.92E-09	2E-11	1.46
Beam RIGHT	5	7.15E-12	2.89E-22	1E-24	1.80E-09	6E-12	1.46
Beam RIGHT	10	7.13E-12	2.82E-22	7E-25	1.76E-09	5E-12	1.47
Beam RIGHT	20	7.17E-12	2.78E-22	1E-24	1.74E-09	8E-12	1.46
Beam RIGHT	30	6.86E-12	2.76E-22	1E-24	1.72E-09	7E-12	1.46
Beam RIGHT	45	5.04E-12	2.49E-22	8E-25	1.55E-09	5E-12	1.65

Table J-4. Neutron Effective Dose (PA) Data at 25 meters.

Orientation from Beam Centerline	Off-Axis Angle	Φ_{TOTAL} [neutrons/cm^2/source e$^-$]	E (PA) [Sv]	δE (PA) [Sv]	E (PA) [Sv/μC]	δE (PA) [Sv/μC]	E Dose-Weighted Average Energy [MeV]
Beam LEFT	-45	4.75E-13	3.32E-23	1E-25	2.07E-10	9E-13	1.49
Beam LEFT	-30	7.95E-13	3.96E-23	3E-25	2.47E-10	2E-12	1.48
Beam LEFT	-20	9.21E-13	4.12E-23	2E-25	2.57E-10	1E-12	1.45
Beam LEFT	-10	9.62E-13	4.19E-23	1E-24	2.61E-10	7E-12	1.45
Beam LEFT	-5	9.55E-13	4.32E-23	5E-25	2.69E-10	3E-12	1.35
Beam LEFT	-2	9.44E-13	4.38E-23	5E-25	2.74E-10	3E-12	1.48
Beam LEFT	-1	9.59E-13	4.96E-23	2E-25	3.10E-10	1E-12	1.60
Beam LEFT	-0.5	1.00E-12	6.03E-23	2E-25	3.76E-10	2E-12	1.81
Beam CENTER	0	1.07E-12	7.68E-23	3E-25	4.79E-10	2E-12	2.32
Beam RIGHT	0.5	1.02E-12	6.28E-23	5E-25	3.92E-10	3E-12	2.02
Beam RIGHT	1	9.67E-13	4.99E-23	3E-25	3.11E-10	2E-12	1.62
Beam RIGHT	2	9.40E-13	4.36E-23	2E-25	2.72E-10	1E-12	1.48
Beam RIGHT	5	9.63E-13	4.64E-23	1E-24	2.90E-10	8E-12	1.41
Beam RIGHT	10	9.35E-13	4.18E-23	6E-25	2.61E-10	3E-12	1.45
Beam RIGHT	20	9.11E-13	4.14E-23	2E-25	2.59E-10	1E-12	1.45
Beam RIGHT	30	7.88E-13	3.97E-23	2E-25	2.48E-10	2E-12	1.48
Beam RIGHT	45	5.00E-13	3.83E-23	2E-24	2.39E-10	1E-11	1.71

Table J-5. Neutron Effective Dose (R-LAT) Data at 25 meters.

Orientation from Beam Centerline	Off-Axis Angle	Φ_{TOTAL} [neutrons/cm^2/source e$^-$]	E (R-LAT) [Sv]	δE (R-LAT) [Sv]	E (R-LAT) [Sv/μC]	δE (R-LAT) [Sv/μC]	E Dose-Weighted Average Energy [MeV]
Beam LEFT	-45	4.75E-13	1.65E-23	7E-26	1.03E-10	5E-13	1.63
Beam LEFT	-30	7.95E-13	1.91E-23	1E-25	1.19E-10	8E-13	1.64
Beam LEFT	-20	9.21E-13	1.98E-23	1E-25	1.24E-10	6E-13	1.62
Beam LEFT	-10	9.62E-13	2.01E-23	5E-25	1.26E-10	3E-12	1.61
Beam LEFT	-5	9.55E-13	2.08E-23	3E-25	1.30E-10	2E-12	1.50
Beam LEFT	-2	9.44E-13	2.12E-23	2E-25	1.32E-10	1E-12	1.65
Beam LEFT	-1	9.59E-13	2.42E-23	9E-26	1.51E-10	6E-13	1.77
Beam LEFT	-0.5	1.00E-12	3.01E-23	1E-25	1.88E-10	8E-13	1.99
Beam CENTER	0	1.07E-12	3.94E-23	2E-25	2.46E-10	1E-12	2.55
Beam RIGHT	0.5	1.02E-12	3.16E-23	3E-25	1.97E-10	2E-12	2.23
Beam RIGHT	1	9.67E-13	2.44E-23	2E-25	1.52E-10	1E-12	1.79
Beam RIGHT	2	9.40E-13	2.11E-23	9E-26	1.31E-10	6E-13	1.65
Beam RIGHT	5	9.63E-13	2.23E-23	6E-25	1.39E-10	4E-12	1.56
Beam RIGHT	10	9.35E-13	2.01E-23	3E-25	1.25E-10	2E-12	1.61
Beam RIGHT	20	9.11E-13	1.99E-23	1E-25	1.25E-10	6E-13	1.61
Beam RIGHT	30	7.88E-13	1.92E-23	1E-25	1.20E-10	8E-13	1.64
Beam RIGHT	45	5.00E-13	1.91E-23	9E-25	1.19E-10	6E-12	1.85

Table J-6. Neutron Effective Dose (ROT) Data at 25 meters.

Orientation from Beam Centerline	Off-Axis Angle	Φ_{TOTAL} [neutrons/cm^2/source e$^-$]	E (ROT) [Sv]	δE (ROT) [Sv]	E (ROT) [Sv/μC]	δE (ROT) [Sv/μC]	E Dose-Weighted Average Energy [MeV]
Beam LEFT	-45	4.75E-13	3.06E-23	1E-25	1.91E-10	9E-13	1.51
Beam LEFT	-30	7.95E-13	3.62E-23	2E-25	2.26E-10	2E-12	1.51
Beam LEFT	-20	9.21E-13	3.77E-23	2E-25	2.35E-10	1E-12	1.48
Beam LEFT	-10	9.62E-13	3.82E-23	1E-24	2.39E-10	6E-12	1.48
Beam LEFT	-5	9.55E-13	3.95E-23	5E-25	2.46E-10	3E-12	1.37
Beam LEFT	-2	9.44E-13	4.01E-23	4E-25	2.50E-10	3E-12	1.51
Beam LEFT	-1	9.59E-13	4.55E-23	2E-25	2.84E-10	1E-12	1.63
Beam LEFT	-0.5	1.00E-12	5.55E-23	2E-25	3.46E-10	1E-12	1.84
Beam CENTER	0	1.07E-12	7.09E-23	3E-25	4.42E-10	2E-12	2.35
Beam RIGHT	0.5	1.02E-12	5.78E-23	5E-25	3.61E-10	3E-12	2.05
Beam RIGHT	1	9.67E-13	4.58E-23	3E-25	2.86E-10	2E-12	1.65
Beam RIGHT	2	9.40E-13	3.99E-23	2E-25	2.49E-10	1E-12	1.51
Beam RIGHT	5	9.63E-13	4.25E-23	1E-24	2.65E-10	7E-12	1.43
Beam RIGHT	10	9.35E-13	3.82E-23	5E-25	2.38E-10	3E-12	1.48
Beam RIGHT	20	9.11E-13	3.79E-23	2E-25	2.37E-10	1E-12	1.48
Beam RIGHT	30	7.88E-13	3.63E-23	2E-25	2.27E-10	1E-12	1.51
Beam RIGHT	45	5.00E-13	3.54E-23	2E-24	2.21E-10	1E-11	1.73

Table J-7. Neutron Effective Dose (PA) Data at 50 meters.

Orientation from Beam Centerline	Off-Axis Angle	Φ_{TOTAL} [neutrons/cm^2/source e$^-$]	E (PA) [Sv]	δE (PA) [Sv]	E (PA) [Sv/μC]	δE (PA) [Sv/μC]	E Dose-Weighted Average Energy [MeV]
Beam LEFT	-45	5.03E-14	5.68E-24	6E-26	3.55E-11	4E-13	1.92
Beam LEFT	-30	9.74E-14	7.33E-24	1E-25	4.57E-11	6E-13	1.66
Beam LEFT	-20	1.14E-13	7.51E-24	7E-26	4.69E-11	5E-13	1.59
Beam LEFT	-10	1.26E-13	8.05E-24	9E-26	5.03E-11	6E-13	1.70
Beam LEFT	-5	1.27E-13	8.00E-24	6E-26	4.99E-11	4E-13	1.59
Beam LEFT	-2	1.28E-13	8.36E-24	7E-26	5.22E-11	4E-13	1.68
Beam LEFT	-1	1.36E-13	9.74E-24	1E-25	6.08E-11	6E-13	1.84
Beam LEFT	-0.5	1.47E-13	1.25E-23	2E-25	7.81E-11	1E-12	2.27
Beam CENTER	0	1.69E-13	1.82E-23	6E-25	1.13E-10	4E-12	2.74
Beam RIGHT	0.5	1.56E-13	1.26E-23	8E-25	7.87E-11	5E-12	2.18
Beam RIGHT	1	1.37E-13	9.82E-24	1E-25	6.13E-11	6E-13	1.85
Beam RIGHT	2	1.29E-13	8.30E-24	7E-26	5.18E-11	4E-13	1.65
Beam RIGHT	5	1.29E-13	7.96E-24	9E-26	4.97E-11	6E-13	1.57
Beam RIGHT	10	1.24E-13	7.79E-24	6E-26	4.86E-11	4E-13	1.57
Beam RIGHT	20	1.15E-13	7.49E-24	8E-26	4.67E-11	5E-13	1.59
Beam RIGHT	30	9.54E-14	7.17E-24	7E-26	4.48E-11	4E-13	1.65
Beam RIGHT	45	5.01E-14	5.58E-24	4E-26	3.49E-11	2E-13	1.89

Table J-8. Neutron Effective Dose (R-LAT) Data at 50 meters.

Orientation from Beam Centerline	Off-Axis Angle	Φ_{TOTAL} [neutrons/cm^2/source e$^-$]	E (R-LAT) [Sv]	δE (R-LAT) [Sv]	E (R-LAT) [Sv/μC]	δE (R-LAT) [Sv/μC]	E Dose-Weighted Average Energy [MeV]
Beam LEFT	-45	5.03E-14	2.87E-24	3E-26	1.79E-11	2E-13	2.08
Beam LEFT	-30	9.74E-14	3.61E-24	5E-26	2.25E-11	3E-13	1.81
Beam LEFT	-20	1.14E-13	3.68E-24	4E-26	2.30E-11	2E-13	1.75
Beam LEFT	-10	1.26E-13	3.96E-24	5E-26	2.47E-11	3E-13	1.88
Beam LEFT	-5	1.27E-13	3.91E-24	3E-26	2.44E-11	2E-13	1.75
Beam LEFT	-2	1.28E-13	4.11E-24	3E-26	2.57E-11	2E-13	1.85
Beam LEFT	-1	1.36E-13	4.86E-24	5E-26	3.03E-11	3E-13	2.04
Beam LEFT	-0.5	1.47E-13	6.42E-24	9E-26	4.01E-11	5E-13	2.51
Beam CENTER	0	1.69E-13	9.60E-24	3E-25	5.99E-11	2E-12	2.98
Beam RIGHT	0.5	1.56E-13	6.43E-24	4E-25	4.01E-11	2E-12	2.39
Beam RIGHT	1	1.37E-13	4.90E-24	5E-26	3.06E-11	3E-13	2.04
Beam RIGHT	2	1.29E-13	4.08E-24	3E-26	2.54E-11	2E-13	1.82
Beam RIGHT	5	1.29E-13	3.89E-24	5E-26	2.43E-11	3E-13	1.73
Beam RIGHT	10	1.24E-13	3.81E-24	3E-26	2.38E-11	2E-13	1.73
Beam RIGHT	20	1.15E-13	3.67E-24	4E-26	2.29E-11	2E-13	1.75
Beam RIGHT	30	9.54E-14	3.54E-24	3E-26	2.21E-11	2E-13	1.80
Beam RIGHT	45	5.01E-14	2.82E-24	2E-26	1.76E-11	1E-13	2.04

Table J-9. Neutron Effective Dose (ROT) Data at 50 meters.

Orientation from Beam Centerline	Off-Axis Angle	Φ_{TOTAL} [neutrons/cm^2/source e$^-$]	E (ROT) [Sv]	δE (ROT) [Sv]	E (ROT) [Sv/μC]	δE (ROT) [Sv/μC]	E Dose-Weighted Average Energy [MeV]
Beam LEFT	-45	5.03E-14	5.27E-24	6E-26	3.29E-11	4E-13	1.94
Beam LEFT	-30	9.74E-14	6.75E-24	1E-25	4.21E-11	6E-13	1.69
Beam LEFT	-20	1.14E-13	6.91E-24	7E-26	4.31E-11	4E-13	1.62
Beam LEFT	-10	1.26E-13	7.41E-24	8E-26	4.62E-11	5E-13	1.73
Beam LEFT	-5	1.27E-13	7.36E-24	6E-26	4.59E-11	4E-13	1.61
Beam LEFT	-2	1.28E-13	7.69E-24	6E-26	4.80E-11	4E-13	1.70
Beam LEFT	-1	1.36E-13	8.98E-24	9E-26	5.60E-11	5E-13	1.87
Beam LEFT	-0.5	1.47E-13	1.16E-23	2E-25	7.22E-11	1E-12	2.30
Beam CENTER	0	1.69E-13	1.69E-23	6E-25	1.05E-10	4E-12	2.76
Beam RIGHT	0.5	1.56E-13	1.17E-23	7E-25	7.27E-11	4E-12	2.20
Beam RIGHT	1	1.37E-13	9.06E-24	9E-26	5.65E-11	6E-13	1.87
Beam RIGHT	2	1.29E-13	7.63E-24	6E-26	4.76E-11	4E-13	1.67
Beam RIGHT	5	1.29E-13	7.31E-24	9E-26	4.56E-11	5E-13	1.60
Beam RIGHT	10	1.24E-13	7.16E-24	6E-26	4.47E-11	4E-13	1.60
Beam RIGHT	20	1.15E-13	6.89E-24	7E-26	4.30E-11	4E-13	1.62
Beam RIGHT	30	9.54E-14	6.61E-24	6E-26	4.13E-11	4E-13	1.67
Beam RIGHT	45	5.01E-14	5.17E-24	4E-26	3.23E-11	2E-13	1.91

Table J-10. Neutron Effective Dose (PA) Data at 100 meters.

Orientation from Beam Centerline	Off-Axis Angle	Φ_{TOTAL} [neutrons/cm^2/source e$^-$]	E (PA) [Sv]	δE (PA) [Sv]	E (PA) [Sv/μC]	δE (PA) [Sv/μC]	E Dose-Weighted Average Energy [MeV]
Beam LEFT	-45	3.94E-15	7.02E-25	1E-26	4.38E-12	8E-14	2.12
Beam LEFT	-30	6.88E-15	9.67E-25	2E-26	6.04E-12	1E-13	1.95
Beam LEFT	-20	8.24E-15	1.04E-24	2E-26	6.48E-12	1E-13	1.85
Beam LEFT	-10	9.03E-15	1.10E-24	1E-26	6.84E-12	8E-14	1.80
Beam LEFT	-5	9.54E-15	1.14E-24	2E-26	7.12E-12	1E-13	1.83
Beam LEFT	-2	9.87E-15	1.24E-24	1E-26	7.75E-12	8E-14	1.91
Beam LEFT	-1	1.13E-14	1.54E-24	2E-26	9.62E-12	1E-13	2.15
Beam LEFT	-0.5	1.36E-14	2.17E-24	7E-26	1.35E-11	4E-13	2.53
Beam CENTER	0	1.81E-14	3.47E-24	3E-25	2.17E-11	2E-12	3.59
Beam RIGHT	0.5	1.45E-14	2.31E-24	1E-25	1.44E-11	7E-13	2.58
Beam RIGHT	1	1.24E-14	1.58E-24	1E-25	9.87E-12	7E-13	2.18
Beam RIGHT	2	1.04E-14	1.28E-24	2E-26	8.02E-12	1E-13	1.97
Beam RIGHT	5	9.64E-15	1.16E-24	2E-26	7.24E-12	1E-13	1.85
Beam RIGHT	10	9.40E-15	1.12E-24	2E-26	7.00E-12	1E-13	1.81
Beam RIGHT	20	8.11E-15	1.03E-24	1E-26	6.45E-12	9E-14	1.85
Beam RIGHT	30	6.90E-15	9.44E-25	2E-26	5.89E-12	1E-13	1.88
Beam RIGHT	45	4.04E-15	7.10E-25	3E-26	4.43E-12	2E-13	2.13

Table J-11. Neutron Effective Dose (R-LAT) Data at 100 meters.

Orientation from Beam Centerline	Off-Axis Angle	Φ_{TOTAL} [neutrons/cm^2/source e$^-$]	E (R-LAT) [Sv]	δE (R-LAT) [Sv]	E (R-LAT) [Sv/μC]	δE (R-LAT) [Sv/μC]	E Dose-Weighted Average Energy [MeV]
Beam LEFT	-45	3.94E-15	3.62E-25	6E-27	2.26E-12	4E-14	2.27
Beam LEFT	-30	6.88E-15	4.89E-25	9E-27	3.06E-12	5E-14	2.10
Beam LEFT	-20	8.24E-15	5.22E-25	9E-27	3.26E-12	6E-14	2.00
Beam LEFT	-10	9.03E-15	5.51E-25	7E-27	3.44E-12	4E-14	1.94
Beam LEFT	-5	9.54E-15	5.74E-25	1E-26	3.58E-12	7E-14	1.99
Beam LEFT	-2	9.87E-15	6.29E-25	7E-27	3.93E-12	4E-14	2.07
Beam LEFT	-1	1.13E-14	7.92E-25	1E-26	4.95E-12	7E-14	2.34
Beam LEFT	-0.5	1.36E-14	1.15E-24	3E-26	7.17E-12	2E-13	2.74
Beam CENTER	0	1.81E-14	1.92E-24	2E-25	1.20E-11	9E-13	3.86
Beam RIGHT	0.5	1.45E-14	1.22E-24	6E-26	7.59E-12	4E-13	2.78
Beam RIGHT	1	1.24E-14	8.12E-25	5E-26	5.07E-12	3E-13	2.36
Beam RIGHT	2	1.04E-14	6.50E-25	1E-26	4.06E-12	7E-14	2.14
Beam RIGHT	5	9.64E-15	5.84E-25	9E-27	3.64E-12	6E-14	2.01
Beam RIGHT	10	9.40E-15	5.63E-25	1E-26	3.51E-12	6E-14	1.96
Beam RIGHT	20	8.11E-15	5.20E-25	7E-27	3.24E-12	4E-14	2.00
Beam RIGHT	30	6.90E-15	4.77E-25	9E-27	2.98E-12	6E-14	2.03
Beam RIGHT	45	4.04E-15	3.66E-25	1E-26	2.28E-12	9E-14	2.26

Table J-12. Neutron Effective Dose (ROT) Data at 100 meters.

Orientation from Beam Centerline	Off-Axis Angle	Φ_{TOTAL} [neutrons/cm^2/source e$^-$]	E (ROT) [Sv]	δE (ROT) [Sv]	E (ROT) [Sv/μC]	δE (ROT) [Sv/μC]	E Dose-Weighted Average Energy [MeV]
Beam LEFT	-45	3.94E-15	6.53E-25	1E-26	4.08E-12	7E-14	2.13
Beam LEFT	-30	6.88E-15	8.98E-25	2E-26	5.60E-12	1E-13	1.96
Beam LEFT	-20	8.24E-15	9.62E-25	2E-26	6.01E-12	1E-13	1.86
Beam LEFT	-10	9.03E-15	1.02E-24	1E-26	6.34E-12	8E-14	1.81
Beam LEFT	-5	9.54E-15	1.06E-24	2E-26	6.60E-12	1E-13	1.85
Beam LEFT	-2	9.87E-15	1.15E-24	1E-26	7.19E-12	8E-14	1.93
Beam LEFT	-1	1.13E-14	1.43E-24	2E-26	8.93E-12	1E-13	2.17
Beam LEFT	-0.5	1.36E-14	2.02E-24	6E-26	1.26E-11	4E-13	2.54
Beam CENTER	0	1.81E-14	3.24E-24	3E-25	2.02E-11	2E-12	3.61
Beam RIGHT	0.5	1.45E-14	2.15E-24	1E-25	1.34E-11	6E-13	2.59
Beam RIGHT	1	1.24E-14	1.47E-24	1E-25	9.17E-12	6E-13	2.20
Beam RIGHT	2	1.04E-14	1.19E-24	2E-26	7.43E-12	1E-13	1.98
Beam RIGHT	5	9.64E-15	1.08E-24	2E-26	6.71E-12	1E-13	1.87
Beam RIGHT	10	9.40E-15	1.04E-24	2E-26	6.49E-12	1E-13	1.83
Beam RIGHT	20	8.11E-15	9.58E-25	1E-26	5.98E-12	8E-14	1.86
Beam RIGHT	30	6.90E-15	8.76E-25	2E-26	5.47E-12	1E-13	1.90
Beam RIGHT	45	4.04E-15	6.60E-25	3E-26	4.12E-12	2E-13	2.14

Table J-13. Neutron Effective Dose (PA) Data at 120 meters.

Orientation from Beam Centerline	Off-Axis Angle	Φ_{TOTAL} [neutrons/cm^2/source e$^-$]	E (PA) [Sv]	δE (PA) [Sv]	E (PA) [Sv/μC]	δE (PA) [Sv/μC]	E Dose-Weighted Average Energy [MeV]
Beam LEFT	-45	1.92E-15	3.69E-25	5E-27	2.30E-12	3E-14	2.19
Beam LEFT	-30	3.24E-15	5.17E-25	9E-27	3.22E-12	6E-14	1.91
Beam LEFT	-20	3.91E-15	5.73E-25	9E-27	3.57E-12	6E-14	1.85
Beam LEFT	-10	4.40E-15	6.40E-25	1E-26	3.99E-12	7E-14	1.94
Beam LEFT	-5	4.80E-15	6.74E-25	3E-26	4.21E-12	2E-13	1.90
Beam LEFT	-2	5.06E-15	7.55E-25	2E-26	4.71E-12	1E-13	2.10
Beam LEFT	-1	5.85E-15	9.31E-25	2E-26	5.81E-12	1E-13	2.26
Beam LEFT	-0.5	6.96E-15	1.21E-24	3E-26	7.57E-12	2E-13	2.57
Beam CENTER	0	9.33E-15	1.90E-24	1E-25	1.19E-11	8E-13	3.11
Beam RIGHT	0.5	7.04E-15	1.25E-24	3E-26	7.83E-12	2E-13	2.69
Beam RIGHT	1	5.93E-15	9.49E-25	2E-26	5.92E-12	1E-13	2.29
Beam RIGHT	2	5.22E-15	7.57E-25	2E-26	4.73E-12	1E-13	2.06
Beam RIGHT	5	4.80E-15	6.79E-25	1E-26	4.24E-12	8E-14	1.96
Beam RIGHT	10	4.61E-15	6.33E-25	2E-26	3.95E-12	1E-13	1.92
Beam RIGHT	20	4.36E-15	6.01E-25	3E-26	3.75E-12	2E-13	1.85
Beam RIGHT	30	3.43E-15	5.26E-25	2E-26	3.29E-12	1E-13	1.92
Beam RIGHT	45	1.98E-15	3.75E-25	1E-26	2.34E-12	6E-14	2.21

Table J-14. Neutron Effective Dose (R-LAT) Data at 120 meters.

Orientation from Beam Centerline	Off-Axis Angle	Φ_{TOTAL} [neutrons/cm^2/source e$^-$]	E (R-LAT) [Sv]	δE (R-LAT) [Sv]	E (R-LAT) [Sv/μC]	δE (R-LAT) [Sv/μC]	E Dose-Weighted Average Energy [MeV]
Beam LEFT	-45	1.92E-15	1.92E-25	2E-27	1.20E-12	2E-14	2.33
Beam LEFT	-30	3.24E-15	2.63E-25	5E-27	1.64E-12	3E-14	2.05
Beam LEFT	-20	3.91E-15	2.91E-25	5E-27	1.81E-12	3E-14	2.00
Beam LEFT	-10	4.40E-15	3.24E-25	6E-27	2.02E-12	4E-14	2.09
Beam LEFT	-5	4.80E-15	3.41E-25	1E-26	2.13E-12	8E-14	2.05
Beam LEFT	-2	5.06E-15	3.86E-25	8E-27	2.41E-12	5E-14	2.28
Beam LEFT	-1	5.85E-15	4.83E-25	1E-26	3.01E-12	6E-14	2.44
Beam LEFT	-0.5	6.96E-15	6.42E-25	1E-26	4.01E-12	9E-14	2.76
Beam CENTER	0	9.33E-15	1.03E-24	7E-26	6.45E-12	4E-13	3.29
Beam RIGHT	0.5	7.04E-15	6.65E-25	2E-26	4.15E-12	1E-13	2.89
Beam RIGHT	1	5.93E-15	4.92E-25	1E-26	3.07E-12	8E-14	2.47
Beam RIGHT	2	5.22E-15	3.86E-25	9E-27	2.41E-12	6E-14	2.23
Beam RIGHT	5	4.80E-15	3.45E-25	7E-27	2.15E-12	4E-14	2.11
Beam RIGHT	10	4.61E-15	3.20E-25	1E-26	2.00E-12	6E-14	2.08
Beam RIGHT	20	4.36E-15	3.03E-25	2E-26	1.89E-12	1E-13	2.00
Beam RIGHT	30	3.43E-15	2.67E-25	9E-27	1.67E-12	6E-14	2.06
Beam RIGHT	45	1.98E-15	1.94E-25	5E-27	1.21E-12	3E-14	2.34

Table J-15. Neutron Effective Dose (ROT) Data at 120 meters.

Orientation from Beam Centerline	Off-Axis Angle	Φ_{TOTAL} [neutrons/cm^2/source e$^-$]	E (ROT) [Sv]	δE (ROT) [Sv]	E (ROT) [Sv/μC]	δE (ROT) [Sv/μC]	E Dose-Weighted Average Energy [MeV]
Beam LEFT	-45	1.92E-15	3.44E-25	4E-27	2.15E-12	3E-14	2.20
Beam LEFT	-30	3.24E-15	4.80E-25	9E-27	3.00E-12	5E-14	1.92
Beam LEFT	-20	3.91E-15	5.32E-25	9E-27	3.32E-12	5E-14	1.86
Beam LEFT	-10	4.40E-15	5.94E-25	1E-26	3.71E-12	7E-14	1.95
Beam LEFT	-5	4.80E-15	6.26E-25	2E-26	3.90E-12	1E-13	1.91
Beam LEFT	-2	5.06E-15	7.01E-25	1E-26	4.38E-12	9E-14	2.11
Beam LEFT	-1	5.85E-15	8.66E-25	2E-26	5.41E-12	1E-13	2.28
Beam LEFT	-0.5	6.96E-15	1.13E-24	3E-26	7.05E-12	2E-13	2.58
Beam CENTER	0	9.33E-15	1.77E-24	1E-25	1.11E-11	7E-13	3.12
Beam RIGHT	0.5	7.04E-15	1.17E-24	3E-26	7.29E-12	2E-13	2.70
Beam RIGHT	1	5.93E-15	8.83E-25	2E-26	5.51E-12	1E-13	2.30
Beam RIGHT	2	5.22E-15	7.03E-25	2E-26	4.39E-12	1E-13	2.07
Beam RIGHT	5	4.80E-15	6.31E-25	1E-26	3.94E-12	8E-14	1.97
Beam RIGHT	10	4.61E-15	5.87E-25	2E-26	3.66E-12	1E-13	1.94
Beam RIGHT	20	4.36E-15	5.58E-25	3E-26	3.48E-12	2E-13	1.87
Beam RIGHT	30	3.43E-15	4.89E-25	2E-26	3.05E-12	1E-13	1.93
Beam RIGHT	45	1.98E-15	3.49E-25	1E-26	2.18E-12	6E-14	2.22

Table J-16. Neutron Effective Dose (PA) Data at 170 meters.

Orientation from Beam Centerline	Off-Axis Angle	Φ_{TOTAL} [neutrons/cm^2/source e$^-$]	E (PA) [Sv]	δE (PA) [Sv]	E (PA) [Sv/μC]	δE (PA) [Sv/μC]	E Dose-Weighted Average Energy [MeV]
Beam LEFT	-45	4.60E-16	9.83E-26	1E-27	6.13E-13	8E-15	2.42
Beam LEFT	-30	8.39E-16	1.51E-25	8E-27	9.45E-13	5E-14	1.84
Beam LEFT	-20	9.62E-16	1.74E-25	5E-27	1.08E-12	3E-14	2.00
Beam LEFT	-10	1.22E-15	1.99E-25	3E-26	1.24E-12	2E-13	2.18
Beam LEFT	-5	1.39E-15	2.43E-25	2E-26	1.52E-12	1E-13	2.48
Beam LEFT	-2	1.42E-15	2.59E-25	7E-27	1.62E-12	5E-14	2.34
Beam LEFT	-1	1.95E-15	3.68E-25	3E-26	2.29E-12	2E-13	2.72
Beam LEFT	-0.5	2.72E-15	5.75E-25	4E-26	3.59E-12	3E-13	3.05
Beam CENTER	0	3.92E-15	9.43E-25	8E-26	5.89E-12	5E-13	3.92
Beam RIGHT	0.5	2.90E-15	6.41E-25	5E-26	4.00E-12	3E-13	3.54
Beam RIGHT	1	2.02E-15	3.86E-25	3E-26	2.41E-12	2E-13	3.02
Beam RIGHT	2	1.47E-15	2.73E-25	1E-26	1.71E-12	9E-14	2.78
Beam RIGHT	5	1.18E-15	2.07E-25	5E-27	1.29E-12	3E-14	2.21
Beam RIGHT	10	1.07E-15	1.89E-25	3E-27	1.18E-12	2E-14	2.12
Beam RIGHT	20	1.02E-15	1.85E-25	8E-27	1.16E-12	5E-14	2.04
Beam RIGHT	30	9.65E-16	1.72E-25	2E-26	1.07E-12	1E-13	1.95
Beam RIGHT	45	4.63E-16	9.81E-26	2E-27	6.12E-13	1E-14	2.39

Table J-17. Neutron Effective Dose (R-LAT) Data at 170 meters.

Orientation from Beam Centerline	Off-Axis Angle	Φ_{TOTAL} [neutrons/cm^2/source e$^-$]	E (R-LAT) [Sv]	δE (R-LAT) [Sv]	E (R-LAT) [Sv/μC]	δE (R-LAT) [Sv/μC]	E Dose-Weighted Average Energy [MeV]
Beam LEFT	-45	4.60E-16	5.17E-26	7E-28	3.23E-13	4E-15	2.56
Beam LEFT	-30	8.39E-16	7.78E-26	4E-27	4.86E-13	2E-14	1.98
Beam LEFT	-20	9.62E-16	8.95E-26	2E-27	5.58E-13	2E-14	2.14
Beam LEFT	-10	1.22E-15	1.02E-25	1E-26	6.37E-13	9E-14	2.34
Beam LEFT	-5	1.39E-15	1.25E-25	1E-26	7.80E-13	7E-14	2.64
Beam LEFT	-2	1.42E-15	1.35E-25	4E-27	8.45E-13	2E-14	2.50
Beam LEFT	-1	1.95E-15	1.96E-25	1E-26	1.22E-12	9E-14	2.91
Beam LEFT	-0.5	2.72E-15	3.16E-25	2E-26	1.97E-12	1E-13	3.24
Beam CENTER	0	3.92E-15	5.31E-25	4E-26	3.31E-12	3E-13	4.14
Beam RIGHT	0.5	2.90E-15	3.54E-25	3E-26	2.21E-12	2E-13	3.77
Beam RIGHT	1	2.02E-15	2.07E-25	1E-26	1.29E-12	9E-14	3.27
Beam RIGHT	2	1.47E-15	1.45E-25	8E-27	9.03E-13	5E-14	3.05
Beam RIGHT	5	1.18E-15	1.07E-25	3E-27	6.65E-13	2E-14	2.38
Beam RIGHT	10	1.07E-15	9.73E-26	2E-27	6.07E-13	1E-14	2.27
Beam RIGHT	20	1.02E-15	9.50E-26	4E-27	5.93E-13	2E-14	2.18
Beam RIGHT	30	9.65E-16	8.73E-26	1E-26	5.45E-13	7E-14	2.08
Beam RIGHT	45	4.63E-16	5.15E-26	9E-28	3.22E-13	6E-15	2.52

Table J-18. Neutron Effective Dose (ROT) Data at 170 meters.

Orientation from Beam Centerline	Off-Axis Angle	Φ_{TOTAL} [neutrons/cm^2/source e$^-$]	E (ROT) [Sv]	δE (ROT) [Sv]	E (ROT) [Sv/μC]	δE (ROT) [Sv/μC]	E Dose-Weighted Average Energy [MeV]
Beam LEFT	-45	4.60E-16	9.17E-26	1E-27	5.72E-13	8E-15	2.43
Beam LEFT	-30	8.39E-16	1.41E-25	7E-27	8.79E-13	4E-14	1.85
Beam LEFT	-20	9.62E-16	1.62E-25	4E-27	1.01E-12	3E-14	2.01
Beam LEFT	-10	1.22E-15	1.85E-25	3E-26	1.16E-12	2E-13	2.19
Beam LEFT	-5	1.39E-15	2.26E-25	2E-26	1.41E-12	1E-13	2.49
Beam LEFT	-2	1.42E-15	2.41E-25	7E-27	1.50E-12	4E-14	2.35
Beam LEFT	-1	1.95E-15	3.43E-25	3E-26	2.14E-12	2E-13	2.73
Beam LEFT	-0.5	2.72E-15	5.37E-25	4E-26	3.35E-12	2E-13	3.06
Beam CENTER	0	3.92E-15	8.82E-25	7E-26	5.50E-12	5E-13	3.93
Beam RIGHT	0.5	2.90E-15	5.99E-25	5E-26	3.74E-12	3E-13	3.55
Beam RIGHT	1	2.02E-15	3.59E-25	3E-26	2.24E-12	2E-13	3.04
Beam RIGHT	2	1.47E-15	2.55E-25	1E-26	1.59E-12	8E-14	2.80
Beam RIGHT	5	1.18E-15	1.92E-25	5E-27	1.20E-12	3E-14	2.22
Beam RIGHT	10	1.07E-15	1.76E-25	3E-27	1.10E-12	2E-14	2.13
Beam RIGHT	20	1.02E-15	1.72E-25	7E-27	1.08E-12	5E-14	2.05
Beam RIGHT	30	9.65E-16	1.60E-25	2E-26	9.96E-13	1E-13	1.96
Beam RIGHT	45	4.63E-16	9.15E-26	2E-27	5.71E-13	1E-14	2.39

APPENIDIX K

TOTAL EFFECTIVE DOSE (PA, R-LAT) DATA

Total effective dose data are given in Table K-1 through Table K-12 and shown in Figure K-1 through K-12.

Table K-1. Total Effective Dose (PA) Data at 10 meters.

Orientation from Beam Centerline	Off-Axis Angle	E (PA) [Sv]	δE (PA) [Sv]	E (PA) [Sv/μC]	δE (PA) [Sv/μC]	% photon	% electron	% neutron
Beam LEFT	-5	5.01E-21	1E-22	3.12E-08	9E-10	60.9%	33%	6.3%
Beam LEFT	-2	1.36E-20	3E-22	8.48E-08	2E-09	45.5%	52%	2.4%
Beam LEFT	-1	3.85E-20	6E-22	2.40E-07	3E-09	43.8%	55%	1.0%
Beam LEFT	-0.5	8.31E-18	2E-20	5.19E-05	1E-07	99.99%	0%	0.01%
Beam CENTER	0	8.17E-17	7E-20	5.10E-04	5E-07	99.84%	0.2%	0.001%
Beam RIGHT	0.5	8.31E-18	2E-20	5.19E-05	1E-07	99.99%	0%	0.01%
Beam RIGHT	1	3.86E-20	3E-22	2.41E-07	2E-09	45.4%	54%	1.0%
Beam RIGHT	2	1.39E-20	2E-22	8.68E-08	2E-09	46.3%	51%	2.4%
Beam RIGHT	5	4.95E-21	2E-22	3.09E-08	1E-09	65.4%	28%	6.4%

Table K-2. Total Effective Dose (R-LAT) Data at 10 meters.

Orientation from Beam Centerline	Off-Axis Angle	E (R-LAT) [Sv]	δE (R-LAT) [Sv]	E (R-LAT) [Sv/μC]	δE (R-LAT) [Sv/μC]	% photon	% electron	% neutron
Beam LEFT	-5	3.73E-21	1E-22	2.33E-08	7E-10	66.4%	29.6%	4.1%
Beam LEFT	-2	9.93E-21	2E-22	6.19E-08	1E-09	51.8%	46.6%	1.6%
Beam LEFT	-1	2.82E-20	4E-22	1.76E-07	3E-09	50.6%	48.8%	0.6%
Beam LEFT	-0.5	7.30E-18	2E-20	4.56E-05	1E-07	99.997%	0.0%	0.003%
Beam CENTER	0	7.16E-17	6E-20	4.47E-04	4E-07	99.882%	0.1%	0.0004%
Beam RIGHT	0.5	7.30E-18	2E-20	4.55E-05	1E-07	99.997%	0.0%	0.003%
Beam RIGHT	1	2.84E-20	3E-22	1.77E-07	2E-09	52.2%	47.2%	0.6%
Beam RIGHT	2	1.02E-20	2E-22	6.35E-08	1E-09	52.6%	45.8%	1.6%
Beam RIGHT	5	3.73E-21	1E-22	2.33E-08	8E-10	70.6%	25.3%	4.1%

Table K-3. Total Effective Dose (PA) Data at 25 meters.

Orientation from Beam Centerline	Off-Axis Angle	E (PA) [Sv]	δE (PA) [Sv]	E (PA) [Sv/μC]	δE (PA) [Sv/μC]	% photon	% electron	% neutron
Beam LEFT	-2	2.97E-21	5E-23	1.86E-08	3E-10	45.6%	52.9%	1.47%
Beam LEFT	-1	8.92E-21	1E-22	5.57E-08	8E-10	41.4%	58.1%	0.56%
Beam LEFT	-0.5	1.46E-18	3E-21	9.12E-06	2E-08	98.7%	1.3%	0.004%
Beam CENTER	0	1.21E-17	1E-20	7.55E-05	6E-08	99.5%	0.5%	0.001%
Beam RIGHT	0.5	1.46E-18	2E-21	9.11E-06	2E-08	98.7%	1.3%	0.004%
Beam RIGHT	1	8.69E-21	1E-22	5.43E-08	6E-10	41.8%	57.6%	0.57%
Beam RIGHT	2	3.13E-21	8E-23	1.95E-08	5E-10	44.1%	54.6%	1.40%

Table K-4. Total Effective Dose (R-LAT) Data at 25 meters.

Orientation from Beam Centerline	Off-Axis Angle	E (R-LAT) [Sv]	δE (R-LAT) [Sv]	E (R-LAT) [Sv/μC]	δE (R-LAT) [Sv/μC]	% photon	% electron	% neutron
Beam LEFT	-2	2.19E-21	4E-23	1.37E-08	2E-10	51.3%	47.8%	0.97%
Beam LEFT	-1	6.53E-21	1E-22	4.07E-08	7E-10	47.6%	52.0%	0.37%
Beam LEFT	-0.5	1.28E-18	2E-21	7.99E-06	1E-08	99.0%	1.0%	0.002%
Beam CENTER	0	1.06E-17	8E-21	6.63E-05	5E-08	99.7%	0.3%	0.0004%
Beam RIGHT	0.5	1.28E-18	2E-21	7.98E-06	1E-08	99.0%	1.0%	0.002%
Beam RIGHT	1	6.37E-21	8E-23	3.97E-08	5E-10	48.1%	51.6%	0.38%
Beam RIGHT	2	2.29E-21	6E-23	1.43E-08	4E-10	49.8%	49.2%	0.92%

Table K-5. Total Effective Dose (PA) Data at 50 meters.

Orientation from Beam Centerline	Off-Axis Angle	E (PA) [Sv]	δE (PA) [Sv]	E (PA) [Sv/μC]	δE (PA) [Sv/μC]	% photon	% electron	% neutron
Beam LEFT	-2	9.62E-22	2E-23	6.01E-09	1E-10	49.1%	50.0%	0.87%
Beam LEFT	-1	2.81E-21	4E-23	1.75E-08	3E-10	42.5%	57.2%	0.35%
Beam LEFT	-0.5	3.52E-19	6E-22	2.20E-06	4E-09	98.1%	1.9%	0.004%
Beam CENTER	0	2.77E-18	2E-21	1.73E-05	1E-08	99.2%	0.8%	0.001%
Beam RIGHT	0.5	3.52E-19	8E-22	2.20E-06	5E-09	98.1%	1.9%	0.004%
Beam RIGHT	1	2.85E-21	6E-23	1.78E-08	4E-10	42.6%	57.1%	0.34%
Beam RIGHT	2	9.55E-22	2E-23	5.96E-09	1E-10	48.8%	50.3%	0.87%

Table K-6. Total Effective Dose (R-LAT) Data at 50 meters.

Orientation from Beam Centerline	Off-Axis Angle	E (R-LAT) [Sv]	δE (R-LAT) [Sv]	E (R-LAT) [Sv/μC]	δE (R-LAT) [Sv/μC]	% photon	% electron	% neutron
Beam LEFT	-2	7.17E-22	2E-23	4.48E-09	1E-10	54.5%	44.9%	0.57%
Beam LEFT	-1	2.07E-21	3E-23	1.29E-08	2E-10	48.4%	51.4%	0.23%
Beam LEFT	-0.5	3.09E-19	5E-22	1.93E-06	3E-09	98.6%	1.4%	0.002%
Beam CENTER	0	2.44E-18	2E-21	1.52E-05	1E-08	99.4%	0.6%	0.0004%
Beam RIGHT	0.5	3.09E-19	7E-22	1.93E-06	4E-09	98.6%	1.4%	0.002%
Beam RIGHT	1	2.10E-21	5E-23	1.31E-08	3E-10	48.5%	51.3%	0.23%
Beam RIGHT	2	7.13E-22	2E-23	4.45E-09	1E-10	54.1%	45.3%	0.57%

Table K-7. Total Effective Dose (PA) Data at 100 meters.

Orientation from Beam Centerline	Off-Axis Angle	E (PA) [Sv]	δE (PA) [Sv]	E (PA) [Sv/μC]	δE (PA) [Sv/μC]	% photon	% electron	% neutron
Beam LEFT	-2	2.76E-22	8E-24	1.72E-09	5E-11	61.3%	38.3%	0.45%
Beam LEFT	-1	8.55E-22	2E-23	5.34E-09	1E-10	47.9%	51.9%	0.18%
Beam LEFT	-0.5	7.80E-20	1E-22	4.87E-07	8E-10	97.3%	2.7%	0.003%
Beam CENTER	0	5.95E-19	4E-22	3.71E-06	3E-09	98.7%	1.3%	0.001%
Beam RIGHT	0.5	7.80E-20	1E-22	4.87E-07	8E-10	97.3%	2.7%	0.003%
Beam RIGHT	1	8.54E-22	2E-23	5.33E-09	1E-10	48.1%	51.8%	0.19%
Beam RIGHT	2	2.79E-22	1E-23	1.74E-09	6E-11	61.7%	37.8%	0.46%

Table K-8. Total Effective Dose (R-LAT) Data at 100 meters.

Orientation from Beam Centerline	Off-Axis Angle	E (R-LAT) [Sv]	δE (R-LAT) [Sv]	E (R-LAT) [Sv/μC]	δE (R-LAT) [Sv/μC]	% photon	% electron	% neutron
Beam LEFT	-2	2.13E-22	6E-24	1.33E-09	4E-11	65.7%	34.0%	0.30%
Beam LEFT	-1	6.42E-22	2E-23	4.01E-09	1E-10	53.4%	46.5%	0.12%
Beam LEFT	-0.5	6.85E-20	1E-22	4.27E-07	6E-10	98.0%	2.0%	0.002%
Beam CENTER	0	5.25E-19	4E-22	3.28E-06	2E-09	99.1%	0.9%	0.0004%
Beam RIGHT	0.5	6.85E-20	1E-22	4.27E-07	7E-10	98.0%	2.0%	0.002%
Beam RIGHT	1	6.42E-22	2E-23	4.00E-09	1E-10	53.6%	46.2%	0.13%
Beam RIGHT	2	2.15E-22	7E-24	1.34E-09	5E-11	66.1%	33.6%	0.30%

Table K-9. Total Effective Dose (PA) Data at 120 meters.

Orientation from Beam Centerline	Off-Axis Angle	E (PA) [Sv]	δE (PA) [Sv]	E (PA) [Sv/μC]	δE (PA) [Sv/μC]	% photon	% electron	% neutron
Beam LEFT	-2	1.98E-22	7E-24	1.24E-09	4E-11	64.9%	34.7%	0.38%
Beam LEFT	-1	6.09E-22	1E-23	3.80E-09	9E-11	48.8%	51.1%	0.15%
Beam LEFT	-0.5	5.14E-20	2E-22	3.21E-07	1E-09	97.0%	3.0%	0.002%
Beam CENTER	0	3.90E-19	5E-22	2.43E-06	3E-09	98.6%	1.4%	0.0005%
Beam RIGHT	0.5	5.14E-20	1E-22	3.21E-07	7E-10	97.1%	2.9%	0.002%
Beam RIGHT	1	6.27E-22	8E-23	3.92E-09	5E-10	52.1%	47.7%	0.15%
Beam RIGHT	2	1.98E-22	7E-24	1.23E-09	5E-11	64.5%	35.1%	0.38%

Table K-10. Total Effective Dose (R-LAT) Data at 120 meters.

Orientation from Beam Centerline	Off-Axis Angle	E (R-LAT) [Sv]	δE (R-LAT) [Sv]	E (R-LAT) [Sv/μC]	δE (R-LAT) [Sv/μC]	% photon	% electron	% neutron
Beam LEFT	-2	1.55E-22	5E-24	9.70E-10	3E-11	68.7%	31.1%	0.25%
Beam LEFT	-1	4.57E-22	1E-23	2.86E-09	6E-11	54.5%	45.4%	0.11%
Beam LEFT	-0.5	4.52E-20	2E-22	2.82E-07	1E-09	97.8%	2.2%	0.001%
Beam CENTER	0	3.44E-19	5E-22	2.15E-06	3E-09	99.0%	1.0%	0.0003%
Beam RIGHT	0.5	4.52E-20	9E-23	2.82E-07	6E-10	97.8%	2.2%	0.001%
Beam RIGHT	1	4.75E-22	7E-23	2.96E-09	4E-10	57.2%	42.7%	0.10%
Beam RIGHT	2	1.54E-22	6E-24	9.64E-10	3E-11	68.4%	31.4%	0.25%

Table K-11. Total Effective Dose (PA) Data at 170 meters.

Orientation from Beam Centerline	Off-Axis Angle	E (PA) [Sv]	δE (PA) [Sv]	E (PA) [Sv/μC]	δE (PA) [Sv/μC]	% photon	% electron	% neutron
Beam LEFT	-1	3.11E-22	2E-23	1.94E-09	1E-10	55.4%	44.5%	0.12%
Beam LEFT	-0.5	2.24E-20	7E-23	1.40E-07	4E-10	96.4%	3.6%	0.003%
Beam CENTER	0	1.68E-19	2E-22	1.05E-06	1E-09	98.1%	1.9%	0.001%
Beam RIGHT	0.5	2.24E-20	6E-23	1.40E-07	4E-10	96.4%	3.6%	0.003%
Beam RIGHT	1	3.06E-22	1E-23	1.91E-09	9E-11	54.7%	45.2%	0.13%

Table K-12. Total Effective Dose (R-LAT) Data at 170 meters.

Orientation from Beam Centerline	Off-Axis Angle	E (R-LAT) [Sv]	δE (R-LAT) [Sv]	E (R-LAT) [Sv/μC]	δE (R-LAT) [Sv/μC]	% photon	% electron	% neutron
Beam LEFT	-1	2.39E-22	1E-23	1.49E-09	7E-11	60.5%	39.5%	0.08%
Beam LEFT	-0.5	1.97E-20	5E-23	1.23E-07	3E-10	97.3%	2.6%	0.002%
Beam CENTER	0	1.49E-19	2E-22	9.29E-07	1E-09	98.6%	1.4%	0.0004%
Beam RIGHT	0.5	1.97E-20	4E-23	1.23E-07	3E-10	97.3%	2.7%	0.002%
Beam RIGHT	1	2.35E-22	1E-23	1.47E-09	7E-11	59.8%	40.1%	0.09%

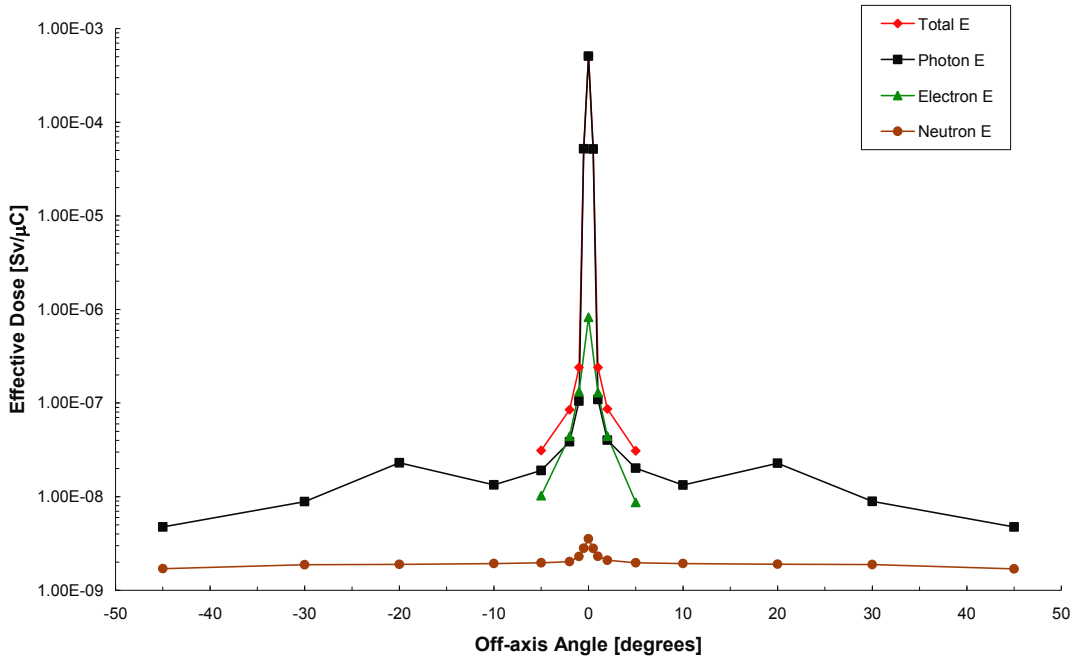

Figure K-1. Effective Dose (PA) at 10 meters.

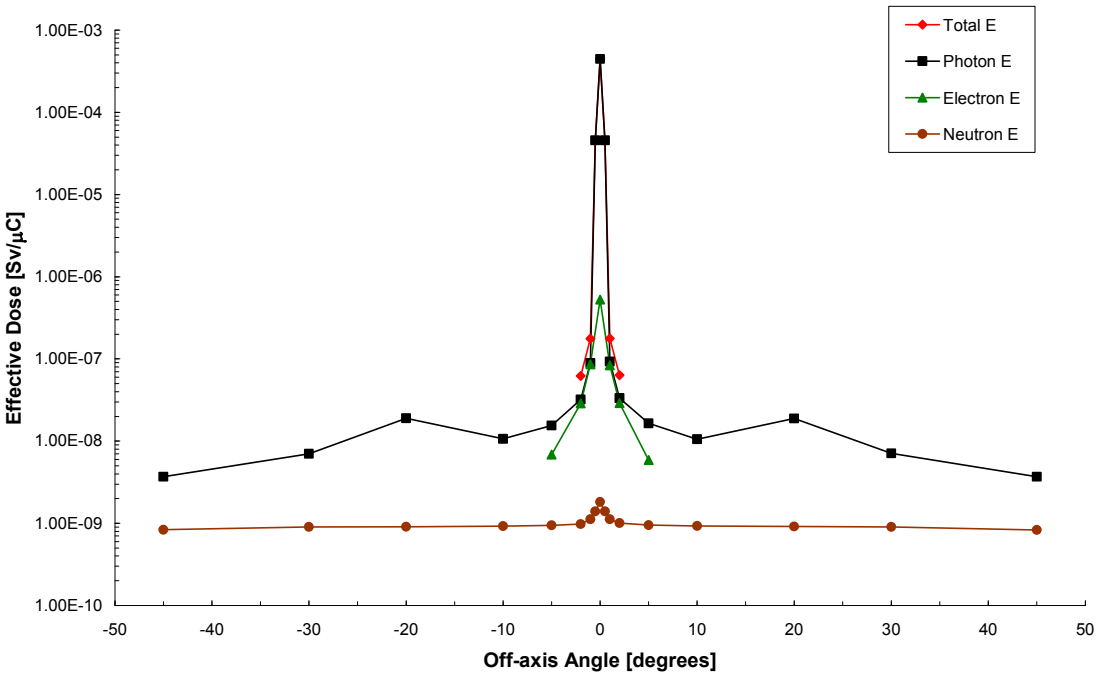

Figure K-2. Effective Dose (R-LAT) at 10 meters.

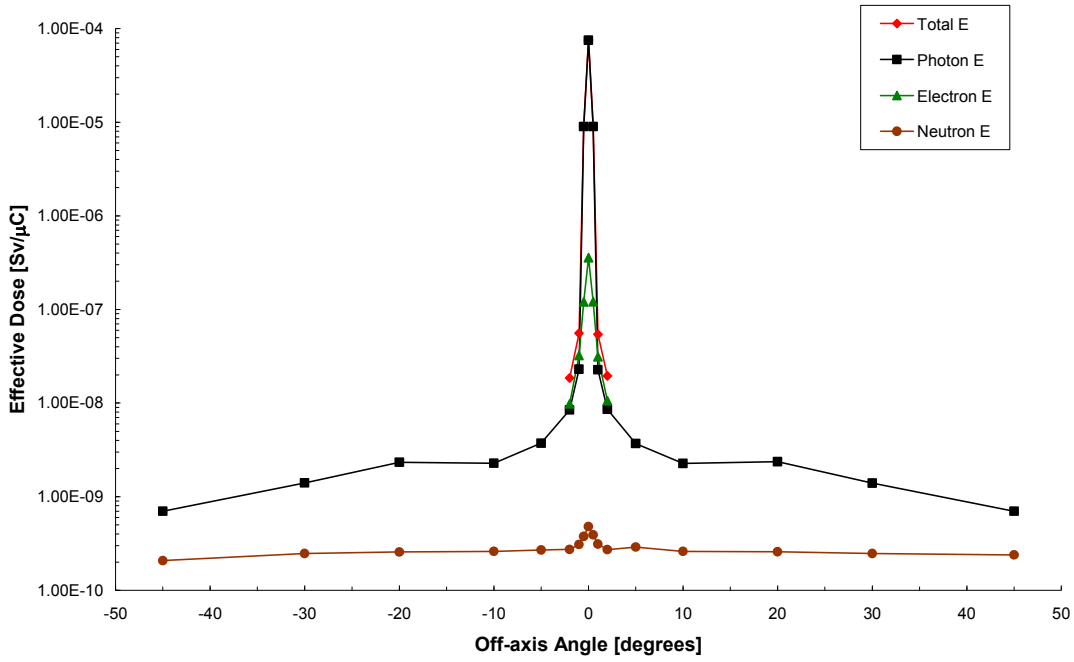

Figure K-3. Effective Dose (PA) at 25 meters.

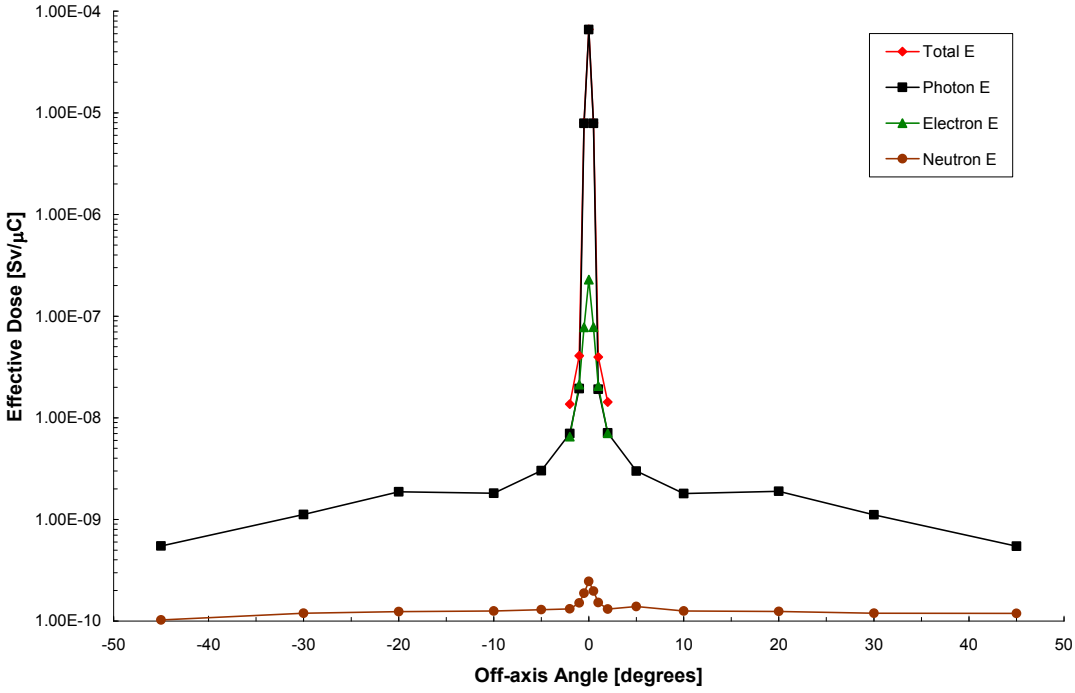

Figure K-4. Effective Dose (R-LAT) at 25 meters.

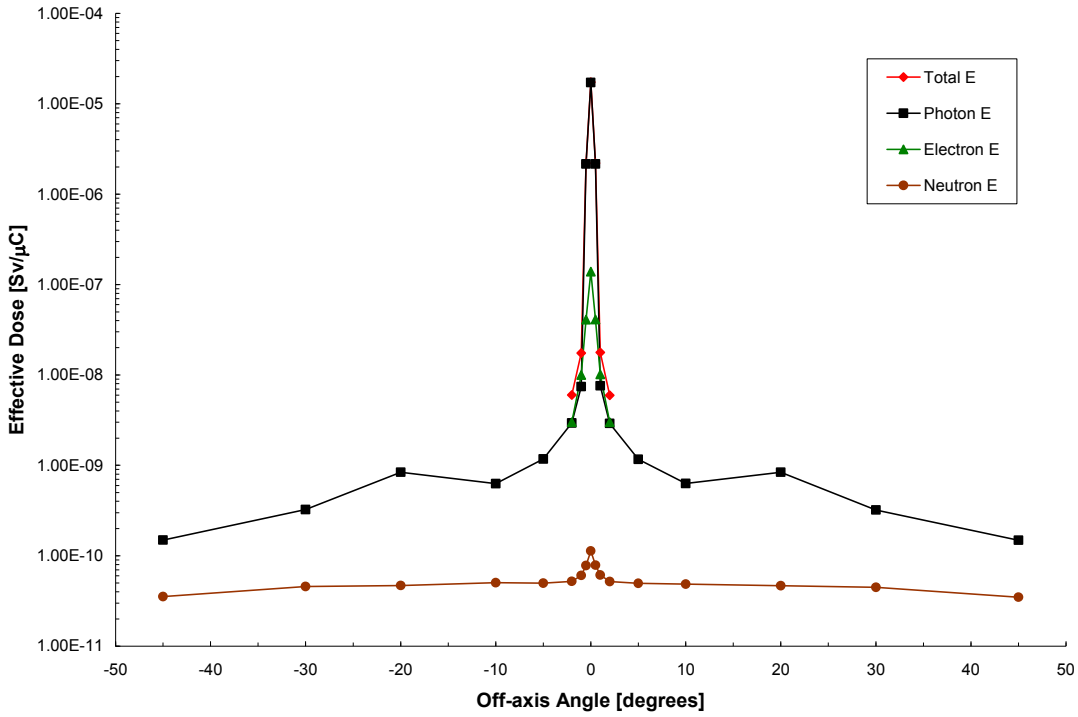

Figure K-5. Effective Dose (PA) at 50 meters.

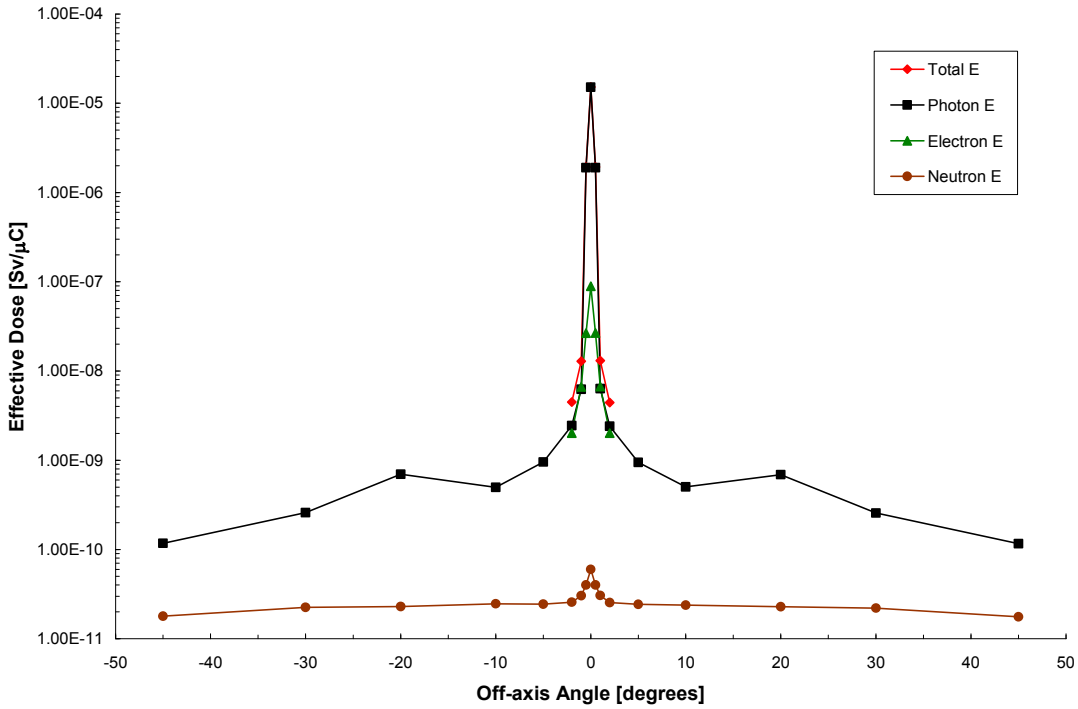

Figure K-6. Effective Dose (R-LAT) at 50 meters.

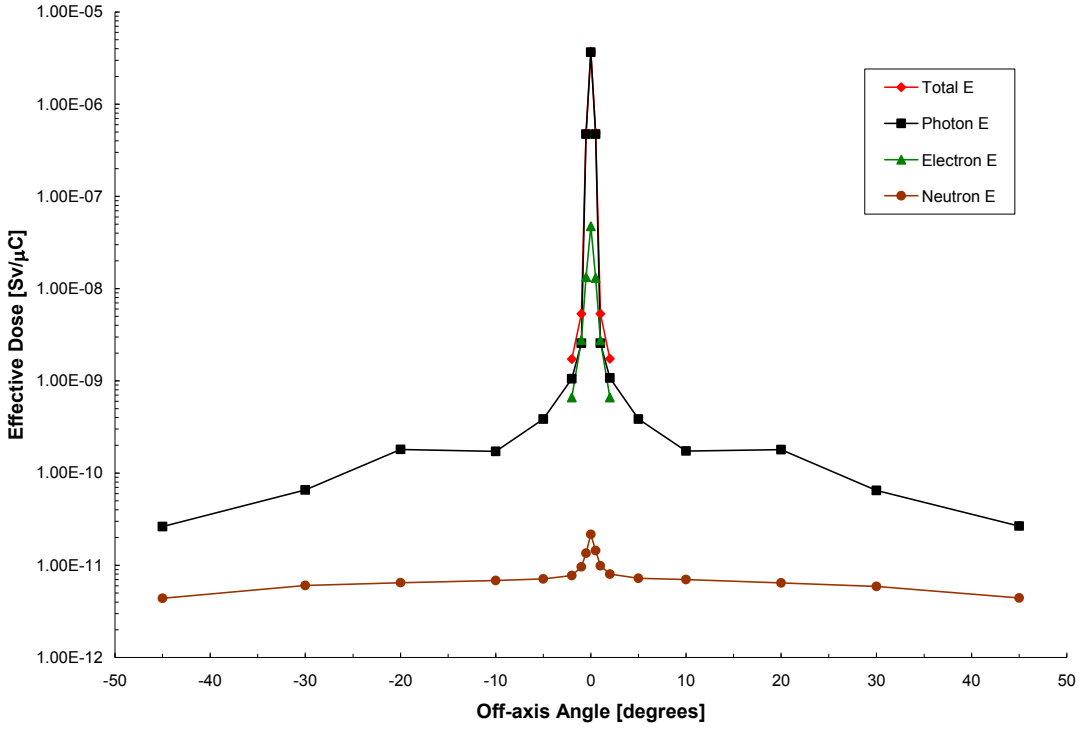

Figure K-7. Effective Dose (PA) at 100 meters.

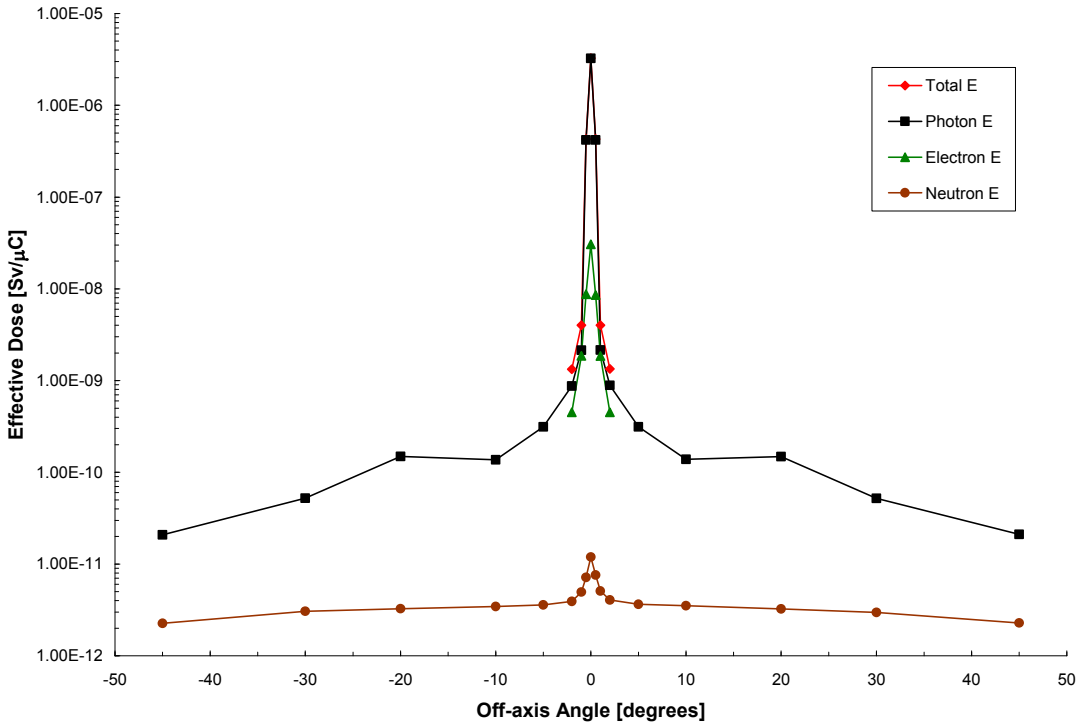

Figure K-8. Effective Dose (R-LAT) at 100 meters.

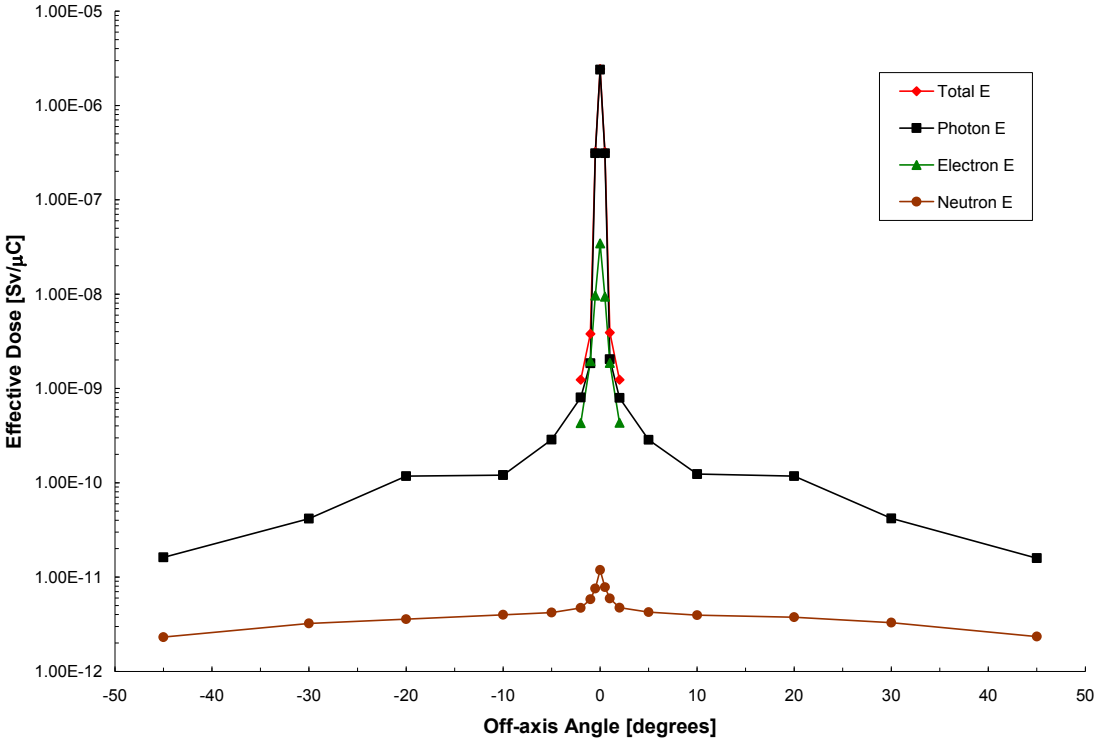

Figure K-9. Effective Dose (PA) at 120 meters.

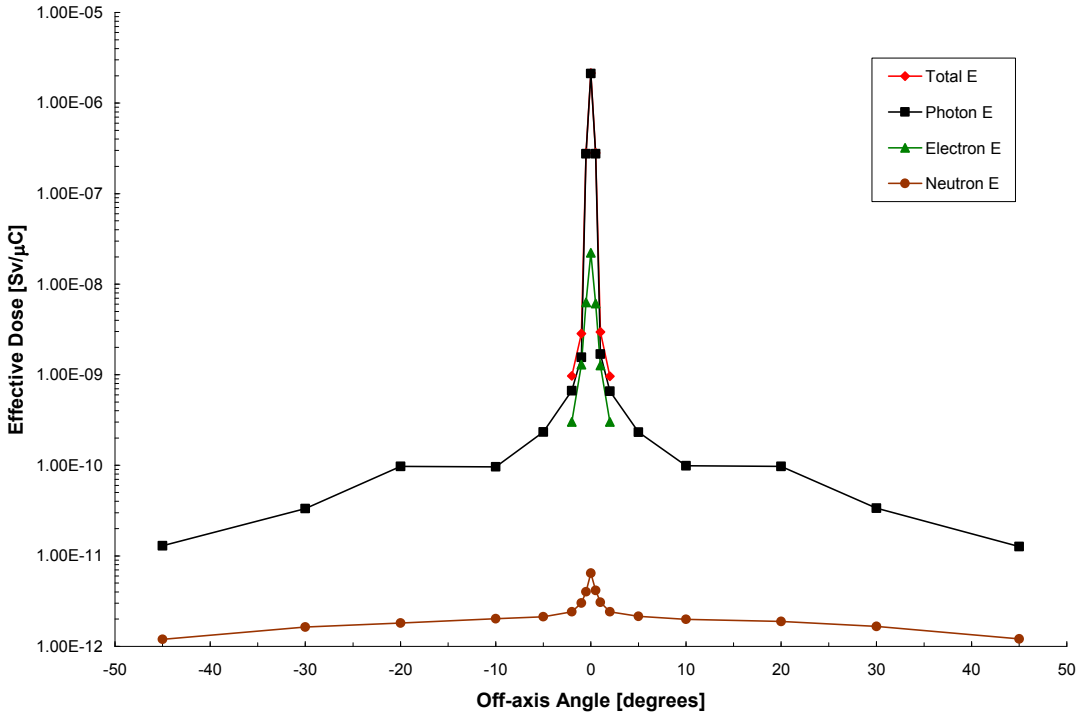

Figure K-10. Effective Dose (R-LAT) at 120 meters.

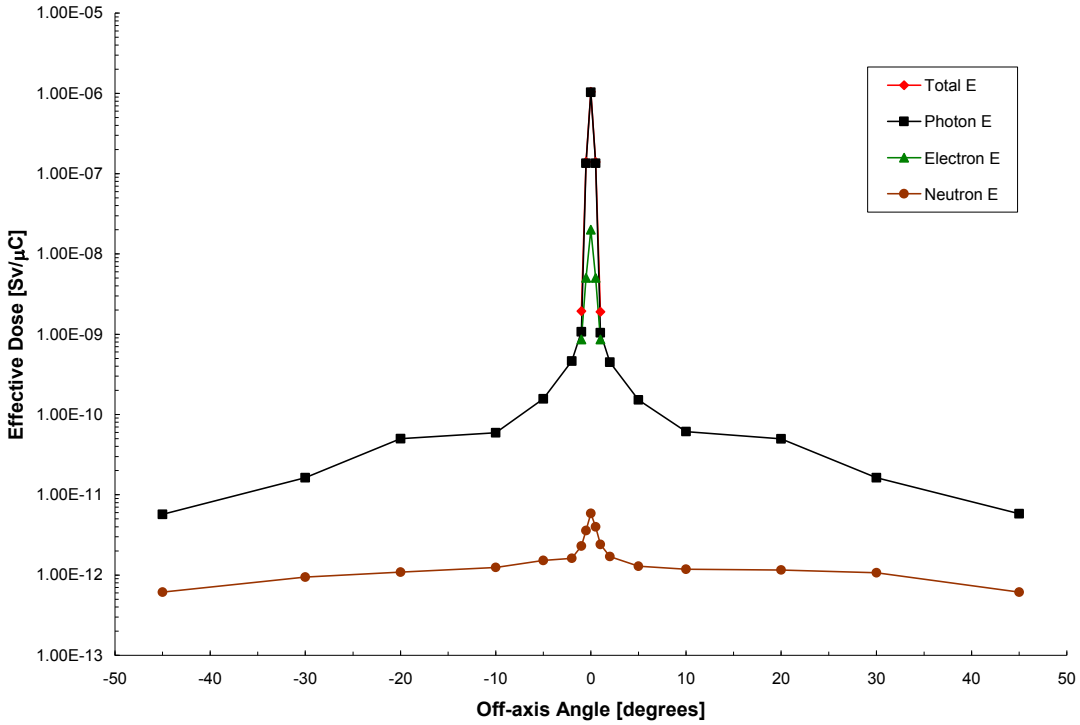

Figure K-11. Effective Dose (PA) at 170 meters.

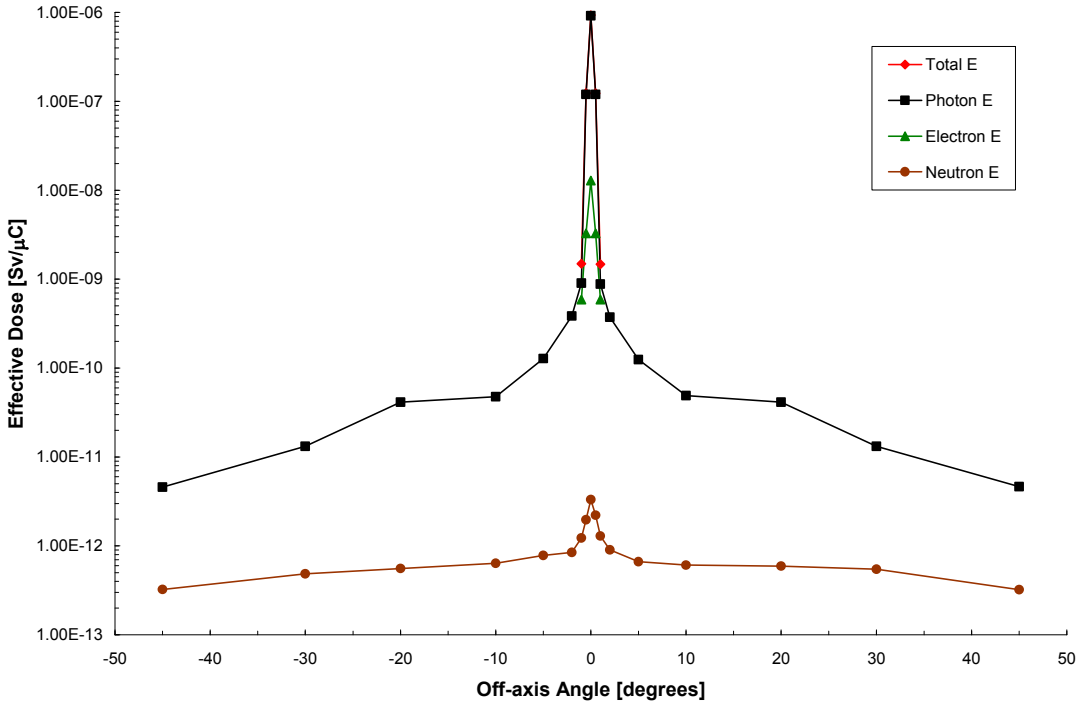

Figure K-12. Effective Dose (R-LAT) at 170 meters.

APPENDIX L

PHOTON H*(15) – H*(30) CALCULATIONS FOR 10 METERS

Table L-1. Photon Ambient Dose Equivalent, H*(15) at 10 meters.

Orientation from Beam Centerline	Off-Axis Angle	Φ_{TOTAL} [photons/cm^2/source e$^-$]	H*(15) [Sv]	δH*(15) [Sv]	H*(15) [Sv/μC]	δH*(15) [Sv/μC]	H*(15) Dose-Weighted Average Energy [MeV]
Beam LEFT	-45	1.80E-10	9.37E-22	5E-24	5.85E-09	3E-11	2.20
Beam LEFT	-30	3.00E-10	1.68E-21	2E-23	1.05E-08	1E-10	2.59
Beam LEFT	-20	5.22E-10	3.78E-21	4E-23	2.36E-08	3E-10	3.59
Beam LEFT	-10	4.58E-10	2.47E-21	5E-23	1.54E-08	3E-10	2.64
Beam LEFT	-5	5.83E-10	3.22E-21	8E-23	2.01E-08	5E-10	2.98
Beam LEFT	-2	9.91E-10	5.86E-21	2E-22	3.66E-08	1E-09	3.49
Beam LEFT	-1	2.20E-09	1.49E-20	4E-22	9.28E-08	3E-09	4.00
Beam LEFT	-0.5	6.28E-07	5.98E-18	1E-20	3.74E-05	8E-08	5.20
Beam CENTER	0	6.48E-06	5.90E-17	5E-20	3.68E-04	3E-07	5.18
Beam RIGHT	0.5	6.27E-07	5.98E-18	1E-20	3.73E-05	8E-08	5.21
Beam RIGHT	1	2.26E-09	1.55E-20	2E-22	9.65E-08	2E-09	3.99
Beam RIGHT	2	1.01E-09	6.07E-21	1E-22	3.79E-08	8E-10	3.52
Beam RIGHT	5	6.06E-10	3.39E-21	1E-22	2.12E-08	9E-10	3.02
Beam RIGHT	10	4.64E-10	2.48E-21	5E-23	1.55E-08	3E-10	2.59
Beam RIGHT	20	5.15E-10	3.73E-21	3E-23	2.33E-08	2E-10	3.61
Beam RIGHT	30	3.03E-10	1.69E-21	2E-23	1.06E-08	1E-10	2.60
Beam RIGHT	45	1.82E-10	9.37E-22	7E-24	5.85E-09	4E-11	2.19

Table L-2. Photon Ambient Dose Equivalent, H*(20) at 10 meters.

Orientation from Beam Centerline	Off-Axis Angle	Φ_{TOTAL} [photons/cm^2/source e$^-$]	H*(20) [Sv]	δH*(20) [Sv]	H*(20) [Sv/μC]	δH*(20) [Sv/μC]	H*(20) Dose-Weighted Average Energy [MeV]
Beam LEFT	-45	1.80E-10	9.66E-22	6E-24	6.03E-09	3E-11	2.26
Beam LEFT	-30	3.00E-10	1.75E-21	2E-23	1.09E-08	1E-10	2.67
Beam LEFT	-20	5.22E-10	4.05E-21	5E-23	2.53E-08	3E-10	3.75
Beam LEFT	-10	4.58E-10	2.58E-21	5E-23	1.61E-08	3E-10	2.75
Beam LEFT	-5	5.83E-10	3.41E-21	9E-23	2.13E-08	5E-10	3.15
Beam LEFT	-2	9.91E-10	6.32E-21	2E-22	3.95E-08	1E-09	3.72
Beam LEFT	-1	2.20E-09	1.63E-20	5E-22	1.02E-07	3E-09	4.25
Beam LEFT	-0.5	6.28E-07	6.82E-18	2E-20	4.26E-05	9E-08	5.47
Beam CENTER	0	6.48E-06	6.71E-17	6E-20	4.19E-04	4E-07	5.46
Beam RIGHT	0.5	6.27E-07	6.82E-18	2E-20	4.26E-05	9E-08	5.47
Beam RIGHT	1	2.26E-09	1.69E-20	3E-22	1.06E-07	2E-09	4.24
Beam RIGHT	2	1.01E-09	6.56E-21	1E-22	4.09E-08	9E-10	3.75
Beam RIGHT	5	6.06E-10	3.60E-21	1E-22	2.25E-08	9E-10	3.20
Beam RIGHT	10	4.64E-10	2.58E-21	5E-23	1.61E-08	3E-10	2.69
Beam RIGHT	20	5.15E-10	4.00E-21	3E-23	2.50E-08	2E-10	3.76
Beam RIGHT	30	3.03E-10	1.76E-21	2E-23	1.10E-08	1E-10	2.68
Beam RIGHT	45	1.82E-10	9.66E-22	7E-24	6.03E-09	4E-11	2.25

Table L-3. Photon Ambient Dose Equivalent, H*(30) at 10 meters.

Orientation from Beam Centerline	Off-Axis Angle	Φ_{TOTAL} [photons/cm^2/source e$^-$]	H*(30) [Sv]	δH*(30) [Sv]	H*(30) [Sv/μC]	δH*(30) [Sv/μC]	H*(30) Dose-Weighted Average Energy [MeV]
Beam LEFT	-45	1.80E-10	9.49E-22	6E-24	5.92E-09	3E-11	2.31
Beam LEFT	-30	3.00E-10	1.73E-21	2E-23	1.08E-08	1E-10	2.75
Beam LEFT	-20	5.22E-10	4.15E-21	5E-23	2.59E-08	3E-10	3.93
Beam LEFT	-10	4.58E-10	2.58E-21	5E-23	1.61E-08	3E-10	2.88
Beam LEFT	-5	5.83E-10	3.49E-21	9E-23	2.18E-08	6E-10	3.39
Beam LEFT	-2	9.91E-10	6.65E-21	2E-22	4.15E-08	1E-09	4.04
Beam LEFT	-1	2.20E-09	1.75E-20	5E-22	1.09E-07	3E-09	4.59
Beam LEFT	-0.5	6.28E-07	7.73E-18	2E-20	4.82E-05	1E-07	5.85
Beam CENTER	0	6.48E-06	7.58E-17	7E-20	4.73E-04	4E-07	5.89
Beam RIGHT	0.5	6.27E-07	7.72E-18	2E-20	4.82E-05	1E-07	5.86
Beam RIGHT	1	2.26E-09	1.81E-20	3E-22	1.13E-07	2E-09	4.58
Beam RIGHT	2	1.01E-09	6.90E-21	1E-22	4.31E-08	9E-10	4.07
Beam RIGHT	5	6.06E-10	3.69E-21	2E-22	2.30E-08	9E-10	3.44
Beam RIGHT	10	4.64E-10	2.57E-21	5E-23	1.61E-08	3E-10	2.81
Beam RIGHT	20	5.15E-10	4.10E-21	3E-23	2.56E-08	2E-10	3.95
Beam RIGHT	30	3.03E-10	1.74E-21	2E-23	1.08E-08	1E-10	2.76
Beam RIGHT	45	1.82E-10	9.49E-22	7E-24	5.92E-09	4E-11	2.30

APPENIDIX M

PHOTON AIR KERMA DATA

Table M-1. Photon Air Kerma at 10 meters.

Orientation from Beam Centerline	Off-Axis Angle	Kerma [Gy]	δKerma [Gy]	Kerma [Gy/μC]	δKerma [Gy/μC]	Kerma-Weighted Average Energy [MeV]
Beam LEFT	-45	8.63E-22	5E-24	5.39E-09	3E-11	2.38
Beam LEFT	-30	1.58E-21	1E-23	9.86E-09	9E-11	2.84
Beam LEFT	-20	3.94E-21	5E-23	2.46E-08	3E-10	4.11
Beam LEFT	-10	2.38E-21	5E-23	1.49E-08	3E-10	3.02
Beam LEFT	-5	3.35E-21	9E-23	2.09E-08	5E-10	3.71
Beam LEFT	-2	6.72E-21	2E-22	4.19E-08	1E-09	4.59
Beam LEFT	-1	1.81E-20	5E-22	1.13E-07	3E-09	5.16
Beam LEFT	-0.5	8.73E-18	2E-20	5.45E-05	1E-07	6.59
Beam CENTER	0	8.60E-17	8E-20	5.37E-04	5E-07	6.57
Beam RIGHT	0.5	8.72E-18	2E-20	5.45E-05	1E-07	6.60
Beam RIGHT	1	1.87E-20	3E-22	1.17E-07	2E-09	5.16
Beam RIGHT	2	6.96E-21	1E-22	4.34E-08	9E-10	4.62
Beam RIGHT	5	3.55E-21	1E-22	2.22E-08	9E-10	3.77
Beam RIGHT	10	2.37E-21	4E-23	1.48E-08	3E-10	2.93
Beam RIGHT	20	3.90E-21	3E-23	2.43E-08	2E-10	4.13
Beam RIGHT	30	1.59E-21	1E-23	9.93E-09	9E-11	2.85
Beam RIGHT	45	8.62E-22	6E-24	5.38E-09	4E-11	2.37

Table M-2. Photon Air Kerma at 25 meters.

Orientation from Beam Centerline	Off-Axis Angle	Kerma [Gy]	δKerma [Gy]	Kerma [Gy/μC]	δKerma [Gy/μC]	Kerma-Weighted Average Energy [MeV]
Beam LEFT	-45	1.27E-22	1E-24	7.96E-10	7E-12	2.42
Beam LEFT	-30	2.51E-22	2E-24	1.57E-09	1E-11	2.86
Beam LEFT	-20	4.14E-22	3E-24	2.58E-09	2E-11	3.15
Beam LEFT	-10	4.08E-22	5E-24	2.55E-09	3E-11	2.92
Beam LEFT	-5	6.57E-22	1E-23	4.10E-09	6E-11	3.67
Beam LEFT	-2	1.48E-21	4E-23	9.24E-09	3E-10	4.38
Beam LEFT	-1	3.98E-21	1E-22	2.49E-08	8E-10	4.91
Beam LEFT	-0.5	1.51E-18	3E-21	9.44E-06	2E-08	6.66
Beam CENTER	0	1.27E-17	1E-20	7.92E-05	6E-08	6.64
Beam RIGHT	0.5	1.51E-18	3E-21	9.43E-06	2E-08	6.66
Beam RIGHT	1	3.91E-21	8E-23	2.44E-08	5E-10	4.97
Beam RIGHT	2	1.50E-21	7E-23	9.38E-09	4E-10	4.41
Beam RIGHT	5	6.51E-22	2E-23	4.06E-09	1E-10	3.67
Beam RIGHT	10	4.06E-22	5E-24	2.53E-09	3E-11	2.90
Beam RIGHT	20	4.19E-22	6E-24	2.62E-09	4E-11	3.13
Beam RIGHT	30	2.50E-22	2E-24	1.56E-09	1E-11	2.86
Beam RIGHT	45	1.27E-22	9E-25	7.95E-10	6E-12	2.40

Table M-3. Photon Air Kerma at 50 meters.

Orientation from Beam Centerline	Off-Axis Angle	Kerma [Gy]	δKerma [Gy]	Kerma [Gy/μC]	δKerma [Gy/μC]	Kerma-Weighted Average Energy [MeV]
Beam LEFT	-45	2.72E-23	6E-25	1.70E-10	3E-12	2.46
Beam LEFT	-30	5.81E-23	7E-25	3.62E-10	4E-12	2.89
Beam LEFT	-20	1.45E-22	2E-24	9.05E-10	1E-11	4.07
Beam LEFT	-10	1.12E-22	2E-24	7.01E-10	1E-11	2.93
Beam LEFT	-5	2.07E-22	4E-24	1.29E-09	3E-11	3.66
Beam LEFT	-2	5.13E-22	1E-23	3.20E-09	6E-11	4.37
Beam LEFT	-1	1.28E-21	2E-23	7.98E-09	1E-10	4.89
Beam LEFT	-0.5	3.62E-19	6E-22	2.26E-06	4E-09	6.75
Beam CENTER	0	2.89E-18	2E-21	1.81E-05	1E-08	6.75
Beam RIGHT	0.5	3.62E-19	8E-22	2.26E-06	5E-09	6.75
Beam RIGHT	1	1.31E-21	6E-23	8.18E-09	4E-10	4.80
Beam RIGHT	2	5.07E-22	1E-23	3.16E-09	7E-11	4.37
Beam RIGHT	5	2.05E-22	4E-24	1.28E-09	2E-11	3.68
Beam RIGHT	10	1.13E-22	2E-24	7.06E-10	1E-11	2.93
Beam RIGHT	20	1.44E-22	7E-24	9.02E-10	4E-11	4.03
Beam RIGHT	30	5.73E-23	8E-25	3.58E-10	5E-12	2.91
Beam RIGHT	45	2.70E-23	4E-25	1.69E-10	3E-12	2.48

Table M-4. Photon Air Kerma at 100 meters.

Orientation from Beam Centerline	Off-Axis Angle	Kerma [Gy]	δKerma [Gy]	Kerma [Gy/μC]	δKerma [Gy/μC]	Kerma-Weighted Average Energy [MeV]
Beam LEFT	-45	4.77E-24	5E-26	2.98E-11	3E-13	2.64
Beam LEFT	-30	1.17E-23	1E-25	7.28E-11	8E-13	2.98
Beam LEFT	-20	3.11E-23	4E-25	1.94E-10	2E-12	4.10
Beam LEFT	-10	3.07E-23	5E-25	1.92E-10	3E-12	3.02
Beam LEFT	-5	6.78E-23	2E-24	4.23E-10	1E-11	3.74
Beam LEFT	-2	1.83E-22	4E-24	1.15E-09	3E-11	4.37
Beam LEFT	-1	4.43E-22	2E-23	2.76E-09	1E-10	4.75
Beam LEFT	-0.5	7.93E-20	1E-22	4.95E-07	7E-10	6.92
Beam CENTER	0	6.16E-19	4E-22	3.85E-06	3E-09	6.94
Beam RIGHT	0.5	7.94E-20	1E-22	4.95E-07	8E-10	6.92
Beam RIGHT	1	4.44E-22	2E-23	2.77E-09	1E-10	4.78
Beam RIGHT	2	1.87E-22	8E-24	1.17E-09	5E-11	4.34
Beam RIGHT	5	6.78E-23	2E-24	4.23E-10	1E-11	3.73
Beam RIGHT	10	3.10E-23	6E-25	1.93E-10	4E-12	3.00
Beam RIGHT	20	3.09E-23	2E-25	1.93E-10	1E-12	4.10
Beam RIGHT	30	1.15E-23	1E-25	7.20E-11	7E-13	3.01
Beam RIGHT	45	4.82E-24	1E-25	3.01E-11	7E-13	2.64

Table M-5. Photon Air Kerma at 120 meters.

Orientation from Beam Centerline	Off-Axis Angle	Kerma [Gy]	δKerma [Gy]	Kerma [Gy/μC]	δKerma [Gy/μC]	Kerma-Weighted Average Energy [MeV]
Beam LEFT	-45	2.93E-24	4E-26	1.83E-11	2E-13	2.73
Beam LEFT	-30	7.41E-24	1E-25	4.63E-11	7E-13	3.00
Beam LEFT	-20	2.02E-23	2E-25	1.26E-10	1E-12	4.10
Beam LEFT	-10	2.15E-23	3E-25	1.34E-10	2E-12	3.03
Beam LEFT	-5	5.03E-23	2E-24	3.14E-10	1E-11	3.75
Beam LEFT	-2	1.40E-22	4E-24	8.75E-10	3E-11	4.40
Beam LEFT	-1	3.19E-22	7E-24	1.99E-09	4E-11	4.86
Beam LEFT	-0.5	5.21E-20	2E-22	3.25E-07	1E-09	6.97
Beam CENTER	0	4.02E-19	6E-22	2.51E-06	4E-09	7.01
Beam RIGHT	0.5	5.21E-20	1E-22	3.25E-07	7E-10	6.97
Beam RIGHT	1	3.62E-22	9E-23	2.26E-09	5E-10	4.40
Beam RIGHT	2	1.38E-22	5E-24	8.64E-10	3E-11	4.40
Beam RIGHT	5	5.00E-23	1E-24	3.12E-10	9E-12	3.82
Beam RIGHT	10	2.20E-23	5E-25	1.37E-10	3E-12	3.07
Beam RIGHT	20	2.02E-23	3E-25	1.26E-10	2E-12	4.13
Beam RIGHT	30	7.45E-24	2E-25	4.65E-11	1E-12	3.02
Beam RIGHT	45	2.88E-24	2E-26	1.80E-11	2E-13	2.72

Table M-6. Photon Air Kerma at 170 meters.

Orientation from Beam Centerline	Off-Axis Angle	Kerma [Gy]	δKerma [Gy]	Kerma [Gy/μC]	δKerma [Gy/μC]	Kerma-Weighted Average Energy [MeV]
Beam LEFT	-45	1.03E-24	1E-26	6.41E-12	7E-14	2.88
Beam LEFT	-30	2.91E-24	5E-26	1.81E-11	3E-13	3.12
Beam LEFT	-20	8.58E-24	1E-25	5.35E-11	9E-13	4.16
Beam LEFT	-10	1.05E-23	2E-25	6.56E-11	1E-12	3.16
Beam LEFT	-5	2.73E-23	1E-24	1.70E-10	6E-12	3.94
Beam LEFT	-2	8.05E-23	3E-24	5.02E-10	2E-11	4.48
Beam LEFT	-1	1.85E-22	9E-24	1.15E-09	6E-11	4.87
Beam LEFT	-0.5	2.26E-20	6E-23	1.41E-07	4E-10	7.12
Beam CENTER	0	1.73E-19	2E-22	1.08E-06	1E-09	7.17
Beam RIGHT	0.5	2.25E-20	4E-23	1.41E-07	3E-10	7.12
Beam RIGHT	1	1.80E-22	6E-24	1.12E-09	4E-11	4.90
Beam RIGHT	2	7.74E-23	2E-24	4.83E-10	1E-11	4.56
Beam RIGHT	5	2.66E-23	6E-25	1.66E-10	4E-12	3.94
Beam RIGHT	10	1.09E-23	6E-25	6.79E-11	4E-12	3.11
Beam RIGHT	20	8.57E-24	9E-26	5.35E-11	6E-13	4.17
Beam RIGHT	30	2.90E-24	3E-26	1.81E-11	2E-13	3.13
Beam RIGHT	45	1.04E-24	2E-26	6.52E-12	1E-13	2.84

APPENIDX N

SPECIAL PHOTON DOSE DRIVER CALCULATIONS

The premise for and methods used in the special dose driver calculation models were presented in Chapter 5. This appendix includes the remainder of the data set for downfield distances of 25 meters through 170 meters. Data for 25 meters are shown in Figure N-1 through Figure N-6. Data for 50 meters are shown in Figure N-7 through Figure N-12. Data for 100 meters are shown in Figure N-13 through Figure N-18. Data for 120 meters are shown in Figure N-19 through Figure N-24. Data for 170 meters are shown in Figure N-25 through Figure N-30.

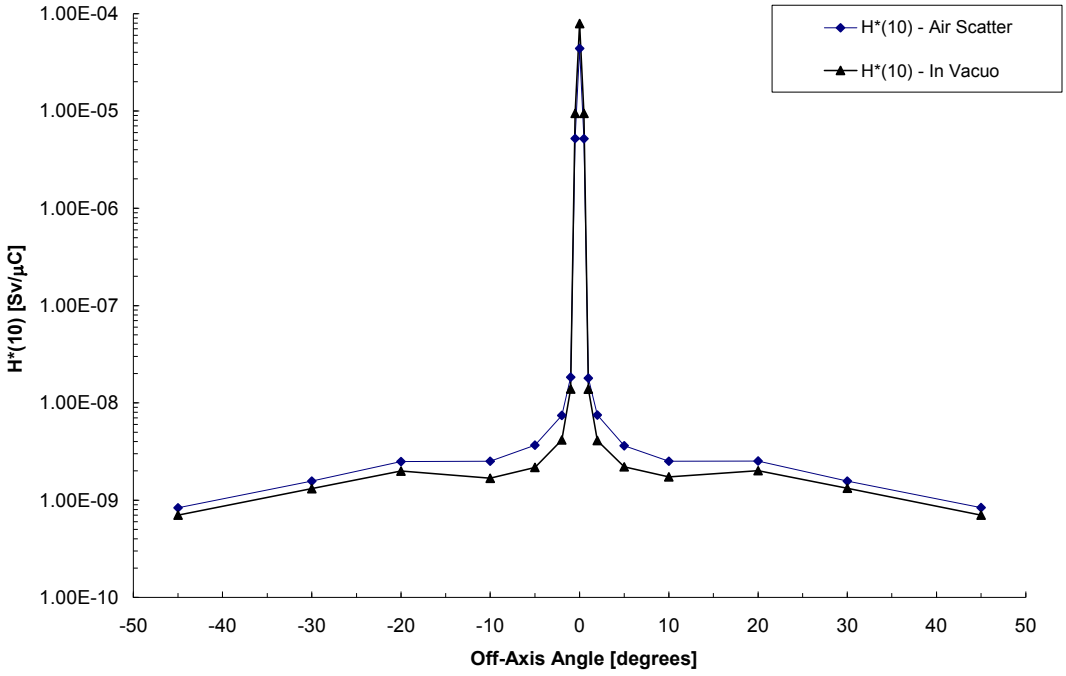

Figure N-1. Comparison of H*(10) in Air and in Vacuo for the System at 25 meters.

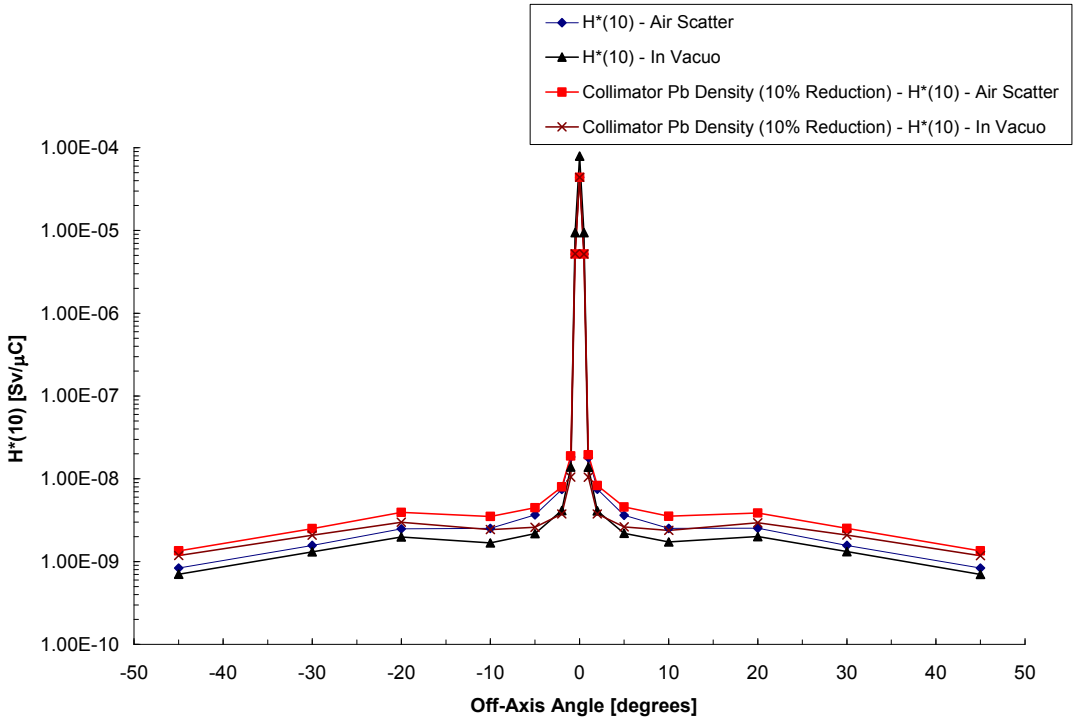

Figure N-2. Comparison of H*(10) in Air, in Vacuo, with a Pb Density Reduction of 10% in the Collimator (in Air), and with a Density Reduction of 10% in the Collimator (in Vacuo) at 25 meters.

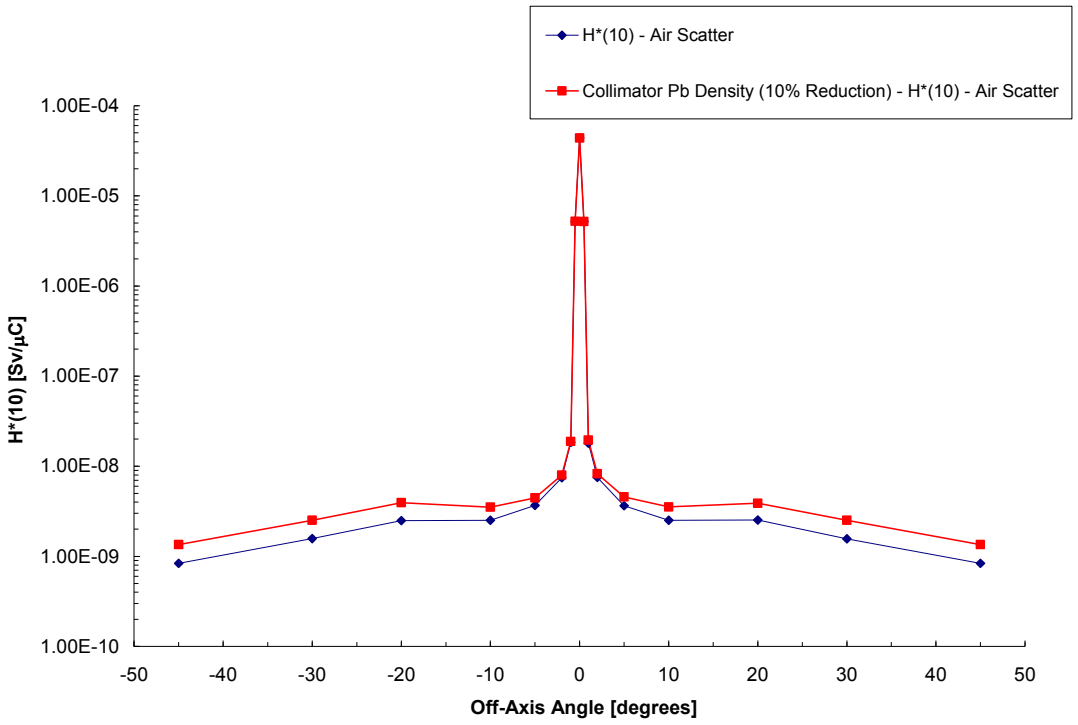

Figure N-3. Comparison of H*(10) for the System (in Air) and H*(10) with a Pb Density Reduction of 10% in the Collimator (in Air) at 25 meters.

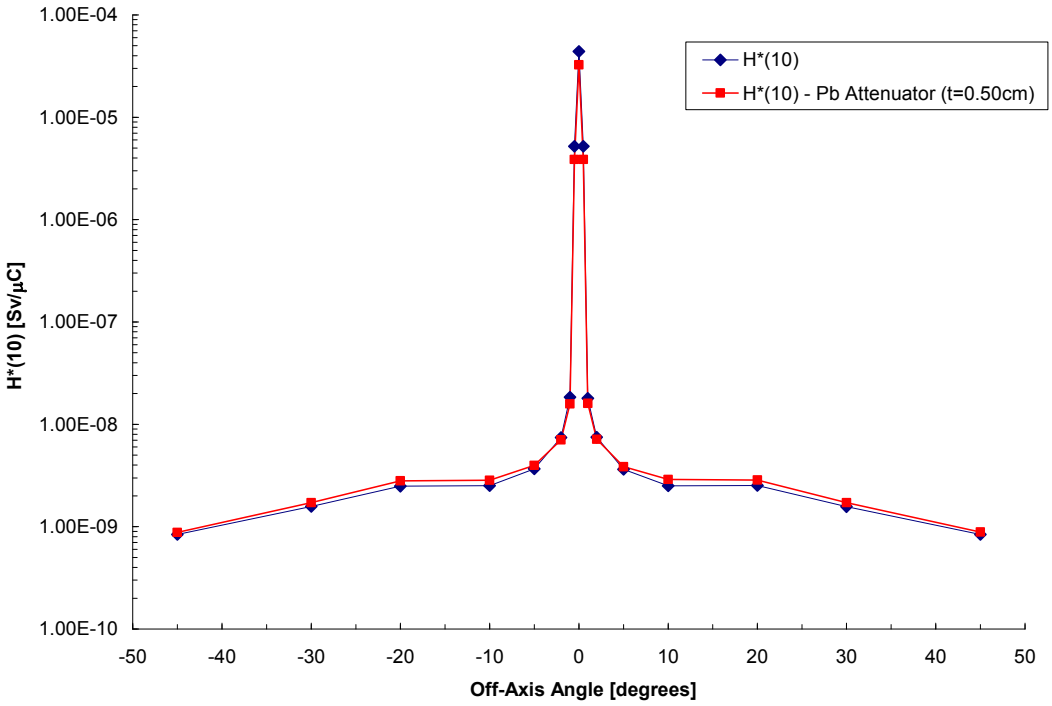

Figure N-4. Comparison of H*(10) for the System (in Air) and the System with a Pb Attenuator (t=0.50 cm) in the Beam Line (in Air) at 25 meters.

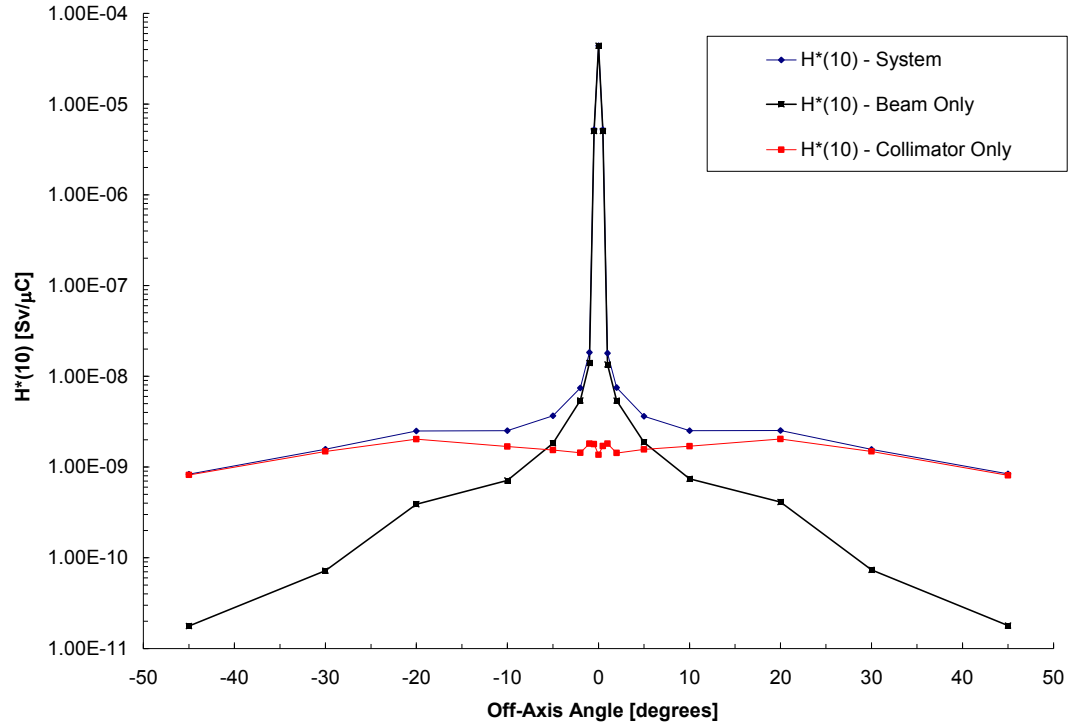

Figure N-5. Comparison of H*(10) for the System (in Air), the Beam Only Contribution, and the Collimator Only Contribution at 25 meters.

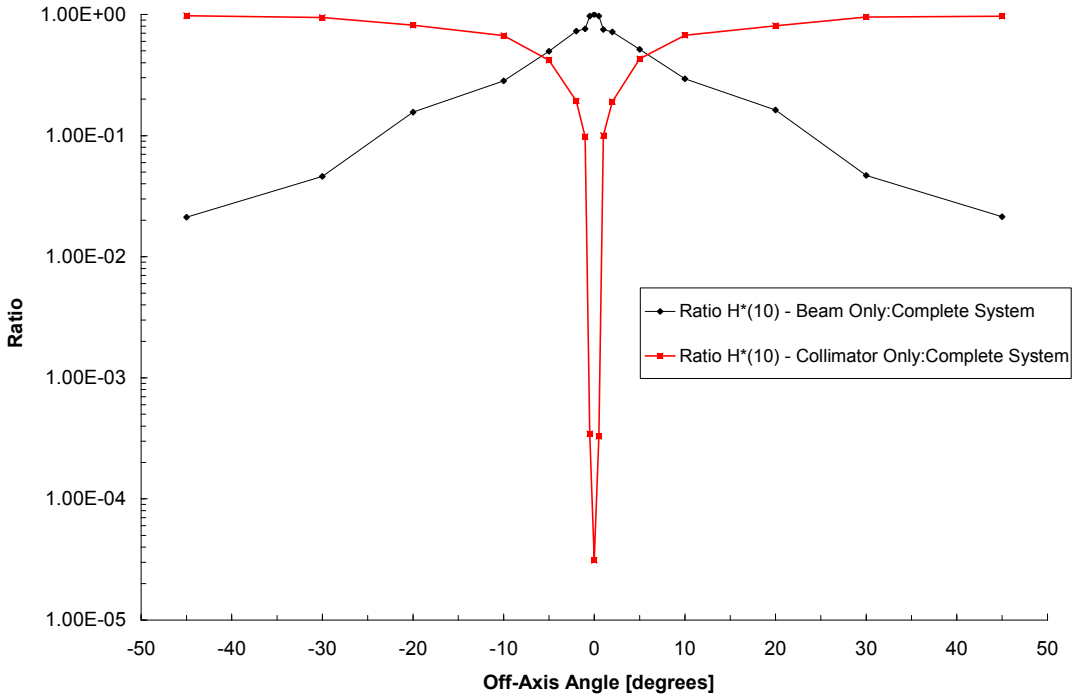

Figure N-6. Ratio of H*(10) for the Beam Only to the System (in Air) and the Collimator Only to the System (in Air) at 25 meters.

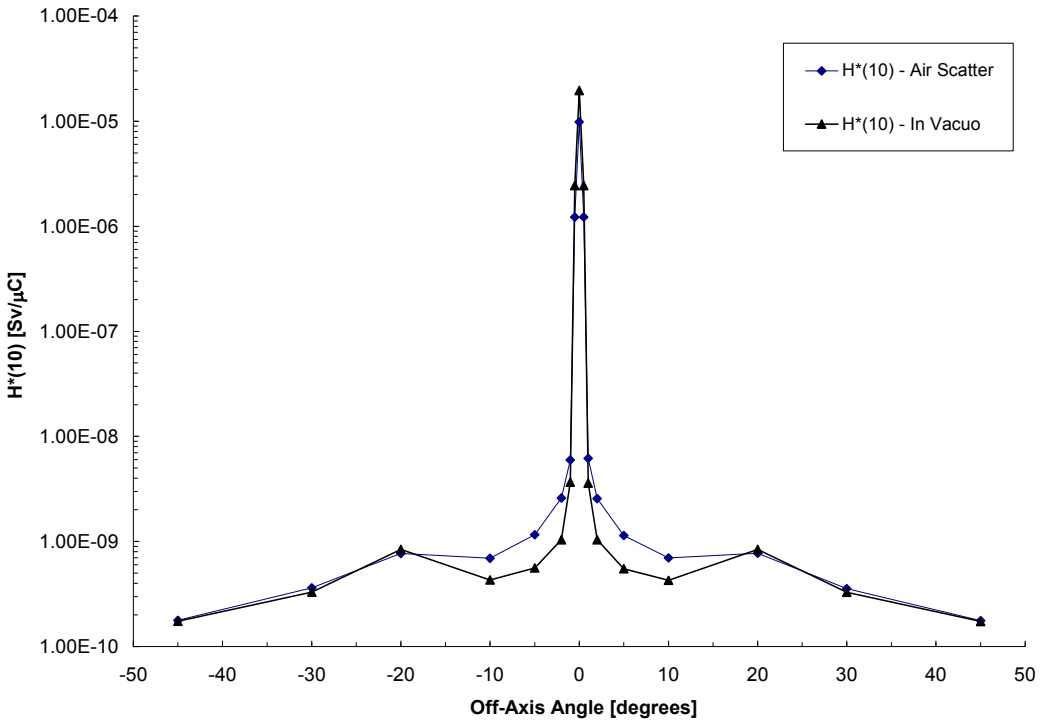

FigureN-7. Comparison of H*(10) in Air and in Vacuo for the System at 50 meters.

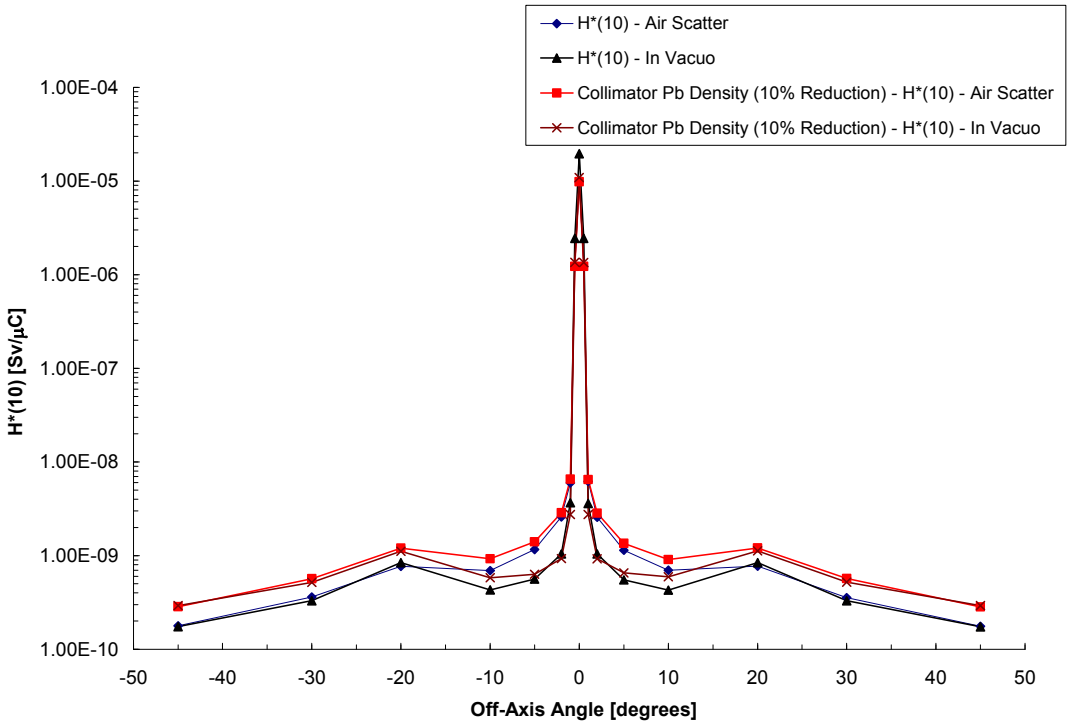

Figure N-8. Comparison of H*(10) in Air, in Vacuo, with a Pb Density Reduction of 10% in the Collimator (in Air), and with a Density Reduction of 10% in the Collimator (in Vacuo) at 50 meters.

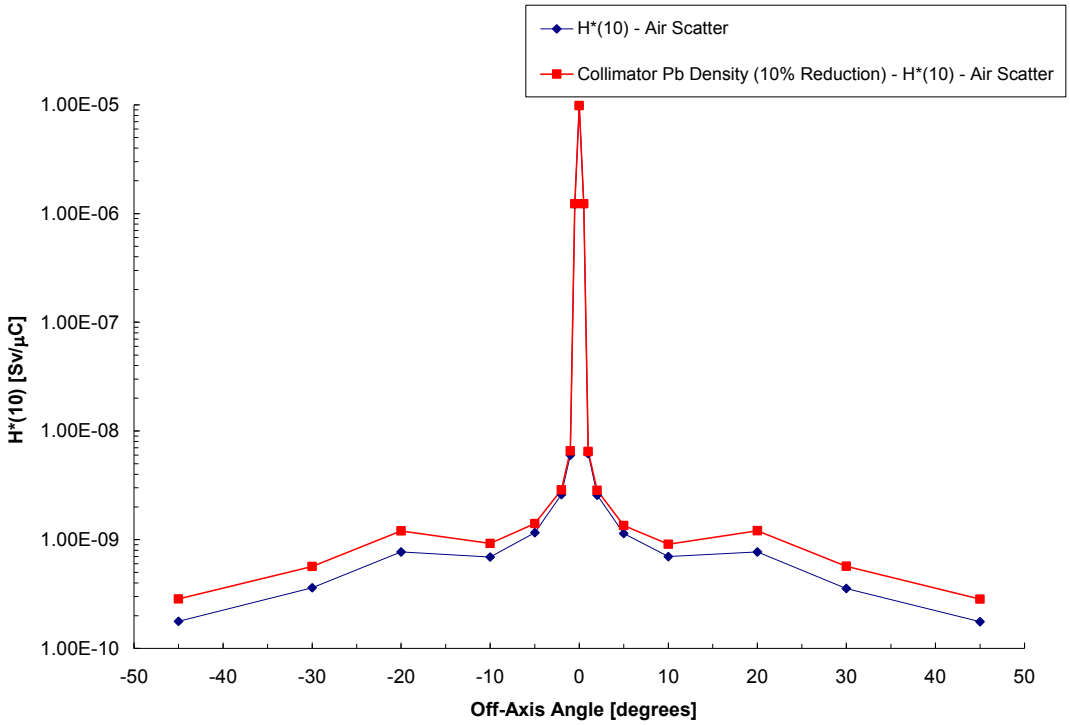

Figure N-9. Comparison of H*(10) for the System (in Air) and H*(10) with a Pb Density Reduction of 10% in the Collimator (in Air) at 50 meters.

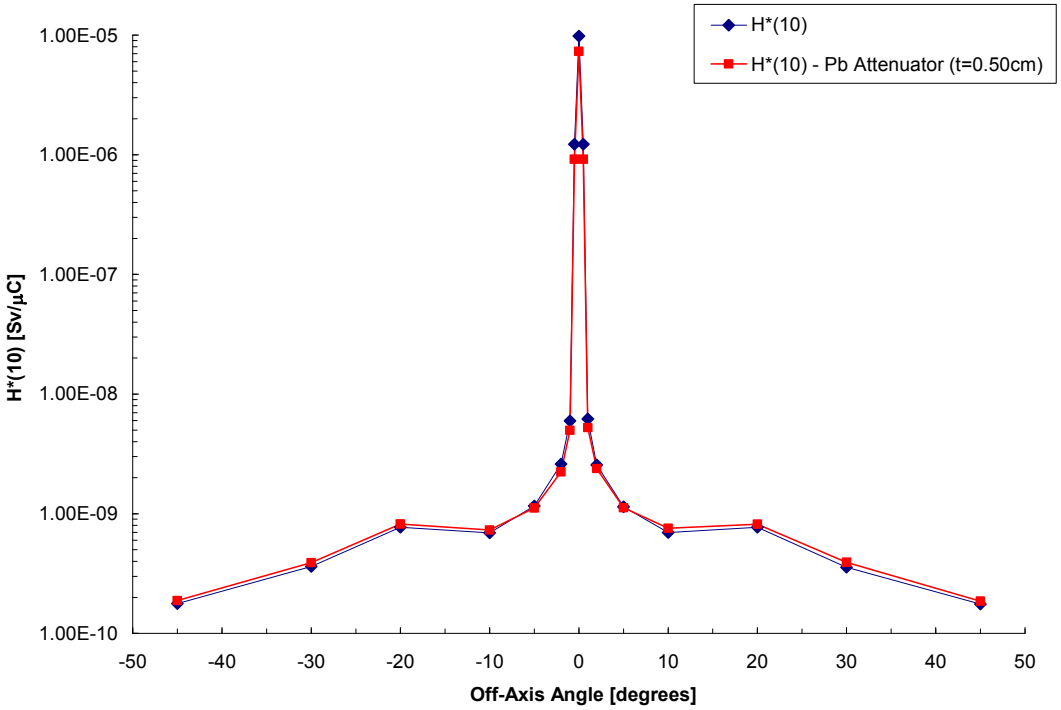

Figure N-10. Comparison of H*(10) for the System (in Air) and the System with a Pb Attenuator (t=0.50 cm) in the Beam Line (in Air) at 50 meters.

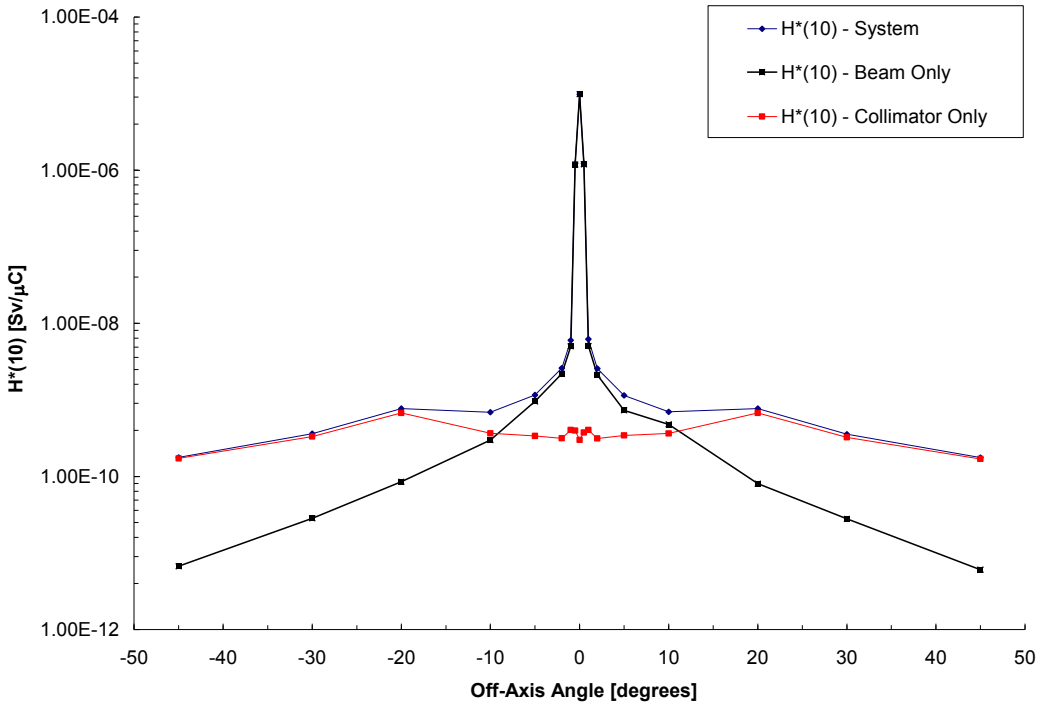

Figure N-11. Comparison of H*(10) for the System (in Air), the Beam Only Contribution, and the Collimator Only Contribution at 50 meters.

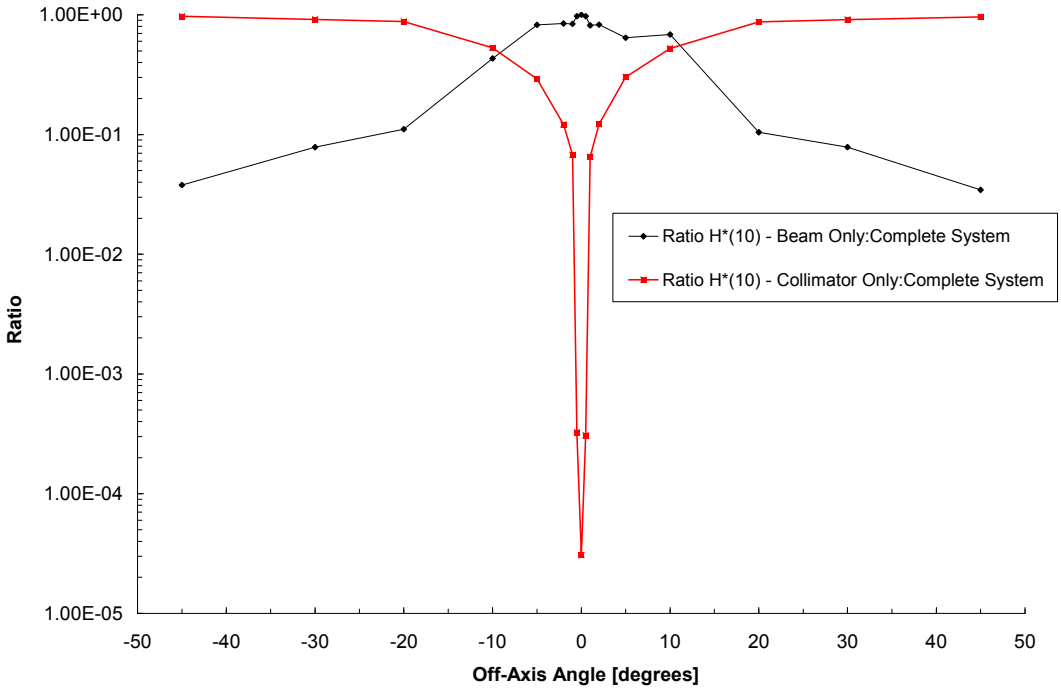

Figure N-12. Ratio of H*(10) for the Beam Only to the System (in Air) and the Collimator Only to the System (in Air) at 50 meters.

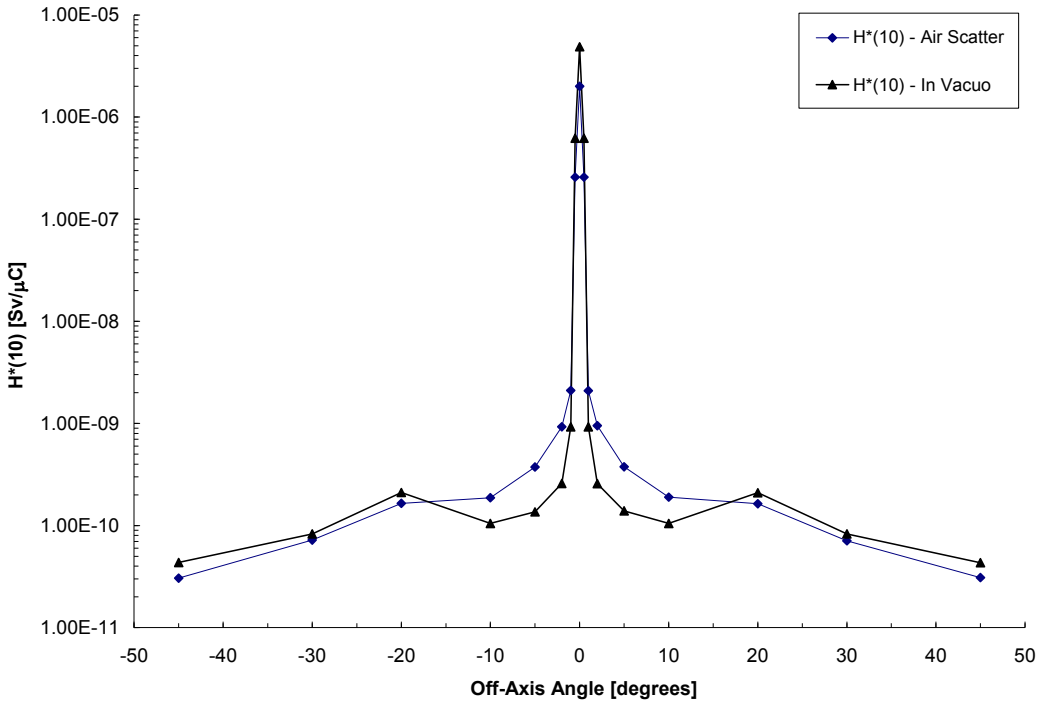

Figure N-13. Comparison of H*(10) in Air and in Vacuo for the System at 100 meters.

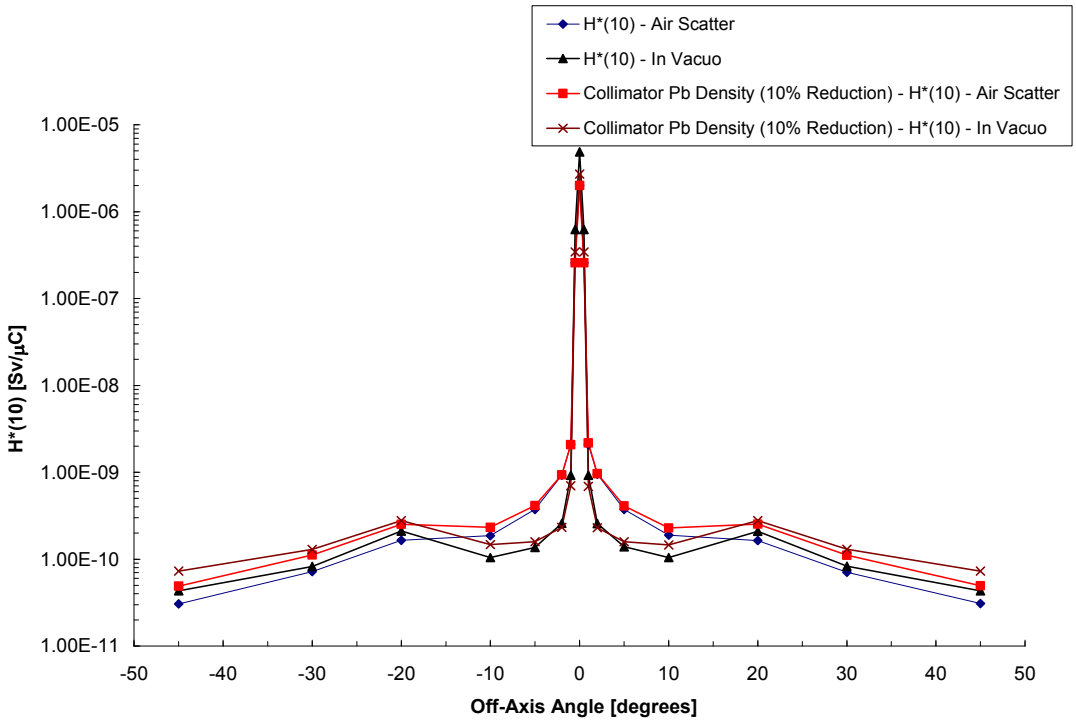

Figure N-14. Comparison of H*(10) in Air, in Vacuo, with a Pb Density Reduction of 10% in the Collimator (in Air), and with a Density Reduction of 10% in the Collimator (in Vacuo) at 100 meters.

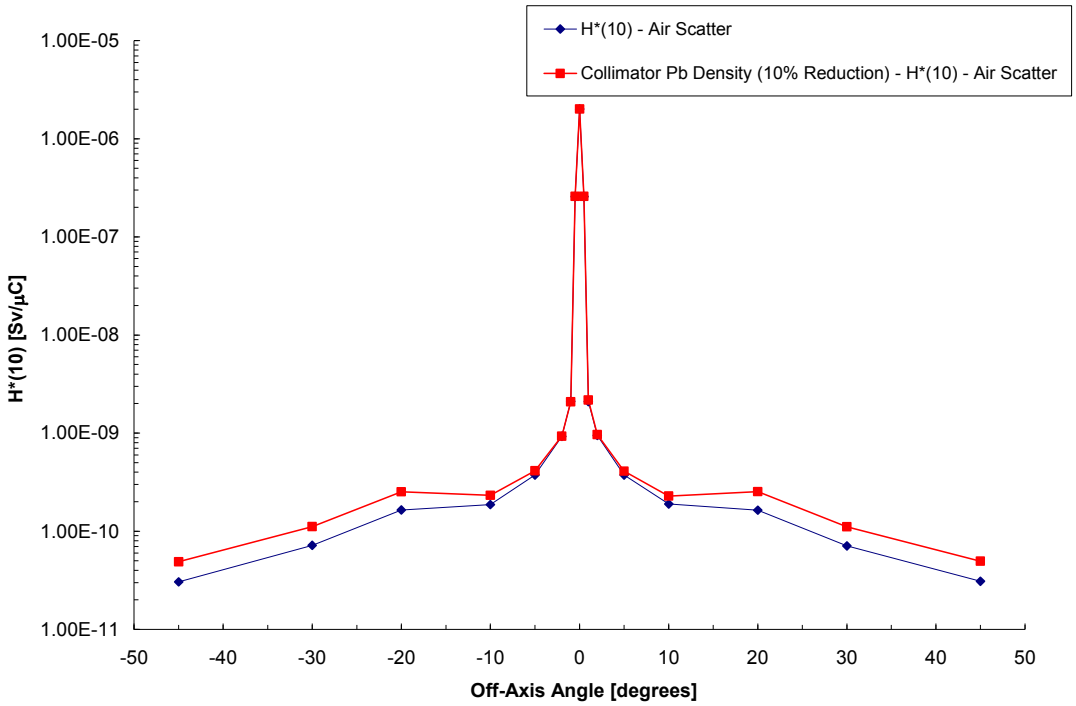

Figure N-15. Comparison of H*(10) for the System (in Air) and H*(10) with a Pb Density Reduction of 10% in the Collimator (in Air) at 100 meters.

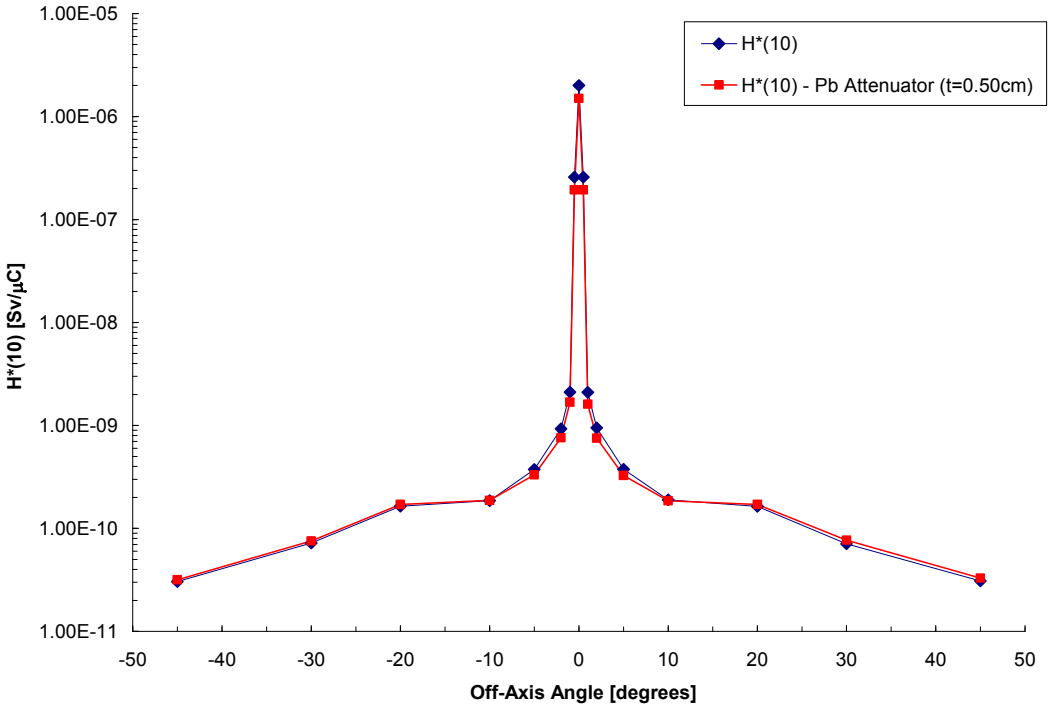

Figure N-16. Comparison of H*(10) for the System (in Air) and the System with a Pb Attenuator (t=0.50 cm) in the Beam Line (in Air) at 100 meters.

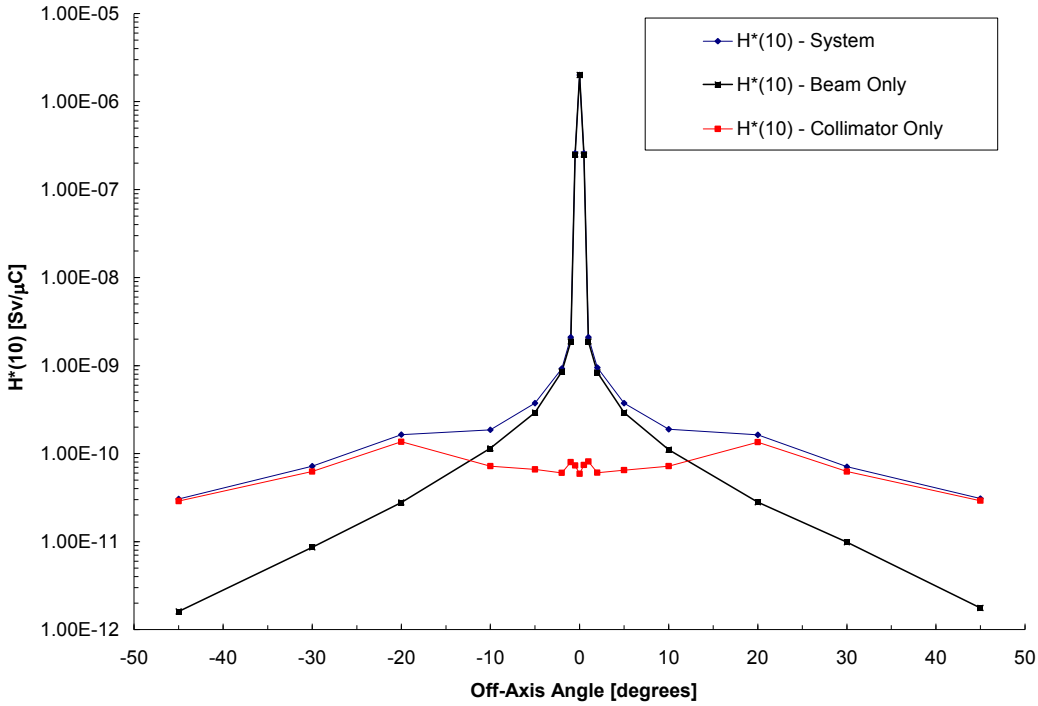

Figure N-17. Comparison of H*(10) for the System (in Air), the Beam Only Contribution, and the Collimator Only Contribution at 100 meters.

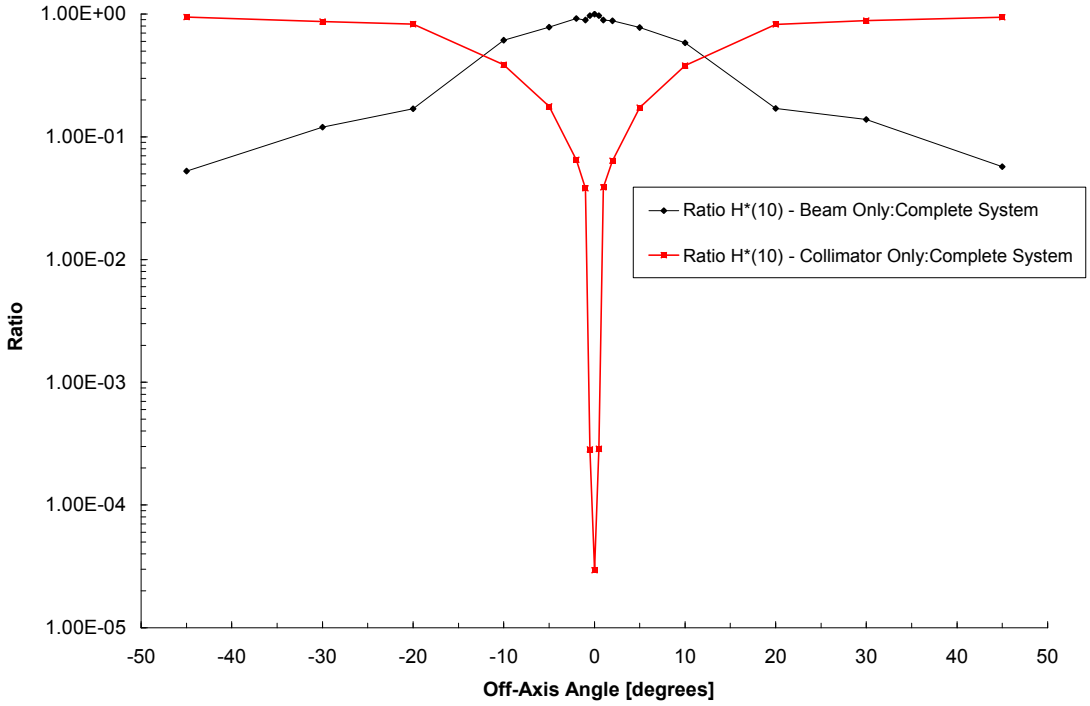

Figure N-18. Ratio of H*(10) for the Beam Only to the System (in Air) and the Collimator Only to the System (in Air) at 100 meters.

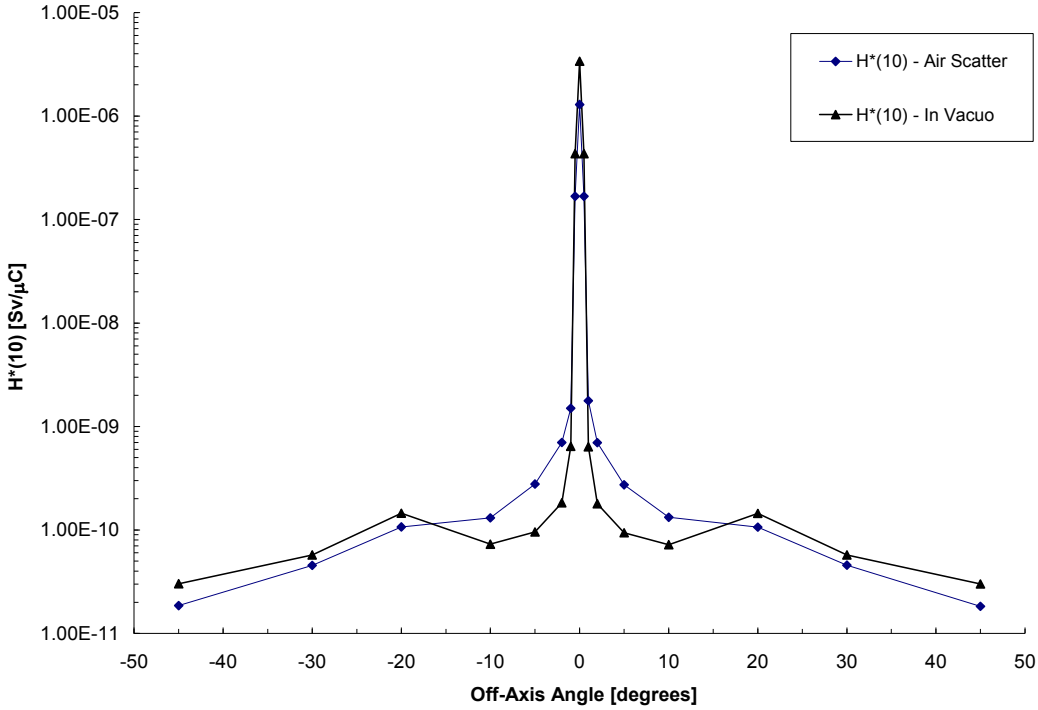

Figure N-19. Comparison of H*(10) in Air and in Vacuo for the System at 120 meters.

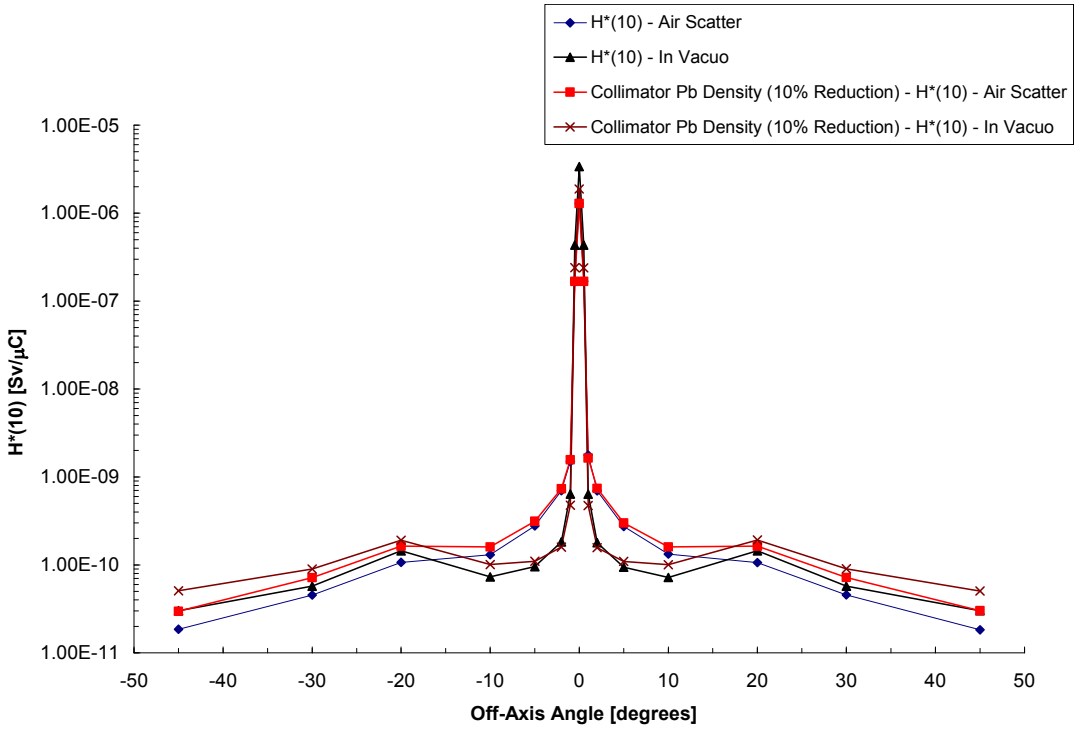

Figure N-20. Comparison of H*(10) in Air, in Vacuo, with a Pb Density Reduction of 10% in the Collimator (in Air), and with a Density Reduction of 10% in the Collimator (in Vacuo) at 120 meters.

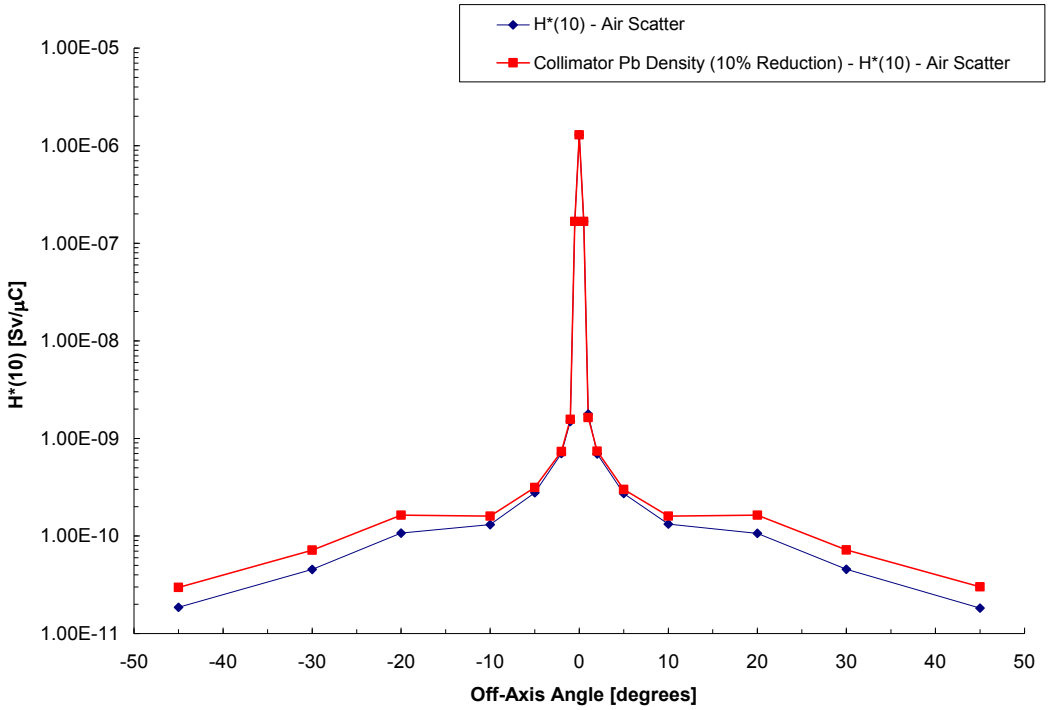

Figure N-21. Comparison of H*(10) for the System (in Air) and H*(10) with a Pb Density Reduction of 10% in the Collimator (in Air) at 120 meters.

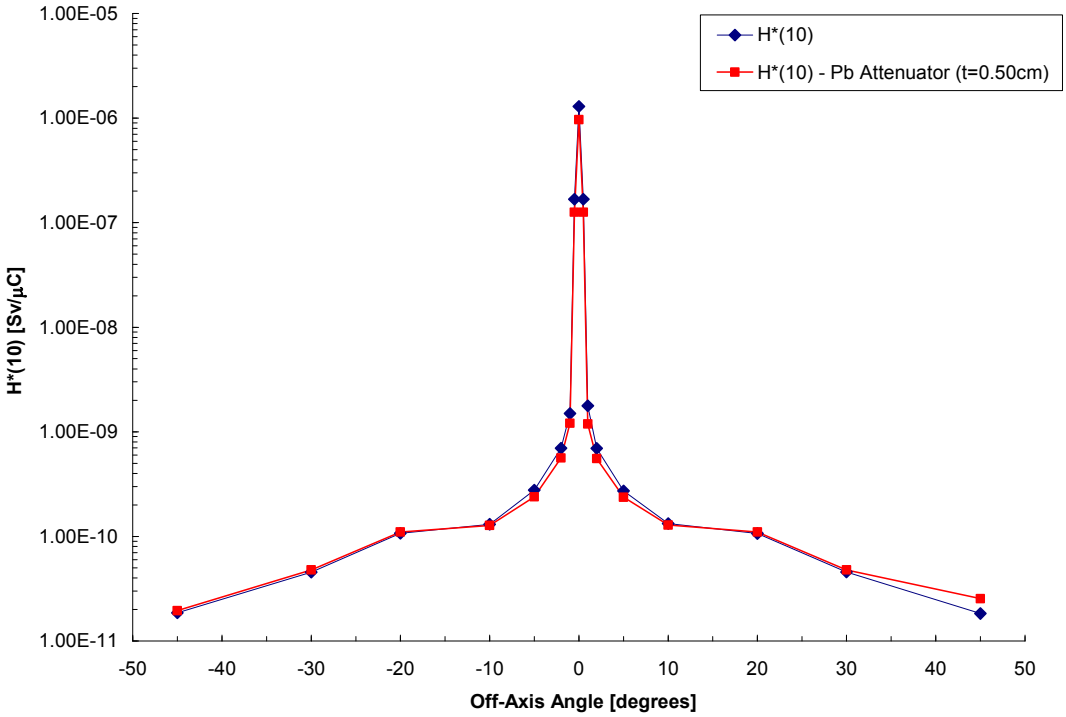

Figure N-22. Comparison of H*(10) for the System (in Air) and the System with a Pb Attenuator (t=0.50 cm) in the Beam Line (in Air) at 120 meters.

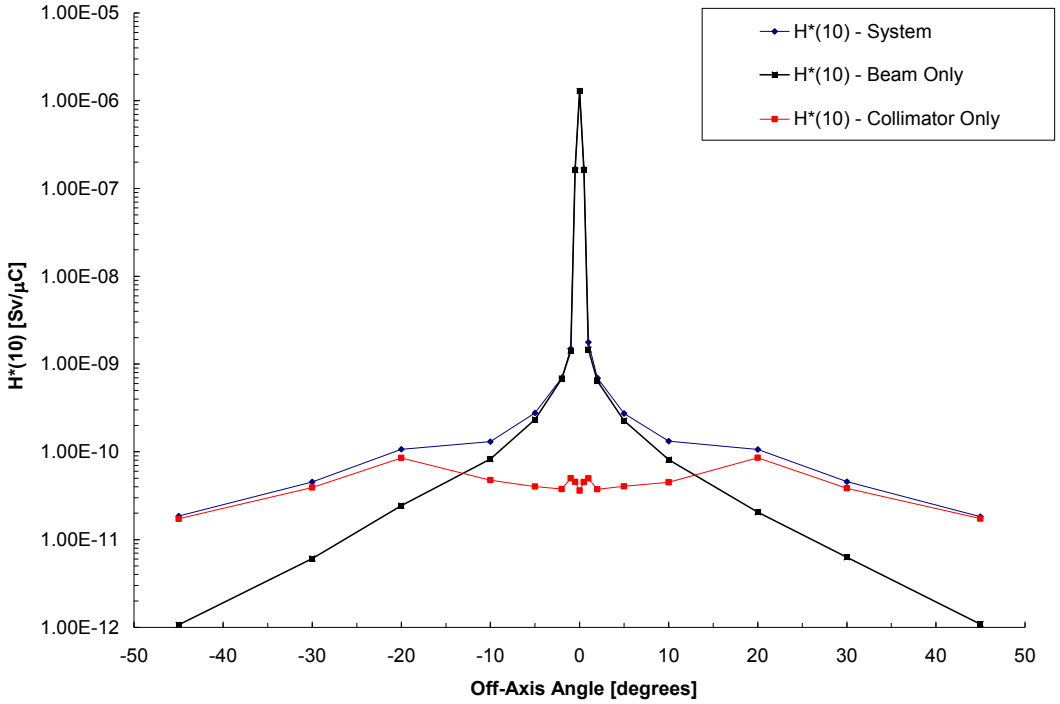

Figure N-23. Comparison of H*(10) for the System (in Air), the Beam Only Contribution, and the Collimator Only Contribution at 120 meters.

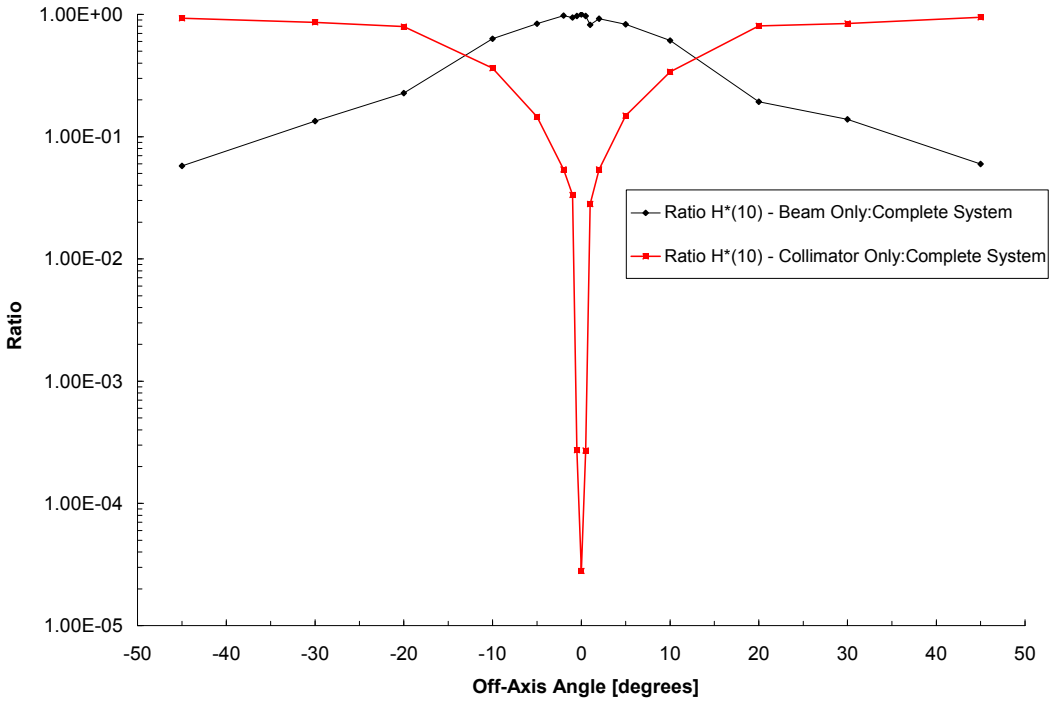

Figure N-24. Ratio of H*(10) for the Beam Only to the System (in Air) and the Collimator Only to the System (in Air) at 120 meters.

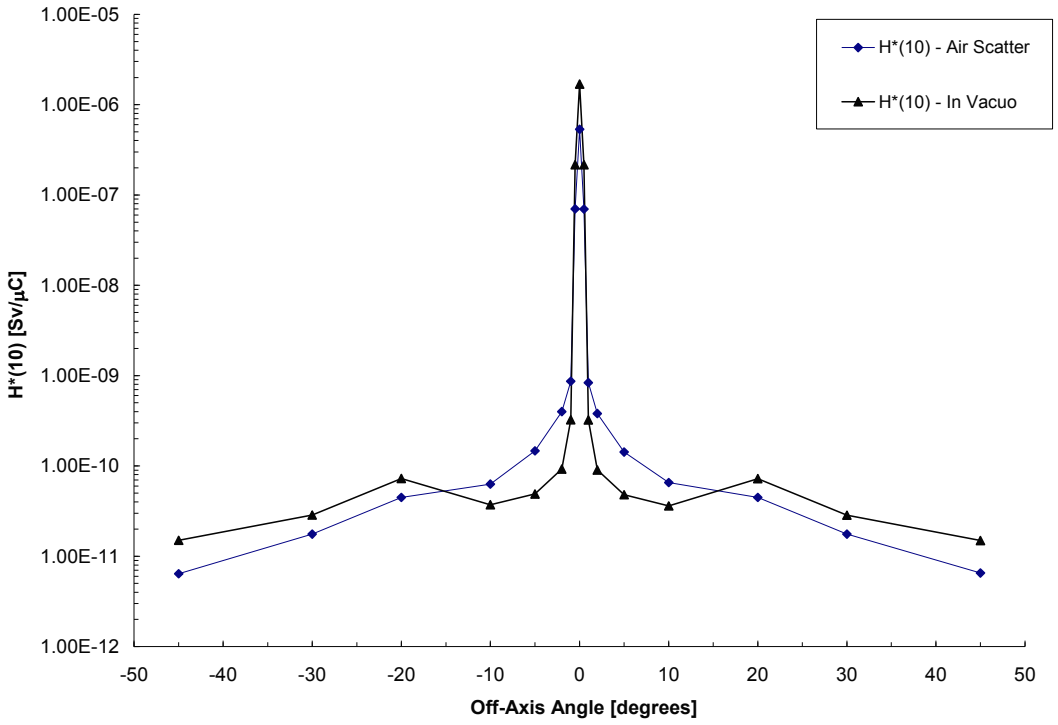

Figure N-25. Comparison of H*(10) in Air and in Vacuo for the System at 170 meters.

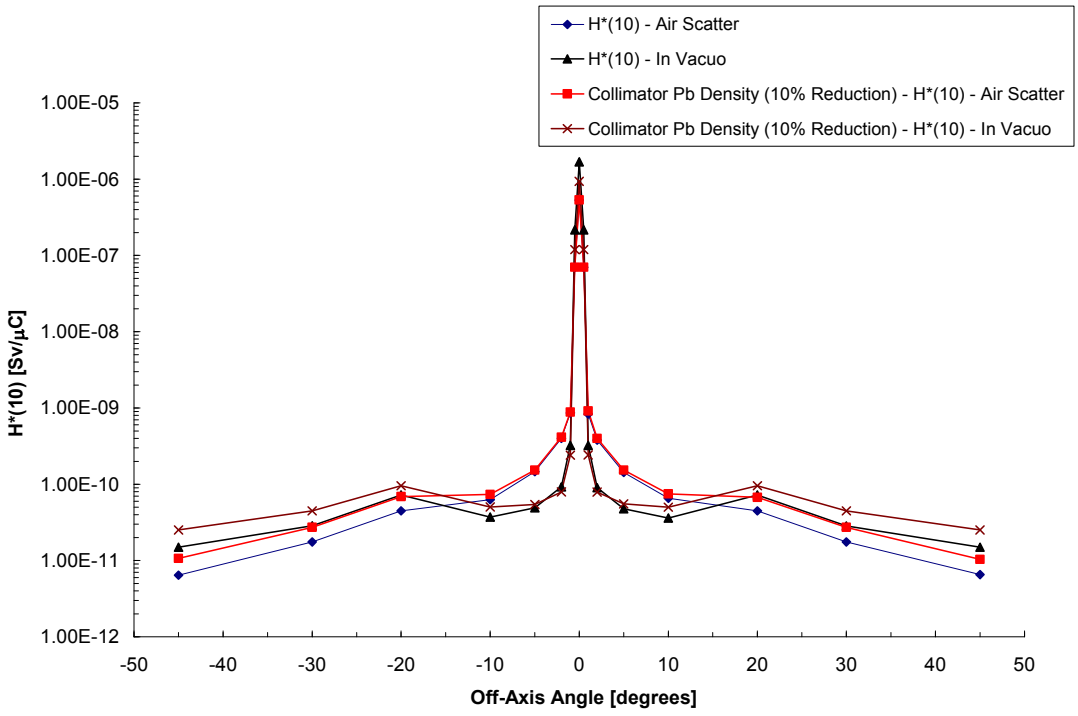

Figure N-26. Comparison of H*(10) in Air, in Vacuo, with a Pb Density Reduction of 10% in the Collimator (in Air), and with a Density Reduction of 10% in the Collimator (in Vacuo) at 170 meters.

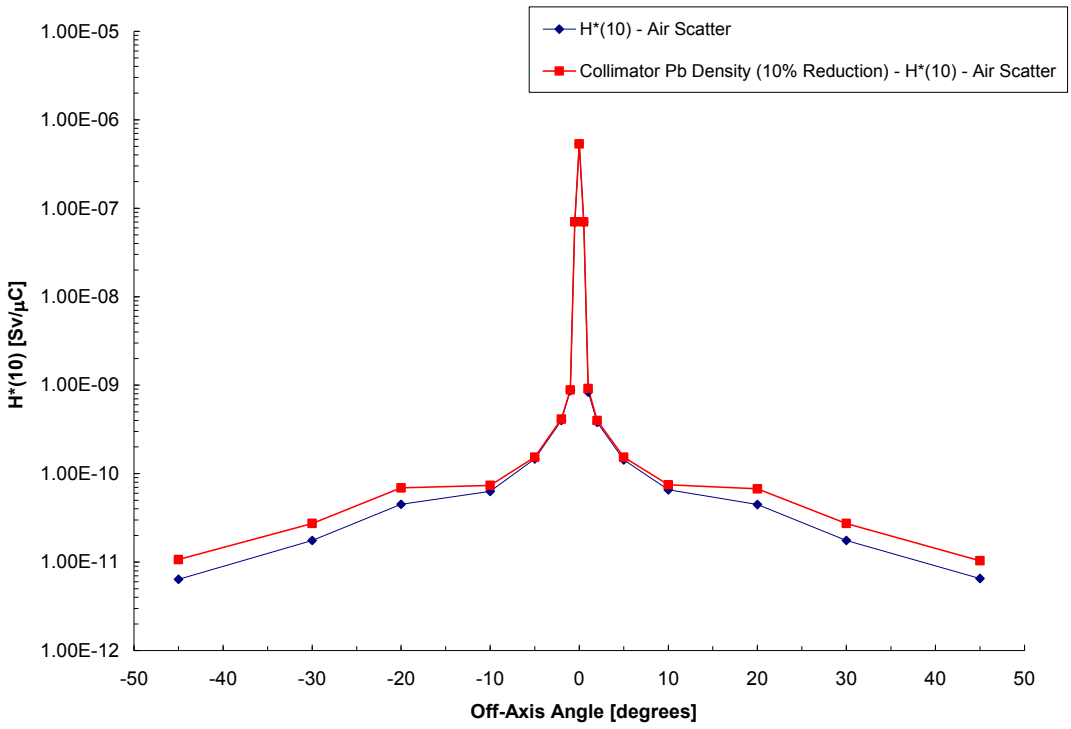

Figure N-27. Comparison of H*(10) for the System (in Air) and H*(10) with a Pb Density Reduction of 10% in the Collimator (in Air) at 170 meters.

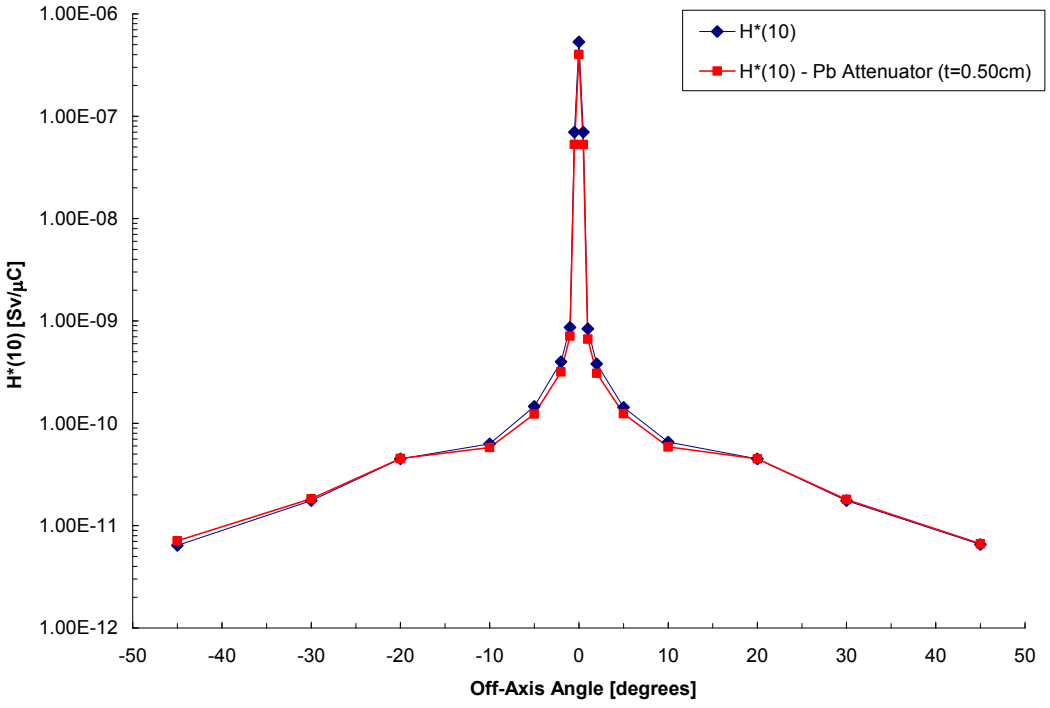

Figure N-28. Comparison of H*(10) for the System (in Air) and the System with a Pb Attenuator (t=0.50 cm) in the Beam Line (in Air) at 170 meters.

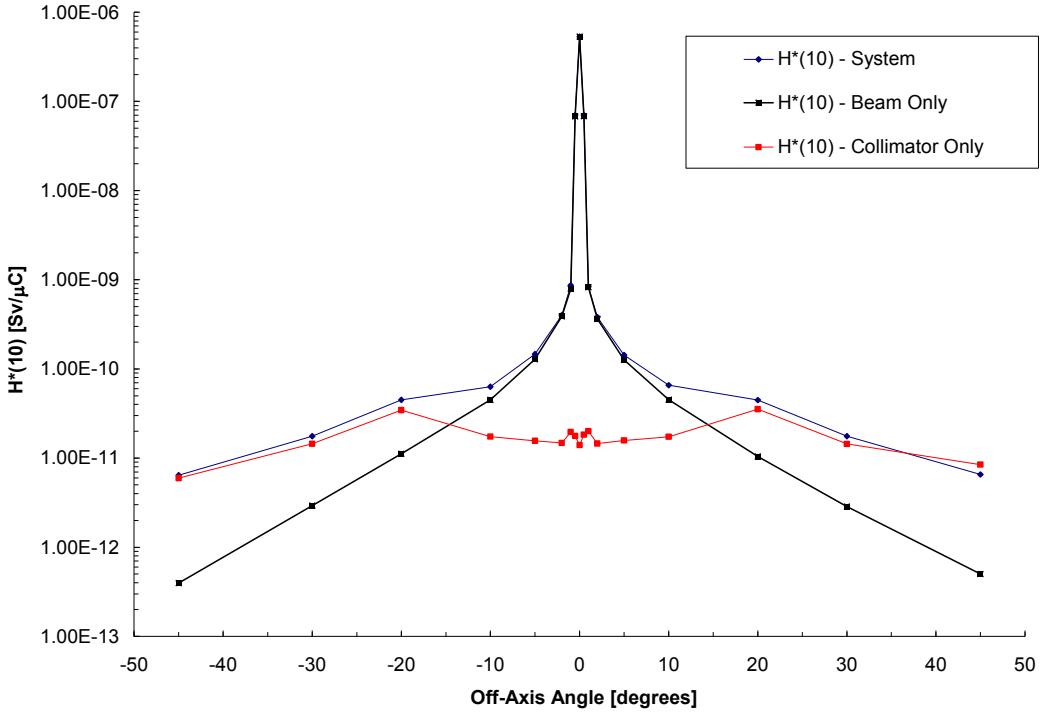

Figure N-29. Comparison of H*(10) for the System (in Air), the Beam Only Contribution, and the Collimator Only Contribution at 170 meters.

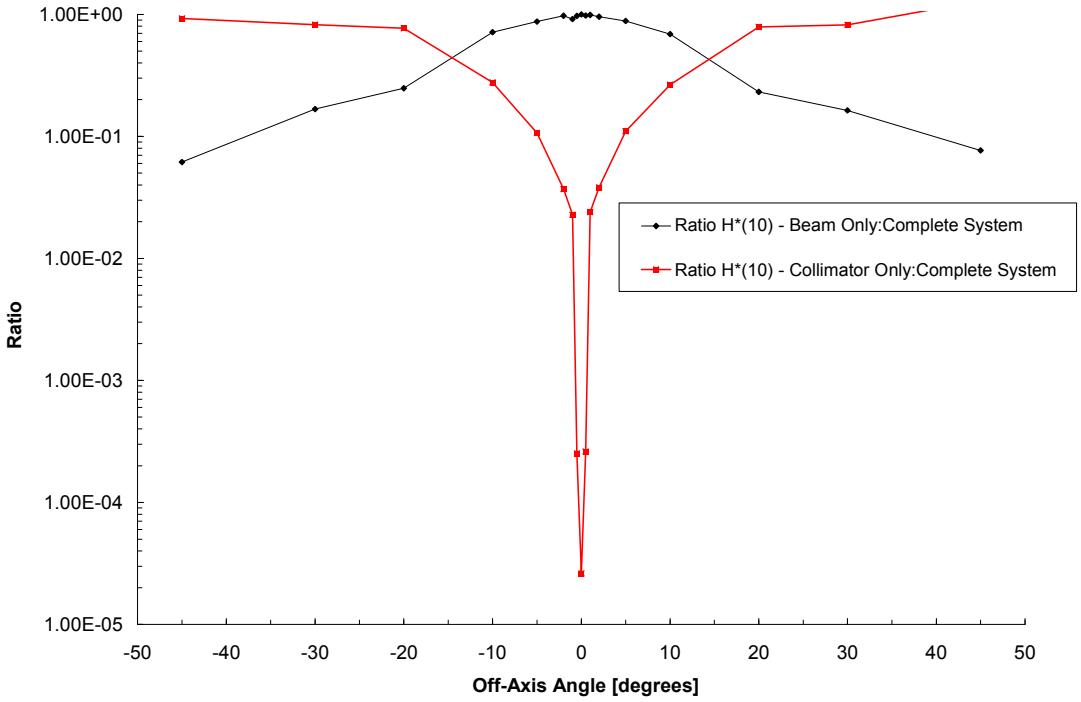

Figure N-30. Ratio of H*(10) for the Beam Only to the System (in Air) and the Collimator Only to the System (in Air) at 170 meters.

APPENIDIX O

DOWNFIELD TOTAL DOSE EQUIVALENT DATA FIT

In order to provide a predictive capability using the results reported in the present work, calculated downfield dose data (total ambient dose equivalent) were fit using a well-developed analytic formula [87] and least squares fitting methodology. The fit is only appropriate for predicting the dose equivalent at a known angle and required downfield distance. For example, the downfield dose equivalent at any distance (up to 200 meters) from the system, along a line extended from the system at a reported angle, can be predicted. The angles where a predicted dose equivalent can be ascertained are 0, 0.5, 1, 2, 5, 10, 20, 30, and 45 degrees (as measured from the beam centerline).

Dose equivalents at angles between those reported angles (i.e. 3 degrees, 15 degrees, etc.) were not fit during the present work and are considered to be undefined. However, all downfield distances along the defined angles up to 200 meters are defined. Since the dose equivalents reported during the present work were essentially symmetrical about the beam centerline, it is appropriate to use the fit at both positive (beam right) and negative (beam left) angles.

The downfield distance, x, and computed total dose equivalent, D, were fit to the following three-parameter empirical formula

$$D = e^{a} x^{b} e^{cx} \tag{O-1}$$

where D is the total dose equivalent, H*(d) in units of Sv/μC and x is the downfield distance in meters. The coefficients a, b, and c in equation (O-1) were determined using a least squares fitting approach and are shown in Table O-1 for each defined angle. A plot of the fit relative to the computed total dose equivalents is shown in Figure O-1. The data between 10 and 30 degrees look distorted, however, a closer examination of the total ambient dose equivalent profile (Section 5.6.4) shows a slight upward trend in the total dose equivalent in the 20 degree detector, especially at closer downfield distances (10 through 50 meters). This explains the bunching of data and crossing of the fit lines in Figure O-1 at these locations.

Table O-1. Fitting Coefficients for Each Defined Off-Axis Angle.

	Formula Coefficients		
Off-axis Angle [degrees]	a	b	c
0	-3.0802	-1.94154	-0.00433
0.5	-5.3423	-1.88767	-0.00429
1	-10.8905	-1.52766	-0.00436
2	-12.3662	-1.33436	-0.01185
5	-11.9232	-2.24713	0.00688
10	-13.6042	-1.87301	-0.00029
20	-12.8527	-2.02117	-0.00151
30	-13.7894	-1.93831	-0.00513
45	-14.2615	-1.98719	-0.00696

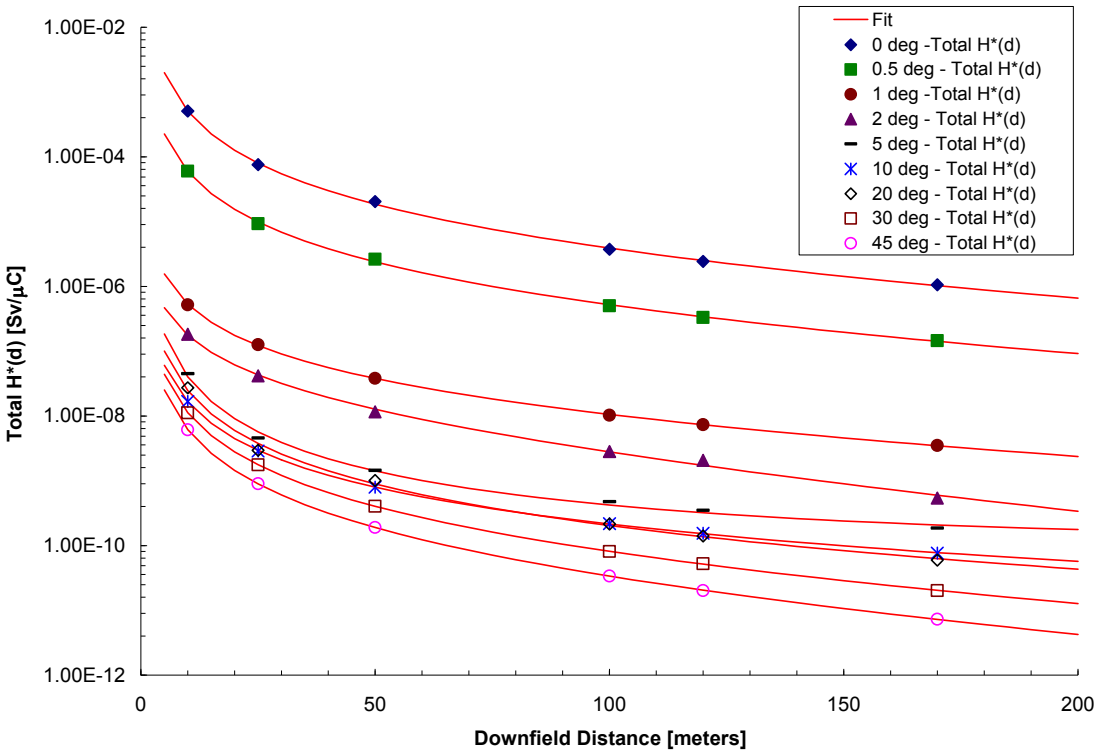

Figure O-1. Data Fit Corresponding to Computed Dose Equivalents.

The process for computing a predictive downfield total dose equivalent is to select an off-axis angle of interest. Use Table O-1 to find the fitting coefficients at the desired off-axis angle of interest and substitute the coefficients into equation (O-1) for a desired downfield distance. Once computed, the total dose equivalents, in units of Sv/μC, obtained from this method need to be normalized to average beam current (μA) and interrogation (run) time (s) as described in Section 4.4.

REFERENCES

[1] X-5 Monte Carlo Team. MCNP – A General Monte Carlo N-Particle Transport Code, Version 5. LA-UR-03-1987. Los Alamos National Laboratory, (2003).

[2] Chadwick, M.B., P. Oblozinsky, M. Herman, et al. ENDF/B-VI.8: Next Generation Evaluated Nuclear Data Library for Nuclear Science and Technology. Nucl Data Sheets, 107, 2931-3118 (2006).

[3] Halbleib, J. A., Kensek, R. P., Mehlhorn, T. A.,Valdez, G. D., Seltzer, S. M. and Berger, M. J. ITS Version 3.0: Integrated TIGER Series of Coupled Electron/Photon Monte Carlo Transport Codes. SAND91-1634 (1992).

[4] Levi, M.A., Rubenstein, D.M., Prepared Testimony before the U.S. Senate Subcommittee on Terrorism, Technology, and Homeland Security, Council on Foreign Relations, (2006).

[5] Rontgen, W.C. On a New Kind of Rays. Science. 3, 227-237 (1896).

[6] Attix, F.H., Introduction to Radiological Physics and Radiation Dosimetry. (New York: John Wiley & Sons, Inc.)(1986) ISBN 0-471-01146-0.

[7] Jones, D.T., ICRU at a Glance. International Commission on Radiation Units & Measurements, http://www.icru.org (Accessed June 2009).

[8] International Commission on Radiological Protection, International Commission on Radiological Protection: History, Policies, Procedures, Elsevier Science Ltd., Oxford (1998).

[9] National Council on Radiation Protection and Measurements (NCRP) Website. http://www.ncrp.org (Accessed June 2009).

[10] Harbs, R., Defense Threat Reduction Agency (DTRA): Combating the Radiological/Nuclear Threat, IEEE Nuclear Science Symposium, Honolulu, Hawaii (2007).

[11] Medalia, J., Detection of Nuclear Weapons and Materials: Science, Technologies and Observations, CRS Report for Congress, R40154, Congressional Research Service (2009).

[12] Idaho National Laboratory, Photonuclear Inspection and Threat Assessment System (PITAS) Overview, INL-08-GA50011-12 (2008).

[13] Jones, J. L., Active, Non-intrusive Inspection Technologies for Homeland Defense, INEEL/CON-03-00181, Idaho National Laboratory (2003).

[14] Jones, J.L., et al., Pulsed Photoneutron Interrogation: The GNT Demonstration System, INEEL/WINCO-1225 (1994).

[15] Jones, J.L., Detection of Pulsed, Bremsstrahlung Induced, Prompt Neutron Capture Gamma-rays with a HPGe Detector, SPIE, 867, p. 202, Crete, Greece (1996).

[16] Jones, J.L., et al., Proof-of-Concept Assessment of a Photofission-Based Interrogation System for the Detection of Shielded Nuclear Material, INEEL/EXT-2000-01523 (2000).

[17] Jones, J.L., et al., Photofission-Based, Nuclear Material Detection: Technology Demonstration, INEEL/EXT- 02-0106 (2002).

[18] Jones, J.L., Yoon, W.L., and Haskell, K.J., Remote Inspections of Cargo Containers for Nuclear Materials: An Initial Experimental and Numerical Assessment, INEEL/EXT-03-00363 (2002).

[19] International Commission on Radiation Units and Measurements. Fundamental Quantities and Units for Ionizing Radiation. ICRU Report 60, (1998).

[20] International Commission on Radiological Protection. Conversion Coefficients for use in Radiological Protection Against External Radiation. ICRP Publication 74 (1997).

[21] International Commission on Radiation Units and Measurements. Conversion Coefficients for Use in Radiological Protection Against External Radiation. ICRU Report 57, (1998).

[22] International Commission on Radiological Protection. The 2007 Recommendations of the International Commission on Radiological Protection. ICRP Publication 103 (2007).

[23] Sutton, M. R., High Energy Neutron Dosimetry. Ph.D. Thesis. Georgia Institute of Technology, Atlanta, GA (2001).

[24] International Commission on Radiation Units and Measurements. Determine of Dose Equivalents Resulting from External Radiation Sources. ICRU Report 39 (1985).

[25] International Commission on Radiation Units and Measurements. Determination of Dose Equivalents from External Radiation Sources – Part 2. ICRU Report 43 (1988).

[26] International Commission on Radiation Units and Measurements. Measurement. Of Dose Equivalents from External Photon and Electron Radiations. ICRU Report 47 (1992).

[27] International Commission on Radiation Units and Measurements. Quantities and Units in Radiat Prot Dosim. ICRU Report 51 (1993).

[28] McDonald, J., Determination of Personal Dose Equivalent in Accelerator Radiation Fields, Pacific Northwest National Laboratory (2008).

[29] MCNP5/MCNPX: Monte Carlo N–Particle Transport Code System Including MCNP5 1.51 and MCNPX 2.6.0 and Data Libraries Abstract. RSICC Code Package CCC-740, http://www-rsicc.ornl.gov (accessed June 2009).

[30] Ferrari, A., Pelliccioni, M. On the Conversion Coefficients from Fluence to Ambient Dose Equivalent. Radiat Prot Dosim. 51, 251-255 (1994).

[31] Ferrari, A., Pelliccioni, M. Fluence-to-Dose Equivalent Conversion Coefficients for Electrons and Photons of Energy up to 10 GeV. Proceedings of the 8th International Conference on Radiation Shielding, Arlington, 2, 893 (1994).

[32] Kim, J.O., Kim, J.K. Dose Equivalent Per Unit Fluence near the Surface of the ICRU Phantom by Including the Secondary Electron Transport for Photons. Radiat Prot Dosim. 83, 211-220 (1999).

[33] Pelliccioni, M. Overview of Fluence-to-Effective Dose and Fluence-to-Ambient Dose Equivalent Conversion Coefficients for High Energy Radiation Calculated Using the Fluka Code. Radiat Prot Dosim. 88, 279-297 (2000).

[34] International Commission on Radiation Units and Measurements. Conceptual Basis for the Determination of Dose Equivalent. ICRU Report 25 (1976).

[35] Dimbylow, P., Francis, T. The Effect of Photon Scatter and Consequent Electron Build-up in Air on the Calculation of Dose Equivalent Quantities in the ICRU Sphere for Photon Energies from 0.662 to 10 MeV. Phys. Med. Biol. 28, 817-828 (1983).

[36] Takasuye, E. Photon Dose Equivalents in Phantoms. MS Thesis. University of Texas at Austin, Austin, TX (1991).

[37] International Commission on Radiological Protection. Data for Use in Protection Against External Radiation. ICRP Publication 51 (1987).

[38] Ferrari, A., Pelliccioni, M. Dose Equivalents for Monoenergetic Electrons Incident on the ICRU Sphere, Radiat Prot Dosim. 55, 207 (1994).

[39] Rogers, D. W., Fluence to Dose Equivalent Conversion Factors Calculated with EGS3 for Electrons from 100 keV to 20 GeV and Photons from 11 keV to 20 GeV. Health Phys. 45, 891–914 (1984).

[40] Greene, D., Williams, P. Linear Accelerators for Radiation Therapy. (New York: Taylor & Francis Group, LLC) (1997) ISBN 0-7503-0476-6.

[41] Brown, K., Tautfest, G. Faraday-Cup Monitors for High-Energy Electron Beams. Rev Sci Instrum. 27, 696-702 (1956).

[42] International Commission on Radiation Units and Measurements. The Dosimetry of Pulsed Radiation. ICRU Report 34 (1982).

[43] Boag, J. Ionization Chambers (Chapter 3) from The Dosimetry of Ionizing Radiation Volume II. Edited by Kase, K., Bjarngard, B., Attix, F. (New York: Academic Press, Inc.) (1987) ISBN 978-0124004030.

[44] AAPM TG-51 Protocol for Clinical Reference Dosimetry of High-Energy Photon and Electron Beams. Med Phys. 26, 1847-1870 (1999).

[45] Dyk, J., MacDonald, J. Penetration of High Energy Electrons in Water. Phys. Med. Biol. 17, 52-65 (1972).

[46] Klevenhagen, S., Physics and Dosimetry of Therapy Electron Beams (Madison, WI: Medical Physics Publishing)(1993) ISBN 978-0944838358.

[47] Aget, H., Rosenwald, J. Polarity Effects for Various Ionization Chambers with Multiple Irradiation Conditions in Electron Beams. Med Phys. 18, 67-72 (1991).

[48] Rogers, D., Ross, C. The Role of Humidity and Other Correction Factors in the AAPM TG-21 Dosimetry Protocol. Med Phys. 15, 40-48 (1988).

[49] Far West Model IC-18 Operation Manual. Far West Technologies, Goleta, CA (2001).

[50] RADCAL Model RC1800 Reference Class Ion Chamber Fact Sheet. RADCAL Corporation, Monrovia, CA (2007).

[51] Krueger, F., Larson, J. Chipmunk IV: Development of and Experience with a New Generation of Radiation Area Monitors for Accelerator Applications. Nucl Instrum Meth A. 495, 20-28 (2002).

[52] Far West Technologies Website. http://www.fwt.com (Accessed June 2009).

[53] Keithley Model 6517B Electrometer User's Manual. 6517B-900-01 Rev A. Keithley Instruments, Inc. (2008).

[54] iServer MicroServer User's Guide. Omega Engineering, Stamford, CT (2008).

[55] National Instruments Website. http://www.ni.com/labview/ (Accessed June 2009).

[56] Turner, J. Atoms, Radiation and Radiation Protection, Second Edition (New York: John Wiley & Sons) (1995) ISBN 0-471-59581-0.

[57] Horowitz, Y. Thermoluminescence and Thermoluminescent Dosimetry (3 Volumes) (Orlando, FL: CRC Press)(1984).

[58] Thermo Scientific. Materials and Assemblies for Thermoluminescent Dosimetry. Product Overview. Franklin, MA (2008).

[59] US Patent #5,354,997: Miller SD. Method for increased sensitivity of radiation detection and measurement. October 11, 1994.

[60] US Patent #5,569,927: Miller SD. Composite material dosimeters. October 29, 1996.

[61] US Patent #5,731,590: Miller SD. Metal oxide composite dosimeter method and material. March 24, 1998.

[62] Landauer, Inc. OSL Website //http:www.osldosimetry.com (Accessed June 2009).

[63] Yukihara, E., McKeever, S. Optically Stimulated Luminescence (OSL) Dosimetry in Medicine. Phys. Med. Biol. 53, R351-R379 (2008).

[64] Bramblett, R., Ewing, R., Bonner, T. A New Type of Neutron Spectrometer. Nucl Instrum Meth. 9, 1-12 (1960).

[65] Sweezy, J. A Multisphere Neutron Spectrometer Measurement of the Georgia Tech Research Reactor Bio-Medical Facility. M.S. Thesis. Georgia Institute of Technology, Atlanta, GA (1996).

[66] Virtual Water Phantom Materials Fact Sheet. CNMC Company, Nashville, TN (2008).

[67] Hertel, N., Davidson, W. The Response f Bonner Spheres to Neutrons from Thermal Energies to 17.3 MeV. Nucl Instrum Methods. A238, 509-516 (1985).

[68] Miller, S. AFITBUNKI: A modified Iterative Code to Unfold Neutron Spectra from Bonner Sphere Detector Data. M.S. Thesis. Air Force Institute of Technology, Air University (1993).

[69] Howell, R., Ferenci, M., Hertel, N., Fullerton, G. Investigation of Secondary Neutron Dose for 18 MV Dynamic MLC IMRT Delivery. Med Phys. 32, 786-793 (2005).

[70] Hales, B. TLD Analysis Undergraduate Research Project. NE4699, Georgia Institute of Technology, Atlanta, GA (2009).

[71] National Institute of Standards and Technology (NIST) PSTAR Database. http://physics.nist.gov/cgi-bin/Star/. (Accessed June 2009).

[72] Woo Yoon, Idaho National Laboratory, private communication, February 2009.

[73] National Institute of Standards and Technology (NIST) ESTAR Database. http://physics.nist.gov/cgi-bin/Star/. (Accessed June 2009).

[74] Steve Seltzer, National Institute of Standards and Technology, private communication, April 2009.

[75] Attix, F. Energy Imparted, Energy Transferred and Net Energy Transferred. Phys Med Biol. 28, 1388 (1983).

[76] American National Standards Institute/Health Physics Society. American National Standard for Dosimetry – Personnel Dosimetry Performance Criteria for Testing. ANSI/HPS N13.11-2009. DRAFT (2009).

[77] International Commission on Radiological Protection. 1990 Recommendations of the International Commission on Radiological Protection. ICRP Publication 60 (1990).

[79] Sutton-Ferenci, M., Hertel, N., Sweezy, J. An Evaluated Set of Neutron, Proton and Photon Fluence-to-Effective-Dose Conversion Coefficients. DDN#: PPO-P00-G-DDN-X-00008. Los Alamos National Laboratory (2001).

[80] Sato, O., Iwai, S., Tanaka, S., Uehara, T., Sakamoto, Y., Yoshizawa, N., Furihata, S. Calculations of Equivalent Dose and Effective Dose Conversion Coefficients for Photons from 1 MeV to 10 GeV. Radiat Prot Dosim. 62, 119 (1995).

[81] Ferrari, A., Pelliccioni, M., Pillon, M. Fluence to Effective Dose and Effective Dose Equivalent Conversion Coefficients for Photons from 50 keV to 10 GeV. Radiat Prot Dosim. 67, 245 (1996).

[82] Ferrari, A., Pelliccioni, M., Pillon, M. Fluence to Effective Dose Conversion Coefficients for Neutrons up to 10 TeV. Radiat Prot Dosim. 71,165 (1997).

[83] Burlin, T., Chan, F. The Influence of Interfaces on Dosimeter Response. Proceedings of the Symposium on Microdosimtery. Edited by H. Ebert. Ispra, Italy, November 1967.

[84] Iglewicz, B., Hoaglin, D. How to Detect and Handle Outliers. (ASI Quality Press) (1993) ISBN 978-0873892476.

[85] Taylor, J. An Introduction to Error Analysis – The Study of Uncertainties in Physical Measurements. Second Edition. (Sausilito, CA: University Science Books) (1997) ISBN 0-935702-75-X.

[86] Rogers, D. The EGSnrc Code System: Monte Carlo Simulation of Electron and Photon Transport. NRCC Report PIRS-701, National Research Council of Canada Ottawa (2006).

[87] Lampley, C.M., Andrews, M.C., Wells, M.B. The Skyshine III Procedure: Calculation of the Effects if Structure Design on Neutron, Primary Gamma-Ray and Secondary Gamma-Ray Dose Rates in Air. (RSIC Code Collection CCC-289) Report RRA T8209A Radiation Research Associates, Fort Worth, TX (1988).